Transactions of the ASME®

Journal of Fluids Engineering

Published Bimonthly by The American Society of Mechanical Engineers

VOLUME 125 • NUMBER 2 • MARCH 2003

Transactions of the ASME, Journal of Fluids Engineering (ISSN 0098-2202) is published bimonthly (Jan., Mar., May, July, Sept., Nov.) by The American Society of Mechanical Engineers, Three Park Avenue, New York, NY 10016. Periodicals postage paid at New York, NY and additional mailing offices.
POSTMASTER: Send address changes to Transactions of the ASME, Journal of Fluids Engineering, c/o THE AMERICAN SOCIETY OF MECHANICAL ENGINEERS, 22 Law Drive, Box 2300, Fairfield, NJ 07007-2300.
CHANGES OF ADDRESS must be received at Society headquarters seven weeks before they are to be effective. Please send old label and new address.
STATEMENT from By-Laws. The Society shall not be responsible for statements or opinions advanced in papers or ... printed in its publications (B7.1, Par. 3).

INDEXED by Applied Mechanics Reviews and Engineering Information, Inc. Canadian Goods & Services Tax Registration #126148048.

TECHNICAL PAPERS

(Contents continued on inside back cover)

This journal is printed on acid-free paper, which exceeds the ANSI Z39.48-1992 specification for permanence of paper and library materials. ♾™
♻ 85% recycled content, including 10% post-consumer fibers.

Journal of Fluids Engineering Volume 125, Number 2 MARCH 2003

TECHNICAL BRIEFS

ANNOUNCEMENTS AND SPECIAL NOTICES

The ASME Journal of Fluids Engineering is abstracted and indexed in the following:

Applied Science & Technology Index, AMR Abstracts Database, Chemical Abstracts, Chemical Engineering and Biotechnology Abstracts (Electronic equivalent of Process and Chemical Engineering), Civil Engineering Abstracts, Computer & Information Systems Abstracts, Corrosion Abstracts, Current Contents, Ei EncompassLit, Electronics & Communications Abstracts, Engineered Materials Abstracts, Engineering Index, Environmental Engineering Abstracts, Environmental Science and Pollution Management, Excerpta Medica, Fluidex, Index to Scientific Reviews, INSPEC, International Building Services Abstracts, Mechanical & Transportation Engineering Abstracts, Mechanical Engineering Abstracts, METADEX (The electronic equivalent of Metals Abstracts and Alloys Index), Petroleum Abstracts, Process and Chemical Engineering, Referativnyi Zhurnal, Science Citation Index, SciSearch (The electronic equivalent of Science Citation Index), Shock and Vibration Digest, Solid State and Superconductivity Abstracts, Theoretical Chemical Engineering

Hydrodynamic Force and Heat/Mass Transfer From Particles, Bubbles, and Drops—The Freeman Scholar Lecture

Efstathios E. Michaelides
School of Engineering and Center for Bioenvironmental Research, Tulane University, New Orleans, LA 70118

Recent advances on the analytical form of the hydrodynamic force and heat/mass transfer from a particle, bubble, or drop are examined critically. Also some of the recent computational studies, which help strengthen or clarify our knowledge of the complex velocity and temperature fields associated with the momentum and heat/mass transfer processes are also mentioned in a succinct way. Whenever possible, the processes of energy/mass exchange and of momentum exchange from spheres and spheroids are examined simultaneously and any common results and possible analogies between these processes are pointed out. This approach results in a better comprehension of the transport processes, which are very similar in nature, as well as in the better understanding of the theoretical expressions that are currently used to model these processes. Of the various terms that appear in the transient equations, emphasis is given to the history terms, which are lesser known and more difficult to calculate. The origin, form, and method of computation of the history terms are pointed out as well as the effects of various parameters on them. Among the other topics examined here are the differences in the governing and derived equations resulting by finite Reynolds and Peclet numbers; the origin, theoretical validity and accuracy of the semi-empirical expressions; the effects of finite internal viscosity and conductivity of the sphere; the effects of small departures from the spherical shape; the effects of the finite concentration; and the transverse, or lift, components of the force on the sphere. [DOI: 10.1115/1.1537258]

1 Introduction

Because the sphere is the simplest three-dimensional shape, heat transfer and fluid dynamics problems pertaining to a sphere have been the subject of the first application of most theoretical methods on the solution of the governing equations, as well as of intellectual curiosity among the scientists. These problems belong to the class of the most fundamental subjects in fluid dynamics and heat/mass transfer that have attracted the attention of many mathematicians, physicists, and engineers. They are also subjects that have numerous practical applications including combustion and propulsion processes, chemical reactions and catalysis processes, mixing and separation processes, boiling and condensation processes, environmental sedimentation and resuspension processes, and biological flow processes. The transport of momentum, heat, and mass is of primary interest in all of these processes. For this reason, calculations are frequently made using the transport coefficients drag coefficient, heat transfer coefficient, or mass transfer coefficient, which emanate from the theory or from experiments pertaining to a sphere.

It is worth mentioning that the subject of transient flow and heat/mass transfer from spheres also finds applications in several cases where the shape of the particles, bubbles or drops is not spherical. For example, one often encounters in boiling processes elongated bubbles or in high Reynolds number flows spheroidal drops. Irregular particles of any shape are common in processes such as coal combustion, chemical catalysis, flocculation and natural sedimentation, and resuspension. In these cases, it is common practice to treat the irregular particles in terms of an ''equivalent diameter'' and apply, as a first approximation, the theory and results that have been derived for spheres. Hence, the transport coefficients of the irregularly shaped particles are given as a first approximation by the transport coefficients of an ''equivalent sphere.'' When more information is available about the shapes of the particles involved in a particular process, a common engineering practice is to apply a theoretical correction, or an empirical correlation to the transport coefficients of the equivalent sphere, which accounts for the departure from spherical shape.

The intent for this review is to be a concise presentation and a critical evaluation of the known analytical expressions, the methods used for the analysis and the results derived for the transient and steady-state momentum, heat, and mass transfer processes from a sphere. Since the subject was first developed almost 200 years ago, a short historical background on the analytical results pertaining to the transport processes is given at first. Secondly, the governing equations for the momentum and heat/mass transfer are presented and compared. Subsequently, the main analytical solutions are presented for the transient hydrodynamic force on a sphere and the transient rate of heat/mass transfer from a sphere at creeping flow conditions. Similar expressions are presented at small but finite values of the Reynolds and Peclet numbers, while emphasis is placed on the form of the resulting equations and the magnitude of the history terms in these equations. For the transient hydrodynamic force, the semi-empirical expressions that extend to high Reynolds numbers are presented and critically examined. A short exposition of the analytical work that has been done in the case of spheroids is also given at creeping flow conditions, with particular reference to an additional history term that appears as a result of the elongated shape of the spheroids. In all cases, the steady-state transport coefficients are presented with useful correlations that can be used in engineering practice or as closure equa-

Contributed by the Fluids Engineering Division for publication in the JOURNAL OF FLUIDS ENGINEERING. Manuscript received by the Fluids Engineering Division Aug. 9, 2002; revised manuscript received Sept. 7, 2002. Editor: J. Katz.

tions in computational studies. The theories and results on the lift induced from the rotation or shear are also examined briefly. Analytical results and certain differences on the transport coefficients resulting from the finite viscosity or the finite conductivity of the sphere are pointed out. Finally, several examples of recent numerical studies are presented that elucidate the theoretical methods and help understand better some of the more complex phenomena associated with the finite concentration of spheres in a flow.

2 Historical Background and Recent Results

2.1 Equation of Motion. The attention to the hydrodynamic force acting on a sphere inside an inviscid fluid first started with the work of Poisson [1] almost 20 years before the publication of what we now call ''the Navier-Stokes equations.'' Poisson solved the potential flow equations around a sphere and determined that the transient force exerted by an inviscid fluid on a spherical object is equal to $1/2 m_f d/dt(V_i - u_i)$, where m_f is the mass of the fluid that has the same volume as the sphere and the term in parenthesis is equal to the uniform velocity of the sphere with respect to the fluid. Therefore, Poisson correctly deduced that the coefficient of what we now call the ''added mass force'' is equal to 1/2. Shortly thereafter, Green [2] extended this result to the flow around an ellipsoid, again in an inviscid fluid and discovered the analogous result that the added mass coefficient of an ellipsoid is also equal to 1/2.

Stokes [3,4] was the first to analyze the motion of a sphere in a viscous fluid. As the first application of the ''Navier-Stokes equations,'' he obtained a solution for the steady-state flow around a sphere moving in an otherwise stagnant viscous fluid and determined that it is equal to: $F = 6\pi\alpha\mu_f V$. The dimensionless drag coefficient which results from this expression is now called ''the Stokes drag coefficient'' and is equal to $c_D = 24/\mathrm{Re}_s$, where Re_s is what we now call the ''Reynolds number'' of the sphere, based on the diameter, 2α, and the relative velocity of the sphere, V.

In a little-known paper to the Academy of Paris, Boussinesq [5] was the first to publish an analytical expression for the transient hydrodynamic force exerted by a viscous fluid on a solid sphere. Based on a mathematical method outlined in his book on the methods of calculation of the rate of heat transfer, Boussinesq [6] presented a succinct method for the solution of the transient equation of the viscous fluid motion around a solid sphere at creeping flow conditions where $\mathrm{Re}_s \to 0$ and derived an analytical expression for the transient hydrodynamic force, which is composed of three terms: the steady-state term, the added mass or virtual mass term and the history term. Three years later, Basset [7,8], apparently unaware of the work of Boussinesq, presented a similar method and derived an identical expression for the transient hydrodynamic force on a solid sphere. While both Boussinesq and Basset derived their expressions for a sphere moving in a stagnant fluid, it is rather trivial to extend their theory to a sphere moving in a fluid of uniform velocity u_i. In this case, the transient hydrodynamic force, $F_i(t)$, may be written as follows:

$$F_i(t) = -6\pi\alpha\mu_f(V_i - u_i) - \frac{1}{2} m_f \frac{d}{dt}(V_i - u_i) - 6\alpha^2\sqrt{\pi\mu_f\rho_f}\int_0^t \frac{\frac{d}{d\tau}(V_i - u_i)}{\sqrt{t-\tau}}\, d\tau. \quad (1)$$

The first term of the above expression is the steady-state term exerted by the viscous fluid and is identical to the Stokes drag. The second term is due to the transient motion of a part of the surrounding fluid. Although the total volume of the fluid that is influenced by the acceleration of the sphere may be considerably higher, the net effect of the fluid acceleration to the transient force exerted on the sphere is equivalent to the simultaneous acceleration of a volume of fluid equal to half the volume of the sphere. This term is often called the added mass or the virtual mass force and is the same as the one originally derived by Poisson [1]. The third term in the equation is due to the diffusion of the vorticity around the sphere and decays as $t^{-1/2}$, which is typical of diffusion processes. It is called the history term/force or sometimes the Basset term or the Basset force. This name is rather ironic when one bears in mind that Boussinesq's work has precedence.

The analyses by Boussinesq and Basset are based on an assumption that neglects the inertia terms in the Navier-Stokes equations. For this reason, Eq. (1) strictly applies to the case of a sphere moving very slowly in the viscous fluid, or creeping flow, a condition which is satisfied only when the Reynolds number of the sphere, Re_s, approaches zero. It must be pointed out that, in the case of a sphere present in a fluid, which is itself in motion, there are two pertinent Reynolds numbers, based on the velocity of the flow and on the relative velocity of the sphere. These two Reynolds numbers are defined as follows:

$$\mathrm{Re} = \frac{2\alpha\rho_f U}{\mu_f} \qquad \mathrm{Re}_s = \frac{2\alpha\rho_f |U - V|}{\mu_f}. \quad (2)$$

It is evident that $\mathrm{Re} > \mathrm{Re}_s$. For the Boussinesq/Basset equation to be valid, the condition $\mathrm{Re}_s \ll 1$ must be satisfied.

The first attempt to solve the full Navier-Stokes equations for a sphere and to derive an expression for the transient force on a solid sphere at finite values of the Reynolds number was made by Whitehead [9] but it was unsuccessful, because of an incorrect matching of the near and far-field conditions around the sphere. Two decades later, Oseen [10,11] used a different asymptotic method, managed to deal successfully with the inertia terms of the Navier-Stokes equations and used the correct matching conditions. He obtained a zeroth-order expression for the velocity perturbation around the sphere, which enabled him to obtain a solution for the hydrodynamic force, valid at finite but small Reynolds numbers ($\mathrm{Re}_s < 1$). The studies by Oseen [10,11] resulted in the extension of the steady-state (Stokes') drag coefficient to an expression, which is often called ''Oseen's drag coefficient'': $c_D = 24/\mathrm{Re}_s(1 + 3/8\,\mathrm{Re}_s)$. Oseen's student, Faxen [12] studied the flow of spheres close to solid boundaries and extended the theory of the transient flow around a sphere to nonuniform flows. His work resulted in the introduction of the now called ''Faxen terms'' in the expression of the hydrodynamic force. These terms account for the nonuniformity in the flow field surrounding the sphere and are expressed in terms of the Laplacian derivatives of the flow field. A more detailed explanation of these terms will be given in Sections 4 and 9. Tchen [13] re-derived the creeping flow equation for a fluid with a time-varying velocity field $u_i(t)$ and included in his derivation the acceleration term that results from any pressure gradient far from the particle. A variant of this expression having a small correction for the effect of the pressure gradient, was used by Corrsin and Lumley [14] for the study of small particles in a time-dependent turbulent flow field. A few years later, Sy et al. [15] also derived the transient equation of motion at very low Reynolds numbers and coined the phrase ''creeping flow.''

Proudman and Pearson [16] used an asymptotic method of higher order to extend Oseen's result for the steady-state motion and to derive the steady-state drag coefficient of a sphere at finite but still small values of the Reynolds number. Sano [17] also followed an asymptotic method and derived an analytical expression for the transient hydrodynamic force on a stationary sphere, when the fluid undergoes a step velocity change. He was first to show that, at finite but small Reynolds numbers ($\mathrm{Re}_s < 1$), the associated history terms decay faster than $t^{-1/2}$, which is predicted by the creeping flow theory.

The more recent paper by Maxey and Riley [18] is considered now as the definitive study on the equation of motion of a solid sphere under creeping flow conditions. The resulting transient equation encompasses unsteady and nonuniform fluid motion as well as body forces acting on the sphere. Their final expression is not in terms of the hydrodynamic force, but actually the Lagrangian equation of the motion of the sphere, from which the hydro-

dynamic force may be easily deduced. In a lesser-known paper, published on the same year, Gatignol [19] also derived a very similar expression for the Lagrangian equation of motion of a solid sphere. Michaelides and Feng [20] derived an extension to this equation that includes the velocity slip on the surface of the sphere and the effects of finite viscosity of the sphere, always under the creeping flow conditions ($Re_s \ll 1$).

The first part of the 1990s saw a great deal of activity and many excellent studies on the analytical expressions as well as computational results on the transient hydrodynamic force. Mei et al. [21] in a semi-analytical study investigated the dependence of this force on the frequency of the flow, for finite values of Re_s. Mei and Adrian [22] discovered that, at high values of Re_s, the history component of the hydrodynamic force essentially decays as t^{-2} and not as $t^{-1/2}$. Lovalenti and Brady [23] used an asymptotic expansion method to obtain a general expression for the unsteady hydrodynamic force on a rigid particle subjected to arbitrary motion. In an appendix of the same article, Hinch [24] gave a physical explanation of the various terms in the analytical expression of the hydrodynamic force, and of their rates of decay. The last two studies show that the processes of acceleration and deceleration of spheres in viscous fluids at finite Reynolds numbers are not reversible with respect to time because of the inertia of the wakes that are formed behind the sphere, while the creeping flow solutions are invariant with respect to time.

As a result of these studies it has become apparent that exact analytical expressions for the transient hydrodynamic force on a sphere may only be obtained at low values of the Reynolds numbers ($Re_s < 1$) and that such solutions at moderate to high Re_s are impossible to obtain analytically. However, several practical applications, and probably the vast majority of them, pertain to flows of moderate to high Re_s. For this reason, in the last few years, the attention of the researchers has been focused on numerical studies, which are very specific in their processes and values of parameters, but give accurate and useful results under conditions the analytical studies cannot tackle. An example of these studies is the one by Chang and Maxey [25,26]. The results of some of the numerical studies, which complement and help elucidate the results of the analytical expressions, will be presented in Sections 7 and 8.

2.2 Heat Transfer Equation. An attempt to determine the age of the earth prompted Jacques Fourier to undertake the first study on the transient rate of heat transfer by conduction from a sphere. He published his theory and results on the heat transfer from spheres in a series of articles to the Academy of Paris, which culminated in his famous book on heat transfer, [27]. This book by Fourier is considered as one of the most important scientific works of the 19th century, as well as the intellectual stimulus for methods adopted in other scientific fields, including the flow of electric currents, [28], and the development of irreversible thermodynamics. Nusselt and others, who worked on the convection mode of heat transfer, basically followed Fourier's method and expressed their results for the rate of heat transferred in terms of a heat transfer coefficient, in analogy with Fourier's expression: $Q = kA\Delta T$. In a 20th century treatise of the subject of conduction, Carslaw and Jaeger [29] basically extended Fourier's ideas on the transient conduction from a solid sphere and other simple geometrical shapes and presented several other analytical solutions on more modern applications of transient heat conduction. It must be pointed out that, because Carlslaw and Jaeger [29] dealt strictly with the subject of conduction, their solutions apply to fluids only under the condition of vanishing Peclet numbers (Pe=Re*Pr).

Although the original work on the steady-state heat transfer from a sphere preceded the studies on the hydrodynamic force, all recent studies on the heat or mass transfer from spheres followed the analogous studies for the determination of the hydrodynamic force and are often based on similar analytical methods. For example, for the calculation of the steady-state rate of heat transfer from a sphere at finite but small Peclet numbers, Acrivos and Taylor [30] used the asymptotic method in [16] to derive an expression for the Nusselt number at finite Peclet numbers. Several other empirical studies in the 1960s and 1970s resulted in correlations for the convective heat transfer coefficients at transient or steady-state processes that are similar to the corresponding expressions for the steady-state drag coefficients.

Regarding the transient equation for the heat transfer from a sphere, Michaelides and Feng [31] used a method similar to the one used in [18] and obtained the first complete analytical solution for the unsteady energy equation valid at creeping flow conditions. They showed for the first time that the general form of the transient energy equation from a sphere at creeping flow conditions also contains a history term. This term is similar in form to the term in the Boussinesq/Basset expression and decays as $t^{-1/2}$. A subsequent study by Feng and Michaelides [32] followed the analytical method used in [23,33] and showed that the energy equation becomes significantly different at small but finite values of the Peclet number and that the history term decays faster than $t^{-1/2}$ when Pe_s is small but finite.

The main results on the momentum transfer from a sphere to a fluid as well as the energy and mass transfer at wide ranges of Re_s and Pe_s may be found in several treatises of these subjects, such as the ones by Leal [34], Kim and Karila [35], and Sirignano [36], or in recent specific review articles, such as the ones by Leal [37] on the motion of fine particles at low Reynolds numbers, Brady and Bossis [38] on the Stokesian formulation of suspension problems, Feuillebois [39] on the asymptotic methods applied to the equation of motion of spheres in viscous liquids, Sirignano [40] on drops and sprays, Stock [41] on particulate dispersion, Michaelides and Feng [42] on the analogies between the heat transfer and motion of particles, Michaelides [43] on the transient equation of motion of particles, Loth [44] on the numerical methods for the treatment of the motion of bubbles, drops, and particles and Koch and Hill [45] on the inertia effects of suspended particles. Some older monographs by Levich [46], Clift et al. [47], Happel and Brenner [48], Govier and Aziz [49], and Soo [50] contain very useful theoretical and empirical results on the motion and heat/mass transfer processes from spheres as well as irregularly shaped particles. In addition, a series of several recent ASME symposia on gas-particle flows, [51–54], comprise a variety of analytical, numerical, and experimental papers on the equation of motion of particles as well as a multitude of industrial applications of the subject.

3 Governing Equations and Time Scales

3.1 Momentum Equation. Consider the problem of the flow of a viscous fluid around a solid sphere of radius α. The fluid velocity field is unsteady and given by the function $u(x_i,t)$ outside the volume occupied by the sphere. If the sphere is solid its velocity is only a function of the time and given as $V(t)$. Otherwise, the velocity of a viscous sphere is given as $V(x_i,t)$. In both cases, the governing equations are: (a) the continuity, or mass conservation, equation

$$\frac{\partial \rho_f}{\partial t} + \rho_f \nabla \cdot \mathbf{u} = 0, \tag{3a}$$

and (b) the momentum conservation equation

$$-\nabla P + \mu_f \nabla^2 \mathbf{u} = \rho_f \left(\frac{\partial \mathbf{u}}{\partial t} + \mathbf{u} \cdot \nabla \mathbf{u} \right). \tag{3b}$$

We may use the diameter of the sphere as the characteristic length of the problem and a conveniently defined characteristic velocity, U, to make the last equation dimensionless. There are two time scales we may choose from in this problem:

a. the momentum diffusion timescale, $\tau_s = 4\alpha^2 \rho_f / \mu_f$, and
b. the momentum advection timescale, $\tau_a = 2\alpha / U$.

In order to render Eq. (3*b*) dimensionless, it is convenient to choose the momentum diffusion timescale as the characteristic scale of the process. Hence, Eq. (3*b*) may be written in dimensionless form as follows:

$$-\nabla^* P^* + \nabla^{*2}\mathbf{u}^* = \frac{\partial \mathbf{u}^*}{\partial t^*} + \mathrm{Re}(\mathbf{u}^*\cdot\nabla^*\mathbf{u}^*). \tag{3c}$$

The Reynolds number of the flow, Re, which was defined in Eq. (2) and is based on the characteristic velocity and the diameter of the sphere, appears as the only parameter of the equation.

Equation (3*b*), or its equivalent (3*c*), is sometimes called ''the Oseen equation.'' It is the full momentum equation and contains the advection term of the fluid flow, $\mathrm{Re}(\mathbf{V}^*\cdot\nabla^*\mathbf{u}^*)$, which was first successfully used by Oseen in the development of an expression for the hydrodynamic force on a sphere. In the case of creeping flow in a quiescent fluid ($\mathrm{Re}\ll 1$), the advection term is negligible and may be dropped out of the equation. Hence, the creeping flow assumption yields the so-called ''Stokes equation,'' which is as follows:

$$\rho_f \frac{\partial \mathbf{u}}{\partial t} = -\nabla P + \mu_f \nabla^2 \mathbf{u}0, \tag{4a}$$

and in dimensionless form

$$-\nabla^* P^* + \nabla^{*2}\mathbf{u}^* = \frac{\partial \mathbf{u}^*}{\partial t^*}. \tag{4b}$$

A characteristic of the Stokes equation is that neither the Reynolds number nor any other dimensionless parameter appears in it. The steady-state solution of Eq. (4*b*) yields the Stokes expression for the hydrodynamic force, while the full unsteady solution yields the Boussinesq-Basset expression, which was given in Section 2.

3.2 Energy and Mass Transfer Equations. The full, or conduction advection, energy equation for a sphere moving with rectilinear relative velocity $\mathbf{V}(\mathbf{t})$ in a fluid where the temperature field is given by the function, $T(x_i,t)$, is as follows:

$$\rho_f c_f \left[\frac{\partial T}{\partial t} + \mathbf{V}\cdot\nabla T\right] = k_f \nabla^2 T, \tag{5a}$$

where k_f is the thermal conductivity of the fluid and c_f is the specific thermal capacity of the fluid. The second term in the square brackets is the so-called advection term, while the term in the right-hand side is the conduction term. One may choose an arbitrary characteristic temperature for this problem, Θ and a characteristic velocity equal to the advection velocity, U. In a similar manner to the development of the dimensionless momentum equation, the characteristic time for the heat diffusion/conduction process, which is equal to $\tau_t = 4\alpha^2\rho_f c_f / k_f$, is chosen as the characteristic time and the diameter of the sphere, 2α, as the characteristic length. Hence, the dimensionless energy equation for the sphere becomes

$$\frac{\partial T^*}{\partial t^*} + \mathrm{Pe}\mathbf{V}^*\cdot\nabla^* T^* = \nabla^{*2} T^*, \tag{5b}$$

where $T^* = T/\Theta$, $V^* = V/U$ and $t^* = t/[4\alpha^2\rho_f c_f U/k_f]$. The Peclet number, Pe, is analogous to the Reynolds number and is equal to $2\alpha\rho_f c_f U/k_f$. It is related to the Reynolds number through the expression $\mathrm{Pe} = \mathrm{RePr}$ ($\mathrm{Pr} = c_f\mu_f/k_f$, the Prandtl number is a dimensionless parameter of the fluid properties). Another Peclet number, based on the relative velocity of the sphere with respect to the fluid, Pe_s, may be defined in analogy with Re_s as follows: $\mathrm{Pe}_s = 2\alpha\rho_f c_f |U-V|/k_f$. It is evident that the dimensionless Peclet number in the full energy equation plays the role of Reynolds number in the momentum equation.

Equation (5*b*) is the energy equation that is analogous to the full momentum equation (3*c*). The governing heat transfer equation, which corresponds to the Stokes equation and is valid in the case of creeping flows, is simply the heat conduction equation. The latter is obtained from (5*b*) under the condition $\mathrm{Pe}\ll 1$ or, equivalently, by neglecting the term that emanates from the advection of energy:

$$\rho_f c_f \frac{\partial T}{\partial t} = k_f \nabla^2 T. \tag{5c}$$

The last expression becomes in dimensionless form

$$\frac{\partial T^*}{\partial t^*} = \nabla^{*2} T^*. \tag{5d}$$

As with the dimensionless Stokes equation, the dimensionless heat transfer equation at creeping flow does not contain any dimensionless parameters. The dimension of the sphere and the effect of the properties of the fluid come into the solution of the problem through the dimensionless expression for the time, $t^* = t/(4\alpha^2\rho_f c_f U/k_f)$.

It is evident that the only difference in the form and the number of terms between the momentum and the energy equations, with or without the advection terms, is the pressure gradient term, ∇P. In the absence of this term, the two equations would have exactly the same form and there would have been a strict mathematical similarity between the transient hydrodynamic force, or transient drag, and the transient rate of heat transfer from the sphere. In the past, certain analytical solutions to the steady-state momentum equation have been obtained without the pressure term and others without the friction term. The former equations yield what was known as the ''friction drag,'' and the latter the ''form drag'' of the sphere. Since the ''friction drag'' is obtained from a governing equation, which is exactly similar in form to the full energy equation, the resulting steady-state ''friction drag coefficient'' would be strictly similar to an appropriately defined Nusselt number for the heat transfer process. From these solutions of the modified momentum governing equations emanate all the results for what is known as the ''similarity'' between the momentum exchange and heat transfer processes. However, it must be emphasized that this ''similarity'' is not applicable in cases when the fluid field is under a finite pressure gradient.

Regarding the mass transfer equations, they are exactly the same in form with the energy (heat transfer) equations. For example, the full equation for the concentration of a species, *i*, which is transported by diffusion and advection from the sphere to the surrounding fluid is as follows:

$$\left[\frac{\partial C_i}{\partial t} + \mathbf{V}\cdot\nabla C_i\right] = D\nabla^2 C_i, \tag{6a}$$

and in dimensionless form

$$\frac{\partial C_i^*}{\partial t^*} + \mathrm{Pe}_m \mathbf{V}^*\cdot\nabla^* C_i^* = \nabla^{*2} C_i^*. \tag{6b}$$

From a comparison of the heat and mass transport equations it is apparent that in the mass transfer equation the temperature, T, is replaced by the concentration of the species, C_i, and that the heat transfer diffusivity ($k_f/\rho_f c_f$) is replaced by the mass diffusivity, D. Hence, the appropriate Peclet number, Pe_m, is defined in terms of the mass diffusivity and is equal to $\mathrm{Pe}_m = 2\alpha U/D$. Under the same initial and boundary conditions, the solutions to the heat transfer equation are also solutions to the mass transfer equation. In the case of the mass transfer, the Sherwood number, which is a dimensionless representation of the coefficient of mass transfer, h_m, ($\mathrm{Sh} = h_m/2\alpha D$) would replace the Nusselt number ($\mathrm{Nu} = h/2\alpha k_f$) in all the resulting analytical or numerical expressions. For brevity, from this point onwards only the heat transfer (or energy) equations and results will be presented. It must be kept in mind, however that all the results on the rate of heat transfer are also applicable to the case of mass transfer and may be very easily obtained by simply changing the pertinent variables.

3.3 Time Scales for Particle-Fluid Interactions. Apart from the time scales defined above, certain other time scales emanate from the interactions of the fluid and the spheres. These time scales are often used in Lagrangian and Eulerian representations of the particle motion, provide a qualitative knowledge of the importance of the fluid-sphere interactions and often result in very convenient simplifications of the momentum and energy exchange processes from a fluid to a sphere. These time scales are related to τ_s and τ_t above, but are formed by using some of the properties of the sphere instead of those of the fluid.

Momentum and thermal timescales for a solid particle are

$$\tau_{sm}=\frac{2\rho_s\alpha^2}{9\mu_f} \quad \text{and} \quad \tau_{st}=\frac{\rho_s c_{ps}\alpha^2}{3k_f}. \tag{7}$$

The first of these, τ_{sm}, emanates from the steady-state Lagrangian equation of motion for a sphere in a fluid subject to Stokesian drag, $m_s dV/dt=6\pi\alpha\mu_f(U-V)$, and the second from the heat transfer expression for conduction, $m_s c_{ps} dTs/dt=4\pi k_f\alpha(T_f-T_s)$. When these Lagrangian equations are made dimensionless by using the timescales τ_{sm} and τ_{st} then the equations appear in their simplest forms, [55,56]:

$$\frac{dV^*}{dt^*}=1-V^* \quad \text{and} \quad \frac{dT_s^*}{dt^*}=1-T_s^*, \tag{8}$$

which may be solved analytically (they have exponential solutions) and render all the calculations for particle and fluid interactions considerably simpler.

It must be pointed out that, because in the case of the bubbles the added mass part of the hydrodynamic force is considerably greater than the other components, a better expression of the momentum timescale is one that incorporates the effect of the added mass on the characteristic time scale, which is as follows:

$$\tau_{sm}=\frac{2\rho_s\alpha^2}{9\mu_f}\left(1+\frac{1}{2}\Delta_A\frac{\rho_f}{\rho_s}\right). \tag{9}$$

Experimental and theoretical evidence support the conjecture that the value for the added mass coefficient, Δ_A, is approximately equal to 1. If $\rho_s/\rho_f \ll 1$, as in the case of most bubbly flows, the characteristic time for bubble-fluid interactions becomes equal to: $\tau_{sm}=\alpha^2\rho_f/9\mu_f$ or $\tau_{sm}=\tau_s/36$.

For any particle-fluid interactions it is also important to have a knowledge of the pertinent fluid flow time scales, τ_f. These are the macroscopic timescales of the fluid that apply to the type of flow and the specific flow domain of the flow. In a laminar flow the pertinent time scale would be equal to L/U, where L is the characteristic lengthscale of the flow domain. For example, the pipe diameter in the case of pipe flows or the height of the flow in the case of channel flows is the lengthscale of the flow domain. In a turbulent flow there are several time scales that are important in the momentum transfer processes. Among these, the most important ones are: the Kolmogorov time scale, τ_{fK}, which is based on the characteristic length of the small eddies, the integral time scale, $\tau_{f\Lambda}$, which is defined with respect to the integral time scale of turbulence, and the macroscopic timescale, τ_{fL}, which is based on the macroscopic characteristic length of the flow, L. The choice of one or another of these time scales depends greatly on the process under consideration and the calculations to be performed, [41,44].

From the considerations of the sphere-fluid interactions, one may define the ratio of the appropriate dimensionless particle-to-fluid time scales, which is usually called the Stokes number, St $=\tau_s/\tau_f$. Here, τ_s stands as a generic symbol for the characteristic time scale of the sphere that is appropriate to the process under consideration, and τ_f is also a generic symbol of the characteristic time of the fluid that is pertinent to the fluid-sphere interactions. The magnitude of the Stokes number yields a qualitative measure of the particle-to-fluid interactions and often serves as a guiding factor for making simplifying assumptions on these interactions. For example, if the Stokes number based on the Kolmogorov time scale is much smaller than unity, $\mathrm{St}_K \ll 1$, one may conclude that the very small spheres are instantaneously advected by the smallest eddies in a turbulent flow. On the other hand if the Stokes number based on the macroscopic timescale is much larger than unity, $\mathrm{St}_L \gg 1$, one may conclude that the fluid motion has very little influence on the motion of the spheres. Stock [41] and Loth [44] in their review articles provide many more details and further elaboration on the particle and fluid time scales, the Stokes numbers that are defined from these timescales and the influence of turbulence on the rectilinear motion and lateral dispersion of particles. The inverse of the Stokes number is the Strouhal number, Sl $=\tau_f/\tau_s$.

4 Solution of the Governing Equations for Creeping Flow

4.1 Assumptions, Method of Derivation, and Analytical Expressions. By the term "creeping flow" it is generally understood that the sphere moves very slowly in the fluid and that the viscous effects dominate over the inertia effects in the flow and any process that may occur in the flowing mixture. In general, the particle Reynolds number must be very small for this type of flow, that is $\mathrm{Re}_s \ll 1$. The creeping flow analytical solutions for the motion of the sphere emanate from the complete and exact solution of Eqs. (3*c*) and (5*b*) in the case of rigid spheres. It is important to note that these solutions have been derived under the following implicit or explicit assumptions for the particle and the velocity field around it:

For the Equation of Motion:

A spherical shape
B infinite fluid domain
C no rotation
D rigid sphere ($\mu_f/\mu_s \ll 1$)
E zero initial relative velocity
F negligible inertia ($\mathrm{Re}_s \ll 1$)

For the Energy Equation:

A spherical shape
B infinite fluid domain
C no rotation
D highly conducting (Bi $\ll 1$ or $k_f/k_s \ll 1$)
E zero initial relative temperature
F negligible advection ($\mathrm{Pe}_s \ll 1$)

Under these assumptions one is able to solve exactly the creeping flow governing equations and to derive exact expressions for the Lagrangian equation of motion and for the energy (heat transfer) equation of a sphere. The common procedure that leads to the solution of the creeping flow momentum and energy equations involves the following steps:

A The decomposition of the velocity or temperature field into an undisturbed outer field and a perturbation component, which is due to the presence of the sphere. The undisturbed components are essentially the flow and temperature fields far from the sphere, while the perturbation components pertain to the disturbance created by the presence of the sphere on the velocity and temperature fields. In the case of creeping flows, where inertia and advection are negligible, the effects of the perturbation fields extend only a few diameters from the center of the sphere.

B The expression of the governing equations, initial conditions, and boundary conditions of the momentum or energy transfer problem in terms of the two components of the decomposed velocity field.

C The adoption of an "auxiliary" velocity or temperature field, whose analytical solution is simple and readily available. This velocity field may be the field created from an impulse on the velocity or the temperature of the sphere. It is important to note

that this auxiliary field is only used in the calculations and does not have to be pertinent to any of the actual processes under consideration.

D The use of Burger's theorem, often referred to as reciprocal, or Green's second theorem, to express the Laplace transform function of the hydrodynamic force or of the heat transfer from a sphere that undergoes any type of process, in terms of the hydrodynamic force or of the heat transfer resulting from this "auxiliary" field.

E The obtaining of an explicit algebraic solution for the hydrodynamic force or for the rate of heat transfer in the Laplace domain.

F The transformation of the expression(s) obtained in step E from the Laplace to the time domain and subsequent rearrangement of the resulting terms and expressions in a form that is suitable for an equation of motion or an energy equation.

More details of these processes and the specific steps that have been used in the derivation of the creeping flow equations of motion and energy transfer from a sphere, respectively, may be found in Maxey and Riley [18] and Michaelides and Feng [31].

Following this general procedure, Maxey and Riley [18] obtained the following dimensional expression for the equation of motion of a rigid sphere in an arbitrary fluid field, whose velocity is given by the function $u_i(x_i,t)$:

$$m_s\frac{dV_i}{dt}=-\frac{1}{2}m_f\frac{d}{dt}\left(V_i-u_i-\frac{\alpha^2}{10}u_{i,jj}\right)-6\pi\alpha\mu_f\left(V_i-u_i-\frac{\alpha^2}{6}u_{i,jj}\right)-\frac{6\pi\alpha^2\mu_f}{\sqrt{\pi\nu_f}}\int_0^t\frac{\frac{d}{d\tau}\left(V_i-u_i-\frac{\alpha^2}{6}u_{i,jj}\right)}{\sqrt{t-\tau}}d\tau+(m_s-m_f)g_i+m_f\frac{Du_i}{Dt}. \quad (10)$$

In the last equation, m_s is the mass of the sphere and m_f is the mass of the fluid that occupies the same volume as that of the sphere. The repeated index (jj) denotes the Laplacian operator, the derivative D/Dt is the total Lagrangian derivative following the particle and all the spatial derivatives are evaluated at the center of the sphere. Of the terms in the above equation, the left-hand side represents the acceleration of the sphere. Of the terms on the right-hand side, one easily recognizes in the first, second, and third terms as the added mass, the steady-state drag, and the history terms of Eq. (1). The other terms in the right-hand side are the gravitational, or body, force and the Lagrangian acceleration term, caused by the acceleration of the fluid. The Laplacian terms in all the parentheses account for the nonuniformity of the fluid velocity field. They are called sometimes "the Faxen terms," because Faxen [12] was the first to derive them. The Faxen terms are second-order corrections for the non-uniformity of the far-from-the-sphere undisturbed fluid velocity field and must be evaluated at the center of the sphere. These terms become zero when the fluid velocity field is uniform and, in this special case, the corresponding terms of Eq. (10) become the same as those of Eq. (1). The Faxen terms scale as α^2/L^2, where L is the macroscopic characteristic length of the fluid velocity field and in most practical applications are very small because $\alpha/L\ll 1$. Therefore, in many practical applications these terms may be neglected.

It is of interest to note that, even though there is a pressure gradient in the fluid, ∇P, this exact equation of the motion of the sphere does not contain a "pressure gradient" term, which would be proportional to $\alpha^3\nabla P$. Such a term has occasionally and erroneously been added in the transient equation of the motion of a sphere in the past. It must be emphasized that the pressure gradient term in the governing equations for the fluid has been accounted for in the derivation of Eq. (10) and that the effect of the pressure gradient of the fluid manifests itself in the added mass term. Therefore, when one uses this equation, the pressure gradient has already been accounted for and it is not necessary to attach to the equation of motion any additional term(s) in order to account for the pressure gradient in the fluid.

It must also be pointed out that Gatignol [19] independently derived a very similar expression for the transient equation of motion of a sphere. Gatignol's study is in French and has received relatively little attention. Equation (10), or simplified versions of it, has found numerous applications and has been used extensively to model the unsteady motion of particles, bubbles, and drops even when the Reynolds number of the flow is finite. Although the expression is ideally suited for Lagrangian applications, attempts have been made to modify and use the full equation or parts of it so that it may be applied to Eulerian studies of rigid particles or bubbles, [57,58].

Following a similar method and under the assumptions for the energy equation presented above, Michaelides and Feng [31] solved the governing equation for the heat/mass transfer and derived an analytical expression for the transient energy equation for a sphere, also valid under creeping flow conditions. For a rigid, isothermal sphere, which is present in a variable and nonuniform fluid temperature field $T_f(x_i,t)$, the final form of the Lagrangian energy equation is as follows:

$$m_s c_s\frac{dT_s}{dt}=-m_f c_f\frac{DT_f}{Dt}-4\pi\alpha k_f\left[T_s-T_f-\frac{1}{6}\alpha^2T_{f,jj}\right]-4\pi\alpha^2k_f\int_0^t\frac{\frac{d}{d\tau}\left[T_s-T_f-\frac{1}{6}\alpha^2T_{f,jj}\right]}{[\pi a_f(t-\tau)]^{1/2}}d\tau. \quad (11)$$

where a_f in the denominator of the last term is the thermal diffusivity of the fluid, which is equal to $k_f/\rho_f c_f$.

The left-hand side of the above equation represents the change of the temperature of the sphere due to the heat transfer. The first term in the right-hand side is analogous to the inertia term of the momentum equation and represents the (Lagrangian) change of temperature of the equivalent mass of the fluid. The second term is the usual conduction term from the sphere to the fluid. This term represents the rate of heat transfer due to the bulk temperature difference between the fluid and the sphere, corrected by the spatial curvature of the temperature field, which is accounted for by the Laplacian term. The second term is analogous to the steady-state drag term of the equation of motion. The last term in the energy equation is a history integral, which results from the diffusion of the temperature gradients in the fluid temperature field and is also corrected for the nonuniformity or curvature of the temperature field (Laplacian term). It is apparent that this term depends on the temporal as well as the spatial variation of the temperature field and is exactly analogous to the history term of the equation of motion. Previous to 1994, [31], this term was unknown and had been absent from all derivations and uses of the energy equation of spheres including particles, bubbles, or drops. As it will be shown in Section 7.4 this term may account for a significant part of the transient heat transfer to a sphere. The Laplacian terms, which are analogous to the Faxen terms of the equation of motion, also scale as α^2/L^2 and are negligible in many practical applications where the particle radius is significantly smaller than the characteristic dimension of the fluid.

It must be emphasized that the added mass term of the equation of motion emanates from the pressure gradient term in the governing Eq. (3*c*). Since the governing equation for energy does not have a term equivalent to ∇P, in the transient energy equation there is no term corresponding to the added mass term. This constitutes the main difference in the functional forms of the equations of motion and temperature variation under creeping flow conditions as well as at finite Reynolds numbers.

Coimbra and Rangel [59] and Coimbra et al. [60] used the method of fractional calculus to derive a similar expression for the energy equation and showed the existence of the same history

term. Their study also includes the radiation effects and, as in the study by Vojir and Michaelides [61], in their derivation they have identified clearly the origin of all the terms. Also, Sazhin et al. [62] essentially derived a similar history integral term for a specific process, while solving the transient of spheres by conduction.

4.2 A Note on the Computation of the History Terms. Integrodifferential equations, such as (10) and (11) generally do not have an explicit analytical solution for the dependent variable (V_i or T_s). Since they are implicit in their dependent variables, V_i or T_s, they must be solved numerically by an iteration method, which consumes a great deal of computational resources in both memory and CPU time when applied to repetitive calculations such as Lagrangian computations of trajectories. For this reason, several Lagrangian simulations on the motion of particles and bubbles performed in the past twenty years have neglected the history term, often without a sound justification or scientific reasoning.

Michaelides [63] and Vojir and Michaelides [61] have devised an analytical method to convert these first-order implicit integrodifferential equations to second-order integrodifferential equations, which are explicit in the dependent variables V_i or T_s. The method used for these transformations is a straightforward transform of Eq. (10) into the Laplace domain and a back transformation into the time domain after some algebraic manipulations. The transformed equations, written in dimensionless form, are as follows:

A. Equation of motion:

$$\frac{4\alpha^4\rho_s^2}{81\mu_f^2}\frac{d^2w_i}{dt^2}+\frac{2\alpha^2\rho_s}{9\mu_f}\gamma\left(2-\frac{9\beta k}{2}\right)\frac{dw_i}{dt}+\gamma^2 w_i$$
$$=-\frac{4\alpha^4\rho_s^2}{81\mu_f^2}\gamma(1-\beta)\frac{d^2u_i}{dt^2}-\frac{2\alpha^2\rho_s}{9\mu_f}\gamma^2(1-\beta)\frac{du_i}{dt}$$
$$+\frac{2\alpha^2\rho_s}{9\mu_f}\gamma^2(1-\beta)\sqrt{\frac{\beta}{\pi}\frac{\alpha^2\rho_s}{\mu_f}}$$
$$\times\int_0^t\frac{\frac{d^2u_i}{d\sigma^2}}{(t-\sigma)^{0.5}}d\sigma+\gamma\sqrt{\frac{\beta}{\pi t}\frac{\alpha^2\rho_s}{\mu_f}}\left[\gamma(1-\beta)\frac{du_i}{dt}\bigg|_{t=0}\right.$$
$$\left.-\gamma(1-\beta)\frac{2g_i\alpha^2\rho_s}{9\mu_f}\right]+\gamma^2(1-\beta)\frac{2g_i\alpha^2\rho_s}{9\mu_f},\qquad(12)$$

with initial conditions:

$$V_i(0)=u_i(0)\qquad(12a)$$

and

$$\frac{d[V_i-u_i]}{dt}\bigg|_{t=0}=-\gamma[1-\beta]\frac{du_i}{dt}\bigg|_{t=0}+\gamma[1-\beta]g_i,\qquad(12b)$$

where the parameter β is the ratio of the densities, $\beta=\rho_f/\rho_s$, and the parameter γ is equal to $(1+0.5\beta)^{-1}$. The solution of Eq. (12) instead of Eq. (10) results in significant computational economy, because there is no need for extensive memory usage and iterations. However, it must be pointed out that Eq. (12) as a second-order equation is not unconditionally stable as Eq. (10) is. A simple analysis yields that the equation becomes unstable in the range $\rho_s/\rho_f<7/4$.

B. Energy equation:

$$\frac{\alpha^4\rho_s^2c_s^2}{k_f^2}\frac{d^2(T_s-T_f)}{dt^2}+\frac{\alpha^2\rho_sc_s}{k_f}(6-9\beta')\frac{d(T_s-T_f)}{dt}+9(T_s-T_f)$$
$$=-\frac{\alpha^4\rho_s^2c_s^2}{k_f^2}(1-\beta')\frac{d^2T_f}{dt^2}-3\frac{\alpha^2\rho_sc_s}{k_f}(1-\beta')\frac{dT_f}{dt}$$
$$+3\frac{\alpha^2\rho_sc_s}{k_f}(1-\beta')\sqrt{\frac{1}{\pi}\frac{\alpha^2\rho_fc_f}{k_f}}\int_0^t\frac{\frac{d^2T_f}{d\sigma^2}}{(t-\sigma)^{0.5}}d\sigma$$
$$+3\sqrt{\frac{1}{\pi t}\frac{\alpha^2\rho_fc_f}{k_f}}(1-\beta')\frac{dT_f}{dt}\bigg|_{t=0},\qquad(13)$$

with initial conditions:

$$T_f(0)=T_s(0),\qquad(13a)$$

and

$$\frac{dT_s}{dt}\bigg|_{t=0}=\beta'\frac{dT_f}{dt}\bigg|_{t=0}.\qquad(13b)$$

In the heat transfer case, the parameter β' is the ratio of the volumetric heat capacities ($\beta'=\rho_fc_f/\rho_sc_s$). Since the ratio of the specific heat capacities c_f/c_s is not very much different from the unit, the ratio β' is of the same order of magnitude as β. As with the equation of motion, the use of the transformed energy equation results in substantial computational savings in all Lagrangian simulations that pertain to energy exchanges between particles and fluids. It must also be pointed out that, even though Eq. (13) is a second-order equation, it is unconditionally stable for all positive values of β'.

Analytical solutions for the momentum and energy equations are still possible to derive when the assumption E is relaxed, that is, when a finite initial relative velocity or initial relative temperature is allowed, [63,64]. In this case, the history terms of the hydrodynamic force and the energy equations in expressions (10) and (11) will become

$$\frac{6\pi\alpha^2\mu_f}{\sqrt{\pi\nu_f}}\int_0^t\frac{\frac{d}{d\tau}\left[V_i-u_i-\frac{\alpha^2}{6}u_{i,jj}\right]}{\sqrt{t-\tau}}d\tau+\frac{6\pi\alpha^2\mu_f[V_i(0)-u_i(0)]}{\sqrt{\pi\nu_f t}},\qquad(10a)$$

and

$$4\pi\alpha^2k_f\int_0^t\frac{\frac{d}{d\tau}\left[T_s-T_f^\infty-\frac{1}{6}\alpha^2T_{f,jj}^\infty\right]}{[\pi a_f(t-\tau)]^{1/2}}d\tau+4\pi\alpha^2k_f\frac{T_s(0)-T_f^\infty(0)}{\sqrt{\pi a_f t}},\qquad(11a)$$

respectively. It must be pointed out that, because the history term decays as $t^{-1/2}$, the full equation of motion and the energy equation are integrable, even at very low values of time. The integral for the velocity and temperature in these cases scales as $t^{1/2}$.

This additional term in the equations of motion and heat transfer offers an answer to the paradoxical result Reeks and McKee [65] observed, while using the creeping flow equation of particles. They noted that when the transient force term is integrated in order to yield the particle velocity, the resulting history terms yield a separate term for the velocity expression, which is proportional to the initial velocity difference that grows with time as $t^{1/2}$. This would mean that the sphere retains a ''memory'' of its initial velocity regardless of the subsequent impulses to which it is subjected. One would arrive at the same paradox in the case of the temperature if one solves the energy Eq. (11) and determines the heat transfer rate, the total rate of heat transfer and the temperature of the sphere. Actually, any term in similar expressions which decays as t^{-n}, and where $n\leqslant 1$, would result in this type of

"memory." The existence of this type of memory is contrary to intuition and to all experimental evidence of the flow and heat transfer processes of particles in a viscous fluid. When a particle is introduced in a viscous fluid with finite velocity (temperature difference), the effect of the viscosity (conductivity) will result in the eventual decay of any initial velocity (temperature) difference, after long times approaching zero. Thus, the initial condition of the velocity or temperature of the particle does not play any role in the determination of its velocity or temperature after a sufficient amount of time. This paradoxical result does not appear if the second terms in the history terms (Eqs. (11*a*) and (11*b*)) are used in the calculations. However, this paradox and the related results notwithstanding, in practice the paradox may not be significant in the calculations of the actual motion or heat transfer from spheres for the following two reasons:

a. When the sphere moves with finite Re_s or Pe_s, the form of the history term is different, as will be shown in the next section. The history terms decay faster and, after integration, there is no memory of the initial relative velocity or relative temperature of the sphere.

b. The concept of an "initial" relative velocity or temperature, while mathematically sound as an initial condition to a partial differential equation, is physically questionable: How does one introduce a sphere in an "initially undisturbed" fluid with a different velocity or temperature? Surely the mechanism of the introduction of the sphere would result in some kind of disturbance to the fluid velocity field, which is not accounted for in the initial and boundary conditions used for the derivation of the pertinent equations. Therefore, one has to reconsider the finite relative velocity as an initial condition of a problem where the sphere is present in an unbounded fluid, which is initially undisturbed by its presence. An interesting approach to this question is through the use of irreversible thermodynamics, where the relative velocity may be described as an internal variable, [66].

Mass transfer due to chemical reactions or phase change results in the changing of the size of a sphere in many practical applications. For example, bubble evaporation or condensation and droplet evaporation or combustion processes will cause the growth or diminution of the size of the sphere. Experimental and analytical studies that take into account the effects of heat transfer, local thermodynamic nonequilibrium and microlayers formed during the evaporation process were performed by Theofanous et al. [67] and Theofanous and Patel [68]. Although they did not explicitly use the energy equation, Magnaudet and Legendre [69] performed a recent study on the hydrodynamic force exerted on an inviscid sphere with variable radius, which may be caused by slow evaporation or condensation. Their study is pertinent to the case of an isothermally condensing bubble and their results essentially apply to small bubbles with $\mu_s/\mu_f \ll 1$ and $\mathrm{Re}_s \ll 1$. The final expression for the unsteady hydrodynamic force with variable radius $\alpha(t)$ is as follows:

$$F_i(t)=4\pi\mu_f\alpha(t)V_i(t)+\frac{2}{3}\pi\rho_f\left(\frac{d[\alpha(t)^3V_i(t)]}{dt}+2\alpha(t)^3\frac{dV_i(t)}{dt}\right)+8\pi\rho\mu_f\int_0^t\exp\left(9\mu_f\int_0^t\frac{d\tau}{\alpha(\tau)^2}d\tau\right)\times\mathrm{erfc}\left(\sqrt{9\mu_f\int_0^t\frac{d\tau}{\alpha(\tau)^2}d\tau}\right)\frac{d[\alpha(\tau)V_i(t)]}{dt}d\tau. \quad (14)$$

Small parentheses in Eq. (14) denote arguments of functions, e.g., time, and not the operation of multiplication. It is obvious that the equation of motion of a growing bubble contains the same terms as Eq. (1) but the form and coefficients of these terms are significantly modified. When the radius of the bubble is constant, the last equation yields the expression derived by Morrison and Stewart [70] for an inviscid bubble and is also identical to the expression derived in [20] for a viscous sphere with perfect slip on its surface.

A similar study on the hydrodynamic force during bubble growth by Thorncroft et al. [71] showed that the added mass part of the hydrodynamic force for a bubble growing close to the wall is also composed of two terms:

$$F_{AM}=\frac{2}{3}\pi\rho_f\alpha^3(t)\left[\frac{dU}{dt}-\frac{dV}{dt}\right]+2\pi\rho_f\alpha^2(t)[U-V]\frac{d\alpha}{dt}. \quad (15)$$

Of these, the first term is the same as the usual added mass term and the second is due to the change of the size of the bubble. When the radius of the sphere is constant, Eq. (15) yields the standard Boussinesq-Basset term for the added mass.

5 Analytical Expressions at Finite Re_s and Pe_s

5.1 Steady-State Force and Heat/Mass Transfer. From the beginning it must be realized that the motion of spheres and the heat transfer from them are inherently unsteady processes when the Reynolds number Re_s exceeds a critical Reynolds number, $\mathrm{Re}_{\mathrm{crit}}$, that lies in the range from 150 to 190, [72]. Above this range, bifurcations occur in the flow field developed by the presence of the sphere and an unsteady wake is formed behind the sphere, [73]. The wake influences greatly the flow field around the sphere and the trajectory of the sphere itself. Mebarek et al. [74] showed that each one of these bifurcations is accompanied by a change in the slope of the steady state component of the hydrodynamic force. At values of $\mathrm{Re}_s > 200$ the instability of the wake increases. In this case, the flow is steady but nonaxisymmetric. At even higher values of Re_s, above 275, the wake becomes unsteady and nonaxisymmetric. These more modern results agree well with experiments performed in the past: Clift et al. [47] present several schematic diagrams and actual photographs of the wake behind a solid sphere and clearly show that, at values of $\mathrm{Re}_s > 400$ unsteady vortices are shed from the back of the sphere. Thus, steady state and axisymmetric conditions for the wake of the sphere imply a relatively low value of Re_s, that is less than 175, as well as steady flow around the sphere.

The first correct solution of the problem of determination of the hydrodynamic force on a sphere at finite Reynolds numbers is attributed to Oseen [10,11]. He did not solve completely for the velocity field around the sphere, but used a simple perturbation method to calculate a first-order correction for the steady-state drag coefficient. His asymptotic expression, $c_D = 24/\mathrm{Re}_s(1 + 3/8\,\mathrm{Re}_s)$, is valid for finite but small values of Re_s. Maxworthy [75] verified experimentally that Oseen's correction is accurate up to $\mathrm{Re}_s = 0.45$. This range covers several practical applications in the chemical industry, where particles are very small and the fluids have high viscosity.

At finite values of Re_s or Pe_s, the nonlinear advection term in the governing momentum and energy Eqs. ((3*b*) and (5*a*)) must be retained in the solution of the equations. In these cases, the vorticity and the temperature gradients around the sphere are transported by the advection of the fluid as well as by the diffusion processes. An analysis of the governing equations reveals that the diffusion part of the process is dominant in an inner region surrounding the sphere with radius $\alpha\,\mathrm{Re}_s^{-1}$ for the momentum problem and $\alpha\mathrm{Pe}_s^{-1}$ for the heat transfer problem. The advection process is dominant at distances far from this region. Close to the sphere defined by the radius $\alpha\,\mathrm{Re}_s^{-1}$ or $\alpha\mathrm{Pe}_s^{-1}$ the two processes advection and diffusion are of the same order of magnitude and their effects must be calculated simultaneously.

The characteristic time of the advection process is α/U, while that of the diffusion process is α^2/ν_f and the two time scales are in general different. Since these characteristic times are in general of different orders of magnitude, the problems of the transport of momentum and energy at finite Reynolds or Peclet numbers may

only be solved asymptotically, usually by a singular perturbation method. Proudman and Pearson [16] employed such a method to calculate the velocity field around a solid sphere and around a cylinder at steady state, which is correct to $O(\mathrm{Re})$. Their method used the expansion of the stream function in suitable polynomials, locally valid in the inner and outer regions of the flow. This expansion and the approximation of the velocity field enabled them to extend Oseen's result and to calculate the steady-state drag coefficient to $O(\mathrm{Re}_s^2)$. Their contribution to the calculation of the steady-state hydrodynamic force is a term of the order of $\mathrm{Re}_s^2 \ln \mathrm{Re}_s$. Their expression for the drag coefficient is as follows:

$$c_D = \frac{24}{\mathrm{Re}_s}\left[1 + \frac{3}{8}\mathrm{Re}_s + \frac{9}{40}\mathrm{Re}_s^2 \ln \mathrm{Re}_s + O(\mathrm{Re}_s^2)\right]. \tag{16}$$

Acrivos and Taylor [30] conducted a similar study for the steady-state energy equation of a spherical particle. They extended the solution to a higher order and derived the following asymptotic expression for the steady-state Nusselt number, valid for finite but small Pe_s:

$$\mathrm{Nu} = 2\left[1 + \frac{1}{2}\mathrm{Pe}_s + \frac{1}{2}\mathrm{Pe}_s^2 \ln \mathrm{Pe}_s + 0.41465\mathrm{Pe}_s^2 + \frac{1}{4}\mathrm{Pe}_s^3 \ln \mathrm{Pe}_s + O(\mathrm{Pe}_s^3)\right]. \tag{17}$$

Because of the heat/mass transfer analogy, the last expression may also be applied to the steady-state mass transfer problem from a sphere when the Sherwood number is substituted for the Nusselt number and the Peclet number is based on the mass diffusivity of the fluid.

Expressions such as (16) and (17) may be used with accuracy in applications of finite but small Reynolds and Peclet numbers in the range from 0 to 0.7. At higher values of these dimensionless parameters, it is advisable to use one of the empirical or semi-empirical expressions for the steady-state drag coefficient and Nusselt number that abound in the literature, such as the Schiller and Nauman's [76] correlation for the drag coefficient c_D:

$$c_D = 24(1 + 0.15\,\mathrm{Re}_s^{0.667})/\mathrm{Re}_s, \tag{18a}$$

or the several other similar in form expressions that were subsequently derived, [47]. In the case of the heat transfer coefficients one may use the analytically derived expression:

$$\mathrm{Nu} = 2 + 0.6\,\mathrm{Re}_s^{0.5}\,\mathrm{Pr}^{0.4}, \tag{18b}$$

or one of the expressions that are similar in form and have been derived by correlations of experimental or numerical results, [77–79]. Several results and expressions for the steady-state transport coefficients, including those applicable for viscous spheres are presented in Sections 7 and 8 below.

5.2 Unsteady Hydrodynamic Force. Sano [17] used an asymptotic analysis and derived an expression for the transient hydrodynamic force acting on a rigid sphere at small but finite values of the Reynolds number, when the sphere undergoes a step change in its velocity of magnitude V:

$$F_i(t) = 6\pi\alpha\mu_f V_i\left\{H(t^*) + \frac{1}{3}\delta(t^*) + \frac{1}{2\sqrt{\pi t^*}} + \frac{3}{8}\mathrm{Re}_s \times\left[\left(1 + \frac{1}{\mathrm{Re}_s^4 t^{*2}}\right)\mathrm{erf}(\mathrm{Re}_s t^{*1/2}) + \frac{1}{(\pi t^*)^{1/2}\mathrm{Re}_s}\left(1 - \frac{1}{2\mathrm{Re}_s^2 t^*}\right)\exp(-\mathrm{Re}_s^2 t^*) - \frac{4}{3(\pi t^*)^{1/2}\mathrm{Re}_s}\right] + \frac{9}{40}\mathrm{Re}_s^2 \ln \mathrm{Re}_s\right\} + O(\mathrm{Re}_s^2). \tag{19}$$

The time variable in Eq. (19) has been made dimensionless by dividing with the characteristic time of the fluid, $\tau_s = 4\alpha^2\rho_f/\mu_f$. The expression in the square brackets results from the contribution of the outer velocity field and is a consequence of the advective terms in the Oseen equations. For this reason, it has been referred to as the ''Oseen contribution,'' [23]. It must be pointed out that the last term of the Oseen contribution cancels the third term in the right-hand side, $(\pi t)^{-1/2}$. The remaining transient terms in Eq. (19) decay exponentially. This rate of decay is faster than the decay of the transient terms of the creeping flow equation. Physically, this happens because the finite velocity difference allows for the faster advection and evolution of the vorticity field around the sphere. While in the creeping flow case the vorticity field around the sphere was transported by viscous diffusion alone, in the case of advection the finite velocity ''carries'' the vorticity field far from the sphere. With the faster decay of the transient terms, a spherical particle does not retain any ''memory'' of its initial velocity, which is characteristic of the $t^{-1/2}$ rate of decay, as mentioned in Section 4. Feuillebois and Lasek [80] also considered the problem of the sphere accelerating at small but finite Reynolds numbers and derived some useful asymptotic results on the properties of the outside boundary layer formed in the viscous fluid.

With the fast development of the numerical methods during the 1980s, computational studies came to complement the analytical results on the transient equation of a sphere. Mei et al. [21] conducted such a numerical study on the motion of a rigid spherical particle at $0 < \mathrm{Re}_s < 50$ when the freestream velocity fluctuates with a small amplitude. The numerical results of this study also point out that, in the low frequency limit, the history term of the hydrodynamic force decays faster than the conventional $t^{-1/2}$ rate. Subsequently, Mei and Adrian [22] obtained an analytical solution for the motion of a solid sphere at very low frequencies ($\mathrm{Sl} \ll \mathrm{Re}_s < 1$). Their results revealed a different history term, which is as follows:

$$\int_0^t \frac{\frac{dV_i}{dt} - \frac{du_i}{dt}}{\left[\left(\frac{\pi\nu_f}{\alpha^2}(t-\tau)\right)^{1/4} + \left(\frac{\pi}{2\alpha\nu_f}\left(\frac{|u_i(\tau)|}{f_H}\right)^3 (t-\tau)^2\right)^{1/2}\right]^2} d\tau,$$

where f_H is a function of the Reynolds number. It is evident that at short times this term matches the classical history term, while at long times it decays asymptotically as t^{-2}. With this type of long-term decay the sphere does not retain any memory of its initial velocity.

Lovalenti and Brady [23,33] essentially followed Sano's method and derived the hydrodynamic force on a sphere undergoing an arbitrary motion. They used a different scheme for rendering the governing equations dimensionless and introduced the product of the Reynolds, Re_s, and Strouhal number, Sl, in their solution. Their solution is also valid for finite but small Reynolds numbers ($0 < \mathrm{Re}_s < 1$). In the case of a solid sphere settling in a stagnant fluid, their equation reduces to the following expression

$$F_i(t) = -6\pi\mu_f\alpha V_i(t) - \frac{2}{3}\pi\alpha\mu_f \mathrm{Re}_s\,\mathrm{Sl}\frac{dV_i}{dt} - \frac{6\mu_f\alpha V_i(t)}{t^{1/2}}(\pi\,\mathrm{Re}_s\,\mathrm{Sl})^{1/2} - \frac{9}{4}\mu_f\alpha(\pi\,\mathrm{Re}_s\,\mathrm{Sl})^{1/2} \times \int_0^t \frac{2}{(t-\tau)^{3/2}}\left[\frac{2}{3} - \frac{1}{A^2}\left[\frac{\pi^{1/2}}{2A}\mathrm{erf}(A) - \exp(-A^2)\right]\right]V_i(\tau)\,d\tau, \tag{20a}$$

where the vector **A** is a measure of the distance traveled by the sphere and is given as follows:

$$\mathbf{A}=\frac{\mathrm{Re}_s}{2}\sqrt{\frac{t-\tau}{\mathrm{Re}_s\,\mathrm{Sl}}}\,\frac{\int_\tau^t \mathbf{V}(q)dq}{t-\tau}. \tag{20b}$$

The Strouhal number, Sl, in the above expressions is the ratio of the characteristic time of the fluid to that of the rigid sphere and is essentially the inverse of the Stokes number.

The studies by Lovalenti and Brady [23,33] also concluded that the unsteady terms of the equation of motion decay faster when the advection terms in the governing equations are retained. Some of the other noteworthy results of this study are that the behavior of the sphere when its motion commences from rest is different than when the sphere starts with a finite velocity. The main physical reason for this is the formation and presence of an unsteady wake behind the sphere, which influences the motion of the sphere. In [33], there is a remarkable appendix by Hinch [24] who presents simple arguments and quick asymptotic methods to explain the physics of the solutions obtained. Hinch reduces the effect of the Oseen contribution, that is, the advection terms in the governing equation, to the action of sources and sinks associated with the presence of the wake behind the sphere. It is apparent from these physical arguments that, with advection, any memory of a possible initial velocity of the sphere fades at long times. Also, because of the differences of the velocity field developed in the surrounding fluid, the acceleration and deceleration processes of the sphere are not achieved with the same force, even though the initial and final velocities of the sphere are the same. Therefore the acceleration and deceleration processes at finite values of Re_s are not symmetric with respect to time. This is in contrast to the case of the creeping flow, where the Boussinesq/Basset expression is invariant with respect to time and implies the same forces in the acceleration and deceleration processes. It must be emphasized at this point that, regardless of this, both the motions at finite and at zero Re_s are irreversible processes from the thermodynamic point of view since they involve finite dissipation.

The asymptotic behavior of the transient hydrodynamic force on a solid sphere has also been the subject of a few more recent theoretical papers by Mei [81] for an oscillating sphere, by Lawrence and Mei [82] for the motion induced by an impulse, and by Lovalenti and Brady [83] for an abrupt change of the velocity of the sphere. Apparently, there is not complete agreement as to the exact form and the long-time behavior of some of the transient terms. This disagreement may be due more to the modeling of the motion of the sphere (e.g., initial and boundary conditions, way of change of the velocity) rather than physical reasons associated with this problem. For example, real spherical particles do not undergo step changes in their velocities and a physical impulse on a sphere inside a viscous fluid is physically different from a Dirac delta function.

Since analytical methods only result in solutions at small Re_s, some needed answers on the transient hydrodynamic force acting on a sphere at higher values of this parameter may only be accomplished by computational studies. This subject bears weight in many engineering applications and is treated in Subsection 7.2.

5.3 Unsteady Heat Transfer. As in the case of the solution of the momentum equation at finite Reynolds numbers, it is also cumbersome to solve the energy equation at finite Peclet numbers. Analytical solutions have been obtained only in the case of finite but small Peclet numbers ($\mathrm{Pe}<1$). The earlier studies on the heat/mass transfer used a given velocity field, usually a steady-state or a very slowly varying velocity field in order to solve the energy equation and derive results for the transient heat transfer. Thus, Choudhury and Drake [84] used the steady-state velocity field obtained in [16] and derived an analytical solution for the rate of heat transfer from a sphere, subject to a varying fluid temperature field. Similarly, Konoplin and Sparrow [85] used a Stokesian velocity profile ($\mathrm{Re}_s \ll 1$) and derived some useful results for the heat transfer and the temperature distribution from a sphere. All these results and the analytical expressions derived from these studies are restricted by the explicit and implicit assumptions pertaining to the choice of the velocity field around the sphere.

As with the case of the hydrodynamic force, analytical results on the heat transfer at finite Pe may only be obtained by asymptotic methods. Using an asymptotic analysis, similar to the one conducted by Sano [17], Feng and Michaelides [86] obtained the following expression for the Nusselt number of a solid sphere undergoing a step temperature change:

$$\mathrm{Nu}=2\left[1+\mathrm{Pe}\left[\frac{1}{2}\,\mathrm{erf}(2\mathrm{Pe}\sqrt{t^*})+\frac{1}{4\mathrm{Pe}\sqrt{\pi t^*}}\exp(-4\mathrm{Pe}^2 t^*)\right]+2\mathrm{Pe}^2\ln(2\mathrm{Pe})\right]+O(\mathrm{Pe}^{1+}), \tag{21}$$

where the time t^* has been made dimensionless by dividing it with the characteristic time of heat diffusion, $4\alpha^2\rho_f c_f/k_f (t^*=t/\tau_t)$.

Feng and Michaelides [32] also performed a study on the energy equation, which is analogous to the one performed by Lovalenti and Brady [23] for the momentum equation. They derived a transient expression for the heat transfer from a solid particle of arbitrary shape, undergoing arbitrary motion, with a velocity $\mathbf{u}^s$. In the special case of a sphere, and for time scales greater than $O(\mathrm{Pe}^{-2})$ their analysis yields the following expression for the total dimensionless heat transfer:

$$\begin{aligned}Q(t^*)=&\frac{4\pi\mathrm{Pe}_s\mathrm{Sl}}{3}\frac{dT^\infty}{dt^*}-4\pi(T_s-T^\infty)-2\pi\sqrt{\mathrm{Pe}_s\mathrm{Sl}}\\&\times\int_0^t\frac{T_s-T^\infty}{\sqrt{t^*-\tau^*}}\frac{\mathrm{erf}|\mathbf{A}'|}{|\mathbf{A}'|}d\tau^*-2\mathrm{Pe}_s\sqrt{\pi}\\&\times\int_0^t\frac{(T_s-T^\infty)|\mathbf{u}^s|}{(t^*-\tau^*)|\mathbf{A}'|}\left[\frac{\sqrt{\pi}}{2|\mathbf{A}'|}\mathrm{erf}|\mathbf{A}'|-\exp(-|\mathbf{A}'|^2)\right]d\tau^*\\&+O(\mathrm{Pe}^{1+}),\end{aligned} \tag{22a}$$

where the vector $\mathbf{A}'$ is analogous to the one in the case of the hydrodynamic force in Eq. (20*a*) and is defined as follows:

$$\mathbf{A}'=\frac{\mathrm{Pe}_s}{2}\left(\frac{t^*-\tau^*}{\mathrm{Pe}_s\mathrm{Sl}}\right)^{1/2}\frac{\int_\tau^t\mathbf{u}^s(\xi)d\xi}{t^*-\tau^*}. \tag{22b}$$

It is evident that the vectors $\mathbf{A}$ and $\mathbf{A}'$ scale as $(t-\tau)^{1/2}$. This result confirms that the history effects in both the expressions decay faster than the corresponding history integrals resulting from the creeping flow solutions.

Of the terms in Eq. (22*a*), the first term represents the contribution of the time-varying undisturbed fluid temperature field, which is far from the particle. The second term is the usual steady-state conduction term. The third and fourth terms are history terms emanating from the temperature gradients, which are simultaneously diffused and advected, since the inception of the heat transfer process. It must be pointed out that this equation is valid at long times after the inception of the process, $[t=O(\mathrm{Pe}^{-2})]$, when the resulting temperature gradients have been convected to distances far from the characteristic Oseen distance $\alpha\mathrm{Pe}^{-1}$. At shorter times, it is the heat diffusion/conduction process that dominates and the expression for the rate of heat transfer is the same as that derived for creeping flow and was presented above in Eq. (11).

Pozrikides [87] also performed an analytical study to determine the transient heat and mass transfer from a suspended particle of arbitrary shape at low Peclet numbers. He used a method of matched asymptotic expansions and obtained the Green's function in order to derive analytical expressions for the transport from a sphere in a fluid undergoing a step temperature change and a sphere in a time-periodic flow. His results are expressed in terms

of the fractional increase of the rate of heat transfer from the case of conduction $[(Q(t)-Q_0)/Q_0$, where Q_0 is the result for pure conduction] and may be summarized as follows:

$$\begin{aligned}&\text{for uniform flow:}\quad (Q(t)-Q_0)/Q_0=1/2\mathrm{Nu}_0\mathrm{Pe}_s\\&\text{for shear flow:}\quad (Q(t)-Q_0)/Q_0=0.257\mathrm{Nu}_0\mathrm{Pe}_s^{1/2}\\&\text{for two-dimensional straining flow:}\\&\quad (Q(t)-Q_0)/Q_0=1.36\mathrm{Nu}_0\mathrm{Pe}_s^{1/2}\\&\text{for axisymmetric straining flow:}\\&\quad (Q(t)-Q_0)/Q_0=2.0\mathrm{Nu}_0\mathrm{Pe}_s^{1/2},\end{aligned}\tag{23}$$

where Pe_s is the instantaneous Peclet number and is a function of time. These expressions show that the velocity field around the sphere influences significantly the rate of heat transfer from the sphere.

6 The Hydrodynamic Force and Heat Transfer for a Spheroid

The similarities in the analytical expressions of the hydrodynamic force and the rate of heat/mass transfer are very well exhibited in the case of a spheroid, with small eccentricity, ε. As ε approaches zero, the spheroid asymptotically approaches the shape of a sphere. Lawrence and Weinbaum [88,89] conducted an analytical study on the motion of a rigid spheroid of revolution with small eccentricity, under creeping flow conditions. Their study used essentially the method employed by Maxey and Riley [18] with the added complexity of domain decomposition to a second-order expansion in terms of the eccentricity, ε. The resulting expression for the transient hydrodynamic force exerted on the spheroid is as follows:

$$\begin{aligned}F_i=-6\pi\mu_f\alpha\Bigg[&(V_i-u_i)\left(1-\frac{\varepsilon}{5}+\frac{37\varepsilon^2}{175}\right)+\frac{\alpha}{\sqrt{\nu\pi}}\left(1-\frac{2\varepsilon}{5}\right.\\&\left.+\frac{81\varepsilon^2}{175}\right)\int_0^t\frac{\overline{d(V_i-u_i)}}{\sqrt{t-\tau}}d\tau+\frac{\alpha^2}{9\nu}\left(1+\frac{\varepsilon}{5}-\frac{26\varepsilon^2}{175}\right)\frac{d(V_i-u_i)}{dt}\\&+\frac{8\alpha\varepsilon^2}{175\sqrt{\pi\nu}}\int_0^t\frac{d(V_i-u_j)}{d\tau}G(t-\tau)d\tau\Bigg],\end{aligned}\tag{24a}$$

where the function G of the last term is frequency dependent and is defined as follows:

$$G(t)=\mathrm{Im}\left[\sqrt{\frac{\pi\phi}{3}}e^{\phi t}-\mathrm{erfc}\sqrt{\phi t}\right],\quad\text{with}\quad\phi=\frac{3}{2}(1+i\sqrt{3}).\tag{24b}$$

A comparison of Eq. (24*a*) with Eq. (1) reveals that the first three terms of (24*a*) are similar to the steady-state drag, the history and the added mass term of the Boussinesq-Basset equation. Their form is the same as the form of the corresponding terms of Eq. (1) with the expected corrections terms due to the eccentricity of the spheroid. The last term of Eq. (24*a*) does not have a counterpart in the Boussinesq-Basset expression. It depends on the eccentricity as well as the frequency of variation of the velocity of the fluid and vanishes asymptotically as ε^2. This is a new history integral term, which emanates from the elongated shape of the immersed object. The presence of such terms in an equation derived under the creeping flow assumption is another indication that the Boussinesq-Basset solution and the Maxey-Riley expression must be modified when there are departures from the assumptions that were listed in Section 4.

The solution of the energy equation for a spheroid yields results, which demonstrate the remarkable similarities between the momentum and heat transfer processes. Feng and Michaelides [90], following the method used in [88,89] decomposed the applied temperature field and also used a second-order expansion of the geometric domain with respect to the eccentricity. They derived the corresponding expression for the heat flux from a spheroid, which is as follows in dimensionless form:

$$\begin{aligned}Q(t^*)=-4\pi\Bigg\{&\left(1+\frac{2}{3}\varepsilon-\frac{1}{45}\varepsilon^2\right)(T_s-T^\infty)+\left(1+\frac{4}{3}\varepsilon-\frac{2}{3}\varepsilon^2\right)\\&\times\int_0^t\frac{\overline{\frac{d}{d\tau^*}(T_s-T^\infty)}}{\sqrt{\pi(t^*-\tau^*)}}d\tau^*+\frac{1}{3}\left(1+\frac{2}{9}\varepsilon+\varepsilon^2\right)\frac{DT^\infty}{Dt^*}\\&+\varepsilon^2\frac{4}{45}\sqrt{\frac{\pi}{3}}\int_0^t\left[\frac{d}{dt^*}(T_s-T^\infty)\right]G'(t^*-\tau^*)d\tau^*\Bigg\}.\end{aligned}\tag{25a}$$

As with the function $G(t^*)$, for the hydrodynamic force expression, the new function $G'(t)$ also depends on the frequency of variation of the temperature field and is defined as follows:

$$G'(t^*)=\mathrm{Im}[\sqrt{\pi\Phi}e^{\Phi t^*}\,\mathrm{erfc}(\sqrt{\Phi t^*})]\qquad\text{and}\qquad\Phi=3e^{i\pi/3}.\tag{25b}$$

The last term in Eq. (25*a*) is analogous to the new history term in Eq. (24*a*) and depends entirely on the eccentricity and the frequency of variation of the external temperature field. The kernels of these terms do not follow the $t^{-1/2}$ decay of the typical history term in creeping flows and depend on the frequency of the variation of the velocity of temperature fields. Regarding the practical significance of these new history terms, Feng and Michaelides [90] showed that, when the frequency of variation of the velocity and temperature fields is not exceedingly high, then the contributions of these terms to the total heat flux and the hydrodynamic force are much smaller than the contributions of the other terms of the corresponding transient equations.

A glance at the equations for the hydrodynamic force and the rate of heat transfer for a spheroid under creeping flow conditions proves that there are remarkable analogies between the two expressions but not a formal mathematical similarity, such as the one Konoplin [91] contemplated and through which one may be able to calculate the results for the one expression by knowing the results of the other. This happens because the numerical coefficients of the correction factors resulting from the eccentricity are entirely different. As with the expressions for spheres, the energy equation for spheroids does not have an added mass term. However, among the similarities of the two expressions one may observe that the two have terms with similar functional forms, that both the expressions comprise the new memory term, which is proportional to ε^2 and that the kernels of this memory term have the same functional form.

One of the conclusions that may by drawn from a simple comparison of the equation of motion and the heat transfer equation for a sphere and a spheroid is that slight departures from the spherical shape result in considerable differences on the form of the two equations as well as on the form of the history term. This leads one to conclude that, by extension, the shape of a particle plays a very important role on the functional form and on the magnitude of the hydrodynamic force and the heart transfer. As a consequence, it is not possible to, a priori, derive with any degree of accuracy the transient equations of motion and heat transfer of particles with irregular shape from the corresponding equations of a sphere. This and similar results on the history terms for cylin-

ders by Chaplin [92] raise questions on the theoretical validity and practical accuracy of the concept and method known as ''equivalent diameter,'' which is often used in the modeling of irregular particles in several chemical and environmental processes including sedimentation, [93]. According to this method, an irregularly shaped particle of volume v essentially behaves as a spherical particle, whose equivalent diameter, d_e, is defined from the equation: $v=1/6\pi(d_e)^3$. Hence, its transport coefficients are approximated by those of the sphere with diameter d_e. Oftentimes, calculations using the method of the equivalent diameter are accompanied by other closure equations pertaining for example, to the sphericity, circularity, or eccentricity of the particles, that emanate from experimental data and, because of this, the final results are sufficiently accurate within their range of applicability, [94].

It appears that the method of the equivalent diameter for the particles, especially when verified and supplemented by empirical data or empirical correlations, is very useful as a first approximation to simple applications of the steady-state motion of irregularly shaped particles. However, it must be borne in mind that the method has very little theoretical justification and should not be used in detailed transient flow calculations or even in steady state calculations beyond the range of applicability of the empirical closure equations.

7 Extension of the Creeping-Flow Solutions to Higher Re—Semi-Empirical Expressions

While all known analytical expressions for the hydrodynamic force and the heat transfer from particles, bubbles, or drops apply to low Reynolds or Peclet numbers, many engineering applications of the transport processes occur at higher ranges of these parameters. Slurry transport and practical pneumatic conveying systems operate in the range $10^1<\mathrm{Re}_s<10^3$; drops in combustion processes may reach Reynolds numbers up to 10^3; bubble columns in chemical processes operate in a range from 0 to 10^3; and particulate flows in the environment may reach Reynolds numbers, Re_s, up to 10^4. Since there is no applicable theory, other than some asymptotic studies, and analytical expressions for $\mathrm{Re}_s>1$, experimental data and empirical correlations have been used for the calculation of the steady state transport coefficients. Usually these correlations are power-law modifications of the Stokes drag coefficient. They emanate from certain sets of experimental data and are applicable only in their corresponding ranges of Re_s. Oftentimes, these correlations are designed to agree with theoretical asymptotic results, such as the Stokes or the Oseen expressions for the steady state drag. Twelve such correlations for the steady-state drag coefficient are listed in [47] and several others are known to exist. The accuracy and reliability of these empirical functions are unpredictable and depend to a great extent on the conditions and experimental accuracy of the original data sets from where they emanate.

7.1 Transient Expressions. Regarding the transient terms of the hydrodynamic force, Odar and Hamilton [95] were the first to propose modifications and correlation functions that extend to the transient terms, following the practice used for the steady state term. They essentially treated the three terms of the Boussinesq-Basset expression (Eq. (1)) as separate forces and multiplied each one of them with a correction function that accounts for the higher Reynolds number. Their proposed extension of the Boussinesq-Basset expression has the following form:

$$F_i=c_1 6\pi\alpha\mu_f(V_i-u_i)+\Delta_A\frac{1}{2}m_f\frac{d(V_i-u_i)}{dt}+\Delta_H\alpha^2\sqrt{\pi\rho_f\mu_f}\int_0^t\frac{\dfrac{d(V_i-u_i)}{d\tau}}{\sqrt{t-\tau}}d\tau, \tag{26}$$

where the functions c_1, Δ_A, and Δ_H are empirical functions determined by experiments. Odar and Hamilton used Schiller and Nauman's [76] correlation for the coefficient $c_1(c_1=1+0.15\,\mathrm{Re}^{0.667})$ and reduced their experimental data to derive the following expressions for the other two coefficients:

$$\Delta_A=1.05-\frac{0.066}{0.12+\mathrm{Ac}^2}\quad\text{and}\quad\Delta_H=2.88+\frac{3.12}{(1+\mathrm{Ac})^3}, \tag{27a}$$

where Ac is the acceleration number defined as:

$$\mathrm{Ac}=\frac{|U-V|^2}{2\alpha\left|\dfrac{dV}{dt}\right|}. \tag{27b}$$

In a subsequent study, Odar [96] verified the accuracy of these coefficients over the suggested range of Re_s. Soon thereafter, Altaweel and Carley [97] performed independently their own experiments for the determination of Δ_A and Δ_H and derived different correlations for these coefficients. They also performed calculations on the importance of these terms and determined under what conditions the history terms were significant, [98].

The use of the semi-empirical expressions became widespread in several applications for the determination of the lateral dispersion of particles and for the transient reaction force exerted on the fluid by particles, bubbles, or drops. Based on these expressions, Shoneborn [99] explained and verified the experimentally observed retardation of spheres in oscillating fluids at very low frequencies.

While there have been several numerical studies that have used Eq. (26) as the fundamental form for the expression of the hydrodynamic force, there is no general agreement on the use of the correlations in Eqs. (27*a*) and (27*b*). The experiments by Karanfilian and Kotas [100], suggest constant values for Δ_A and Δ_H of 0.5 and 6, respectively, for the lower values of Re_s. The same authors attribute the effect of the acceleration number solely to the coefficient c_1 and suggest the correlation $c_1=c_{1s}(1+1/\mathrm{Ac})^{1.2}$, where c_{1s} is the value of the steady state drag coefficient. Temkin and Mehta [101] also suggested that the acceleration number affects only c_1 and recommended a different correlation for it. On the other hand, Tsuji et al. [102] in an extensive experimental study of gas-solid flows confirmed the expressions by Odar and Hamilton [95] and concluded that the accuracy of their correlations as given in Eq. (20) extends to Reynolds numbers up to 16,000.

Darwin [103] proposed an experimental method to measure independently the added mass coefficient of a bubble, by a determination of the deformation of a plane surface perpendicular to the trajectory of the bubble. Based on this method, Bataille et al. [104] measured the added mass coefficient and found out that it is consistently equal to 1/2 in the range $500<\mathrm{Re}_s<1000$, when some of the bubbles are not even spherical. Mei et al. [21], Rivero et al. [105], and Auton et al. [106] confirmed that the potential flow solution, which yields the value $\Delta_A=1$ for the coefficient of the added mass term is correct, and that neither the Reynolds number nor the acceleration number influence this term. These recent results call for the reinterpretation of the experimental data for the total hydrodynamic force that has resulted in the semi-empirical correlations.

The general practice of separating the transient force into three independent components and using the empirical values for Δ_A and Δ_H somehow was crowned with success (by this it is meant agreement with the experimental data) and became very popular in engineering calculations in the last 30 years. The reasons for this accuracy and popularity of the expression are the relative ease of calculations with the aid of computers and the close agreement of the results with experimental data. This agreement is due to the following reasons:

a. the semi-empirical equations have a sound experimental basis, that is, they are essentially correlations of experimental results, and,
b. the semi-empirical expressions have always been used in calculations to determine the total hydrodynamic force, and not any of its three parts.

It must be recalled that the pertinent experiments, from which the empirical coefficients emanate, measured the total hydrodynamic force on the sphere under various conditions. Then, by a series of assumptions and deductions, the experimentalist estimated the three parts of Eq. (26) and, hence, determined experimentally the three coefficients. Similarly, for any verification of the derived expressions that followed, the resulting equation was used as a single entity to always calculate the total hydrodynamic force and not any parts of it separately, and then to compare the results with other experiments, similar to the ones from which the force was determined in the first place. Because of this determination and verification of the results, it would have been rather surprising if close agreement between experiment and ''theory'' were not obtained. It appears that this fortuitous agreement, which is based on a circular argument, is the reason why the semi-empirical expressions are still considered accurate and used in some engineering calculations. The derived results for the total hydrodynamic force can be trusted within their range of applicability because they have a sound experimental basis.

Regardless of the perceived accuracy of the semi-empirical expressions, it is a fact that they are based on a form of the hydrodynamic force that was derived under conditions where the Reynolds numbers approach zero, but the expressions themselves were developed to be used at very high Reynolds numbers. A glance at Eqs. (1), (19), and (20*a*) will prove that the form of the function of the hydrodynamic force changes dramatically, when the Reynolds number is finite. Therefore, there is no a priori theoretical justification to using the functional form of expressions such as Eq. (26) for the total hydrodynamic force at higher values of Re_s. Any agreement of the semi-empirical expressions with experimental results is fortuitous and due to the fact that the semi-empirical expressions are essentially correlations of sets of experimental data. Therefore, when they are applied under similar conditions, they yield similar results. While using a semi-empirical equation, one has only to ensure that the range of validity of the coefficients in terms of Re_s and Ac covers the range of the calculations. However, if the conditions change, for example, if the frequency of variation of the fluid field is significantly different than the frequency of the experimental data, the semi-empirical expressions would fail. It is believed that differences in the conditions of the underlying experiments account for the manifest differences of the correlations proposed in [95,98,100].

It must be emphasized that the hydrodynamic force on a sphere is a single entity and not three different forces. For this reason there was never conducted (and it is not possible to conduct) a physical experiment, which would independently generate the values of the several individual terms for a semi-empirical equation, such as Eq. (26). With the development of numerical techniques, it is now possible to infer the value of these terms by separating the effect of the pressure term and of the steady-state results in the solution of the governing equations. Recent numerical studies by Chang and Maxey [25,26] have separated the pressure effect and computed the history term for a sphere in the cases of oscillatory and accelerated motion. These studies also cast doubts on the validity and accuracy of Eq. (26) when it comes to the behavior of the history term and do not support the decomposition of the total transient hydrodynamic force.

Kim et al. [107] developed a more recent version of a semi-empirical expression, based on numerical results rather than experimental data. They used the same process of decomposition of the hydrodynamic force into several components, and concentrated their attention to the history term. They used the standard drag coefficient curve for the steady state component, a coefficient equal to 1/2 for the added mass coefficient, a convolution integral for the usual history term and another function to account for any initial difference of the velocity between the fluid and the sphere. Thus, they derived an expression that applies to a stationary or oscillating fluid in the range $0<\mathrm{Re}_s<150$ and appears as follows:

$$m_s\frac{dV_i}{dt}=-\frac{1}{2}c_{D0}\pi\alpha^2\rho_f(V_i-u_i)|V_i-u_i|-\frac{1}{2}m_f\left(\frac{dV_i}{dt}-\frac{Du_i}{Dt}\right)$$
$$-6\pi\alpha\mu_f\int_{0^+}^{t}K(t-\tau,\tau)\frac{d}{d\tau}(V_i-u_i)d\tau-6\pi\alpha\mu_f K_1(t)$$
$$\times[V_i(0^+)-u_i(0^+)+V_i(0^-)-u_i(0^-)]+(m_s-m_f)g_i$$
$$+m_f\frac{Du_i}{Dt}, \tag{28}$$

where the functions K and K_1 are determined from series numerical data after ensuring that their limits at $\mathrm{Re}_s=0$ for low and high frequencies agree well with analytical and asymptotic solutions. Kim et al. [107] claim very good accuracy of their expression in the range $0<\mathrm{Re}_s<150$ and $0.2>\beta>0.005$. Given that accurate computations of the unsteady motion of a particle in high Reynolds numbers is a recently developed area, it is almost certain that several other semi-empirical expressions similar to the last equation will appear in the near future. Bagchi and Balachandar [108] essentially followed a similar approach and derived a semi-empirical equation based on their computational results.

In the case of heat transfer there are no known semi-empirical expressions to be applied to higher Peclet numbers under transient conditions. However, there are several experimental correlations for the steady-state heat transfer coefficients, such as Eq. (18*b*), which can be found in textbooks and treatises of the general subject of heat transfer, [78,109]. These correlations are analogous to the widely used experimental correlation for the steady-state drag coefficients.

It is apparent from the above that analytical solutions for the transient hydrodynamic force and the heat/mass transfer rates may only be obtained in the case of low Reynolds or Peclet numbers and this for a solid sphere only. Although these studies yield very good results on the form of the expressions for the hydrodynamic force and for the rate of heat transfer at finite but small values of the dimensionless numbers Re_s and Pe_s, and perhaps some guidance on the form of these expressions at higher Re_s and Pe_s, they do not provide any quantitative results that may be used in applications that pertain to higher values of these parameters. This only leaves numerical studies to provide answers as to the functional form of the hydrodynamic force and to the rate of heat transfer from a sphere at higher values of Re_s and Pe_s.

7.2 Numerical Results on the Hydrodynamic Force at Higher Re. Numerical (computational) studies are very specific to the exact values of the parameters used in the derivation of the results and do not provide as much insight as an analytical solution. However, at the present state of the art, computer capacity and numerical techniques are advanced enough to yield reliable results for the transient behavior of rigid as well as deformable spheres in infinite or bounded fluids. It is not the scope of this manuscript to cover the area of computational fluid dynamics as applied to the transport coefficients of the sphere, but a short discussion of certain numerical results, which provide an insight to the transient behavior of spheres, is appropriate. For a more in-depth analysis the reader is directed to the recent review articles by Matsumoto and Takagi [110] and Loth [44] that cover the numerical methods extensively.

At first, it must be mentioned that several of the recent analytical studies also contain a numerical component, [21], where some part of the problem was studied, or elucidated by a numerical computation. Secondly, there are several numerical studies, which provide answers to the steady-state hydrodynamic force and rate of heat transfer from a viscous or a solid sphere, with different

degrees of success and accuracy, [111–113]. The relevance and accuracy of the results of these earlier studies is discussed in three recent numerical studies on the steady-state heat transfer coefficient and drag coefficient for viscous spheres by Feng and Michaelides [114–116]. The latter studies use a novel numerical technique that allows one to extend the range of the numerical results to values of the parameters Re_s and Pe_s up to 1000. This value is close to the upper end of the practical limit, where some viscous spheres retain their spherical shape, [117].

Regarding the transient hydrodynamic force, Chang and Maxey [25,26] conducted a purely numerical study, based on a spectral method, for the oscillatory motion and for the accelerated motion of a single sphere in an infinite fluid domain up to $\mathrm{Re}_s=40$. The first study shows how important the transient effects are on the flow structure around the sphere, by comparing steady-state results with transient results at the same values of Re_s. It was observed that flow separation occurs in the decelerating portion of the flow field under oscillation even at values of Re_s below 20. In some cases the strongly decelerating flow completely detaches itself from the sphere and an inner reverse flow surrounds the sphere instantaneously. The corresponding steady-state results show that at these values of Re_s there is no separation. The flow separation and similar effects of the transient behavior observed in the numerical results affect considerably the transport coefficients of the sphere, both momentum exchange and heat transfer.

Chang and Maxey [25,26] also devised a way to separate the effect of the pressure on the hydrodynamic force and essentially separated the added mass component. They found out that, under both oscillatory motion and constantly accelerating or decelerating flow, this component is adequately represented by $\Delta_A=1$ in the ranges $0<\mathrm{Re}_s<40$ and $0.5<\mathrm{Sl}<10$. This is the exact value of the potential flow theory, which was first deduced by Poisson [1] and also appears in the Boussinesq-Basset expression (Eq. (1)). The correlation by Odar and Hamilton (Eqs. (27*a*) and (27*b*)), [95], yields the coefficient $\Delta_A=1$ only when $\mathrm{Ac}=0$. The results in [25] on the history term are also rather surprising: their computations show that in the case of oscillatory flow, the history term is adequately described by the Boussinesq-Basset expression, even at the high range of the Reynolds numbers examined. They concluded that, in this case, the results obtained by using Eq. (1) differ very little from the numerical results and, hence, there is no advantage in using the semi-empirical expression. They also found out in the case of the accelerating/decelerating flow that the Boussinesq-Basset expression adequately represents the numerical data in the initial stages of motion. However, in the final stage of the motion, the numerical results indicate that the kernel of the history integral decayed faster than $t^{-1/2}$ and that the rate of decay became exponential, except in the case of a sphere brought to rest where the decay rate was still algebraic but faster than $t^{-1/2}$.

The studies of Rivero et al. [105], Magnaudet et al. [118], and Chang and Maxey [25] also explain a flaw in the studies that resulted in semi-empirical expressions: For the decomposition of the experimental data most of these studies have stipulated that in sinusoidal flows the history term vanishes at phase angles equal to $\phi=\pi/4$ and $3\pi/4$. Based on this stipulation and given an expression for the steady-state term, a correlation for the added mass term was determined and, hence, another correlation for the history term was deduced from the residual of the total force. The results by Rivero et al. [105] and Chang and Maxey [25] show that the history component of the hydrodynamic force does not vanish at $\phi=3\pi/4$, but at a slightly lower phase angle. Therefore, the findings of the recent numerical studies cast further doubts on the validity of the decomposition by Odar and Hamilton [95], as well as of all the similar studies that used the same assumptions for the determination of the coefficients of semi-empirical expressions.

Among the other numerical studies for a single object, Chaplin [92] calculated the history forces on a stationary cylinder in a viscous fluid based on the asymptotic properties of the wake. The motions he considered are oscillatory motion, impulsive start and stop as well as reverse flow. He examined values of Re_s in the range 2 to 40 and found a qualitative agreement on the decay rates of the kernel with the results of Mei and Lawrence [119], although he points out that this agreement deteriorates in the high values of Re_s considered. Chaplin's results also show that, even for a cylinder, the history term of the hydrodynamic force finally decays as t^{-1}, $[t^{0.5}\log(t)]^{-1}$ and $t^{-0.5}$, in the cases of an impulsive start, stop, and reverse motion, respectively.

Kim et al. [120] examined the unsteady three-dimensional interactions between a single advected cylindrical vortex tube and a fixed spherical particle whose diameter is of the same order of magnitude as the initial diameter of the vortex. They also investigated the viscous flow interactions between a pair of vortex tubes advected by a uniform freestream and a spherical particle that is suddenly placed and held fixed in space. The values of Re_s in this study reach 100. The lift force on the sphere is calculated as well as the deviation of the rectilinear drag due to the action of the transverse force. Massudi and Sirignano [121] extended these results from a solid sphere to an evaporating droplet. This type of study is the first step towards understanding the two-way interactions between the small-scale turbulence and a sphere.

Given that the transient behavior of a single particle in a viscous fluid is complex, inter-particle interactions in a fluid are even more complicated and can only be examined numerically. Among these studies, Kim et al. [122] used a three-dimensional algorithm to obtain the drag and lift on two stationary spheres (placed close together) in a uniform fluid velocity. Chiang and Kleinstreuer [123] used a finite element code to determine the transport coefficients of three spheres in a linear array. The study by Feng and Joseph [124] demonstrates the complexity of the unsteady motion of several spheres in a quiescent fluid, even at creeping flow conditions. They found out that had the spheres been allowed to move freely, coalescence would have occurred and that the Nusselt number of the second and third spheres are greatly influenced by the wake shed by the leading sphere. Cheng and Papanicolaou [125] used an approach that is based on the analysis of periodic Green's functions and calculated the force on a periodic array of spheres in a viscous flow at small Re_s. Their analysis considers asymptotically, in the low limit, the effect of the concentration of the spherical particles in the flow.

7.3 Numerical Results on the Transient Heat Transfer. As with the case of momentum transfer, results for the transient heat/mass transfer at high Reynolds or Peclet numbers may only be derived by asymptotic or numerical methods. Abramzon and Elata [113] assumed a Stokesian velocity distribution around the sphere and solved numerically the energy transfer equations to derive results on the transient Nusselt number of spheres. Because the Stokesian velocity distribution implies $\mathrm{Re}_s \ll 1$ and, since $\mathrm{Pe}=\mathrm{Re}^*\mathrm{Pr}$, their results for high Pe are implicitly restricted to very low values of Pr ($\mathrm{Pr}=\mu_f c_f/k_f$). Similarly, Chiang and Kleinstreuer [126] used a known velocity profile and drag forces between the spheres to derive the steady-state heat and mass transfer coefficients for an array of three evaporating drops. Pozrikides [127] used a matched asymptotic expansion, obtained the double-periodic Green's function and used numerical computations to derive the rate heat transfer from a semi-infinite line of small evaporating particles. Balachandar and Ha [128] used a direct numerical simulation to address the effect of unsteadiness on the heat transfer at high Peclet and Reynolds numbers. They considered the processes of step temperature change in the temperature of the fluid and of the particle as well as a sinusoidal temperature change and performed computations up to $\mathrm{Re}_s=250$. They expressed their results in terms of an effective Nusselt number, and confirmed that at finite Pe_s the history term initially decays as $t^{-1/2}$, and at later stages of the processes it decays at a faster rate. In general, they observed that the behavior of the history term in the energy equation is very similar to its behavior in the equation of motion as described in the previous subsection.

7.4 The Effect of the History Term(s). It appears that the functional form of the history term is well known, and has a unique functional form only in the case of creeping flow conditions. At finite Re_s or Pe_s the functional form of the history term depends on the actual transient process of temperature or velocity change. In many cases the functional form of the history term in both the equation of motion and the heat transfer equation is only known asymptotically, [22–24,129]. For this reason, at finite Re_s or Pe_s it is not easy to determine the effect of the history term on the magnitude of the hydrodynamic force with a great deal of accuracy. However, all researchers agree that the history terms decay faster than the creeping flow rate of $t^{-1/2}$ when Re_s and Pe_s are finite. Therefore, the influence of the history term on the magnitude of the hydrodynamic force or on the heat transfer would be weaker at finite Re_s or Pe_s than at creeping flow conditions.

The main reason for the interest on the effect of the history term is that this term is difficult to compute, as was shown in Section 4.3. If this term does not contribute substantially to the total hydrodynamic force or heat transfer, then neglecting the term and its effects simplifies and shortens repetitive computations considerably. The a priori knowledge of the significance of the history terms in Lagrangian computations is particularly important in cases where the nature of the problem examined requires the computation of trajectories of a very large number of particles, [130]. Such repetitive computations can be simplified considerably if the history term may be neglected.

Hjemfelt and Mocros [131] were the first to compute the effect of the several parts of the hydrodynamic force for a particle in a turbulent flow field. They parametrized their data with respect to a dimensionless parameter related to the Stokes number, $(18\beta St)^{-1/2}$ and concluded that the effect of the history term as well as all the other transient terms may be a priori neglected only at very low values of the density ratio $\beta=\rho_f/\rho_s$. Their results also indicate that the history term may be neglected when the Stokes number and the density ratio satisfy the condition $St < 2/9^*\beta^{-1/2}$. Vojir and Michaelides [61] computed the effect of the history term during Lagrangian computations of the particle motion in simulated sinusoidal and randomly varying velocity fields. They concluded that the effect of the history term is significant in the range $0.7<\beta<0.002$ as well as at very high values of the Stokes number ($St>10$) or, equivalently, low values of the Strouhal number. They also found out that the effect of the history term on the total distance traveled by a particle is by far more significant when the fluid velocity field varies monotonically than when the fluctuations are random. Druzhinin and Ostrovsky [132] also conducted a numerical study of the effect of the history term in a rotating flow and concluded that the history term reduces the drift of the particles and modifies their rotation in the azimuthal direction. The experimental and numerical study by Domgin et al. [133] concluded that the history term may be neglected for bubbly flows, and that the decay rate of the kernel proposed by Mei and Adrian [22], t^{-2}, agrees slightly better with the experimental results than the original decay rate $t^{-1/2}$, which was proposed in [5] and [7]. The study by Domgin et al. [133] also confirmed the statistical results in [61]. Other recent studies by Launey and Huillier [134] and Abbad and Souhar [135] confirm the fact that the history terms may be neglected when either the Stokes number is high or the density ratio β very low.

Given that several fluid dynamics experimental techniques, such as the LDV and the PIV methods, are based on the assumption that the velocity of very small particles is equal to the local velocity of the fluid, Thomas [136] conducted a numerical study to determine the influence of the history term on the statistical quantities that emanate from the LDV velocity data. He used essentially the creeping flow equation of motion of particles without the gravitational term and concluded that the inclusion of the history term in the calculations has a considerable influence on the experimentally observed rms velocity deviation. He also concluded that small, light particles are better suited as seeding in LDV studies. In studies that use very light particles, a correction for the gravity/buoyancy is necessary for the interpretation of the velocity field data.

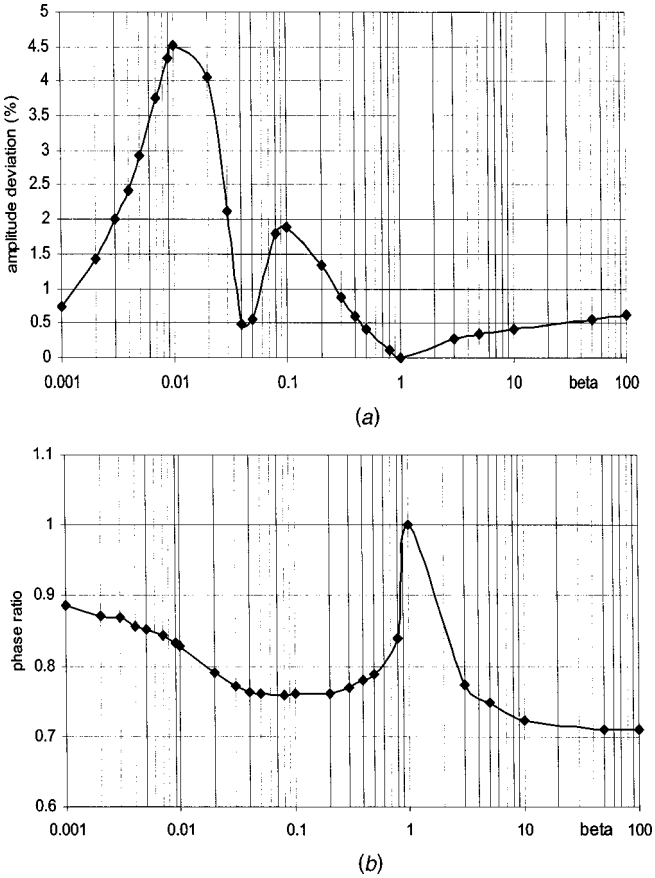

Fig. 1 The effect of the history term on the amplitude (*a*) and phase lag (*b*) of the temperature of a rigid sphere

Regarding the effect of the history terms on the heat transfer from a sphere, Gay and Michaelides [137] conducted a thorough numerical study to compute the effect of the history term on the heat transferred to a sphere at creeping flow conditions and considered three processes: (a) a step variation of the fluid temperature; (b) a ramp change of the fluid temperature; and, (c) a sinusoidal variation. The main parameters for this study are the volumetric heat capacity ratio $\beta'=\rho_f c_f/\rho_s c_s$ and the Stokes number, St. They concluded that the history term is of importance in the computations of the transient heat flux when the ratio of the volumetric heat capacities, β', is between 0.002 and 0.5. This is the range for liquid-solid flows and droplet flows in heavier gases. They also found almost no effect of the history term on the heat transfer for bubbles ($\beta'>10$). Typical results of these computations for a sinusoidal variation of the fluid temperature field are depicted in Figs. 1(*a*) (amplitude ratio) and 1(*b*) (phase difference). Also, Michaelides and Feng [138] conducted a study for creeping as well as low Reynolds number flow and heat transfer. They determined the fractional error associated with neglecting the history terms as a function of the particle's Stokes number, St. Some of the results of [138] are depicted in Fig. 2, where it shown that the history term plays an important role at intermediate Stokes numbers. This occurs because at low St the particles follow almost exactly the fluid streamlines and at high St the fluid has very little impact on the flow and the heat transfer from the particle. The results of [137,138] show that neglecting the history term in the energy equation of a rigid sphere leads to an underes-

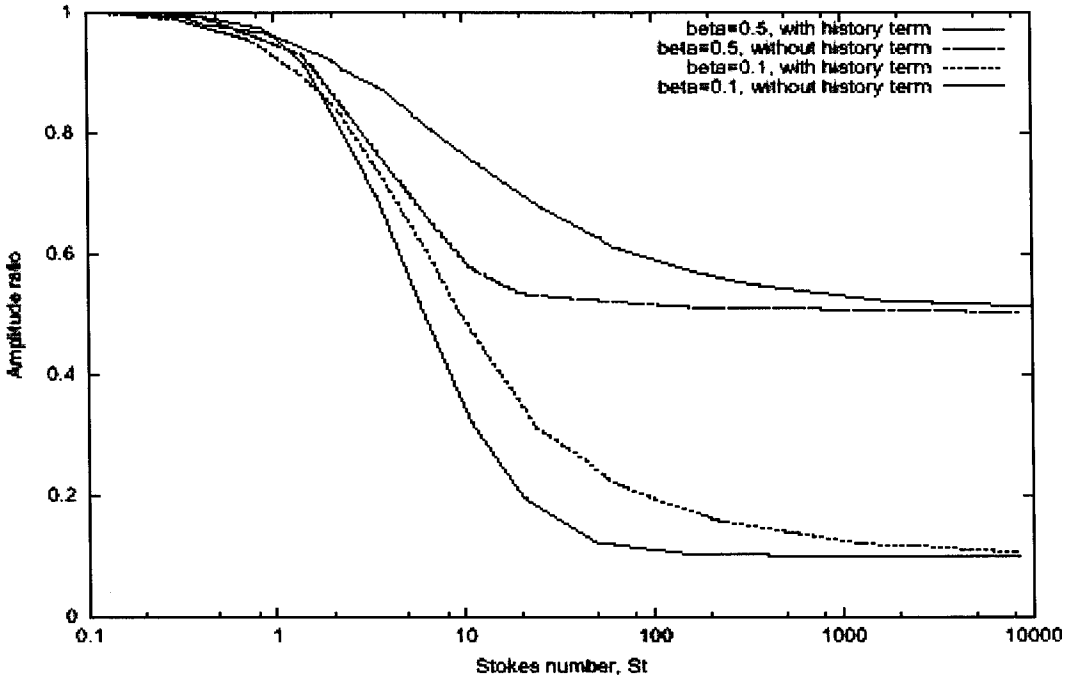

Fig. 2 The effect of the Stokes number on the heat transfer from rigid particles with and without the history term

timation of the instantaneous rate of heat transfer by 10–15 percent and that this error may reach up to 35 percent in extreme cases.

7.5 Steady-State Expressions. The Effect of Other Parameters. It is apparent from the treatment of the transient terms, that in many practical applications and most engineering calculations on the flow and heat transfer from particles, bubbles, and drops, it is sufficient to know only the steady state part of the sphere-to-fluid interactions. The steady-state part of the transient expressions is often the dominant part of the hydrodynamic force or rate of heat transfer and, hence, its accurate determination is critical to the accuracy of the computations. In this case, it is sufficient for a practicing engineer to know the steady-state drag coefficient or the convective heat transfer coefficient in order to perform calculations, such as the sizing of plant components or the design of chemical reactors. For this reason, a great deal of experimental work in the past 60 years was spent on the task of determining the steady-state component of the transport coefficients. The results of the experimental studies are usually empirical correlations of expressions for the drag coefficient or for the Nusselt number.

An excellent compilation of all the experimental work that was performed in the 1960s and 1970s may be found in Happel and Brenner [48] and Clift et al. [47]. A ''universal'' curve for the steady-state drag coefficient and several recommended expressions, emanating from experimental data or numerical studies and spanning the range $0<\mathrm{Re}_s<4000$, may be found in Clift et al. [47] as well as several other similar monographs and texts [48,139]. At low Reynolds numbers most of these expressions yield the equations derived by Stokes [4] and Oseen [11]. At higher Re_s most correlations resemble the power-law expansion by Schiller and Nauman [76]. It must be pointed out that, when Re_s is greater than 20, a visible wake is formed behind the sphere that grows in size with the Reynolds number. As mentioned in Section 5, when $\mathrm{Re}_s>400$ this wake becomes unstable and vortices are shed behind the sphere, thus making any motion of the sphere unsteady. Despite of this unsteadiness in the motion, it has been confirmed that the universal curve for the drag coefficient, which is mostly derived from experimental data, leads to reasonably accurate calculations for time-averaged results, such as the average velocity and total distance traveled by a particle.

The effects of irregular particle shape (nonsphericity), flow turbulence, flow compressibility, etc., are often given as corrections to this universal drag coefficient curve in the form of functions of the turbulence intensity, eccentricity, or Mach number:

$$c_D(\overline{u'^2},\varepsilon,\mathrm{Ma}\ldots)=c_D f_1(\overline{u'^2}) f_2(\varepsilon) f_3(\mathrm{Ma})\ldots. \tag{29}$$

For example, Carlson and Hoglund [140] derived the following empirical relationship for the function $f_3(\mathrm{Ma})$, which is used in many computations pertaining to particles in shock waves and other compressible flow fields:

$$f_3(\mathrm{Ma})=\frac{1+\exp\left(-\dfrac{0.427}{\mathrm{Ma}^{4.63}}-\dfrac{3}{\mathrm{Re}_s^{0.88}}\right)}{1+\dfrac{\mathrm{Ma}}{\mathrm{Re}_s}\left[3.82+1.28\exp\left(-1.25\dfrac{\mathrm{Re}_s}{\mathrm{Ma}}\right)\right]}, \tag{30}$$

where Ma is the Mach number based on the relative velocity of the particle with respect to the fluid. It appears that, for small particles, the drag coefficient decreases due to a rarefaction effect, while, for large particles, it increases because of the associated compressibility effects.

When using these empirical expressions for the functions f_1, f_2, f_3, etc., one must be aware that they are derived from a limited number of experimental data or, more recently, from numerical studies. Therefore, their accuracy is strictly limited to the range of conditions prescribed in the experimental study from which these functions originate.

As with the case of the equation of motion, most practical studies on the transient heat transfer from spheres use a quasi-steady approach, and a function for the steady-state heat transfer coefficient, which originate from experimental or numerical studies. The analytical result for conduction or creeping flow conditions, first derived by Fourier [27], may be written in the form that usually appears now as $\mathrm{Nu}=2$. Acrivos and Taylor [30] derived asymptotic solutions that are applicable at the limit of creeping flow as well as at small but finite Pe_s. The final forms of their expressions are as follows:

$$\mathrm{Nu}=0.991\mathrm{Pe}_s^{1/3}+0.922 \tag{31}$$

for Stokesian flow ($\mathrm{Re}_s \ll 1$) and

$$\mathrm{Nu}=0.991\mathrm{Pe}_s^{1/3}\left(1+\frac{1}{16}\mathrm{Re}_s+\frac{3}{160}\mathrm{Re}_s^2\ln\mathrm{Re}_s+O(\mathrm{Re}_s^2)\right) \tag{32}$$

for steady-state flows at small but finite Reynolds numbers.

At large Reynolds or Peclet numbers, the experimental studies by Ranz and Marshall [141] and Whitaker [76] resulted in the following two correlations which are widely used in engineering calculations and the design of systems:

$$\mathrm{Nu}=2.0+0.6(\mathrm{Re}_s)^{1/2}(\mathrm{Pr}_s)^{1/3}, \tag{33a}$$

and

$$\mathrm{Nu}=2+(0.4\,\mathrm{Re}_s^{1/2}+0.06\,\mathrm{Re}_s^{2/3})\mathrm{Pr}^{0.4}. \tag{33b}$$

These correlations are applicable up to $\mathrm{Re}_s=10^4$.

The asymptotic study by Polyanin [142] provides a plethora of asymptotic results on the heat and mass transfer coefficients of spheres at low Pe_s, including cases where heat and mass transfer take place simultaneously, combustion or evaporation/condensation processes, for example. Also, the experimental results by Yuge [143] are being widely used in convective heat transfer applications. Corrections to this equation for the effect of the eccentricity of the sphere and the flow turbulence are known to exist or may be derived directly from experimental studies, such as the ones by Bankoff and Mason [144], Gilbert and Angelino [145], or Hayward and Pei [146]. In analogy with the corresponding studies for the expressions of the drag coefficient, the results of these studies would be expressions of the Nusselt number that have the following functional form:

$$\mathrm{Nu}(\overline{u'^2},\varepsilon,\mathrm{Ma}\ldots)=\mathrm{Nu}_0 f_1(\overline{u'^2})f_2(\varepsilon)f_3(\mathrm{Ma})\ldots. \tag{34}$$

8 The Effects of Finite Viscosity or Conductivity of the Sphere

8.1 Transient Expressions. Most of the results for the hydrodynamic force and the heat transfer mentioned in the previous sections pertain to a rigid sphere or a sphere with viscosity much greater than the viscosity of the surrounding fluid ($\mu_s/\mu_f \gg 1$). Analytical solutions pertaining to the other limit of the viscosity ratio, that of inviscid bubbles, $\mu_s/\mu_f \ll 1$, have also been derived analytically in the past by Chen [147], Morrison and Stewart [70], Lhuillier [148], and Leal [34]. Auton et al. [106] studied the effect of rotation on the transient motion of an inviscid sphere, while Drew and Lahey [149,150] examined the added mass component and the lift force induced on an inviscid sphere in a rotating and a straining flow field. Mei et al. [151] conducted an analytical/numerical study on the history term of the hydrodynamic force acting on a spherical bubble and derived results, which were later confirmed by an experimental investigation by Park et al. [152].

In an analogous manner, most of the heat transfer studies, which pertain to the steady-state heat transfer coefficients, have been derived for cases where $k_s/k_f \gg 1$ or $k_f/k_s \gg 1$. Under these conditions, the problems of momentum and energy transfer have only one significant characteristic time scale, which is based on the viscosity or conductivity of the surrounding fluid. In this case, the solution of the governing equations can be achieved by well-established exact or asymptotic mathematical methods as was shown in Sections 4 and 5.

When the viscosity or conductivity of the sphere is comparable to the viscosity or conductivity of the fluid, the Navier-Stokes and the energy transfer equations must be applied to the two fluid domains which are inside and outside the sphere and are depicted in Fig. 3. Hence, for a viscous or conducting sphere there are two characteristic timescales to the momentum or energy transfer problems:

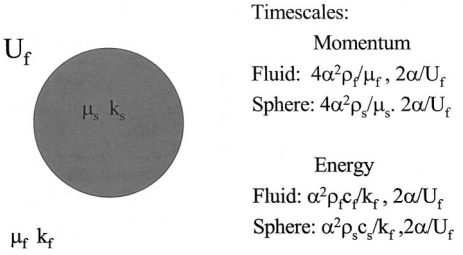

Fig. 3 Spatial domains and timescales in the case of a viscous sphere

a. the time scale of momentum or energy transfer inside the geometrical domain of the sphere, and
b. the time scale of momentum or energy transfer outside the geometrical domain of the sphere.

Because of this, an analytical solution of the governing equations for a viscous sphere is impossible to derive, even in the simplest case of creeping flow. Chisnell [153] recognized this fact and obtained asymptotic solutions for the velocity of drops immediately after the commencement of the process (short time domain) and long after the commencement of the motion process (long time domain). Full analytical solutions in this case may only be obtained not in the time domain but in the Laplace or the Fourier domain. Sy and Lightfoot [154] attempted to derive a closed-form solution for the transient hydrodynamic force in the case of a sphere, but applied wrongly the velocity boundary condition on the interface. As a result they derived a final expression, which is erroneous. The boundary conditions and final expression of this study were repeated in an otherwise very informative monograph by Kim and Karila [35]. Galindo and Gerbeth [155] were the first to derive a correct expression for the hydrodynamic force on a viscous sphere under creeping flow conditions in the Laplace or the Fourier domain, which is as follows:

$$\overline{F_i}=-6\pi\alpha\mu_f[\overline{V_i}-\overline{u_i}]\left\{\frac{\chi_f^2}{9}+(\chi_f+1)-\frac{(\chi_f+1)^2 f(\chi_s)}{[\chi_s^3-\chi_s^2\tanh(\chi_{ss})-2f(\chi_s)]\lambda+(\chi_f+3)f(\chi_s)}\right\}, \tag{35}$$

where the overbar denotes Laplace domain functions and χ represents the two dimensionless timescales in the Laplace domain:

$$\chi_f=\sqrt{\frac{s\alpha^2}{\nu_f}} \quad \text{and} \quad \chi_s=\sqrt{\frac{s\alpha^2}{\nu_s}} \tag{35a}$$

and the function f(χ) is as follows:

$$f(\chi)=(\chi^2+3)\tanh(\chi)-3\chi. \tag{35b}$$

Michaelides and Feng [20] performed a similar study that included the effect of the viscosity ratio, $\lambda=\mu_s/\mu_f$, as well as allowed for the existence of finite velocity slip on the surface of the sphere. Their result in the case of no-slip at the interface is an expression, which is identical to Eq. (35). An expression similar to the Maxey-Riley equation may be derived from Eq. (35) at the limit $\lambda\to\infty$, while an expression identical to the one derived in [70] for an inviscid bubble may be derived at the opposite limit, $\lambda\to 0$. One of the unexpected results of [20] is that the same expression for the transient hydrodynamic force that applies to an inviscid bubble also applies to a sphere of finite viscosity, $\lambda>0$, with perfect slip at the interface. This leads one to conclude that if extremely small particles (nanoparticles) are to be modeled as a continuum with finite velocity slip allowed at their interface with a fluid, then the values of their drag coefficients would be between the values for the drag coefficients of bubbles and the drag coef-

ficients of rigid particles. Asymptotic solutions of Eq. (35) have also been derived at short as well as long times from the inception of the motion of the sphere. The long-time transient solutions are independent of the internal viscosity of the sphere because any transient effects have dissipated in the finite geometrical domain within the radius of the sphere.

Regarding the heat transfer from a sphere whose conductivity is of the same order of magnitude as the conductivity of the fluid (that is, the Biot number is neither close to zero nor approaching infinity), Feng et al. [156] proved that, because of the existence of the two time scales, a closed-form analytical solution in the time domain cannot be derived in the time domain, even under the creeping flow conditions ($Pe_s \ll 1$). In this case, the rate of heat transfer to the sphere in the Laplace domain as follows:

$$\overline{Q} = -4\pi\alpha k_f \frac{f'(\chi_s')}{[f'(\chi_s') + \sigma(1+\chi_f'\alpha)\sinh(\chi_s' R)]} \left[(1+\chi_f'\alpha)\overline{T_f^0}(\mathbf{x}=0) + \left(\frac{1}{2} + \frac{1}{6}\chi_f'\alpha\right)\alpha^2\nabla^2\overline{T_f^0}(x=0) \right] + \left[\frac{(1+\chi_f'\alpha)}{s} T_s(0,0) + \frac{\alpha^2}{6s}(\nabla^2 T_p)(0,0) \right] + \frac{\alpha k_p (1+\chi_f'\alpha)}{s[f'(\chi_s') + \sigma(1+\chi_f'\alpha)\sinh(\chi_s'\alpha)]} \times \int_{V_s} \nabla T_p(\mathbf{x},0)\cdot\nabla\left[\frac{\sinh(\chi_s' r)}{r}\right] dV, \tag{36}$$

where σ is the ratio of the thermal conductivity ($\sigma = k_f/k_s$) and the variables χ_f' and χ_s' are the dimensionless variables analogous to those of Eq. (35*a*), defined in terms of the energy diffusivity of the sphere:

$$\chi_f' = \sqrt{\frac{s\rho_f c_f}{k_f}} \quad \text{and} \quad \chi_s' = \sqrt{\frac{s\rho_s c_s}{k_s}}. \tag{36a}$$

The function $f'(\chi)$ is analogous to $f(\chi)$ above and is defined as

$$f'(\chi) = \chi\alpha\cosh(\chi\alpha) - \sinh(\chi\alpha). \tag{36b}$$

A glance at Eqs. (35) and (36) shows that, as in the case of the spheroids, there are several analogies in the expressions of the momentum and energy equations, but not a strict similarity that can be used in formal calculations. Thus, one has to calculate independently the hydrodynamic force and the heat flux from viscous spheres.

It must be pointed out that, in the special cases when the analytical transformation of Eqs. (35) and (36) onto the time domain can be accomplished, several history terms appear that are different than the typical history term of Eq. (1) in their functional form as well as the details of their kernels. Yang and Leal [157], Galindo and Gerbeth [155] and Michaelides and Feng [20] have derived several of these terms. The functional form, kernels and other parameters of these history terms are significantly different from the typical history term of Eq. (1). This leads to the conclusion that the history term emanating from the Boussinesq-Basset expression is a special case, which applies only to the restricted conditions underlying its derivation, and that there is a group of history terms that appear when one or more of the restrictions applied to the Basset-Boussinesq theory are relaxed.

8.2 Steady-state Expressions for the Hydrodynamic Force. Given the virtual impossibility for analytical solutions to provide simple working expressions for the hydrodynamic force and heat transfer coefficient of a viscous sphere and the fact that for many practical applications a knowledge of the steady state part of these expressions is sufficient for engineering calculations and design work, analytical, experimental, and numerical studies have filled this void and have provided us with sufficiently accurate expressions and data on the transport coefficients of viscous spheres (bubbles and drops). Two of the earlier analytical studies on this subject are those by Hadamard [158] and Rybczynski [159]. These studies resulted in the following expression for the drag coefficient, which is valid at creeping flow conditions ($Re_s \ll 1$):

$$c_D = \frac{8}{Re_s}\left(\frac{3\lambda+2}{\lambda+1}\right). \tag{37}$$

This expression yields the Stokes law for a solid particle, $c_D = 24/Re_s$ at $\lambda\to\infty$ and $c_D = 16/Re_s$ for an inviscid bubble at $\lambda\to 0$. At the other end of the spectrum, when $Re_s \gg 1$, an asymptotic solution by Happer and Moore [160] yields the following expression for the drag coefficient of an inviscid sphere, which applies to the flow of spherical bubbles at high Reynolds numbers:

$$c_D = \frac{48}{Re_s}\left(1 + \frac{3}{2}\lambda\right). \tag{38}$$

The hydrodynamic force on all objects depends very much on their shape, and viscous spheres are deformable and do not retain their spherical shape under all flow conditions. Therefore, a key question in the motion of viscous spheres in fluids is whether or not they maintain their spherical shape at higher Reynolds numbers. The subjects of the deformation of viscous spheres at higher Reynolds numbers as well as the trajectory oscillations that result from this deformation have been well studied experimentally and computationally, [36,161–168]. Also, the formation, shape, and size drops are reviewed in a recent article, [169]. In general, the shape of a viscous sphere depends on the Reynolds and Bond (or Weber) numbers, and the resulting shape is one of the primary variables that determines the total transient or steady-state hydrodynamic force, as well as the rate of heat transfer. When viscous spheres depart from their spherical shape, they become oblate spheroids (drops) or develop a hemispherical shape (bubbles) that may grow to become Taylor bubbles, which are bullet shaped.

The answer to the question of whether or not a drop or a bubble maintains its spherical shape at high Reynolds numbers has been given in the past by empirical data and more recently by numerical studies: The experimental results by Winnikow and Chao [117] on the free fall and rise of drops in liquids show that a liquid drop will remain spherical when the dimensionless Bond number, Bo, is less than or equal to 0.2; that is, when

$$Bo = \frac{4g\alpha^2|\rho_s - \rho_f|}{\sigma_s} \leq 0.2, \tag{39}$$

where σ_s is the surface tension of the sphere. The experimental work by Winnikow and Chao [117] shows that drops of m-nitrotoluene in water ($\lambda = 2.2$) with $d = 3.1$ mm remain spherical at $Re_s = 506$. According to the criterion $Bo < 0.2$, simple calculations show that water droplets in air will maintain their spherical shape at values of Re_s up to 470. In the case of substances with high surface tension such as liquid metals, the corresponding Re_s would be much larger, up to 1150 for mercury droplets in air. It must be pointed out that Loth [44] prefers the criterion $Bo < 0.14$ for spheres to retain their shape, which is based on the experimental study by Garner and Lihou [170]. The adoption of this criterion implies that water droplets in air maintain their spherical shape up to $Re_s = 395$ and mercury droplets in air maintain their spherical shape up to $Re_s = 1000$. Regardless of the value used in the Bond number criterion, the fact remains that viscous drops retain their spherical shape at relatively high values of Re_s and, therefore, the knowledge of their transport coefficients up to these high values is necessary in some computations.

There are several numerical studies on the drag coefficient and heat transfer coefficient for viscous bubbles or drops that retain their spherical shape. One of the first such studies is by LeClair and Hamielek [171], who used a finite difference technique to compute the drag coefficients of drops at relatively low values of Re_s. Rivkind et al. [112] Rivkind and Ryskin [172] and Oliver and Chung [173] used similar numerical techniques and extended the range of Re_s for the drag coefficients of viscous spheres to approximately 100. Beyond this value of Re_s it is known that a

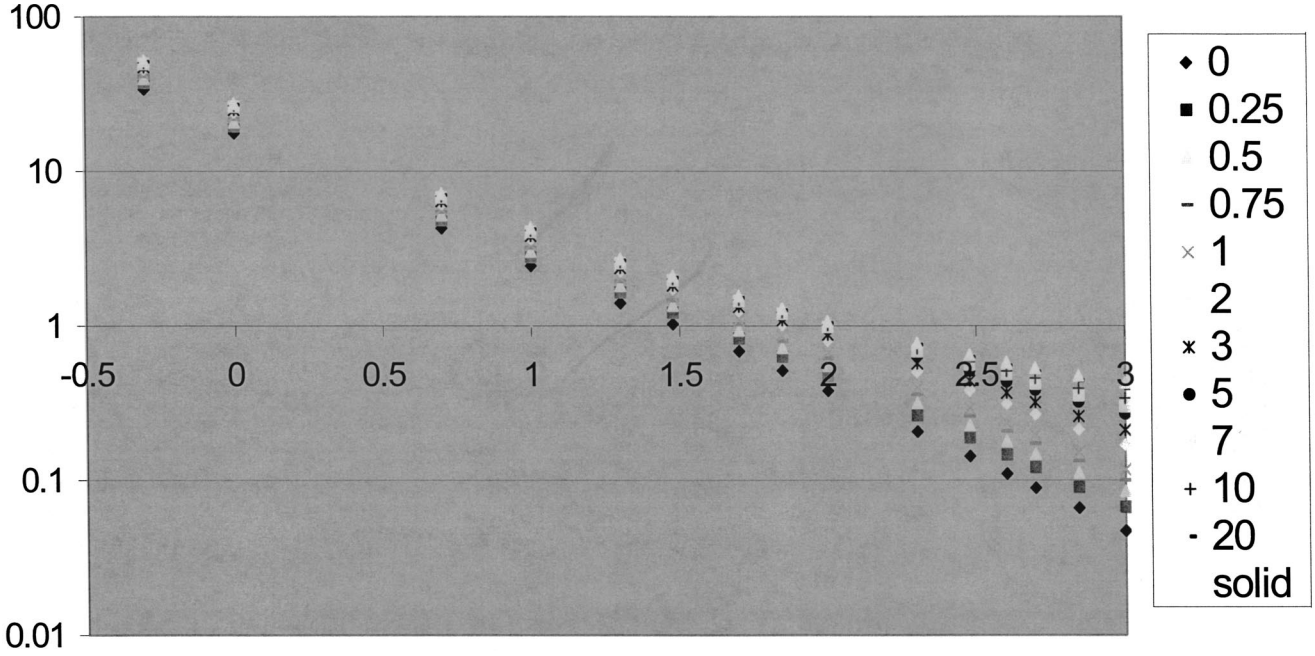

Fig. 4 Drag coefficients of viscous spheres

boundary layer is formed at the exterior of the sphere. The capture of the effects of this boundary layer requires a different technique or a hybrid type of computational grid. Feng and Michaelides [116] used faster computers and a hybrid grid to capture the outside boundary layer for solid and viscous spheres and thus conducted computations up to $\mathrm{Re}_s=1000$. Their results are shown pictorially in Fig. 4, where it is observed that there are several regularities and trends of the numerical data that would lead to accurate empirical correlations which are useful in repetitive engineering calculations. These correlations of the numerical data in terms of the parameters Re_s and λ are briefly summarized here:

$$c_D(\mathrm{Re}_s,\lambda)=\frac{2-\lambda}{2}c_D(\mathrm{Re}_s,0)+\frac{4\lambda}{6+\lambda}c_D(\mathrm{Re}_s,2) \quad \text{for } 0\leqslant\lambda\leqslant 2, \quad \text{and} \quad 5<\mathrm{Re}_s\leqslant 1000, \tag{40a}$$

and

$$c_D(\mathrm{Re}_s,\lambda)=\frac{4}{\lambda+2}c_D(\mathrm{Re}_s,2)+\frac{\lambda-2}{\lambda+2}c_D(\mathrm{Re}_s,\infty) \quad \text{for } 2\leqslant\lambda\leqslant\infty, \quad \text{and} \quad 5<\mathrm{Re}_s\leqslant 1000 \tag{40b}$$

where the functions $c_D(\mathrm{Re}_s,0)$, $c_D(\mathrm{Re}_s,2)$, and $c_D(\mathrm{Re}_s,\infty)$ are given by the following expressions:

$$c_D(\mathrm{Re}_s,0)=\frac{48}{\mathrm{Re}_s}\left(1+\frac{2.21}{\sqrt{\mathrm{Re}_s}}-\frac{2.14}{\mathrm{Re}_s}\right) \tag{41a}$$

$$c_D(\mathrm{Re}_s,2)=17.0\,\mathrm{Re}_s^{-2/3} \tag{41b}$$

and

$$c_D(\mathrm{Re}_s,\infty)=\frac{24}{\mathrm{Re}_s}\left(1+\frac{1}{6}\mathrm{Re}_s^{2/3}\right). \tag{41c}$$

The expressions for $c_D(\mathrm{Re}_s,0)$ and $c_D(\mathrm{Re}_s,\infty)$ in the above expressions are routinely used correlations for the drag coefficients of bubbles and solid particles. Expression (41*b*) is a simple correlation of the computational results that are shown in Fig. 4 for $\lambda=2$.

In the low-values range of Re_s, which is not covered by the above expressions, the following expression is recommended:

$$c_D=\frac{8}{\mathrm{Re}_s}\frac{3\lambda+2}{\lambda+1}\left(1+0.05\frac{3\lambda+2}{\lambda+1}\mathrm{Re}_s\right)-0.01\frac{3\lambda+2}{\lambda+1}\mathrm{Re}_s\ln(\mathrm{Re}_s) \quad 0\leqslant\mathrm{Re}_s\leqslant 5. \tag{42}$$

This expression reduces to the Haddamard-Rybszynski solution at $\mathrm{Re}_s=0$ and to the Oliver and Chung [173] expression for small but finite Re_s. The form of the last term of Eq. (42) is derived from the natural next-order expansion in terms of Re_s. Although the intention was to use this expression up to $\mathrm{Re}_s=5$, it was actually concluded that the last equation accurately represents the numerical results up to $\mathrm{Re}_s=20$. It must be pointed out that the standard deviation of the correlations (40), (41), and (42) from the numerical results is 2.1 percent and the maximum error is 4.6 percent.

The drag coefficient of inviscid spheres (bubbles) is of particular importance in practical applications, such as boiling and aeration. It is generally accepted that surfactants and material impurities play a very important role in the determination of the drag coefficient of bubbles. The drag coefficient of clean spherical bubbles is often approximated by the expression [174]

$$c_{D0}=\min\left(\frac{16}{\mathrm{Re}_s}(1+0.15\,\mathrm{Re}_s^{0.687}),\frac{48}{\mathrm{Re}_s}\right), \tag{43}$$

which is consistent with the previous correlations when $\lambda\to 0$. When the bubbles become bigger, their shape is distorted and they form hemispheres. Consequently their drag coefficient depends strongly on the surface tension, which is a determinant of their shape. In this case the drag coefficient is independent of the Reynolds number and may be given by the expression:

$$c_D=\frac{8}{3}\frac{Eo}{Eo+4}, \tag{44}$$

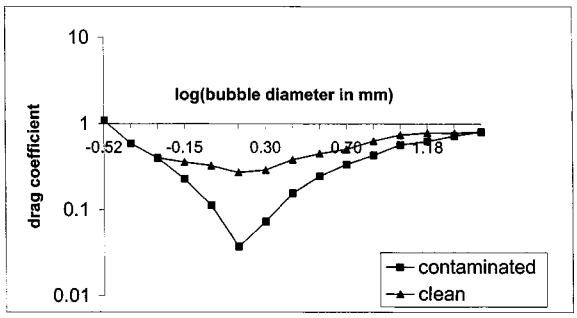

Fig. 5 Drag coefficients for bubbles as a function of their diameter

which is valid for fairly large hemispherical bubbles (up to 3 cm diameter). However, it was observed in many studies that the presence of even traces of surfactants or other impurities in the water causes an increase in the value of the drag coefficient as it is shown in Fig. 5. It is generally accepted that when even traces of surfactants appear in the system, the drag coefficient of a bubble may take any value in the enclosed region of the three curves that appear in Fig. 5, [34,47].

Two recent experimental studies on the subject have provided evidence that impurities alone do not cause this change in the shape of a bubble and the modification of the drag coefficient. The experimental study by Tomiyama [174] claims that the method of a bubble's initial release from the nozzle also determines its drag coefficient and the trajectory it follows. When bubbles are released with small initial deformation, their shape remains close to spherical, their drag coefficient is higher and their motion is rectilinear or zigzag on a plane. However, when the bubbles are released with high initial deformation, their shape continues to be ellipsoidal with high aspect ratio, their drag coefficient is higher and their motion is helical or rectilinear. In a similar study, Wu and Gharib [175] also found that the initial method of the release of bubbles (whether they are released from a narrow or a wide tube) plays a role in the eventual shape, the rise velocity, and the drag coefficient. Thus, Wu and Gharib [175] were able to observe spherical bubbles of large diameters in clean water systems that behaved as bubbles with surfactants. Prosperetti [176] has named this phenomenon ''the Leonardo effect'' and has put forward the following conjecture for its explanation: Both types of bubbles when released from their tubes are contaminated. However, the shape oscillations that occur after detachment are strong enough to clean the bubble surface from its contaminants. In most practical cases, the water contains a sufficient concentration of contaminants for the bubble surface to become immediately contaminated. However, in the case of a very pure system, the recontamination process of the surface is so slow that the bubble remains clean for the finite duration of the experiment. A consequence of this conjecture is that the large spherical bubbles created by this method are unstable and, given sufficient time, will flatten. Since this is a problem with many practical applications and great intellectual curiosity, it is expected that it will attract a number of studies in the near future.

8.3 Steady-State Expressions for the Heat Transfer Coefficient of Viscous Spheres. The study by Bowman et al. [177] was among the first to point out the differences in the heat/mass transfer from solid and viscous spheres. Since most of the practical problems of the heat and mass transfer from drops and bubbles are related to processes such as boiling, condensation, evaporation, or combustion, the mass transfer at the boundary of the sphere plays an important role in the determination of the rate of heat transfer. For this reason an evaporation parameter, which is sometimes called the Spalding transfer number, B, plays an important role in the heat and mass transfer expressions from drops and bubbles:

$$B=\frac{h^{\infty}-h^{\alpha}+h_{\mathrm{comb}}}{h_{fg}} \tag{45}$$

where h is the enthalpy, the superscript α denotes conditions at the radius of the sphere, the superscript ∞ conditions at infinity, h_{fg} is the latent heat of vaporization, and h_{comb} is the heat of combustion. In many studies the effects of the transport coefficients of viscous spheres are given in terms of the transport coefficients of solid spheres with corrections in terms of B, obtained from experimental, analytical, or numerical data. For example, Abramzon and Sirignano [178] expressed the Nusselt number in the case of evaporating drops as follows:

$$\mathrm{Nu}=2\frac{\log(1+B)}{B}\left(1+\frac{K}{2}\frac{\mathrm{Re}^{1/2}\,\mathrm{Pr}^{1/3}}{f(B)}\right) \tag{46}$$

where K is a constant and $f(B)$ is a function of B that can be correlated from the numerical results of Abramzon and Sirignano [178]. In the case $B=0$, the above equation yields the expression for the Nusselt number of a solid sphere (Eq. (33*a*)). Similar expressions have appeared for the Sherwood number, which is used in cases of mass transfer from bubbles or drops, as well as for the drag coefficient. More details on the derivation and the form of these functions as well as the effects of the phase change on the transport coefficients of bubbles and drops may be found in Chigier [179,180], Chigier and McGreath [181], Crespo and Linian [182], Clift et al. [47], Law [183], Williams [184], and Sirignano [36,40].

If mass exchange is negligible, its effect may be isolated in the functions of the Spalding coefficient, B, as in the last expression, or, if the effect of the mass transfer from the sphere is negligible on the heat transfer process (e.g., in the case of heating of subcooled drops) one needs to have accurate expressions for the heat transfer from a viscous sphere that does not exchange mass. Because of this, several analytical and numerical studies have been conducted to determine the heat transfer coefficient of a viscous sphere without the exchange of mass. Levich [46] provided an asymptotic first-order solution for a liquid sphere at very large Pe under the condition of creeping flow ($\mathrm{Re}\ll 1$):

$$\mathrm{Nu}=\left[\frac{4}{3\pi}\frac{1}{1+\lambda}\mathrm{Pe}\right]^{1/2}. \tag{47}$$

Feng and Michaelides [79,114] conducted two numerical studies on the subject of heat transfer from a viscous sphere at constant volume and derived useful correlations, first at high Re_s and any Pe_s, [114], and then at any Re_s and Pe_s, [79]. Their results in correlation form are as follows:

A At small but finite Re_s($0<\mathrm{Re}_s<1$) and $\mathrm{Pe}_s>10$, the general expression for the Nusselt number is as follows:

$$\mathrm{Nu}(\lambda,\mathrm{Pe}_s,\mathrm{Re}_s)=\left(\frac{0.651}{1+0.95\lambda}\mathrm{Pe}_s^{1/2}+\frac{0.991\lambda}{1+\lambda}\mathrm{Pe}_s^{1/3}\right)(1+\alpha(\mathrm{Re}_s))+\left(\frac{1.65(1-\alpha(\mathrm{Re}_s))}{1+0.95\lambda}+\frac{\lambda}{1+\lambda}\right), \tag{48a}$$

where the function $a(\mathrm{Re}_s)$ is expressed as follows:

$$\alpha(\mathrm{Re}_s)=\frac{0.61\,\mathrm{Re}_s}{\mathrm{Re}_s+21}+0.032. \tag{48b}$$

B As with the case of the expression of the drag coefficient, for higher Re_s the analysis of the data revealed that the best correlations of the numerical data are obtained when the general expression for the Nusselt number is given in terms of the following three functions:

B1 The correlation of Nu for an inviscid sphere ($\lambda=0$), which is as follows:

$$\mathrm{Nu}(0,\mathrm{Pe}_s,\mathrm{Re}_s)=0.651\mathrm{Pe}_s^{1/2}\left(1.032+\frac{0.61\,\mathrm{Re}_s}{\mathrm{Re}_s+21}\right)+\left(1.60-\frac{0.61\,\mathrm{Re}_s}{\mathrm{Re}_s+21}\right). \tag{49a}$$

B2 The corresponding function of Nu for a solid sphere ($\lambda=\infty$), which is as follows:

$$\mathrm{Nu}(\infty,\mathrm{Pe},\mathrm{Re})=0.852\mathrm{Pe}^{1/3}(1+0.233\,\mathrm{Re}^{0.287})+1.3-0.182\,\mathrm{Re}^{0.355}. \tag{49b}$$

B3 The corresponding function of Nu for a sphere with viscosity ratio equal to 2 ($\lambda=2.0$), which was derived from the numerical results and is as follows:

$$\mathrm{Nu}(2,\mathrm{Pe}_s,\mathrm{Re}_s)=0.64\mathrm{Pe}_s^{0.43}(1+0.233\,\mathrm{Re}_s^{0.287})+1.41-0.15\,\mathrm{Re}_s^{0.287}. \tag{49c}$$

The final correlations for the heat transfer coefficients may be given by the following expressions in the two subranges $0\leqslant\lambda<2$ and $2<\lambda\leqslant\infty$:

$$\mathrm{Nu}(\mathrm{Pe}_s,\mathrm{Re}_s,\lambda)=\frac{2-\lambda}{2}\mathrm{Nu}(\mathrm{Pe}_s,\mathrm{Re}_s,0)+\frac{4\lambda}{6+\lambda}\mathrm{Nu}(\mathrm{Pe}_s,\mathrm{Re}_s,2)\quad\text{for } 0\leqslant\lambda\leqslant2,\quad\text{and}\quad 10\leqslant\mathrm{Pe}_s\leqslant1000 \tag{50a}$$

and

$$\mathrm{Nu}(\mathrm{Pe}_s,\mathrm{Re}_s,\lambda)=\frac{4}{\lambda+2}\mathrm{Nu}(\mathrm{Pe}_s,\mathrm{Re}_s,2)+\frac{\lambda-2}{\lambda+2}\mathrm{Nu}(\mathrm{Pe}_s,\mathrm{Re}_s,\infty)\quad\text{for } 2\leqslant\lambda\leqslant\infty,\quad\text{and}\quad 10\leqslant\mathrm{Pe}_s\leqslant1000. \tag{50b}$$

For the case of smaller values of $\mathrm{Pe}_s<10$, no correlation of $\mathrm{Nu}(\mathrm{Pe}_s,\mathrm{Re}_s,\lambda)$ of satisfactory accuracy was obtained from the numerical data. For applications in the range $0<\mathrm{Pe}_s<10$, it is recommended that one consults the original numerical results in [79], which are given in tabular form.

9 Transverse (Lift) Force and the Effect of Boundaries

a. Lift Force. Particle rotation combined with finite relative velocity, or fluid velocity gradients (shear) even in the absence of particle rotation, will induce a transverse component in the hydrodynamic force on the sphere, which is often called the ''lift force.'' This transverse component of the hydrodynamic force has two parts. The first is due to the particle rotation, is independent of the viscosity, and is frequently referred to as ''the Magnus force.'' In a quiescent and irrotational fluid, the expression for the Magnus force is

$$\mathbf{F}_{LM}=\pi a^3\rho_f[\boldsymbol{\Omega}_p\otimes(\mathbf{V}-\mathbf{U})]. \tag{51}$$

The Magnus force is the result of pressure induced because of the streamline asymmetry that results from the rotation of the sphere. It is the contribution of the outer velocity field disturbance, far from the sphere, caused by the rotating sphere. The Magnus force is independent of the fluid viscosity and, therefore, it appears in viscous as well as in inviscid flows.

The second part of the transverse hydrodynamic force is the shear-induced lift and does not necessitate rotation of the sphere. It was first derived by Saffman [185] and, for this reason, it is oftentimes referred to as ''the Saffman force.'' Saffman [185,186] followed the work by Proudman and Pearson [16] and Childress [187] and performed an asymptotic domain expansion of the velocity field around the sphere. He derived the following expression for the magnitude of the shear-induced lift:

$$F_{LS}=K\rho_f a^2\kappa^{1/2}\nu^{-1/2}, \tag{52}$$

where K is a constant equal to 6.44 and κ is the fluid velocity shear, evaluated at the center of the sphere. Sufficient conditions for the validity of the above expression are very low Re_s as well as

$$V\ll(\kappa\nu)^{1/2},\quad \kappa a^2/\nu\ll1\quad\text{and}\quad a^2\Omega/\nu\ll1, \tag{52a}$$

which would imply one of the following two alternatives:

a. either very low particle velocity, shear and angular rotation for the particle, or
b. extremely high kinematic viscosity for the fluid if the particle has finite velocity, shear or angular rotation.

The first alternative is compatible with the assumptions implied in the derivation of the Basset-Boussinesq equation. The second alternative implies very high viscosity in combination with finite shear or rotation and is not strictly compatible with the implied conditions of the Basset-Boussinesq equation.

It must be pointed out that the appearance of the lift force is related to the inertia of the particle and that it is inconsistent with the governing equations from which the creeping flow solutions have been derived. Under the creeping flow conditions and the assumptions underlined in Section 4, a sphere only experiences a symmetric force that opposes its rectilinear motion. Transverse forces do not appear in creeping flow conditions, because the flow domain resulting from the introduction of the sphere is symmetric, [34]. At finite Re_s transverse forces may appear if the velocity field has an asymmetry. However, most of the analytical and numerical derivations of drag coefficients at finite Re_s implicitly assume that the velocity field is symmetric.

Both the Magnus and the Saffman parts of the transverse hydrodynamic force, or the lift force, are much weaker than the rectilinear components of the hydrodynamic force, the drag force. However, the lift force plays an important role in the migration of bubbles, drops, and particles towards the walls of cylindrical pipes. This happens because these objects have to travel relatively very short distances in order to approach the walls of the pipe and a weak force would be sufficient to induce them to travel such short distances, thus contributing significantly to radial diffusion or dispersion, wall deposition [188], mixing, and separation processes [189,190].

Among the recent developments on the lift forces exerted by a viscous fluid on a sphere, Auton [191] derived an expression for the lift induced by the rotational motion of the fluid at higher Re_s. Tsuji et al. [192] measured experimentally the shear-induced lift on bubbles and concluded that the expression by Saffman yields satisfactory results on the magnitude of the force. McLaughlin [193] relaxed some of the assumptions used by Saffman and derived a correction to the expression by Saffman in terms of the shear, κ. This correction improved the accuracy of Saffman's equation and extended the range of its applicability. McLaughlin's theoretical work was later confirmed experimentally by Cherukat et al. [194] for a solid sphere near a wall. The experimental results by Sridhar and Katz [195] suggest that the magnitude of the lift component of the hydrodynamic force of bubbles and particles is higher than the values predicted by the theory. Mei and Klausner [196] also derived a correlation for the lift coefficient of a bubble in a shear flow field by a numerical method at high values of Re_s. However, their results only considered the outer expansion and not the inner expansion of the problem as pointed out by Magnaudet and Legendre [197]. An essentially numerical article by Legendre and Magnaudet [198] has shed some clarity on the mathematical formulation of the problem as well as the physical mechanisms that contribute to the lift of the sphere in inertia-

dominated flows. Another experimental study by Tomiyama et al. [199] on bubbles in shear flows concluded that the lift coefficient of larger bubbles depends on the surface tension (the Eotvos number) and that rising bubbles tend to accumulate close to the walls if their radii are less than 6 mm, while bigger bubbles with radii higher that 6 mm tend to migrate towards the center of the apparatus.

As with the steady-state drag force, the magnitude of the Magnus lift force is often expressed as a function of a dimensionless lift coefficient, c_{LM}, which is then correlated by experimental data. A recent investigation by Oesterle and Bui-Dinh [200] yields the following empirical expression for the lift coefficient of a sphere rotating in an infinite fluid:

$$c_{LM}=0.45+\left(\frac{\mathrm{Re}_R}{\mathrm{Re}_s}-0.45\right)\exp(-0.05684\,\mathrm{Re}_R^{0.4}\,\mathrm{Re}_s^{0.3}) \quad \text{for} \quad \mathrm{Re}_R<140 \tag{53}$$

where Re_R is the Reynolds number based on the rotational speed of the sphere:

$$\mathrm{Re}_R=\frac{4\rho_f\alpha^2|\mathbf{\Omega}|}{\mu_f}. \tag{54}$$

The lift coefficient is in general a monotonically decreasing function of the Reynolds number, Re_s, as shown by many, including Rubinow and Keller [201], Dennis et al. [202] and Oesterle and Bui-Dihn [200].

The lift of growing bubbles that are formed close to a wall is very important in the boiling and evaporation processes, because the global rate of the heat transfer greatly depends on the amount of vapor which is in contact with the wall or in the immediate vicinity of the wall. In this case, the lift due to shear facilitates the detachment of small spherical bubbles from the wall and subsequently the nucleation and the commencement of the growth process of other bubbles. Thorncroft et al. [71] studied the growth and detachment of bubbles from a surface and concluded that the growth of a bubble close to a wall enhances the lift force exerted by the shear. In their analytical and computational study they derived the following expression for the lift due to the shear:

$$F_{SL}=\frac{1}{2}|U-V|(U-V)\pi\rho_f\alpha^2(t)\kappa^{1/2}\left\{\left[\frac{1.46J}{\mathrm{Re}_s^{1/2}}\right]^2+\left[\frac{3}{4}\kappa^{1/2}\right]^2\right\}^{1/2}, \tag{55}$$

where J is a scalar function of the dimensionless shear rate and the Reynolds number. The augmented lift force in this case facilitates the detachment of the bubble from the wall, reduces the amount of vapor close to this wall, and, thus, contributes to the enhancement of the heat transfer from the wall to the bulk fluid.

The shear-induced lift on solid spheres attached to a wall where other similar spheres are present, known as suspension flow, was studied numerically by Feng and Michaelides [203]. Their results show that the instantaneous hydrodynamic force exerted by the suspension flow on a solid particle attached to a wall is increased by a factor of 2–4 by the presence of similar particles in the flow field. The augmentation includes both the lift and the drag component of the hydrodynamic force and is caused by the interactions of the suspended spherical particles with the stationary particle when they are in close proximity, within 1–2 diameters. In this case, it is the hydrodynamic interactions between pairs or triplets of particles that result in the augmentation of the lift and drag components of the force. As a result of this type of hydrodynamic interaction, a particle that lays on a horizontal boundary may be lifted and become suspended in the flow without any physical collisions with other particles in the suspension.

Regardless of the method of evaluation of the lift component, the ratio of the transverse to the longitudinal component of the hydrodynamic force, F_L/F_D, is of the order of $\alpha(\kappa/\nu)^{1/2}$. This is necessarily a very small number according to all the assumptions used in the derivation of the lift forces (Eq. (52*a*)). Despite this, the transverse component of the hydrodynamic force is very important because it determines the lateral migration and dispersion of spheres, and plays an important role in several phenomena, such as bubble detachment during boiling and particle sedimentation and resuspension in water quality models. For this reason, the accurate knowledge of this transverse component is of paramount importance for engineering calculations that pertain to such processes. It is common practice in such engineering calculations to superpose an expression for the transverse or lift component, such as Eq. (51) or (52) with an expression for the transient hydrodynamic force in the longitudinal direction, such as Eqs. (1), (10), or (19), and thus calculate the longitudinal and transverse motion of particles, bubbles, and drops. The result of such a superposition is that the transient hydrodynamic force on a sphere appears to have a lateral, albeit steady-state, component in addition to the longitudinal component. Although this superposition is not justified on analytical grounds, it is very convenient to use and the results obtained appear to be accurate, since they agree fairly well with experimental data. When one uses this superposition, it is important to ensure that the necessary conditions for the validity of the expressions used for the several components of the hydrodynamic force are not violated. In most of the cases this means that there is very low relative velocity and rotation between the sphere and the fluid, and that the local shear is small.

b. Effect of the Walls on the Motion of Particles. The motion of particles, bubbles and drops in the vicinity of a wall is very important in many practical applications ranging from boiling to particulate and slurry transport. As was mentioned above, the lift on small bubbles influences the rate of heat transfer from a surface during several practical processes. In particulate transport processes, particle collisions with the walls result in pipeline erosion and particle adhesion to the walls cause scale buildup and oftentimes pipeline clogging. The effect of a wall in general is to retard the motion of particles in both the parallel and the perpendicular direction to the wall, thus reducing the rate of mass transport. In addition, the presence of particles and bubbles in boundary layers and mixing layers significantly modifies the stability and transport properties of these layers. Although the effect of the particles and bubbles on the boundary layers is not the subject of this article, there is a great deal of recent experimental and analytical work on this subject, which may be found in Aggarwal [204], Moursali et al. [205] Climent and Magnaudet [206] Narayanan et al. [207] Marie et al. [208] Joia et al. [209] Tran-Cong et al. [210] Druhzinin and Elghobashi [211], and Felton and Loth [212].

The first to consider the motion and to derive an expression for the hydrodynamic force on a particle in rectilinear motion parallel to a wall was Faxen [12]. He used the method of reflections for the movement of the sphere under creeping flow conditions and obtained an asymptotic solution for the total force acting on a sphere that settles in an orthogonal circular cylinder, when the trajectory of the center of the sphere is the centerline of the cylinder. In this case, the ratio of the particle diameter to the characteristic distance, or diameter, of the cylinder, Ξ, is the most important parameter that affects the hydrodynamic force. Faxen's expression for the hydrodynamic force may be given in terms of a wall drag multiplier, K_{wall}, which is the ratio of the steady-state hydrodynamic force in the presence of the wall to the Stokesian force ($6\pi\mu\alpha V$) that a sphere experiences in an unbounded flow. By using the same method of reflections Bohlin [213] obtained a higher order approximation for the wall drag multiplier, which may be written as follows:

$$K_{\text{wall}}=\frac{1}{1-2.01443\Xi+2.088777\Xi^3-6.94813\Xi^5-1.372\Xi^6+3.87\Xi^8-4.19\Xi^{10}+\ldots}. \tag{56}$$

Haberman and Sayre [214] developed a theoretical method to compute the wall correction factor, K_{wall}, for spheres settling in cylinders up to very high values of Ξ, and later Paine and Scherr [215] used this method in order to compute K_{wall}, and tabulated their results for several values of the diameter ratio in the range $0\leqslant\Xi\leqslant 0.9$. A comparison between the expression by Bohlin (Eq. (56)) and the exact theory by Haberman and Sayre [214] shows that Eq. (56) yields accurate results only up to $\Xi=0.6$.

Apart from the analytical/computational studies, there are also several experimental studies pertaining to the settling of a sphere along the centerline of an orthogonal circular cylinder or next to a plane wall. Among them, the experimental studies by Iwaoka and Ishii [216] and Miyamura et al. [217] show good agreement with the theoretical solutions by Faxen [12], Bohlin [213] and Paine and Scherr [215]. The recent study on this subject by Masmoudi et al. [218] must also be mentioned. They devised an elaborate experimental apparatus to measure with higher accuracy the position and trajectory of a particle in a vessel and, thus, to determine the interaction between the particle and the walls of the vessel.

An excellent exposition of the studies on the settling of spheres in enclosures of any shape may be found in the treatise by Happel and Brenner [48], who devoted an entire chapter to discuss the wall effects on the motion of a single sphere. They considered creeping as well as inertia flows, and stipulated that the total effect on the hydrodynamic force acting on the sphere is a simple linear combination of the separate effects of proximity to the outside boundary and inertia. Thus the total correction factor for the hydrodynamic force acting on a sphere is given by the expression

$$K=K_{\text{wall}}+K_{\text{inertia}}-1, \tag{57}$$

where K_{wall} is the wall effect at creeping flow as defined above and, K_{inertia} is the additional correction factor due to the inertia effects of the flow at higher Re_s. Equation (57) simply implies that the drag on a sphere is composed of two additive terms: one term is due to the effect of the cylindrical boundary and the other is due to the flow inertia effect. The latter is usually obtained from one of the empirical correlations for the drag coefficient at high Reynolds numbers, such as the one by Schiller and Nauman [76].

Equation (57) is essentially a conjecture that is based on the experimental data by Fayon and Happel [219]. The data set pertains to a diameter ratio, Ξ, in the range of 0.1250 to 0.3125 and Reynolds numbers in the range 0.1 to 40. Feng and Michaelides [220] conducted a more general numerical study for a wider range of Ξ and Re_s that is applied to cylindrical as well as prismatic enclosures. They concluded that the two effects of inertia and of flow confinement are not always additive and may not be combined as Eq. (57) implies. Because of this, in calculating the hydrodynamic force on a sphere, it is more accurate to use computational or experimental data that are not restricted by this assumption.

Regarding the radial migration of particles in pressure-driven flows in pipes and small capillaries, Poiseuille [221] was the first to perform a study in order to model blood flow and, for this reason, such flows now bear his name. Wang and Skalak [222] studied analytically the flow of an array of spheres located at the centerline of a cylindrical tube under creeping flow conditions and calculated the pressure drop in the cylinder with the particle size and inter-particle distance as parameters. Westborg and Hassager [223] studied numerically the creeping motion of elongated bubbles inside capillary tubes and Xu and Michaelides [224] extended these results to flows at finite Reynolds numbers and determined the hydrodynamic force on ellipsoids and spheres inside cylindrical tubes.

Of particular interest in Poiseuille flows with suspended rigid or deformable spheres is the transverse motion and the calculation of the transverse, or migration, velocity of these spheres, caused by interactions with the walls. By using the method of reflections, Brenner and Happel [225] solved the problem of a rigid sphere moving in the axial direction in a Poiseuille flow and obtained asymptotic solutions for the drag force and torque. Later, Cox and Brenner [226] extended this approach to rigid particles of irregular shapes, and derived the following expression for the migration velocity of a sphere that is falling close to a wall:

$$V_r=\frac{6\pi V_s^2}{\nu}h, \tag{58}$$

where V_s is the sedimentation velocity and h is an integral of the Green's function for the point force representing the sphere. The last expression is valid under the conditions $\text{Re}_s\ll\alpha/l_w\ll 1$, where l_w is the distance of the center of the sphere from the wall. The implications of this condition are that the sphere is far from the wall and creeping flow. Cox and Hsu [227] evaluated this integral for the case of a sphere and derived the following asymptotic expression for the migration velocity:

$$V_r=\frac{3}{64}\text{Re}_s V_s, \tag{59}$$

also valid under the conditions $\text{Re}_s\ll\alpha/l_w\ll 1$. The fact that this expression implies that the migration velocity of the sphere is independent from its distance from the wall does not constitute a paradox, because the expression is valid only at distances sufficiently far from the wall as expressed by the condition $\alpha/l_w\ll 1$.

Vasseur and Cox [228] derived analytically an expression for the lateral migration velocity of a sphere that falls in a quiescent fluid in the proximity of a plane wall. Their expression for the lateral velocity is as follows:

$$V_r=\frac{3}{8}\frac{\alpha V_z^2}{\nu}\left[\left(\frac{\nu}{l_w V_z}\right)^2+2.219\left(\frac{\nu}{l_w V_z}\right)^{5/2}\right], \tag{60}$$

where V_z is the (vertical) sedimentation velocity and the terms in the two parentheses are the inverse of a Reynolds number based on the distance from the wall. This expression was later confirmed by the experimental data of Cherukat and McLaughlin [229] to be valid up to $\text{Re}_s=3.0$.

The experimental studies by Segre and Silberberg [230] with neutrally buoyant spheres demonstrated that particles in a pressure-driven Poiseuille flow experience a radial force and tend to align at a distance which is at approximately 0.6 pipe radii away from the centerline. This shows that there exists an equilibrium position where the radial force is zero and, thus, particles tend to accumulate in this position. Two-dimensional numerical studies have also concluded that there is an equilibrium position for cylinders at a distance of 0.4234 half-channel width away from the centerline for both a single and for a group of naturally buoyant cylinders in a pressure-driven channel flow [231]. Mortazavi and Tryggvason [232] studied the lateral migration of two-dimensional drops in Poiseuille flows and found that drops either move halfway between the pipe centerline and the wall, as Segre and Sielverding [230] also observed, or they oscillate around an off-center equilibrium position. More recently, Joseph and his coworkers [233,234] studied the lift force in two dimensions by examining the behavior of a circular particle in a plane Poiseuille flow and the motion of circular particles in two-dimensional pressure-driven flows using a finite element method.

One of the lesser known studies on the lift of a sphere is that by Feuillebois and Lasek [235] who, starting from the creeping flow equations for the angular momentum of a sphere, discovered the existence of a history term in the angular momentum equation, the history couple. Although this history couple is weak, it contributes to the transient rotation and transverse motion of spheres.

All the above studies pertain to the transverse motion of a sphere, whose main direction of motion is parallel to a wall. Regarding the flow of a sphere perpendicular to a wall, Brenner [236] obtained asymptotically a first-order correction for the drag coefficient of a small rigid sphere moving towards the wall and concluded that the Stokes' drag coefficient increased by a factor equal to $1.25(\alpha/h)$, where h is the distance of the particle from the wall. Brenner's results indicate that the hydrodynamic force on the particle increases dramatically when the particle approaches close to the wall. The study by Kalio [237] indicates that the influence of the wall on the drag of the particles is important when the particle is within 20 diameters from the wall.

In the case of turbulent flows, analysis and experiments have shown that, despite the increased drag coefficient, the process of turbophoresis tends to bring the particles close to the wall, where the turbulent fluctuations are weaker. However, when the particle concentration at the wall becomes high, the accumulation of particles close to the wall results in a ''drift velocity'' towards the center, which is the result of the high particle concentration gradient. The balance of the two driving forces, turbulence and concentration, yields an equilibrium condition. Models that are based on this equilibrium predict fairly well the particle behavior close to the wall in turbulent pipe flow. Portela et al. [238] found that the local equilibrium models predict well the particulate concentration, except very close to the wall ($y^+<20$) where the turbulent fluctuations are very weak and turbophoresis cannot even be defined in a physically meaningful way. A great deal of information on the motion of particles close to the walls, the collisions with the walls and inter-particle collisions may be found in the monograph by Crowe et al., [239] the experimental article by Sommerfeld and Hubber [240] the recent review article by Sommerfeld [241], the numerical study on particles in large-eddy simulations by Yamamoto et al. [242], as well as in several other research articles that were presented in the proceedings of the last two international conferences on multiphase flow [243,244].

Regarding bubble flows, a recent experimental study on the effect of a vertical wall on rising bubbles and the collisions of the bubble with the wall by De Vries et al. [245] found that, upon collision with the wall, the wake of the bubbles impinges on the wall and becomes a coherent, approximately spherical vortex, which plays an important role in the dynamics of the collision process. A numerical study by Lyubimov et al. [246] examined the vibrations of bubbles close to the walls at microgravity conditions.

It must be pointed out that our knowledge of the lift component of the hydrodynamic force, that is, both the Saffman and the Magnus components, and of the effect of the walls on the motion of a sphere is not based on any rigorous derivation of the transient equation of motion that originates from the solution of the governing equations (which would include both the longitudinal as well as the transverse motion) but on specific analytical and numerical studies at steady state. For this reason, one has to be aware that the rectilinear transient equations of motion mentioned in all the previous sections implicitly assume that there is no rotation of the sphere, no significant shear in the flow and, in most cases, that the sphere is in an unbounded fluid. For this reason, the addition of the lift or wall effect on a rigorously derived transient equation for the rectilinear motion of a particle must be viewed as an *ad hoc* assumption, which has been justified by validation with experiments, but has its own limitations in the range of applicability.

10 The Effect of Concentration on the Steady-State Drag and Added Mass Coefficient

While most of the theories and experiments on spheres have been developed for single spheres, the majority of practical applications involve the flow of many particles, bubbles, or drops. Interactions of the spheres and the formation of clusters and groups of spheres with correlated motions play an important role on the value of the hydrodynamic force exerted by the fluid and on the temperature field developed. Hence, the motion and rate of heat transfer from the spheres to the fluid depends on these interactions, which become more pronounced as the concentration of the spheres increases. In general, it is accepted that one may use the results and apply the theory of a single sphere inside a flow mixture of monodisperse spheres if the average distance between the centers of the spheres is greater than 4α, that is, if the outer surfaces of the spheres are separated by a distance, greater than one diameter. Such mixtures are known as dilute mixtures. Simple geometric arguments show that the average concentration of the spheres in dilute mixtures is lower than approximately 6 percent. For concentrations higher than 6 percent, the concentration of the mixture is one of the variables that should be accounted for in the calculation of hydrodynamic force and rate of heat transfer.

Regarding the steady state of the hydrodynamic force, Richardson and Zaki [247] carried out one of the earlier series of experiments on the sedimentation of particles in a quiescent fluid, and by correlating the settling velocity of the particles to the concentration of the mixture, they concluded that the drag coefficient increases by a factor equal to $(1-\varphi)^{-K}$, where K is a weak function of the Reynolds number given by the relation: $K=4.45\,\mathrm{Re}^{0.1}$. Because of the spread of their data, it is apparent that the exponent K may attain any value in the range 2.5 to 5.7. Rowe [248] conducted experiments with arrays of solid spheres in water and air and found out that the drag coefficient of the array is inversely proportional to the dimensionless separation distance of the spheres. His experimental data suggest an exponent, K, closer to the value of 3. The experimental study by Aidi et al. [249] on the sedimentation of polydisperse solutions showed that the analytical solution by Batchelor and Wen [250,251] is accurate enough and also that the hydrodynamic interactions between several spheres are of importance in the determination of the average value of the hydrodynamic force in sedimentation processes. More recently, Di Felice [252] used several sets of data available in the literature, including those by Richardson and Zaki [247] and derived the following correlation, which is recommended in the range $10^{-2}<\mathrm{Re}<10^4$:

$$c_D=c_{D0}(1-\phi)^{-\mathrm{K}} \text{ with } K=3.7-0.65\exp\left[-\frac{(1.5-\log \mathrm{Re}_s)^2}{2}\right]. \tag{61}$$

The subject of interacting particles, bubbles and drops is rather difficult to investigate experimentally, but ideally suited for computational simulations where different initial conditions may be examined and statistical results are relatively easy to derive. Modern computational techniques and more powerful computers have allowed the numerical modeling of large groups of spheres. As a result we learn more and have a better understanding of the behavior of large groups of particles, drops, and bubbles. Recently, finite element methods (FEM) and the lattice Bolzmann method (LBM) have enabled scientists and engineers to perform ''thought experiments'' of groups of interacting spheres and thus to determine the effect of interactions on the hydrodynamic force exerted on individual spheres. The LBM [253–255] is an ideally suited method for the determination of the interaction of groups of cylinders and spheres, and has enabled the simulation of processes involving very large groups of particles.

Kaneda [256] used an asymptotic method to derive the steady-state component of the hydrodynamic force on an array of solid spheres at very small, but not negligible, Reynolds number and at

very low concentration. His study showed the following functional relationship for the average drag coefficient, c_D:

$$c_d = 1 + (\sqrt{2}/3)\phi^{1/2} + (\sqrt{2}/40)\phi^{-1/2}\,\mathrm{Re}_s^2. \tag{62}$$

This expression is valid at distances where the inertia of the sphere is important, that is, at distances far from the Brinkman screening length. In the case of an array of spheres, the Brinkman screening length is equal to $\phi^{1/2}$ and the range of applicability of this expression is $\phi^{1/2} \gg \mathrm{Re}_s$. Kaneda [256] also concluded that in the opposite limit, $\phi^{1/2} \ll \mathrm{Re}_s$, the Oseen [11] correction to the Stokes drag is valid for the average drag coefficient, even in the case of an array with several interacting particles. Working with arrays of two-dimensional particles in flows at finite Reynolds numbers and using the LBM, Koch and Ladd [257] and Rojas and Koplik [258] also confirmed that the Oseen relationship for the steady-state component of the hydrodynamic force, $c_D = 1 + 3/8\,\mathrm{Re}_s$, applies to particles at small but finite Reynolds numbers.

Using the LBM for a packed bed of particles, Koch and Sangani [259] performed calculations on the rectilinear drag coefficients with fixed arrays of spheres (essentially a well-organized porous medium) and found out that the steady-state drag component is scaled as Re_s^2 in high-concentration suspensions and depends on the concentration. They obtained the following functional relationship of the steady-state part of the hydrodynamic force for concentrations higher than 40 percent, which is valid at finite but small values of Re_s:

$$c_d = c_{d0}(\phi) + c_{d1}(\phi)\mathrm{Re}_s^2. \tag{63}$$

The first function of this expression, which is the equivalent of the dimensionless Stokes drag force, is given by the formula

$$c_{d0} = \frac{1 + 3(\phi/2)^{1/2} + 2.11\phi \ln\phi + 16.14\phi}{1 + 0.681\phi - 8.48\phi^2 + 8.16\phi^3}. \tag{64}$$

The ratio of the functions, c_{d1}/c_{d0}, diminishes with increasing concentration of the solid particles. Apparently the second term of Eq. (63) is very small in comparison to the first and, because of this, Koch and Sangani [259] claim that the nonlinear (Re_s^2) behavior of the steady-state part of the average hydrodynamic force for close-packed arrays is difficult to observe in experimental studies.

Koch and Hill [45] also performed LBM studies at higher Reynolds numbers and found out that the steady-state component of the hydrodynamic force increases linearly with Re_s according to the following correlation:

$$c_d = c_{d0}(\phi) + [0.0673 + 0.212\phi + 0.0232(1-\phi)^{-5}]\mathrm{Re}_s, \tag{65}$$

where the function $c_{d0}(\phi)$ is the same as in Eq. (64). Koch and Hill [45] concluded that this expression agrees well with the experimental results and the empirical relation derived by Ergun [260] for packed beds of particles.

Bubbles have been always modeled as inviscid and weightless spheres moving in a fluid, which is often idealized as inviscid. Because in this case the added mass term is much greater than all the components of the hydrodynamic force, such spheres accelerate as if their masses were equal to the mass of the fluid occupying half their volume, that is $m_s = 2/3\pi\rho_f\alpha^3$. In the case of several bubbles in a fluid with concentration ϕ, the added mass coefficient, Δ_A, is a function of the concentration of the bubbles. Zuber [261] used a cell model for the flow of groups of bubbles to obtain analytically the correction to the added mass coefficient:

$$\Delta_A = \frac{1 + 2\phi}{1 - \phi}. \tag{66}$$

This expression is very simple to use in repetitive computations and according to Sangani et al. [58] it applies in a wide variety of cases.

Van Wijngaarten [262] performed an asymptotic analytical study in the case of a swarm of bubbles that are impulsively accelerated and concluded that, on the order of ϕ^2, the added mass coefficient of the group with concentration ϕ is equal to

$$\Delta_A = 1 + 2.76\phi + O(\phi^2). \tag{67}$$

Most of the recent studies and much of our knowledge on the behavior of interacting bubbles emanate from computer simulations. Spelt and Sangani [263] performed such a simulation and determined the influence of the fluid pseudo-turbulence, that is, the velocity fluctuations of the fluid, as well as the effect of the concentration of bubbles on the hydrodynamic force and the drag coefficient. They found that there is a weak dependence of the added mass coefficient on the fluid velocity fluctuations, but a significant dependence of the added mass on the bubble concentration. Their final expression, which is accurate for $\phi < 0.3$, when put in a form similar to that of Zuber's expression, becomes

$$\Delta_A = \frac{1 + 2\phi + 0.225\phi A}{1 - \phi} \tag{68}$$

where A is a dimensionless measure of the temporal velocity fluctuations of the fluid. With a similar analysis the same authors obtained the following expression for the viscous drag coefficient for a swarm of bubbles in a viscous fluid:

$$c_d = \frac{1 + 0.15\phi A}{(1-\phi)^2}. \tag{69}$$

The observation that c_d increases slightly with the velocity fluctuations of the fluid, is also consistent with the study by Sangani and Didwania [264].

In an experimental study on the interactions of two bubbles in proximity rising in a quiescent fluid, Duineveld [265] concluded that the steady-state component of the average hydrodynamic force increases up to 60 percent when the two bubbles approach each other and their centerline distance is lower than 5α. Such influence of the proximity of bubbles on the drag coefficient is a consequence of the inertia effects and of the wake formed behind the bubbles. For this reason the drag depends greatly on the value of the Reynolds number, Re_s, of the bubbles.

Oftentimes, large groups of interacting spheres may be approximated and treated as porous media with porosity κ, which depends on the concentration of the media [266]. Clouds or large groups of such smaller spheres may be approximated as larger porous spheres that are transported in a fluid medium. Beavers and Joseph [267] and Saffman [268] developed the foundations for the treatment of the boundary conditions in such porous spheres and Jones [269] obtained the expression for the steady-state hydrodynamic force on a porous sphere at creeping flow conditions:

$$\mathbf{F} = 6\pi\alpha\mu_f(\mathbf{U} - \mathbf{V})\,\frac{2\zeta^2(1 + 2\eta\zeta^{-1})}{2\zeta^2 + 3 + 6\eta\zeta + 6\eta\zeta^{-1}}, \tag{70}$$

where ζ is the inverse of the dimensionless permeability of the sphere ($\zeta = \alpha/\kappa^{1/2}$, with κ being the permeability of the sphere) and η is a dimensionless constant that depends on the properties of the porous medium. Feng and Michaelides [129] used an asymptotic expansion and extended this result to finite Reynolds numbers, Re_s, for the porous sphere as follows:

$$\mathbf{F}=6\pi\alpha\mu_f(\mathbf{U}-\mathbf{V})\frac{2\left(1+\frac{\eta}{\zeta}\right)\zeta^2}{4\eta\zeta+2\zeta^2+3\frac{\eta}{\zeta}+1}$$

$$\times\left[1+\mathrm{Re}_s\frac{3\left(1+\frac{\eta}{\zeta}\right)\zeta^2}{4\left(4\eta\zeta+2\zeta^2+3\frac{\eta}{\zeta}+1\right)}\right.$$

$$\left.+\mathrm{Re}_s^2\ln(\mathrm{Re}_s)\frac{9\left(1+\frac{\eta}{\zeta}\right)^2\zeta^4}{10\left(4\eta\zeta+2\zeta^2+3\frac{\eta}{\zeta}+1\right)^2}\right], \qquad (71)$$

where Re_s is the Reynolds number of the whole cloud of small spheres based on its relative velocity. It must be pointed out that Eq. (71) yields the correct behavior in the extreme cases of zero and infinite permeability: for a solid sphere ($\kappa\to\infty$) the last expression yields the hydrodynamic force obtained by Proudman and Pearson [16], while at low permeability ($\kappa\to0$) it yields the result by Joseph and Tao [270]. At creeping flow ($\mathrm{Re}_s=0$) it yields the force predicted by Saffman [268].

Acknowledgments

The author is thankful to the NSF, LEQSF, NASA, DOE, ONR, DWSA, and to the Tulane-Xavier Center for Bioenvironmental Research for their support of the several parts of his original research, which resulted in this article. He is also grateful to the selection committee of the ASME Freeman Scholar Award, which made this article possible.

Nomenclature

Latin Symbols

a = heat diffusivity
A = vector defined in Eq. (11)
Ac = acceleration number
Bi = Biot number
c = specific heat capacity
C = mass concentration
c_D = drag coefficient
c_d = average drag coefficient
D = diffusivity coefficient
d = diameter
d_e = equivalent diameter
erf = error function
erfc = complementary error function
f_H = function of the history term
F = force
g = gravitational acceleration
G = functions defined in Eqs. (17*a*) and (18*a*)
H = the Heaviside function
k = conductivity
K = constant or function
m = mass
Nu = Nusselt number
P = pressure
Pe = Peclet number
Pr = Prandtl number
Q = rate of heat transfer
Re = Reynolds number
Sl = Strouhal number
Sh = Sherwood number
St = Stokes number
t = time
T = temperature
u = fluid velocity
U = characteristic velocity
v = volume
V = sphere velocity

Greek Symbols

α = radius
β = density ratio
β' = heat capacity ratio
γ = parameter ($=1+1/2\beta$)
$\delta(t)$ = Kronecker delta
Δ_A = added mass coefficient
Δ_H = history term coefficient
ε = eccentricity
ζ = dimensionless permeability
η = dimensionless constant
θ = temperature
κ = rate of shear, permeability
λ = viscosity ratio
μ = dynamic viscosity
ν = kinematic viscosity
Ξ = dimensionless distance
ρ = density
σ = conductivity ratio
τ = dummy variable with units of time
φ = concentration of particles, bubbles or drops
χ = dimensionless timescale
Ω = angular velocity

Superscripts

$*$ = dimensionless
∞ = pertains to undisturbed flow
T = total
$'$ = pertains to heat/mass transfer

Subscripts

f = pertains to fluid
i = vector component
jj = laplacian operator
K = pertains to Kolmogorov lengthscale
L = characteristic dimension
LM = Magnus lift
LS = Saffman lift
m = pertains to mass
M = pertains to momentum
r = radial
s = pertains to sphere
t = thermal
w = pertains to a wall/boundary
z = longitudinal
Λ = pertains to integral timescale

References

[1] Poisson, S. A., 1831, ''Memoire sur les Mouvements Simultanes d'un Pendule et de L'air Environnemant,'' Mem. Acad. Sci., Paris, **9**, p. 521–523.
[2] Green, G., 1833, ''Researches on the Vibration of Pendulums in Fluid Media,'' Trans. - R. Soc. Edinbrgh, **13**, pp. 54–68.
[3] Stokes, G. G., 1845, ''On the Theories of Internal Friction of the Fluids in Motion,'' Trans. Cambridge Philos. Soc., **8**, pp. 287–319.
[4] Stokes, G. G., 1851, ''On the Effect of the Internal Friction of Fluids on the Motion of a Pendulum,'' Trans. Cambridge Philos. Soc., **9**, pp. 8–106.
[5] Boussinesq, V. J., 1885, ''Sur la Resistance qu' Oppose un Liquide Indéfini en Repos . . . ,'' C. R., Acad. Sci., **100**, pp. 935–937.
[6] Boussinesq, J., 1885, *Applications L'etude des Potentiels*, Blanchard, Paris (re-edition 1969).
[7] Basset, A. B., 1888, *Treatise on Hydrodynamics*, Bell, London.
[8] Basset, A. B., 1888, ''On the Motion of a Sphere in a Viscous Liquid,'' Philos. Trans. R. Soc. London, Ser. A, **179**, pp. 43–63.
[9] Whitehead, A. N., 1889, ''Second Approximation to Viscous Fluid Motion. A Sphere Moving Steadily in a Straight Line,'' Q. J. Math., **23**, pp. 143–152.
[10] Oseen, C. W., 1910, ''Uber die Stokes'sche Formel und Uber eine verwandte Aufgabe in der Hydrodynamik,'' Ark. Mat., Astron. Fys., **6**(29).
[11] Oseen, C. W., 1913, ''Uber den Goltigkeitsbereich der Stokesschen Widerstandsformel,'' Ark. Mat., Astron. Fys., **9**(19).

[12] Faxen, H., 1922, ''Der Widerstand gegen die Bewegung einer starren Kugel in einer zum den Flussigkeit, die zwischen zwei parallelen Ebenen Winden eingeschlossen ist,'' Ann. Phys. (Leipzig), **68**, pp. 89–119.
[13] Tchen, C. M., 1949, ''Mean Values and Correlation Problems Connected With the Motion of Small Particles Suspended in a Turbulent Fluid,'' doctoral dissertation, Technical University of Delft, Delft, The Netherlands.
[14] Corssin, S., and Lumley, J. L., 1957, ''On the Equation of Motion of a Particle in a Turbulent Fluid,'' Appl. Sci. Res., Sect. A, **6**, pp. 114–116.
[15] Sy, F., Taunton, J. W., and Lightfoot, E. N., 1970, ''Transient Creeping Flow Around Spheres,'' AIChE J., **16**, pp. 386–391.
[16] Proudman, I., and Pearson, J. R. A., 1956, ''Expansions at Small Reynolds Numbers for the Flow Past a Sphere and a Circular Cylinder,'' J. Fluid Mech., **2**, pp. 237–262.
[17] Sano, T., 1981, ''Unsteady Flow Past a Sphere at Low Reynolds Number,'' J. Fluid Mech., **112**, pp. 433–441.
[18] Maxey, M. R., and Riley, J. J., 1983, ''Equation of Motion of a Small Rigid Sphere in a Non-Uniform Flow,'' Phys. Fluids, **26**, pp. 883–889.
[19] Gatignol, D., 1983, ''The Faxen Formulas for a Rigid Particle in an Unsteady Non-Uniform Stokes Flow,'' J. Mec. Theor. Appl., **1**, pp. 143–154.
[20] Michaelides, E. E., and Feng, Z.-G., 1995, ''The Equation of Motion of a Small Viscous Sphere in an Unsteady Flow With Interface Slip,'' Int. J. Multiphase Flow, **21**, pp. 315–321.
[21] Mei, R., Lawrence, C. J., and Adrian, R. J., 1991, ''Unsteady Drag on a Sphere at Finite Reynolds Number With Small Fluctuations in the Free-Stream Velocity,'' J. Fluid Mech., **233**, pp. 613–631.
[22] Mei, R., and Adrian, R. J., 1992, ''Flow Past a Sphere With an Oscillation in the Free-Stream and Unsteady Drag at Finite Reynolds Number,'' J. Fluid Mech., **237**, pp. 323–341.
[23] Lovalenti, P. M., and Brady, J. F., 1993, ''The Hydrodynamic Force on a Rigid Particle Undergoing Arbitrary Time-Dependent Motion at Small Reynolds Numbers,'' J. Fluid Mech., **256**, pp. 561–601.
[24] Hinch, E. J., 1993, ''The Approach to Steady State in Oseen Flows,'' J. Fluid Mech., **256**, pp. 601–603.
[25] Chang, E. J., and Maxey, M. R., 1994, ''Unsteady Flow About a Sphere at Low to Moderate Reynolds Number. Part 1, Oscillatory Motion,'' J. Fluid Mech., **277**, pp. 347–379.
[26] Chang, E. J., and Maxey, M. R., 1995, ''Unsteady Flow About a Sphere at Low to Moderate Reynolds Number. Part 2. Accelerated Motion,'' J. Fluid Mech., **303**, pp. 133–153.
[27] Fourier, J., 1822, *Theorie Analytique de la Chaleur*, Paris.
[28] Tait, P. G., 1885, *Scientific Papers*, A. & C. Black, Edinburgh.
[29] Carslaw, H. S., and Jaeger, J. C., 1947, *Conduction of Heat in Solids*, Oxford University Press, Oxford, UK.
[30] Acrivos, A., and Taylor, T. E., 1962, ''Heat and Mass Transfer from Single Spheres in Stokes Flow,'' Phys. Fluids, **5**, pp. 387–394.
[31] Michaelides, E. E., and Feng, Z. G., 1994, ''Heat Transfer From a Rigid Sphere in a Non-Uniform Flow and Temperature Field,'' Int. J. Heat Mass Transf., **37**, pp. 2069–2076.
[32] Feng, Z.-G., and Michaelides, E. E., 1998, ''Transient Heat Transfer From a Particle With Arbitrary Shape and Motion,'' ASME J. Heat Transfer, **120**, pp. 674–681.
[33] Lovalenti, P. M., and Brady, J. F., 1993, ''The Force on a Bubble, Drop or Particle in Arbitrary Time-Dependent Motion at Small Reynolds Numbers,'' Phys. Fluids A, **5**, pp. 2104–2116.
[34] Leal, L. G., 1992, *Laminar Flow and Convective Transport Processes*, Butterworth-Heineman, Boston.
[35] Kim, S., and Karila, S. J., 1991, *Microhydrodynamics: Principles and Selected Applications*, Butterworth-Heineman, Boston.
[36] Sirignano, W. A., 1999, *Fluid Dynamics and Transport of Droplets and Sprays*, Cambridge University Press, Cambridge, UK.
[37] Leal, L. G., 1980, ''Particle Motions in a Viscous Fluid,'' Annu. Rev. Fluid Mech., **12**, pp. 435–476.
[38] Brady, J. F., and Bossis, G., 1988, ''Stokesian Dynamics,'' Annu. Rev. Fluid Mech., **20**, pp. 111–157.
[39] Feuillebois, F., 1989, ''Some Theoretical Results for the Motion of Solid Spherical Particles on a Viscous Fluid,'' Multiphase Sci. Technol., **4**, pp. 583–794.
[40] Sirignano, W. A., 1993, ''Fluid Dynamics of Sprays,'' ASME J. Fluids Eng., **115**, pp. 345–378.
[41] Stock, D. E., 1996, ''Particle Dispersion in Flowing Gases,'' ASME J. Fluids Eng., **118**, pp. 4–17.
[42] Michaelides, E. E., and Feng, Z.-G., 1996, ''Analogies Between the Transient Momentum and Energy Equations of Particles,'' Prog. Energy Combust. Sci., **22**, pp. 147–163.
[43] Michaelides, E., 1997, ''Review—The Transient Equation of Motion for Particles, Bubbles, and Droplets,'' ASME J. Fluids Eng., **119**, pp. 233–247.
[44] Loth, E., 2000, ''Numerical Approaches for the Motion of Dispersed Particles, Droplets, or Bubbles,'' Prog. Energy Combust. Sci., **26**, pp. 161–223.
[45] Koch, D. L., and Hill, R. J., 2001, ''Inertial Effects in Suspension and Porous Media Flows,'' Annu. Rev. Fluid Mech., **33**, pp. 619–647.
[46] Levich, V. G., 1962, *Physicochemical Hydrodynamics*, Prentice-Hall, Englewood Cliffs, NJ.
[47] Clift, R., Grace, J. R., and Weber, M. E., 1978, *Bubbles, Drops and Particles*, Academic Press, New York.
[48] Happel, J., and Brenner, H., 1986, *Low Reynolds Number Hydrodynamics*, Martinus Nijhoff, Dordrecht, The Netherlands (reprint, orig. publ. 1963).
[49] Govier, G. W., and Aziz, K., 1977, *The Flow of Complex Mixtures in Pipes*, Kruger Publ., Huntington (reprint).
[50] Soo, S. L., 1990, *Multiphase Fluid Dynamics*, Science Press, Beijing.
[51] Stock, D. E., Reeks, M. W., Tsuji, Y., Michaelides, E. E., and Gautam, M., 1993, *Gas-Particle Flows*, FED-Vol. 166, ASME, New York.
[52] Stock, D. E., Reeks, M. W., Tsuji, Y., Michaelides, E. E., and Gautam, M., 1995, *Gas-Particle Flows*, FED-Vol. 228, ASME, New York.
[53] Stock, D. E., Reeks, M. W., Tsuji, Y., Michaelides, E. E., and Gautam, M., 1997, *Gas-Particle Flows–1997*, ASME, New York.
[54] Stock, D. E., Reeks, M. W., Tsuji, Y., Michaelides, E. E., and Gautam, M., 1999, *Gas-Particle Flows–1999*, ASME, New York.
[55] Michaelides, E. E., 1988, ''On the Drag Coefficient and the Correct Integration of the Equation of Motion of Particles in Gases,'' ASME J. Fluids Eng., **110**, pp. 339–342.
[56] Barton, I. E., 1996, ''Exponential-Lagrangian Tracking Schemes Applied to Stokes Law,'' ASME J. Fluids Eng., **118**, pp. 85–89.
[57] Dodemand, E., Prud'homme, R., and Kuentzmann, P., 1995, ''Influence of Unsteady Forces Acting on a Particle in a Suspension Application to the Sound Propagation,'' Int. J. Multiphase Flow, **21**, pp. 27–51.
[58] Sangani, A. S., Zhang, D. Z., and Prosperetti, A., 1991, ''The Added Mass, Basset and Viscous Drag Coefficients in Nondilute Bubbly Liquids Undergoing Small-Amplitude Oscillatory Motion,'' Phys. Fluids A, **3**, pp. 2955–2970.
[59] Coimbra, C. F. M., and Rangel, R. H., 1997, ''General Solution of the Particle Momentum Equation in Unsteady Stokes Flows,'' J. Fluid Mech., **370**, pp. 53–72.
[60] Coimbra, C. F. M., Edwards, D. K., and Rangel, R. H., 1998, ''Heat Transfer in a Homogenous Suspension Including Radiation and History Effects,'' J. Thermophys. Heat Transfer, **12**, pp. 304–312.
[61] Vojir, D. J., and Michaelides, E. E., 1994, ''The Effect of the History Term on the Motion of Rigid Spheres in a Viscous Fluid,'' Int. J. Multiphase Flow, **20**, pp. 547–556.
[62] Sazhin, S. S., Goldstein, V. A., and Heikal, M. R., 2001, ''A Transient Formulation of Newton's Cooling Law for Spherical Bodies,'' ASME J. Heat Transfer, **123**, pp. 63–64.
[63] Michaelides, E. E., 1992, ''A Novel Way of Computing the Basset Term in Unsteady Multiphase Flow Computations,'' Phys. Fluids A, **4**, pp. 1579–1582.
[64] Maxey, M. R., 1987, ''The Motion of Small Spherical Particles in a Cellular Flow Field,'' Phys. Fluids, **30**, pp. 1915–1928.
[65] Reeks, M. W., and McKee, S., 1984, ''The Dispersive Effects of Basset History Forces on Particle Motion in Turbulent Flow,'' Phys. Fluids, **27**, pp. 1573–1582.
[66] Lhuillier, D., 2001, ''Internal Variables and the Non-Equilibrium Thermodynamics of Colloidal Suspensions,'' J. Non-Newtonian Fluid Mech., **96**, pp. 19–30.
[67] Theofanous, T. G., Bohrer, T. H., Chang, M. C., and Patel, P. D., 1978, ''Experiments and Universal Growth Relations for Vapor Bubbles with Microlayers,'' ASME J. Heat Transfer, **100**, pp. 41–48.
[68] Theofanous, T. G., and Patel, P. D., 1976, ''Universal Relations for Bubble Growth,'' Int. J. Heat Mass Transf., **19**, pp. 425–429.
[69] Magnaudet, J., and Legendre, D., 1998, ''The Viscous Drag Force on a Spherical Bubble With a Time-Dependent Radius,'' Phys. Fluids, **10**, pp. 550–554.
[70] Morrison, F. A., and Stewart, M. B., 1976, ''Small Bubble Motion in an Accelerating Fluid,'' ASME J. Appl. Mech., **97**, pp. 399–402.
[71] Thorncroft, G. E., Klausner, J. F., and Mei, R., 2001, ''Bubble Forces and Detachment Models,'' Multiph. Sci. Technol., **13**(3–4), pp. 35–76.
[72] Ormieres, D., and Provancal, M., 1999, ''Transition to Turbulence in the Wake of a Sphere,'' Phys. Rev. Lett., **83**, pp. 80–83.
[73] Ghidersa, B., and Dusek, J., 2000, ''Breaking of Axisymmetry and Onset of Unsteadiness in the Wake of a Sphere,'' J. Fluid Mech., **423**, pp. 33–69.
[74] Mebarek, M., Bouchet, G., Gidhersa, B., and Dusek, J., 2002, ''Hydrodynamical Forces Acting on a Rigid Fixed Sphere Placed in a Uniform Flow,'' Int. J. Numer. Methods Fluids, in print.
[75] Maxworthy, T., 1965, ''Accurate Measurements of a Sphere Drag at Low Reynolds Numbers,'' J. Fluid Mech., **23**, pp. 369–372.
[76] Schiller, L., and Nauman, A., 1933, ''Uber die grundlegende Berechnung bei der Schwekraftaufbereitung,'' Ver. Deutch. Ing., **44**, pp. 318–320.
[77] Whitaker, S., 1972, ''Forced Convection Heat Transfer Correlations for Flow in Pipes Past Flat Plates, Single Cylinders, Single Spheres, and for Flow in Packed Beds and Tubes Bundles,'' AIChE J., **18**, pp. 361–371.
[78] Incropera, F. P., and DeWitt, C. P., 1985, *Fundamentals of Heat and Mass Transfer*, John Wiley and Sons, New York.
[79] Feng, Z.-G., and Michaelides, E. E., 2001, ''Heat and Mass Transfer Coefficients of Viscous Spheres,'' Int. J. Heat Mass Transf., **44**, pp. 4445–4454.
[80] Feuillebois, F., and Lasek, A., 1980, ''Boundary Layer on a Sphere Accelerating From Rest,'' *Boundary and Interior Layers—Computational and Asymptotic Methods*, J. J. H. Miller, ed., Boole Press, Dublin.
[81] Mei, R., 1994, ''Flow due to an Oscillating Sphere and an Expression for Unsteady Drag on the Sphere at Finite Reynolds Numbers,'' J. Fluid Mech., **270**, pp. 133–174.
[82] Lawrence, C. J., and Mei, R., 1995, ''Long-Time Behavior of the Drag on a Body in Impulsive Motion,'' J. Fluid Mech., **283**, pp. 307–332.
[83] Lovalenti, P. M., and Brady, J. F., 1995, ''Force on a Body in Response to an Abrupt Change in Velocity at Small but Finite Reynolds Number,'' J. Fluid Mech., **293**, pp. 35–46.
[84] Choudhury, P. N., and Drake, D. G., 1971, ''Unsteady Heat Transfer from a Sphere in a Low Reynolds Number Flow,'' Q. J. Mech. Appl. Math., **24**, pp. 23–36.

[85] Konoplin, N., and Sparrow, E. M., 1972, ''Unsteady Heat Transfer and Temperature for Stokesian Flow About a Sphere,'' ASME J. Heat Transfer, **94**, pp. 266–272.
[86] Feng, Z.-G., and Michaelides, E. E., 1996, ''Unsteady Heat Transfer from a Spherical Particle at Finite Peclet Numbers,'' ASME J. Fluids Eng., **118**, pp. 96–102.
[87] Pozrikidis, C., 1997, ''Unsteady Heat or Mass Transport from a Suspended Particle at Low Peclet Numbers,'' J. Fluid Mech., **289**, pp. 652–688.
[88] Lawrence, C. J., and Weinbaum, S., 1986, ''The Force on an Axisymmetric Body in Linearized Time-Dependent Motion: A New Memory Term,'' J. Fluid Mech., **171**, pp. 209–218.
[89] Lawrence, C. J., and Weinbaum, S., 1988, ''The Unsteady Force on a Body at Low Reynolds Number: The Axisymmetric Motion of a Spheroid,'' J. Fluid Mech., **189**, pp. 463–498.
[90] Feng, Z.-G., and Michaelides, E. E., 1997, ''Transient Heat and Mass Transfer From a Spheroid,'' AIChE J., **43**, pp. 609–616.
[91] Konoplin, N., 1971, ''Gravitationally Induced Acceleration of Spheres in a Creeping Flow,'' AIChE J., **17**, pp. 1502–1503.
[92] Chaplin, J. R., 1999, ''History Forces and the Unsteady Wake of a Cylinder,'' J. Fluid Mech., **393**, pp. 99–121.
[93] Julien, P. Y., 1995, *Erosion and Sedimentation*, Cambridge Press, Cambridge, UK.
[94] Loseno, C., and Easson, W. J., ''Free Falling of Irregular Particles,'' *Proceedings of the 4th International Conference on Multiphase Flow*, E. E. Michaelides, ed., New Orleans, LA.
[95] Odar, F., and Hamilton, W. S., 1964, ''Forces on a Sphere Accelerating in a Viscous Fluid,'' J. Fluid Mech., **18**, pp. 302–303.
[96] Odar, F., 1966, ''Verification of the Proposed Equation for Calculation of the Forces on a Sphere Accelerating in a Viscous Fluid,'' J. Fluid Mech., **25**, pp. 591–592.
[97] Al-taweel, A. M., and Carley, J. F., 1971, ''Dynamics of Single Spheres in Pulsated Flowing Liquids: Part I. Experimental Methods and Results,'' AIChE Symp. Sr., **67**(116), pp. 114–123.
[98] Al-taweel, A. M., and Carley, J. F., 1972, ''Dynamics of Single Spheres in Pulsated Flowing Liquids: Part II. Modeling and Interpretation of Results,'' AIChE Symp. Ser., **67**(116), pp. 124–131.
[99] Schoneborn, P. R., 1975, ''The Interaction Between a Single Sphere and an Oscillating Fluid,'' Int. J. Multiphase Flow, **2**, pp. 307–317.
[100] Karanfilian, S. K., and Kotas, T. J., 1978, ''Drag on a Sphere in Unsteady Motion in a Liquid at Rest,'' J. Fluid Mech., **87**, pp. 85–96.
[101] Temkin, S., and Mehta, H. K., 1982, ''Droplet Drag in an Accelerating and Decelerating Flow,'' J. Fluid Mech., **116**, pp. 297–313.
[102] Tsuji, Y., Kato, N., and Tanaka, T., 1991, ''Experiments on the Unsteady Drag and Wake of a Sphere at High Reynolds Numbers,'' Int. J. Multiphase Flow, **17**, pp. 343–354.
[103] Darwin, C., 1953, ''A Note on Hydrodynamics,'' Proc. Roy. Soc., **49**, pp. 342–353.
[104] Bataille, J., Lance, M., and Marie, J. L., 1990, ''Bubbly Turbulent Shear Flows,'' J. Kim, U. Rohatgi, and M. Hashemi, eds., FED-Vol. 99, ASME, New York, pp. 1–7.
[105] Rivero, M., Magnaudet, J., and Fabre, J., 1991, ''Quelques Resultats Nouveaux Concernants les Forces Exercées sur une Inclusion Spherique par Ecoulement Accelere,'' C. R. Acad. Sci., Ser. II: Mec., Phys., Chim., Sci. Terre Univers, **312**, ser. II, pp. 1499–1506.
[106] Auton, T. R., Hunt, J. R. C., and Prud'homme, M., 1988, ''The Force Exerted on a Body in Inviscid Unsteady Non-Uniform Rotational Flow,'' J. Fluid Mech., **197**, pp. 241–257.
[107] Kim, I., Elghobashi, S., and Sirignano, W. A., 1998, ''On the Equation for Spherical-Particle Motion: Effect of Reynolds and Acceleration Numbers,'' J. Fluid Mech., **367**, pp. 221–253.
[108] Bagchi, P., and Balachandar, S., 2001, ''On the Effect of Nonuniformity and the Generalization of the Equation of Motion of a Particle,'' *Proceedings of the 4th International Conference on Multiphase Flow*, E. E. Michaelides, ed., New Orleans, LA.
[109] Kaviani, M., 1994, *Principles of Convective Heat Transfer*, Springer-Verlag, New York.
[110] Matsumoto, Y., and Takagi, S., 1998, ''Numerical Simulations of Multiphase Flows,'' Computational Fluid Dyn. Rev., **4**, pp. 994–1010.
[111] LeClair, B. P., Hamielec, A. E., and Pruppracher, H. R., 1970, ''A Numerical Study of the Drag on a Sphere at Intermediate Reynolds and Peclet Numbers,'' J. Atmos. Sci., **27**, pp. 308–319.
[112] Rivkind, V. Y., Ryskin, G. M., and Ishbein, G. A., 1976, ''Flow Around a Spherical Drop in a Fluid Medium at Intermediate Reynolds Numbers,'' Appl. Math. Mech., **40**, pp. 687–691.
[113] Abramzon, B., and Elata, C., 1984, ''Heat Transfer from a Single Sphere in Stokes Flow,'' Int. J. Heat Mass Transf., **27**, pp. 687–695.
[114] Feng, Z.-G., and Michaelides, E. E., 2000, ''A Numerical Study on the Transient Heat Transfer From a Sphere at High Reynolds and Peclet Numbers,'' Int. J. Heat Mass Transf., **43**, pp. 219–229.
[115] Feng, Z.-G., and Michaelides, E. E., 2000, ''Mass and Heat Transfer From Fluid Spheres at Low Reynolds Numbers,'' Powder Technol., **112**, pp. 63–69.
[116] Feng, Z.-G., and Michaelides, E. E., 2001, ''Drag Coefficients of Viscous Spheres at Intermediate and High Reynolds Numbers,'' ASME J. Fluids Eng., **123**, pp. 841–849.
[117] Winnikow, S., and Chao, B. T., 1966, ''Droplet Motion in Purified Systems,'' Phys. Fluids, **9**, pp. 50–61.
[118] Magnaudet, J., Rivero, M., and Fabre, J., 1995, ''Accelerated Flows Past a Rigid Sphere or a Spherical Bubble. Part 1. Steady Straining Flow,'' J. Fluid Mech., **284**, pp. 97–135.
[119] Mei, R., and Lawrence, C. J., 1996, ''The Flow Field due to a Body in Impulsive Motion,'' J. Fluid Mech., **325**, pp. 79–111.
[120] Kim, I., Elghobashi, S., and Sirignano, W. A., 1997, ''Unsteady Flow Interactions Between a Pair of Advected Vortex Tubes and a Rigid Sphere,'' J. Multiphase Flow, **23**, pp. 1–23.
[121] Masoudi, M., and Sirignano, W. A., 2000, ''Collision of a Vortex with a Vaporizing Droplet,'' Int. J. Multiphase Flow, **26**, pp. 1925–1949.
[122] Kim, I., Elghobashi, S., and Sirignano, W. A., 1993, ''Three-Dimensional Flow Over Two Spheres Placed Side by Side,'' J. Fluid Mech., **246**, pp. 465–488.
[123] Chiang, H., and Kleinstreuer, C., 1993, ''Numerical Analysis of Variable-Fluid-Property Effects on the Convective Heat and Mass Transfer of Fuel Droplets,'' Combust. Flame, **92**, pp. 459–464.
[124] Feng, J., and Joseph, D. D., 1995, ''The Unsteady Motion of Solid Bodies in Creeping Flows,'' J. Fluid Mech., **303**, pp. 83–102.
[125] Cheng, H., and Papanicolaou, G., 1997, ''Flow Past Periodic Arrays of Spheres at Low Reynolds Number,'' J. Fluid Mech., **335**, pp. 189–212.
[126] Chiang, H., and Kleinstreuer, C., 1992, ''Transient Heat and Mass Transfer of Interacting Vaporizing Droplets in a Linear Array,'' Int. J. Heat Mass Transf., **35**, pp. 2675–2682.
[127] Pozrikidis, C., 2000, ''Conductive Mass Transport From a Semi-Infinite Lattice of Particles,'' Int. J. Heat Mass Transf., **43**, pp. 493–502.
[128] Balachandar, S., and Ha, M. Y., 2001, ''Unsteady Heat Transfer From a Sphere in a Uniform Cross-Flow,'' Phys. Fluids, **13**(12), pp. 3714–3728.
[129] Feng, Z.-G., and Michaelides, E. E., 1998, ''Motion of a Permeable Sphere at Finite but Small Reynolds Numbers,'' Phys. Fluids, **10**, pp. 1375–1383.
[130] Graham, D. J., and Moyeed, R. A., 2002, ''How Many Particles for My Lagrangian Simulations?'' Powder Technol., **114**, pp. 254–259.
[131] Hjelmfelt, A. T., and Mockros, L. F., 1966, ''Motion of Discrete Particles in a Turbulent Fluid,'' Appl. Sci. Res., **16**, pp. 149–161.
[132] Druzhinin, O. A., and Ostrovsky, L. A., 1994, ''The Influence of Basset Force on Particle Dynamics in Two Dimensional Flows,'' Physica D, **76**, pp. 34–43.
[133] Domgin, J.-F., Huilier, D. G. F., Karl, J.-J., Gardin, P., and Burnage, H., 1998, ''Experimental and Numerical Study of Rigid Particles, Droplets, and Bubbles Motion in Quiescent and Turbulent Flows—Influence of the History Force,'' Third International Conference on Multiphase Flow, ICMF-98, Lyon, France.
[134] Launey, K., and Huillier, D., 1999, ''On the Influence of the Non-Stationary Forces on the Particles Dispersion,'' *Proceedings of the ASME*, ASME, New York, FEDSM99-7874, San Fransisco, CA.
[135] Abbad, M., and Souhar, M., 2001, ''Experimentation on the History Force Acting on Rigid or Fluid Particles at Low Reynolds Number in an Oscillating Frame,'' *Proceedings of the 4th International Conference on Multiphase Flow*, E. E. Michaelides, ed., New Orleans, LA.
[136] Thomas, P. J., 1997, ''A Numerical Study of the Influence of the Basset Force on the Statistics of LDV Velocity Data Sampled in a Flow Region With a Large Spatial Velocity Gradient,'' Exp. Fluids, **23**, pp. 48–53.
[137] Gay, M., and Michaelides, E. E., 2002, ''Effect of the History Term on the Transient Energy Equation for a Sphere,'' Int. J. Heat Mass Transf., in print.
[138] Michaelides, E. E., and Feng, Z.-G., 2002, ''History Terms in the Heat and Mass Transfer Equations of Particles,'' *Proc. 12th Intern. Conf. on Heat Transfer*, Elsevier, Amsterdam, Paper No. 991.
[139] White, F. M., 1985, *Viscous Fluid Flow*, McGraw-Hill, New York.
[140] Carlson, D. J., and Hoglund, R. F., 1964, ''Particle Drag and Heat Transfer in Rocket Nozzles,'' AIAA J., **2**, pp. 1980–1984.
[141] Ranz, W. E., and Marshall, W. R., 1952, ''Evaporation From Drops,'' Chem. Eng. Prog., **48**, pp. 141–146.
[142] Polyanin, A. D., 1984, ''An Asymptotic Analysis of Some Nonlinear Boundary Value Problems of Convective Mass and Heat Transfer of Reacting Particles With the Flow,'' Int. J. Heat Mass Transf., **27**, pp. 163–189.
[143] Yuge, T., 1960, ''Experiments on Heat Transfer from Spheres Including Combined Natural and Forced Convection,'' ASME J. Heat Transfer, **82**, pp. 214–220.
[144] Bankoff, S. G., and Mason, J. P., 1962, ''Heat Transfer from the Surface of a Steam Bubble in Turbulent Subcooled Liquid Stream,'' AIChE J., **8**, pp. 30–33.
[145] Gilbert, H., and Angellino, H., 1974, ''Transfere de Matiere entre une Sphere Soumise a des Vibrations et un Liquide en Mouvement,'' Int. J. Heat Mass Transf., **17**, pp. 625–632.
[146] Hayward, G. L., and Pei, D. C. T., 1978, ''Local Heat Transfer from a Single Sphere to a Turbulent Air Stream,'' Int. J. Heat Mass Transf., **21**, pp. 35–41.
[147] Chen, J. L. S., 1974, ''Growth of the Boundary Layer on a Spherical Gas Bubble,'' ASME J. Appl. Mech., **41**, pp. 873–878.
[148] Lhuillier, D., 1982, ''Forces d'Inertie sur une Bulle en Expansion se Deplacant dans un Fluide,'' C. R. Acad. Sci., Paris, **295**, pp. 95–106.
[149] Drew, D. A., and Lahey, R. T., 1987, ''The Virtual Mass and Lift Force on a Sphere in Rotating and Straining Inviscid Flow,'' Int. J. Multiphase Flow, **13**, pp. 113–121.
[150] Drew, D. A., and Lahey, R. T., 1990, ''Some Supplemental Analysis on the Virtual Mass and Lift Force on a Sphere in a Rotating and Straining Inviscid Flow,'' Int. J. Multiphase Flow, **16**, pp. 1127–1130.
[151] Mei, R., Klausner, J. F., and Lawrence, C. J., 1994, ''A Note on the History Force on a Spherical Bubble at Finite Reynolds Number,'' Phys. Fluids, **6**, pp. 418–420.
[152] Park, W. C., Klausner, J. F., and Mei, R., 1995, ''Unsteady Forces on Spherical Bubbles,'' Exp. Fluids, **19**, pp. 167–172.

[153] Chisnell, R. F., 1987, ''The Unsteady Motion of a Drop Moving Vertically Under Gravity,'' J. Fluid Mech., **176**, pp. 434–464.
[154] Sy, F., and Lightfoot, 1971, ''Transient Creeping Flow Around Fluid Spheres,'' AIChE J., **17**, pp. 177–181.
[155] Galindo, V., and Gerbeth, G., 1993, ''A Note on the Force on an Accelerating Spherical Drop at Low Reynolds Numbers,'' Phys. Fluids, **5**, pp. 3290–3292.
[156] Feng, Z. G., Michaelides, E. E., and Scibilia, M.-F., 1996, ''The Energy Equation of a Sphere in an Unsteady and Non-Uniform Temperature Field,'' Rev. Gen. Therm., **35**, pp. 5–13.
[157] Yang, S.-M., and Leal, L. G., 1991, ''A Note on Memory-Integral Contributions to the Force of an Accelerating Spherical Drop at Low Reynolds Number,'' Phys. Fluids A, **3**, pp. 1822–1824.
[158] Hadamard, J. S., 1911, ''Mouvement Permanent Lent d'une Sphere Liquide et Visqueuse dans un Liquide Visqueux,'' C. R. Acad. Sci., Paris, **152**, pp. 1735–1752.
[159] Rybczynski, W., 1911, ''On the Translatory Motion of a Fluid Sphere in a Viscous Medium,'' Bull. Acad. Sci., Cracow, Series A, **p.** 40.
[160] Harper, J. F., and Moore, D. W., 1968, ''The Motion of a Spherical Liquid Drop at High Reynolds Number,'' J. Fluid Mech., **32**, pp. 367–391.
[161] Ryskin, G., and Leal, L. G., 1983, ''Numerical Simulation of a Free Boundary Problem in Fluid Mechanics—Part III: Bubble Deformation in an Axysymmetric Straining Flow,'' J. Fluid Mech., **148**, pp. 37–54.
[162] Fan, L.-S., and Tsuchiya, K., 1990, *Bubble Wake Dynamics in Liquids and Liquid Solid Suspensions*, Butterworth-Heinemann, Stoneham, MA.
[163] Takagi, S., Prosperetti, A., and Matsumoto, Y., 1994, ''Drag Coefficient of a Gas Bubble in an Axisymmetric Shear Flow,'' Phys. Fluids, **6**(9), pp. 3186–3188.
[164] Tomiyama, A., Miyoshi, K., Tamai, H., Zun, I., and Sakaguchi, T., 1998, ''A Bubble Tracking Method for the Prediction of Spatial-Evolution of Bubble Flow in a Vertical Pipe,'' *Proceedings of the ICMF-98*, Lyon, France.
[165] Ford, B., and Loth, E., 1998, ''Forces on Ellipsoidal Bubbles in a Turbulent Shear Layer,'' Phys. Fluids, **10**(1), pp. 178–188.
[166] Fujiwara, A., Tokuhiro, A., Hishida, K., and Maeda, M., 1998, ''Investigation of Oscillatory Bubble Motion Using a Dual Shadow Technique and Its Surrounding Flow Field by LIF-PIV,'' *Proceedings of the 3th International Conference on Multiphase Flow*, ICMF-98, Lyon, France.
[167] Fujiwara, A., Tokuhiro, A., Hishida, K., and Maeda, M., 2001, ''Flow Structure Around Rising Bubble Measured by PIV/LIF (Effect of Shear Rate and Bubble Size),'' *Proceedings of the 4th International Conference on Multiphase Flow*, E. E. Michaelides, ed., New Orleans, LA.
[168] Tokuhiro, A., Maekawa, M., Iizuka, K., Hishida, K., and Maeda, M., 1998, ''Turbulent Flow Past a Bubble and an Ellipsoid Using Shadow-Image and PIV Techniques,'' Int. J. Multiphase Flow, **24**, pp. 1383–1406.
[169] Sirignano, W. A., and Mehring, C., 2000, ''Review of Theory of Distortion and Disintegration of Liquid Streams,'' Prog. Energy Combust. Sci., **26**, pp. 609–655.
[170] Garner, F. H., and Lihou, D. A., 1965, *DECHEMA–Monograph*, **55**, pp. 155–178.
[171] LeClair, B. P., and Hamielec, A. E., 1972, ''A Theoretical and Experimental Study of the Internal Circulation in Water Drops Falling at Terminal Velocity in Air,'' J. Atmos. Sci., **29**(2), pp. 728–740.
[172] Rivkind, V. Y., and Ryskin, G. M., 1976, ''Flow Structure in Motion of a Spherical Drop at Intermediate Reynolds Numbers,'' Fluid Mech.-Sov. Res., **11**(1), pp. 5–12.
[173] Oliver, D. L., and Chung, J. N., 1987, ''Flow About a Fluid Sphere at Low to Moderate Reynolds Numbers,'' J. Fluid Mech., **177**, pp. 1–18.
[174] Tomiyama, A., 2001, ''Reconsideration of Three Fundamental Problems in Modeling Bubbly Flows,'' *39th European Two-Phase Flow Group Meeting*, Aveiro, Portugal.
[175] Wu, M., and Gharib, M., 2002, ''Experimental Studies on the Shape and Path of Small Air Bubbles Rising in Clean Water,'' Phys. Fluids, **14**, pp. L49–L52.
[176] Prosperetti, A., 2002, ''Some Problems Associated With the Formation and Flow of Bubbles,'' *14th Congress of Theoretical and Applied Mechanics*, Blacksburg, VA.
[177] Bowman, C. W., Ward, D. M., Johnson, A. I., and Trans, O., 1961, ''Mass Transfer From Fluid and Solid Spheres at Low Reynolds Numbers,'' Can. J. Chem. Eng., **39**, pp. 9–13.
[178] Abramzon, B., and Sirignano, W. A., 1989, ''Droplet Vaporization for Spray Combustion Calculations,'' Int. J. Heat Mass Transf., **32**, pp. 1605–1618.
[179] Chigier, N. A., 1976, ''The Atomization and Burning of Liquid Fuel Sprays,'' Prog. Energy Combust. Sci., **2**, pp. 97–114.
[180] Chigier, N. A., 1981, *Energy, Combustion and Environment*, McGraw-Hill, New York.
[181] Chigier, N. A., and McCreath, C. G., 1974, ''Combustion of Droplets in Sprays,'' Acta Astronaut., **1**, pp. 687–710.
[182] Crespo, A., and Linan, A., 1975, ''Unsteady Effects in Droplet Evaporation and Combustion,'' Combust. Sci. Technol., **1**, pp. 9–18.
[183] Law, C. K., 1982, ''Recent Advances in Droplet Vaporization and Combustion,'' Prog. Energy Combust. Sci., **8**, pp. 171–201.
[184] Williams, A., 1985, *Combustion Theory: The Fundamental Theory of Chemically Reacting Flow Systems*, Benjamin-Cummings, Menlo Park, CA.
[185] Saffman, P. G., 1965, ''The Lift on a Small Sphere in a Slow Shear Flow,'' J. Fluid Mech., **22**, pp. 385–398.
[186] Saffman, P. G., 1968, ''The Lift on a Small Sphere in a Slow Shear Flow-Corrigendum,'' J. Fluid Mech., **31**, pp. 624–625.
[187] Childress, S., 1964, ''The Slow Motion of a Sphere in a Rotating Viscous Fluid,'' J. Fluid Mech., **20**, pp. 305–314.
[188] Fan, F. G., and Ahmadi, G., 2000, ''Wall Deposition of Small Ellipsoids From Turbulent Air Flows—A Brownian Dynamics Simulation,'' J. Aerosol. Sci., **31**(10), pp. 1205–1229.
[189] Crowe, C., Chung, J. N., and Troutt, T. R., 1988, ''Particle Mixing in Free Shear Flows,'' Prog. Energy Combust. Sci., **14**, pp. 171–194.
[190] Bohnet, M., Gottschalk, O., and Morweiser, M., 1997, ''Modern Design of Aerocyclones,'' Adv. Powder Technol., **8**(2), pp. 137–161.
[191] Auton, T. R., 1987, ''The Lift Force on a Spherical Body in a Rotational Flow,'' J. Fluid Mech., **183**, pp. 199–218.
[192] Tsuji, Y., Morikawa, Y., and Mizuno, O., 1985, ''Experimental Measurements of the Magnus Force on a Rotating Sphere at Low Reynolds Numbers Bubble in an Axisymmetric Shear Flow,'' ASME J. Fluids Eng., **107**, pp. 484–498.
[193] McLaughlin, J. B., 1991, ''Inertial Migration of a Small Sphere in Linear Shear Flows,'' J. Fluid Mech., **224**, pp. 261–274.
[194] Cherukat, P., McLaughlin, J. B., and Graham, A. L., 1994, ''The Inertial Lift on a Rigid Sphere Translating in a Linear Shear Flow Field,'' Int. J. Multiphase Flow, **20**, pp. 339–353.
[195] Sridhar, G., and Katz, J., 1995, ''Drag and Lift Forces on Microscopic Bubbles Entrained by a Vortex,'' Phys. Fluids, **7**(2), pp. 389–399.
[196] Mei, R., and Klausner, J. F., 1994, ''Shear Lift Force on Spherical Bubbles,'' Int. J. Heat Mass Transf., **15**(1), pp. 62–65.
[197] Magnaudet, J., and Legendre, D., 1998, ''Some Aspects of the Lift Force on a Spherical Bubble,'' *In Fascination of Fluid Dynamics*, A. Biesheuvel and G. F. van Heijst, eds., Kluwer Academic, Dordrecht, The Netherlands, pp. 441–461.
[198] Legendre, D., and Magnaudet, J., 1997, ''A Note on the Lift Force on a Spherical Bubble or Drop in a Low Reynolds Number Linear Shear Flow,'' Phys. Fluids, **9**, pp. 3572–3574.
[199] Tomiyama, A., Tamai, H., Zun, I., and Hosokawa, S., ''Transverse Migration of Single Bubbles in Simple Shear Flows,'' *Proceedings 2nd Int. Symposium on Two-Phase Flow Modeling and Experimentation*, **2**, pp. 941–948.
[200] Oesterle, B., and Dihn, Bui, 1998, ''Experiments on the Lift of a Spinning Sphere in the Range of Intermediate Reynolds Numbers,'' Exp. Fluids, **25**, pp. 16–22.
[201] Rubinow, S. I., and Keller, J. B., 1961, ''The Transverse Force on a Spinning Sphere Moving in a Viscous Fluid,'' J. Fluid Mech., **11**, pp. 447–459.
[202] Dennis, S. C. R., Singh, S. N., and Ingham, D. B., 1980, ''The Steady Flow Due to a Rotating Sphere at Low and Moderate Reynolds Numbers,'' J. Fluid Mech., **101**, pp. 257–279.
[203] Feng, Z.-G., and Michaelides, E. E., 2002, ''Inter-Particle Forces and Lift on a Particle Attached to a Solid Boundary in Suspension Flow,'' Phys. Fluids, **14**, pp. 49–60.
[204] Aggarwal, S. K., Chen, G., Yapo, J. B., Grinstein, F. F., and Kailasanath, K., 1992, ''Numerical Simulation of Particle Dynamics in Planar Shear Layers,'' AIAA Paper No. 92-0107.
[205] Moursali, E., Marie, J. L., and Bataille, J., 1995, ''An Upward Turbulent Bubbly Boundary Layer Along a Vertical Flat Plate,'' Int. J. Multiphase Flow, **21**, pp. 107–117.
[206] Climent, E., and Magnaudet, J., 1998, ''Modifications d'une Couche de Melange Verticale Induites par la Presence de Bulles,'' Academie des Sciences Paris **326**(11b), pp. 627–634.
[207] Narayanan, C., Lakehal, D., and Yadigaroglu, G., 2002, ''Linear Stability Analysis of Particle-Laden Mixing Layers Using Lagrangian Particle Tracking,'' Powder Technol., **125**, pp. 122–130.
[208] Marie, J. L., Moursali, E., and Tran-Cong, S., 1997, ''Similarity Law and Turbulence Intensity Profiles in a Bubbly Boundary Layer at Low Void Fraction,'' Int. J. Multiphase Flow, **23**, pp. 227–247.
[209] Joia, I. A., Ushijima, T., and Perkins, R. J., 1997, ''Numerical Study of Bubble and Particle Motion in Turbulent Boundary Layer Using Proper Orthogonal Decomposition,'' Appl. Sci. Res., **57**, pp. 263–277.
[210] Tran-Cong, S., Marie, J. L., and Perkins, R. J., 2001, ''Bubble Migration in a Turbulent Boundary Layer—The Influence of Coherent Structures,'' *Proceedings of the 4th International Conference on Multiphase Flow*, E. E. Michaelides, ed., New Orleans, LA.
[211] Druzhinin, O. A., and Elghobashi, S. E., 2001, ''Direct Numerical Simulation of a Three-Dimensional Spatially Developing Bubble-Laden Mixing Layer with Two-Way Coupling,'' J. Fluid Mech., **429**, pp. 23–61.
[212] Felton, K., and Loth, E., 2002, ''Diffusion of Spherical Bubbles in a Turbulent Boundary Layer,'' Int. J. Multiphase Flow, **28**, pp. 69–92.
[213] Bohlin, T., 1960, ''Terminal Velocities of Solid Spheres in Cylindrical Enclosures,'' *Transactions of the Royal Institute of Technology*, Stockholm, Report No. 155.
[214] Haberman, W. L., and Sayre, R. M., 1958, ''Motion of Rigid and Fluid Spheres in Stationary and Moving Liquids Inside Cylindrical Tubes,'' Report No. 1143, David Taylor Model Basin, U.S. Navy, Washington, DC.
[215] Paine, P. L., and Scherr, P., 1975, ''Drag Coefficients for the Movement of Rigid Spheres Through Liquid-Filled Cylindrical Pores,'' Biophys. J., **15**, pp. 1087–1091.
[216] Iwaoka, M., and Ishii, T., 1979, ''Experimental Wall Correction Factors of Single Solid Spheres in Circular Cylinders,'' J. Chem. Eng. Jpn., **12**, pp. 239–242.
[217] Miyamura, A., Iwasaki, S., and Ishii, T., 1981, ''Experimental Wall Correction Factors of Single Solid Spheres in Triangular and Square Cylinders, and Parallel Plates,'' Int. J. Multiphase Flow, **7**, pp. 41–46.
[218] Masmoudi, K., Lecoq, N., Anthore, R., Bostel, F., and Feuillebois, F., 2002, ''Accurate Measurement of Hydrodynamic Interactions Between a Particle and Walls,'' Exp. Fluids, **32**, pp. 55–65.
[219] Fayon, A. M., and Happel, J., ''Effect of a Cylindrical Boundary on a Fixed

Rigid Sphere in a Moving Viscous Fluid,'' AIChE J., **6**, pp. 55–58.
[220] Feng, Z.-G., and Michaelides, E. E., 2002, ''Hydrodynamic Force on Spheres in Cylindrical and Prismatic Enclosures,'' Int. J. Multiphase Flow, **28**, pp. 479–496.
[221] Poiseuille, J. L. M., 1841, ''Recherches sur le Mouvement du Sang dans les Vein Capillaires,'' Mem. Acad. Roy. Sci., **7**, pp. 105–175.
[222] Wang, H., and Skalak, R., 1969, ''Viscous Flow in a Cylindrical Tube Containing a Line of Spherical Particles,'' J. Fluid Mech., **38**, pp. 75–96.
[223] Westborg, H., and Hassager, O., 1989, ''Creeping Motion of Long Bubbles and Drops in Capillary Tubes,'' J. Colloid Interface Sci., **133**, pp. 135–147.
[224] Xu, Q., and Michaelides, E. E., 1996, ''A Numerical Study of the Flow Over Ellipsoidal Objects Inside a Cylindrical Tube,'' Int. J. Numer. Methods Fluids, **22**, pp. 1075–1088.
[225] Brenner, H., and Happel, J., 1958, ''Slow Viscous Flow Past a Sphere in a Cylindrical Tube,'' J. Fluid Mech., **4**, pp. 195–213.
[226] Cox, R. G., and Brenner, H., 1967, ''The Slow Motion of a Sphere through a Viscous Fluid Towards a Plane Surface,'' Chem. Eng. Sci., **22**, pp. 1753–1777.
[227] Cox, R. G., and Hsu, S. K., 1977, ''The Lateral Migration of Solid Spheres in a Laminar Flow Near a Plane,'' Int. J. Multiphase Flow, **3**, pp. 201–222.
[228] Vasseur, P., and Cox, R. G., 1976, ''The Lateral Migration of Spherical Particles in Two-Dimensional Shear Flow,'' J. Fluid Mech., **78**, pp. 385–413.
[229] Cherukat, P., and McLaughlin, J. B., 1990, ''Wall-Induced Lift on a Sphere,'' Int. J. Multiphase Flow, **16**(5), pp. 899–907.
[230] Segre, G., and Silberberg, A., 1962, ''Behavior of Macroscopic Rigid Spheres in Poiseuille Flow,'' J. Fluid Mech., **14**, pp. 115–157.
[231] Inamuro, T., Maeba, K., and Ogino, F., 2000, ''Flow Between Parallel Walls Containing the Lines of Neutrally Buoyant Circular Cylinders,'' Int. J. Multiphase Flow, **26**, pp. 1981–2004.
[232] Mortazavi, S., and Tryggvason, G., 2000, ''A Numerical Study of the Motion of Drops in Poiseuille Flow. Part 1: Lateral Migration of One Drop,'' J. Fluid Mech., **411**, pp. 325–350.
[233] Joseph, D. D., Ocando, D., and Huang, P. Y., 2002, ''Slip Velocity and Lift,'' J. Fluid Mech., in print.
[234] Patankar, N., Ko, T., Choi, H. G., and Joseph, D. D., 2001, ''A Correlation for the Lift-Off of Many Particles in Plane Poiseuille Flows of Newtonian Fluids,'' J. Fluid Mech., **445**, pp. 55–76.
[235] Feuillebois, F., and Lasek, A., 1978, ''On the Rotational Historic Term in Non-Stationary Shear Flow,'' Q. J. Mech. Appl. Math., **31**, pp. 435–443.
[236] Brenner, H., 1961, ''The Slow Motion of a Sphere Through a Viscous Fluid Toward a Plane Surface,'' Chem. Eng. Sci., **16**, pp. 242–251.
[237] Kalio, G. A., 1993, ''Random Walk Modeling of Particle Deposition,'' *Gas-Solid Flows–1993*, Stock et al., eds., ASME FED Vol. 166, ASME, New York, pp. 161–167.
[238] Portela, L. M., Cota, P., and Oliemans, R. V. A., 2002, ''Numerical Study of the Near-Wall Behavior of Particles in Turbulent Pipe Flows,'' Powder Technol., **125**, pp. 149–157.
[239] Crowe, C. T., Sommerfeld, M., and Tsuji, Y., 1998, *Multiphase Flows with Droplets and Particles*, CRC Press, Boca Raton, FL.
[240] Sommerfeld, M., and Huber, N., 1999, ''Experimental Analysis and Modelling of Particle-Wall Collisions,'' Int. J. Multiphase Flow, **25**, pp. 1457–1489.
[241] Sommerfeld, M., 2000, ''Theoretical and Experimental Modelling of Particulate Flow,'' *Von Karman Institute for Fluid Dynamics Series*, B. Rhode, ed., Von Karman Institute, Saint Genese, Belgium.
[242] Yamamoto, Y., Potthoff, M., Tanaka, T., Kajishima, T., and Tsuji, Y., 2001, ''Large-Eddy Simulation of Turbulent Gas-Particle Flow in a Vertical Channel: Effect of Considering Inter-Particle Collisions,'' J. Fluid Mech., **442**, pp. 303–334.
[243] Michaelides, E. E., ed., 2001, *Proceedings of the 4th International Conference on Multiphase Flow*, New Orleans, LA.
[244] ICMF-98 1998, ''Proceedings of the 3rd International Conference on Multiphase Flow,'' Lyon, France.
[245] De Vries, A. W. G., Biesheuvel, A., and Van Wijngaarden, L., 2001, ''Notes on the Path and Wake of a Gas Bubble Rising in Pure Water,'' *Proceedings of the 4th International Conference on Multiphase Flow*, E. E. Michaelides, ed., New Orleans, LA.
[246] Lyubimov, D. V., Lyubimova, T. P., Meradji, S., and Roux, B., 2001, ''Unsteady Motion and Deformation of a Gaseous Bubble in a Vibrating Liquid in Zero Gravity,'' *Proceedings of the 4th International Conference on Multiphase Flow*, E. E. Michaelides, ed., New Orleans, LA.
[247] Richardson, J. F., and Zaki, W. N., 1954, ''The Fall Velocities of Spheres in Viscous Fluids,'' Trans. Inst. Chem. Eng., **32**, pp. 35–41.
[248] Rowe, P. N., 1961, ''The Drag Coefficient of a Sphere,'' Trans. Inst. Chem. Eng., **39**, pp. 175–181.
[249] Aidi, M., Feuillebois, F., Lasek, A., Anthore, R., Petipas, C., and Auvray, X., 1989, ''Mesure de la Vitese de Sedimentation d' une Suspension par Absorption de Rayons X,'' Rev. Phys. Appl., **24**, pp. 1077–1084.
[250] Batchelor, G. K., and Wen, C. S., 1983, ''Sedimentation in a Dilute Polydisperse System of Interacting Spheres. Part 2. Numerical Results,'' J. Fluid Mech., **137**, pp. 467–468.
[251] Batchelor, G. K., and Wen, C. S., 1982, ''Sedimentation in a Dilute Polydisperse System of Interacting Spheres—Part II: Numerical Results,'' J. Fluid Mech., **124**, pp. 495–511.
[252] Di Felice, R., 1994, ''The Voidage Function for Fluid-Particle Interaction Systems,'' Int. J. Multiphase Flow, **20**, pp. 153–162.
[253] Ladd, A. J. C., 1994, ''Numerical Simulations of Particulate Suspensions via a Discretized Boltzmann Equation—Part I: Theoretical Foundation,'' J. Fluid Mech., **271**, pp. 285–310.
[254] Ladd, A. J. C., 1994, ''Numerical Simulations of Particulate Suspensions via a Discretized Boltzmann Equation—Part II: Numerical Results,'' J. Fluid Mech., **271**, pp. 311–332.
[255] Aidun, C. K., Lu, Y.-N., and Ding, E.-J., 1998, ''Direct Analysis of Particulate Suspensions With Inertia Using the Discrete Boltzmann Equation,'' J. Fluid Mech., **373**, pp. 287–303.
[256] Kaneda, Y., 1986, ''The Drag on a Sparse Random Array of Fixed Spheres in Flow at Small but Finite Reynolds Number,'' J. Fluid Mech., **167**, pp. 455–463.
[257] Koch, D. L., and Ladd, A. J. C., 1997, ''Moderate Reynolds Number Flows Through Periodic and Random Arrays of Aligned Cylinders,'' J. Fluid Mech., **349**, pp. 31–66.
[258] Rojas, S., and Koplik, J., 1998, ''Non-Linear Flow in Porous Media,'' Phys. Rev. E, **E58**(4), pp. 4776–4782.
[259] Koch, D. L., and Sangani, A. S., 1999, ''Particle Pressure and Marginal Stability Limits for a Homogeneous Monodisperse Gas Fluidized Bed: Kinetic Theory and Numerical Calculations,'' J. Fluid Mech., **400**, pp. 229–263.
[260] Ergun, S., 1952, ''Fluid Flow Through Packed Columns,'' Chem. Eng. Prog., **48**, pp. 93–98.
[261] Zuber, N., 1964, ''On the Dispersed Two-Phase Flow in the Laminar Flow Regime,'' Chem. Eng. Sci., **19**, pp. 897–917.
[262] van Wijngaarden, L., 1976, ''Hydrodynamic Interaction Between Bubbles in a Liquid,'' J. Fluid Mech., **77**, pp. 27–44.
[263] Spelt, P. D. M., and Sangani, A. S., 1998, ''Properties and Averaged Equations for Flows of Bubbly Liquids,'' *In Fascination of Fluid Dynamics*, A. Biesheuvel, and G. F. van Heijst, eds., Kluwer Academic, Dordrecht, pp. 337–386.
[264] Sangani, A. S., and Didwania, A. K., 1993, ''Dynamic Simulation of Flows of Bubbly Liquids at Large Reynolds Numbers,'' J. Fluid Mech., **250**, pp. 307–337.
[265] Duineveld, P. C., 1998, ''Bouncing and Coalescence of Bubble Pairs,'' *In Fascination of Fluid Dynamics*, A. Biesheuvel, and G. F. van Heijst, eds., Kluwer Academic, Dordrecht, pp. 409–439.
[266] Neale, G., Epstein, N., and Nader, W., 1973, ''Creeping Flow Relative to Permeable Spheres,'' Chem. Eng. Sci., **28**, pp. 1865–1874.
[267] Beavers, G. S., and Joseph, D. D., 1967, ''Boundary Conditions at a Naturally Permeable Wall,'' J. Fluid Mech., **30**, pp. 197–207.
[268] Saffman, P. G., 1971, ''On the Boundary Condition at the Surface of a Porous Medium,'' Stud. Appl. Math., **50**, pp. 93–101.
[269] Jones, I. P., 1973, ''Low Reynolds Number Flow Past a Porous Spherical Shell,'' Proc. Cambridge Philos. Soc., **73**, pp. 231–238.
[270] Joseph, D. D., and Tao, L. N., 1964, ''The Effect of Permeability on the Slow Motion of a Porous Sphere in a Viscous Liquid,'' ZAMP, **44**, pp. 361–364.

Modeling and Qualitative Experiments on Swirling Bubbly Flows: Single Bubble With Rossby Number of Order 1

F. Magaud
A. F. Najafi[1]
J. R. Angilella
M. Souhar

Laboratoire d'Energétique et de Mécanique Théorique et Appliquée, LEMTA, CNRS-UMR 7563 ENSEM-INPL, 2, avenue de la Forêt de Haye, B.P. 160, 54504 Vandoeuvre Cedex, France

The behavior of an isolated bubble in a single-phase swirling flow is investigated theoretically and experimentally. The Rossby number is such that the liquid flow can be approximated by a solid-body rotation superposed to a uniform axial velocity. The equations of the motion of the bubble are solved analytically and numerically, by assuming that the bubble is small and does not modify the water flow. Two kinds of bubbles have been considered: clean bubbles and bubbles with a contaminated interface. In the latter case the bubble is treated as a solid sphere. In both cases a critical angular velocity ω_c for the rotating device is found. When $\omega<\omega_c$ the trajectory of the bubble is a conical spiral which converges to the pipe axis, and when $\omega>\omega_c$ the trajectory is a cosine conical spiral: the bubble migrates to the center in an oscillating manner. The numerical value of ω_c, together with the terminal velocity of the bubble, are found to be in good agreement with experimental observations, provided the bubble is treated as a solid sphere. [DOI: 10.1115/1.1539870]

1 Introduction

Single-phase swirling flows are widely used in industrial devices such as cyclonic separators, combustion chambers, Francis turbines, or Kaplan turbines. They are also visible in geophysical science (cyclones, siphons, etc.). In confined ducts, swirling flows can be obtained by superposing a rotating flow to an axial flow. Fluid points have quasi-helical trajectories, and the direction of their velocity vector continuously changes with their axial and radial coordinates. Rotation can be obtained in several manners in these single-phase flows. Indeed, three different kinds of methods emerge in the literature (Gupta et al. [1]), so that the various experimental works are not easy to analyze and compare. One can quote the experimental analyses of Weske and Sturov [2], Kitoh [3], and Jacquin [4], to name but a few. In addition, numerous theoretical analyses have also been performed: Talbot [5], Bradshaw [6], Rochino and Lavan [7], Lilley and Chigier [8], Gibson and Younis [9], and Kobayashi and Yoda [10]. However, the predictive power of such models remains rather poor, and the problem of the creation and control of swirling flows is still open today.

In the case of two-phase gas-liquid flows, very few references are available (see, for example, Baur [11], Greenspan and Ungarish [12], and Greenspan [13]), so that one cannot predict correctly the distribution of the phases in a swirling multiphase flow. When the gaseous phase is dispersed (bubbles), the analysis is also complicated, because of particle-particle interactions and of particle-turbulence interactions. This is the reason why, in the present paper, we focus on the movement of an isolated bubble in a swirling flow with Rossby number of order 1. Our goal is to analyze the trajectory of the bubble for various rotation rates of the liquid flow.

We shall first describe the mathematical modeling of the problem, then we will solve the equations analytically and numerically, and finally we compare our results to available experimental visualizations.

2 Visualization of Experimental Bubble Trajectories

Our experiment consists in a fixed vertical pipe of inner radius $R=0.03$ m (Fig. 1). At the bottom of the pipe a rotating honeycomb provides a rotating flow. Any gas-liquid mixture flowing into the device through the honeycomb is then forced to segregate because of the radial pressure gradient. The photographs of Fig. 2(*a*) illustrate this effect. (The bulk velocity of gas is 0.0064 m/s, and the bulk velocity of water is 1 m/s.)

The device can also be used to investigate the trajectory of a *single* bubble (or a train of bubbles), by means of a needle which tip can be placed at any position in the front section of the honeycomb. Such trajectories are shown on the photographs of Fig. 2(*b*). The effect of the rotation is clearly visible, as for $N=522$ rpm the bubble trajectory is close to the pipe axis. In the present paper we will investigate the case of a single bubble moving in the liquid flow. The bulk velocity of the liquid flow in our experiments is $W_0=1$ m/s.

Continuous flow rates are obtained by means of a classical loop (see Baur [11] and Baur et al. [14]). The control parameters of the liquid flow are the flow rate ($W_0\times\pi R^2$), and the angular velocity of the honeycomb ω. The needle is bent so that bubbles are injected without radial velocity, and also to avoid the appearance of air in its wake. The bubble injection frequency is taken to be small, so that bubble/bubble interactions can be neglected.

Camera visualizations enable to measure the vertical coordinate (z) and the deviated horizontal coordinate (X) of the bubble (see Fig. 1). Indeed, because the refraction index of air, Plexiglas, and water are different, the horizontal coordinate measured by the camera has to be corrected. This correction can be done by making use of the classical Snell-Descartes law.

Visualizations are performed using a standard camera (30 frames per second) and a VTR. The X and z-coordinates are determined on the screen by using a reticle which is moved by hand. Relative errors are of the order of $\pm 5\%$. In addition, we can estimate the order of magnitude of the equivalent bubble radius: $2a\simeq 3\text{ mm}\pm 20\%$.

[1]Present address: Mechanical Engineering Department, Sharif University of Technology, P.O. Box 11365/9567, Tehran, Iran.

Contributed by the Fluids Engineering Division for publication in the JOURNAL OF FLUIDS ENGINEERING. Manuscript received by the Fluids Engineering Division July 25, 2001; revised manuscript received October 21, 2002. Associate Editor: Y. Matsumoto.

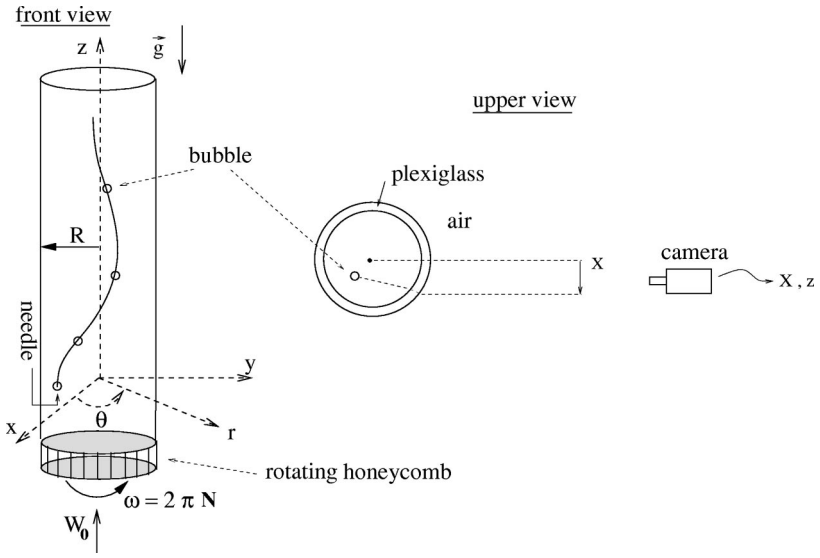

Fig. 1 Sketch of the pipe flow and of the rotating honeycomb. The inner radius of the pipe is $R=0.03$ m. The liquid/gas mixture flows through the honeycomb. Alternatively, the gaseous phase can also be injected by means of a needle.

The liquid velocity profiles at various cross sections of the pipe are obtained by means of a hot wire anemometer DANTEC 55R1, provided by an electronic device DISA55M01 (Baur [11]). These measures show that the velocity profile is close to a solid-body rotation, and this point will be discussed in the next section.

Four runs have been performed in the present analysis. They correspond to different rotation frequencies ($N=\omega/2\pi$). The various parameters of these runs are shown in Table 1 (see next section).

3 Mathematical Modeling of Bubble Trajectory

In order to describe the flow and the bubble trajectory we use the cylindrical coordinates system (r,θ,z) as sketched on Fig. 1. The angular velocity of the device is ω, its radius is R, and W_0 denotes the bulk velocity. The experiments of Weske and Sturov [2] in air flow show that if the Rossby number

$$\mathrm{Ro}=\frac{W_0}{R\omega}$$

is larger than 0.6, and if the Reynolds number is large enough (this condition is satisfied in the present work), then the axial velocity profile $w_c(r)$ is approximately uniform, and the azimuthal velocity profile $v_c(r)$ corresponds to a solid-body rotation over a large part of the cross section, up to the height $z/2R\simeq 10$. This result is also in agreement with our water flow experiments. Figure 3 shows our experimental velocity profiles at sections $z/R=2.4$ and $z/R=12$ when $\mathrm{Ro}=0.6$ (Baur [11]). These profiles are close to a solid-body rotation near the axis of the pipe (solid lines, Fig. 3). This result has also been confirmed by numerical computations performed with the Fluent CFD code (Najafi et al. [15]), with the Reynolds stresses turbulence model. (Indeed, the classical $k-\varepsilon$ turbulence model is not suitable to describe such a rotating flow, because of the anisotropy of the eddy viscosity. See, for example, Ref. [3].) Note that the axial velocity profile is nearly uniform in the vicinity of the pipe axis only. However, because bubbles migrate rapidly near the center, the assumption of uniform axial velocity can be done at first order.

We therefore assume that the velocity field $\mathbf{V}_c$ of the continuous phase (liquid) is of the form

$$\mathbf{V}_c=(u_c,v_c,w_c)\simeq(0,\omega r,W_0), \qquad (1)$$

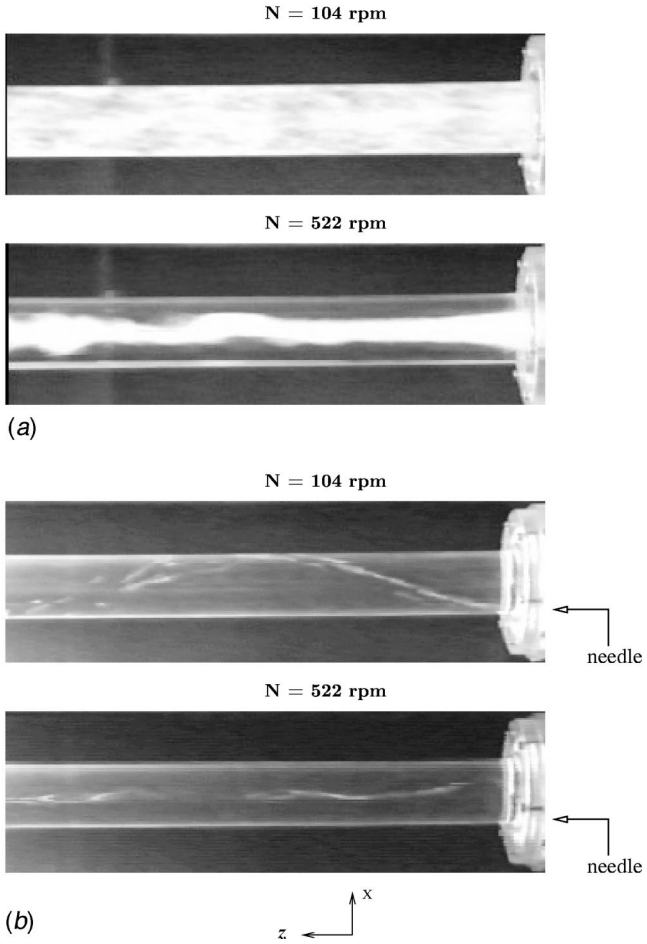

Fig. 2 Photographs showing the device at work, for two different rotation rates. The honeycomb is located on the right-hand side of the photographs. In case (*a*) a liquid/gas mixture flows through the honeycomb. In case (*b*) a train of bubbles is introduced by means of the needle. The tip of the needle is locate outside the visualization frame. The effect of swirling is clearly visible here, as it makes the light phase converge to the vicinity of the pipe axis.

Table 1 Parameters used in the four experiments

N	R	ω	W_0	Fr	γ	a_*	Ro	$\mathrm{Re}=2W_0R/\nu_c$
522 rpm	3 cm	54.7 s^{-1}	1 m/s	9.14	0.001	0.05	0.61	$6\ 10^4$
313 rpm	3 cm	32.8 s^{-1}	1 m/s	3.28	0.001	0.05	1.02	$6\ 10^4$
209 rpm	3 cm	21.9 s^{-1}	1 m/s	1.46	0.001	0.05	1.52	$6\ 10^4$
104 rpm	3 cm	10.9 s^{-1}	1 m/s	0.36	0.001	0.05	3.1	$6\ 10^4$

where the index c denotes the continuous phase. We then consider a small bubble (also denoted as "particle") injected at the bottom of the pipe. The bubble is assumed to be passive, spherical, with radius a. In this case the forces acting up on the particle are

$$\mathbf{F}=\mathbf{F}_p+\mathbf{F}_m+\mathbf{F}_d+\mathbf{F}_g+\mathbf{F}_l=\rho_d\mathcal{V}\frac{d\mathbf{V}_d}{dt}, \tag{2}$$

where the index d denotes the dispersed phase, ρ is the density, and $\mathcal{V}=4\pi a^3/3$ is the volume of the bubble.

$\mathbf{F}_p$ is the action of the pressure gradient (without the gravity term which we have included in the buoyancy force $\mathbf{F}_g$): $\mathbf{F}_p=\rho_c\mathcal{V}D\mathbf{V}_c/Dt$.

$\mathbf{F}_m$ denotes the added mass: $\mathbf{F}_m=C_a\rho_c\mathcal{V}D(\mathbf{V}_c-\mathbf{V}_d)/Dt$, where $C_a=1/2$ is the added-mass coefficient of a sphere in an inviscid fluid.

$\mathbf{F}_d$ is the drag: $\mathbf{F}_d=-(1/2)\rho_c C_d\pi a^2(\mathbf{V}_d-\mathbf{V}_c)\|\mathbf{V}_d-\mathbf{V}_c\|$, where $C_d=C_d(\mathrm{Re}_p)$ denotes the drag coefficient which depends on the Reynolds number of the particle $\mathrm{Re}_p=2a\|\mathbf{V}_d-\mathbf{V}_c\|/\nu_c$, where ν_c is the kinematic viscosity of the liquid. The value of C_d for a wide range of Re_p is obtained from correlations given in Ref. [16].

$\mathbf{F}_g$ is the buoyancy: $\mathbf{F}_g=-\mathcal{V}(\rho_c-\rho_d)\mathbf{g}$.

$\mathbf{F}_l$ is the lift force, which is given by $\mathbf{F}_l=\rho_c\mathcal{V}C_l(\mathbf{V}_c-\mathbf{V}_d)\times\mathbf{\Omega}$, where $\mathbf{\Omega}=\mathrm{curl}\mathbf{V}_c$ and $C_l\simeq 1/2$ is the lift coefficient (Auton [17]).

By writing $\gamma=\rho_d/\rho_c$ we are led to

$$\frac{d\mathbf{V}_d}{dt}=\frac{1+C_a}{\gamma+C_a}\frac{D\mathbf{V}_c}{Dt}-\frac{1-\gamma}{\gamma+C_a}\mathbf{g}-\frac{3}{8}\frac{C_d}{a(\gamma+C_a)}(\mathbf{V}_d-\mathbf{V}_c)\|\mathbf{V}_d-\mathbf{V}_c\|+\frac{C_l}{\gamma+C_a}(\mathbf{V}_c-\mathbf{V}_d)\times\mathbf{\Omega}, \tag{3}$$

and from Eq. (1) we get

$$\frac{D\mathbf{V}_c}{Dt}=(-\omega^2 r,0,0)\quad\text{and}\quad\mathbf{\Omega}=(0,0,2\omega). \tag{4}$$

If the position of the bubble at time t is $(r(t),\theta(t),z(t))$, then

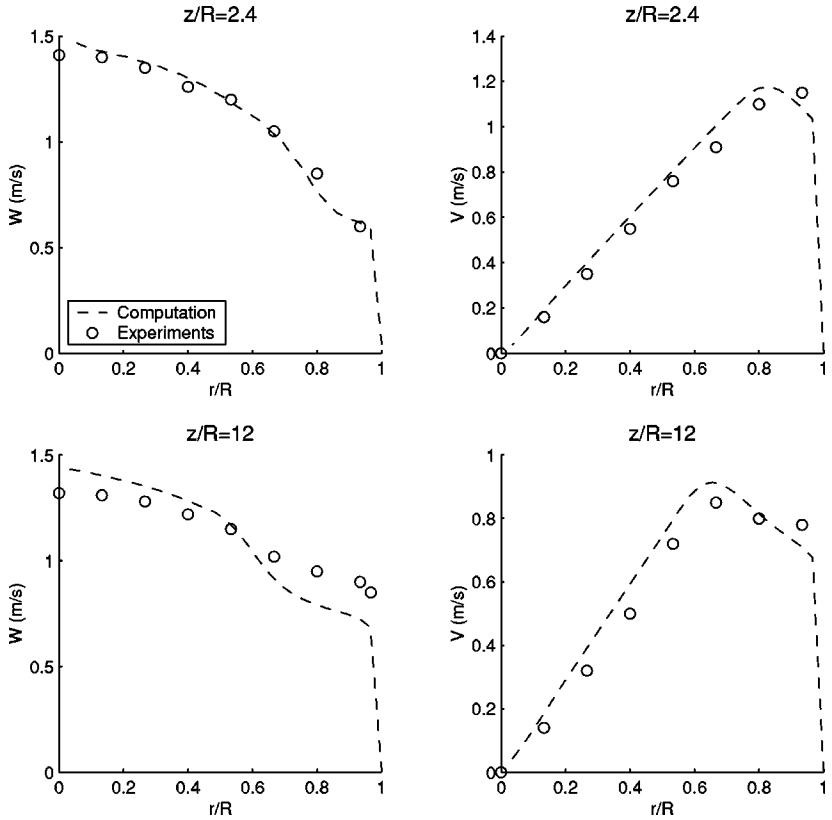

Fig. 3 Mean velocity profiles at sections $z/R=2.4$ and $z/R=12$ obtained from experiments and numerical computation (CFD code Fluent with Reynolds stresses (RSM) turbulence model). The Rossby number is Ro=0.59. In the vicinity of the center the velocity is close to a solid body rotation. The Rossby number in the four cases considered in the present paper will be larger than this one, and the corresponding velocity profiles will therefore be approximated by a solid-body rotation.

$$\mathbf{V}_d=(\dot r,r\dot\theta,\dot z)\quad\text{and}\quad\frac{d\mathbf{V}_d}{dt}=(\ddot r-r\dot\theta^2,2\dot r\dot\theta+r\ddot\theta,\ddot z),\tag{5}$$

where $\dot X$ denotes dX/dt.

By writing

$$r_*=r/R,\quad z_*=z/R,\quad t_*=\omega t,\quad\text{and}\quad a_*=a/R,$$

and by scaling velocities by $R\omega$, Eq. (3) in polar coordinates reads (Souhar [18])

$$\ddot r_*-r_*\dot\theta^2=-C_1r_*-\frac{3}{8}C_3\|\mathbf{V}_g\|\dot r_*-2C_4r_*(\dot\theta-1),\tag{6}$$

$$2\dot r_*\dot\theta+r_*\ddot\theta=-\frac{3}{8}C_3\|\mathbf{V}_g\|r_*(\dot\theta-1)+2C_4\dot r_*,\tag{7}$$

$$\ddot z_*=\frac{C_2}{\mathrm{Fr}}-\frac{3}{8}C_3\|\mathbf{V}_g\|(\dot z_*-R_0),\tag{8}$$

where

$$C_1=\frac{1+C_a}{\gamma+C_a},\quad C_2=\frac{1-\gamma}{\gamma+C_a},\quad C_3=\frac{C_d}{(\gamma+C_a)a_*},\quad C_4=\frac{C_l}{\gamma+C_a}.$$

The nondimensional number Fr is the pseudo-Froude number:

$$\mathrm{Fr}=\frac{R\omega^2}{g},$$

and

$$\mathbf{V}_g=(\dot r_*,r_*(\dot\theta-1),\dot z_*-R_0)$$

is the nondimensional slip velocity. At the initial time $t=0$ we take the slip velocity to be zero, that is

$$r_*=r_{*,0},\quad\theta=\theta_0,\quad z_*=z_{*,0},\tag{9}$$

$$\dot r_*=0,\quad\dot\theta=1,\quad\dot z_*=R_0.\tag{10}$$

One could argue that, since the needle is fixed, the initial velocity of the bubble should theoretically be zero. Nevertheless, the gas flow rate through the needle is very small, because the detachment frequency is very low. The time required for bubble formation is therefore non-negligible. During this time the bubble is stretched, and tends to follow the liquid, so we can reasonably assume that its initial slip velocity is small. Further analyses should help to clarify this point. Note that the initial velocity of the bubble does not affect significantly its migration towards the axis of the pipe.

In the following the index $*$ will be dropped for r, z, and t, as well as for r_0 and z_0. Table 1 shows the various parameters and nondimensional numbers corresponding to the four runs.

4 Resolution of the Equations

Because the density of water is much larger than that of air ($\gamma=O(10^{-3})$) we have

$$C_1\simeq3,\quad C_2\simeq2,\quad\text{and}\quad C_4\simeq1,$$

and

$$C_3\simeq2C_d/a_*.$$

If bubbles are assumed to be clean, then $C_d\sim1/\mathrm{Re}_p$ at leading order for small or moderate particle Reynolds numbers. The drag is therefore a linear function of the slip velocity, and this case is investigated in the next section (linear-drag analysis).

Nevertheless, our bubbles might have contaminated interfaces, so that a no-slip boundary condition could apply at their surface (see for example Ref. [16], pp. 35–41, for an interesting discussion). In this case, bubbles have to be treated like solid spheres and one can therefore set $C_d\simeq$constant, as soon as Re_p is of order 10^3. This case is investigated in Subsection 4.2 (nonlinear drag theory).

Both the linear-drag analysis and the non-linear drag analysis will be compared to qualitative visualizations and numerical results.

4.1 Linear-Drag Analysis. When the drag coefficient is of the form $C_d\simeq k/\mathrm{Re}_p$, that is when Re_p is small ($k=24$ for clean bubbles) or for some large Re_p with $k=48$ (see correlations given in Ref. [16]), one can find an analytical solution. In this case Eq. (7) leads to

$$2\dot r(\dot\theta-1)+r\ddot\theta=-fr(\dot\theta-1),\tag{11}$$

where

$$f=\frac{3k}{8}\frac{\nu_c}{\omega a^2}.$$

Equation (11) can be readily integrated, and leads to

$$\dot\theta-1=(\dot\theta_0-1)\left(\frac{r_0}{r(t)}\right)^2e^{-ft}.\tag{12}$$

We therefore observe that, if $\dot\theta_0=1$, then $\dot\theta(t)=1$ is the only solution for θ. This solution corresponds to a movement without azimuthal slip. In other words, in the rotating reference frame, a bubble has a two-dimensional movement (i.e., its trajectory is included in a rotating vertical plane with an angular velocity ω).

The whole system (6)–(8) therefore reduces to a set of linear equations

$$\ddot r+f\dot r+2r=0,\tag{13}$$

$$\dot\theta(t)=1,\tag{14}$$

$$\ddot z+f\dot z-f\mathrm{Ro}-\frac{2}{\mathrm{Fr}}=0.\tag{15}$$

In contrast, when $\dot\theta_0\neq1$, we obtain a strongly nonlinear equation for r, and this case will not be treated in the present paper.

Equations (13) and (15), together with the initial conditions (9) and (10) can be readily integrated. Equation (13) has two different kinds of solutions, according to whether $f>2\sqrt2$ or not. In other words, there exists a critical angular velocity:

$$\omega_c=\frac{3k}{16\sqrt2}\frac{\nu_c}{a^2}$$

which enables to characterize the transition between two regimes. These two solutions are

$$r(t)=r_0e^{-ft/2}\left(\cosh\frac{t\sqrt\Delta}{2}+\frac{f}{\sqrt\Delta}\sinh\frac{\sqrt\Delta}{2}t\right),$$

$$\text{when }\ \omega<\omega_c,\ \text{(nonoscillating regime)}\tag{16}$$

$$r(t)=r_0e^{-ft/2}\left(\cos\frac{t\sqrt\Delta}{2}+\frac{f}{\sqrt\Delta}\sin\frac{\sqrt\Delta}{2}t\right),$$

$$\text{when }\ \omega>\omega_c,\ \text{(oscillating regime)}\tag{17}$$

where $\Delta=|f^2-8|$. In both cases the z component reads

$$z(t)=z_0-\frac{2}{f^2\mathrm{Fr}}(1-e^{-ft})+\left(\frac{2}{f\mathrm{Fr}}+\mathrm{Ro}\right)t.\tag{18}$$

In particular, the nondimensional terminal vertical velocity of the bubble is

$$\dot z_\infty=\mathrm{Ro}+\frac{2}{f\mathrm{Fr}}.\tag{19}$$

The terminal (dimensional) slip-velocity of the bubble is $16ga^2/3k\nu_c$ and the particle Reynolds number Re_p is

$$\mathrm{Re}_p = \frac{32}{3k}\frac{ga^3}{\nu_c^2}.$$

The correlation $C_d \simeq k/\mathrm{Re}_p$ given in Ref. [16] is valid for $\mathrm{Re}_p < \mathrm{Re}_{p,\mathrm{lim}}$, where $\mathrm{Re}_{p,\mathrm{lim}}$ is of order unity. Hence, the linear-drag analysis is valid for bubbles with radius

$$a < a_{\mathrm{lim}} = \left(\frac{3k}{32}\frac{\nu_c^2}{g}\mathrm{Re}_{p,\mathrm{lim}}\right)^{1/3}.$$

In the case of water, a_{lim} is of the order of 360 μm, which is smaller than the actual bubble radius of our experiments. Therefore, this analysis will not be compared to experimental results.

4.2 Nonlinear Drag Analysis. When the bubble is taken to be a solid sphere, the no-slip boundary condition at the bubble interface drastically modifies the drag coefficient. In this case we have $C_d \simeq 0.44$ as soon as Re_p is of the order of 10^3, and Eqs. (16)–(18) in the case $\dot{\theta}=1$, lead to

$$\ddot{r} + F\dot{r} + 2r = 0, \tag{20}$$

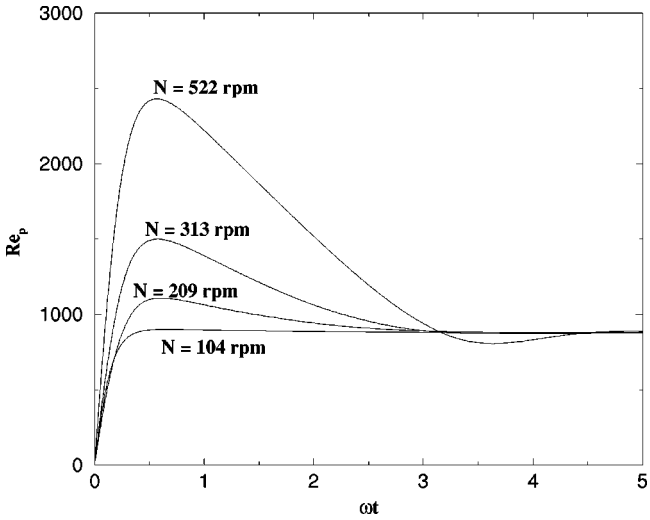

Fig. 4 Plot of the computed particle Reynolds number, for the four runs

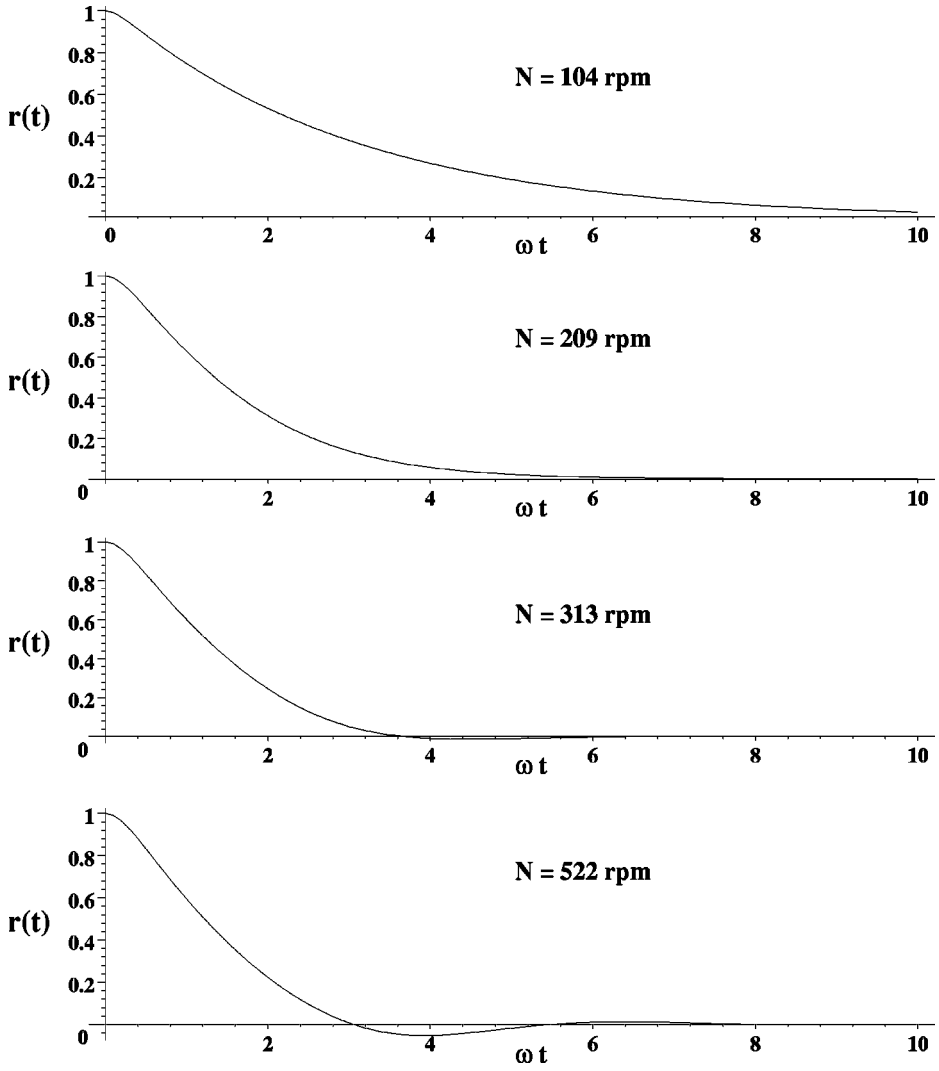

Fig. 5 Plot of the decay of the *r*-coordinate in the four cases considered in this paper, obtained from the numerical computation. As predicted by the analysis, the oscillating regime appears when *N* is larger than about 200 rpm.

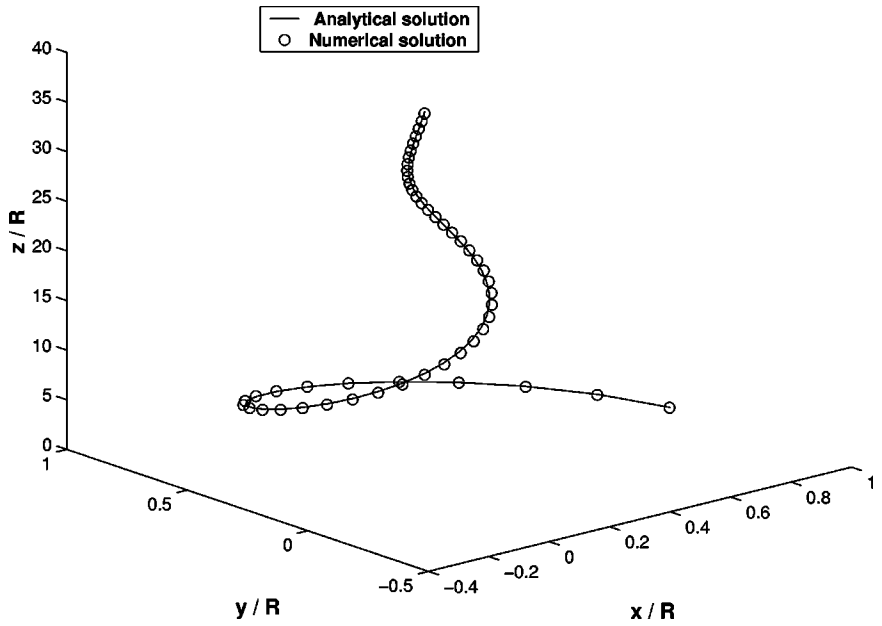

Fig. 6 Plot of the analytical solution (16)–(17) of the nonlinear drag analysis (solid line), together with the full numerical solution (symbol ○) of the basic equations of motion (6)–(8) when $N=104$ rpm

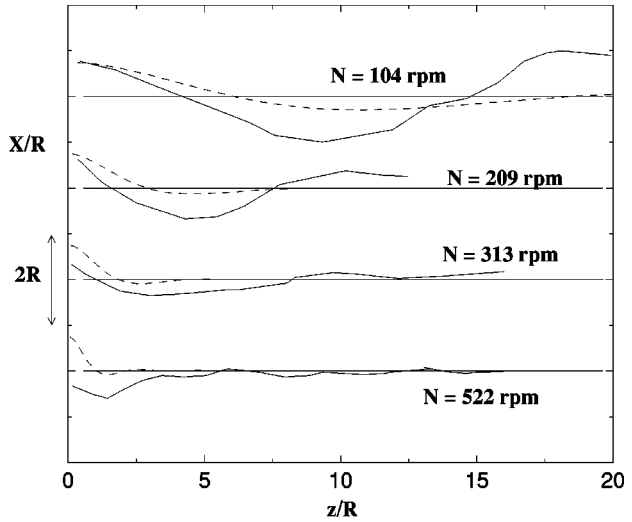

Fig. 7 Comparison between experimental trajectories (solid lines) and computed trajectories (dashed lines)

$$\ddot{z}+F(\dot{z}-\mathrm{Ro})-\frac{2}{\mathrm{Fr}}=0, \tag{21}$$

where

$$F=\frac{3}{4}\frac{C_d}{a_*}(\dot{r}^2+(\dot{z}-\mathrm{Ro})^2)^{1/2}, \tag{22}$$

with initial conditions given by (9) and (10). These equations cannot be solved exactly, and this is the reason why a numerical solver is used below. Nevertheless, we can simplify these equations by considering the short-time solution first, then the long-time solution.

For *short times*, we have $\dot{z}(t)-\mathrm{Ro}\simeq 0$, as the initial condition is $\dot{z}(0)-\mathrm{Ro}=0$. Hence, in Eq. (21) the term $-2/\mathrm{Fr}$ can only be balanced by $\ddot{z}$. We then solve $\ddot{z}-2/\mathrm{Fr}\simeq 0$, $\dot{z}(0)-\mathrm{Ro}=0$, and this leads to

$$\dot{z}(t)\simeq \mathrm{Ro}+2t/\mathrm{Fr}, \quad t\to 0.$$

Similarly, since $\dot{r}(0)=0$ and $r(0)=r_0\sim 1$, the term $2r$ in Eq. (20) can only be balanced by $\ddot{r}$ for short times. This leads to the solution

$$r(t)\simeq r_0(1-t^2), \quad t\to 0.$$

For *long times*, $|\dot{r}|$ decreases to 0 and $|\dot{z}-\mathrm{Ro}|$ increases to the terminal slip velocity. So we assume that the vertical slip velocity is much larger than the radial slip velocity, that is $|\dot{r}|\ll|\dot{z}-\mathrm{Ro}|$. Equation (21) is then approximated by

$$\ddot{z}+\alpha(\dot{z}-\mathrm{Ro})^2-\frac{2}{\mathrm{Fr}}=0, \tag{23}$$

where we have set $\alpha=3C_d/(4a_*)$. The solution of this last equation is

$$\dot{z}(t)=\mathrm{Ro}+\sqrt{\frac{2}{\alpha\mathrm{Fr}}}\tanh\left(\frac{2}{\alpha\mathrm{Fr}}(\alpha t-c_1)\right), \tag{24}$$

where c_1 is an integration constant which can be determined by matching the long-time solution with the short-time solution. Therefore, the bubble velocity tends exponentially to the terminal velocity:

$$\dot{z}_\infty=\mathrm{Ro}+\sqrt{\frac{2}{\alpha\mathrm{Fr}}}=\mathrm{Ro}+\sqrt{\frac{8a_*}{3C_d\mathrm{Fr}}}. \tag{25}$$

As expected, this is the classical terminal velocity of a buoyant sphere with large Reynolds number in a still fluid. In dimensional units this velocity reads

$$\dot{z}_\infty\times R\omega-W_0=\sqrt{\frac{8}{3C_d}}\sqrt{ag}\approx 0.29\ \mathrm{m/s}. \tag{26}$$

This value will be compared to experimental results in the following section.

By injecting solution (24), with $\tanh(.)\simeq 1$, in Eq. (20) we obtain a linear equation

$$\ddot{r}+\sqrt{\frac{2\alpha}{\mathrm{Fr}}}\dot{r}+2r=0, \tag{27}$$

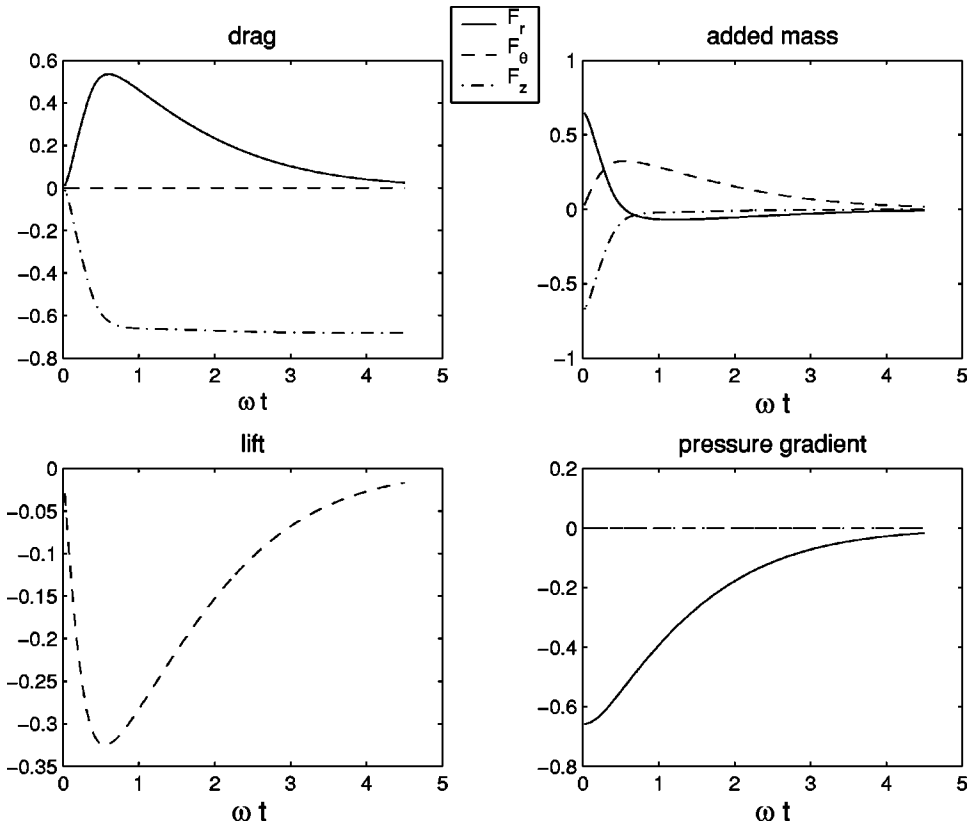

Fig. 8 Evolution of the forces acting on the particle, for the run $N=209$ rpm

which displays two different solutions according to whether $2\alpha/\mathrm{Fr}>8$ or not. We therefore conclude that, like in the linear-drag theory, there exists two regimes which are characterized by the critical angular velocity:

$$\omega_c=\frac{\sqrt{3}}{4}\sqrt{\frac{C_d g}{a}}. \tag{28}$$

For bubbles with diameter $2a\simeq 3$ mm we obtain $\omega_c\simeq 20$ rad/s, that is $N_c\simeq 200$ rpm, in agreement with experimental observations (Baur [11]). The solution of Eq. (27) is given by (16)–(17) with $f=\sqrt{2\alpha/\mathrm{Fr}}$, and its integration constants have been obtained by matching the long-time solution with the short-time solution.

In the next section we compare the model to experimental and numerical results.

5 Results

First of all we observe that the terminal velocity $\dot{z}_\infty$ predicted by the linear-drag model (Eq. (19)) is not in agreement with experiments. Indeed, the experimental terminal velocity given in the literature and in Baur [11] is about 0.25 m/s, whereas the terminal velocity given by Eq. (19) is about four times larger than this. This confirms that the linear-drag analysis is not valid.

In contrast, the terminal velocity predicted by the nonlinear-drag model (Eq. (26)) is in agreement with these experimental results. This confirms that the drag of the bubble must be nonlinear in the experiment, and that the solid-sphere assumption is acceptable. This might be due to the fact that our bubbles are highly contaminated, so that a no-slip boundary condition applies at the gas-liquid interface. In addition we have plotted the evolution of the particle Reynolds number for the four runs (Fig. 4). We observe that the values of the Reynolds number are in agreement with the fact that $C_d\simeq$ constant.

The analytical approach (for either large or small particle Reynolds number) predicts that two regimes exist, according to whether N is smaller or larger than a critical value N_c. Indeed, when the rotating frequency N of the device is larger than the critical value $N_c\simeq 200$ rpm (obtained from Eq. (28)), the decay of the r-coordinate is pseudo-periodical. This is confirmed by numerical computations (Fig. 5) of bubble trajectories. When $N=104$ rpm the decay of r is monotonic. In contrast, for $N=209$, 313, and 522 rpm, a pseudo-periodical regime appears.

The physical interpretation of these two regimes can be done by considering the movement equation in the radial direction (6). In the right-hand side of this equation, the first term corresponds to the pressure gradient force (with added mass), the second term corresponds to the drag force, and the third term is the radial component of the lift, which is zero when $\dot{\theta}=1$. If the drag is removed from this equation, then we obtain an oscillating solution whatever ω. In contrast, if the pressure gradient term is removed, then $C_1\simeq 1$, the equation is of order one in $\dot{r}$, and no oscillating regime can appear. The oscillating regime therefore appears when the radial pressure gradient force dominates over the other radial forces.

Because $\theta=t$, we observe that the bubble trajectory, when $N<N_c$, is a logarithmic conical spiral of the form

$$r(\theta)\propto e^{-C\theta}, \tag{29}$$

$$z(\theta)\propto\theta, \tag{30}$$

(where C is a constant). When $N>N_c$ the trajectory is a logarithmic cosine conical spiral of the form

$$r(\theta)\propto e^{-C\theta}(A\cos(C_1\theta)+B\sin(C_1\theta)), \tag{31}$$

$$z(\theta)\propto\theta. \tag{32}$$

Such an oscillating behavior has been observed experimentally, and the measured critical velocity N_c is in agreement with the one calculated in Ref. [11].

In order to check the validity of the analytical resolution we have plotted the solution of the nonlinear drag analysis on Fig. 6, together with the full numerical solution of Eqs. (6)–(8). (These have been obtained by making use of a fourth-order Runge-Kutta scheme.) The numerical solution is found to be in rather good agreement with the nonlinear drag theory, especially when the time required for the particle to reach its terminal velocity is short.

The comparison between model and experiments is less easy. From Fig. 2(*b*) we can estimate the deviated horizontal coordinate X (as sketched on Fig. 1) and the vertical coordinate z. From the theoretical particle coordinate (r,θ) we obtain the theoretical X coordinate by making use of elementary optical calculations. The result is shown on Fig. 7. Even if experimental and theoretical trajectories do not fit at all, they are roughly similar.

The evolution of the forces acting on the particle can be easily obtained from the numerical computation. These forces have been detailed on Fig. 8, for the run $N=209$ rpm. They are written in units of $M\times R\omega^2$, where M is the mass of water within the volume $\mathcal{V}$. We observe that, for short times, the radial component of the pressure gradient force $\mathbf{F}_p.\mathbf{e}_r$ dominates and is negative. As expected, this force is responsible for the migration of the bubble towards the center. A positive radial drag appears, as a consequence of the radial slip of the bubble during the migration. As expected, the azimuthal drag is zero. We also observe that an orthoradial negative lift appears during the radial migration. This is because the slip velocity of the particle has an inward component. As soon as the migration is complete, the lift vanishes. Also, at short times, the added mass is non-negligible, due to the acceleration of the bubble. The order of magnitude of all these forces is rather similar, but they act at different times. As expected, only the vertical component of the drag exists for long times, and is balanced by the buoyancy force, not plotted here.

6 Conclusion

The model presented in this paper shows some agreement with available experimental results. The terminal velocity of the bubble is well predicted only if bubbles are treated as solid spheres. This suggests that our bubbles might be highly contaminated, so that a no-slip boundary condition applies at the gas-liquid interface.

The critical frequency ω_c above which a pseudo-periodical regime appears has been calculated analytically (Eq. (28)). Its value is in agreement with the experiment. When $\omega>\omega_c$ the bubble converges to the center in an oscillating manner, i.e., the bubble crosses the axis periodically.

These calculations can also be used to estimate the typical height required for the particle to reach the axis (i.e., the overall length-scale of the envelope of the particle trajectory). This suggests that this elementary model could be used to design phase separators in the limit of small void fractions.

When the Rossby number is smaller than 0.6 the velocity profile of the continuous phase can no longer be approximated by a Rankine vortex. However, even in the single-phase case this problem is still open, [15]. In addition, when the void fraction increases, the liquid/gas interactions are much more complex, and the problem requires different theoretical approaches.

Further analyses are therefore necessary to investigate the phases separator for a large range of Rossby numbers and void fractions.

Nomenclature

N = rotation frequency of the honeycomb
index d = dispersed phase (air bubble)
index c = continuous phase (water)
x, y, z = Cartesian coordinates of the bubble
r, θ, z = cylindrical polar coordinates of the bubble
$\dot{X}=dX/dt$ = time derivative of $X(t)$
$X_0=X(0)$ = initial value of $X(t)$
R = radius of the pipe
a = radius of the bubble
$\mathcal{V}$ = volume of the bubble
$a_*=a/R$ = nondimensional radius of the bubble
W_0 = axial velocity of the continuous phase
ω = angular velocity of the continuous phase
$\mathbf{V}_c=(u_c,v_c,w_c)$ = velocity field of the continuous phase in cylindrical polar coordinates
$\mathbf{F}_p$, $\mathbf{F}_m$, $\mathbf{F}_d$, $\mathbf{F}_g$, $\mathbf{F}_l$ = forces acting on the bubble (respectively, pressure gradient, added mass, drag, buoyancy, and lift)
C_a, C_l, C_d = respectively, added-mass coefficient, lift coefficient, and drag coefficient
C_1, C_2, C_3 = various constants
ρ_d, ρ_c = densities
$\gamma=\rho_d/\rho_c$ = density ratio
ν_c = kinematic viscosity of the continuous phase
$\mathbf{\Omega}=\text{curl}\,\mathbf{V}_c$ = vorticity field of the continuous phase
$\text{Fr}=R\omega^2/g$ = Froude number
$\text{Ro}=W_0/R\omega$ = Rossby number
$\text{Re}=2W_0R/\nu_c$ = Reynolds number
$\text{Re}_p=2a\|\mathbf{V}_d-\mathbf{V}_c\|/\nu_c$ = particle Reynolds number

References

[1] Gupta, A., Lilley, D. G., and Syred, N., 1984, *Swirl Flow, Energy & Engineering Sciences Series*, Abacus Press.
[2] Weske, D. R., and Sturov, G. Ye., 1974, "Experimental Study of Turbulent Swirled Flows in a Cylindrical Tube," FLUID MECHANICS-Soviet Research, **3**(1).
[3] Kitoh, Osami, 1991, "Experimental Study of Turbulent Swirling Flow in a Straight Pipe," Journal of Fluid Mechanics, **225**, pp. 445–479.
[4] Jacquin, L., 1988, "Etude théorique et expérimentale de la turbulence homogène en rotation," ONERA, Technical note.
[5] Talbot, L., 1954, "Laminar Swirling Pipe Flow," Trans. of the ASME, **21**(1), pp. 1–7.
[6] Bradshaw, P., 1969, "The Analogy Between Streamline Curvature and Buoyancy in Turbulent Shear Flow," Journal of Fluid Mechanics, **36**, p. 77.
[7] Rochino, A., and Lavan, Z., 1969, "Analytical Investigations of Incompressible Turbulent Swirling Flow in Stationary Ducts," Trans. of the ASME, pp. 151–158.
[8] Lilley, D. G., and Chigier, N. A., 1971, "Non Isotropic Turbulent Stress Distribution in Swirling Flows From Mean Value Distribution," Int. J. Heat Mass Transf., **14**, p. 573.
[9] Gibson, N. M., and Younis, B. A., 1986, "Calculation of Swirling Flow Jets With a Reynolds Stress Closure," Physics of Fluids, **29**, p. 38.
[10] Kobayashi, T., and Yoda, M., 1987, "Modified $k-\varepsilon$ Model for Turbulent Swirling Flow," Int. J. JSME, **30**, p. 66.
[11] Baur, L., 1995, "Contribution Expérimentale à l'Étude d'Écoulements Diphasiques de Type Swirling," Ph.D. thesis, Institut National Polytechnique de Lorraine (INPL), Nancy, France.
[12] Greenspan, H. P., and Ungarish, M., 1985, "On the Centrifugal Separation of a Bulk Mixture," Int. J. Multiphase Flow, **11**(6), pp. 825–835.
[13] Greenspan, H. P., 1993, "On the Centrifugal Separation of a Mixture," Journal of Fluid Mechanics, **127**, pp. 91–101.
[14] Baur, L., Izrar, B., Lusseyran, F., and Souhar, M., 1996, "Etude des Écoulements à Bulle Tourbillonants," La houille blanche, **1**(2), pp. 64–70.
[15] Najafi, A. F., Angilella, J. R., Souhar, M., and Sadeghipour, M. S., 2002, "Turbulence Modeling in a Swirling Pipe Flow and Comparison With Experiments," to be submitted.
[16] Clift, R., Grace, J. R., and Weber, M. E., 1978, *Bubbles, Drops and Particles*, Academic Press, San Diego, CA.
[17] Auton, T. R., 1984, "The Dynamics of Bubbles, Drops and Particles in Motion in Liquids," Ph.D. dissertation, Cambridge University, Cambridge, UK.
[18] Souhar, M., 1995, "Note sur les Trajectoires de Bulles Isolées dans un Ecoulement de Type Swirling à Grand Nombre de Rossby," LEMTA internal report.

Simulation of Swirling Gas-Particle Flows Using Different Time Scales for the Closure of Two-Phase Velocity Correlation in the Second-Order Moment Two-Phase Turbulence Model[1]

Y. Yu

L. X. Zhou[2]

Department of Engineering Mechanics,
State Key Laboratory of Clean Coal Combustion,
Tsinghua University,
Beijing, P. R. China

C. G. Zheng

Z. H. Liu

National Laboratory of Coal Combustion,
Huazhong University of Science and Technology,
Wuhan, P. R. China

Three different time scales—the gas turbulence integral time scale, the particle relaxation time, and the eddy interaction time—are used for closing the dissipation term in the transport equation of two-phase velocity correlation of the second-order moment two-phase turbulence model. The mass-weighted averaged second-order moment (MSM) model is used to simulate swirling turbulent gas-particle flows with a swirl number of 0.47. The prediction results are compared with the PDPA measurement results taking from references. Good agreement is obtained between the predicted and measured particle axial and tangential time-averaged velocities. There is some discrepancy between the predicted and measured particle axial and tangential fluctuation velocities. The results indicate that the time scale has an important effect. It is found that the predictions using the eddy interaction time scale give the right tendency—for example, the particle tangential fluctuation velocity is smaller than the gas tangential fluctuation velocity, as that given by the PDPA measurements. [DOI: 10.1115/1.1538630]

Introduction

The gas-particle velocity correlation plays an important role in the closure of second-order moment two-phase turbulence models. It is the correlation between the particle fluctuation velocity and the gas fluctuation velocity seen by particles. Physically, it represents the interaction between the gas and particle Reynolds stresses or turbulent kinetic energies by the drag force, lift force, etc., and its closure will affect the final prediction results of particle Reynolds stresses, if the gas Reynolds stresses can be reasonably predicted using an appropriate gas turbulence model, such as the second-order moment model. Zhou and Chen [1] proposed the second-order moment two-phase turbulence model, derived and closed the transport equation of two-phase velocity correlation based on Reynolds expansion and an assumption that the summation of normal components for the dissipation tensor of two-phase velocity correlation is proportional to the dissipation of gas turbulent kinetic energy, with an integral time scale of gas turbulence. Zhou and Xu [2] started from the Zaichik's algebraic closure expression and improved it using the Lagrangian analysis given by Wang and Stock [3], Huang and Stock [4], accounting for the crossing-trajectory effect, inertial effect, and continuity effect. Alternatively, Simonin et al. [5] derived the gas-particle velocity correlation equation based on the joint PDF equation in the gas and particle velocity space and closed it using the Langevin equation. He proposed three types of closure models of two-phase velocity correlation. In this paper, the effect of time scales in closing the two-phase velocity correlation equation is studied. The mass-weighed averaged second-order moment (MSM) two-phase turbulence model with different time scales in the closure of dissipation term of two-phase velocity correlation equation is used to simulate swirling gas-particle flows and the predictions are compared with PDPA measurements made in [6] for swirling gas-particle flows with a swirl number of 0.47.

The Mass-Weighed Averaged Second-Order Moment (MSM) Two-Phase Turbulence Model

The original second-order moment two-phase turbulence model is obtained by time averaging, [1]. The advantage of mass-weighed averaging over the time averaging is that the former can remarkably reduce the number of correlation equations. The mass-weighed averaging for turbulent gas-particle flows is an extension of the Favre averaging for single-phase compressible flows to two-phase flows. Let us define $\rho_p=\alpha_p\rho_{pm}$; $\rho_g=\alpha_p\rho_{gm}$; $\alpha_p+\alpha_g=1$, where ρ_p, ρ_g are apparent particle and gas densities, ρ_{pm}, ρ_{gm} are particle and gas material densities. When neglecting the forces other than drag and gravitational forces, the fluctuation of particle source term due to reaction, and defining the mass-weighted averaging by

$$\phi_k=\tilde{\phi}_k+\phi_k''; \quad \tilde{\phi}_k=\overline{\alpha_k\rho_{km}\phi_k}/\overline{\alpha_k\rho_{km}} \quad (k=p,g)$$

$$\tilde{\phi}_k''=\overline{\alpha_k\rho_{km}\phi_k''}/\overline{\alpha_k\rho_{km}}=0.$$

and taking the time-averaging for the volume fraction, pressure, and shear stresses,

$$\alpha_k=\overline{\alpha}_k+\alpha_k'; \quad p=\overline{p}+p'; \quad \tau_{ji}=\overline{\tau}_{ji}+\tau_{ji}'.$$

[1]The research results, sponsored by the Special Funds for Major State Basic Research Project, PRC.

[2]To whom correspondence should be addressed.

Contributed by the Fluids Engineering Division for publication in the JOURNAL OF FLUIDS ENGINEERING. Manuscript received by the Fluids Engineering Division January 19, 2000; revised manuscript received October 17, 2002. Associate Editor: Y. Matsumoto.

The generalized closed form of mass-weighed averaged continuity, momentum, and gas and particle Reynolds stress equations for isothermal gas-particle flows can be obtained as follows:

$$\text{continuity equation:} \quad \frac{\partial \overline{\alpha}_k}{\partial t} + \frac{\partial \overline{\alpha}_k \widetilde{u}_{kj}}{\partial x_j} = 0, \tag{1}$$

momentum equation:

$$\frac{\partial \overline{\alpha}_k \rho_{km} \widetilde{u}_{ki}}{\partial t} + \frac{\partial \overline{\alpha}_k \rho_{km} \widetilde{u}_{kj} \widetilde{u}_{ki}}{\partial x_j} = \overline{\alpha}_k \rho_{km} g_i - \overline{\alpha}_k \frac{\partial \overline{p}}{\partial x_i} + \frac{\partial \overline{\alpha}_k \overline{\tau}_{kji}}{\partial x_j} - \frac{\partial \overline{\alpha}_k \rho_{km} \overline{\overline{u''_{kj} u''_{ki}}}}{\partial x_j}, \tag{2}$$

and Reynolds stress equation:

$$\frac{\partial \overline{\alpha}_k \rho_{km} \overline{\overline{u''_{ki} u''_{kj}}}}{\partial t} + \frac{\partial \overline{\alpha}_k \rho_{km} \widetilde{u}_{kk} \overline{\overline{u''_{ki} u''_{kj}}}}{\partial x_k} bf = D_{k,ij} + P_{k,ij} + \Pi_{k,ij} - \varepsilon_{k,ij} + S_{k,ij}, \tag{3}$$

where ρ_p, ρ_g are particle and gas apparent densities, ρ_{pm}, ρ_{gm} are corresponding material densities, the subscript k denotes gas phase g or particle phase p, and also denotes the summation of derivatives in all coordinate directions, the one-bar symbol denotes time averaging, the wave or double-bar symbols denote mass-weighted averaging, the superscript two primes denote the fluctuation value in mass-weighed averaging, $D_{k,ij}$, $P_{k,ij}$, $\Pi_{k,ij}$, $\varepsilon_{k,ij}$, $S_{k,ij}$ stand for the diffusion term, shear production term, pressure-strain term, dissipation term, and gas-particle interaction term, respectively, in the Reynolds stress equation. These terms in their closed form are

$$P_{k,ij} = -\overline{\alpha}_k \rho_{km} \left(\overline{\overline{u''_{kk} u''_{ki}}} \frac{\partial \widetilde{u}_{kj}}{\partial x_k} + \overline{\overline{u''_{kk} u''_{kj}}} \frac{\partial \widetilde{u}_{ki}}{\partial x_k} \right);$$

$$D_{k,ij} = \frac{\partial}{\partial x_k} \left(c_k \overline{\alpha}_k \rho_{km} \frac{k_k}{\varepsilon_k} \overline{\overline{u''_{kk} u''_{kl}}} \frac{\partial \overline{\overline{u''_{ki} u''_{kj}}}}{\partial x_1} \right);$$

$$\Pi_{g,ij} = \Pi_{g,ij,1} + \Pi_{g,ij,2}; \quad \Pi_{p,ij} = 0; \quad \varepsilon_{p,ij} = 0;$$

$$\varepsilon_{g,ij} = \frac{2}{3} \delta_{ij} \overline{\alpha}_g \rho_{gm} \varepsilon_g;$$

$$\Pi_{g,ij,1} = -C_{g1} (\varepsilon_g / k_g) \alpha_g \rho_{gm} \left(\overline{\overline{u''_{gi} u''_{gj}}} - \frac{2}{3} \delta_{ij} k_g \right);$$

$$\Pi_{g,ij,2} = -C_{g2} \left(P_{g,ij} - \frac{2}{3} \delta_{ij} P_g \right);$$

$$S_{k,ij} = \frac{\overline{\alpha}_p \rho_{pm}}{\tau_{rp}} (\overline{\overline{u''_{gi} u''_{kj}}} + \overline{\overline{u''_{gj} u''_{ki}}} - \overline{\overline{u''_{pi} u''_{kj}}} - \overline{\overline{u''_{pj} u''_{ki}}}).$$

For closing the equation of two-phase velocity correlation, the closure of diffusion and pressure-strain terms is similar to that used in Reynolds stress equation. The key point is the closure of dissipation term. The dissipation can be considered as an isotropic one. Assume that its dissipation is proportional to the summation of all normal components divided by a time scale. This time scale can be taken as the gas turbulence scale $\tau_t = C_\mu k/\varepsilon$, i.e., the gas turbulent kinetic energy divided by its dissipation rate, as that used in the original USM model, [1]. Simonin [4] takes a time scale of the gas turbulence seen by particles $\tau_t = l/\beta k/\varepsilon$, based on the results for nonsettling particles in homogeneous flows. It can also be taken as the particle relaxation time. Alternatively, this time scale can be taken as the eddy interaction time, expressing the crossing-trajectory effect—the particle trajectory differs from the gas eddy's trajectory. So the eddy interaction time is taken as the smaller one from the gas turbulence time scale and the particle relaxation time, as that was done in the particle trajectory model. The closed form of the equation of $\overline{\overline{u''_{gi} u''_{pj}}}$ is

$$\frac{\partial}{\partial t} (\overline{\alpha}_p \rho_{pm} \overline{\overline{u''_{gi} u''_{pj}}}) + \frac{\partial}{\partial x_k} (\overline{\alpha}_p \rho_{pm} \widetilde{u}_{pk} \overline{\overline{u''_{gi} u''_{pj}}}) = D_{gp,ij} + P_{gp,ij} + S_{gp,ij} + \Pi_{gp,ij} - \varepsilon_{gp,ij} \tag{4}$$

where

$$D_{gp,ij} = \frac{\partial}{\partial x_k} \left(C_{gp3} \overline{\alpha}_p \widetilde{\rho}_p \tau_{rp} \overline{\overline{u''_{pk} u''_{pm}}} \frac{\partial \overline{\overline{u''_{gi} u''_{pj}}}}{\partial x_m} \right)$$

$$P_{gp,ij} = -\overline{\alpha}_p \rho_{pm} \left(\overline{\overline{u''_{pk} u''_{gi}}} \frac{\partial \widetilde{u}_{pj}}{\partial x_k} + \overline{\overline{u''_{gk} u''_{pj}}} \frac{\partial \widetilde{u}_{gi}}{\partial x_k} \right);$$

$$S_{gp,ij} = -\frac{\overline{\alpha}_p \rho_{pm}}{\tau_{rp}} \left[(\overline{\overline{u''_{gi} u''_{pj}}} - \overline{\overline{u''_{gi} u''_{gj}}}) - \frac{\overline{\alpha}_p \rho_{pm}}{\overline{\alpha}_g \rho_{gm}} (\overline{\overline{u''_{gi} u''_{pj}}} - \overline{\overline{u''_{pi} u''_{pj}}}) \right];$$

$$\Pi_{gp,ij} = \Pi_{gp,ij,1} + \Pi_{gp,ij,2}$$

$$\Pi_{gp,ij,1} = -\frac{C_{gp1}}{\tau_{rp}} \alpha_p \rho_{pm} \left(\overline{\overline{u''_{gi} u''_{pj}}} - \frac{1}{3} \delta_{ij} \overline{\overline{u''_{gk} u''_{pk}}} \right);$$

$$\Pi_{gp,ij,2} = -C_{gp2} \left(P_{gp,ij} - \frac{2}{3} \delta_{ij} \sqrt{G_{gk} G_{pk}} \right)$$

$$\varepsilon_{gp,ij} = c_{gp} \frac{\overline{\alpha}_p \rho_{pm}}{\tau_{rp}} \overline{\overline{u''_{gk} u''_{pk}}} \delta_{ij} \text{(Version1)}$$

$$\varepsilon_{gp,ij} = c_{gp} \frac{\overline{\alpha}_g \rho_{gm}}{\tau_T} \overline{\overline{u''_{gk} u''_{pk}}} \delta_{ij} \text{(Version2)}$$

$$\varepsilon_{gp,ij} = c_{gp} \frac{\overline{\alpha}_p \rho_{pm}}{\tau_e} \overline{\overline{u''_{gk} u''_{pk}}} \delta_{ij} \text{(Version3)} \qquad \tau_e = \min[\tau_{rp}, \tau_T],$$

$$\tau_T = k/\varepsilon.$$

Equations (3) to (4) express the mass-weighed averaged USM model or the MUSM model.

Simulation of Swirling Gas-Particle Flows

The MSM model is used to simulate swirling gas-particle flows with a swirl number of 0.47, measured by PAPA, [6]. In order to save the computation time the gas-particle fluctuation velocity correlation transport equation is simplified to an algebraic expression, and an isotropic diffusion coefficient is used in diffusion terms of two-phase Reynolds stress transport equations. Notice that the last approximation is taken only in the diffusion term of the Reynolds stress transport equations, but both the Reynolds stresses and diffusion terms in the momentum equations are anisotropic. For example, we have

$$D_{g,ij} = \frac{\partial}{\partial x_k} \left(\overline{\alpha}_g \frac{\mu_e}{\sigma_k} \frac{\partial \overline{\overline{u''_{gi} u''_{gj}}}}{\partial x_k} \right); \quad D_{p,ij} = \frac{\partial}{\partial x_k} \left(\overline{\alpha}_p \frac{\mu_{pe}}{\sigma_{pk}} \frac{\partial \overline{\overline{u''_{gi} u''_{gj}}}}{\partial x_k} \right)$$

$$\overline{\overline{u''_{gi} u''_{pj}}} = (1 - \lambda_{gp1} - \lambda_{gp2}) \frac{1}{3} \delta_{ij} \overline{\overline{u''_{gk} u''_{pk}}} - \lambda_{gp1} \tau_e \left(\overline{\overline{u''_{pk} u''_{gi}}} \frac{\partial \widetilde{u}_{pj}}{\partial x_k} + \overline{\overline{u''_{gk} u''_{pj}}} \frac{\partial \widetilde{u}_{gi}}{\partial x_k} \right) + \lambda_{gp2} \overline{\overline{u''_{gi} u''_{gj}}}$$

$$\mu_e = c_\mu \overline{\alpha}_g \rho_{gm} \frac{k_g^2}{\varepsilon_g} + \mu; \quad \mu_{pe} = c_{\mu p} \overline{\alpha}_p \rho_{pm} \frac{k_p^2}{|S_{pg}|}$$

For boundary conditions, the inlet two-phase velocities, normal components of Reynolds stresses, and particle number density or volume fraction are given by experiments; the shear stresses are given by the eddy-viscosity assumption; the fully-developed flow

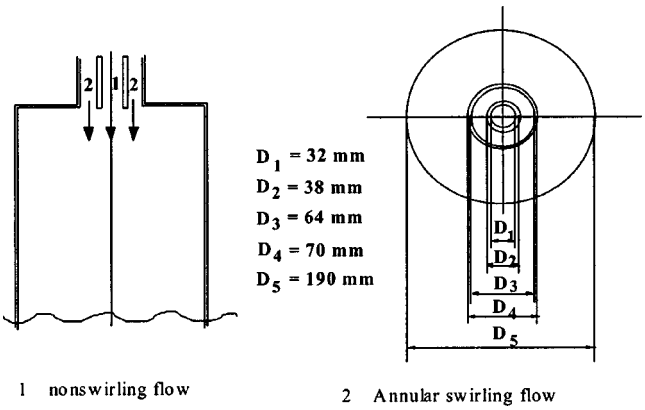

Fig. 1 Geometrical configuration and sizes of the chamber

condition of two phases are taken at the exit; at the walls no-slip condition is used for gas velocity, and the gas Reynolds stress components as well as gas velocities are determined via production term including the effect of wall functions for near-wall grid nodes. Zero normal velocity, zero gradients of longitudinal and tangential velocities and normal components of Reynolds stresses, and zero mass flux at the walls are used for the particle phase. At the axis the symmetrical condition is adopted for two phases. The numerical method is an extended version of SIMPLEC algorithm for two-phase flows.

The swirling gas-particle flows with $s=0.47$, [6], were simulated. The geometrical configuration and sizes of the chamber are shown in Fig. 1. The grid nodes are 32×20. The length of the chamber is 950 mm. The particle phase is glass beads with diameters 30 μm and density 2.15×10^3 kg/m^3. The inlet flow parameters are: central mass flow velocity 9.9 g/s, annular mass flow velocity 38.5 g/s, particle mass loading 0.034.

The convergence criteria for gas and particle phases are mass sources less than 1.0×10^{-3} and 1.0×10^{-2}, respectively. The computer code consists of about 10,000 statements in FORTRAN–77 language. It takes about 66 minutes for running a case using the Visual Fortran Version 6.0 system in a Pentium 200 MMX PC computer.

Simulation Results and Discussion

Figures 2 and 3 give the predicted time-averaged particle axial and tangential velocities, respectively. It can be seen that the predictions are in good agreement with the measurement results. Figures 4 and 5 show the particle axial and tangential fluctuation velocities, respectively. The particle fluctuation velocities are underpredicted, in particular in the axial direction. Up to now, for swirling flows, nearly all two-fluid models and Eulerian-Lagrangian models underpredict the particle fluctuation velocities. Figure 6 gives the measured gas and particle tangential fluctuation velocities in experiments. The particle tangential fluctuation velocity is smaller than the gas tangential fluctuation velocity, since the particles initially have only the axial momentum and the particle tangential velocity is caused by the gas tangential velocity of swirling secondary air. Figures 7 to 9 show the comparison between the gas and particle tangential fluctuation velocities, predicted using the MSM model with different time scales in the dissipation term of the two-phase velocity correlation equation. Figure 7 indicates that the MSM model with the eddy interaction time scale expressing the crossing-trajectory effect properly predicts that the particle tangential fluctuation velocity is smaller than the gas one, as observed in experiments. Figures 8 and 9 give the comparison between the gas and particle tangential fluctuation

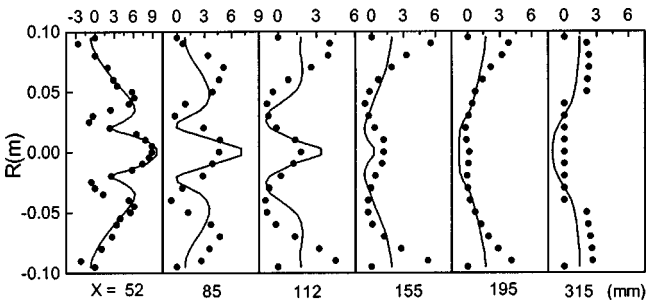

Fig. 2 Particle axial velocity(——MSM, ●exp.)

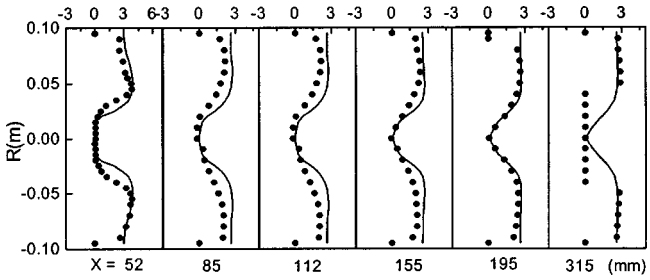

Fig. 3 Particle tangential velocity(——MSM, ●exp.)

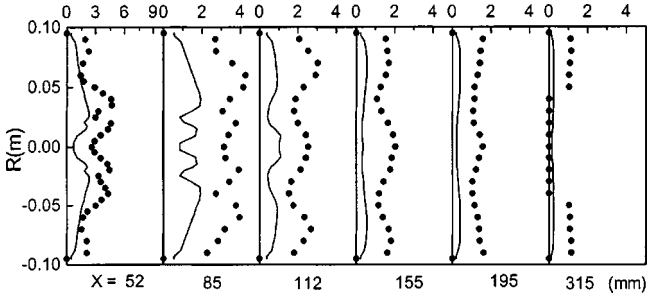

Fig. 4 Particle axial fluctuation velocity(——MSM, ●exp.)

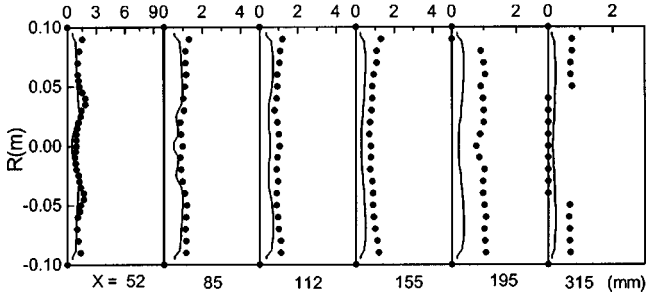

Fig. 5 Particle tangential fluctuation velocity(——MSM, ●exp.)

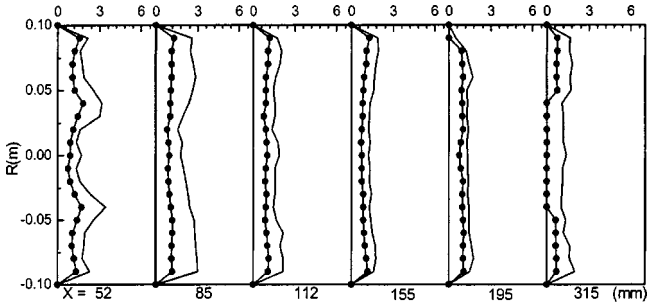

Fig. 6 Two-phase tangential fluctuation velocity (experiment, ——gas, ●particle)

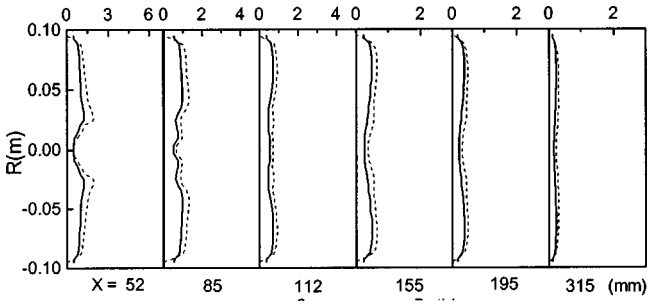

Fig. 7 Two-phase tangential fluctuation velocities (MSM, ——particle, — — —gas; $\tau_e = \min[\tau_{rp}, \tau_T]$, $\tau_T = k/\varepsilon$)

velocities, predicted using the MSM model with two different time scales—the gas turbulence time scale and the particle relaxation time in the dissipation term of two-phase fluctuation velocity correlation equation. The gas turbulence time is the characteristic time scale of the large eddies in the gas phase. It can be seen that the gas turbulence time scale gives the wrong tendency—the particle tangential fluctuation velocity is larger than the gas one. On the other hand, the particle relaxation time gives the result near to that given by the time scale accounting for the crossing-trajectory effect. These results indicate that in the present case the particle relaxation time is much smaller than the gas turbulence time scale.

Conclusions

1. The mass-weighed averaged second-order moment (MSM) two-phase turbulence model predicts the averaged particle axial and tangential velocities of swirling flows very well.
2. The MSM model underpredicts the particle fluctuation velocities, in particular in the axial direction.
3. The time scale in the dissipation term of two-phase velocity correlation equation plays an important role in predicting the relationship between gas and particle fluctuation velocities.
4. The eddy interaction time, accounting for the crossing-trajectory effect, is the best time scale.

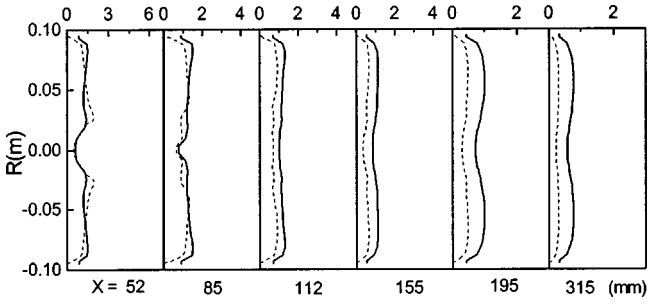

Fig. 8 Two-phase tangential fluctuation velocities (MSM, ——particle, — — —gas; $\tau_e = k/\varepsilon$)

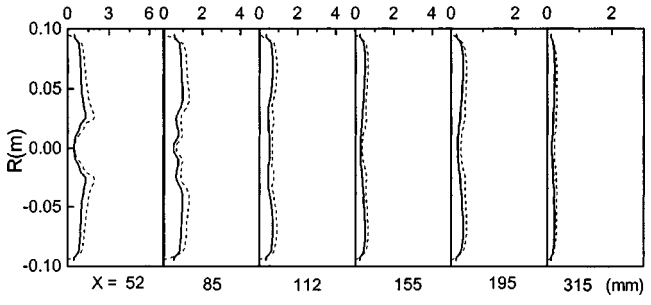

Fig. 9 Two-phase tangential fluctuation velocities (MSM, ——particle, — — —gas; $\tau_e = \tau_{rp}$)

Acknowledgement

This study was sponsored by the Special Funds for Major State Basic Research Project, PRC, under the grant G-1999-0222-08.

Nomenclature

c = empirical constants
D = diffusion term in Reynolds stress equations
g = gravitational acceleration
k = turbulent kinetic energy
N = particle number density
n = number density fluctuation
P = production term of Reynolds stresses or turbulent kinetic energy
p = pressure
S = source term due to gas-particle interaction
t = time
u = velocity
x = coordinate

Greek

α = volume fraction
δ = unit tensor
ε = dissipation rate of Reynolds stress or turbulent kinetic energy
ϕ = generalized variable
Π = pressure-strain term
ρ = density
τ = relaxation time; shear stress
μ, ν = dynamic and kinematic viscosities

Subscripts

g = gas
i, j, k, l = coordinates directions
k = generalized symbol denoting particle or gas
m = material
p = particle
r = relaxation

References

[1] Zhou, L. X., and Chen, T., 2001, ''Simulation of Strongly Swirling Flows Using USM and *k-ε-kp* Two-Phase Turbulence Models,'' Powder Technol., **114**(1–3), pp. 1–11.
[2] Zhou, L. X., and Xu, Y., Fan, L. S., and Li, Y., 2001, ''Simulation of Swirling Gas-Particle Flows Using an Improved Second-Order Moment Two-Phase Turbulence Model,'' Powder Technol., **116**, pp. 178–189.
[3] Wang, L. P., and Stock, D. E., 1993, ''Dispersion of Heavy Particles by Turbulent Motion,'' J. Atmos. Sci., **50**, pp. 1897–1913.
[4] Huang, X. Y., and Stock, D. E., 1994, ''Using the Monte-Carlo Process to Simulate Two-Dimensional Heavy Particle Dispersion in a Uniformly Sheared Turbulent Flow,'' Numerical Methods in Multiphase Flows, ASME, New York, ASME-FED-**185**, pp. 243–249.
[5] Simonin, O., Deutsch, E., and Minier, J. P., 1993, ''Eulerian Prediction of the Fluid-Particle Correlated Motion in Turbulent Two-Phase Flows,'' Appl. Sci. Res., **51**, pp. 275–283.
[6] Sommerfeld, M., and Qiu, H. H., 1991, ''Detailed Measurements in a Swirling Particulate Two-Phase Flow by a Phase-Doppler Anemometer,'' Int. J. Heat Fluid Flow, **12**, pp. 15–32.

Effect of Unsteady Wake Passing Frequency on Boundary Layer Transition, Experimental Investigation, and Wavelet Analysis

M. T. Schobeiri

K. Read

Turbomachinery Performance and
Flow Research Laboratory,
Texas A&M University,
College Station, TX 77843-3123

J. Lewalle

Department of Mechanical and
Aerospace Engineering,
Syracuse University,
Syracuse, NY

Detailed experimental and theoretical investigations were carried out to study the effect of unsteady wake passing frequency on the boundary layer transition along the concave surface of a curved plate under a zero longitudinal pressure gradient. Periodic unsteady flow with different passing frequencies is generated utilizing an unsteady flow research facility with a rotating cascade of rods positioned upstream of the curved plate. Extensive unsteady boundary layer measurements are carried out. The data are analyzed using conventional and wavelet-based methods. Local time scales are defined as those of the most energetic fluctuations, and are calculated from wavelet transforms of the velocity signals. The dominant time scales are mapped as functions of the distance to the plate, the downstream location, and the phase relative to the wake-passing. Furthermore, conditional sampling is applied, laminar and turbulent time scales are calculated and the effects of wake passing frequency on these scales are shown. [DOI: 10.1115/1.1537253]

Introduction

Development in the field of turbomachinery computational fluid dynamics (CFD) has reached an advanced level that allows detailed computation of the complex three-dimensional viscous flow through a turbomachinery stage using Navier-Stokes codes. Case presentations at the past conferences by ASME International Gas Turbine Institute (IGTI) demonstrated the capability of different CFD-methods to calculate various flow quantities in a remarkably detailed fashion. The efficiency and loss calculations, however, revealed a significant discrepancy between the experiment and the numerical calculation. Considering the physical aspects of the computation, two major issues may be considered primarily responsible for the above discrepancy, namely the turbulence and the laminar-turbulent boundary layer transition modeling. The latter directly impacts the accuracy of the loss, efficiency and heat transfer calculations of the blade and the turbomachinery stage.

Boundary layer transition and its modeling has been the subject of intensive research for the past three decades. Investigations by Evans [1,2], Walker [3–6], Walker and Gostelow [7], among others, studied the effect of unsteadiness and turbulence on compressor stage performance and aerodynamics. Comprehensive studies by Schultz et al. [8] and Poensgen and Gallus [9,10] investigated three-dimensional wake decay characteristics within compressor cascades. Significant impact on turbine blade heat transfer and aerodynamics were reported by Hodson [11,12], Hodson and Addison [13], Blair [14], Blair et al. [15], Dring et al. [16,17], and Joslyn et al. [18]. Wittig and his co-researchers, [19], and Dullenkopf [20] conducted a series of extensive studies investigating wake effects on gas turbine heat transfer. Investigations by Gaugler [21] and Schobeiri et al. [22] show that the existing correlations primarily developed for external aerodynamics applications are not capable of correctly predicting the unsteady transition behavior of gas turbine blades. The detailed study by Mayle [23] and the followup discussion by Walker [6] underscore the role and the significance of transition in turbomachinery.

The significance of the unsteady flow effect on the efficiency and performance of compressor and turbine stages was recognized in the early fifties by Speidel [24], who utilized a symmetric profile and an oscillating wire for generating the unsteady flow and found a direct correlation between the Strouhal number and the profile loss coefficient. He attributed the increase of the profile loss coefficient to the decrease of the length of the laminar boundary layer. Following the boundary layer transition studies by Speidel [24], Pfeil and his co-researchers Pache [25], Eifler [26–29], Herbst [30], and Schröder [31] concentrated their efforts on investigating the transition process of unsteady boundary layers. Using a flat plate and varying the pressure gradient and the wake-induced unsteady inlet flow condition, by changing the number, diameter, and frequency of the rods, Pfeil et al. [32] generated wake-induced transition, where intermittently laminar and turbulent states of the boundary layer were observed. Their studies show that the wakes affect the onset and length of transition. Based on the results of their experimental investigations, Pfeil and his co-researchers established a generally accepted unsteady boundary layer transition model. The innovative data published by Pfeil and Herbst [29] along with their model were instrumental in describing the intermittency function.

Proper modeling of the unsteady laminar-turbulent boundary transition process requires that the parameters describing the structure of the impinging unsteady wakes, the blade pressure gradient, the freestream turbulence, and the surface roughness be included into a comprehensive transition model. Thus, the creation of such a model by a deductive process involving flow equations over the range of parameters cannot be effective. Considering this situation, an inductive approach is necessary to understand the basic physics of unsteady boundary layer transition, essential for its efficient modeling. In a recent study, Schobeiri and Radke [33] investigated the effect of the wake-induced unsteady flow and curvature on the boundary layer transition along the concave side of a curved plate, where zero and negative pressure gradients were established. The experiments clearly revealed that the periodic wake impingement and the gen-

Contributed by the Fluids Engineering Division for publication in the JOURNAL OF FLUIDS ENGINEERING. Manuscript received by the Fluids Engineering Division July 31, 2001; revised manuscript received June 14, 2002. Associate Editor: T. B. Gatski.

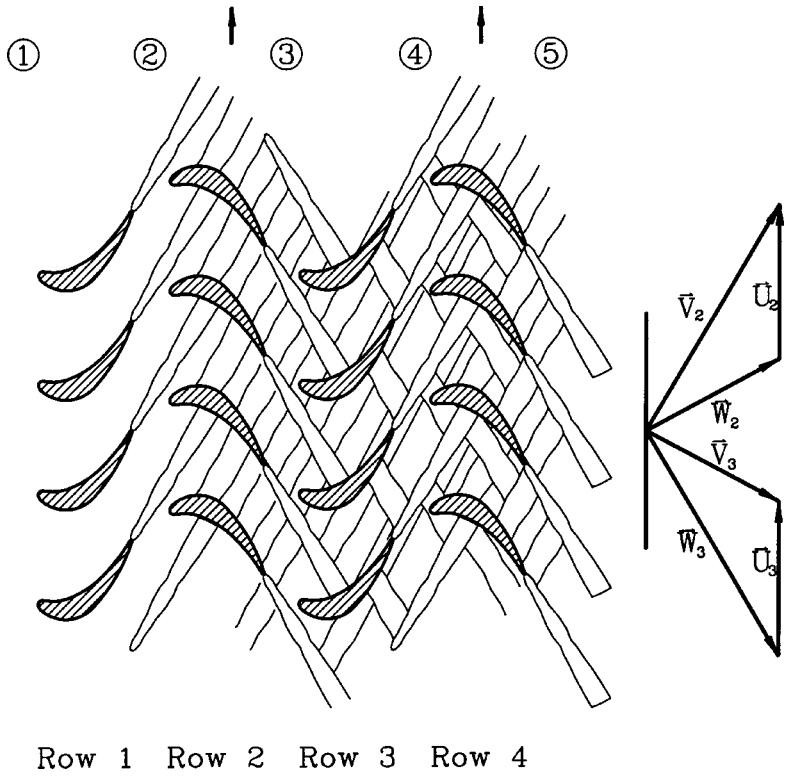

Fig. 1 Schematic of unsteady wake flow propagation through a multistage turbine in an absolute and relative frame of reference. Note the number of wakes through each row.

eration of highly turbulent intensity cores, as a result of intensive interaction and the mutual mixing process of the incoming wakes, affect the transition. Since the issue of the wake-induced unsteady boundary layer development directly involves the question of wake development and decay, in a parallel study, Schobeiri et al. [34] also investigated, theoretically and experimentally, the structure of the unsteady wakes to comprehend the *phenomenon and the physics* of the wake development and decay as well as the mutual interaction between wakes under the turbomachinery specific conditions. The results and the knowledge acquired by these investigations are currently being implemented into a transition model.

A schematic picture of the wake flow within a multi-stage turbine in an absolute and relative frame of reference is shown in Fig. 1. The structure of the unsteady turbulent flow changes by passing successively through the stator and rotor rows. Leaving the first stator blade row, the wake flow generated at the stator exit impinges on the second blade row (rotor) with a spatial frequency related to the spacing of the preceding stator blades. Due to the frame of reference change, the second cascade is exposed to a periodic unsteady turbulent flow that affects the boundary layer flow pattern, velocity, turbulence stress distributions and, particularly for cooled blades, the heat transfer characteristics of the succeeding row. The third row (second stator) is subjected to two sets of unsteady wakes that originate from the first two rows. These sets of wakes impinge on the third row and convect with different velocity deficits, phase displacements and turbulence structure. The latter is already affected by the mutual interaction, dissipation and mixing of the involved individual wakes. At the exit of the third row, as the result of an intensive interaction and mixing, the deterministic character of the periodic unsteady flow is, to some extent, degenerated into a highly stochastic flow. From this point on, the downstream rows are subjected to a highly turbulent flow, with an intensity distribution far above the inlet. This complex flow picture is deduced from the investigations by Arndt [35], who observed that the stator-rotor and the rotor-rotor interactions have significant influence on the flow through the multistage LP turbine he investigated; however, he did not perform boundary layer investigations. The above flow picture, which was modeled by Schobeiri et al. [36] indicated that the boundary layer transition along the blade of each row within a multistage arrangement is subjected to distinctively different unsteady flow structures.

The objective of this research is to provide experimental information essential for the development of a comprehensive transition model and to analytically evaluate the turbulence scales. Detailed unsteady flow measurements along the concave side of a curved plate were performed to generate a complete picture of the unsteady boundary layer behavior. Wake-spacing is varied which inherently results in a change of frequency of the impinging wakes and the freestream turbulence. This variation, as discussed previously, models the unsteady flow within a multistage turbine. A detailed analysis of the unsteady flow picture and turbulent intermittency is followed by the wavelet analysis of the unsteady boundary layer discussing the determination of time scales (and implicitly the length scales).

Experimental Research Facility

The experimental data for this paper were obtained using the same research facility described in the paper by Schobeiri and Radke [33]. The detailed design description and performance can be found in the paper by Schobeiri and Pardivala [37]. Thus, only a brief description of the facility and its components is given in this section.

The facility consists of a large centrifugal fan, a settling chamber, a nozzle, a wake generator, and a test section (Fig. 2). The fan can generate a maximum mean velocity of 36 m/s and a maximum Reynolds number (based on the test section inlet height) of 8.8 $\times 10^5$. For the simulation of the unsteady inlet flow condition and

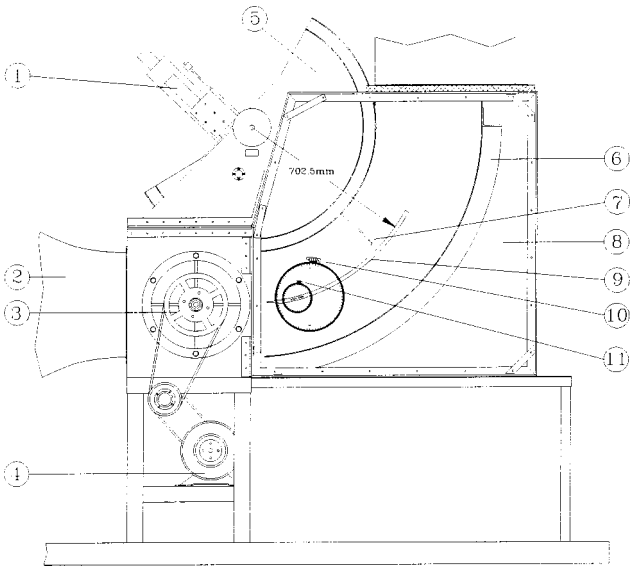

Fig. 2 Test section: 1–traversing system; 2–nozzle; 3–wake generator; 4–electric motor; 5–convex wall; 6–concave wall; 7–hot-wire probe; 8–plexiglass wall; 9–curved plate; 10–vernier; 11–vernier

the wake flow pattern downstream of a rotor row, as sketched in Fig. 1, a *squirrel cage* type wake generator of Fig. 2 is utilized. Similar wake generators were successfully utilized by Pfeil and his co-researchers, [26–29], and by Liu and Rodi [38]. Each rod generates two wakes with every revolution of the wake generator, one *primary* and one *secondary* wake, each at horizontal distances of 252.9 mm and 556.4 mm, respectively, from the leading edge. The experimental investigations by Schobeiri and Pardivala [37], and Schobeiri and Radke [33] in accordance with those reported by Liu and Rodi [38], have shown that by correct adjustments of the plate location, as well as the proper choice of the number of cylindrical rods, clean periodic unsteady wakes with clearly isolated turbulence structure can be established which allow time-dependent boundary layer simulation and measurements. In addition, this type of wake generator has the unique capability of simulating the unsteady wake flow through a multistage turbomachine. The wake generator can incorporate up to 30 cylindrical rods that are arranged circumferentially on two parallel rotating disks. The rotating disks are driven by a frequency controlled electric motor with a maximum rotational speed of 1750 rpm. A fiber-optic sensor directly monitors the angular frequency of the wake generator and also serves as the triggering mechanism for data transfer and for ensemble averaging. In order to simulate the wake width and spacing, the diameter and number of rods can be varied. For the present investigation, three sets of rods with a diameter of 2 mm were used. The geometric, inlet flow, and the unsteady flow specifications are given in Table 1. A frequency parameter Ω is introduced that appropriately reflects the unsteady character of the flow dominated by the wakes and their spacing. It is related to the Strouhal number and is defined as $\Omega=\sigma/\phi$ with $\sigma=s_0/s_r$ and $\phi=V/U$ as the ratio of the inlet velocity V and the circumferential velocity of the wake generator U. The values for Ω are varied as specified in Table 1 and cover approximately a broad range of Ω encountered in turbomachinery.

The test section, shown in Fig. 2, is located downstream of the wake generator and consists of a convex top wall, a curved plate for boundary layer measurements, a concave bottom wall and two vertical plexiglass side walls. The convex wall assembly is designed to allow precise radial and circumferential traversing of the probes. The curved plate, which simulated the pressure surface of a turbine blade with the specifications listed in Table 1, is inserted mid-height of the test section in Fig. 2. The plate is mounted between the two plexiglass side walls, where its axial and angular position can be precisely varied by a positioning system consisting of a disk, in which the curved plate is mounted eccentric to the center, and two angular verniers shown in Fig. 2. This positioning system allows variation of the pressure gradient and the fine adjustment of the leading edge position to avoid inception of separation bubbles. It incorporated static pressure ports mounted flush with the surface at arc length spacings of 36.8 mm. The ports were connected to a scanivalve for the pressure measurement purposes. For flow visualization, the static pressure ports were also connected to a manometer bank to detect any possible leading edge flow separation.

The concave bottom wall is designed to slide horizontally within two T-slots in the bottom wall of the wake generator. A favorable or an adverse streamwise pressure gradient within the test section can be created by moving the concave wall in and out inside the T-slots. The movable concave wall also serves for better adjustment of the flow angle relative to the curved plate, thus preventing flow separation at the plate leading edge. The two curved walls have static pressure ports mounted flush with the surface at regular arc lengths of 50 mm. Similar to the curved plate, the static pressure ports of the concave wall are connected to a manometer bank for visualization purposes.

For boundary layer measurement along the concave surface of the curved plate, a computer controlled traversing system with a stepper motor, decoder, and encoder is mounted vertically on the base plate of the convex wall assembly. The system is capable of traversing probes in small steps with a minimum of 2.5 μm. This is specifically useful for boundary layer investigations where the measurement of the laminar sublayer is of particular interest. Positioning of the probe in the longitudinal direction is achieved by rotating the entire convex wall assembly about its center of curvature. To capture the major portion of the transition onset, the plate was traversed in a longitudinal direction in steps of 2 deg,

Table 1 Specifications of inlet flow, curved plate, and wake generator characteristics

Parameters	Values	Parameters	Values
Nozzle exit Raynolds number	$\mathrm{Re}_h=0.43\times10^6$	Nozzle exit turbulent intensity	$Tu=1.20\%$
Nozzle exit height	$h=420.00$ mm	Nozzle exit width	$w=593.00$ mm
Curved plate surface arc length	$s_0=690$ mm	Curved plate width	$w=593.00$ mm
Curved plate curvature radius	$r_C=702.5$ mm	Curved plate leading edge rad.	$r_{\mathrm{LE}}=1.0$ mm
Curved plate thickness	$t=15.00$ mm	Curved plate Re-number	$\mathrm{Re}_s=0.54\times10^6$
Steady reference (no rods)	$s_R=\infty$ mm	$\Omega=$parameter steady case	$\Omega=0.0$
Set 1 rod spacing	$s_R=188.4$ mm	$\Omega=$parameter for cluster 1	$\Omega=1.725$
Set 2 rod spacing	$s_R=94.2$ mm	$\Omega=$parameter for cluster 2	$\Omega=3.443$
Set 3 rod spacing	$s_R=62.8$ mm	$\Omega=$parameter for cluster 3	$\Omega=5.166$
Rod diameter	$d_R=2.0$ mm	No. of rods in set 2	$n_R=10$
No. of rods in set 1	$n_R=5$	No. of rods in set 3	$n_R=15$

within 50% of the plate. From this point on, up to 75% of the plate, an increased step of 3 deg was used. Finally the final 25% was traversed in steps of 5 deg. The slider of the traversing system incorporates a specially designed single hot-wire boundary layer probe, which is parallel to a distance pin. The function of the distance pin, which is of similar shape to the hot-wire probe, is to keep the hot-wire probe about 0.1 mm above the plate surface. By touching the surface, an electric circuit is activated by the pin that marks the reference zero point.

Instrumentation, Data Acquisition, Reduction

The data acquisition system is controlled by a personal computer, in which a 12-bit A/D-board (analog to digital conversion) is installed. The instantaneous velocity signal is obtained using a constant temperature hot-wire anemometer system (TSI-IFA 100). Based on numerous spectral measurements within the wake, the low pass filter of the signal conditioner is set to 20 kHz. All the measurements in the present study were made using a tungsten hot-wire sensor of 4 μm in diameter mounted on a custom designed single-wire boundary layer probe. For unsteady boundary layer measurements, a triggering system is implemented for data collection and tracking the number of cycles to later aid in the calculation of ensemble-averaged quantities of the periodic unsteady wakes. In order to ensure a high level of accuracy, the new calibration method described in John and Schobeiri [39] was used for all hot-wire calibration. The instantaneous velocity components are calculated from the temperature compensated instantaneous voltages using the calibration coefficients. The instantaneous velocity can be represented in the following form:

$$U=\overline{U}+u \tag{1}$$

where $\overline{U}$ is the mean (time-averaged) velocity and u is the turbulent fluctuation component. The mean velocity, also known as the time-average, is given by

$$\overline{U}=\frac{1}{N}\sum_{j=1}^{N} U_j \tag{2}$$

where N is the total number of samples at one radial location. A sampling rate of 1 kHz was used for the investigation of steady flow (no wakes). Good convergence was found for $N=16384$ samples. The root mean square value of the turbulent velocity fluctuation is obtained from the instantaneous and mean velocity by

$$u=\sqrt{\frac{1}{N}\sum_{j=1}^{N}(U_j-\overline{U})^2} \tag{3}$$

and the local turbulence intensity is defined as

$$Tu_{\mathrm{loc}}=\frac{u}{\overline{U}}\times 100=\frac{1}{\overline{U}}\sqrt{\frac{1}{N}\sum_{j=1}^{N}(U_j-\overline{U})^2}\times 100. \tag{4}$$

For certain presentations of the turbulence intensity it is appropriate to nondimensionalize with respect to a reference velocity for a particular boundary layer. This reference turbulence intensity is given by

$$Tu=\frac{u}{U_{\mathrm{ref}}}\times 100. \tag{5}$$

The unsteady data were reduced by the ensemble-averaging method. In order to keep the amount of the produced data and the required data analysis time under control, an extensive preliminary frequency study was performed prior to the final data acquisition and analysis (see [4]) study dealt with the variation of the number of samples per wake generator revolutions and the number of total revolutions to determine the optimum settings for convergence of the ensemble-averaged quantities. As a result, a sampling rate of 2.56 kHz was found to exactly reproduce the same ensemble-averaged velocity and turbulence intensity distributions that were found by utilizing sampling rates of 5 to 10 kHz. Utilizing this sampling rate, at each radial (lateral) position, 512 samples were taken for each of $n=300$ revolutions of the wake generator. The data were ensemble-averaged with respect to the rotation period (200 ms) of the wake generator. Thus, the ensemble-averaged results calculated over the 300 revolutions show n_R wake passings.

The ensemble-averaged fluctuation velocity and the turbulence intensity are calculated from the instantaneous samples by

$$\langle U_i(t_i)\rangle=\frac{1}{N}\sum_{j=1}^{N} U_{ij}(t_i) \tag{6}$$

$$\langle u_i(t_i)\rangle=\sqrt{\frac{1}{N}\sum_{j=1}^{N}[U_{ij}(t_i)-\langle U_i(t_i)\rangle]^2} \tag{7}$$

$$\langle Tu_i(t_i)\rangle=\frac{\langle u_i(t_i)\rangle}{\overline{U}}\times 100 \tag{8}$$

where $j=1,2,\ldots N$, and N is the total number of periods (i.e., 300 revolutions), and $I=1,2,\ldots M$, where M is the number of samples taken per period ($M=512$). U_{ref} is the reference velocity for the particular boundary layer traverse.

Measurements, Results, Discussion

Steady, Time-Averaged Velocity Distributions. Before taking the unsteady flow measurements, the boundary layer velocity and turbulence intensity distributions were measured under steady flow conditions in the lateral direction along the concave side of the plate for different longitudinal positions s/s_0. The measurements were conducted under the same inlet flow conditions (inlet velocity, turbulence intensity, Reynolds number) and the same pressure gradient in the longitudinal direction) as reported by Schobeiri and Radke [33]. Thus, for the steady-state reference case, identical results were obtained to which we refer for further discussion.

To study the effect of unsteady wake passing frequency, caused by varying the rod spacing, three different periodic unsteady flows with the frequency parameters $\Omega=1.725$, 3.443, and 5.166 defined in Table 1 were investigated. These Ω-values correspond to the wake-induced unsteady flow established by 5, 10, and 15 rods. This arrangement allows doubling and tripling the impinging wake frequency as sketched in Fig. 1. As mentioned previously, each rod generates a primary and a secondary wake with every revolution of the wake generator. For the 5-rod case, the signals of these two wakes on a velocity trace are observed to be clearly isolated, indicating no mutual interaction. In the 10-rod case, however, visible interaction of the two wakes are observed simulating the unsteady flow situation past the second row (first rotor) shown in Fig. 1. The observation of the velocity traces of the 15-rod case reveals an early mixing of the secondary wakes before they reach the primary wakes resulting in a high freestream turbulence.

The time-averaged nondimensionalized velocity distribution for $\Omega=1.725$, 3.443, and 5.166 that correspond to 5, 10, and 15 rods are presented in Fig. 3(*a*,*b*,*c*) for different longitudinal positions s/s_0. Boundary layer measurements were taken extremely close to the wall with the resolution of $y^+=2$, thereby requiring a wall correction which is necessary when utilizing a hot-wire measuring scheme. As seen, for all three Ω-values, the laminar sublayer within the y^+-range of 2 to 8 is well described by the linear wall function, which is shown by the solid lines. Although these figures do not reveal any unsteady details, they show clearly the transitional behavior of the velocity profiles within the given range, defined in Fig. 3. Further details of boundary layer transition and development are shown in Fig. 4(*a*,*b*,*c*), where the contour of the time-averaged turbulence intensity in the longitudinal direction is plotted in the lateral direction y/d ($d=10$ mm). Starting with Ω

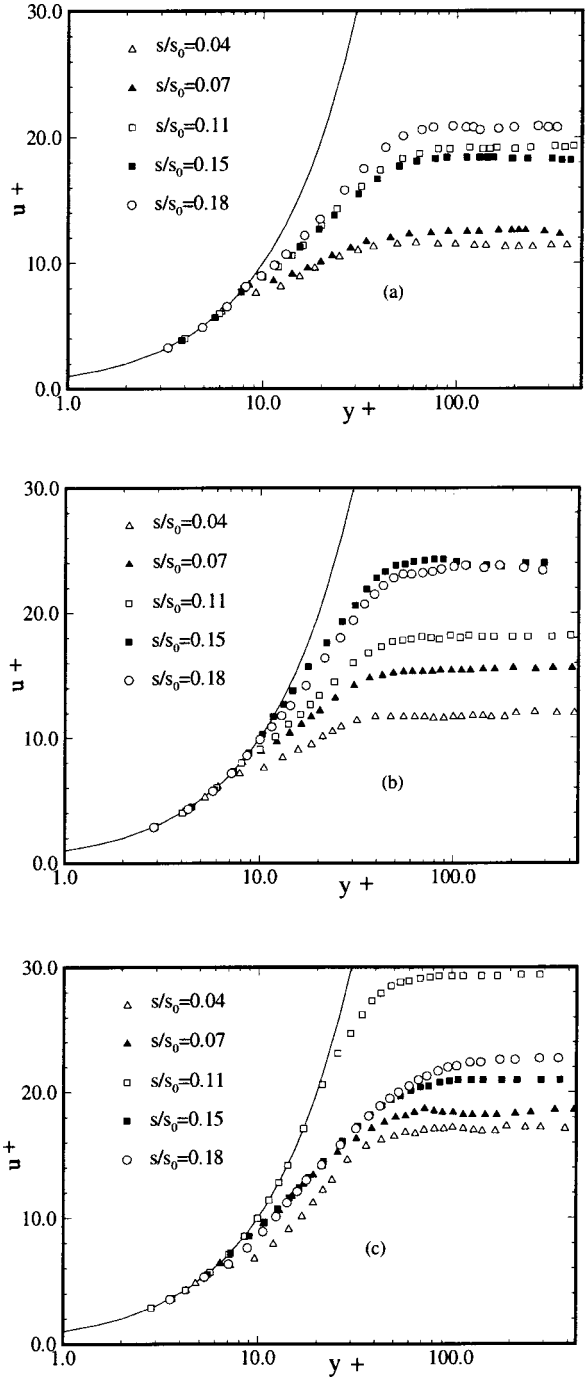

Fig. 3 Time-averaged velocity profiles at the leading edge for (*a*) 5 rods, (*b*) 10 rods, and (*c*) 15 rods

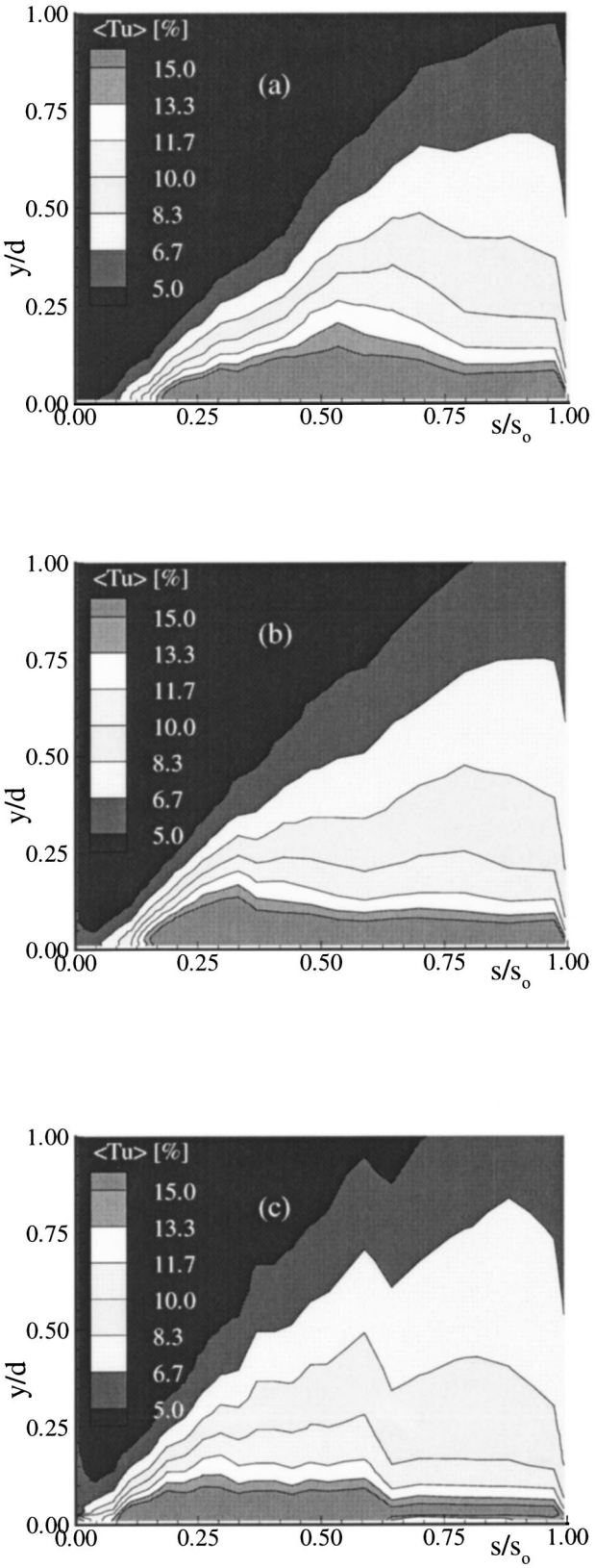

Fig. 4 Time-averaged turbulence intensity contours for (*a*) 5 rods, (*b*) 10 rods, and (*c*) 15 rods

$=1.725$ (5 rods), the wall region exhibits a compact high turbulence intensity core of above 15% with the center located at $s/s_0 \approx 0.50$. Increasing the frequency by reducing the rod spacing ($\Omega = 3.443$, 10 rods) results in a shift of the center of the turbulence intensity core toward the leading edge, indicating an earlier beginning of the transition process (for comparison with steady-state, see Schobeiri and Radke [33]). Two mechanisms may be responsible for this shift. First, a higher impinging frequency of the wake strips with excessive energy transport to the boundary layer, second, earlier mixing of the secondary wakes results in an increase of the freestream turbulence level. Further increase of the frequency as a result of reducing the spacing (Fig. 4(*c*), $\Omega = 5.166$, 15 rods) shows a farther upstream movement of the transition process which can be attributed to the same mechanisms mentioned above. These experimental results are in accord with those by Liu and Rodi [38]) but are in disagreement with the

earlier statement by Pfeil et al. [31], and Pfeil and Herbst [29], which investigated the onset of transition on a flat plate utilizing the boundary layer integral quantities such as displacement and momentum thicknesses. They kept the inlet velocity, the wake generator frequency and the position of their flat plate constant, and measured the time-averaged boundary layer velocities for seven different rod spacings. Reducing the wake spacing by increasing the rod number, caused a significant variation in the time-averaged displacement and momentum thicknesses along the plate within the range 20% to 100% of the length. Close to the plate leading edge, in the range of 0% to 20% of the length, only small variations were distinguishable. Pfeil et al. [31] presented their original idea of a transition model and concluded that, by keeping the flow and rod velocity constant, the variation of spacing (increasing the rod numbers) would show no influence on the position of forced transition start $x_{f,tr}$. This conclusion was drawn primarily from the distribution of the time-averaged integral quantities such as displacement and momentum thicknesses without the presentation of experimental evidence essential to rectify the conclusion. However, time-averaged quantities cannot sufficiently explain the detailed physical picture of the unsteady boundary layer behavior. It should be pointed out that Herbst [30] had a data acquisition and processing system which only allowed for time-averaged and limited ensemble-averaged results. Based on their (at that time) limited information, Pfeil et al. [31] successfully established a transition model which is generally accepted and, to a large extent, is supported by the present experimental investigation.

Longitudinal Propagation of the Unsteady Wake Within the Boundary Layer. During one rod passing period, the wake induced boundary layer development undergoes a sequence of different states as shown in Figs. 5 and 6 for $\Omega=1.725$ and 5.166, that pertain to 5 and 15 rods. (Note: the plots contained in Fig. 5 are identical to the corresponding figure in the study by Schobeiri and Radke [33] and were reproduced with new data.) These contour plots display the turbulence intensity distributions at different lateral positions y/d with nondimensional time (t/τ) as a parameter. Since this sequence is periodic, we start with $t/\tau=0.25$, in Fig. 5(*b*), where the quasi-steady ''primary'' boundary layer (as defined by Schobeiri and Radke [33]) transition starts at $s/s_0 \approx 0.20$ and extends to the trailing edge of the plate. The primary boundary layer has a high turbulence intensity core located around $s/s_0 \approx 0.50$ and is externally disturbed by a wake strip originating from a passing wake. As Fig. 5(*b*) reveals, the tail of this strip travels as an external periodic disturbance over the primary boundary layer.

At $t/\tau=0.49$, shown in Fig. 5(*c*), a wake strip hits the plate's leading edge and forms an isolated core with a turbulence intensity higher than that of the wake strip itself. While convecting downstream, the turbulence intensities of the isolated core continuously increase, resulting in a periodic wake induced boundary layer transition with a high turbulence intensity core (13%) close to the wall, Fig. 5(*d*). By moving farther downstream at $t/\tau=0.72$, 0.96, 0.02 (or 1.02), Figs. 5(*d,e,a*) the periodic boundary layer coalesces with the primary boundary layer resulting in a strong deformation of the latter and generating a high turbulence intensity core. After the boundary layer portion of this strip is totally penetrated into the primary boundary layer at $t/\tau=0.49$, becalmed regions are formed behind the wake strip. Increasing the parameter Ω to 5.166 (pertaining to 15 rods) by reducing the rod spacing (i.e., increasing wake-passing frequency and freestream turbulence) has moved the onset of the boundary layer transition closer to the leading edge, as shown in Fig. 6(*a–d*). This statement is supported by Figs. 7 and 8, which will be discussed in the following section. Similar boundary layer flow patterns were revealed for $\Omega=3.443$ (10 rods). Once the individual primary boundary layer transition pattern has been established, the wake strip traveling downstream as an external periodic disturbance apparently does not, by itself, significantly affect the transition onset, but it clearly causes a deformation of the boundary layer picture. Similar observations were made by Pfeil et al. [31] and later by Addison and Hodson [40,41]. Comprehensive investigations by Orth [42,43] and Schobeiri and Radke [33] indicate a similar boundary layer pattern.

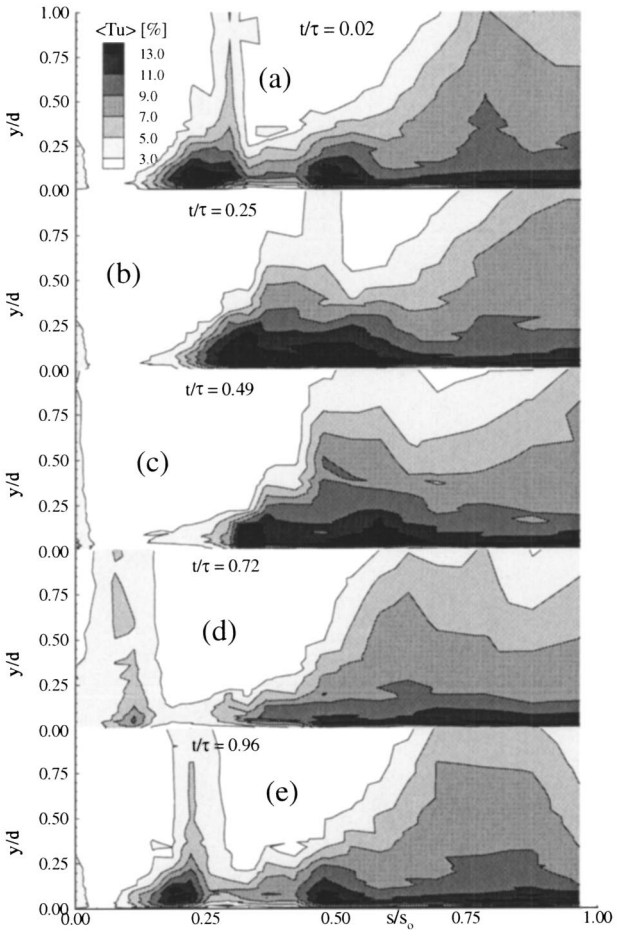

Fig. 5 Ensemble-averaged turbulence intensity contours at $t/\tau=0.02, 0.25, 0.49, 0.72, 0.96$ for 5 rods

Velocity and Turbulence Intensity Distribution. A picture of the temporal-spatial ensemble-averaged velocity band in the vicinity of the wall at $y=0.3$ mm is given in Fig. 7(*a,b,c*) for $\Omega=1.725$, 3.443, 5.166 pertaining to 5, 10, and 15 rods. Close to the leading edge at $s/s_0 \approx 0.07$, the ensemble-averaged nondimensional velocity distribution $\langle U\rangle/U_{\text{ref}}$ shown in Fig. 7(*a*) is not affected by the presence of a very thin laminar boundary layer. However, as a result of the growing viscous boundary layer, a continuous deceleration and deformation in the longitudinal direction, is visible. After passing through a Tollmien-Schlichting wave-dominated region, $s/s_0 \approx 0.10-0.15$, this deceleration and deformation leads to generation of turbulent spots propagating with velocities that range between $0.36U_{\text{ref}}$ and $0.60U_{\text{ref}}$. Note that these values refer to a band of ensemble-averaged velocities and are not identical to the leading and trailing edge velocities which are found in literature. The process of turbulent spot generation within the boundary layer starts at $s/s_0 \approx 0.17$, which can be interpreted as the onset of the boundary layer transition. By moving downstream, the distinctively periodic flow within the boundary layer is continuously degenerating and becoming fully stochastic (starting at $s/s_0 \approx 0.75$ with random fluctuations in t/τ-direction). In contrast to Fig. 7, where the velocity contour was presented close to the surface ($y=0.3$ mm), Fig. 8(*a,b,c*) exhibits the velocity contours at the edge of the boundary layer

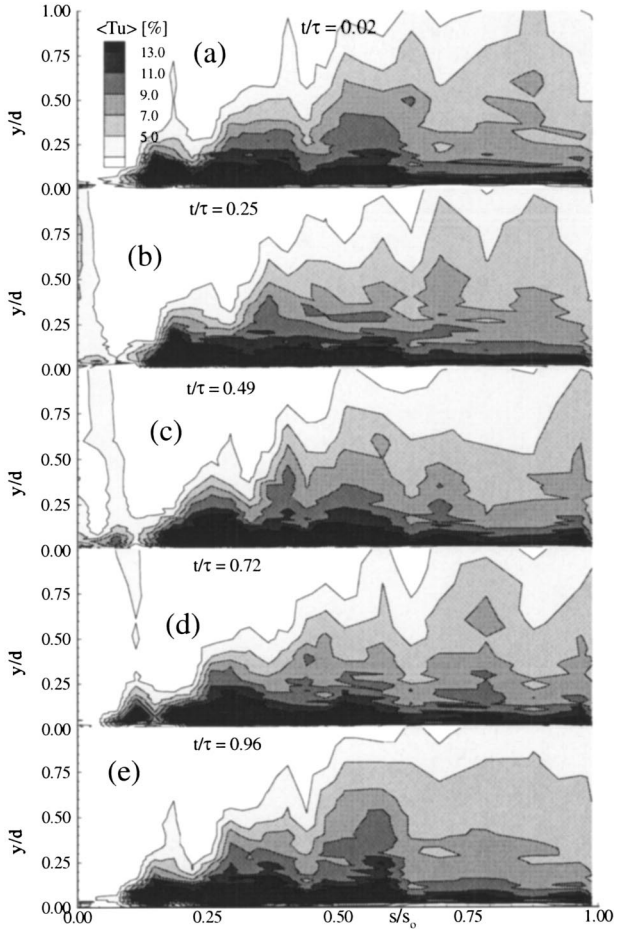

Fig. 6 Ensemble-averaged turbulence intensity contours at $t/\tau = 0.02, 0.25, 0.49, 0.72, 0.96$ for 15 rods

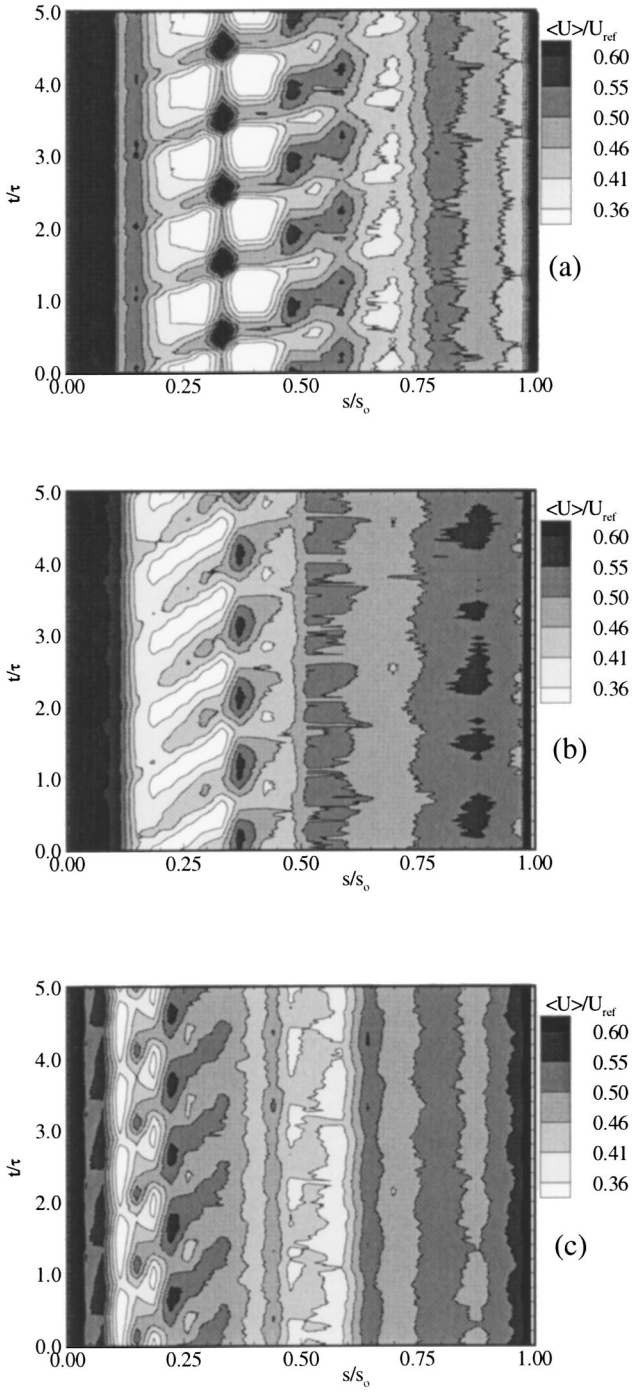

Fig. 7 Ensemble-averaged nondimensional velocity in the temporal-spatial domain at $y = 0.3$ mm for (*a*) 5 rods, (*b*) 10 rods, and (*c*) 15 rods

($y = 2.5$ mm) for $\Omega = 1.725$, 3.443, and 5.166 pertaining to 5, 10, and 15 rods. In Fig. 7 the wake can be identified by high velocity regions along the wake centerline (due to profile switching underneath the wake as clearly shown by Schobeiri and Radke [33]) whereas in Fig. 8 the wake can be identified by low velocity regions (wake velocity deficit).

The entire set of ensemble-averaged data, from which only a few were discussed above, were utilized to generate the ensemble-averaged turbulence intensity contour plot for two different lateral positions $y = 0.3$ mm and 2.5 mm presented in Figs. 9(*a,b,c*) and 10(*a,b,c*). As shown in Fig. 9(*a*) ($\Omega = 1.725$, 5 rods), the boundary layer is periodically disturbed by the high turbulence intensity wake strips. These strips are contained between the wake leading edge and the wake trailing edge (marked in the plots). Outside the wake strips undisturbed low turbulence regions are observed with significantly lower intensity levels indicating the absence of any visible wake interaction. These regions are observed between the plate leading edge and the streamwise position of $s/s_0 \approx 0.3$. Increasing the unsteady parameter Ω by reducing the rod spacing (Fig. 9(*b,c*) with $\Omega = 3.443$, 5.166 rods) results in an earlier transition start compared to the above 5 rod case. In contrast to Fig. 9, where the turbulence intensity contour was presented close to the surface at the lateral position $y = 0.3$ mm, Fig. 10(*a,b,c*), exhibits the turbulence intensity contours at the edge of the boundary layer with $y = 2.5$ mm for $\Omega = 1.725$, 3.443, and 5.166 pertaining to 5, 10, and 15 rods. For both lateral positions, the wake flow regime is identified by periodic high turbulence intensity regions that are characteristic for the wake development along the wake centerline.

The turbulence intensity distributions exhibited in Figs. 9 and 10 present a fairly clear and consistent picture about the transition start and end process and the influence of the wake structure and interaction on the transition. In accord with the previous discussions, two mechanisms are considered instrumental in affecting the above transition start. First, an increased impinging frequency of the primary wakes based on reducing the rod spacing cause a formation of wakes, whose initial spacing corresponds to the rod spacing. These wakes convect downstream while the individual wake widths continually increase (see Schobeiri et al. [34]) until they have reached approximately the size of the rod spacing. At

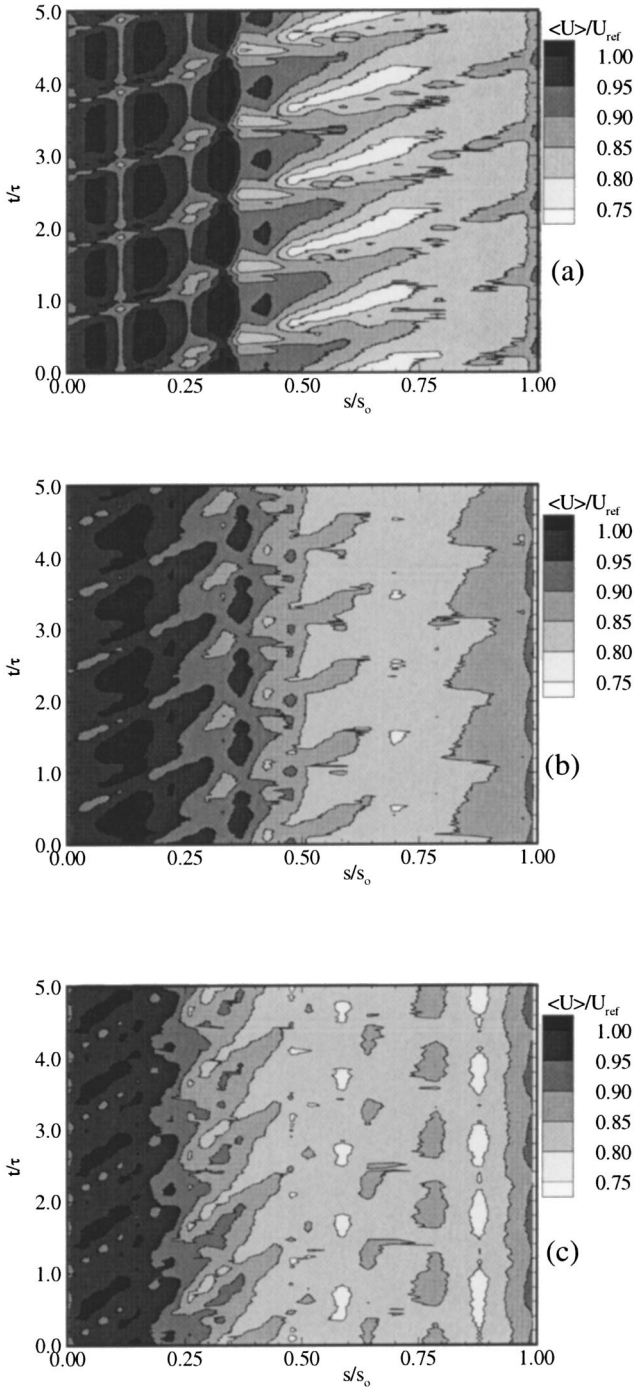

Fig. 8 Ensemble-averaged nondimensional velocity in the temporal-spatial domain at $y=2.5$ mm for (*a*) 5 rods, (*b*) 10 rods, and (*c*) 15 rods

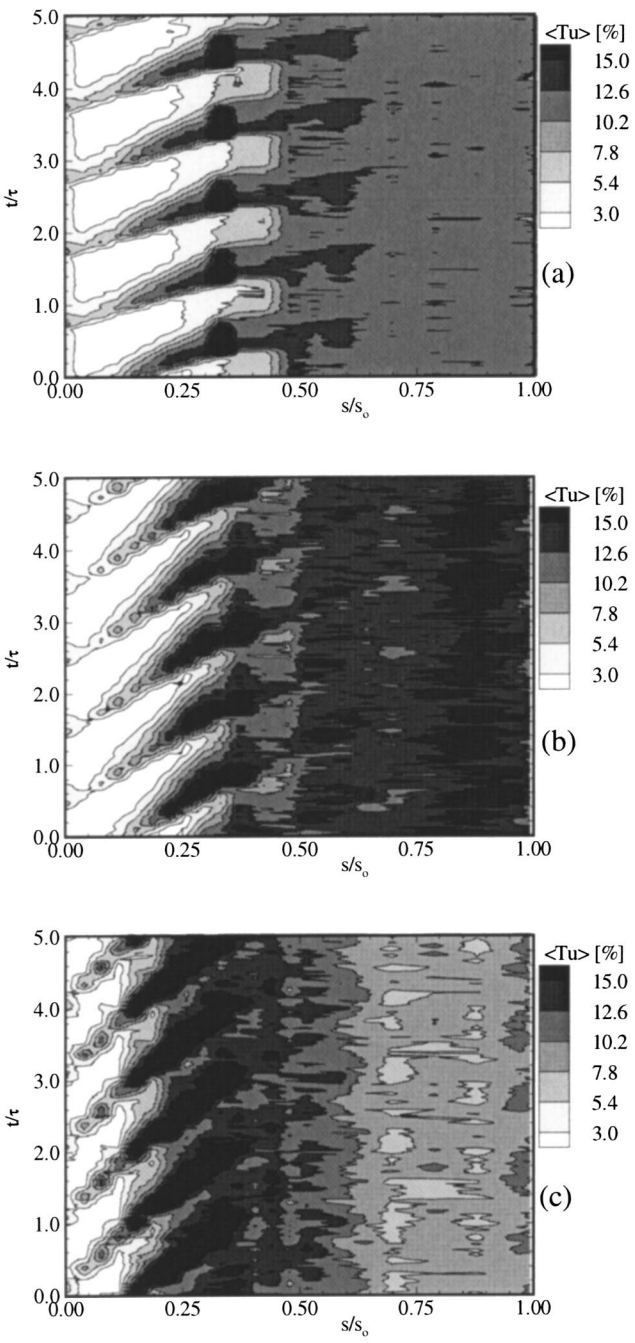

Fig. 9 Ensemble-averaged reference turbulence intensity in the temporal-spatial domain at $y=0.3$ mm for (*a*) 5 rods, (*b*) 10 rods, and (*c*) 15 rods

this point, a strong wake mixing and interaction follows that generates a highly turbulent flow regime with an intensity of $Tu=15\%$. By decreasing the rod spacing, thereby increasing the wake impinging frequency, the wake interaction occurs earlier. This flow regime introduces an excessive turbulent kinetic energy transport to the boundary layer causing a shift of transition toward the leading edge. Second, an earlier mixing of the secondary wakes due to the growth of their width leads to higher freestream turbulence which inherently affects the onset of the transition. It is conceivable that the combination of these two mechanisms would make an additional contribution to the shift of transition. However, due to the complexity of the flow situation, a quantifying statement cannot be made at this time. Finally, an increase of Ω (Fig. 9(*c*) with $\Omega=5.166$, 15 rods) results in a higher freestream turbulence and increased impinging frequency and thus a significant shift of the transition toward the leading edge as the consequence of the mechanisms discussed above (for comparison with steady-state see Schobeiri and Radke [33]).

Spot Detection and Intermittency Factors. Discrimination between laminar and turbulent regions of the flow from hot-wire records is based on the presence of small-scale fluctuations within the turbulent patches. Hedley and Keffer [44] surveyed a number

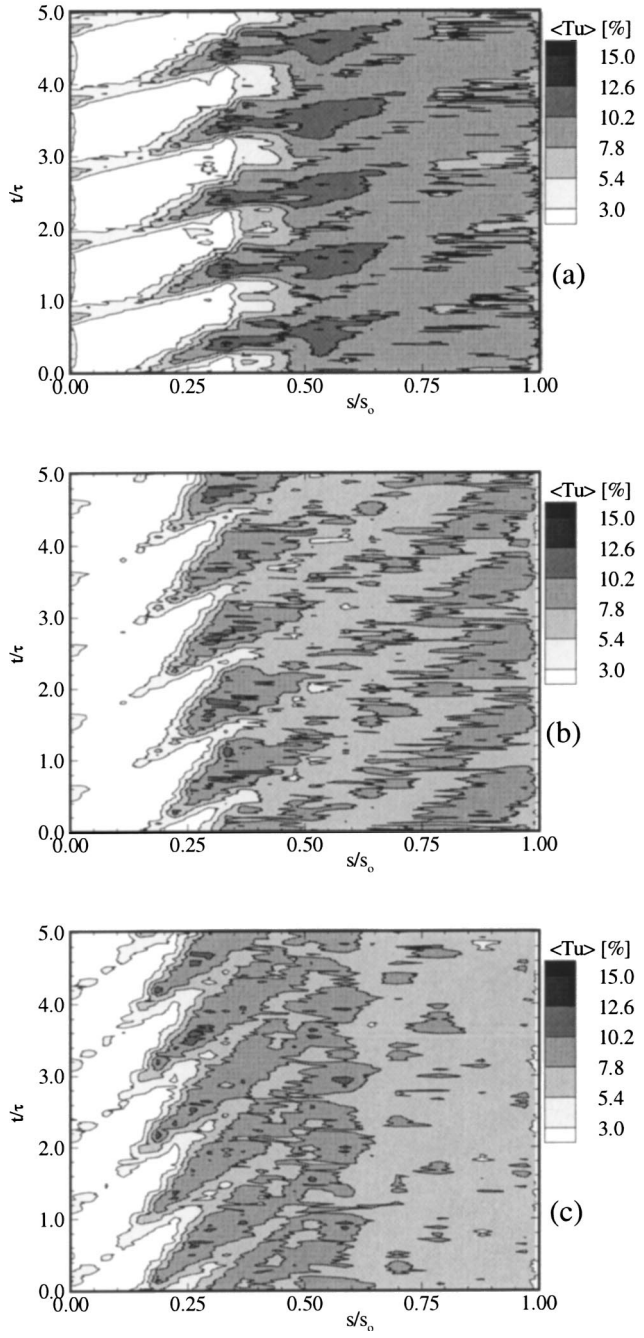

Fig. 10 Ensemble-averaged reference turbulence intensity in the temporal-spatial domain at $y=2.5$ mm for (*a*) 5 rods, (*b*) 10 rods, and (*c*) 15 rods

of options and issued recommendations for the discrimination algorithms. Variants were later suggested by Antonia [45]. We summarize some of the steps for background.

The small-scale fluctuations translate into high-frequency regions in the time traces of the velocity (''discriminator'' signal). Small-scale features are enhanced by double differentiation of the discriminator signal, and squaring eliminated irrelevant sign information, resulting in a ''detector'' function. Smoothing over scales of the order of the Taylor microscale fills the gaps between the small-scale patches, yielding the ''criterion'' function. This criterion function is compared to a threshold, resulting in the ''indicator'' function (0 at points where the criterion function is less than the threshold, 1 otherwise). The indicator function is used to mask parts of the data in the calculation of conditional statistics (see Antonia [45]). The average value of the indicator function measures the fraction of the time during which a signal is identified as turbulent, and is called the intermittency factor. All told, the construction of the indicator function requires the choice of a discriminator signal (in this instance, streamwise velocity is available), an order of differentiation, (second derivatives were used following the recommendation of Hedley and Keffer [44] a smoothing scale (selected to be the sampling rate, in the absence of reliable estimates of the local Taylor microscale), and a threshold (selected at 1 rms of the detector function, in the absence of realistic estimates of an absolute threshold). We tested the results for sensitivity to the last two parameters, using a range of smoothing scales and thresholds. No significant differences were observed, so that the results presented below are insensitive to the parameters used in the intermittency algorithm.

Ensemble-averages of the indicator functions represent the variations of intermittency factor in relation to the phases of the rods. Figures 11 and 12 present the ensemble-averaged intermittency for two passing periods. Figure 11(*a,b,c*) exhibit the intermittency behavior of the boundary layer at a wall distance of $y=0.1$ mm for $\Omega=1.725$, 3.443, and 5.155 that corresponds to 5, 10, and 15 rods, respectively. Figure 12(*a,b,c*) display the intermittency behavior at a distance $y=10$ mm from the wall for the same frequencies as in Fig. 11(*a,b,c*).

Intermittency distribution outside the boundary layer at $y=10$ mm is shown in Fig. 12(*a*). Except for the narrow wake strips, Fig. 12(*a*) shows the virtual absence of turbulence (as defined by our criterion) with $\langle\gamma\rangle\approx 0.0$ corresponding to the wake passings. The wake strips with highly turbulent core convect downstream and undergo a decay process while the individual wake widths continually increase until they have reached approximately the size of the rod spacing. For $\Omega=1.725$ (5 rods), this occurs at $s/s_0\approx 0.9$. At this point, a process of wake mixing follows that generates an intermittency pattern ranging from $\langle\gamma\rangle\approx 0.2$ to $\langle\gamma\rangle\approx 1.0$. The dominant feature is the abrupt change in direction of the turbulent strip at the distance $s/s_0\approx 0.45$. Recalling that the angle of a line on this plot is a measure of the translation velocity of the observed feature, we see that the turbulent patches travel initially at a higher speed (freestream), then at lower speed. Moving closer to the wall at $y=0.1$ mm, we observe similar intermittency patterns within the boundary layer as shown in Fig. 11(*a*). The *nonturbulent* regions ($\langle\gamma\rangle\approx 0.0$) separated from the turbulent wake strips with sharply defined contours, indicate the intermittent nature of the boundary layer. Similar to the case shown in Fig. 12(*a*), we observe a sudden change in direction of the turbulent strip at the distance $s/s_0\approx 0.45$. We interpret this as representing the sudden shift from a flow dominated by the convection of wakes by the freestream to the propagation of boundary layer spots (or other turbulent structures) at a lower speed.

Increasing the number of the rods ($\Omega=3.443$, 10 rods) as shown in Figs. 11(*b*) and 12(*b*) results in closer spacing between the wakes. As a consequence, the mixing point of the wakes and the onset of wake-induced transition experience a shift toward the leading edge. Compared to the 5-rod case discussed above, the nonturbulent regions with $\langle\gamma\rangle\approx 0.0$ shown in Figs. 11(*b*) and 12(*b*) have become narrower. Further increasing the rod number ($\Omega=5.166$,15 rods) as shown in Figs. 11(*c*) and 12(*c*) results in a strong mutual interaction of the wakes that determines the intermittency picture of the unsteady flow pattern. In any event, the close spacing of the wakes in the 15-rod case ensures the longer dominance of wake turbulence relative to the 10 and 5-rod cases. As Fig. 11(*c*) indicates, the higher freestream turbulence generated by the wake mixing process predominantly affects the onset of the boundary layer transition. Interestingly, the calming effect of the periodic unsteady wake discussed previously is maintained and causes the very narrow nonturbulent region with $\langle\gamma\rangle\approx 0.0$ exhibited in Fig. 12(*c*) to widen as shown in Fig. 11(*c*).

Intermittency Analysis. The contour plots of the intermit-

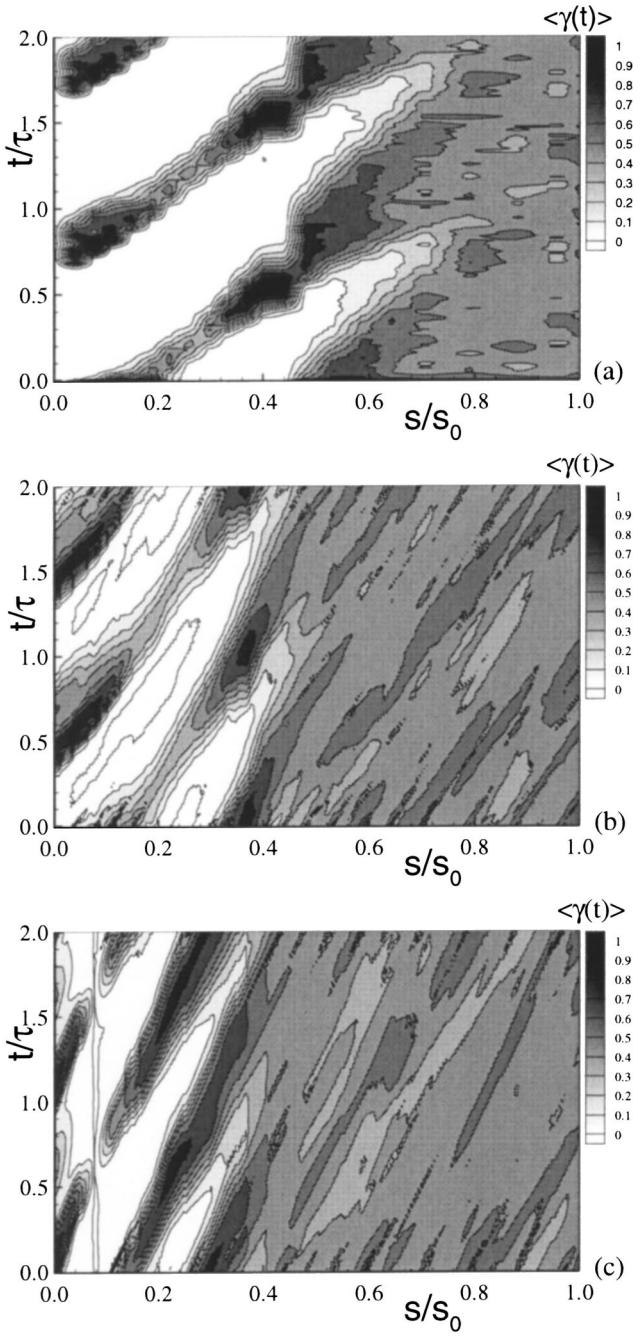

Fig. 11 Ensemble-averaged intermittency γ in temporal-spatial domain at $y=0.1$ mm for (*a*) 5 rods, (*b*) 10 rods, and (*c*) 15 rods

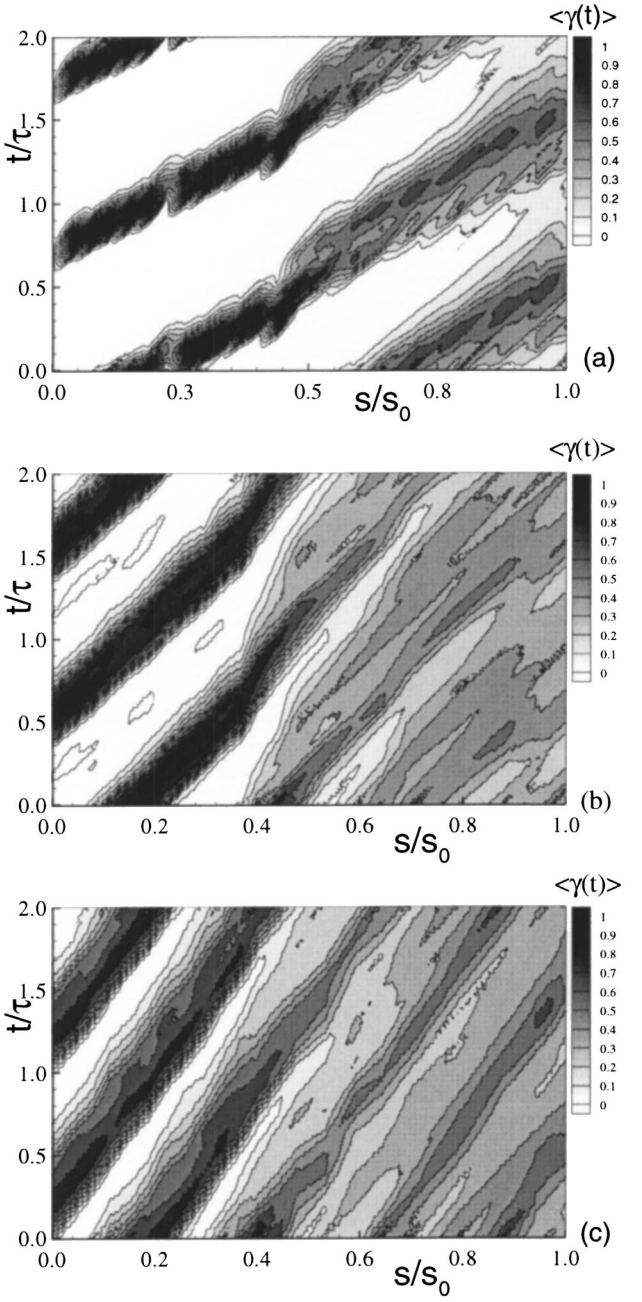

Fig. 12 Ensemble-averaged intermittency γ in temporal-spatial domain at $y=10.0$ mm for (*a*) 5 rods, (*b*) 10 rods, and (*c*) 15 rods

tency distributions in Figs. 11 and 12 clearly show the unsteady nature of the boundary layer transition process and serve for better understanding the physics of unsteady boundary layer transition. In this form, however, they cannot be used to quantitatively describe the complex unsteady transition process. To establish the basic relations essential for a quantitative description of the unsteady boundary layer transition, we resort to the fundamental studies by Schobeiri and his co-workers, [34] and [46], that deal with the physics of steady and unsteady wake development in a curved environment. These studies show clearly that the turbulence structure of the steady and unsteady wake flow is determined by the wake defect, which is a Gaussian function. Following the above studies, we define a dimensionless parameter

$$\zeta=\frac{U_w t}{b}=\frac{y}{b}\quad\text{with}\quad b=\frac{1}{\sqrt{\pi}}\int_{-\infty}^{+\infty}\Gamma\, d\xi_2 \tag{9}$$

that relates the wake-passing time t with the wake-passing velocity in lateral direction U_w and the intermittency width b. The latter is directly related to the wake width introduced by Schobeiri and his co-workers, [34] and [46]. In an analogous way to find the defect function, we define the relative intermittency function Γ as

$$\Gamma=\frac{\langle\gamma_i(t_i)\rangle-\langle\gamma_i(t_i)\rangle_{\min}}{\langle\gamma_i(t_i)\rangle_{\max}-\langle\gamma_i(t_i)\rangle_{\min}}. \tag{10}$$

In the above equation, $\langle\gamma_i(t_i)\rangle$ is the time-dependent ensemble-averaged intermittency function, which determines the transitional nature of an unsteady boundary layer. The maximum intermit-

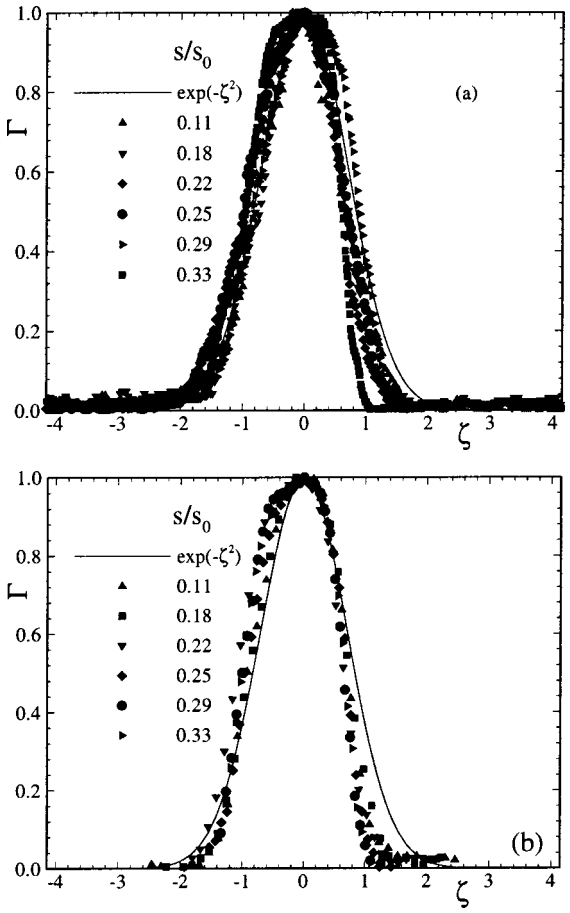

Fig. 13 Relative intermittency as a function of nondimensionalized lateral coordinate for (*a*) 3 rods and (*b*) 15 rods

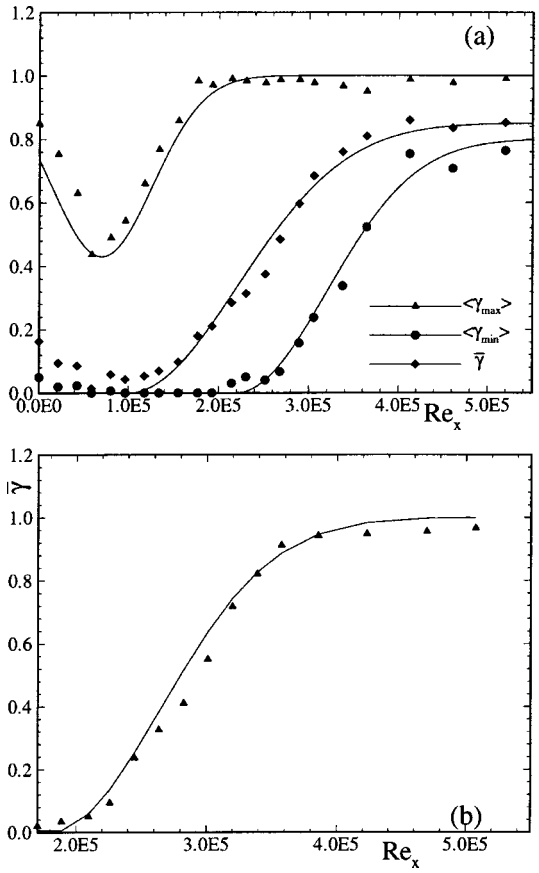

Fig. 14 Maximum, minimum, and time-averaged intermittency distributions as a function of axial Reynolds number for (*a*) 3 rods and (*b*) no rods (steady case)

tency $\langle \gamma_i(t_i) \rangle_{\max}$ exhibits the time-dependent ensemble-averaged intermittency value inside the wake vortical core. Finally, the minimum intermittency $\langle \gamma_i(t_i) \rangle_{\min}$ represents the ensemble-averaged intermittency values outside the wake vortical core.

Further analysis of the intermittency data for $\Omega = 1.725$ (5 rods), $\Omega = 3.443$ (10 rods), and $\Omega = 5.166$ (15 rods) clearly indicated that the relative intermittency Γ closely follows a Gaussian distribution. These new results gave impetus to perform a new set of unsteady boundary layer measurements for a frequency parameter of $\Omega = 1.033$, which corresponds to 3-rods configuration. The data were taken at a sampling rate of 10 kHz and much smaller Δy-increments. As representatives, Fig. 13(*a*,*b*) shows Γ for frequency parameter values of $\Omega = 1.033$ (3 rods) and $\Omega = 5.166$ (15 rods) with the dimensionless longitudinal distance s/s_0 as a parameter. The symbols represent the experimental data. As shown, the measured relative intermittency Γ for wakes impinging on the concave surface presented in this paper follow closely a Gaussian distribution, which is given by

$$\Gamma = e^{-\zeta^2}. \tag{11}$$

Here, ζ is the nondimensionalized variable defined in Eq. (9). Although the relative intermittency function described by Eq. (11) has been derived for the unsteady boundary layer at zero pressure gradient, the recent boundary layer study along a turbine blade under periodic unsteady flow by Schobeiri and Chakka [47] shows that the intermittency function Γ described by Eq. (11) is also valid for different pressure gradients characteristic of a turbine cascade. These results indicate the universal character of the relative intermittency function.

With the relative intermittency function given by Eq. (11), the time-dependent intermittency function $\langle \gamma_i(t_i) \rangle$ is completely determined if additional information about the minimum and maximum intermittency functions $\langle \gamma_i(t_i) \rangle_{\min}$ and $\langle \gamma_i(t_i) \rangle_{\max}$ are available. As a representative example for the cases investigated in this study, the distributions of $\langle \gamma_i(t_i) \rangle_{\min}$, $\langle \gamma_i(t_i) \rangle_{\max}$, and the averaged $\overline{\gamma}$ in the streamwise direction are plotted in Fig. 14(*a*) for $\Omega = 1.033$ (3 rods) for $y = 0.1$ mm. The steady-state case (no rod) shown in Fig. 14(*b*) serves as the basis of comparison for these maximum and minimum values. In the steady-state case, the intermittency starts to rise from zero at a streamwise Reynolds number $\mathrm{Re}_{x,s} \approx 2 \times 10^5$ and gradually approaches the unity, corresponding to the fully turbulent state. This is typical of natural transition and follows the intermittency function introduced by Narasimha [48]. As shown in Fig. 14(*a*), at each particular streamwise location with a given Reynolds number, for example $\mathrm{Re}_x = 1 \times 10^5$, two corresponding, distinctively different intermittency states are periodically present. At this location, $\langle \gamma_i(t_i) \rangle_{\max}$ corresponds to the condition when the wake with the high turbulence intensity core impinges on the plate surface at a particular instant of time. Once the wake has passed over the surface, the same streamwise location is exposed to a low turbulence intensity flow regime with an intermittency state of $\langle \gamma_i(t_i) \rangle_{\min}$, where no wake is present. As seen, $\langle \gamma_i(t_i) \rangle_{\min}$ has the tendency to follow the course of the steady (no-wake) intermittency distribution exhibited in Fig. 14(*b*), with a gradual increase from an initial *nonturbulent* state with a value of zero approaching a final state of 0.8. This was expected as $\langle \gamma_i(t_i) \rangle_{\min}$ is calculated outside the wake region where the turbulence intensity is relatively small. On the other hand, $\langle \gamma_i(t_i) \rangle_{\max}$ reveals a fundamentally different behavior that needs to be discussed further. As Fig. 14(*a*) shows, the wake flow

Table 2 Constants in the intermittency correlation

	Reduced Frequency, Ω			
Const.	**1.033**	**1.725**	**3.441**	**5.166**
c_1	0.57	0.22	0.50	0.35
c_2	0.80	0.85	0.80	0.83
c_3	1.00	0.82	0.80	0.80
c_4	0.85	0.92	0.92	0.94

with an intermittency close to unity impinges on the blade surface. By convecting downstream, its turbulent fluctuations undergo a strong damping by the wall shear stress forces. The process of damping continues until $\langle \gamma_i(t_i)\rangle_{\max}$ reaches a minimum. At this point, the wall shear forces are not able to further suppress the turbulent fluctuations. As a consequence, the intermittency again increases to approach the unity, showing the combined effect of *wake-induced* and *natural transition* due to an increased turbulence intensity level. The damping process of the high turbulence intensity wake flow, discussed above, explains the phenomena of *the becalming* effect of a wake-induced transition observed first by several researchers including Pfeil and Herbst [29–31], Schobeiri and Radke [33], and Halstead et al. [49]. The intermittencies $\langle \gamma_i(t_i)\rangle_{\min}$ and $\langle \gamma_i(t_i)\rangle_{\max}$ precisely describe the physical events exhibited in Figs. 5 and 6. Figure 14(*a*) also shows the average intermittency $\overline{\gamma}$ which is a result of the integral effect of periodic wakes with respect to time. The maximum intermittency is described by

$$\langle \gamma(t)\rangle_{\max} = 1.0 - c_1 e^{-(\mathrm{Re}_x - \mathrm{Re}_{x,s}/\mathrm{Re}_{x,s} - \mathrm{Re}_{x,e})^2} \tag{12}$$

where the constant c_1 depends on Ω. The minimum intermittency is described by

$$\langle \gamma(t)\rangle_{\min} = c_2(1.0 - e^{-(\mathrm{Re}_x - \mathrm{Re}_{x,s}/\mathrm{Re}_{x,s} - \mathrm{Re}_{x,e})^2}) \tag{13}$$

where the constants c_2 are again dependent on Ω. And, the time-averaged intermittency is described by

$$\overline{\gamma} = c_4(1.0 - c_3 e^{-(\mathrm{Re} - \mathrm{Re}_{x,t}/\mathrm{Re}_{x,t} - \mathrm{Re}_{x,e})^2}). \tag{14}$$

The combined effects of $\langle \gamma_i(t_i)\rangle_{\max}$ and $\langle \gamma_i(t_i)\rangle_{\min}$ can be seen in the expression for $\overline{\gamma}$ through the constants c_3 and c_4. The four constants for the frequencies under investigation are given in Table 2. For natural transition, the above constants approach unity.

Spectral Analysis

Wavelet Tools: Local Spectral Discrimination. The emerging complexity of the flow makes it imperative to quantify the active scales so that modeling can include more of the relevant physics. Fourier methods, and variants thereof, have been the traditional method of spectral analysis of experimental data. However, it has long been apparent that the analysis of complex (non-periodic, non-Gaussian) signals would benefit from a compromise between the sequential and the spectral views. Indeed, while a Fourier spectrum is very effective at identifying the wake passing frequency, it is ill-suited to the spectral analysis of the turbulence associated with these wakes. Wavelet methods have evolved over the past few years (Daubechies [50] and Farge [51]) as a versatile substitute for earlier time-frequency approaches. Mathematical derivations, specific algorithms and alternative techniques, with examples of applications to experimental data, can be found in literature. Wavelet methods allow quantitative measurements of both duration and time of occurrence, and establish the compromise between their respective accuracies. In this study, we have used the continuous Mexican hat wavelet g_2,

$$g_2(t) = (t^2 - 1)e^{-t^2/2}. \tag{15}$$

Time t and duration κ^{-1} become two independent variables, and the wavelet transform of the signal $f(t)$ is defined by

$$f_g(\kappa, t) = \int_{-\infty}^{\infty} \kappa^{1/2} f(\tau) g_2(\kappa(\tau - t))\, d\tau. \tag{16}$$

The duration can be related (Higuchi et al. [52]) to an equivalent frequency ϕ. For the Mexican hat wavelet, we have

$$\frac{\phi}{\kappa} = \frac{\sqrt{2.5}}{2\pi}. \tag{17}$$

This relation has been used to reduce all wavelet durations to equivalent frequencies in the results presented below. Essential for the purpose of this study is the ability to distribute the total energy of the signal among a spectrum of frequencies at each instant. This result is embodied in the Parseval theorem

$$\int_{-\infty}^{\infty} |f(t)|^2 dt = \frac{1}{\pi} \int_0^{\infty} d\kappa \int_{-\infty}^{\infty} dt |f_g(\kappa, t)|^2 = \int_0^{\infty} 2E(\kappa)\, d\kappa. \tag{18}$$

In Eq. (18), the expression $|f_g(\kappa,t)|^2/2\pi$ can be interpreted as the *local* spectral energy density. The factor $1/\pi$ in Eq. (18) is specific to the Mexican hat wavelet Eq. (15). The mean energy spectrum $E(\kappa)$ obtained by time integration of the local spectrum is equivalent to the Fourier power spectrum. Conditional mean spectra (Higuchi et al. [52], Lewalle [53], and Lewalle et al. [54]) obtained by integrating the local spectral energy density only during a portion of the sampling time (e.g., while in the wakes, or in laminar regions only (Hedley and Keffer [45])) adds flexibility to the processing of the data, and the results will illustrate the merits of this approach. Finally, dominant frequencies (energy-containing scales) are obtained from the peak of the product of the power spectrum and the frequency. This method is applicable to mean wavelet spectra, with or without conditioning, as well as Fourier spectra. In the following sections, the ''dominant time scale'' is identified as the inverse of the frequency of the largest energy content.

Dominant Scales: Ensemble Variations. During one cycle of the wake generator, the time scales of the turbulence in the freestream can be expected to vary with the basic periodicity imposed by the number of rods. These time scales could be calculated within the framework of Fourier methods by the following algorithm. For each given phase, a window containing at least a few cycles of the expected dominant frequency would be picked, and the Fourier power spectrum calculated within this window, cumulatively for successive cycles. The wavelet local energy spectrum provides a simpler alternative that relies only on individual flow events (rather than on their repetition within a larger window). Ensemble energy spectra $E(\phi)$ can be calculated simply by summing the local energy spectra at fixed phases. The algorithm underlying the following results is as follows:

1 calculation of the wavelet transform according to Eq. (16);
2 squaring to obtain the local spectral energy density (Eq. 18);
3 multiplication by κ to identify the energy content;
4 average the time scales for all times in each ensemble;
5 at each time, search for the maximum of the curve $\kappa|f_g(\kappa,t)|^2/2\pi$ versus κ; and finally
6 at each time, express the dominant κ as an equivalent frequency (Eq. (16)) and its inverse time scale.

The dominant time scales, relevant to modeling, are plotted in Figs. 15(*a,b,c*) at $y = 10$ mm and 16(*a,b,c*) at $y = 0.75$ mm, in each case with 5, 10, and 15 rods successively. Figure 15(*a*) shows a pattern very similar to the intermittency plots, with the switch from freestream to wall-dominated turbulence at matching locations. As the small-scale turbulence develops, the energy-containing scales fall below the sampling rate for these very long time series. This will be discussed in our conclusions, but we note that comparison of the results is possible nonetheless. The present data show clearly the effect of the wakes and their passing frequency, both quantitatively as measured by the shading scale and

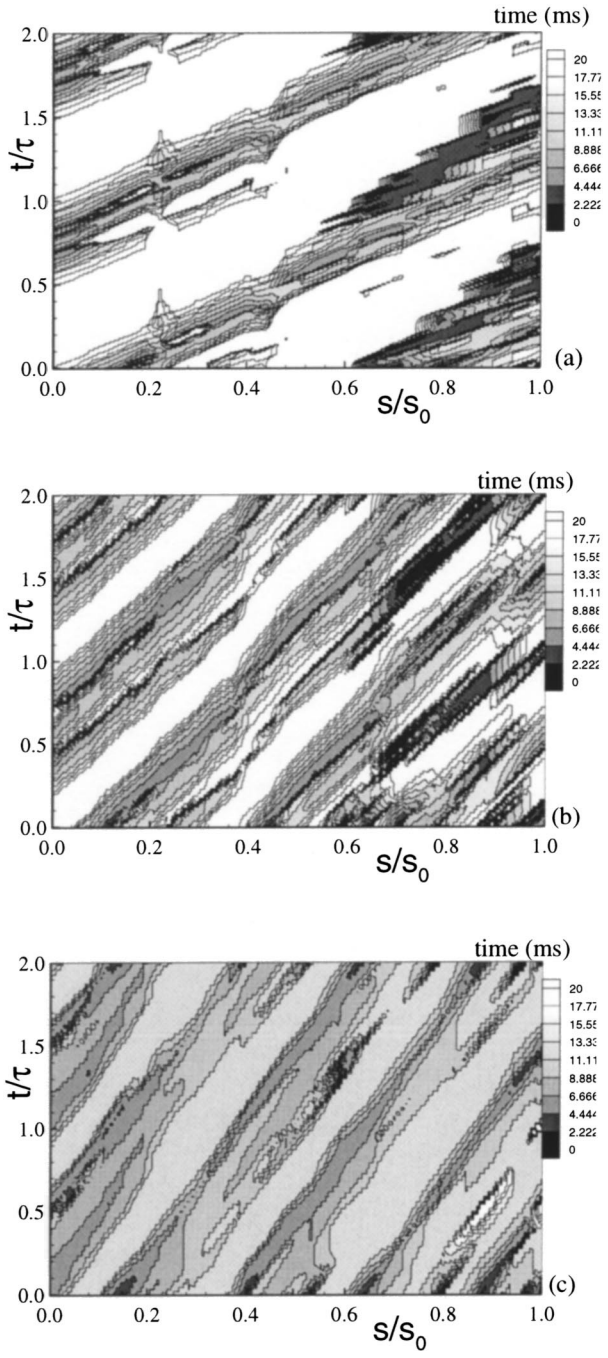

Fig. 15 Ensemble-averaged dominant time scales in temporal-spatial domain at $y=10.0$ mm, wake passing frequencies for (*a*) 5 rods, (*b*) 10 rods, (*c*) 15 rods

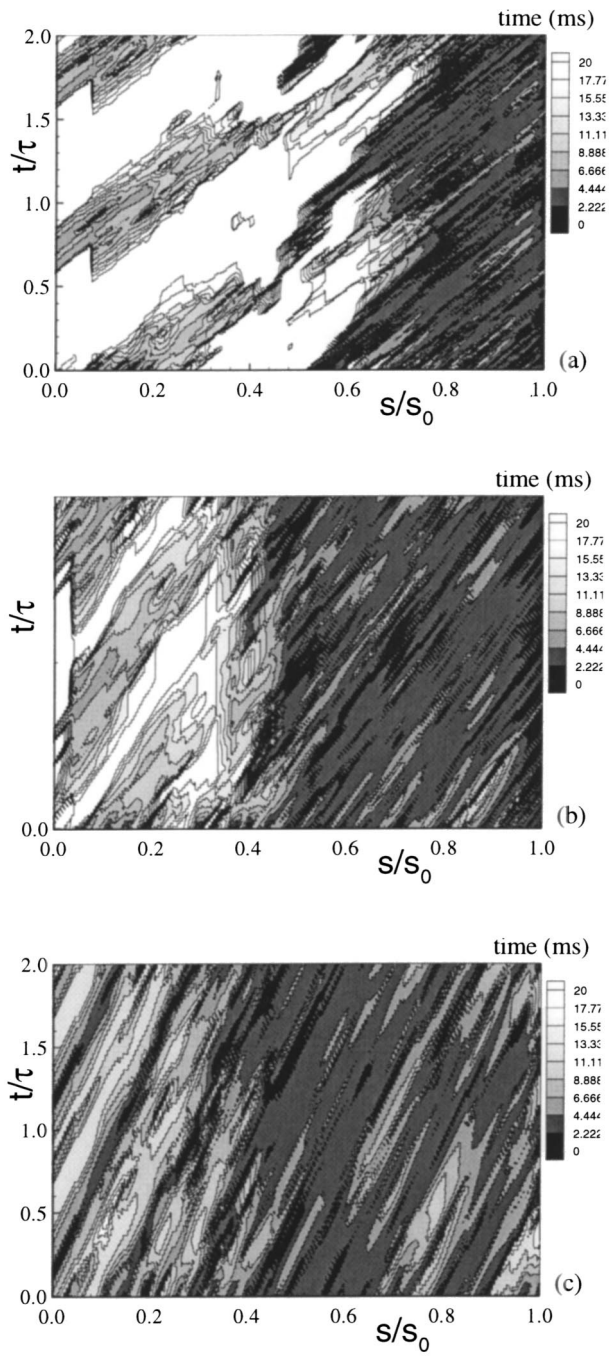

Fig. 16 Ensemble-averaged dominant time scales in temporal-spatial domain at $y=0.75$ mm, wake passing frequencies for (*a*) 5 rods, (*b*) 10 rods, (*c*) 15 rods

qualitatively as shown by the pattern of small scale activity beyond $s/s_0 \approx 0.6$. In the 10-rod case (Fig. 15(*b*)), the secondary (double) wake-passing is observed clearly until the boundary layer turbulence wipes out the weaker wake beyond $s/s_0 \approx 0.8$. The 15-rod case (Fig. 15(*c*)) is yet more complicated, with the double wake observable from $s/s_0 = 0.0$ to 0.25 and from 0.6 to 0.9. This may be due to interactions of a given wake with lagged spots from the previous wake as they travel at different speeds.

Closer to the wall, the interactions between wake-generated scales and boundary layer generated scales complicate the map (Fig. (16*a*)) for the 5-rod case. The double wake-passing can be observed at this level. The transition to smaller scales is virtually complete by $s/s_0 \approx 0.8$ for this case, $s/s_0 \approx 0.55$ for the 10-rod case (Fig. 16(*b*)) and $s/s_0 \approx 0.4$ for the 15-rod case (Fig. 16(*c*)). This is consistent with the propagation speed being slower for the boundary layer structures, and with these structures generating the smallest observable scales. Generally, we note that the energy-containing time scales are dependent on the wake-passing frequency (see bars with each plot). The shortest time scales, more and more dominant as the flow evolves, reflect a mixture of nominally laminar and turbulent regions. The following section establishes a discrimination between them.

Dominant Scales: Conditional Sampling. In the construction of the ensemble power spectrum explained above, we can elect to include only contributions that meet a combination of

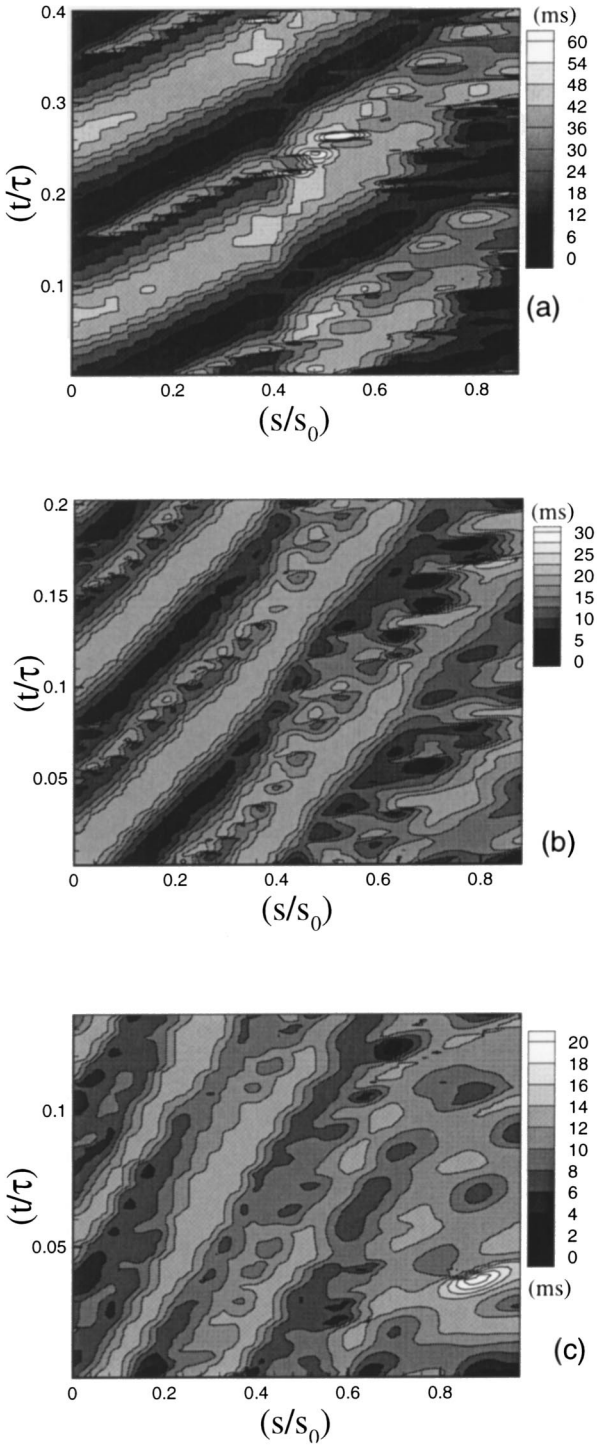

Fig. 17 Ensemble-averaged dominant "laminar" time scales in temporal-spatial domain at $y=10$ mm for (*a*) 5 rods, (*b*) 10 rods, (*c*) 15 rods

criteria, of which phase is only one component. Of most direct interest would be the mapping of turbulent scales. Time scales associated with the nominally laminar regions of flow will be mapped, to illustrate the feasibility of the concept and the substantial differences with the unconditional statistics presented in the previous subsection. Figure 17(*a*,*b*,*c*) presents the results for ensemble plots of "laminar" scales. Initially comparable to the unconditional scales in the intervals between wakes, they are notably larger in all regions of the plots where the intermittency factor is not very small. Thus, at large s/s_0, the energy content of the long time-scale ("laminar") region is overwhelmed by that of intermittent turbulent patches in the calculation of the unconditional time scales (Figs. 15 and 16).

The comparison of the results for ensemble-averaged turbulence intensity Figs. 9, 10, the intermittency, Figs. 11, 12 and the dominant time scales (Figs. 15 and 16) is informative. The turbulence intensity plots indicated an early increase in the random fluctuations. This is confirmed by inspection of the velocity traces, in which few quiescent intervals and no locally periodic wave trains can be observed. In contrast, the intermittency factor remains relatively small, even after the footprint of the wakes has been mixed into a more uniform flow at large s/s_0. This apparent contradiction is resolved by examining the respective contents of the intermittency and turbulence level algorithms. The intermittency algorithm is designed to detect small-scale fluctuations generated by a spectral transfer of energy. Thus, the longer time scales coincide with a relatively low intermittency factor, but do not presume a low energy content for the corresponding fluctuations. The parts of the signal associated with high-turbulence intensities (energy content) also have weak small-scale content, and their typical duration is roughly proportional to the intervals between wake passings. This can be seen from the numerical values on the scales for Figs. 15–17. Furthermore, an estimation of the typical sizes of these "eddies" can be obtained as the product of their time scale and their convection speed, yielding a size larger than the distance to the wall by at least one order of magnitude. We conclude that these long-duration events are better characterized as the alternance of accelerated and decelerated flow resulting from wake passings, than as turbulent eddies. The emerging picture, to be tested in future studies, is that relatively few turbulent patches (possibly turbulent spots) evolve primarily due to the buffeting of the boundary layer by the passing wakes; and that the wakes and spots, traveling at different speeds, induce large-scale nonturbulent fluctuations in streamwise velocity.

Conclusions

The effects of periodic unsteady wake-passing frequency on the boundary layer transition and development along the concave surface of a constant curvature plate at zero pressure gradient was experimentally investigated. The measurements were carried out utilizing an unsteady flow research facility with a rotating cascade of rods positioned upstream of the curved plate. Keeping the rotational speed of the wake generator constant, three different passing frequencies were investigated by varying the rod spacing. Two mechanisms were established by this variation: first, an earlier mixing of the secondary wakes due to the reduction of their spacing that led to higher freestream turbulence. Secondly, increased impinging frequency of the primary wake strips introduced an excessive turbulence kinetic energy transport to the boundary layer. Based on the experimental investigations and their analysis the following conclusions are drawn:

- The boundary layer transition behavior was significantly affected by the wake-induced unsteady flow. Lower Ω generated isolated unsteady wakes with no visible mutual interaction, simulating the inlet flow condition to the second row of a turbomachine. The wake-induced unsteady flow significantly affected the boundary layer transition behavior leading to the formation of a wake induced boundary layer transition and a primary boundary layer with a quasi-steady character that was periodically disturbed by wake strips and the wall. Increasing the parameter of Ω resulted in a change of the boundary layer development process, turbulence distribution, sport generation, and a shift of the transition onset toward the leading edge.
- Further increase of Ω, simulating the unsteady flow through the third and fourth row of a multistage turbine with higher impinging frequency and smaller wake spacing associated with earlier mixing of the secondary wakes, resulted in higher freestream

Table 3 Uncertainty in velocity measurement for hot-wire probe

$\bar{U}$ (m/s)	3	5	12
$\omega\bar{U}/U$ (%)$_{red}$	5.78	2.41	1.40

turbulence and a significant shift of the transition toward the leading edge as a consequence of the mechanisms discussed above.

• Further analysis of intermittency data revealed a universal pattern of the relative intermittency factor that follows a Gaussian distribution. The minimum intermittency factor, $\langle\gamma_{min}\rangle$, represented the boundary layer behavior between the turbulent wake strips. It was shown to follow the natural transition process as the freestream was almost nonturbulent. On the other hand, $\langle\gamma_{max}\rangle$ being the value inside the turbulent core, started with a high value and went through a minimum, which indicates the start of wake induced transition. This was due to the viscous damping of the turbulent core by the boundary layer.

• Concerning the wavelet analysis, in some regions of the flow, the calculated dominant time scales reach the lower limit set by the data acquisition rate. These limits reached in regions where small-scale turbulence production within the boundary layer is expected to be significant. The transition from longer to smaller time scales is continuous and smooth. Further studies will examine the effect of the sampling rate on the accuracy of turbulence intensities and time scales. We also note that wavelet methods do not introduce further aliasing or harmonics, since they only rely on local information (as few as three data points at the smaller scales).

• The long time-series are necessary to yield stable statistics presented in this paper. Detailed study of the high frequency boundary layer turbulence will be the subject of future work.

• The effect of the wake-passing frequency on the dominant (mainly laminar) time scales shows that the flow is not turbulent between wakes. The frequency scaling is dictated by the intervals between wakes, not because of local turbulence structure. The local turbulence is more likely determined by the three-dimensional nature of the flow induced by the layering of (and velocity difference between) wake turbulence and boundary layer turbulence. This layering is likely to induce streamwise vorticity and enhanced mixing associated with three-dimensional flow.

• Turbulence intensity alone may not be good diagnostic of turbulent transport in these very nonhomogenous flows. The complex distribution of velocity fluctuations at different time scales is exposed by the combination of methods presented in this paper. Further studies will address the spectral resolution of active fluctuations as they affect transport and its modeling in turbomachinery flows.

Uncertainty Analysis

The Kline and McClintock [55] uncertainty analysis method was used to determine the uncertainty in the velocity after calibration and data reduction for the single-wire probe. In addition, the uncertainty in the heat transfer measurements was also determined. The Kline and McClintock method determines the uncertainty for a 95% confidence level. The uncertainty in velocity for the single-wire probe after data reduction is given in Table 3. As shown, the uncertainty in velocity increases as the flow velocity decreases. This is due to the pneumatic pressure transducer having a large uncertainty during calibration.

Nomenclature

c = chord plate length (see Table 1)
d = lateral position above the plate surface $d=10$ mm
h = nozzle height (see Table 1)
Re_h = Reynolds number based on nozzle height
Re_c = Reynolds number based on curved plate chord
T = wake generator period
Tu = reference turbulence intensity
$\langle Tu\rangle$ = ensemble-averaged reference turbulence intensity
u = fluctuation velocity
$\langle u\rangle$ = ensemble-averaged fluctuation velocity
u^+ = nondimensional velocity $u^+=u/u_\tau$
$\bar{U}$ = time-averaged mean velocity parallel to the surface
U_{ref} = reference local velocity at a distance of $d=10$ mm above the plate surface
y = lateral distance from plate surface
y^+ = nondimensional wall distance $y^+=u_\tau y/\nu$
ν = kinematic viscosity of air
ρ = density of air
τ = one wake-passing period

Subscripts

in = inlet to test section
loc = local
ref = reference

References

[1] Evans, R. L., 1978, "Boundary-Layer Development on an Axial-Flow Compressor Stator Blade," ASME J. Eng. Power, **100**, pp. 287–293.
[2] Evans, R. L., 1982, "Boundary Layer Transition and Separation on a Compressor Rotor Airfoil," ASME J. Eng. Power, **104**, pp. 251–253.
[3] Walker, G. J., 1974, "The Unsteady Nature of Boundary Layer Transition on an Axial-Flow Compressor Blade," ASME Paper No. 74-GT-135.
[4] Walker, G. J., 1982, "The Turbulent Boundary Layer on an Axial Compressor Blade," ASME Paper No. 82-GT-52.
[5] Walker, G. J., 1989, "Transitional Flow on Axial Turbomachine Blading," AIAA J., **27**, pp. 595–602.
[6] Walker, G. J., 1993, "The Role of Laminar-Turbulent Transition in Gas Turbine Engines: A Discussion," ASME J. Turbomach., **115**, pp. 207–217.
[7] Walker, G. J., and Gostelow, J. P., 1990, "The Effect of Adverse Pressure Gradients on the Nature and the Length of Boundary Layer Transition," ASME J. Turbomach., **112**, pp. 196–205.
[8] Schultz, H. D., Gallus, H. E., Lakshminarayana, B., "Three-Dimensional Separated Flow Field in the Endwall Region of an Annular Compressor Cascade in the Presence of Rotor-Stator Interaction, Part 2—Unsteady Flow and Pressure Field," ASME J. Turbomach., **112**, pp. 679–690.
[9] Poensgen, C., and Gallus, H. E., 1991, "Three-Dimensional Wake Decay Inside of a Compressor Cascade and Its Influence on the Downstream Flow Field: Part I—Wake Decay Characteristics in the Flow Passage," ASME J. Turbomach., **113**, pp. 180–189.
[10] Poensgen, C., Gallus, H. E., 1991, "Three-Dimensional Wake Decay Inside of a Compressor Cascade and Its Influence on the Downstream Flow Field: Part II—Unsteady Flow Field Downstream of the Stator," ASME J. Turbomach., **113**, pp. 190–197.
[11] Hodson, H. P., 1984, "Measurement of Wake-Generated Unsteadiness in the Rotor Passage of Axial Flow Turbines," ASME Paper No. 84-GT-189.
[12] Hodson, H. P., 1984, "Boundary Layer and Loss Measurements on the Rotor of an Axial Flow Turbine," ASME J. Eng. Gas Turbines Power, **106**, pp. 181–192.
[13] Hodson, H. P., and Addison, J. S., 1989, "Wake-Boundary Layer Interactions in an Axial Flow Turbine Rotor at Off-Design Conditions," ASME J. Turbomach., **111**, pp. 181–192.
[14] Blair, M. F., 1983, "The Effect of Free Stream Turbulence on the Turbulence Structure and Mean Profile Development," ASME J. Heat Transfer, **105**, pp. 33–47.
[15] Blair, M. F., Dring, R. P., and Joslyn, H. D., 1988, "The Effect of Turbulence and Stator/Rotor Interactions on Turbine Heat Transfer," Part 1: ASME Paper No. 88-GT-125; Part II: ASME Paper No. 88-GT-5.
[16] Dring, R. P., Joslyn, H. D., Hardin, L. W., and Wagner, J. H., 1982, "Turbine Rotor-Stator Interaction," ASME Paper No. 82-GT-3.
[17] Dring, R. P., Blair, M. F., Joslyn, H. D., Power, G. D., and Verdon, J. M., 1986. "The Effect of Inlet Turbulence and Rotor/Stator Interactions on the Aerodynamics and Heat Transfer of a Large Scale Rotating Turbine Model," NASA CR 4079.
[18] Joslyn, H. D., Dring, R. O., and Sharma, P., 1983, "Unsteady Three-Dimensional Turbine Aerodynamics," ASME J. Eng. Power, **105**, pp. 322–331.
[19] Wittig, S., Schulz, A., Dullenkopf, K., and Fairbank, J., 1988, "Effects of Free-Stream Turbulence and Wake Characteristics on the Heat Transfer Along a Cooled Gas Turbine Blade," ASME Paper No. 88-GT-179.
[20] Dullenkopf, K., 1992, "Untersuchungen zum Einfluβ periodisch instationärer Nachlaufströmungen auf den Wärmeübergang konvektiv gekühlter Gasturbinenschaufeln," dissertation der Technischen Hochschule Karlsruhe, Germany.
[21] Gaugler, R., 1985, "A Review and Analysis of Boundary Layer Transition Data for Turbine Application," ASME Paper No. 85-GT-83.
[22] Schobeiri, T., McFarland, E., and Yeh, F., 1991, "Aerodynamics and Heat

Transfer Investigations on a High Reynolds Number Turbine Cascade,'' NASA TM 103260.
[23] Mayle, R. E., 1991, ''The Role of Laminar-Turbulent Transition in Gas Turbine Engines,'' ASME J. Turbomach., **113**, pp. 509–537.
[24] Speidel, L., 1952, ''Beeinflussung der laminaren Grenzschicht durch periodische Störung der Zuströmung,'' Z. Flugwiss., **5**(9), pp. 270–275.
[25] Pache, W., 1976, ''Zur Frage der Entwicklung von Strömungsgrenzsschichten bei instationärer Zuströmung in Turbomachinen,'' dissertation D-17, Technische Hochschule, Darmstadt, Germany.
[26] Pfeil, H., and Eifler, J., 1975, ''Zur Frage der Schubspannungsverteilung für die ebenen freien turbulenten Strömungen,'' Forschung, Ing.-Wes., **41**(4), pp. 105–112.
[27] Pfeil, H., and Eifler, J., 1975, ''Messungen im turbulenten Nachlauf des Einzelzylinders,'' Forschung, Ing.-Wes., **41**(5), pp. 137–145.
[28] Pfeil, H., and Eifler, J., 1976, ''Turbulenzverhältnisse hinter rotierenden Zylindergittern,'' VDI-Zeitschrift für Forschung im Ingenieurwesen, **42**(1).
[29] Pfeil, H., and Herbst R., 1979, ''Transition Procedure of Instationary Boundary Layers,'' ASME Paper No. 79-GT-128.
[30] Herbst, R., 1980, ''Entwicklung von Grenzschichten bei instationärer Zuströmung,'' dissertation der Technischen Hochschule Darmstadt, Germany, D-17.
[31] Schröder, T., 1985, ''Entwicklung des instationären Nachlaufs hinter quer zur Strömungsrichtung bewegten Zylindern und dessen Einfluß auf das Umschalgverhalten von ebenen Grenzschichten stromabwärts angeordneter Versuchskörper,'' dissertation der Technischen Hochschule Darmstadt, D-17, Germany.
[32] Pfeil, H., Herbst, R., and Schröder, T., 1983, ''Investigation of the Laminar Turbulent Transition of Boundary Layers Disturbed by Wakes,'' ASME J. Eng. Power, **105**, pp. 130–137.
[33] Schobeiri, M. T., and Radke, R. E., 1994, ''Effects of Periodic Unsteady Wake Flow and Pressure Gradient on Boundary Layer Transition along the Concave Surface of a Curved Plate,'' ASME Paper No. 94-GT-327.
[34] Schobeiri, M. T., John, J., and Pappu, K., 1996, ''Development of Two-Dimensional Wakes Within Curved Channel: Theoretical Framework and Experimental Investigations,'' ASME J. Turbomach., **118**, pp. 506–518.
[35] Arndt, N., 1993, ''Blade Row Interaction in a Multi-Stage Low Pressure Turbine,'' ASME J. Turbomach., **115**, pp. 137–146.
[36] Schobeiri, M. T., Pappu, K., and Wright, L., 1995, ''Experimental Study of the Unsteady Boundary Layer Behavior on A Turbine Cascade,'' ASME Paper No. 95-GT-435.
[37] Schobeiri, T., and Pardivala, D., 1992, ''Development of a Subsonic Flow Research Facility for Simulating the Turbomachinery Flow and Investigating its Effects on Boundary Layer Transition, Wake Development and Heat Transfer,'' *Fourth International Symposium on Transport Phenomena and Dynamics of Rotating Machinery*, ISROMAC, pp. 98–114.
[38] Liu, X., and Rodi, W., 1991, ''Experiments on Transitional Boundary Layers With Wake-Induced Unsteadiness,'' J. Fluid Mech., **231**, pp. 229–256.
[39] John, J., and Schobeiri, T., 1993, ''A simple and Accurate Method for Calibrating X-Probes,'' ASME J. Fluids Eng., **115**, pp. 148–152.
[40] Addison, J. S., and Hodson, H. P., 1990, ''Unsteady Transition in an Axial-Flow Turbine—Part 1: Measurements on the Turbine Rotor,'' ASME J. Turbomach., **112**, pp. 206–214.
[41] Addison, J. S., and Hodson, H. P., 1990, ''Unsteady Transition in an Axial-Flow Turbine—Part 2: Cascade Measurements and Modelling,'' ASME J. Turbomach., **112**, pp. 215–221.
[42] Orth, U., 1991, ''Entwicklung des instationären Nachlaufs hinter quer zur Strömungsrichtung bewegten Zylindern und dessen Einfluß auf das Umschlagverhalten von ebenen Grenzschichten stromabwärts angeordneter Versuchskörper,'' dissertation D-17, Technische Hochschule Darmstadt.
[43] Orth, U., 1992, ''Unsteady Boundary Layer Transition in Flow Periodically Disturbed by Wakes,'' ASME Paper No. 92-GT-283.
[44] Hedley, T. B., and Keffer, J. F., 1974, ''Turbulent/Non-turbulent decisions in an intermittent flow,'' J. Fluid Mech., **64**, pp. 625–644.
[45] Antonia, R. A., 1981, ''Conditional Sampling in Turbulence Measurement,'' Annu. Rev. Fluid Mech., **13**, pp. 131–156.
[46] John, J., and Schobeiri, M. T., 1996, ''Development of Two-Dimensional Wakes in a Curved Channel at Positive Pressure Gradient,'' ASME J. Fluids Eng., **118**, pp. 292–299.
[47] Schobeiri, M. T., and Chakka, P., 1998, ''Unsteady Wake Effects on Boundary Layer Transition and Heat Transfer Characteristics of a Turbine Blade,'' ASME Paper No. 98-GT-291.
[48] Narasimha, R., 1957, ''On the Distribution of Intermittency in the Transition Region of a Boundary Layer,'' J. Aerosp. Sci., **24**, pp. 711–712.
[49] Halstead, E. D., et al., 1995, ''Boundary Layer Development in Axial Compressors and Turbines: Parts 1 to 4,'' ASME Paper No. 95-GT-461 to 95-GT-464.
[50] Daubechies, I., 1992, *Ten Lectures on Wavelets*, S.I.A.M.
[51] Farge, M., 1992, ''Wavelet Transforms and their Applications to Turbulence,'' Annu. Rev. Fluid Mech., **24**, pp. 395–457.
[52] Higuchi, H., Lewalle, J., and Crane, P., 1994, ''On the Structure of a Two-Dimensional Wake Behind a Pair of Flat Plates,'' Phys. Fluids A, **6**, pp. 297–305.
[53] Lewalle, J., 1994, ''Wavelet Analysis of Experimental Data: Some Methods and the Underlying Physics,'' AIAA Paper No. 94-2281.
[54] Lewalle, J., Aspis, D. E., and Sohn, K. H., 1997, ''Demonstration of Wavelet Techniques in Spectral Analysis of Bypass Transition Data,'' NASA TP-3555.
[55] Kline, S. J., and McKlintock, F. A., ''Describing Uncertainties in Single-Sample Experiments,'' Mech. Eng. (Am. Soc. Mech. Eng.), **75**, Jan., pp. 3–8.

A Comparison of Spreading Angles of Turbulent Wedges in Velocity and Thermal Boundary Layers

S. Zhong

T. P. Chong

School of Engineering,
University of Manchester,
Manchester M13 9PL, UK

H. P. Hodson

Whittle Lab,
Department of Engineering,
University of Cambridge,
Cambridge CB3 0DY, UK

Turbulent wedges induced by a three-dimensional surface roughness placed in a laminar boundary layer over a flat plate were visualized for the first time using both shear-sensitive and temperature-sensitive liquid crystals. The experiments were carried out at zero pressure gradient and two different levels of favorable pressure gradients. The purpose of this investigation was to examine the spreading angles of turbulent wedges indicated by their associated surface shear stresses and heat transfer characteristics and hence obtain further insight about the difference in the behavior of transitional momentum and thermal boundary layers when a streamwise pressure gradient exists. It was found that under a zero pressure gradient the spreading angles indicated by the two types of liquid crystals are the same, but the difference increases as the level of favorable pressure gradient increases with the angle indicated by temperature-sensitive liquid crystals being smaller. The results from the present study suggest that the spanwise growth of a turbulent region is smaller in a thermal boundary layer than in its momentum counterpart and this seems to be responsible for the inconsistency in transition zone length indicated by the distribution of heat transfer rate and boundary layer shape factor reported in the literature. This finding would have an important implication to the transition modeling of thermal boundary layers over gas turbine blades. [DOI: 10.1115/1.1539871]

Introduction

Liquid crystals have been used in heat transfer and aerodynamic tests as a cost-effective full surface flow visualization and measurement tool for sometime, [1–5]. The coating of liquid crystals displays different color upon changes in certain flow parameters and gives a vivid visual impression of the characteristics of a surface flow. With the improvement in formulation, liquid crystals that respond solely to changes in a single flow parameter have become available commercially in 1990s. Currently two types of liquid crystals are commonly used, i.e., shear-sensitive liquid crystals and temperature-sensitive (thermochromic) liquid crystals. The former display different color upon changes in surface shear stress, providing information about the surface shear stress distribution, [2,3]. The latter change color as surface temperature varies. Once the surface heat flux is determined either by direct measurements or via the use of heat transfer models, the heat transfer rate at the wall can be obtained from the surface temperature, [4,5].

The availability of both temperature-sensitive and shear-sensitive liquid crystals offers an effective way of correlating the heat transfer and aerodynamic characteristics of a nonisothermal flow field, thus providing a means of examining the validity of the Reynolds analogy. The problem of particular interest to the present study is the different effects that pressure gradients exert on the momentum and heat transfer process in a boundary layer undergoing transition from laminar to turbulent. As reported by Blair [6] and Sharma [7], when a favorable pressure gradient exists, the transition zone length indicated by the distribution of heat transfer rate along the wall is longer than that indicated by the boundary layer shape factor (The opposite is true when an adverse pressure gradient is present.) Blair suggested that it is because at the presence of a favorable pressure gradient, the fully turbulent structure, which the heat transfer process directly depends upon, requires a longer streamwise distance to develop than the fully turbulent mean velocity profile, [6]. Such a discrepancy questions the adequacy of the Reynolds analogy, which relates skin friction to heat transfer and has been widely adopted by turbomachine designers for sometime.

Since boundary layer transition starts by formation and growth of localized turbulent regions, i.e., turbulent spots [8], a better understanding of the above phenomenon should be achieved by examining a fundamental issue, i.e., how a turbulent region grows in a laminar background under the influence of pressure gradients as indicated by wall heat transfer and surface shear stress, respectively. In the present work, such a turbulent region is generated by a surface roughness placed on a flat plate along which a laminar boundary layer is developing. The turbulent region diverges in the spanwise direction as it propagates downstream, forming a turbulent wedge. Turbulent wedges produced by a surface roughness have been studied for sometime because they closely resemble the behavior of a train of turbulent spots, which are the active features in a transitional boundary layer, in terms of their spanwise growth, [9]. It has been found that the turbulent wedge is composed of a fully turbulent core bounded by a transitional (intermittently turbulent) region, and in a zero pressure gradient boundary layer the wedge diverges with a half included angle of about 10 deg, [9,10].

In this paper, both temperature-sensitive and shear-sensitive liquid crystals were used to visualize the development of turbulent wedges in laminar boundary layers under a zero pressure gradient and two different levels of favorable pressure gradients. The purpose of this work is to investigate the different effects of pressure gradients on the momentum and heat transfer processes involved in the growth of turbulent region in a laminar boundary layer, and thus obtain further insight about the difference in the behavior of transitional momentum and thermal boundary layers. The result

Contributed by the Fluids Engineering Division for publication in the JOURNAL OF FLUIDS ENGINEERING. Manuscript received by the Fluids Engineering Division January 15, 2002; revised manuscript received September 16, 2002. Associate Editor: V. Ötügen.

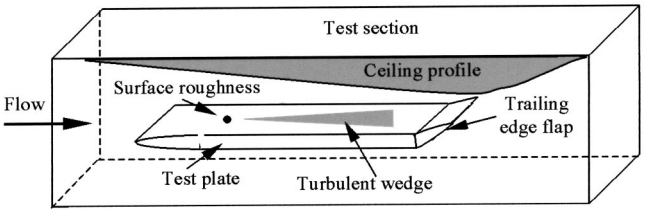

Fig. 1 Schematic diagram of the test section

from the present study would be expected to have an important implication to the modeling of transition in boundary layers over gas turbine blades [11].

Experimental Facility

The experiment was conducted in the Farnborough wind tunnel at the Goldstein Laboratory, the Manchester School of Engineering. The wind tunnel has a test section of 460 mm×207 mm. The maximum velocity in the test section is about 28 m/s and the freestream turbulence intensity is about 0.3%. Both the top and two side-walls of the test section are made of glass to allow optical access. A test plate 25 mm thick and 625 mm long was mounted horizontally across the entire width of the test section. The plate has a 1:3 superelliptical leading edge, which according to Narasimha and Prasad [12], helps to minimize flow separation and premature transition at the leading edge. A schematic sketch of the test section is shown in Fig. 1. In the present experiment, the state of the boundary layer was checked by surface oil flow tests. It was found that by setting the plate at a one-degree negative incidence and the trailing edge flap at 20 deg a fully attached laminar boundary layer around the leading edge was obtained. Spanwise surface pressure measurements also confirmed that the boundary layer flow was two-dimensional over 75% spanwise width of the plate.

For the tests with shear-sensitive liquid crystals, the transparent thermoplastic test surface was coated with water-based matt black paint before the liquid crystal coating was applied. The water-based black paint is free of chemical contaminants and thus prolongs the life of the liquid crystals. In order to track the thermal footprint of the turbulent wedge, another plate consisting of multiple layers (see Fig. 2) was constructed. The test surface was heated uniformly with a 0.1 mm thick metalized film, which was connected to a DC power supply through metal foil strips adhered along the edges of the film. A 14 mm thick Styrofoam sheet was glued to the back of the test plate to reduce the heat loss by conduction.

The favorable streamwise pressure gradients were achieved by attaching a flat transparent thermoplastic sheet at different angles to the ceiling of the test section (see Fig. 1). At the maximum operating velocity, the two wedge angles used in the present experiment produced accelerating flows with a constant pressure gradient parameter $K=0.25\times10^{-6}$ and 1.0×10^{-6}, respectively. The corresponding velocity and pressure gradient distributions for these two cases are shown in Fig. 3. Tests were also carried out at a zero pressure gradient boundary layer ($K=0$) to provide baseline data for comparison.

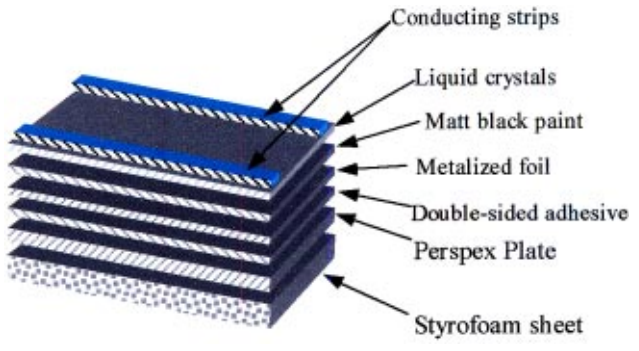

Fig. 2 Schematic diagram of the heated plate used with temperature-sensitive liquid crystals

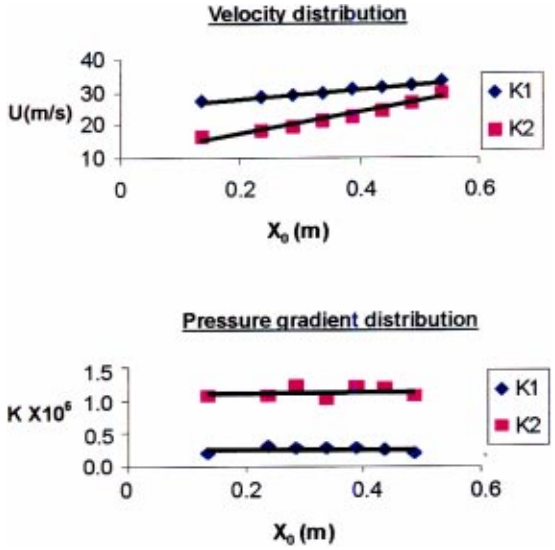

Fig. 3 Velocity and pressure gradient distributions for the mild (K1) and strong (K2) pressure gradient cases

The turbulent wedge was generated by a 1.1 mm diameter metal sphere, which was glued on the test surface at a distance of 187 mm from the leading edge. The local boundary layer thickness was about 2 mm and the Reynolds number based on the local momentum thickness ranged from 200 to 450 for the three test cases. According to Hall [13], a critical Reynolds number Re_d of 500 has to be reached in order to initiate a turbulent wedge immediately downstream to the roughness. Here $Re_d=ud/\nu$, d is the height of the roughness which is the diameter of the sphere and u is the velocity in the undisturbed boundary layer at the height of the roughness. In the present experiment, this Reynolds number was estimated to be at least 1000 for all the test cases and is substantially greater than the critical Reynolds number.

The Liquid Crystal Techniques

Shear-Sensitive Liquid Crystals. Shear-sensitive (chiral nematic) liquid crystals are capable of responding to different levels of surface shear stress by color changes, [2]. As the shear stress increases, the color of the liquid crystals coating will shift from rusty red through the visible spectrum to violet. Since at the same Reynolds number, the surface shear stress underneath a turbulent boundary layer is considerably higher than that in its laminar counterpart, the color variations displayed by the crystals can be used to differentiate a turbulent region from its laminar background thus providing the information about the growth of a turbulent wedge.

The shear-sensitive liquid crystal slurry used in the tests was supplied by Hallcrest Ltd. and it is formulated for tests at a freeestream velocity up to 30 m/s. To apply shear-sensitive liquid crystals to the test surface, the slurry was first heated to its clearing point at about 50°C and then brushed along the surface using an artist paintbrush. The crystals form a sticky wet film over the surface with an estimated thickness of about 30 μm based on the amount of crystals used and area of coverage. The film will be sheared slightly and reach a dynamic equilibrium under the im-

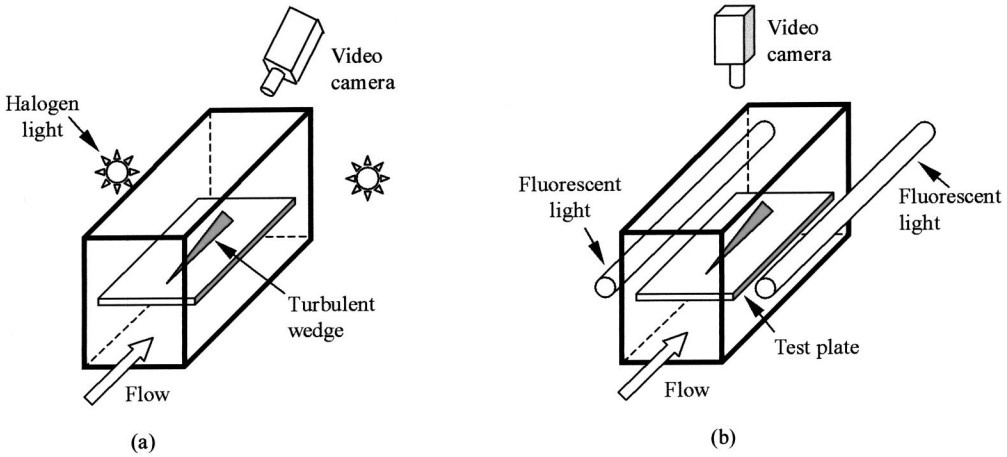

Fig. 4 Schematic diagrams showing the lighting and recording arrangement in (*a*) shear-sensitive and (*b*) temperature-sensitive liquid crystal tests

pact of the local time-averaged surface shear stress. But it is believed that the displacement of the crystal top layer is small and does not alter the no-slip condition at the wall.

Two 1 KW halogen lights were found to give desirable illumination of the liquid crystals when projected from downstream at each side of the test section. The liquid crystal color changes produced by the turbulent wedge were recorded at an angle of 54.5 deg to the horizontal plane through the top glass window from a downstream viewpoint (see Fig. 4(*a*)). No attempt was made to calibrate the crystal color play against shear stress in the present tests.

Temperature-Sensitive Liquid Crystals. Temperature-sensitive (encapsulated cholesteric) liquid crystals show variations of color from red through the visible spectrum to blue as temperature increases. Since at the same Reynolds number a turbulent boundary layer exhibits a higher heat transfer rate than a laminar boundary layer, under the same surface heat flux the surface temperature beneath a turbulent boundary layer will be lower than its laminar counterpart, making the thermal footprint of a turbulent region visible. This method has been used successfully by Zhong et al. [5] to visualize the growth and development of individual artificially created spots in a water tunnel experiment.

The temperature-sensitive liquid crystal slurry used in this experiment was supplied by Thermographic Measurements Ltd. It has an active color bandwidth of 5°C, showing red at 22°C and blue at 27°C. The slurry was mixed with adequate amount of binder and sprayed on to the test surface using an artistic airbrush. The crystals form a dry surface coating with a thickness not exceeding 30 μm. Two 60 W fluorescent strip lights were clamped at each side of the test section to provide a uniform illumination to the crystal coating (see Fig. 4(*b*)). The liquid crystal images were recorded with the axis of a video camera normal to the test surface.

The calibration of temperature-sensitive liquid crystals color play followed a standard procedure. The crystal color play was calibrated against the temperature reading from a thermocouple glued on the surface with the same lighting and recording arrangement in the experiment. The color information was recorded using a digital video camera and was subsequently processed in Matlab. Upon loading into the Matlab, the color signals at each pixel were represented in form of red, green, and blue color component (RGB). The RGB signals can be further converted into color signals represented in form of hue, saturation, and intensity (HSI signals). Among the HSI signals, hue signal alone is commonly used as the color index in processing temperature-sensitive liquid crystal images since it is a simple and monotonic function of liquid crystal temperature and is independent of the local illumination strength [14]. The calibrated relation between temperature and hue for the crystal coating used in the present experiment is shown in Fig. 5.

The electrical power used to heat the surface was controlled by a DC power supply with digital display of current and voltage settings. In order to maximize the color variations shown by the crystals, the power was adjusted to a level that the surface under a laminar boundary layer began to show blue color. The magnitudes of current and voltage were recorded for each test case, allowing the heat flux applied to the surface to be calculated.

Flow Visualization Results

In the present experiment, all the color information was recorded using a digital video camera. Figures 6 and 7 show the surface color variations (raw data) displayed by both shear-sensitive and temperature-sensitive liquid crystals at zero, mild and strong favorable pressure gradients, respectively. In Fig. 6, the laminar region appears in rusty red whereas the turbulent region associated with higher shear shows green color, making the turbulent wedge clearly visible. Distinct color variations were also observed from the temperature-sensitive liquid crystals (Fig. 7) which showed reddish color in the turbulent region and blue in the laminar region respectively. It can be seen that the spreading angle of the wedge decreases as the level of favorable pressure gradient

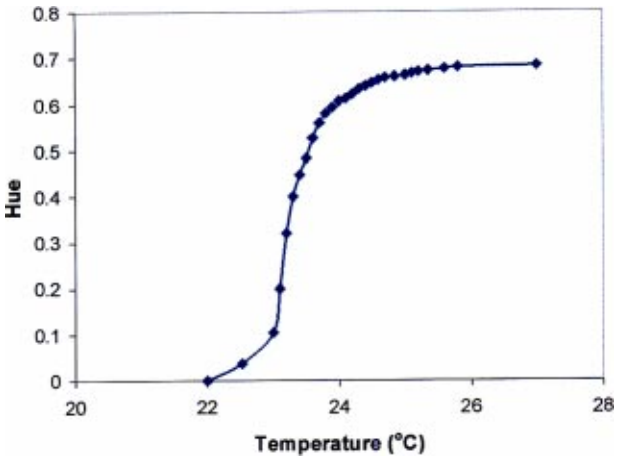

Fig. 5 Typical hue-temperature calibration curve for temperature-sensitive liquid crystals

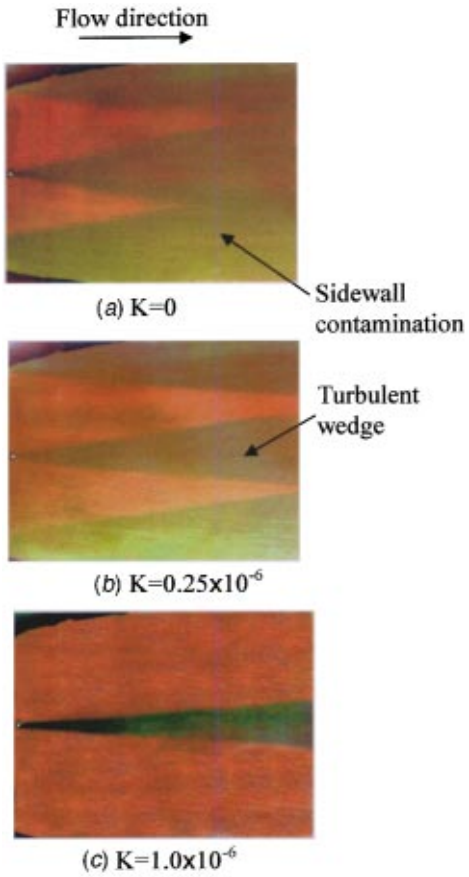

Fig. 6 Turbulent wedge shown by shear-sensitive liquid crystals (raw data)

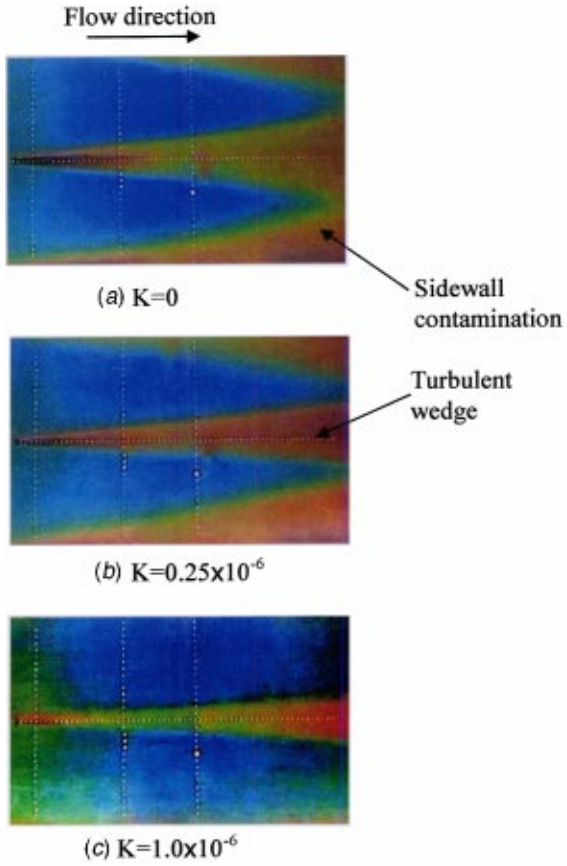

Fig. 7 Turbulent wedge shown by temperature-sensitive liquid crystals (raw data)

increases, which is consistent with the observations made by others researchers on turbulent spots using other experimental methods such as hot-wires, [15,16]. The side-wall contamination zones on each side of the plate are also clearly visible. It is seen that the side-wall contamination zone is smaller at the mild pressure gradient than that to the zero pressure gradient case and at the strong favorable pressure gradient it almost disappears completely.

It should be noted that the images obtained with shear-sensitive liquid crystals were taken at an oblique angle from a downstream viewpoint (see Fig. 4(*a*)). Hence the lateral spreading angle of the turbulent wedge obtained directly from the original images is expected to be larger than its actual value. Therefore a perspective transformation of the images is necessary to correct this error before the results can be compared with those from the temperature-sensitive liquid crystal images which were taken with the camera axis normal to the test surface. The transformation was performed in Matlab by taking into account the camera position relative to the plate and the camera settings with the algorithm documented by González [17].

In order to determine the lateral spreading angle of the turbulent wedge more accurately, the color information of the images was represented in form of hue, saturation and intensity signals. For the images from temperature-sensitive liquid crystals, hue was further converted into temperature using the color calibration curve shown in Fig. 5. In the present test, since the total heat flux required to heat the surface was known, the convective heat flux can be calculated by subtracting the heat losses radiation from the top surface and conduction from the back of the model. The convective heat transfer rate from the surface can then be determined by dividing the convective heat flux by the temperature difference between the surface and freestream. A more detailed description of this method was given in Clark et al. [10]. For the images from shear-sensitive liquid crystals, since the color calibration was not carried out, the color intensity was used directly to obtain the spreading angle of turbulent wedges. Here the color intensity is used instead of hue, since the intensity signal shows more pronounced variations across the turbulent wedge. It is known that the color changes in shear-sensitive liquid crystals depend on both the magnitude of shear stress and angle between the shear vector and the viewing direction, [3]. However, the direction effect is considered to be small in the present test since in an averaged sense its variation is not greater than 10 deg which is the spot spreading angle for the zero-pressure-gradient case. The contours of color intensity (shear stress) and heat transfer coefficient deduced from the liquid crystal images are shown in Fig. 8 and 9, respectively.

Typical spanwise distributions of heat transfer rate and color intensity obtained from the two types of liquid crystals are given in Fig. 10. It can be seen that the heat transfer rate stays at a constant level in the laminar flow region and increases dramatically to the turbulent level inside the core of the turbulent wedge (Fig. 10(*a*)). In contrast, the color intensity shown by the shear-sensitive liquid crystals is high in the laminar region and is considerably lower inside the wedge (Fig. 10(*b*)). Note the fluctuations in the color intensity were caused by the strokes of the brush used to apply the crystal coating.

The boundary of the turbulent wedge can be determined by taking the intersection point of the line representing the nearly constant heat transfer rate/color intensity in the laminar region to the line that depicts the steep change near the boundary of the wedge as shown in Fig. 10. It can be seen that the edge at $x = 162.5$ mm is located at about $z = 25$ mm for both types of crystals at the zero pressure gradient. This process was repeated on

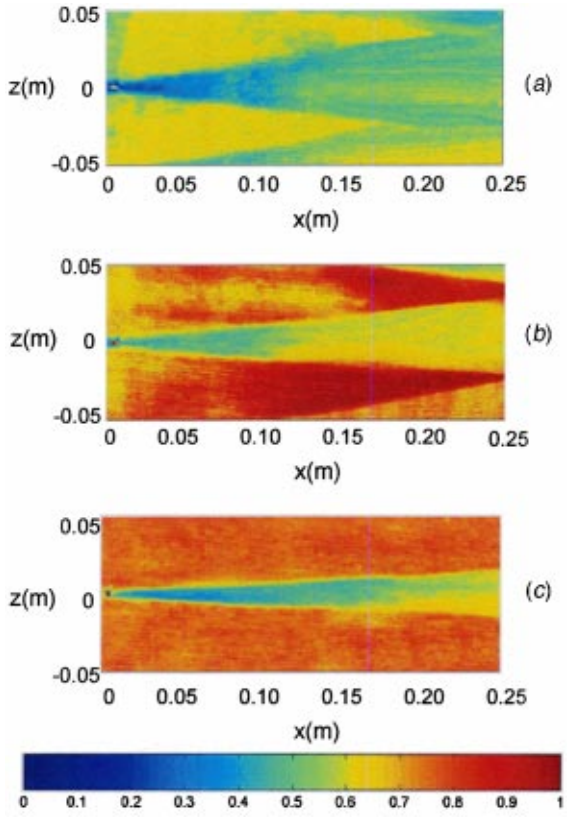

Fig. 8 Contours of color intensity obtained from shear-sensitive liquid crystals, (*a*) $K=0$, (*b*) $K=0.25\times10^{-6}$, (*c*) $K=1.0\times10^{-6}$

both sides of the turbulent wedge at several streamwise locations. Finally the wedge spreading angle was taken as the half included angle between two straight lines that depict the envelope of the wedge (see Fig. 11). A summary of the spreading angles found for all of the test cases is given in Table 1.

The main sources of errors in determining the relative values of spreading angle obtained from the two types of liquid crystals are the spatial resolution of liquid crystal images and the uncertainty associated with perspective transformation of the images from shear-sensitive liquid crystals. For the present experimental setup, the spatial resolution is 0.5 mm/pixel and the error due to perspective transformation is 0.2, 0.14, and 0.05 deg for $K=0$, 0.25 $\times^{-6}$ and 1×10^{-6}, respectively. Therefore for the above three test cases, the total error in the spreading angles is estimated to be ±0.6, ±0.4, and ±0.3 deg, respectively, for temperature-sensitive liquid crystals and ±0.7, ±0.5, and ±0.3 deg, respectively, for shear-sensitive liquid crystals.

Discussion of Results

Comparing the results shown in Table 1, one can see that the spreading angle indicated by the temperature-sensitive liquid crystals was nearly the same as that by the shear-sensitive liquid crystals in the zero pressure gradient case. However, at the mild favorable pressure gradient, the spreading angle of the thermal footprint was about 20% smaller than that of the shear stress footprint of the turbulent wedges. The difference is more pronounced at the strong pressure gradient where a difference of 31% was found. These results suggest that a turbulent region grows in the spanwise direction at different rates in momentum and thermal boundary layers. In a transitional boundary layer, a smaller spreading angle corresponds to a slower spanwise growth of turbulent spots and a longer transition zone length thus results. The finding from the present study appears to be consistent with the finding of Blair [6], i.e., in a transitional flow subject to a favorable pressure gradient, the thermal boundary layer establishes the fully turbulent flow state more slowly than its momentum counterpart. The difference in the spreading angle observed in the present experiment seems to provide an explanation for the inconsistency in transition zone length indicated by the distribution of heat transfer rate and boundary layer shape factor reported by Blair [6] and Sharma [7].

In the present experiment, turbulent wedges were found to spread at an average angle of 6.4 deg in a zero-pressure-gradient boundary layer. This result is consistent with that of Zhong et al. [5] who obtained a 6.5 deg angle for turbulent spots in zero-pressure-gradient flow using temperature-sensitive liquid crystals. However, this value is smaller than the widely reported values of 10 deg, [9,16,18]. Since the local Reynolds number based on the momentum thickness at the roughness is about 450 which is reasonably large, it is unlikely that the smaller angle is due to the low Reynolds number effect. In order to identify the cause for the smaller spreading angle obtained, a series of supplementary measurements were carried out using hot wires and an array of surface-mounted hot films for the zero-pressure-gradient case.

It is known that a turbulent wedge contains a fully turbulent core bounded by an intermittently turbulent region as shown in Fig. 11. Therefore it is worth checking if the smaller spreading angle obtained is because the liquid crystals only responded to the fully turbulent region in the turbulent wedge. A spanwise array of DANTEC surface-mounted hot films were consequently fixed across the edge of the turbulent wedge ($z=25$ mm) detected by the liquid crystals at a streamwise location 162.5 mm downstream of the surface roughness. The spacing between consecutive sensors was about 7 mm and the signals were sampled simultaneously at 5 KHz. It is clear from the signals shown in Fig. 12 that at $z=12.3$ mm from wedge centerline the flow was fully turbulent suggesting that the measurement point was inside the turbulent core, whereas at $z=33.3$ mm the flow was laminar indicating that it was outside the wedge. It can also be seen that the flow was intermittently turbulent at $z=19.3$ mm and was almost laminar with very occasional burst of turbulence at $z=26.3$ mm. Therefore the edge of the turbulent wedge detected by the liquid crystals ($z=25$ mm) is located in the outer part of the transitional region. This suggests that the sensitivity of the crystals is sufficient to respond to the intermittently turbulent flow and is not the cause for the smaller spreading angle found. Furthermore, it can be seen that the region associated with the rapid changes in heat transfer and shear stress from the laminar level to turbulent level shown in Fig. 10 actually corresponds in location to the transitional region in Fig. 11.

Now that the sensitivity issue of the liquid crystals is excluded, it is felt that the only reason for the smaller spreading angle found must be that the spanwise cross section of the wedge has a three-dimensional shape and thus a smaller width at the wall than further away in the boundary layer as shown in Fig. 13. This is similar to the ''overhang'' observed by Gad-el-Hak et al. [19] at the leading edge of a turbulent spot. In order to verify this hypothesis, simultaneous measurements were carried out using surface-mounted hot films and a hot wire at $x=162.5$ mm from the roughness. The hot wire was fixed at 0.6 mm above the surface and at a spanwise location ($z=26.3$ mm) slightly outside the edge detected by the crystal coatings. The signals obtained from the hot wire and two film gauges are shown in Fig. 13. It can be seen that although the hot wire clearly picked up the turbulent flow as the film gauge located at $z=19.3$ mm did, the film gauge directly beneath the hot wire saw an essentially laminar flow. This observation confirms the presence of an overhang in the spanwise direction. Being such, the spreading angle of the wedge in the outer part of the boundary layer has to be larger than that at the wall in order to acquire a larger spanwise width. Therefore a smaller spreading angle measured at the wall with liquid crystals is not

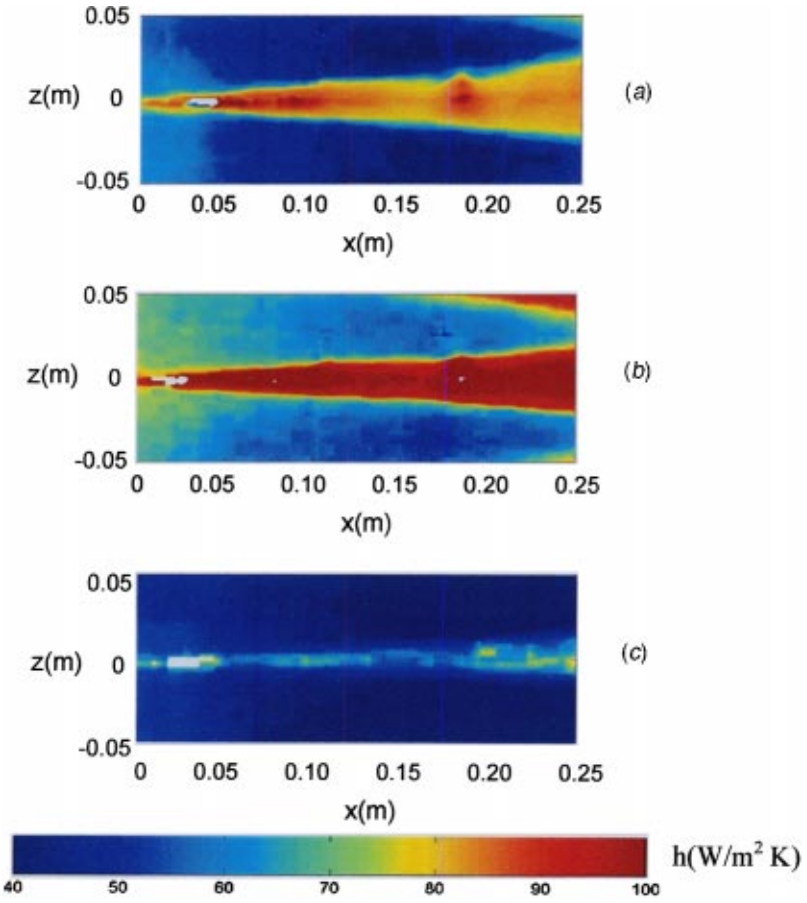

Fig. 9 Contours of heat transfer coefficient obtained from temperature-sensitive liquid crystals, (*a*) $K=0$, (*b*) $K=0.25\times10^{-6}$, (*c*) $K=1.0\times10^{-6}$

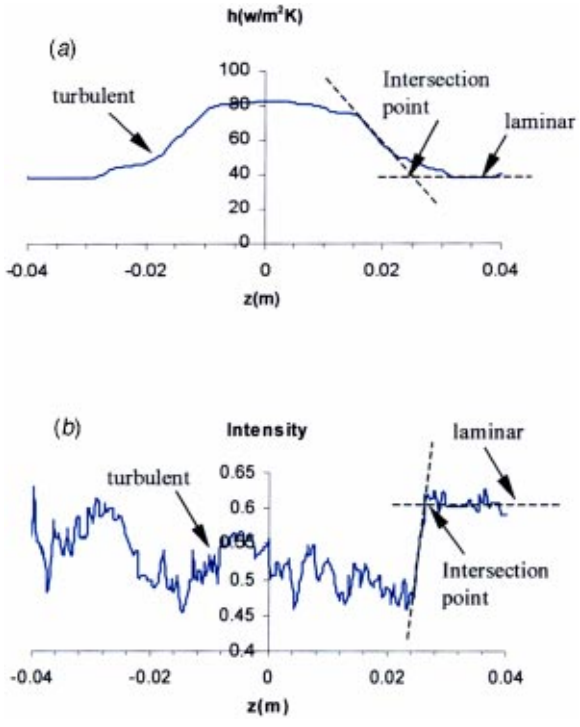

Fig. 10 Spanwise distributions of (*a*) heat transfer rate from temperature-sensitive liquid crystals and (*b*) color intensity from shear-sensitive liquid crystals at $x=162.5$ mm ($K=0$)

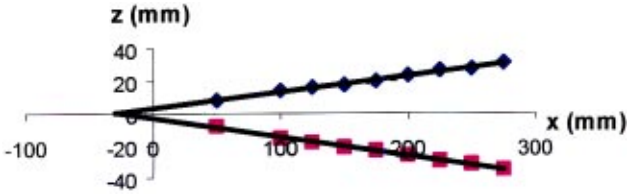

Fig. 11 Linear best-fit of the boundaries of a turbulent wedge ($x=162.5$ mm, $K=0$). The symbols represent the edge of the wedge found from the liquid crystal images at a number of streamwise locations.

Table 1 Summary of spreading angles of turbulent wedges

K	0	0.25×10^{-6}	1.0×10^{-6}
SSLC(°)	6.4	5.5	3.4
TSLC(°)	6.3	4.4	2.4
Difference (%)	0.3	20	31

unexpected. It is also worth noting that almost all the researchers who obtained a larger spreading angle used hot wires as the key experimental apparatus for their measurement. Because of the physical size of a hot wire, the measurement has to be carried out at a certain distance away from the wall where the edge of the turbulent wedge stretches further outwards than at the wall in the spanwise direction.

Based on the above results from the supplementary measurements with surface-mounted hot films and a hot wire, the reason

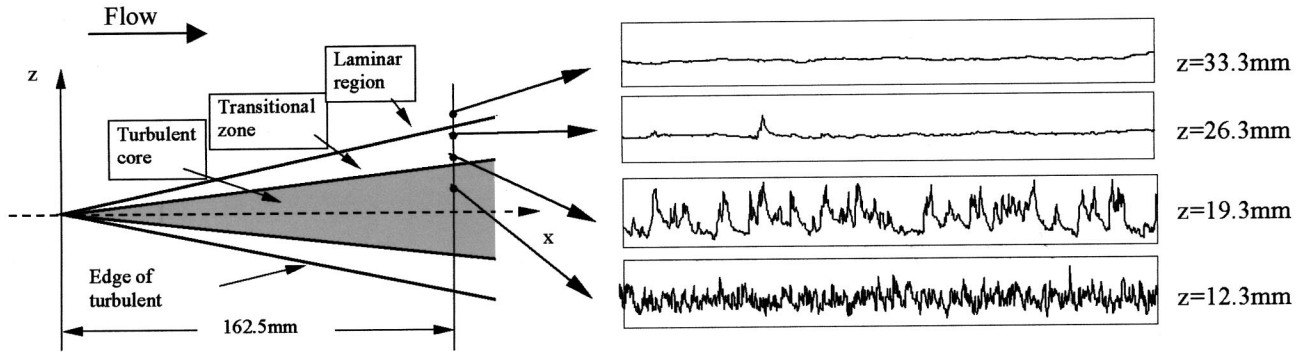

Fig. 12 Signals from a spanwise array of surface-mounted hot films at $x=162.5$ mm ($K=0$)

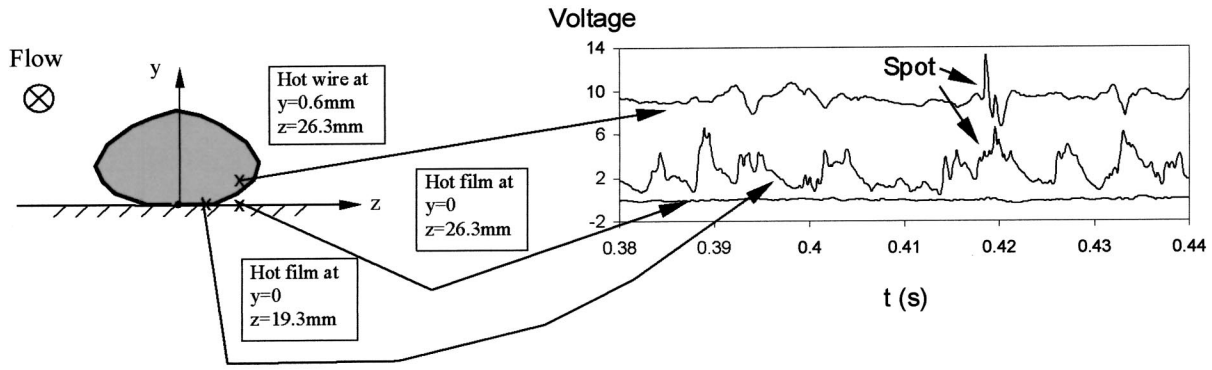

Fig. 13 Comparison of signals from surface-mounted hot films and a hot-wire at $x=162.5$ mm ($K=0$)

for the smaller spreading angle obtained with liquid crystal coatings becomes clear. It is because the spanwise cross section of the wedge has a smaller width at the wall than further away in the boundary layer rather than the insensitivity of the crystal coating. Therefore the results from the present study are valid.

Conclusion

Turbulent wedges induced by a three-dimensional surface roughness placed in a laminar boundary layer over a flat plate were studied for the first time using both shear-sensitive and temperature-sensitive liquid crystals. The experiments were carried out at a zero pressure gradient and two favorable pressure gradients. The purpose of this investigation was to examine the spreading angles of turbulent wedges as indicated by their associated surface shear stresses and heat transfer characteristics and hence obtain further insight about the difference in the behavior of transitional momentum and thermal boundary layers when a streamwise pressure gradient exists.

It was found that under a zero pressure gradient the spreading angles indicated by the two types of liquid crystals are the same, but the difference increases as the level of favorable pressure gradient increases with the angles indicated by temperature-sensitive liquid crystals being smaller. Since in a transitional boundary layer a smaller spreading angle corresponds to a slower spanwise growth of turbulent spots and thus a longer transition zone length, the result from the present study implies that under a favorable pressure gradient the thermal boundary layer will reach a fully turbulent state more slowly than its momentum counterpart. This finding seems to provide an explanation for the inconsistency in the transition zone length indicated by momentum transfer and heat transfer parameters reported in the literature.

With more evidence accumulated to support, this finding should have an important implication to the modeling of transitional boundary layers over gas turbine blades. It suggests that when the turbulent spot based transition models are employed, different empirical relations for the spot growth rate have to be used in order to obtain the correct transition zone length for momentum and thermal boundary layers, respectively. This study also showed that the spreading angle of a turbulent spot/turbulent wedge at the wall is different from that further away in the boundary layer due to its three-dimensional cross-sectional shape. Therefore for more accurate prediction of both surface shear stress and heat transfer rate the spot characteristics measured at the wall should be used.

Acknowledgments

The work reported in this paper is sponsored by the Engineering and Physics Science Research Council in the UK.

Nomenclature

h = convective heat transfer coefficient, W/m^2K
K = pressure gradient parameter, $\mathbf{K}=\nu/U^2(dU/dx_0)$
Re = Reynolds number
T = surface temperature, °C
U = freestream velocity, ms^{-1}
x_0 = streamwise distance from leading edge of test plate, m
x = streamwise distance from surface roughness, m
z = spanwise distance from centerline of turbulent wedge, m
ν = kinematic viscosity, $m^2\,s^{-1}$

References

[1] Klein, E. J., and Margozzi, A. P., 1968, "Exploratory Investigation on the Measurement of Skin Friction by Means of Liquid Crystals," NASA TM-X-1774.
[2] Reda, D. C., and Wilder, M. C., 1997, "Simultaneous, Full-Surface Visualizations of Transition and Separation Using Liquid Crystal Coatings," AIAA J., **35**(4), pp. 615–616.
[3] Reda, D., Wilder, M. C., Farina, D. J., and Zilliac, G., 1997, "New Method-

ology for the Measurement of Surface Shear Stress Vector Distributions,'' AIAA J., **35**(**4**), pp. 608–614.
[4] Ireland, P. T., Wang, Z., and Jones, T. V., 1993, *Liquid Crystal heat Transfer Measurements*, Von Karman Institute for Fluid Dynamics 1992–1993 Lecture Series.
[5] Zhong, S., Kittichaikarn, C., Hodson, H. P., and Ireland, P. T., 2000, ''Visualization of Turbulent Spots Under the Influence of Adverse Pressure Gradients,'' Exp. Fluids, **28**, pp. 385–393.
[6] Blair, M. F., 1982, ''Influence of Free-Stream Turbulence on Boundary Layer Transition in Favorable Pressure Gradients,'' ASME Journal of Engineering for Power, **104**, pp. 743–750.
[7] Sharma, O. P., 1987, ''Momentum and Thermal Boundary Layers on Turbine Airfoil Suction Surfaces,'' AIAA Paper No. 87-1918.
[8] Emmons, H. W., 1951, ''The Laminar-Turbulent Transition in a Boundary Layer—Part I,'' J. Aerosp. Sci., **18**(**7**), pp. 490–498.
[9] Schubauer, G. B., and Klebanoff, P. S., 1955, ''Contribution on the Mechanism of Boundary Layer Transition,'' NACA TN-3489.
[10] Clark, J. P., Magari, P. J., and Jones, T. V., 1993, ''On the Distribution of Heat Transfer Coefficients in Turbulent and Transitional Wedges,'' Int. J. Heat Fluid Flow, **14**(**2**), pp. 217–222.
[11] Mayle, R. E., 1991, ''The Role of Laminar-Turbulent Transition in Gas Turbine Engines,'' ASME Paper No. 91-GT-261.
[12] Narasimha, R., and Prasad, S. N., 1994, ''Leading Edge Shape for Flat Plate Boundary Layer Studies,'' Exp. Fluids, **17**, pp. 358–360.
[13] Hall, G. R., 1967, ''Interaction of the Wake From Bluff Bodies With an Initially Laminar Boundary Layer,'' AIAA J., **5**, pp. 1386–1392.
[14] Wang, Z., Ireland, P. T., Jones, T. V., and Davenport, R., 1994, ''A Color Image Processing System for Transient Liquid Crystal Heat Transfer Experiments,'' ASME Paper NO. 94-GT-290.
[15] Sankaran, R., Chamber, A. J., and Antonia, R. A., 1986, ''The Influence of a Favorable Pressure Gradient on the Growth of a Turbulent Spot,'' *Proceedings of the 9th Australian Fluid Mechanics Conference*, University of Auckland, New Zealand.
[16] Gostelow, J. P., Melwani, N., and Walker, G. J., 1996, ''Effects of Streamwise Pressure Gradient on Turbulent Spot Development,'' ASME J. Turbomach., **118**, pp. 737–743.
[17] González, R. C., 1993, *Digital Image Processing*, Addison-Wesley, Reading, MA.
[18] Wygnanski, I., Zilberman, M., and Harritonidis, J., 1982, ''On the Spreading of a Turbulent Spot in the Absence of a Pressure Gradient,'' J. Fluid Mech., **123**, pp. 69–90.
[19] Gad-el-Hak, M., Blackwelder, R. F., and Riley, J. J., 1981, ''On the Growth of Turbulent Regions in a Laminar Boundary Layers,'' J. Fluid Mech., **110**, pp. 73–99.

Hongze Lai
Graduate Research Assistant

Jonathan W. Naughton[1]
Assistant Professor,
e-mail: naughton@uwyo.edu

William R. Lindberg
Professor
e-mail: lindberg@uwyo.edu

Department of Mechanical Engineering,
University of Wyoming,
Laramie, WY 82071

An Experimental Investigation of Starting Impinging Jets

Impulsively started impinging jets were experimentally investigated in a water tank utilizing a fluorescent dye technique. The jets were examined prior to and subsequent to impingement. The impingement surfaces included a flat surface and a two-dimensional semicircular concave surface. The normalized jet-to-surface distance and the jet Reynolds number were varied in this study. Using digitized flow visualization images, the jet trajectories, front velocities, growth rates, and convective velocities of large-scale turbulent structures were quantified. A central conclusion of this investigation is that, for all cases studied, the jet-front velocity varies with the square root of time. These results are important to applications that might use starting or pulsed jets for heat transfer enhancement and in combustion processes. [DOI: 10.1115/1.1537255]

Introduction

This paper reports the results of an experimental study of starting impinging jets. Starting impinging jets are of interest in a variety of applications, including enhanced heat transfer, mixing, and combustion processes. This interest results from potential increase in mixing, surface shear stress, and heat transfer rates relative to steady impinging jets. A starting impinging jet can be treated as a starting free jet before impingement and a starting wall jet thereafter. Although steady wall jets have been studied in detail (see Refs. [1] and [2] for reviews), the starting wall jet that forms after the jet impinges on a surface has received little attention. Prior investigations of free starting jets (see, for example, Refs. [3–5]) have revealed that the front velocity is proportional to the square root of time and is about half of the centerline velocity in a steady jet at the same location. Lahbabi et al. [3] point out that the advancing jet width is proportional to the distance from the jet exit. Steady radial wall jets have been extensively studied using both similarity analysis and experiments (see, for example, Refs. [6–8]). These studies have shown that the maximum velocity is inversely proportional to the radial length scale, and the jet width is proportional to the same length scale. One study has considered the impingement of an unsteady (pulsating) jet on a surface, with the objective of studying the enhanced heat transfer characteristics, [9]. To the authors' knowledge, the trajectory and front velocities of a starting wall jet after impingement have not been investigated.

In the present study, incompressible, homogenous, axisymmetric, impulsively started turbulent jets are experimentally investigated using quantitative flow visualization. Flow visualization has been effectively used in the past to characterize unsteady jet flows, particularly the jet front propagation (see, for example, Refs. [3], [5]). Both the starting free jet and starting wall-jet flows have been studied with an emphasis on the measurement of jet trajectories, front velocities, growth rates, and convective velocities of turbulent structures. In addition to investigating jet impingement on flat surfaces, jet impingement on one curved surface has also been studied to investigate the effect of surface curvature on the wall-jet development.

The results from this study suggest that, when nondimensionalized using the appropriate variables, the front velocity of the starting wall jet behaves in the same manner as a starting free jet. This similarity complements previous research that showed that the functional variation of the mean jet velocity with the trajectory path length is of the same form in both the steady free jet and the steady wall jet, [8]. The front velocity of a wall jet developing on a surface with curvature also exhibits the same functional behavior as normally impinging and free starting jets. It is concluded that all of these physical similarities occur because these flows are inertially dominated, with wall shear playing only a minor role in the initial transient flow dynamics.

Experimental Setup

The experimental system is shown in Fig. 1, where a schematic of the starting jet is shown in (a), and the flow visualization system is shown in (b). The experiments are carried out in a Plexiglas tank of 1.2 m$\times$1.2 m cross section and 0.7 m deep. A smaller tank is filled with fluorescein sodium dyed water and is positioned above the large tank. The apparatus provides a water jet that impulsively issues from a nozzle into a large tank of quiescent water and impinges on a surface. The nozzle has an exit diameter d_0 of 3.18 mm, and an upstream contraction ratio of 8 provides a uniformly distributed velocity profile at the jet exit. The jet velocity, which is calculated from the flow rate and the nozzle diameter, is controlled by the water level difference between the two tanks. A solenoid valve is used to start the jet impulsively so that no significant amount of dyed water is released prior to starting the jet.

For the majority of the plane wall impingement studies, the water surface in the tank is used as the impingement surface, primarily for the ease of adjusting the jet-exit-to-impingement-point distance (H). The surface tension of tap water is sufficient to suppress any disturbances, and, although there may be some boundary slip, it can be shown that boundary shear is not important to the propagation of the wall jet (this point is discussed in the Appendix). To investigate the effect of curvature on impingement, the plane surface is replaced by a solid curved surface. A fluorescent dye technique is used to visualize the flow. Fluorescein sodium dyed water fills the tubing leading to the jet exit before an experiment begins. To observe the jet, the test section is illuminated from either the sides or the bottom of the tank using two focused filament lights that produce a light sheet approximately 0.5 cm thick. The time-dependent jet-flow behavior is recorded using a 768$\times$484 pixel CCD camera with a zoom lens (12.5–75 mm) that is mounted perpendicularly to the illumination plane. The camera is computer controlled using an image capture board and imaging software. Digital images are first buffered in the image capture board and then are transferred to the computer for storage and analysis. By storing a series of images during a test, a dynamic picture of starting jet development is captured.

The experimental conditions for each test are summarized in Table 1, and the coordinate frame and important parameters for

[1]To whom correspondence should be addressed.

Contributed by the Fluids Engineering Division for publication in the JOURNAL OF FLUIDS ENGINEERING. Manuscript received by the Fluids Engineering Division December 20, 2001; revised manuscript received September 19, 2002. Associate Editor: V. Ötügen.

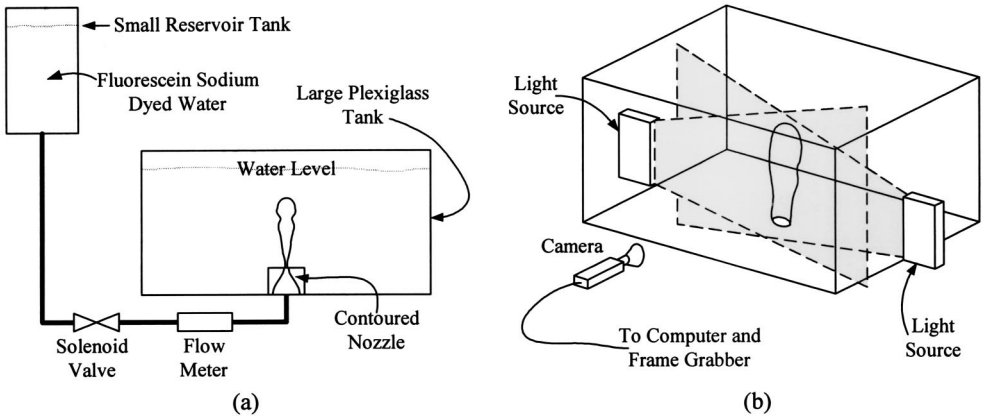

Fig. 1 Schematic of experimental setup: (*a*) starting jet test apparatus, and (*b*) flow visualization arrangement

free and impinging jets are shown in Fig. 2. Cases 1–5 were selected to cover a range of impingement heights and a small range of Reynolds numbers for jet impingement on a flat surface. Past experimental results have shown that the free jet behavior is a weak function of Reynolds number, [3,4], and impinging jets are independent of impingement height when H is greater than several jet diameters, [7]. Results from the free jet portions of these tests validated the quantitative visualization technique used here, whereas the wall-jet portions of these experiments established the appropriate scaling for wall jets in the absence of curvature. Case 6 was then used to compare the scaling for the wall jet with curvature with the more detailed results for the wall jet without curvature.

Image Analysis Approach

The digital images that captured jet development were examined quantitatively and qualitatively. For example, the edge-enhanced images were analyzed to determine the jet-front position of both the free and impinging jets. In addition, analysis of the steady portion of the jet allowed for the determination of the jet width and convective velocities. A brief description of these quantitative methods used is given below, but a complete description can be found in Lai et al. [10]. In addition, digitally enhanced sequential images were examined in slow motion in order to observe many of the details of the evolving flow.

Jet-Front Analysis. To ensure consistency and reduce subjectivity in determining the jet-front location, an automatic image-processing procedure was developed and applied to the sequence of images in each experiment. First, the background image was subtracted from all jet images. Next, an edge detection algorithm based on local derivative operators, [11], was applied to the images. This analysis yielded a sequence of images in which the jet edge was highlighted.

Sequences of edge-enhanced images are shown in Figs. 3 (jet impinging on a horizontal free surface) and 4 (jet impinging on a curved surface). These images show the starting jet at several different times during its evolution. These series of images demonstrate the ability of this analysis procedure to highlight the jet front and other large-scale features of the flow. Note that the lower boundary of the wall jet in Fig. 3 is not visible due to the lack of scattered light in this region caused by low dye concentration and partial blockage of the illuminating source by the jet front. In Fig. 4, the jet boundary that appears to intersect the wall is an artifact due to light reflection from the wall.

Several qualitative observations can be made from these images. First, both figures display an initial free jet that impacts on the wall and, after a transition period, evolves into a wall jet. In both cases, it is evident that the macroscopic motion contains fine

Table 1 Details of experimental conditions

Case	# of Tests	Re_d	H/d_0	Impingement Surface
1	1	7550	114	horizontal free
2	1	6600	147	horizontal free
3	1	6700	109	horizontal free
4	3	5400	115	horizontal free
5	10	7800	83	horizontal free
6	5	4200	63	curved

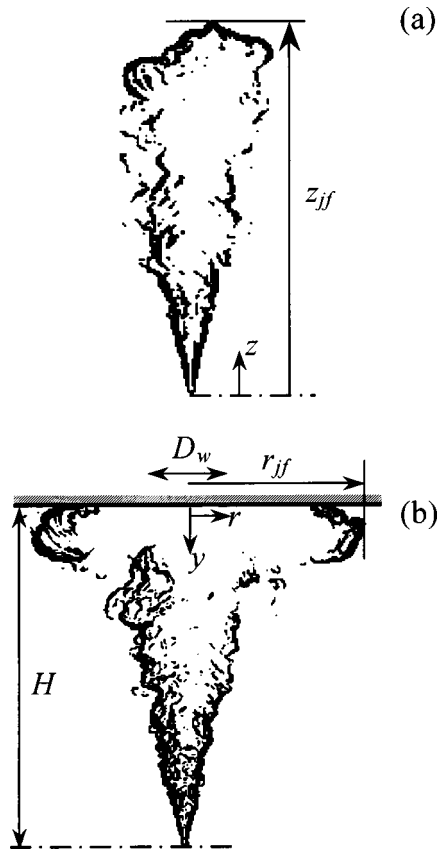

Fig. 2 Edge-enhanced images with important parameters: (*a*) starting free jet and (*b*) wall jet

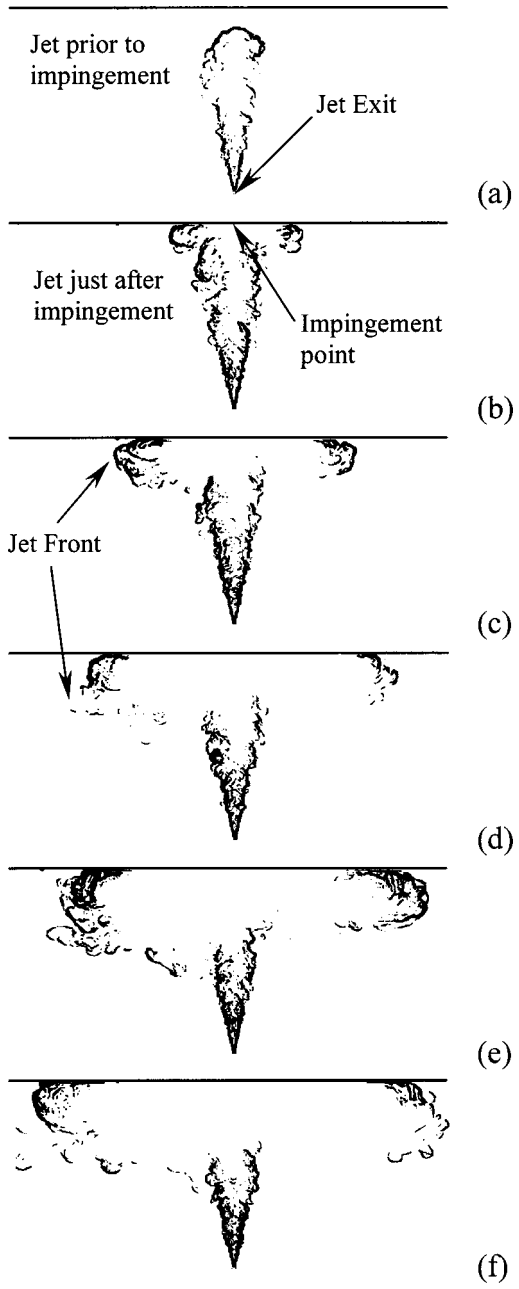

Fig. 3 Edge enhanced images of a starting jet impinging on a flat surface (case 4). The images shown were captured at (*a*) 2070, (*b*) 3670, (*c*) 6530, (*d*) 10620, (*e*) 15980, and (*f*) 21470 $U_0 t/d_0$.

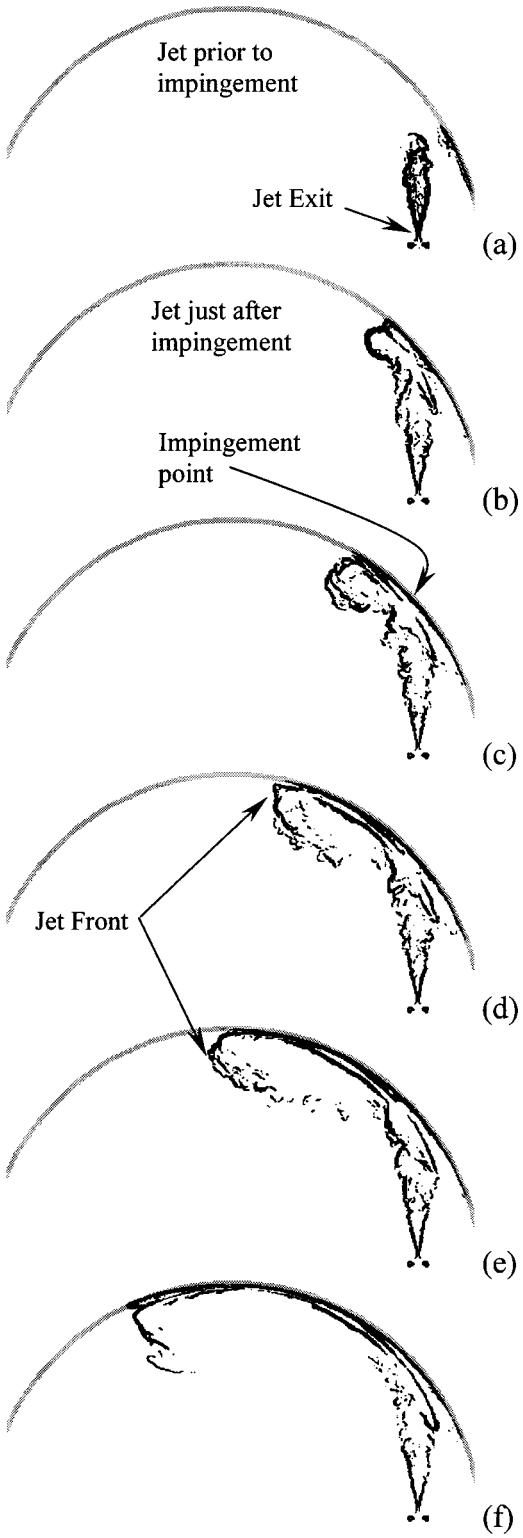

Fig. 4 Edge enhanced images of a starting jet impinging on a curved surface (case 6). The images shown were captured at (*a*) 730, (*b*) 1480, (*c*) 2230, (*d*) 3740, (*e*) 5260, and (*f*) 7920 $U_0 t/d_0$.

detail that varies from image to image. In particular, the structure that makes up the jet front is strongly vortical, with embedded turbulent structure. Another observation is that the wall jet along the curved surface travels at a higher rate than the wall jet on the flat surface. This occurs because the initial jet momentum in the curved wall jet deflects primarily in one direction, whereas the momentum in the flat wall jet spreads radially.

The location on the jet edge farthest from the origin (the jet-front position) was determined in each image. To avoid picking an isolated point, a front point was not considered valid unless there were other edge points in the 3×3 pixel neighborhood surrounding it. Once a front point was identified, its location was stored along with the time of the image. By determining the distance traveled by the jet front between several frames, the jet-front velocity was determined.

Jet Width Determination. In addition to identifying the jet-front position, the width of the jet could also be estimated. Since the fluorescent dye acted as a passive scalar, its signal was used as an indicator of the mixing between the jet and the ambient fluid. Regions of high intensity existed at the jet exit, but the intensity

decreased as the unseeded ambient fluid mixed with the jet. Gray level values of certain points inside the steady wall-jet region were retrieved from the images, and, by determining the location of a specified gray level value, the wall-jet width was determined at various distances from the impingement point.

Convective Velocity. Observations of the time evolution of these impinging radial flows clearly revealed the advection of turbulent structures (whose origins were difficult to identify). It was concluded that these structures were significant elements in the flow and should be investigated. The experimental methodology involved examining the time variation of the image gray levels at fixed locations. Analyzing these intensity signals at several points revealed the passage of turbulent structures. By determining the time it took for these structures to traverse the distance between consecutive points, the convective velocity was determined.

Uncertainty. The uncertainties of the measurements made in this study are discussed in this section. The uncertainties in jet-front position are $\pm 0.8\, d_0$ in space and $\pm 1.2\, d_0/U_0$ in time. The uncertainty on Reynolds number is related to the uncertainty of a flow meter, which results in a 5% error in Re_d. Where ensemble averaging has been used (for example: to determine the mean jet front position), the run-to-run variations significantly exceed the measurement uncertainty. Thus a 95% confidence interval around the mean value is used in those cases. Details of the uncertainty analysis can be found in Ref. [12].

Results

The focus of this study is the trajectory and the front velocity of the starting free jet and impinging wall jet. The results for starting free jets, determined from enhanced images such as those in Fig. 2, are presented and compared with previous studies to validate the quantitative flow visualization approach used here. Next, the results are presented for starting jets impinging on flat and curved surfaces. Finally, the width and convective velocities in the steady wall-jet region are discussed.

Jet Trajectory. The propagation of the starting free jet has been studied previously (see, for example, Refs. [3–5]). Using appropriate nondimensionalization, the jet-front position (z_{jf}/d_0) can be expressed as

$$z_{jf}/d_0 = \alpha (tU_0/d_0)^{1/2} + \beta. \tag{1}$$

The experimentally determined jet-front position and linear least-squares fits using Eq. (1) for cases 1–4 are plotted in Fig. 5. The data for $\mathrm{Re}_d = 5400$ are the ensemble average of three runs. The virtual origin effects, reflected by the term β in Eq. (1), are often neglected because β is close to zero. The lines included in Fig. 5 have slopes α of 2.3 and 2.6. The latter value has been found using an experimental method similar to that used here, [5]. As in previous studies, α does not appear to depend strongly on Re_d, [3–5]. These results indicate that the methods used in the present experiment to determine advancing jet front location yield values similar to those found in other studies.

After impingement on a flat surface, the jet propagates along the surface as a wall jet. As with the starting free jet, two parameters can be used to characterize a wall jet: the initial wall-jet momentum flux and the initial wall-jet diameter. These quantities scale as follows:

$$\frac{M_i}{\rho} \sim U_0 d_0^2, \tag{2}$$

$$D_w \sim H, \tag{3}$$

where M_i is the initial momentum flux per unit mass (conservation of momentum prior to and following impingement) and D_w is the diameter of the initial wall jet (immediately following impingement). Based on these parameters, it is suggested that the appropriate scales for these wall-jet flows are H and $H^2/(d_0 U_0)$ for length and time, respectively.

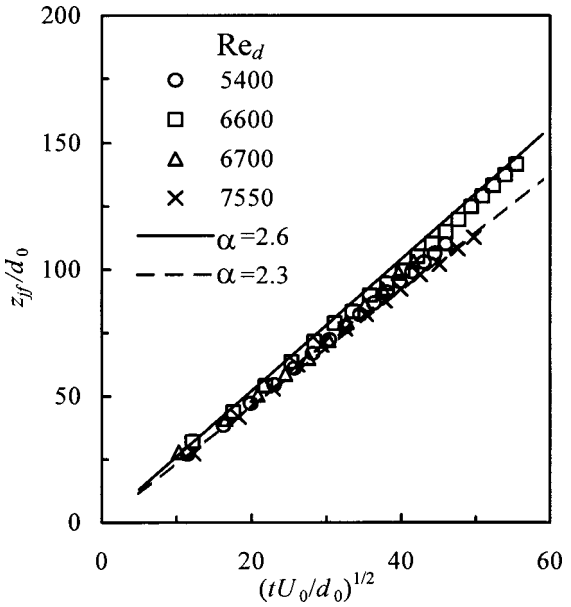

Fig. 5 Free-jet front trajectory

In Fig. 6, the nondimensional wall-jet front trajectories measured for two Reynolds numbers are plotted versus the square root of nondimensional time. The data points for case 5 are the ensemble average of 10 runs, whereas those for case 4 are the ensemble average of 3 runs.

Although the wall jet originates from the impingement of the free jet on the surface, data in the impingement region are not shown in Fig. 6 because the jet transitions from a free jet to a wall jet in this region. Outside this impingement region, the wall jet develops as if it originates from a location within the impingement region (defined as the virtual origin of the wall jet). For convenience, a new time coordinate t_w is defined, where $t_w = 0$ corresponds to the time at which the jet impinges on the surface.

The collapse of the data in Fig. 6 supports the chosen nondimensional parameters. The data are fit closely by a line indicating

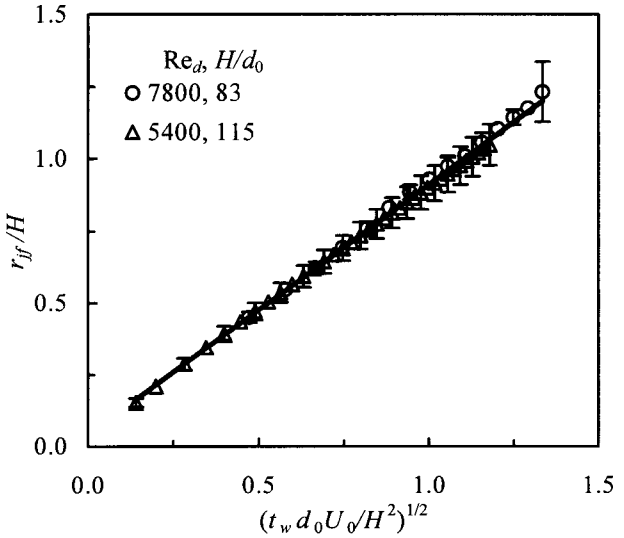

Fig. 6 Radial wall-jet front trajectory with linear least-squares fit of the data (solid line) shown

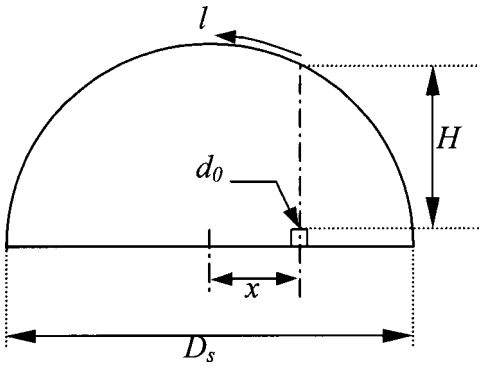

Fig. 7 Important parameters for a jet impinging on a curved surface

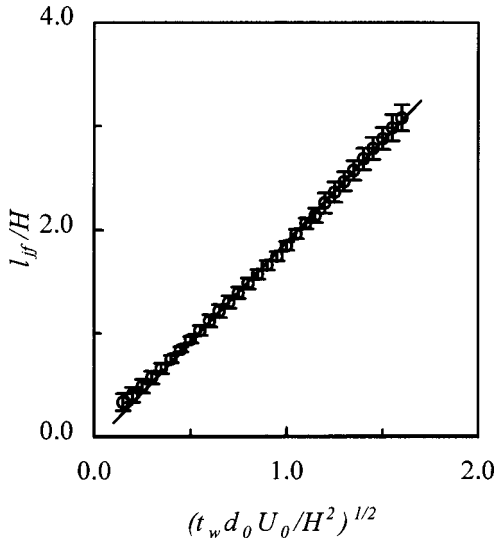

Fig. 8 Jet-front trajectory of the wall jet along a circular-arc surface for case 6 with a linear least-squares fit of the data (solid line) shown

that the normalized jet front of the radial wall jet increases linearly with the square root of normalized time. The equation of this line may be written as

$$r_{jf}/H = \alpha(t_w d_0 U_0/H^2)^{1/2} + \beta, \tag{4}$$

where $\beta \sim 0$. For this case, the slope α is 0.87.

A further objective of this study is to determine if jets impinging on a circular surface behave in a manner similar to jets impinging on a flat surface. To investigate curvature effects, a solid circular-arc surface with a diameter of 190 jet diameters ($D_s/d_0 = 190$) is placed in the large tank. The jet origin is located at 67 jet diameters from the center of curvature ($x/d_0 = 67$). At this x/d_0 location, the jet axis intersects the solid curved surface at a distance of 63 jet diameters from the jet exit ($H/d_0 = 63$). A schematic of the experimental setup and the important parameters for this case are shown in Fig. 7. A new coordinate l is defined for the wall jet impinging on a semicircle surface, where l is the arc length from the impingement point to the projected jet-front point on the semicircular surface.

The jet-front trajectory of the wall jet impinging on the curved surface determined by ensemble averaging is plotted in Fig. 8 using the same scaling that is used for the flat impingement case. The data again show that the nondimensional jet-front location (l_{jf}/H) increases proportionally to the square root of nondimensional time. Although similarities exist between flat impingement and curved impingement, the jet-front propagation rate of the curved wall jet ($\alpha = 1.94$) is more than double that of the flat impingement case ($\alpha = 0.87$). As suggested by Figs. 3 and 4, this difference in propagation rate is most likely due to the radial spread of momentum flux in the flat impingement case, whereas the curved wall jet is spreading primarily in one direction. The sensitivity of this result to curvature can only be assessed with additional tests in which the curvature is varied.

Jet Structure. Careful observation of sequences of flow visualization frames provides insight into the difference in the growth rates observed for the normal impingement on a flat surface and the curved surface impingement case. In the normally impinging jet, a vortex forms at the jet front upon impingement. This vortex grows in size (radially and normally to the wall) as the jet spreads such that its size scales with the impingement-point-to- jet-front distance. High momentum wall-jet fluid that overtakes this vortex is entrained. In contrast, a much smaller, flatter vortex forms when the impingement occurs on the curved surface. This vortex quickly moves away from the impingement point and growth in the size of the vortex is slow. Although this vortex still entrains higher momentum wall-jet fluid that overtakes it, it does so at a much slower rate than the normally impinging jet. Observations of the evolving flow indicate that the rotation induced by the wall curvature is of the same order as the induced rotation of the vortex, in contrast to the vortex structure of the flat plate impingement flow.

The wall jet starting vortex is apparently unrelated to the starting vortex of the impulsively started free jet, as has been discussed by Gharib et al. [13]. At the time of impingement, t_i, the "formation number" ($U_0 t_i/d_0$) for the present free jet flows is of the order of 50, and the formation number of the first image acquired following startup of the free jet is of the order of 10. Gharib et al. [13] conclude that the free jet initial vortex is overtaken by the free jet for formation numbers greater than 4. Thus, the starting vortex of the free jet should not have a significant effect on the wall jet flows discussed here.

Steady Jet Width. After the propagating jet front passes, the flow behind the front approaches a steady flow with increasing time. In the present experiments, the run-time limit imposed by the size of the tank is insufficient to determine the steady flow behavior by time-averaging alone. Therefore, the values determined from images from several runs are averaged. The region within the dashed lines (indicated by (1) in Fig. 9) is the steady wall-jet region. This region must be carefully chosen to avoid the

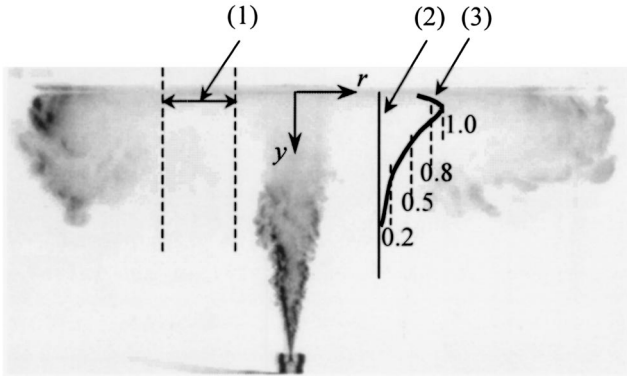

Fig. 9 Definitions of coordinate system and normalized intensity level profile: (1) the "steady" wall-jet region; (2) a scan line; and (3) a normalized intensity profile on the scan line. The image is the negative of an instantaneous result and is shown only for location reference.

influence of the impingement region and the leading vortex region, where strong mixing and three-dimensional flow occur. Note that the points in this region are steady only after the leading vortex has passed, which occurs at different times for different locations.

Scan lines (such as the one indicated by (2) in Fig. 9) at nine radial locations spaced approximately 15 mm apart are selected in the steady wall-jet region. The normalized average image intensity $\overline{I}_{\mathrm{norm},j}$ along each scan line is calculated for a given run j of case 5 as follows. First, the intensity at each location (r,y) along a scan line is summed for N_j images. These values are then normalized by the maximum summed intensity along that scan line:

$$\overline{I}_{\mathrm{norm},j}(r,y)=\frac{\Sigma_{i=1}^{N_j} I_i(r,y)}{\max\left(\Sigma_{i=1}^{N_j} I_i(r,y)\right)}, \tag{5}$$

where $I_i(r,y)$ is the intensity in a given image and N_j is the number of images in that given run. Next, the normalized average intensity $\overline{I}_{\mathrm{norm}}(r,y)$ (see the line labeled (3) in Fig. 9) for the case is determined by averaging over all runs for a given case:

$$\overline{I}_{\mathrm{norm}}(r,y)=\frac{\Sigma_{j=1}^{N} \overline{I}_{\mathrm{norm},j}(r,y)}{N}, \tag{6}$$

where N is the number of runs.

The width of a steady wall jet is usually defined as the distance from the wall where the velocity is half of the maximum velocity, [1,8]. In the present research, the jet width is defined using the normalized image intensity profile, [14], as shown in Fig. 9. In this figure, the normalized intensity is the bold line indicated by (3). Averaged, normalized-intensity profiles $\overline{I}_{\mathrm{norm}}(r,y)$ at nine locations are shown in Fig. 10. Although there is only an inexact connection between intensity and dye concentration due to nonuniform illumination, camera sensitivity, and scattering effects, the normalized intensity is used to determine a concentration thickness.

In this study, the steady jet width has been determined for three normalized-intensity levels (0.8, 0.5, and 0.2), as shown in Fig. 9. The lower the intensity level, the closer the points are to the jet edge (see Fig. 10). The jet width, as defined by these normalized-intensity levels, changes linearly with increasing radius as shown in Fig. 11. The $\overline{I}_{\mathrm{norm}}=0.2$ width seems to exhibit the largest deviation from a line, but this deviation is likely due to the greater sensitivity of this normalized-intensity level to the sample size used here. The last $\overline{I}_{\mathrm{norm}}=0.2$ point may also be affected by the leading vortex structure. The plot shows that the choice of intensity level does not affect the linear relationship between the width and the radius. This conclusion is consistent with the previous research by Poreh et al. [15]. The three wall-jet widths in Fig. 11 appear to intersect when extrapolated to a point on the r axis. To verify this intersection, the experimental data are fit using the following linear equation:

$$\frac{h}{r_w}=k\left(\frac{r}{r_w}-1\right), \tag{7}$$

where r_w is the intersection of the line on the r-axis, and k is the slope. The values of r_w and k are tabulated in Table 2 for each of the jet boundaries indicated in Fig. 11. The three values of r_w are close to one another, which suggests that r_w is the virtual origin of the steady wall jet. The values of k bracket the accepted value of 0.09 for the spreading rate based on the point where the velocity has dropped to half the maximum velocity, [1]. Assuming the same virtual origin indicated by the concentration thickness, the predicted wall-jet width using the 0.09 value is indicated in Fig. 11 and lies close to the 0.5 concentration thickness value.

Convective Velocity of Coherent Structures. Large-scale structures that convect in the direction of the mean velocity are the primary mechanisms for the transport of mass and momentum in the jet. These structures are not always evident in the images, but their existence is suggested by intensity changes at locations along the jet that indicate their passage.

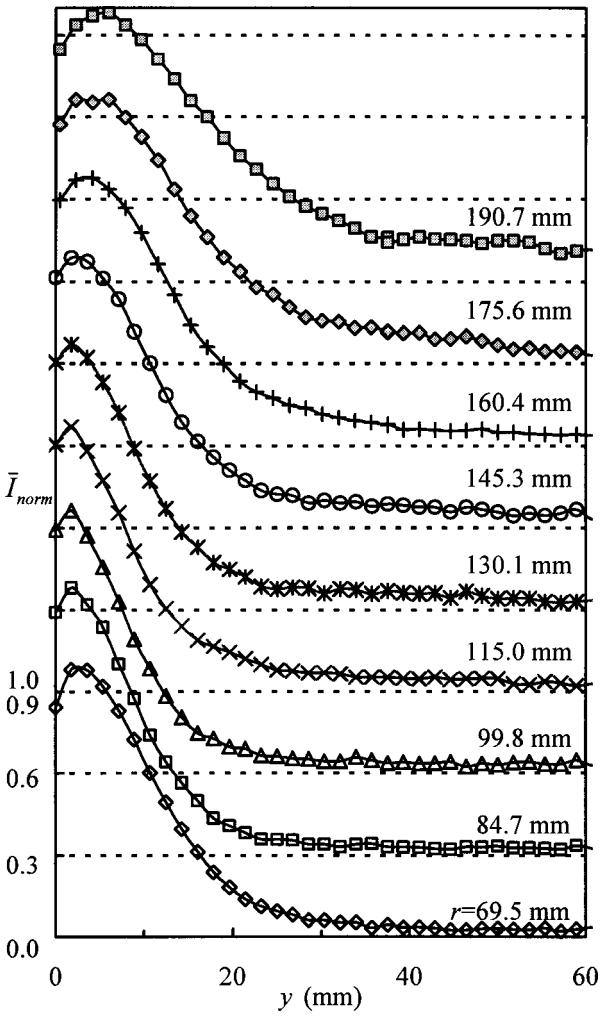

Fig. 10 Normalized intensity profiles at nine radial locations for case 5 (horizontal dashed lines denote the base lines for the subsequent radial locations)

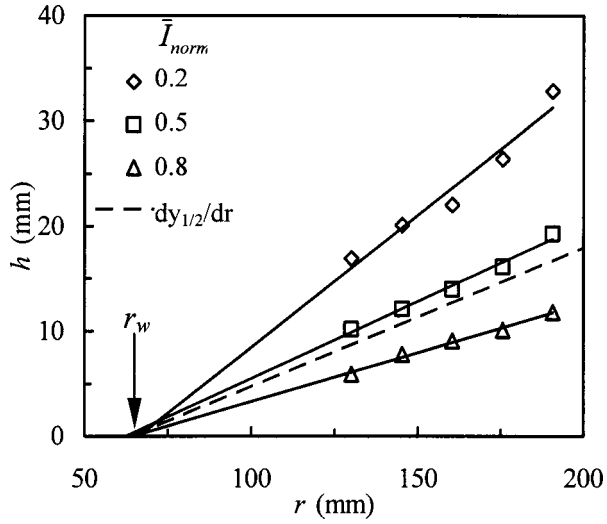

Fig. 11 Radial wall-jet width at three normalized-intensity levels for case 5

Table 2 Linear fit parameters for the wall-jet width (case 5)

$\overline{I}_{\text{norm}}$	k	r_w (mm)
0.2	0.251	66.5
0.5	0.147	62.5
0.8	0.093	64.3

Certain patterns are evident in Fig. 12 where intensities are shown as a function of time at selected values of (r,y) for the wall jet region of case 5. Nine radial locations are shown where the y-value for each location is chosen to be coincident with the maximum normalized average intensity (i.e., $\overline{I}_{\text{norm}}=1.0$). The slanted solid lines identify disturbances indicative of large-scale structures as they move radially outward. Flow disturbances are revealed by intensity variations evident at each of the locations in Fig. 12. By following the peaks or troughs of these disturbances as they travel radially outward, their radial propagation velocity is determined. By repeating such calculations for many structures over ten runs, the average convective velocity of these coherent structures at several radial locations can be determined. Convective velocities have been calculated from plots such as Fig. 12 using intensity variations from locations where the normalized intensities are 0.5 and 1.0. The calculated convective velocities at these locations are equal to or greater than the jet-front velocity for $1.0<r/r_w<3.0$, the range in which these velocities have been determined.

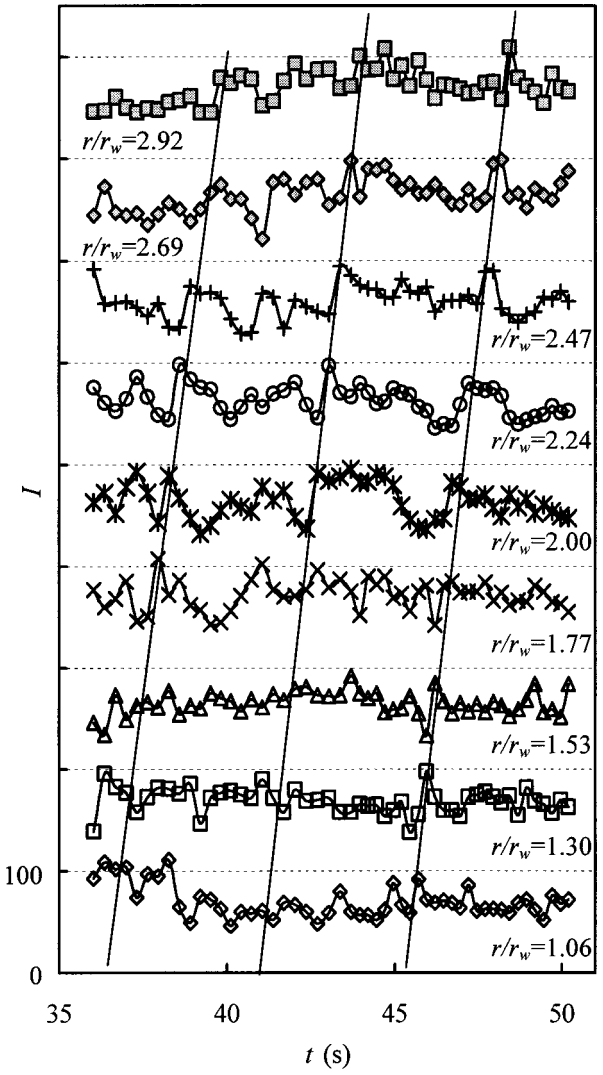

Fig. 12 Intensity fluctuations at nine selected radial locations for case 5. The horizontal dashed lines denote zero intensity for each of the radial locations. The slanted solid lines indicate the propagation of a large-scale structure.

Conclusions

The impulsively started impinging jet has been experimentally investigated in a series of flow visualization experiments performed in a water tank. The transient, impinging jet studies have been directed toward further understanding the dynamics of starting jets impinging on flat and curved surfaces. The quantitative flow visualization results from the starting free jet and steady wall jet compare favorably to prior studies.

When starting jets impinge normally to a flat surface, the jet front propagates radially along the surface at a rate proportional to the square root of time. The same functional behavior is found for a starting jet impinging at an angle to a curved surface. However, the curved wall jet front propagates at a faster rate than the front velocity of a comparable radial wall jet that forms when a jet impinges normally on a flat surface. This result is attributed to the constrained growth direction of the curved wall jet and not to curvature effects. It is important to note that the jet-front velocity of all of the impinged wall jets behaves similarly to that of the starting free jet.

In the steady region of the jet impinging on the flat surface (i.e., following passage of the initial vortical front), both the growth rate and the convective velocities have been investigated. As found in previous studies, the steady wall jet appears to grow linearly from a virtual origin. In addition, the convective velocity of observed coherent structures propagates at a velocity equal to or greater than the local mean velocity of the steady wall-jet flow.

This study provides jet propagation rates that could be important in the development of combustion or heat transfer systems based on unsteady injection. In a combustion application, the propagation of the wall jet front indicates the penetration of an injected fuel in gasoline direct injection process. In heat transfer applications, the jet front dictates the onset of transient heat transfer. The leading front vortex is observed to provide very strong entrainment, so enhanced mixing could be accomplished by periodic jet flows in many applications.

The implications of transient impinging jets to mixing/entraining flows suggest the need for further study. The importance of these flows in a variety of applications together with the need for understanding the basic mechanisms of these flows have stimulated further work in this area, which will be reported at a later date. For example, impingement surfaces with other curvatures should be studied to determine the effects of wall curvature. Repeating similar experiments on flat inclined plates should provide clarification of the roles of curvature and inclined impingement in governing the jet front velocity. Finally, this study has pointed out the striking similarity in the jet-front velocity in starting free jets and impinged wall jets. Such similarity suggests a physical equivalence in these various cases, where inertial and free shear effects are dominant over wall stresses.

Acknowledgments

The authors would like to recognize the collaboration with Prof. Bronek Sendyka of Cracow University of Technology whose interest in gasoline direct injection (GDI) processes stimulated this work. Additionally, suggestions contributed by Dr. James L. Smith and the reviewers of this manuscript are gratefully acknowledged. We would like to thank Jeremy Bennington and Lucas Neubert for their help with the experiments.

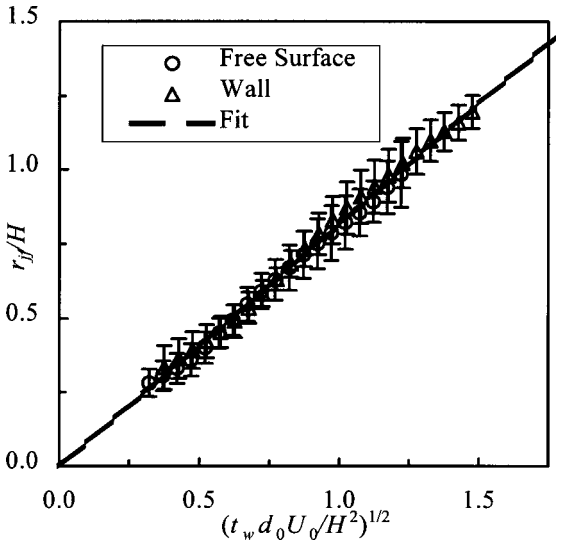

Fig. 13 Comparison of jet-front propagation for a jet impinging on a free surface and a jet impinging on a wall

Appendix

A brief scaling argument is presented in this appendix to demonstrate that the wall shear stress plays only a minor role in the dynamics of impinging jet behavior. After impingement, a mean radial velocity $U_r(r)$ and a jet thickness $h(r)$ characterize the spreading radial wall jet. At any radial location, the radial momentum flux $J(r)$ may be scaled as

$$J(r) \sim \rho U_r^2 A_r \sim \rho U_r^2 (2\pi r h), \tag{8}$$

where $A_r(r)$ is the radial jet flow area $(2\pi rh)$. The net radial force, from a radius beyond the initial jet impact zone $(R_o \gg r_w)$ out to a radius of R, resulting from wall shear stress may be written as

$$F_D(R) \int_{R_1}^{R} \left[\frac{1}{2}\rho U_r^2(r)\right] C_f (2\pi r dr) \sim \int_{R_1}^{R} \frac{1}{2} C_f \frac{J(r)}{h(r)} dr, \tag{9}$$

where C_f is a local wall skin-friction coefficient $(\sim 10^{-3})$. Beyond the initial transition region, the radius r is much larger than R_1, and, behind the leading jet front, the radial momentum flux is constant $(J(r) \sim J_1)$ in the absence of wall friction. Thus, one may write the above expression as

$$\frac{F_D}{J_1} \sim \left(\frac{\overline{C_f}}{2k}\right) \ln\left[\frac{R/r_w - 1}{R_1/r_w - 1}\right], \tag{10}$$

where Eq. (8) has been employed for $h(r)$. This scaling indicates that the contribution of the wall shear stress to the radial momentum flux J_1 is small (less than 1%, for $R/r_w < 150$). For the initial advancing front, the inviscid displacement of surrounding fluid is the dominant mechanism controlling the flow dynamics, rather than the wall stresses. The similarity of the frontal velocities for all of the cases studied (with and without wall shear) is further justification for this conclusion.

To demonstrate the validity of the argument given above, the propagation of a jet impinging on a wall is compared to a jet impinging on a free surface in Fig. 13. The ensemble-averaged results indicate that, as suggested above, there is virtually no difference in the jet-front propagation rate for the two different cases.

Nomenclature

A_r = area of wall jet width
C_f = skin friction coefficient
$\overline{C_f}$ = average skin friction coefficient
D_w = initial wall jet diameter
D_s = diameter of the semicircular surface
F_D = radial force due to shear stress
H = jet-exit-to-impingement-point distance
I = pixel intensity value in gray level scales (0–255)
$\overline{I}_{\text{norm},j}$ = normalized average image intensity for run j
I_{norm} = normalized average image intensity for a case
J = radial momentum flux of wall jet
M_i = initial momentum flux per unit mass
N_j = number of images
N = number of runs
R = radius limit of integration
Re_d = jet Reynolds number $= U_0 d_0 / \upsilon$
U_0 = jet-exit velocity
U_r = mean radial velocity of wall jet
d_0 = diameter of the nozzle
h = wall-jet width
i = index for an image in a particular run
j = index for a run in a particular case
k = steady wall jet growth rate
l = coordinate along the semicircular surface
l_{jf} = jet-front position for jet impinging on semicircular surface
r,y = radial and wall-normal coordinates in the wall jet
r_{jf} = wall-jet front location
r_w = virtual origin of wall jet
t = time
t_i = time of jet impingement
t_w = time associated with wall jet origin
x = the orthogonal distance from the semicircle center to the jet centerline
z = axial coordinate in the free jet
z_{jf} = free-jet front location
α = starting jet propagation coefficient
β = virtual origin of starting jet
ρ = fluid density
υ = kinematic viscosity
0 = exit conditions
1 = first point of integration in wall jet

References

[1] Launder, B. E., and Rodi, W., 1983, "The Turbulent Wall Jet—Measurements and Modeling," Annu. Rev. Fluid Mech., **15**, pp. 429–459.
[2] Launder, B. E., and Rodi, W., 1981, "The Turbulent Wall Jet," Prog. Aerosp. Sci., **19**, pp. 81–128.
[3] Lahbabi, F. Z., Boree, J., Nuglisch, H. J., and Charnay G., 1993, "Analysis of Starting and Steady Turbulent Jets by Imaging Processing Techniques," *Proceedings of the 1993 ASME Winter Annual Meeting*, ASME-FED-Vol. 172, ASME, New York, pp. 315–321.
[4] Johari, H., Zhang, Q., Rose, M. J., and Bourque, S. M., 1995, "Impulsively Started Turbulent Jets," AIAA J., **35**, pp. 657–662.
[5] Sangras, R., Kwon, O. C., and Faeth, G. M., 2002, "Self-Preserving Properties of Unsteady Round Nonbuoyant Turbulent Starting Jets and Puffs in Still Fluids," ASME J. Heat Transfer, **124**, pp. 460–469.
[6] Bakke, P., 1957, "An Experimental Investigation of a Wall Jet," J. Fluid Mech., **2**, pp. 467–472.
[7] Beltaos, S., and Rajaratnam, N., 1977, "Impingement of Axisymmetric Developing Jets," J. Hydraul. Res., **15**, pp. 311–325.
[8] Rajaratnam, N., 1976, *Turbulent Jets*, *Developments in Water Science*, Elsevier Amsterdam, pp. 231–240.
[9] Mladin, E.-C., and Zumbrunnen, D. A., 2000, "Alterations to Coherent Flow Structures and Heat Transfer due to Pulsations in an Impinging Air-Jet," Int. J. Therm. Sci., **39**, pp. 236–248.
[10] Lai, H., Naughton, J. W., and Lindberg, W. R., 2000, "Quantitative Light Sheet Imaging of a Turbulent Impinging Jet," *Proceedings of the 9th International Symposium on Flow Visualization*, I. Grant and G. M. Carlomagno, eds., Edinburgh, Scotland, Paper No. 368.
[11] Gonzalez, R. C., and Wintz, P., 1987, *Digital Image Processing*, Addison-Wesley, Reading, MA, pp. 334–359.
[12] Lai, H., 1999, "An Experimental Investigation of Starting Impinging Jets," M.S. thesis, Department of Mechanical Engineering, University of Wyoming, Laramie, WY, July.
[13] Gharib, M., Rambod, E., and Shariff, K., 1998, "A Universal Time Scale for Vortex Ring Formation," J. Fluid Mech., **360**, pp. 121—140.
[14] Naughton, J. W., Cattafesta, III, L. N., and Settles, G. S., 1997, "An Experimental Study of Compressible Turbulent Mixing Enhancement in Swirling Jets," J. Fluid Mech., **330**, pp. 271—305.
[15] Poreh, M., Tsuei, Y. G., and Cermak, J. E., 1967, "Investigation of a Turbulent Radial Wall Jet," ASME J. Appl. Mech., **34**, pp. 457—463.

Satoshi Watanabe
Associate Professor,
Department of Mechanical Engineering Science,
Kyushu University,
6-10-1 Hakozaki,
Higashi-ku, Fukuoka 812-8581, Japan
and
Visiting Associate,
Division of Applied Science and Engineering,
California Institute of Technology,
1200 E. California Boulevard,
Pasadena, CA 91125

Christopher E. Brennen
Division of Engineering and Applied Science,
California Institute of Technology,
Pasadena, CA 91125

Dynamics of a Cavitating Propeller in a Water Tunnel

This study investigates the unsteady dynamics and inherent instabilities of a cavitating propeller operating in a water tunnel. First, the steady characteristics of the cavitating propeller such as the thrust coefficient are obtained by applying continuity and momentum equations to a simple one-dimensional flow tube model. The effects of the tunnel walls as well as those of the propeller operating conditions (advance ratio and cavitation number) are explored. Then the transfer matrix of the cavitating propeller (considered to be the most appropriate way to describe the dynamics of propeller) is obtained by combining the simple stream tube model with the conventional cavity model using the quasi-static cavitation compliance and mass flow gain factor representation. Finally, the surge instability of a cavitating propeller observed by Duttweiler and Brennen (2001) is examined by coupling the present model of the cavitation with a dynamic model for the water tunnel. This analysis shows that the effect of tunnel walls is to promote the surge instability.
[DOI: 10.1115/1.1524588]

1 Introduction

In devices such as pumps, turbines, and marine propellers, cavitation has many adverse effects including material erosion and performance degradation. In addition, it can give rise to instabilities that do not occur in single phase flow. For example, high-speed turbopumps often suffer from severe shaft vibrations due to cavitation instabilities such as cavitation surge and rotating cavitation. With ship's propellers, the fluctuating cavity volume due to the interaction between the propeller and the wake of ship hull can be a significant source of noise and even severe structural vibration of the ship. The large body of work on propeller-hull interactions has been summarized by Weitendorf [1].

Recently, a surge instability, which had not been previously reported, was observed by Duttweiler and Brennen [2] in their experimental work on a cavitating propeller operated in a water tunnel. The phenomenon seems to be similar to the well-known cavitation surge in pumps (Brennen [3]). This suggests that the dynamics of a cavitating propeller are system-dependent, whereas many investigators have implicitly assumed that propellers in water tunnels have dynamic characteristics similar to those operating in open conditions. In the past, studies of the cavitation dynamics of pumps developed the concept of a transfer matrix, which characterizes the relationship between the fluctuating pressure and mass flow rate at inlet and outlet (Brennen and Acosta [4]). In determining the elements of transfer matrix, two important parameters were introduced, namely the cavitation compliance and the mass flow gain factor. The cavitation compliance models the effective compressibility of a cavitating flow. The mass flow gain factor represents the response of the cavity volume to incoming mass flow rate variations. Later, this modeling of cavitating pumps led to the important conclusion that cavitation surge and rotating cavitation of pumps are caused by a positive mass flow gain factor (Brennen [5] and Tsujimoto et al. [6]). The above background suggests that it is useful to use the transfer matrix approach to describe the dynamics of a cavitating propeller in a water tunnel and to use this technique to explore the stability of these flows. In the present study, we construct a one-dimensional flow tube model that includes the effects of the tunnel walls as well as cavities on the propeller. First, we study the steady flow characteristics including the thrust force in order to examine the effects of tunnel walls. Then, the transfer matrix approach is used to model the dynamics of the cavitating propeller, and calculations are made for several cases with assumed cavitation characteristics. Finally, we examine the stability of these cavitating flows by coupling the propeller model with the dynamics of the water tunnel.

2 Outline of the One-dimensional Flow Tube Analysis

2.1 Formulation of the Problem. Consider the one-dimensional flow through a cavitating propeller in a water tunnel as shown in Fig. 1. The propeller (cross-sectional area a_p) is located on the centerline of the tunnel whose cross-sectional area is A. We consider a stream tube containing the propeller whose volumetric flow rate is denoted by q. For simplicity, it will be assumed that the flow is uniformly distributed across the propeller stream tube and is one-dimensional. Friction and mixing losses between the inner and outer flows are neglected. The low-frequency unsteady characteristics of the cavitating propeller will be analyzed under the assumption that the flow can be represented by a series of quasi-static states.

Referring to the propeller stream tube, the incoming and outgoing volumetric flow rates are different due to the rate of change of the cavity volume, dV_c/dt, where V_c is the total cavity volume on the propeller blades. The continuity relation yields

$$u_1 a_1 - u_p^- a_p = -\int_{-\infty}^{0} \frac{\partial a}{\partial t} dx \tag{1}$$

$$u_2 a_2 - u_p^+ a_p = \int_{0}^{\infty} \frac{\partial a}{\partial t} dx \tag{2}$$

$$u_p^+ a_p - u_p^- a_p = dV_c/dt \tag{3}$$

$$u_2 a_2 + U_2(A - a_2) - u_1 A = dV_c/dt \tag{4}$$

where u and U denote velocities in the inner and outer flows, a denotes cross-sectional area of the inner tube, and the subscripts 1, 2, and p, respectively, denote quantities far upstream, far downstream, and at the propeller. Superscripts $+$ and $-$, respectively, denote the outlet from and the inlet to the propeller. It has been assumed that the velocities in the inner and the outer flows are the same far upstream. The right-hand sides of Eqs. (1) and (2) represent the volume change of the stream tube upstream and downstream of the propeller; later these will be ignored for simplicity.

The relation between the pressures far upstream and far downstream is obtained by applying Bernoulli's equation in the outer flow as follows:

Contributed by the Fluids Engineering Division for publication in the JOURNAL OF FLUIDS ENGINEERING. Manuscript received by the Fluids Engineering Division February 1, 2002; revised manuscript received August 15, 2002. Associate Editor: S. L. Ceccio.

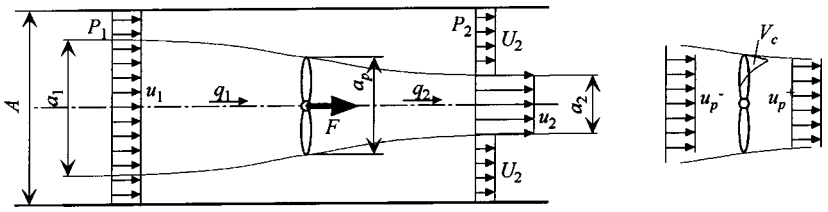

Fig. 1 Propeller being operated at the center of axis

$$P_2-P_1=\frac{1}{2}\rho(u_1^2-U_2^2)-\rho\int_{-\infty}^{\infty}\frac{\partial U}{\partial t}dx \tag{5}$$

where the last term of the right-hand side is the inertia effect in the control volume.

Now, we calculate the thrust force F produced by the propeller in three ways. First, applying the momentum theorem to a control volume containing all the tunnel flow, we obtain

$$\rho u_1^2A+P_1A+F=\rho U_2^2(A-a_2)+\rho u_2^2a_2+P_2A+dM/dt.$$

The last term in the right-hand side is rate of the change of the momentum in the control volume, represented by

$$\begin{aligned}\frac{dM}{dt}&=\rho\frac{d}{dt}\int_{-\infty}^{\infty}[ua+U(A-a)]dx\\&=\rho\frac{d}{dt}\left\{\int_{-\infty}^{\infty}[ua+U(A-a)-u_1A]dx+\int_{-\infty}^{\infty}u_1Adx\right\}\\&=\rho\frac{d}{dt}\left\{\int_0^{\infty}\frac{dV_c}{dt}dx+A\int_{-\infty}^{\infty}u_1dx\right\}\\&=\rho\int_0^{\infty}\frac{d^2V_c}{dt^2}dx+\rho A\int_{-\infty}^{\infty}\frac{du_1}{dt}dx\end{aligned}$$

which yields

$$\begin{aligned}F=&\frac{1}{2}\rho(u_1-U_2)A(2u_2+U_2-u_1)+\rho(u_2+U_2)\frac{dV_c}{dt}\\&+\left[\rho A\int_{-\infty}^{\infty}\frac{\partial(u_1-U)}{\partial t}dx+\rho\int_0^{\infty}\frac{d^2V_c}{dt^2}dx\right].\end{aligned}\tag{6}$$

Second, we obtain the total pressure difference across the propeller from the Euler head,

$$\Delta p^T=\rho U_Tv_p=\rho U_T(U_T-u_p^+\cot\beta)-\rho\frac{c}{\sin\beta}\frac{du_p^+}{dt},$$

where β and c, respectively, denote the discharge flow angle and the chord length of the blade. The last term in this equation represents the inertia effect of the fluid in the blade passage. Since the static pressure difference $p_{\text{out}}-p_{\text{in}}$ is given by

$$p_{\text{out}}-p_{\text{in}}=\frac{1}{2}\rho(U_T^2-u_p^{+2}\cot^2\beta)-\rho\frac{c}{\sin\beta}\frac{du_p^+}{dt}$$

and the thrust force can be computed as

$$\begin{aligned}F&=(p_{\text{out}}-p_{\text{in}})a_p+\rho(u_p^{+2}-u_p^{-2})a_p\\&=\frac{1}{2}\rho(U_T^2-u_p^{+2}\cot^2\beta)a_p+\rho(u_p^++u_p^-)\frac{dV_c}{dt}-\rho\frac{a_pc}{\sin\beta}\frac{du_p^+}{dt}.\end{aligned}\tag{7}$$

Third, the pressures p_{in} and p_{out} may be related to the upstream and downstream conditions using Bernoulli's equation:

$$p_{\text{in}}=P_1+\frac{1}{2}\rho u_1^2-\frac{1}{2}\rho u_p^{-2}-\rho\int_{-\infty}^{0}\frac{\partial u}{\partial t}dx$$

where the last term is the inertance in the stream tube. Applying Bernoulli's equation between the outlet of the propeller and far downstream, we obtain

$$\begin{aligned}p_{\text{out}}&=P_2+\frac{1}{2}\rho\left(u_2^2+v_p^{+2}\frac{a_p}{a_2}\right)-\frac{1}{2}\rho(u_p^{+2}+v_p^{+2})+\rho\int_0^{\infty}\frac{\partial u}{\partial t}dx\\&=P_2+\frac{1}{2}\rho u_2^2-\frac{1}{2}\rho u_p^{+2}+\frac{1}{2}\rho(U_T-u_p^+\cot\beta)^2\left(\frac{a_p}{a_2}-1\right)\\&\quad+\rho\int_0^{\infty}\frac{\partial u}{\partial t}dx.\end{aligned}$$

Then the thrust force F follows as

$$\begin{aligned}F&=(p_{\text{out}}-p_{\text{in}})a_p+\rho(u_p^{+2}-u_p^{-2})a_p\\&=\frac{1}{2}\rho\left[(u_2^2-U_2^2)+(U_T-u_p^+\cot\beta)^2\left(\frac{a_p}{a_2}-1\right)\right]a_p\\&\quad-\frac{1}{2}\rho(u_p^++u_p^-)\frac{dV_c}{dt}+\rho a_p\int_{-\infty}^{\infty}\frac{\partial(u-U)}{\partial t}dx.\end{aligned}\tag{8}$$

For the purpose of the general discussion, we have considered all possible unsteady effects in the above formulation, namely the effects of volume change of the stream tubes in Eqs. (1) and (2), the inertia effects upstream and downstream of the propeller in Eqs. (5), (6), and (8), and the inertia effect in the propeller in Eq. (7) as well as the effects of the cavity volume change dV_c/dt in Eqs. (3) and (4). To evaluate many of these terms, we need to know the shape of the stream tube, which is beyond the scope of the present one-dimensional stream tube analysis. Consequently, some compromises are needed in order to proceed. First we neglect the stream tube volume changes in Eqs. (1) and (2) on the basis that these cancel and thus produce no net perturbation within the water tunnel. We note, however, that this superficial argument may need further examination. Second, we neglect the inertance terms in Eqs. (5), (6), and (8) on the basis that past experience has suggested that we can consider these contributions to be lumped into the other inertance contributions in the tunnel circuit. Again this may need additional examination in the future. In summary, we choose to examine only the unsteady effects associated with dV_c/dt in Eqs. (3) and (4).

Summarizing, we note that the eight equations (1) through (8) contain eight unknowns U_2, u_2, u_p^+, u_p^-, a_1, a_2, F, and P_2 assuming that the propeller operating parameters u_1, P_1, u_T, the discharge flow angle, β, and the rate of change of the cavity volume, dV_c/dt, are given. Information on the discharge flow angle β especially for cavitating conditions will be discussed in the following subsection. The rate of change of the cavity volume, dV_c/dt, will be modeled in Section 2.3.

2.2 Discharge Flow Angle. To quantify the discharge flow angle β, we resort to an empirical model for the deviation angle, θ

(the difference between the discharge blade angle β_2 and the discharge flow angle β), which takes into account the fact that the deviation will be increased by the presence of cavities on the propeller blades. Specifically, we adopt the following empirical model for the deviation angle:

$$\theta = 0 \qquad \text{for } \lambda > \lambda_{cr}$$

$$\theta = \left(\beta_2 - \tan^{-1}\frac{u_p}{U_T}\right)\left(1 - \frac{\lambda}{\lambda_{cr}}\right)^2 \quad \text{for } \lambda > \lambda_{cr} \tag{9}$$

where we have introduced the parameter $\lambda = \sigma/2\alpha$, where $\sigma = 2(p_{\text{in}} - p_v)/\rho U_T^2$ is the operating cavitation number of the propeller and $\alpha = \beta_1 - \tan^{-1}(u_p/u_T)$ is the incidence angle on the propeller blades. The argument for this single parameter representation, $\theta(\lambda)$, is that classical linear theory (Tulin [7] and Brennen [8]) shows that the cavity length to chord ratio is a function only of λ and consequently the expected deviation should similarly be a function of λ. Though nonlinear and three-dimensional effects may generate departures from this simple functional dependence, it seems appropriate to proceed with this simplification in this approximate analysis.

Equation (9) has the properties that, if the cavity is small (λ is large), the flow discharges from the propeller parallel to the blade. At the other extreme, when the cavity is very long ($\lambda \to 0$), the propeller performance will be degraded and the flow turning angle through the propeller diminished (there may be a certain small λ at which the propeller breaks down but this detail is neglected for simplicity.) The critical value, λ_{cr}, below which the deviation begins, could be determined theoretically or empirically. This study will use a typical value of $\lambda_{cr} = 1$.

2.3 Cavity Volume Change. We assume that the cavity volume $V_c(p_{\text{in}}, u_p^-)$ is a function of the inlet pressure p_{in} and inflow velocity u_p^-. Then, the rate of change of the cavity volume can be expressed as

$$\frac{dV_c}{dt} = -K\frac{dp_{\text{in}}}{dt} - M\frac{du_p^-}{dt} \tag{10}$$

where $K = -\partial V_c/\partial p_{\text{in}}$ and $M = -\partial V_c/\partial u_p^-$ are, respectively, the cavitation compliance and the mass flow gain factor (Brennen and Acosta [4]). These important parameters are nondimensionalized as follows:

$$\frac{K^*}{2\pi} = -\frac{\partial V_c/a_p R}{\partial \sigma} = -\frac{\rho U_T^2/2}{a_p R}\frac{\partial V_c}{\partial p_{\text{in}}} = \frac{\rho R^2 \Omega^2}{2\pi R^3}K = \frac{1}{2\pi}\frac{\rho \Omega^2}{R}K$$

$$M^* = -\frac{\partial V_c/a_p R}{\partial u_p^-/U_T} = -\frac{U_T}{a_p R}\frac{\partial V_c}{\partial u_p^-} = \frac{R\Omega}{\pi R^3}M = \frac{\Omega}{\pi R^2}M$$

where Ω is the rotational frequency of the propeller, and K^* and M^* are nondimensional values of the cavitation compliance and the mass flow gain factor used by Duttweiler and Brennen [2]. In this study, the values of K and M are estimated using free streamline theory (Otsuka et al. [9] and Watanabe et al. [10]).

3 Steady Calculation

In this section, we discuss the steady flow solutions of Eqs. (1) to (8) by eliminating the unsteady terms. Then, Eqs. (1)–(10) can be solved provided the operating conditions u_1, P_1, U_T and the discharge flow angle, β, are specified. For the purposes of illustration, we choose to present results for typical blade angles, β_1 and β_2, of 25 deg. Moreover, the results are best presented using the following nondimensional parameters; the advance ratio J_1, a propeller flow coefficient J_p and a thrust coefficient of the propeller C_T defined as follows:

$$J_1 = \pi u_1/U_T$$

$$J_p = \pi\phi = \pi u_p/U_T$$

$$C_T = F/\tfrac{1}{2}\rho U_T^2 a_p$$

where ϕ is the propeller flow coefficient (also used in describing pump flows). As shown later, if we decrease the incoming velocity u_1, the inner flow tube expands far upstream and its cross-sectional area a_1 reaches that of the tunnel, A, at a certain value of u_1. When the incoming velocity is smaller than this value, Eq. (5) no longer applies. In such cases, the steady solution is obtained by setting $a_1 = A$ and $U_2 = 0$, and eliminating Eq. (4), because it becomes identical to the combination of Eqs. (1)–(3).

3.1 Noncavitating Results. Results for the noncavitating case (no deviation angle) are shown in Fig. 2. Various values of the cross-sectional area ratio, A/a_p, were selected in order to examine the effect of the presence of the tunnel walls. The case with $A/a_p = 1$ corresponds closely to that of a typical axial flow pump, because all the flow from upstream proceeds through the propeller (assuming no tip leakage flow for simplicity) and there is no outer flow. For the cases with $A/a_p = 2$ and 10, a critical advance ratio (approximately 0.58 and 0.12 for $A/a_p = 2$ and 10, respectively) exists at which the cross-sectional area of stream tube far upstream a_1 equals to that of the duct A. Below the critical advance ratio, the propeller works like an axial flow pump with all fluid flowing through the propeller. The results for $A/a_p = 10$ have been found to adequately represent the open condition ($A/a_p = \infty$) except at very low advance ratios, where the analysis breaks down for reasons discussed elsewhere.

Figures 2(*a*)–(*c*) present the thrust coefficient C_T, the propeller flow coefficient J_p, and the cross-sectional areas a_1/a_p and a_2/a_p plotted against the advance ratio J_1. For $A/a_p = 2$ and 10, as the advance ratio decreases, the flow coefficient decreases gradually and the thrust coefficient increases gradually. This is because, as the advance ratio is decreased, the propeller is taking fluid from a wider upstream stream tube. The variations of the thrust coefficient and the flow coefficient are more gradual than those for $A/a_p = 1$. However, below the critical advance ratio where the propeller works like an axial flow pump, the flow coefficient rapidly decreases and the thrust coefficient rapidly increases, and these variations are more significant than for $A/a_p = 1$. The decrease in the flow coefficient is related directly to the advance ratio, so that the slope of the flow coefficient in Fig. 2(c) gets steeper as the duct gets wider.

Given these steady operating characteristics, it is valuable to consider the quasi-static response to low frequency fluctuations of the incoming flow velocity u_1. For illustrative purposes, we compare the case of $A/a_p = 2$ with that for a pump ($A/a_p = 1$). Consider first the case when the advance ratio is larger than the critical advance ratio. As the upstream flow velocity varies, the flow rate through the propeller varies less when $A/a_p = 2$ than when $A/a_p = 1$ (Fig. 2(b)). However, when the advance ratio is smaller than the critical value, this trend is reversed. If the propeller were cavitating, these results would suggest that, at larger advance ratios, the mass flow gain factor will be smaller for $A/a_p = 2$ than that for $A/a_p = 1$, whereas at smaller advance ratios, the mass flow gain factor will be larger for $A/a_p = 2$. This is important since the mass flow gain factor is responsible for cavitation instabilities of turbomachinery and a large mass flow gain factor implies a more unstable system.

The surge instability of a cavitating propeller, reported by Duttweiler and Brennen [2], is an example of cavitation instability caused by a positive mass flow gain factor. They examined two different configurations of the propeller, one in which the propeller is operated in front of a support fairing, and the other in which the propeller is operated downstream of that fairing, and observed a violent surge instability only for the latter case. The explanation for this difference is unknown, but one explanation might be as follows. The presence of the fairing can be considered to be the blockage, so that the effective flow path upstream of the propeller is smaller for the case with the propeller operated downstream of

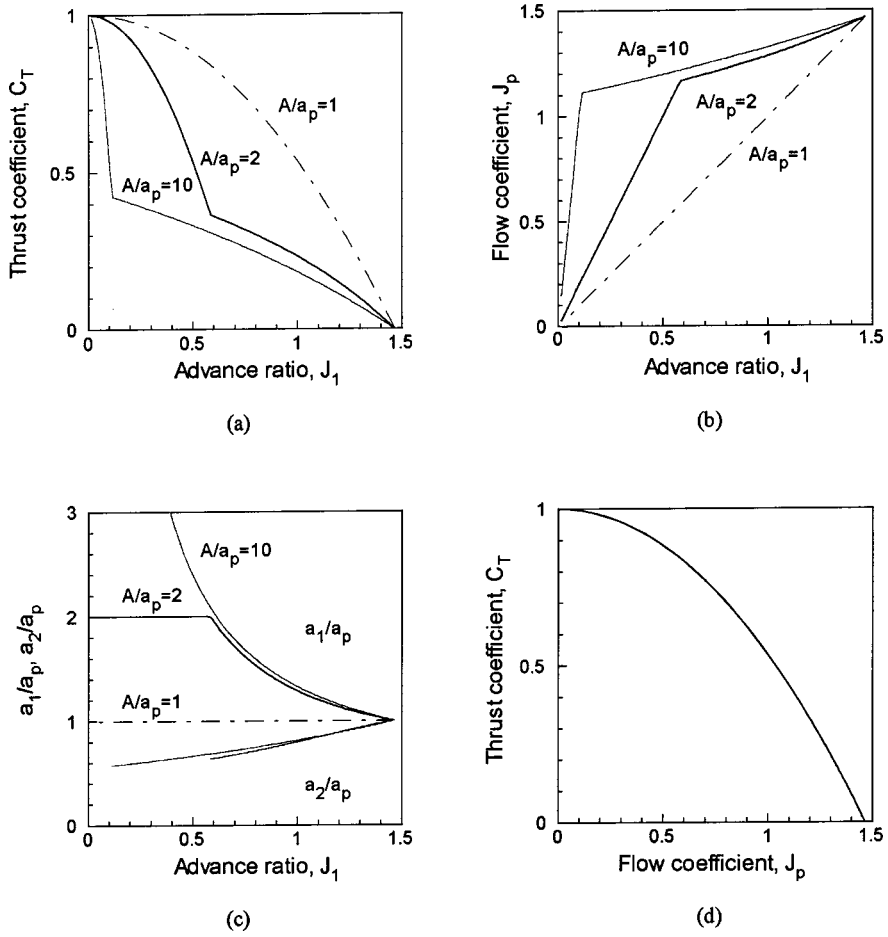

Fig. 2 Steady characteristics of noncavitating propeller with the constant exit flow angle of $\beta=25$ deg. The propeller is located at the center of the duct with cross-sectional areas of $A/a_p=1$, 2, and 10.

the fairing. Figure 2(b) indicates that the critical value of the advance ratio is larger when the propeller is operated in the narrower duct. So, as the advance ratio decreases, the propeller could readily shift into operation as a pump. The result would be that the mass flow gain factor is larger for the propeller operated downstream of the fairing.

3.2 The Case With Cavitation. Figures 3(a) and (b) present the thrust coefficient C_T and the flow coefficient J_p plotted against the advance ratio J_1 for various cavitation numbers, σ. Recall that in this model the presence of the cavitation affects the results only by altering the exit flow angle (Eq. (9)). Figure 4 shows the thrust coefficient C_T plotted against the cavitation num-

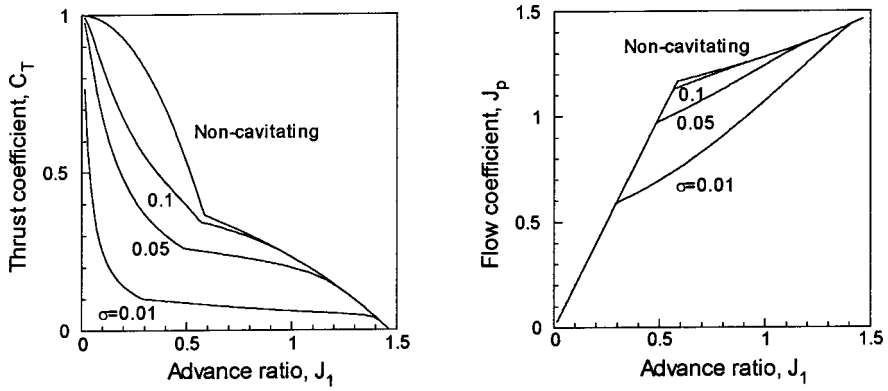

Fig. 3 Effect of cavitation number on thrust coefficient C_T and propeller flow coefficient Jp. The presence of cavitation is taken into account through the deviation angle of the flow exiting from the propeller [$A/a_p=2$].

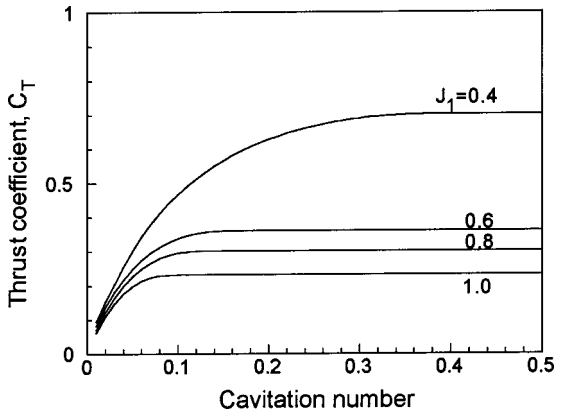

Fig. 4 Thrust coefficient C_T versus cavitation number σ for various advance ratios J_1. The effects of cavitation are taken into account through the deviation angle of the exit flow.

ber σ for various advance ratios J_1. Note that the deterioration of the thrust coefficient as a result of cavitation is well simulated by introducing the deviation angle due to the presence of cavitation modeled by Eq. (9).

Note also that the flow coefficient has a steeper slope against the advance ratio for smaller cavitation numbers as shown in Fig. 3(*b*). This is because, as the cavitation number is decreased, the thrust coefficient decreases because of the losses through the deviation angle associated with the presence of cavitation on the propeller blades. Then the flow rate through the propeller must decrease to compensate for the decreased thrust. The steeper slope of the flow coefficient against the advance ratio means that the flow rate through the propeller is more sensitive to the upstream flow variation and the mass flow gain factor is larger because a small advance ratio change makes a large propeller flow rate change. This will tend to promote a surge instability.

4 Quasi-Steady Analysis

In this section, we analyze the low-frequency unsteady characteristics of the cavitating propeller. The system of equations consists of nonlinear equations. However, in order to utilize the conventional transfer function methodology, we linearize the problem. For example, the upstream flow velocity is expressed by

$$u_1=\overline{u_1}+\mathrm{Re}[\tilde{u}_1\exp(j\omega t)].$$

After substituting similar expressions for all the unknowns, Eqs. (1)–(8) are then divided into steady and unsteady parts and linearized under the assumption of small fluctuations. The unsteady parts of the equations consist of linear equations for the unsteady components, the eight unknowns U_2, u_2, u_p^+, u_p^-, a_1, a_2, F, and P_2 as well as the quantities, u_1, P_1, β, and dV_c/dt. The unsteady component of β is obtained by the linearized version of Eq. (9), which diminishes for larger values of σ. The rate of the change of cavity volume dV_c/dt is given by Eq. (10).

The total mass flow rate and static pressure downst ream of the propeller are defined downstream of the mixing of the flows in the inner and outer stream tubes. The mass flow rate and pressure after the mixing, m_2 and P_2', are obtained by applying continuity and momentum conservation as follows:

$$m_2=\rho[u_2a_2+U_2(A-a_2)]=\rho u_2'A$$

$$P_2A+\rho u_2^2a_2+\rho U_2^2(A-a_2)=P_2'A+\rho u_2'^2A.$$

Using these equations, we can relate the downstream fluctuations to the inlet fluctuations using the conventional transfer matrix (Brennen [3]):

$$\begin{Bmatrix}\tilde{p}_2^T\\ \tilde{m}_2\end{Bmatrix}=\begin{bmatrix}T_{11} & T_{12}\\ T_{21} & T_{22}\end{bmatrix}\begin{Bmatrix}\tilde{p}_1^T\\ \tilde{m}_1\end{Bmatrix}$$

where p^T and m are total pressure and mass flow rate, respectively.

4.1 Example Calculations. Figure 5 presents a typical calculation of the transfer matrix for an advance ratio of $J_1=1.0$ and duct cross-sectional areas of $A/a_p=1$, 2 and 10. For illustrative purposes, values of the compliance and mass flow gain factor $(K^*/2\pi,M^*)$ of (0.1,1.0) are selected since these values are typical of those obtained by previous researchers, [3–5]. The change of the exit flow angle β is neglected for simplicity, assuming $\sigma=\infty$. Note that T_{21} takes a similar value for all cases while there are large differences in the other elements of transfer matrix. If we consider the case with no discharge mass flow fluctuations, the

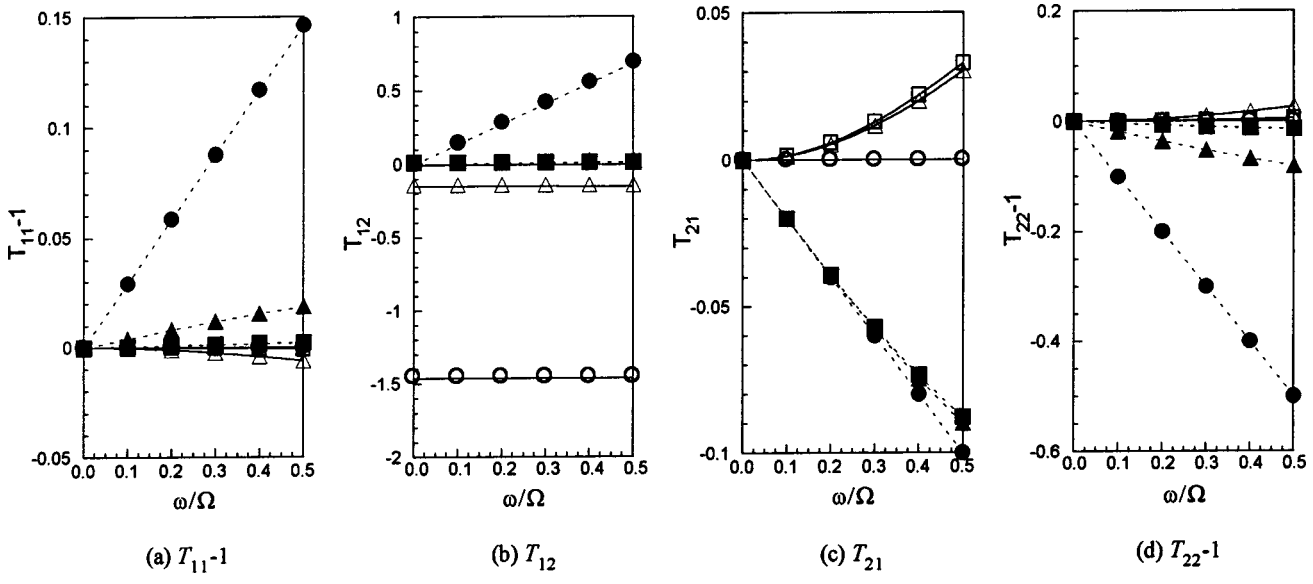

Fig. 5 Calculated transfer matrices of the cavitating propeller for an advance ratio, $J_1=1.0$, and $(K^*/2\pi,M^*)=(0.1,1.0)$ and for various values of $A/a_p=1$(○ ●), 2(△ ▲), and 10(□ ■), where open and closed symbols denote real and imaginary parts of matrix elements, respectively. The change of the exit flow angle of β is neglected.

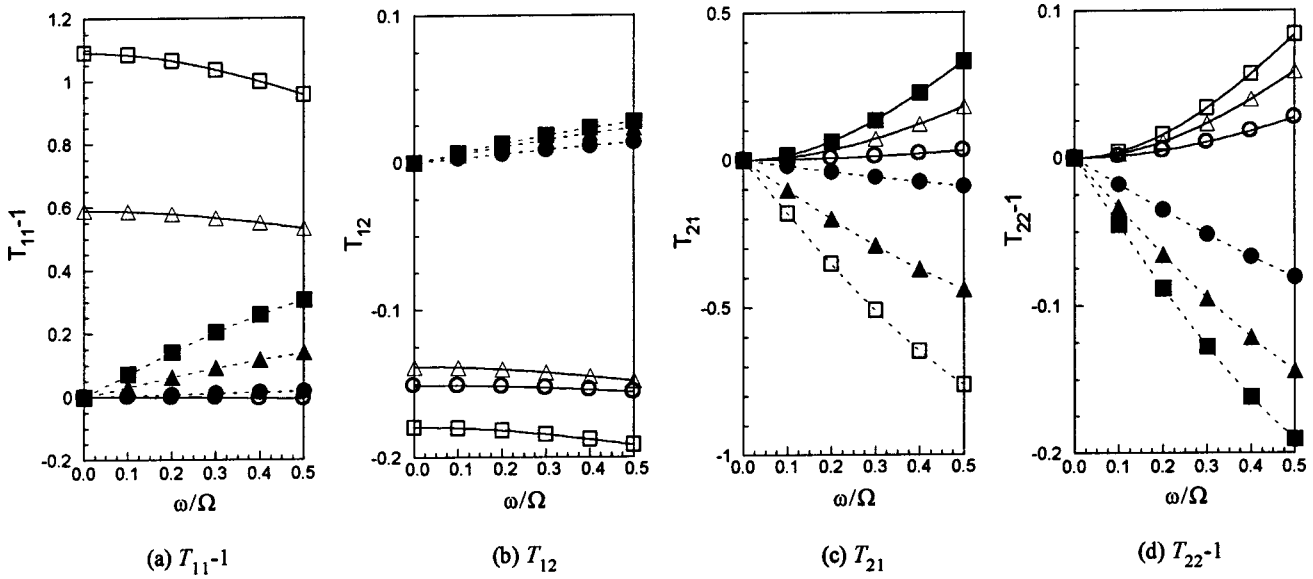

Fig. 6 Calculated transfer matrices of the cavitating propeller with $A/a_p=2$ and an advance ratio, $J_1=1.0$, for the various cavitation numbers $\sigma=\infty$(○ ●), 0.05(△ ▲), and 0.01(□ ■), where open and closed symbols denote real and imaginary parts of matrix elements, respectively

propeller operated in a wider duct (for example $A/a_p=10$) might be the most stable because of the large negative impedance with the small imaginary part of T_{22} and the large imaginary part of T_{21}.

Figure 6 shows the transfer matrix for an advance ratio of $J_1=1.0$, a duct cross-sectional area of $A/a_p=2$ and various cavitation numbers. The values of $(K^*/2\pi,M^*)$ are again set to be (0.1,1.0) for all cases. Head deterioration due to the presence of cavitation is implicitly included through the assumed changes in the deviation angle β. All elements are affected by the head deterioration, but the stability does not seem to be significantly changed. The imaginary parts of both T_{21} and T_{22} are increased by the head deterioration.

4.2 Coupling With Streamline Theory. Otsuka et al. [9] and Watanabe et al. [10] have obtained the cavitation compliance and mass flow gain factor of cavitating cascades by a free streamline theory. Here, we utilize their results in order to assess appropriately values of $K^*/2\pi$ and M^*. The values of $(K^*/2\pi,M^*)$ obtained by those investigations are shown in Fig. 7 for typical values for the solidity (1.0), the stagger angle ($\beta=25.0$ deg) and the number of blades ($Z_N=5$). Because Otsuka et al. and Watanabe et al. examine only two-dimensional flows around foils, the cavity size per blade is treated as a cross-sectional area V_{cpb} (not a volume) and the scaling as $V_c=Z_NRV_{cpb}/2$ is used as a best estimate. Note that $(K^*/2\pi,M^*)$ are functions of the parameter $\lambda=\sigma/2\alpha$, where σ is cavitation number at inlet to the propeller.

Now, rather than use the fixed values of K^* and M^*, we calculate the transfer function using the above relations between $(K^*/2\pi,M^*)$ and $\lambda=\sigma/2\alpha$. Results are shown in Figs. 8 and 9 for $A/a_p=2$ and 10, respectively. Three cases with different upstream cavitation numbers $\sigma_{up}=0.15$, 0.20, and 0.5 are examined. The advance ratio J_1 is 1.0, which is larger than the critical value. Note that, only for the case with $\sigma_{up}=0.15$, is the parameter $\lambda=\sigma/2\alpha$ less than unity and therefore only in this case is there head deterioration with increasing deviation angle. The cavitation compliance $K^*/2\pi$ varies from 0.018 to 0.172 for $A/a_p=2$ and from

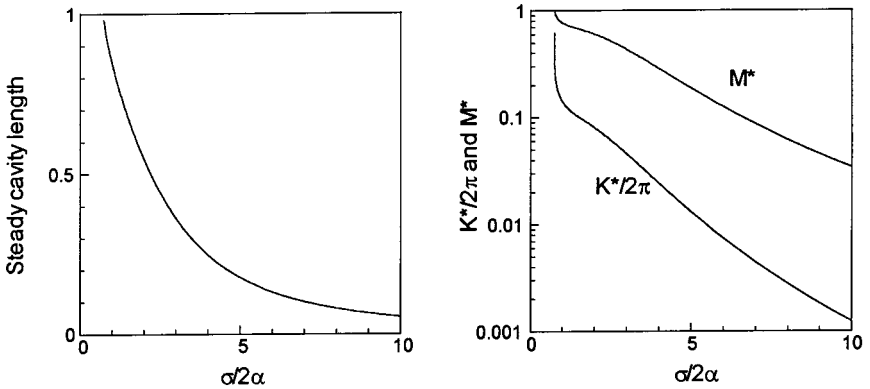

Fig. 7 Steady cavity length and the quasi-static cavitation compliance and mass flow gain factor plotted against $\sigma/2\alpha$ obtained by a free streamline theory (Watanabe et al. [10]). [solidity=1.0, stagger angle $\beta=25.0$ deg, $Z_N=5$].

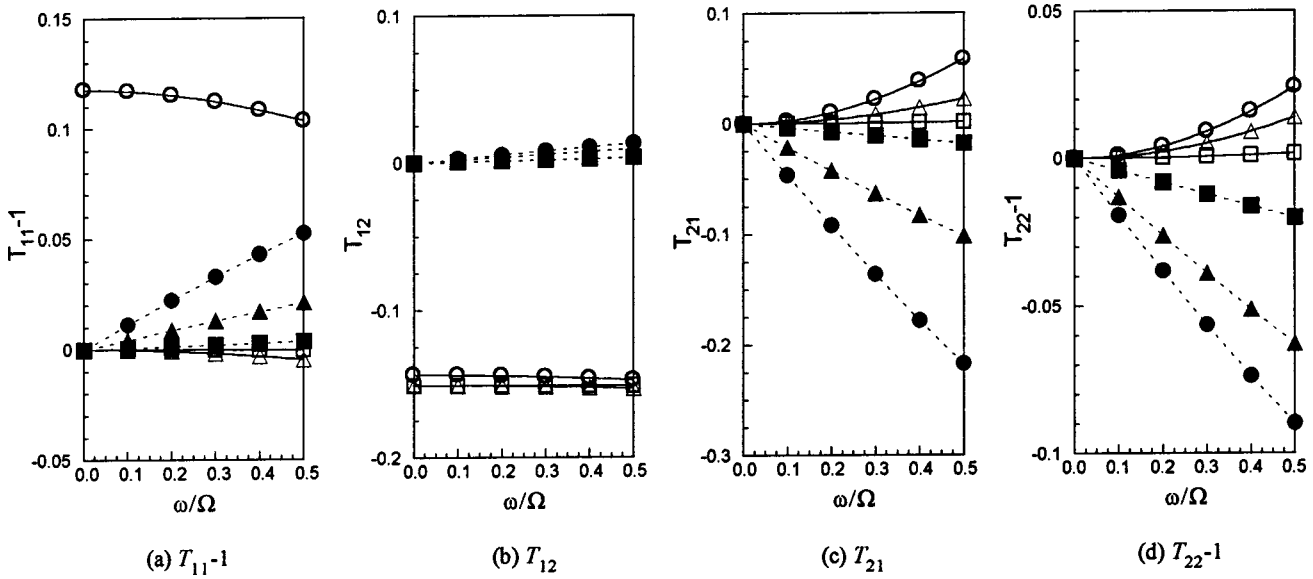

Fig. 8 Calculated transfer matrices of the cavitating propeller with $A/a_p=2$ and an advance ratio, $J_1=1.0$, for the various cavitation numbers $\sigma_{up}=0.15$(○ ●), 0.20(△ ▲), and 0.50(□ ■), where open and closed symbols denote real and imaginary parts of matrix elements, respectively. The values of cavitation compliance and mass flow gain factor are obtained from Fig. 7.

0.009 to 0.143 for $A/a_p=10$. The mass flow gain factor M^* varies from 0.231 to 0.831 for $A/a_p=2$ and from 0.140 to 0.777 for $A/a_p=10$. These values are slightly smaller for the case with $A/a_p=10$. This is because, as shown in Fig. 2(*b*), the flow coefficient is slightly larger for the case with $A/a_p=10$, and this results in a smaller incidence angle.

From Figs. 8 and 9, it is seen that T_{21} takes similar values for all the cavitation numbers, while the other elements of the transfer matrix are much affected by the presence of cavitation. Note that the elements $T_{11}-1$, T_{12} and $T_{22}-1$ are much smaller for the case with $A/a_p=10$, whereas the element T_{21} is the same order for both cases. This implies that the propeller with $A/a_p=10$ is more stable since the imaginary part of T_{22} is smaller; in other words the effective mass flow gain factor is smaller.

The advance ratio J_1 is also an important parameter, because there is a critical value which separates normal operation from pump-like operation. It would be interesting to compare the transfer matrices for normal and pump-like operations, but unfortunately the free streamline theory is only applicable to high flow rates and high advance ratios.

4.3 Facility and Cavitation Dynamics. We now consider the dynamics of the whole system of the water tunnel, taking the experimental arrangement used by Duttweiler and Brennen [2] as an example. Figure 10 shows the schematic of the facility and cavitation dynamics used by Duttweiler and Brennen. The facility dynamics are characterized by (i) the compliance, $C_{ot}[=405]$, of the overflow tank that allows control of the pressure within the

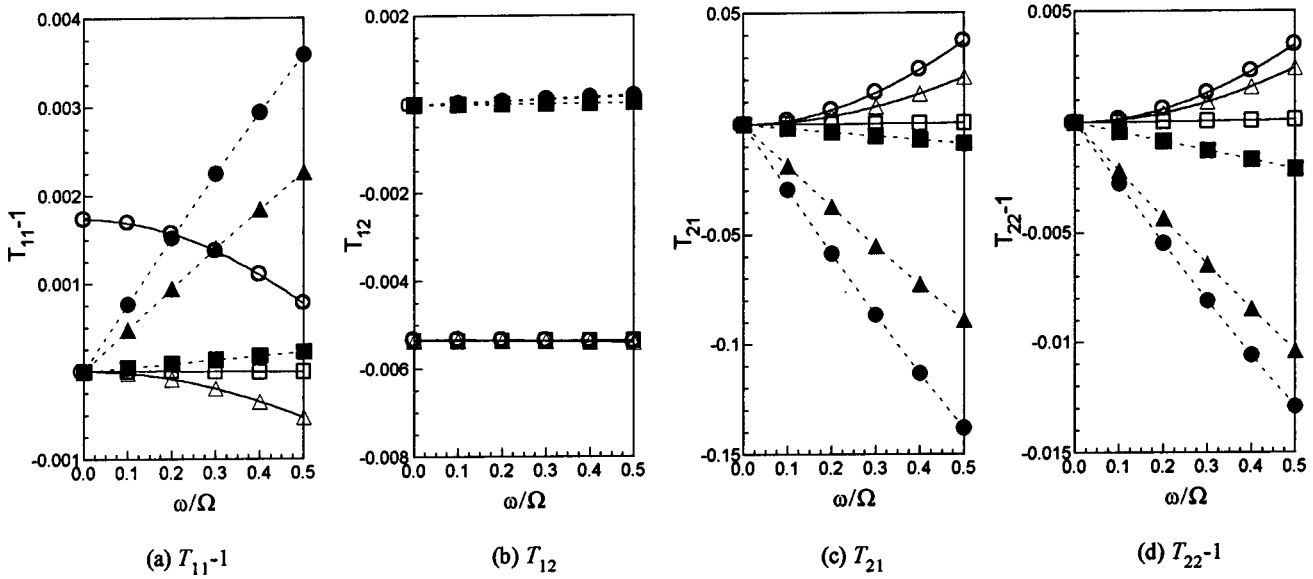

Fig. 9 Calculated transfer matrices of the cavitating propeller with $A/a_p=10$ and an advance ratio, $J_1=1.0$, for the various cavitation numbers $\sigma_{up}=0.15$(○ ●), 0.20(△ ▲), and 0.50(□ ■), where open and closed symbols denote real and imaginary parts of matrix elements, respectively. The values of cavitation compliance and mass flow gain factor are obtained from Fig. 7.

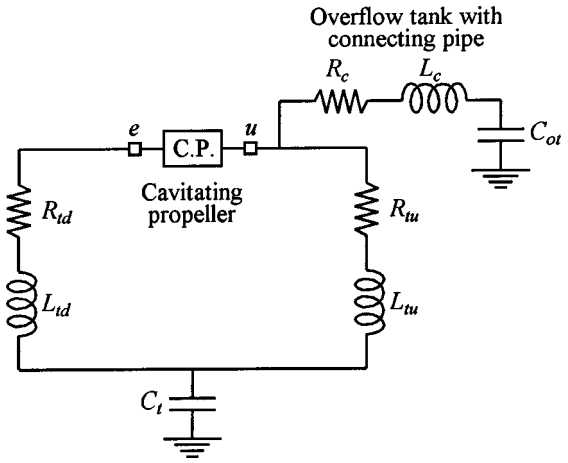

Fig. 10 Schematic of facility and cavitation dynamics

facility and therefore has the only deliberate free surface, (ii) the resistance, $R_c[=0.0295]$, and inertance, $L_c[=57.3]$, of the pipe connecting the tunnel with the overflow tank, (iii) the compliance, $C_t[=1970]$, associated with the expansion and contraction of the walls of the tunnel, and (iv) the resistances, $R_{tu}[=0.0]$ and $R_{td}[=0.0]$, and inertances, $L_{tu}[=0.953]$ and $L_{td}[=2.10]$, associated with the typical flow paths upstream and downstream of the cavitating propeller. The parameters used by Duttweiler and Brennen [2] were normalized using the propeller radius, R, and the propeller rotation frequency, Ω, to obtain the values shown in the square brackets after each symbol.

The dynamics of the system can be characterized by considering the response of the system to a fluctuating mass flow rate, $\tilde{m}_e$, injected at some specific location, e, in the system (Fig. 10). We define a system impedance, Z, as follows:

$$Z=\frac{\tilde{p}_e^T}{\tilde{m}_e}$$

where $\tilde{p}_e^T$ is the total pressure fluctuation at e. Note that, in general, the impedance Z is complex.

Using the present methodology coupled with the dynamics of the water tunnel identified by Duttweiler and Brennen [2], we have calculated the system impedance Z for the case with advance ratio $J_1=0.64$ and cavitation number $\sigma_{up}=0.25$. The real part of Z is plotted in Fig. 11 against the normalized frequency, ω/Ω. In calculating the transfer matrix of propeller, we set $A/a_p=3.16$ and $Z_N=6$ and the cavitation characteristics (M,K) shown in Fig. 7 were used. The positive peak at $\omega/\Omega=0.007$ is largely due to the impedance of overflow tank. The shallow negative peak around

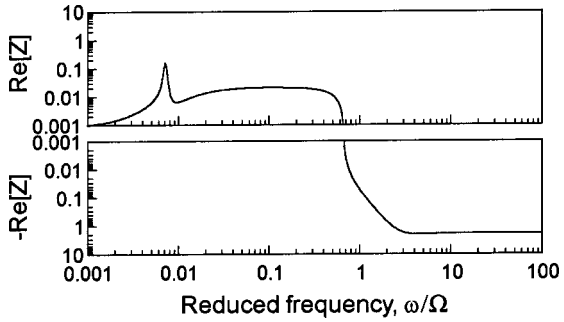

Fig. 11 Example of the system impedance, *Z*. Mass flow fluctuation is imposed at point *e* in Fig. 10. Real part of the system impedance is plotted against the various excited frequencies. [$J_1=0.64$, $\sigma_{up}=0.25$. *K and *M** are evaluated from Fig. 7.]**

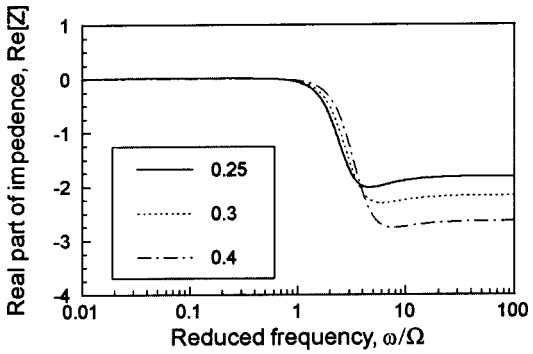

Fig. 12 Real part of the system impedance for various upstream cavitation numbers, σ_{up}. [$J_1=0.64$. *K and *M** are evaluated from Fig. 7.]**

$\omega/\Omega=3$ might indicate the existence of surge instability, but the frequency is much higher than the value of $\omega/\Omega=0.2$ observed in the experiments of Duttweiler and Brennen [2]. Moreover, if we compare the present result with the system impedance obtained by Duttweiler and Brennen, we find that the frequency obtained by the present analysis is still much higher than the experimental values and the peak is much shallower. The explanation for this discrepancy is unknown, but the following may be pertinent. In the pump cases, the elements T_{21} and $T_{22}-1$ are purely imaginary when the cavitation compliance and mass flow gain factor considered are purely real. On the other hand, in the propeller cases, T_{21} and $T_{22}-1$ are complex because of our one-dimensional flow tube model. Complex values of T_{21} and $T_{22}-1$ mean that the system responds as if we have complex values of the cavitation compliance and mass flow gain factor.

Figure 12 shows the real part of system impedance for the case with three different cavitation numbers $\sigma_{up}=0.25$, 0.2, and 0.15. The frequency at the negative peak decreases as the cavitation number is decreased, but is still larger than the experimental value of $\omega/\Omega=0.2$. One possible explanation for the discrepancy is that the model considers only the sheet cavitation on the blade surface. However, a large volume change in the tip cavity during a surge cycle was clearly observed in experiments by Duttweiler and Brennen [2]. It is important to note that the present one-dimensional stream tube model may lose validity at the lower advance ratios, where the flow around the propeller is very three-dimensional. However, because the surge instability is a system instability in which the large amount of fluid is accelerated one-dimensionally by the volume change of cavities, the present method is expected to be applicable even at those low advance ratios provided we could evaluate the cavitation compliance and the mass flow gain factor of all the cavitation including the tip vortex cavities. The unsteady characteristics of tip vortex cavities need further investigation.

Figure 13 shows the values of $\sigma/2\alpha$ just upstream of the propeller plotted in the $\sigma_{up}-J_1$ plane obtained by the present steady analysis. According to the linear theory [11], cavitation instabilities of a two-dimensional cascade are dependent only on the parameter $\sigma/2\alpha$. The instability boundary obtained by Duttweiler and Brennen [2] is also plotted in the figure. We can see that the value of $\sigma/2\alpha$ is nearly constant along the instability boundary, which means that the stability depends on the local condition at the propeller inlet rather than the advance ratio or upstream cavitation number.

5 Conclusion

This paper has evaluated the quasi-static transfer matrices for a cavitating propeller operating in a water tunnel. Simple flow models based on a one-dimensional flow tube analysis are used. The effects of the presence of cavitation, and of the blockage due to

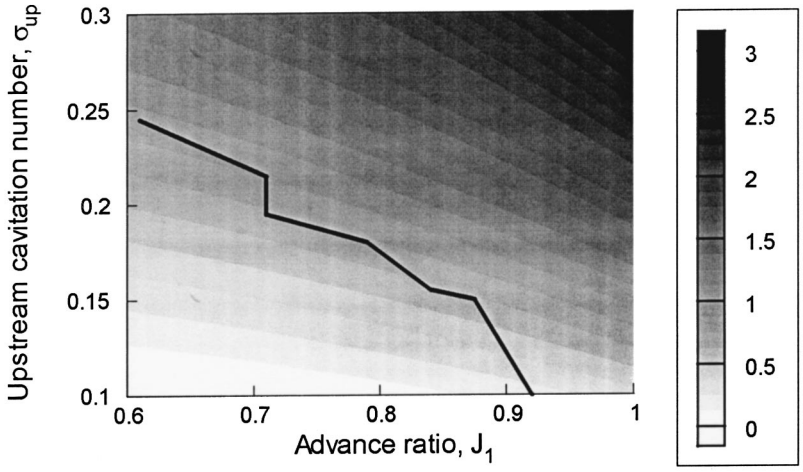

Fig. 13 The ratio of cavitation number to twice of incidence angle, $\sigma/2\alpha$, is plotted for various upstream conditions σ_{up} and J_1. The solid line represents the boundary of the onset of surge instability observed by Duttweiler and Brennen [2], showing that the surge instability occurs in the region below this line.

the tunnel walls are examined. The former is modeled by the head deterioration through the deviation of the exit flow, and the conventional cavitation characteristics, the cavitation compliance and the mass flow gain factor. These characteristics are estimated by a free streamline theory.

It is found that the presence of the tunnel wall has a large effect on the stability of propeller operation. In an open condition, the flow rate through the propeller is not very sensitive to the advance ratio. However, in the presence of the tunnel walls, the propeller flow rate changes much more in response to the advance ratio change. This implies that, if there are flow rate fluctuations, the flow rate through the propeller varies more when there are tunnel walls and this may result in unstable operation of the propeller. When the advance ratio is the same, the flow rate through the propeller is smaller and the incidence angle is larger if the propeller is operated in a tunnel with a smaller cross-sectional area. Large incidence angles can result in the flow instabilities and enhance the occurrence of cavitation. Transfer matrices for the cavitating propeller are evaluated by assuming the flow is quasi-static. The transfer matrices show that the propeller operating in the narrower tunnel is much more unstable. If the propeller is operated in a wider tunnel or in an open condition, the effects of a mass flow gain factor are reduced because the variation of the propeller flow rate is smaller even when the total flow rate changes substantially.

Finally, we have tried to obtain the frequency of surge instability from the system impedance, but failed. One of the possible explanations for the discrepancy is that the model considers only sheet cavitation on the blade surface. A large volume change in the tip cavity during a surge cycle was also observed in experiments and may well contribute to the discrepancy.

Nomenclature

A = cross-sectional area of water tunnel
a = cross-sectional area of inner stream tube
C_{ot}, C_t = compliance of overflow tank and water tunnel
C_T = thrust coefficient
c = chord length
F = thrust force of propeller
J_1, J_p = advance ratio and flow coefficient
K^* = cavitation compliance
L_c = innertance of the connecting duct between water tunnel and overflow tank
L_{tu}, L_{td} = innertance of the duct upstream and downstream of the tunnel
M^* = mass flow gain factor
m = mass flow rate
P_1, P_2 = static pressure far upstream and downstream
p_{in} and p_{out} = static pressure at inlet and outlet of propeller
p^T = total pressure
p_v = vapor pressure
q = volumetric flow rate of the stream tube
R = propeller radius
R_c = resistance of the connecting duct between water tunnel and overflow tank
R_{tu}, R_{td} = resistance of the duct upstream and downstream of the tunnel
U = axial velocity in the outer stream tube
U_T = rotational velocity of propeller
u = axial velocity component in inner stream tube
T_{ij} = elements of transfer matrix
V_c = cavity volume on the propeller blade
v = tangential velocity component in inner stream tube
Z = system impedance
α = incidence angle
β = discharge flow angle
β_1, β_2 = inlet and outlet blade angles of propeller
λ = parameter defined by $\sigma/2\alpha$
σ, σ_{up} = cavitation numbers at propeller inlet and far upstream
Ω = rotational frequency of propeller
ω = angular frequency of fluctuations

Superscripts

$\bar{}$ = steady (mean) components of variables
$\sim$ = unsteady components of variables
$+$, $-$ = variables just upstream and downstream of propeller

Subscripts

1,2 = far upstream and downstream
e = at the point of excitation in the system shown in Fig. 10
p = at the propeller

References

[1] Weitendorf, E. A., 1989, ''25 Years Research on Propeller Excited Pressure Fluctuations and Cavitation,'' *Proc. ASME Int. Symp. On Cavitation Noise and Erosion in Fluid Systems*, ASME, New York, **FED-18**, pp. 1–10.

[2] Duttweiler, M. E., and Brennen, C. E., 2002, ''Surge Instability on a Cavitating Propeller,'' J. Fluid Mech., **458**, pp. 133–152.

[3] Brennen, C. E., 1994, *Hydrodynamics of Pumps*, Oxford University Press and Concept ETI, New York.

[4] Brennen, C. E., and Acosta, A. J., 1973, ''Theoretical, Quasi-Static Analyses of Cavitation Compliance in Turbopumps,'' J. Spacecr. Rockets, **10**(3), pp. 175–180.

[5] Brennen, C. E., 1978, ''Bubbly Flow Model for the Dynamic Characteristics of Cavitating Pumps,'' J. Fluid Mech., **89**, pp. 223–240.

[6] Tsujimoto, Y., Kamijo, K., and Yoshida, Y., 1993, ''A Theoretical Analysis of Rotating Cavitation in Inducers,'' ASME J. Fluids Eng., **115**, pp. 135–141.

[7] Tulin, M. P., 1953, ''Steady, Two-Dimensional Cavity Flows About Slender Bodies,'' Tech. Report 834, David Taylor Model Basin.

[8] Brennen, C. E., 1995, *Cavitation and Bubble Dynamics*, Oxford University Press, New York.

[9] Otsuka, S., Tsujimoto, Y., Kamijo, K., and Furuya, O., 1996, ''Frequency Dependence of Mass Flow Gain Factor and Cavitation Compliance of Cavitating Inducers,'' ASME J. Fluids Eng., **118**, pp. 400–408.

[10] Watanabe, S., Tsujimoto, Y., Kamijo, K., and Furuya, O., 1998, ''An Analysis of Cavitation Characteristics by Singularity Method,'' Trans. Jpn. Soc. Mech. Eng., Ser. B, **64**(621), pp. 1285–1292 (in Japanese).

[11] Watanabe, S., Sato, K., Tsujimoto, Y., and Kamijo, K., 1999, ''Analysis of Rotating Cavitation in a Finite Pitch Cascade Using a Closed Cavity Model,'' ASME J. Fluids Eng., **121**(4), pp. 834–840.

Experimental Analysis of an Axial Inducer Influence of the Shape of the Blade Leading Edge on the Performances in Cavitating Regime

F. Bakir
S. Kouidri
R. Noguera
R. Rey

ENSAM–Centre de Paris,
151, boulevard de l'Hôpital,
75013 Paris, France

The aim of this paper is to analyze, from experimental results, the influence of the shape of the leading edge and its sharpening on the cavitating behavior of an inducer. The studied inducer is designed according to a methodology developed at LEMFI. Successive cutting and sharpening (four cuts, which modify up to 20 percent of the blade chord at the tip), were made to modify the shape of the leading edge. For the various geometries, the experimental results obtained on the LEMFI test rig are presented as follows. Noncavitating Regime: Overall performances at 1450 rpm. Cavitating Regime: (1) The development of the cavitation versus the cavitation number, (2) the description of the various cavitation pictures, and (3) the pressure fluctuations measured at the wall at 150 mm downstream of the trailing edge for various flow rates and inlet pressures. The CFD simulations carried out under CFX-Blade Gen+ on this range of inducers are presented to explain certain aspects observed. [DOI: 10.1115/1.1539872]

Introduction

The inducer is generally placed upstream of a centrifugal or mixed flow impeller in order to improve its cavitation resistance. Both rotors are on the same drive shaft, turn at the same speed, and work in series. Designed to reduce cavitation, the inducer, due to the generated pressure rise, allows the main impeller to function in best supplied conditions. This configuration is usually used in many industrial applications: nuclear industry, petroleum, agrobusiness, chemistry, and especially cryogenic propellant pumping. This device allows higher rotational speeds which make pumps more compact and economical. Although these machines are very useful nowadays, several aspects of their operation and their behavior need to be further mastered. The design methodologies found in the literature, [1,2], still today, completely do not explain the influence of the constructive geometrical parameters of the inducers on their performances.

To improve the design method and to appreciate certain phenomena conditioning the reliability of these machines, their maximum performances and their application limits, the experimentation is always used, [3–5].

During this work, mainly experimental, it is proposed to study the influence of the shape of the leading edge on the inducer performances. From an initial inducer, four other inducers by successive cuttings of the inlet edge are obtained.

This step has the advantage of ensuring the same geometrical base for the various configurations. The objective is to analyze the influence of this operation on the surging behavior of the inducer. This enables us to supplement the design rules worked out in [6].

After each cutting three geometrical parameters of design change: the T ratio (this parameter represents the ratio of angular sector of tip and hub delimited per one blade), meridian stacking, and azimuth stacking. The experimental study will make it possible to quantify the simultaneous influence of these last three parameters. The associated parametric study presented below will give qualitative indications on the influence of each one of these parameters.

1 Inducers Configurations and Test Rig

An axial inducer (Fig. 1), respecting the design rules already suggested, [6], and taking into account the constraints imposed by the test bench of our laboratory (external diameter fixed by the transparent envelop, high cylindrical hub imposed by the bearing and the shaft line), is carried out. The inducer named A1 is designed for nominal operating conditions corresponding to a flow coefficient of $\varphi=0.38$, a rotational speed of 1450 rpm and a pressure coefficient of $\psi=0.15$. It consists of three blades without camber and with constant thickness and a sharpened leading edge. The rolling up angles at the hub and at the tip are $[\theta_{TE}-\theta_{LE}]_{\text{Hub}}=384\,\text{deg}$ and $[\theta_{TE}-\theta_{LE}]_{\text{Tip}}=339\,\text{deg}$ respectively, (the angle's origin is taken on the hub and at the leading edge. The angle is positive in the clockwise direction). The ratio $T=0.88$ is higher than the value recommended in the literature (close to 0.7), [7].

To observe the influence of this ratio and the sharpening of the leading edge, four successive cuttings and sharpenings were carried out on the inducer A1 (Fig. 1). The obtained configurations are indicated by a letter and a number: The numbers from 2 to 5 indicate the number of the cutting (number 1 relates to the initial inducer) and the letter A indicates a sharpened leading edge and B is a nonsharpened leading edge. For the B series inducers, a light rounded on leading edge is carried out.

The leading edge cuttings are carried out according to a linear variation of the ratio T (see Table 1 and Fig. 1 for the cutting quantity).

The sharpening of the leading edge is carried out on the suction side in such a way that after each cutting the new leading edge obtained is not sharpened. For all cases, the sharpening length of each blade, is spread out on zero mm at the hub, 15 mm at the average radius, and 25 mm at the tip (see details in Fig. 2). The main constructive parameters of the inducers are shown in Table 1.

Contributed by the Fluids Engineering Division for publication in the JOURNAL OF FLUIDS ENGINEERING. Manuscript received by the Fluids Engineering Division May 29, 2001; revised manuscript received Sept. 17, 2002. Associate Editor: Y. Tsujimoto.

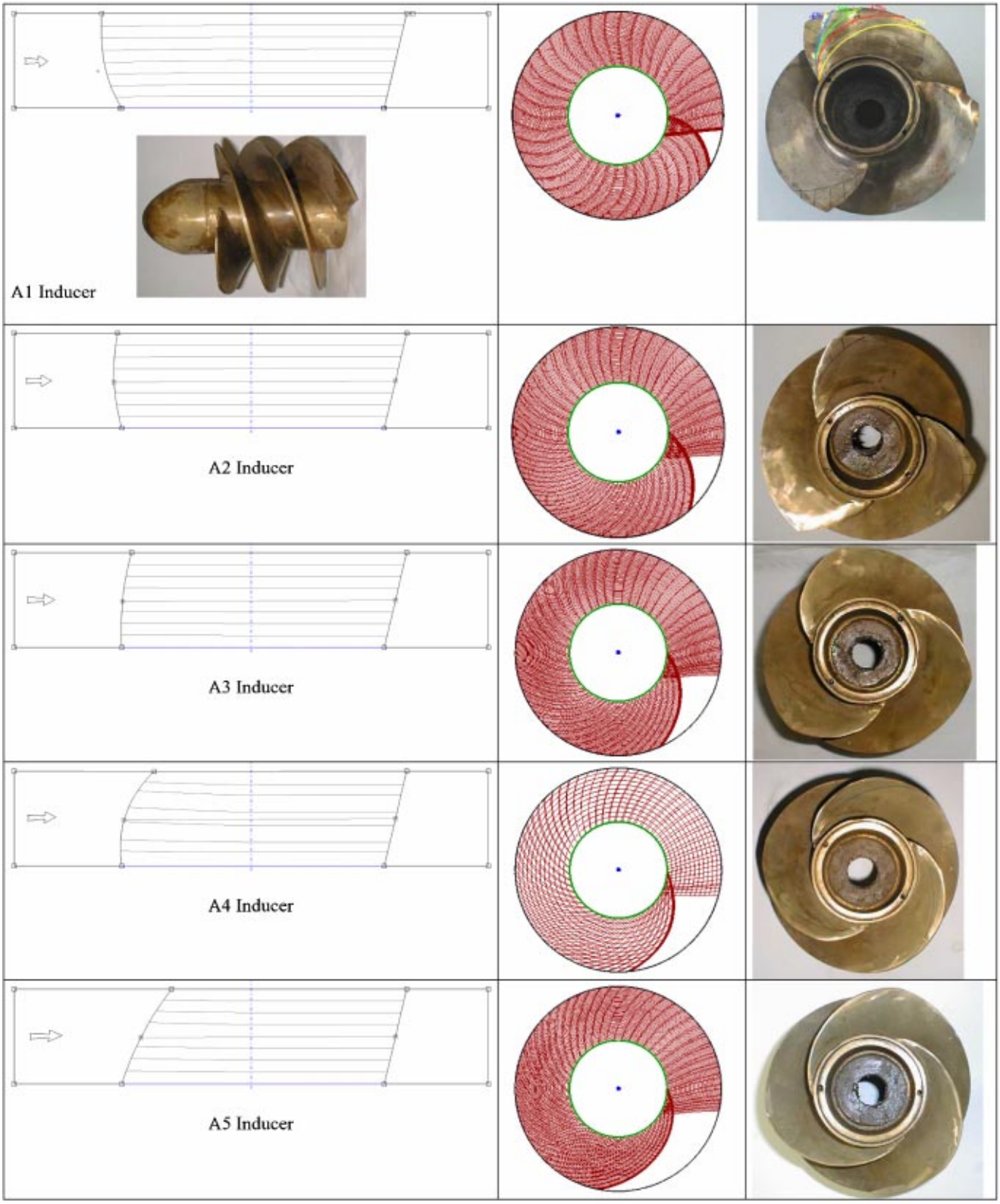

Fig. 1 Inducers configurations

General Overview of the Experimental Facilities. In order to compare the experimental behavior of the various inducers obtained under the same operating conditions, the LEMFI-Paris pump test rig (Fig. 3) composed of the following main elements is used:

- two storage tanks with a capacity of 4 m3 each, connected by a pipe of 350 mm in diameter. They can be loaded and emptied by means of two electrical control valves.
- a liquid ring vacuum pump is used to control the pressure at the free surface inside the storage tanks.

Table 1 Main constructive parameters of the inducers

Flow coefficient	0.38
Head coefficient	0.15
Rotational speed	1450 rpm
Blades number	3
Blade angle (axial definition): (this angle is constant from inlet to outlet)	Hub:65.5 deg Tip:74.5 deg
Blade thickness	5 mm
Tip-to-hub ratio	0.494
Tip diameter	235 mm
Tip clearance	0.4 mm
Stagger angle	Hub:65.5 deg Tip:74.5 deg

	Hub $\theta_{LE}:\theta_{TE}$	50 percent span $\theta_{LE}:\theta_{TE}$	Tip $\theta_{LE}:\theta_{TE}$	Ratio: T	Solidity hub:tip
B1 & A1	0:384	10:373	29:368	0.880	3.5:2.95
B2 & A2	0:384	22:373	47:368	0.835	3.5:2.80
B3 & A3	0:384	33:373	65:368	0.790	3.5:2.65
B4 & A4	0:384	44:373	83:368	0.745	3.5:2.50
B5 & A5	0:384	55:373	101:368	0.700	3.5:2.35

• a 22 kW DC motor powered by a variable frequency controller was used to drive the tested inducer. The electric efficiency of the motor is given by the manufacturer. The rotational speed is measured using a magnetic tachometer (accuracy 0.1 percent).

• a motorized control valve serves to adjust precisely the flow rate.

• the inducer equipped with a transparent acrylic cover.

• a circulation centrifugal pump installed in series with the impeller in order to overcome the circuit losses.

• various measurement instruments and devices:

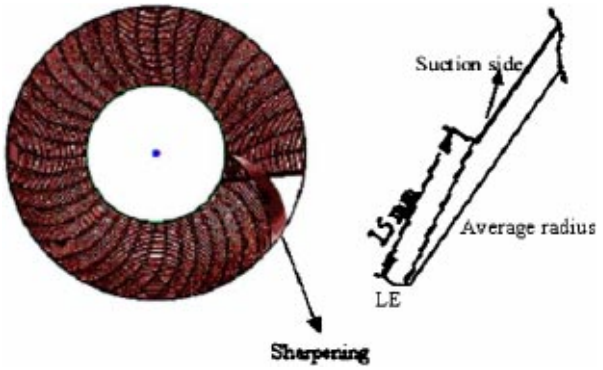

Fig. 2 Sketch sharpened leading edge

• ultrasonic flow meter (accuracy 1 percent), placed at the inducer inlet.

• two piezoresistif manometers (accuracy 1 percent). They are positioned at the inlet and outlet sections and measure the average tip pressure on four points.

• a temperature probe (accuracy 1 percent): the average temperature during the tests presented below is 18°C.

• two dynamic pressure sensors KISTLER brand 601A type, flush mounted over the transparent cover, one at 20 mm upstream from the leading edge of the impeller and the other at 150 mm downstream from the trailing edge. Their specifications are range 0–250 bar, and natural frequency >150 kHz. The pressure fluctuations were measured by these sensors and amplified then treated with a spectrum analyzer (Lecroy 930A). All the signals were identified and stored in a personal computer for further analysis.

2 Experimental Results for the Inducer A1

2.1 Overall Performances. The characteristic flow rate pressure in a noncavitating regime and the cavitating tests of the A1 inducer, at 1450 rpm, are summarized on Fig. 4. It is noted at the design flow rate that an efficiency of 57 percent and a value of a critical cavitation number σ_c of 0.05 (the critical value corresponds to a drop of 3 percent of the total pressure variation) corresponding to a number S of 310 is a modest value for an inducer. If the centrifugal pumps suction specific speed S is limited to 250, the first generation of industrial inducers reaches 450 and the high-performance propellers greatly surpass 600.

2.2 Development of Cavitation With the Cavitation Number. Figure 5 presents, for $Q/Qn=1.09$ at 1450 rpm, the appearance of the cavitation pocket versus σ. The first significant vapor pockets start to appear, at the tip, on both sides of the blade near $\sigma=0.25$. As σ decreases these pockets advance towards the trailing edge and also towards the hub. At $\sigma=0.045$ the passage of water is strongly blocked by the vapor pocket and at that time a significant drop in performance of the inducer is noted.

2.3 Presentation of the Figures of Cavitation Versus the Flow Rate. The figures of cavitation visualized during the tests are typical and are in general in conformity with those presented in the literature [8]. However, the alternate pocket described in [9] were not observed. Figure 6 presents the most representative images. One can thus identify:

• in partial flow the backflow vortex cavitation returning upstream of the inducer (Fig. 6(*a*)): the importance of this torch increases for the low flow rates.

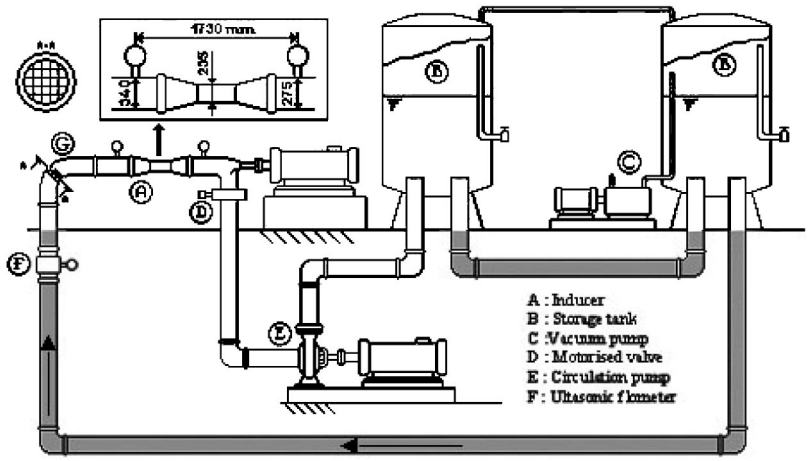

Fig. 3 Hydrodynamic test bench of the LEMFI–Paris

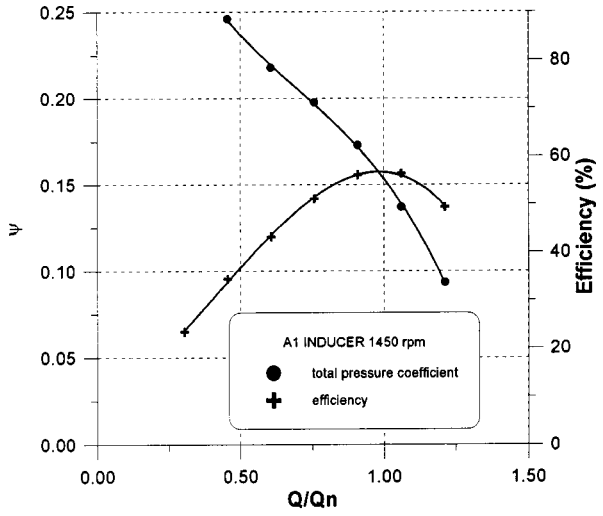

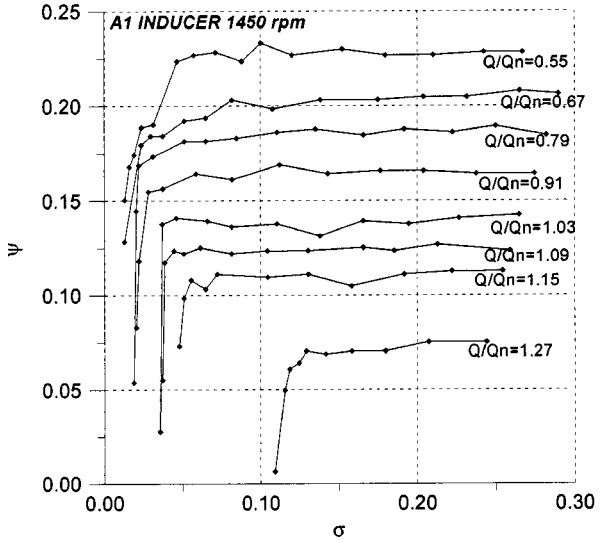

Fig. 4 Experimental performances of the inducer A1 (uncertainty in $N\pm2$ rpm, in efficiency ±1 percent, in $\sigma\pm0.002$, in $Q/Qn\pm0.02$, in $\psi\pm0.002$)

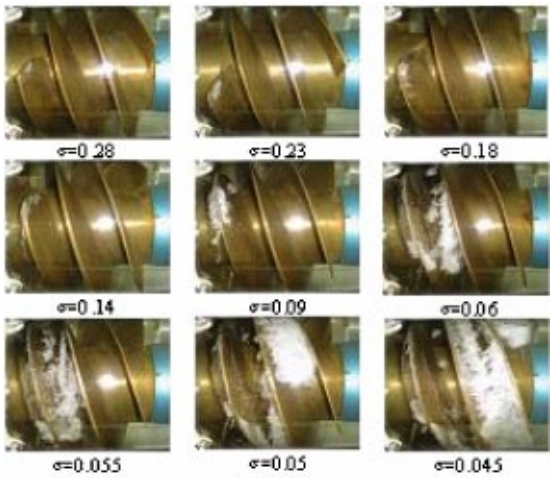

Fig. 5 Appearance of the cavities of cavitation $N=1450$ rpm, $Q/Qn=1.09$ (uncertainty in $N\pm2$ rpm, in $\sigma\pm0.002$, in $Q/Qn\pm0.02$)

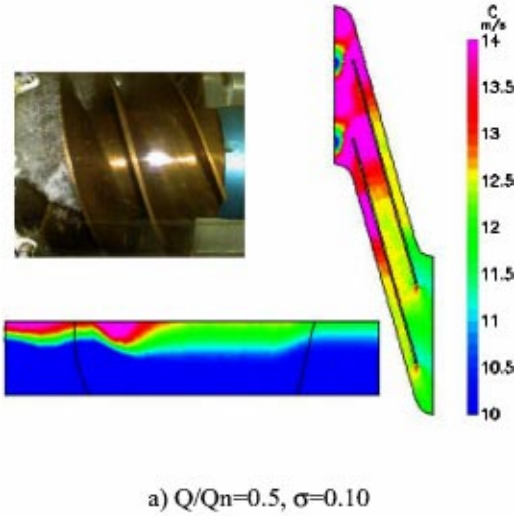

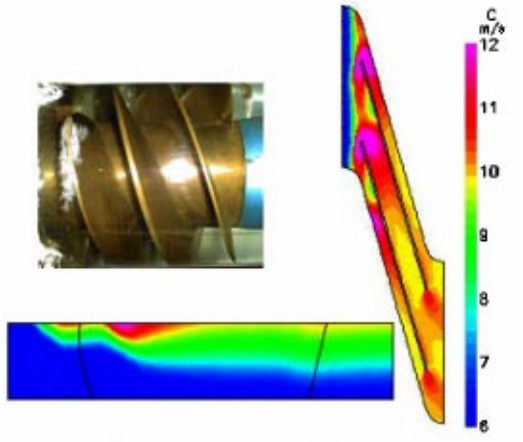

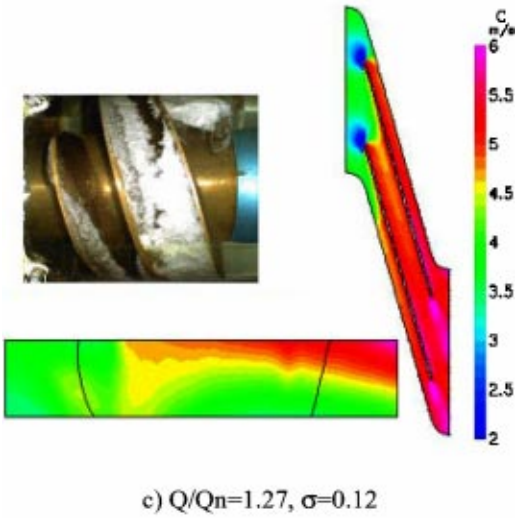

Fig. 6 Various figures of cavitation, A1 inducer 1450 rpm (uncertainty in $N\pm2$ rpm, in $\sigma\pm0.002$, in $Q/Qn\pm0.02$)

• the cavitation attached to the blade observed in the nominal flow rate (Fig. 6(*b*)).

• for high flow rates, stable cavities developed on both sides of the blade, characterizing the phenomenon of blockage which is accompanied by a fast rise of the critical σ (Fig. 6(*c*)).

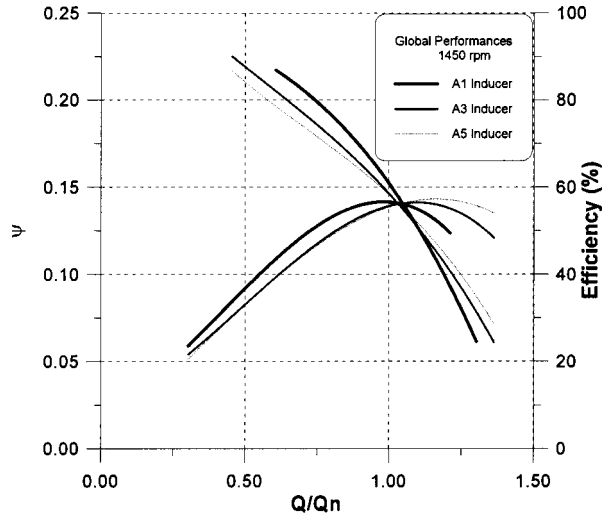

Fig. 7 Overall performances of the inducers A1, A3, and A5, experimental results (uncertainty in $N \pm 2$ rpm, in efficiency ± 1 percent, in $Q/Qn \pm 0.02$, in $\psi \pm 0.002$)

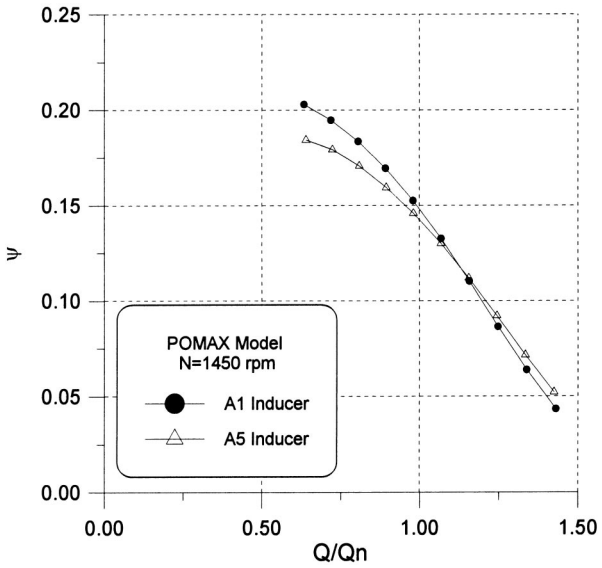

Fig. 8 Overall performances of the inducers A1 and A5, POMAX model

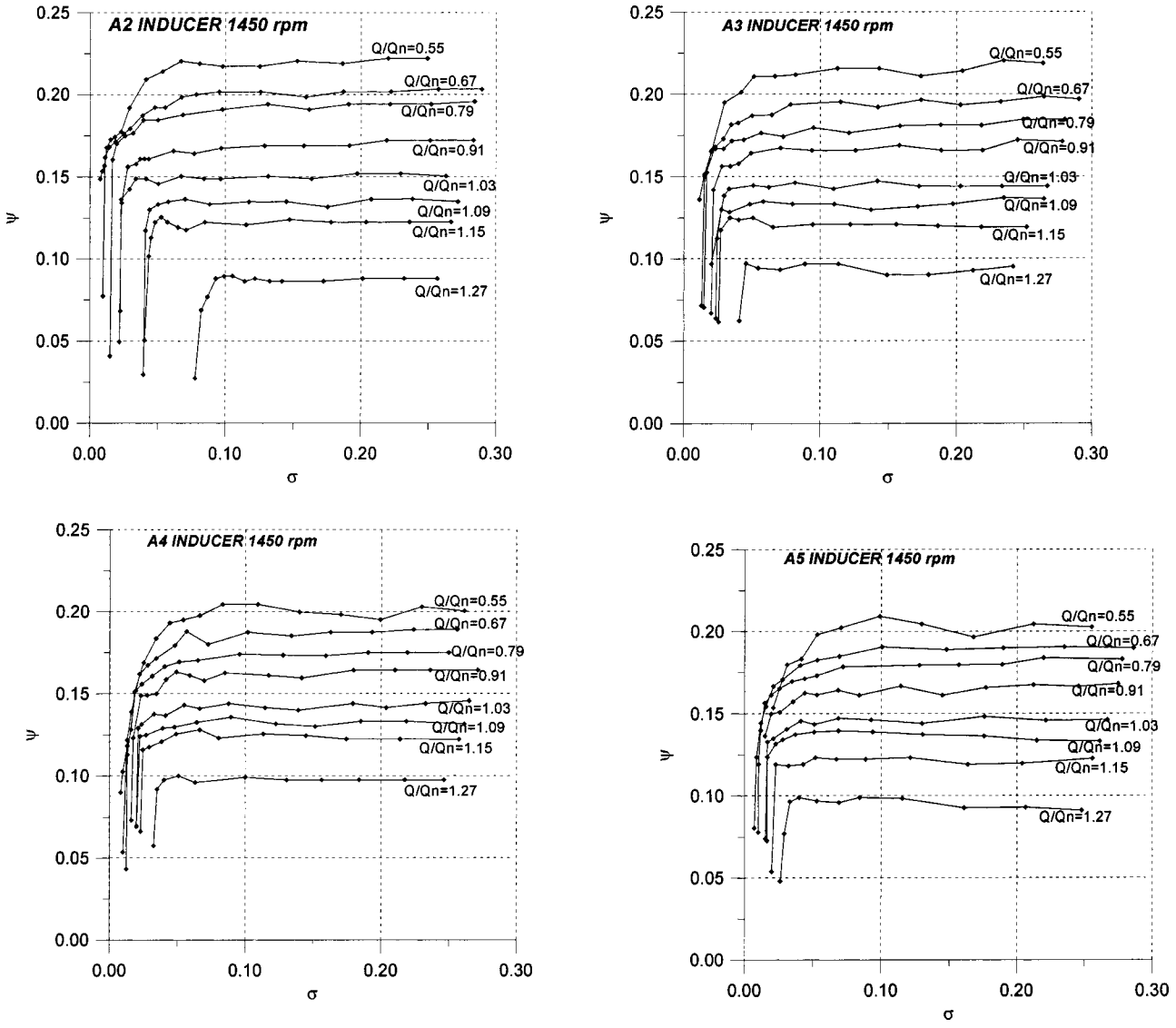

Fig. 9 Evolution of the head versus σ available inducers A2 to A5 (uncertainty in $N \pm 2$ rpm, in $\sigma \pm 0.002$, in $Q/Qn \pm 0.02$, in $\psi \pm 0.002$)

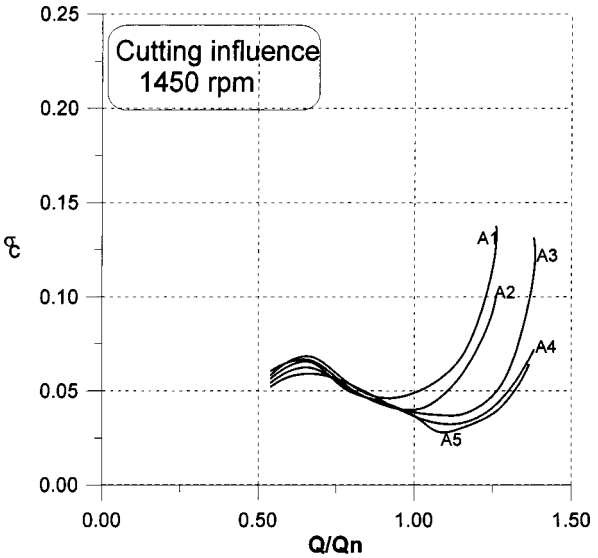

Fig. 10 Cutting influence (uncertainty in $N\pm 2$ rpm, in $\sigma_c \pm 0.002$, in $Q/Qn\pm 0.02$)

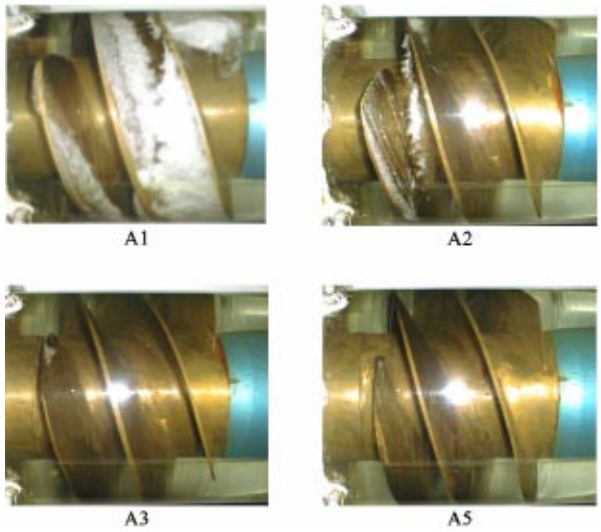

Fig. 11 Cutting influence—figures of cavitation, $N=1450$ rpm, $Q/Qn=1.27$, $\sigma=0.12$ (uncertainty in $N\pm 2$ rpm, in $\sigma\pm 0.002$, in $Q/Qn\pm 0.02$)

The development of cavitation is almost identical in the three inducer channels.

The appearance of the cavitation figures above is related to the organization of the kinematics of flow in the inducer. Indeed the CFD simulation carried out with CFX-BladeGen+, (three-dimensional Navier-Stokes code with a zero-equation type turbulence model and a not-structured grid generator with tetrahedral elements) in a steady flow condition and with several flow rates on the inducer A1 confirms this result. The simulation conditions are: $N=1450$ rpm, with the condition of the mass flow rate im

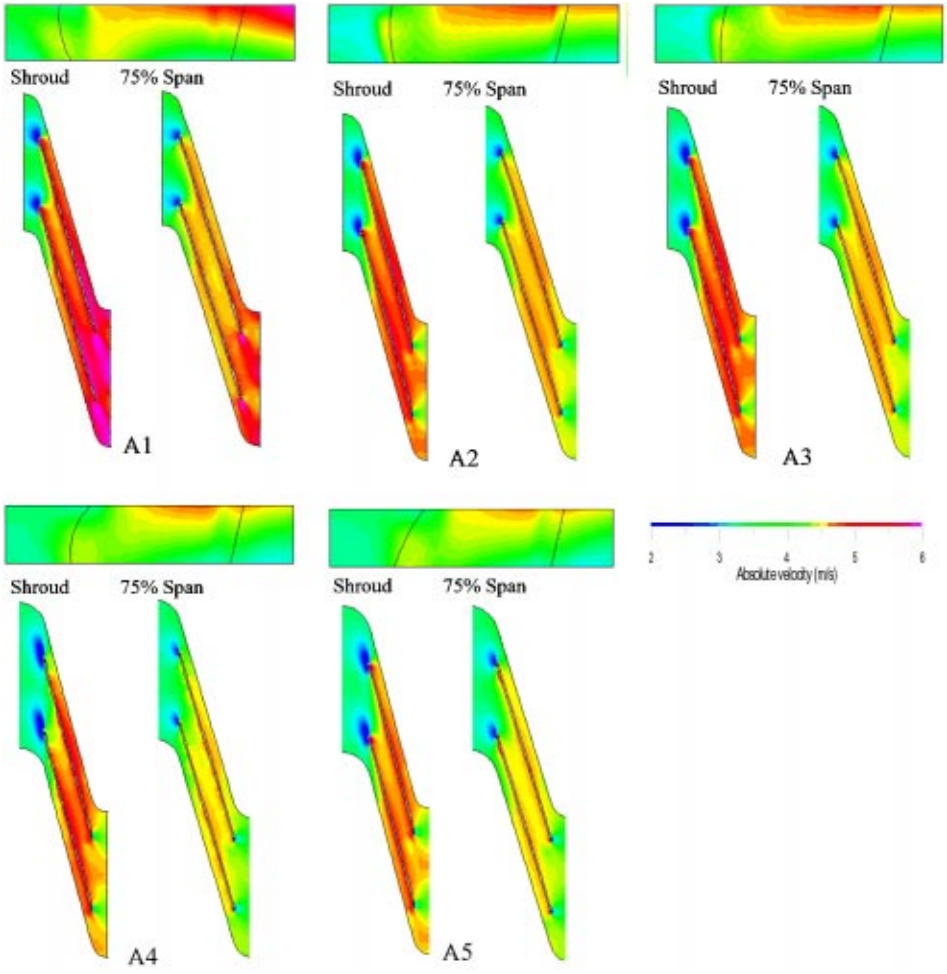

Fig. 12 Cutting influence—BladeGen+calculation, $N=1450$ rpm, $Q/Qn=1.27$, $\sigma=0.25$

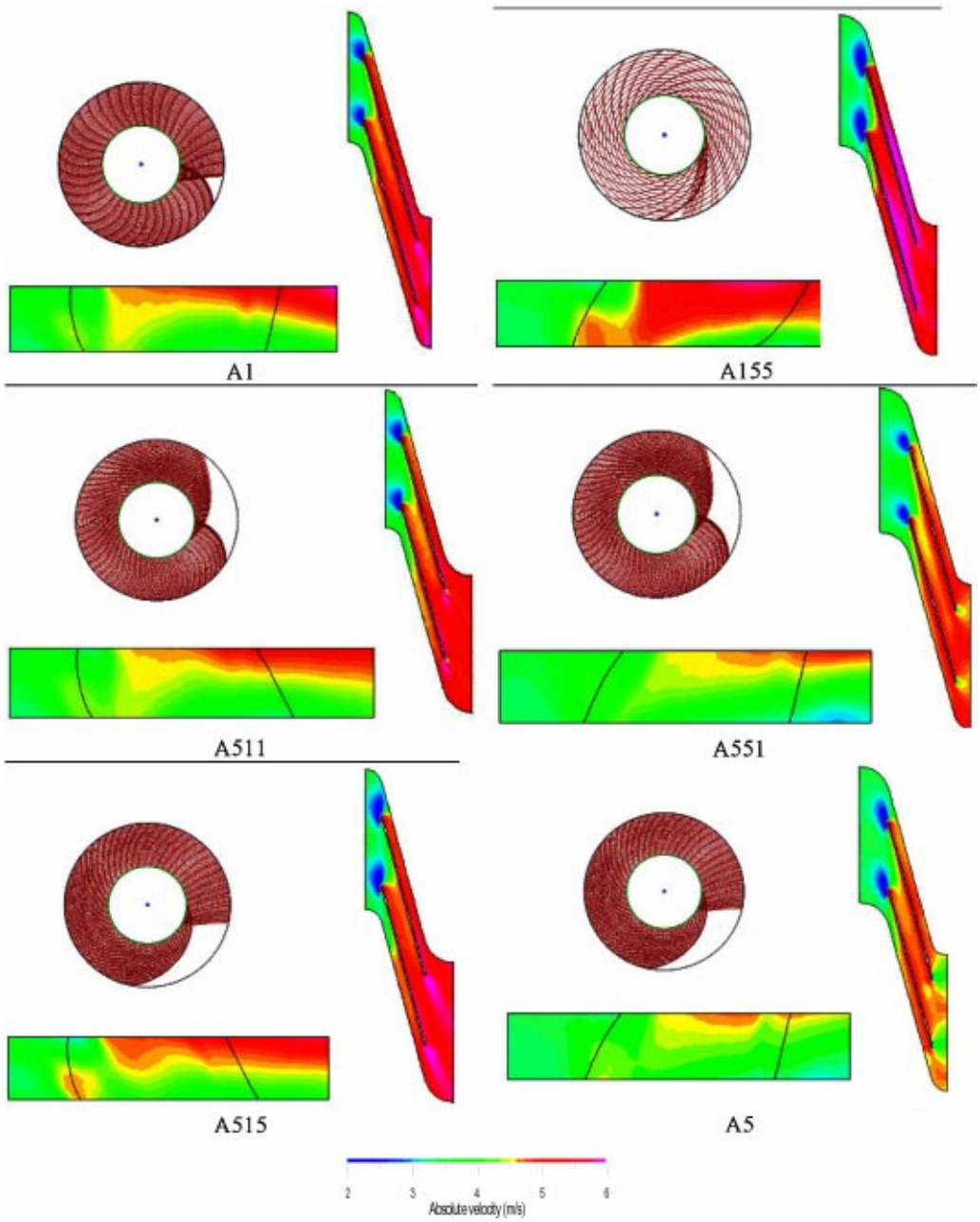

Fig. 13 Parametric study—BladeGen+calculation, $N=1450$ rpm, $Q/Qn=1.27$, $\sigma=0.25$

posed at the outlet and static pressure at the inlet. The tip clearance is not considered here. The mesh size is approximately 45,000 nodes.

Figure 6 presents the absolute velocity fields for three flow rates: the meridian (on the suction side) and blade to blade at the tip. In conformity with the experimentation, the high velocities (favorable place to cavitation appearance) are, respectively, localized: towards the inlet at low flow rates (Fig. 6(*a*)), on the blade at the design flow rate (Fig. 6(*b*)), and towards the outlet at a high flow rate (Fig. 6(*c*)).

3 Influence of the Cut of the Leading Edge

3.1 Noncavitating Tests. The overall performances of the A1, A3, and A5 inducers are given in Fig. 7. A rotation of the characteristic curves pressure-flow rate around the design point is observed. The maximum efficiency point is moved to a higher flow rate as we increase the leading edge sweep. The inducers produce more pressure above the nominal flow rate. This still authorizes the coupling of these inducers with centrifugal pumps. This phenomenon is mainly linked to the reduction of the cord due to the cutting. The simulation, done by the design software POMAX developed at the Lemfi, [10], and taking into account the radial equilibrium, confirms this aspect in Fig. 8 for the inducer A1 and A5.

3.2 Tests in the Cavitating Regime. Figure 9 presents the cavitating performances at 1450 rpm for inducers A2 to A5: evolution of the head coefficient versus the cavitation number allowing the determination of the critical cavitation number. Figure 10 presents the critical cavitation number versus the flow rate for A1 to A5 inducers. A clear improvement of these performances at the nominal flow rate and above the nominal flow rate is noted. For $Q/Qn=1.15$, for example, the σ_C varies from 0.06 ($S=280$) to

0.025 ($S=510$). It is pointed out that an optimized inducer is that which, on a wide scale of flow rate, has a high pressure coefficient (for better stuff the centrifugal impeller), a lowest critical cavitation number, and weak pressure fluctuations.

This quantitative result is strongly correlated by the images of cavitation presented in Fig. 11. The progressive disappearance of cavitation bubbles with different cuttings is noted (these tests are carried out under the same speed rotation 1450 rpm, $\sigma=0.12$, and flow rate $Q/Qn=1.27$).

This disappearance of cavitation bubbles with different cuttings is related to the favorable reorganization of the velocity field at the inducer. This result was recently confirmed by the numerical study carried out by Arnone and al. on the PLOX inducer of Ariane 5, [11].

To confirm this explanation a simulation is carried out using the CFD software CFX-BladeGen+ in a steady flow condition and over a design flow rate ($Q/Qn=1,3$) on the five inducers A1 to A5. The conditions of simulation are identical to those previously shown. Figure 12 presents the distribution of absolute velocity in meridian (on the suction side) and blade to blade (at the tip and at 75 percent of the hub) views. The velocities are decelerated, more and more, after each cutting. The velocities distribution is more favorable to appearance of the cavitation for inducer A1. The tendency of disappearance of cavitation bubbles with cuttings is confirmed for the same reason.

To qualify the influence of the three parameters which change after each cutting, simulations under BladeGen+ are carried out (same conditions of simulation as previously) on four other virtual inducers called A155, A511, A551, and A515. The three numbers state, respectively, that the ratio T, meridian stacking, and azimuth stacking correspond to those of the machines A1 or A5. For example, the machine A155 has the same ratio T as that of A1, the meridian stacking of A5, and the azimuth stacking of A5.

Figure 13 presents for the two inducers A1 and A5 and the four new machines, on the meridian (on the suction side) and blade to blade (of tip) views, the absolute velocity distribution. The detailed analysis of these results shows the importance of the influence of each one of the three geometric parameters, in particular the ratio T and the meridian stacking.

- The comparison of the two inducers A1 and A155 shows a more accelerated velocity fields for the machine A155 in spite of both stacking of A5.
- The two inducers A511 and A551 are different only by meridian stacking. The machine A551 would be most powerful.
- The comparison between A551 and A5, different only by azimuth stacking, shows a small slowing down in the inducer A5.

The machine A5 has the velocity fields less accelerated. Therefore, it would be the machine where the appearance cavitation figures are delayed compared to the other machines.

3.3 Instabilities of Operation. One of the aspects limiting the use of the inducers is related to the presence of instabilities of operation in the cavitating mode, [4,8]. The influence of cuttings, on the pressure fluctuations measured with dynamic pressure sensor Kistler placed at 150 mm downstream of the trailing edge of the inducers A1, A2, A4, and A5, is presented here. The inducers are compared under the same operation conditions.

These results are illustrated in Fig. 14 (128 points of measures for each inducer, in the flow rate σ field). A clear decrease, except in the vicinity of $Q/Qn=0.6$ in the level of fluctuations according to various cuttings, is noted. This reduction of the level of fluctuations is due to the disappearance of the cavitation figures. The degradation observed in the vicinity of $Q/Qn=0.6$ is related to the appearance of oscillating cavitation whose amplitude increases with the cuttings.

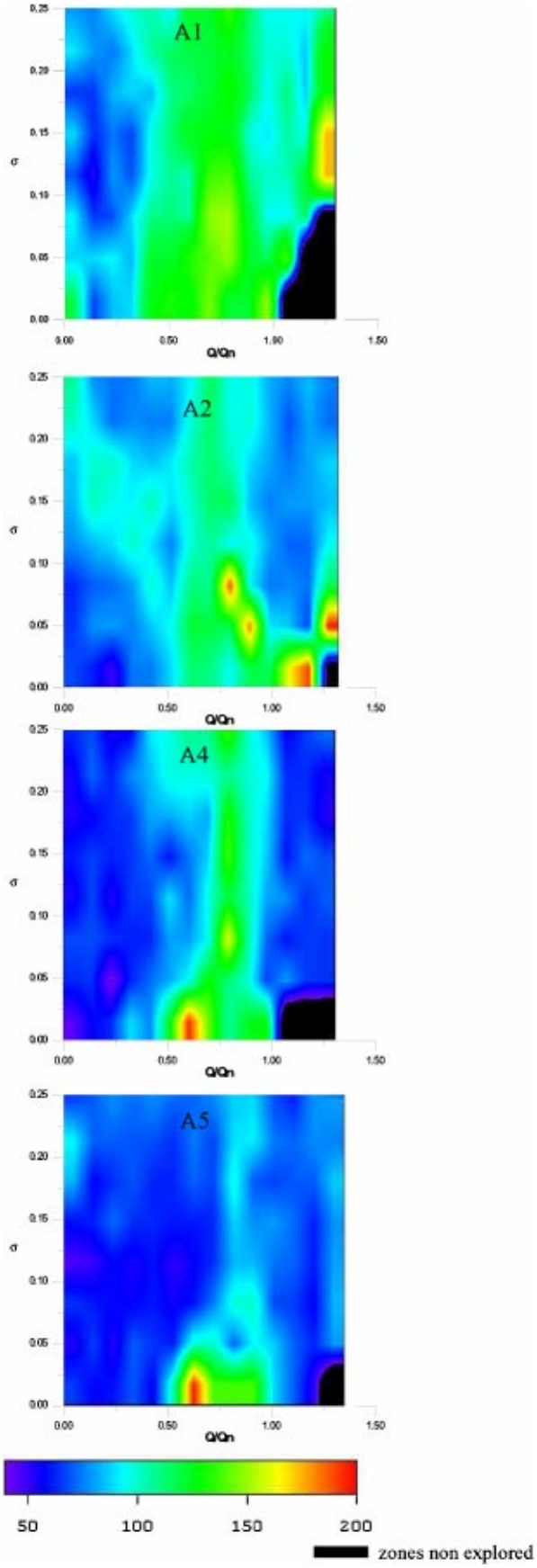

Fig. 14 Influence of the various cuttings on the fluctuations in pressure downstream from the inducer $N=1450$ rpm (uncertainty in $N\pm2$ rpm, in $\sigma\pm0.002$, in $Q/Qn\pm0.02$, in $\Delta p_f\pm0.002$)

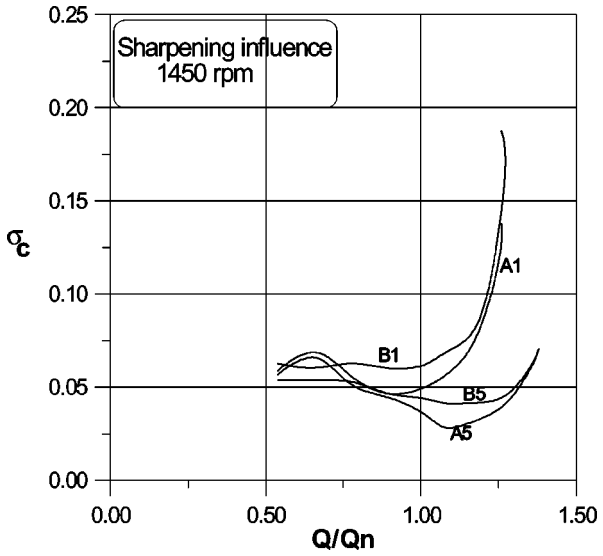

Fig. 15 Sharpening influence (uncertainty in $N\pm 2$ rpm, in $\sigma_c \pm 0.002$, in $Q/Qn\pm 0.02$)

4 Influence of the Sharpening of the Leading Edge

To show the influence of sharpening Fig. 15 presents, for the inducers A1–A5 and B1–B5, the evolution of the critical cavitation number versus the flow rate. Only an improvement around the nominal flow rate is noted. Apart from this nominal point a significant improvement is not observed.

5 Conclusion

The interest of this work is to describe the leading edge shape influence on the performances of an inducer's range. A full experiment was carried out in the cavitating regime related to several geometries of inducers obtained by successive cutting and sharpening of the leading edge. These tests underlined the dominating influence of these constructive parameters. The increase in the slope of the leading edge makes it possible to significantly improve the cavitating performances at high flow rate and to attenuate the pressure fluctuations.

In order to reduce the critical cavitation number, we shown for these studied inducers the interest to incline the leading edge towards the outlet in the meridian view and towards the back for the front view. The performance improvements were observed until a ratio $T=0.7$ was reached. A test with a lower ratio was not carried out in the experiments for two reasons: first, we didn't observe a significant improvement of the critical cavitation number σ_C between the inducers A4 and A5, and secondly, in order to conserve the inducer A5 for other visualisation tests. Sharpening improves these same performances in the vicinity of the nominal flow rate. All these tests: pressure fluctuations, cavitation figures, and overall performances constitute a database which will be used as reference for numerical simulations.

Acknowledgments

This study was carried out with the support of FAPMO. The test bench was renovated and equipped with the financial assistance from the ANVAR. We would like to thank them.

Nomenclature

g = acceleration due to gravity (m^2/s)
N = rotational speed of inducer (rpm)
$\mathrm{NPSP}=p_{t(\mathrm{inlet})}-p_v$ = net positive suction pressure (Pa)
$\mathrm{NPSH}=\mathrm{NPSP}/\rho g$ = net positive suction head (m)
p_t = total pressure (Pa)
p_v = liquid vapor pressure (Pa)
Q = flow rate (m^3/s)
Q_n = nominal flow rate of A1 inducer (m^3/s)
Re = tip radius (m)
$S=52.9326$
$\cdot\omega\sqrt{Q}/(g\cdot\mathrm{NPSH})^{0,75}$ = suction specific speed
$U_t=\omega\,\mathrm{Re}$ = peripheral velocity (m/s)
$T=[\theta_{TE}-\theta_{LE}]_{\mathrm{Tip}}$ $/[\theta_{TE}-\theta_{LE}]_{\mathrm{Hub}}$ = ratio rolling up angle
$\Delta p=p_{t(\mathrm{outlet})}-p_{t(\mathrm{inlet})}$ = total pressure variation (Pa)
Δp_f = pressure fluctuations (mbar)
$\varphi=Q/\omega\,\mathrm{Re}^3$ = flow coefficient
$\psi=\Delta p/\rho U_t^2$ = pressure coefficient
θ_{LE} = leading edge azimuthal angle (deg)
θ_{TE} = trealing edge azimuthal angle (deg)
ρ = liquid density (kg/m^3)
$\sigma=\mathrm{NPSP}/\rho U_t^2$ = cavitation number
σ_c = critical cavitation number (corresponds to a drop of 3 percent of the total pressure variation)
ω = angular velocity (rad/s)

References

[1] Lakshminarayana, B., 1982, "Fluid Dynamics of Inducers. A Review," ASME J. Fluids Eng., **4**, pp. 411–427.
[2] NASA, 1971, "Liquid Rocket Engine Turbopump Inducers," SP 8052, May.
[3] Geai, P., 1997, "Observations of Oscillating Cavitation of an Inducer," ASME J. Fluids Eng., **119**, p. 742.
[4] Tsujimoto, Y., Yoshida, Y., Maekawa, Y., Watanabe, S., and Hashimoto, T. 1997, "Observations of Oscillating Cavitation of an Inducer," ASME J. Fluids Eng., **119**, pp. 775–781.
[5] Hashimoto, T., Yoshida, M., Watanabe, M., Kamijo, K., and Tsujimoto, Y., 1997, "Experimental Study on Rotating Cavitation of Rocket Propellant Pump Inducers," J. Propul. Power, **13**, pp. 488–494.
[6] Bakir, F., Kouidri, S., Noguera, R., and Rey, R., 1998, "Design and Analysis of Axial Inducers Performances," ASME Fluid Machinery Forum, Washington DC, Paper No. FEDSM98-5118.
[7] Acosta, A. J., 1993, "Flow in Inducer Pumps, an Aperçu," *Proceedings 4th International Symposium on Transport Phenomena and Dynamics of Rotating Machinery*, Honolulu, Vol. A., ISROMAC, pp. 1–13.
[8] Offtinger, C., Henry, C., and Morel, R., 1996, "Instabilité de fonctionnement en débit partiel d'un inducteur fretté. Comparaison avec le cas non fretté," *3ème Journée Cavitation*, SHF, Grenoble France, pp. 31–38 (in French).
[9] Huang, J. D., Aoki, M., and Zhang, J. T., 1998, "Alternate Blade Cavitation on Inducer," JSME Int J. Ser., B. **41**(1), pp. 1–6.
[10] Noguera, R., Rey, R., Massouh, F., Bakir, F., and Kouidri, S., 1993, "Design and Analysis of Axial Pumps," *ASME Fluids Engineering, Second Pumping Machinery Symposium*, ASME, New York, pp. 95–111.
[11] Arnone, A., Boncinelli, P., Capuani, A., Spano, E., and Rebattet, C., 2001, "Ariane 5 TPLOX Inducer Design Strategies to Enhance Cavitating Performance," *Proceedings, Fourth International Symposium on Cavitation*, CAV2001 Session B7.004, Pasadena, CA, June 20–23.

Y. Kinoue
T. Setoguchi
T. H. Kim
K. Kaneko

Department of Mechanical Engineering,
Saga University,
1, Honjo
Saga 840-8502, Japan

M. Inoue
Department of Mechanical Engineering Science,
Kyushu University,
6-10-1 Hakozaki, Higashi-ku
Fukuoka 812-8581, Japan

Mechanism of Hysteretic Characteristics of Wells Turbine for Wave Power Conversion

A Wells turbine for wave power conversion has hysteretic characteristics in a reciprocating flow. The counterclockwise hysteretic loop of the Wells turbine is opposite to the clockwise one of the well-known dynamic stall of an airfoil. In this paper, the mechanism of the hysteretic behavior was elucidated by an unsteady three-dimensional Navier-Stokes numerical simulation. It was found that the hysteretic behavior was associated with a streamwise vortical flow appearing near the blade suction surface. In the accelerating process of axial flow velocity, the vortex is intensified to enlarge the flow separation area on the blade suction surface. In the decelerating flow process, the flow separation area is reduced because of the weakened vortex. Therefore, the aerodynamic performance in the accelerating flow process is lower than in the decelerating flow process, unlike the dynamic stall. Based on the vortex theorem, the mechanism to vary the intensity of the vortex can be explained by the trailing vortices associated with the change in the blade circulation. [DOI: 10.1115/1.1538629]

Introduction

In the past two decades, worldwide efforts have been devoted to the development of energy conversion from ocean waves. One of the most applicable devices for wave energy is the combination of an oscillating water column (OWC) as a primary converter and a self-rectifying air turbine as a secondary one (Fig. 1).

The Wells turbine is one of the most suitable air turbine for energy conversion from oscillating air flow. Usually, the unsteady characteristics of Wells turbine are predicted by computer simulation on the basis of the steady characteristics, [1]. It seems to be reasonable to employ such a quasi-steady analysis because the nondimensional wave frequency (based on the relative velocity and the blade chord length) is the order of 10^{-4}. However, it results in inaccurate predictions of the performance, since the Wells turbine has hysteretic characteristics in an unsteady flow, [2–4].

Dynamic stall of an airfoil is well known as an unsteady aerodynamic phenomenon which has hysteretic characteristics, and a lot of researchers have reported many kinds of aspects of dynamic stall of an airfoil, [5–8]. But the hysteretic loop of the lift-attack angle characteristics of the dynamic stall is counterclockwise and opposite to the clockwise one of the Wells turbine. So the mechanism of the hysteretic characteristics of Wells turbine should be clarified for the better design of the system for wave power conversion.

In order to investigate the mechanism of the hysteretic behavior of the Wells turbine, unsteady, three-dimensional Navier-Stokes numerical simulations were conducted for the flow field around a blade of the Wells turbine.

Numerical Analysis

Numerical simulations in this paper were made of the Wells turbine, the hysteretic behavior of which was investigated experimentally by Inoue et al. [2]. Summaries of the experiments are briefly mentioned. The test rig consists of a 1.4-m-diameter cylinder with a piston disk, a rectangular settling chamber, and a 0.3-m-diameter test section with a bell mouth entry and a diffuser exit. The turbine rotor is placed at the center of the test section, and can be operated at arbitrary rotating speed. A sinusoidal axial air flow is produced by controlling the motion of the piston (0.167 Hz of frequency in this paper). The unsteady turbine performances were examined in one-half period of the sinusoidal change in axial flow velocity. Experimental results of the half-part of the full cyclic hysteretic characteristics by Alcorn and Beattie [4] reveal almost similar results to Inoue et al. [2]. Table 1 shows the specifications of the turbine rotor used in this study. Model testing was made in such the way that the turbine rotating speed was set at zero axial flow velocity condition once, then the turbine output torque T, the air flow Q and the total pressure drop across the rotor ΔP_0 were measured while keeping the turbine speed constant. The Reynolds number based on the blade chord length and relative velocity at mean radius is about 2.4×10^5.

A commercial code, FLUENT 5, was used for the numerical analysis. The unsteady three-dimensional and filtered Navier-Stokes equations were discretized by the finite volume method. The rotating frame fixed to turbine rotor was adopted. The second-order accuracy upwind differencing scheme was used for the convection term and the second-order accuracy implicit method was used for the time discretization. The RNG-SGS model, [9], which is an LES model, was used to calculate the subgrid-scale turbulent viscosity. The unsteady calculations were made in one-half period of the sinusoidal change in an axial flow velocity.

The computational domain was extended four and eight blade chord lengths upstream and downstream of the blade, respectively, as shown in Fig. 2. Figure 3 shows the perspective view of the grids. The structured, hexahedral grids of O-type were used around the blade, while H-type grids were used for the upstream and downstream regions. The total number of grids is approximately 560,000. Three grids were embedded in the region of tip clearance. The calculation for finer grids (approximately 703,000 grids, six grids for tip clearance) was made to check the grid dependency of the calculation for the objective (560,000) grids.

Nonslip boundary conditions were used for the hub surface, the pressure and suction side of the rotor surfaces. The moving casing wall was used because of the rotating frame of reference. Periodic boundary conditions were used for the surfaces of circumferential sides. On the upstream boundary, the inlet velocities were given at each time step, where the axial velocities were given from the flowrate and the circumferential velocities were given from the rotor rotating speed. On the downstream boundary, the static pressures were set at each time step. The results of the steady flow

Contributed by the Fluids Engineering Division for publication in the JOURNAL OF FLUIDS ENGINEERING. Manuscript received by the Fluids Engineering Division June 13, 2002; revised manuscript received October 21, 2002. Associate Editor: Y. Tsujimoto.

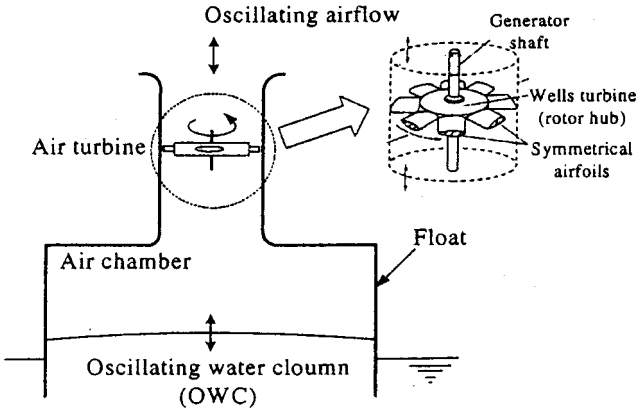

Fig. 1 Schematic view for OWC device

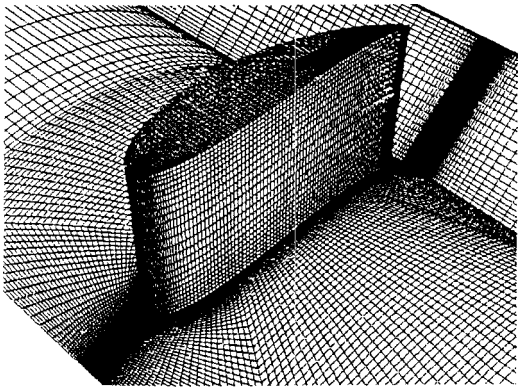

Fig. 3 Perspective view of grids

calculation for attack angle $\alpha_R = 0$ deg were used as the initial condition, which corresponded to the experimental condition. The nondimensional distance of the first grid point from the blade surface was less than 5.0 based on the friction velocity and the kinematic viscosity of air.

Numerical Results

Figure 4 shows the experimental, [2], and calculated results of hysteretic behaviors of the total pressure coefficient C_A and the torque coefficient C_T against the attack angle α_R in one-half period of the sinusoidal flow. Figure 4(*a*) shows the experimental and calculated values of C_A, and Fig. 4(*b*) the experimental and calculated values of C_T. These coefficients are defined as follows:

$$C_A = \Delta P_0 Q / (\varrho (v_a^2 + U_R^2) z b l v_a / 2) \tag{1}$$

$$C_T = T / (\rho (v_a^2 + U_R^2) z b l r_R / 2) \tag{2}$$

$$\alpha_R = \tan^{-1}(v_a / U_R) \tag{3}$$

where ΔP_0 denotes the total pressure drop across the rotor, Q air flow rate, ρ density of air, v_a axial velocity, U_R circumferential velocity at midspan, z number of blades, b span of the blade, T torque of the rotor, r_R radius at midspan, and α_R attack angle.

Table 1 Turbine models

Blade Profile	NACA0020
Number of blades z	6
Blade chord length l	90 mm
Solidity at tip σ_t	0.57
Aspect ratio AR	0.5
Tip radius R_t	149 mm
Tip clearance TC	1 mm
Setting angle γ	0 deg

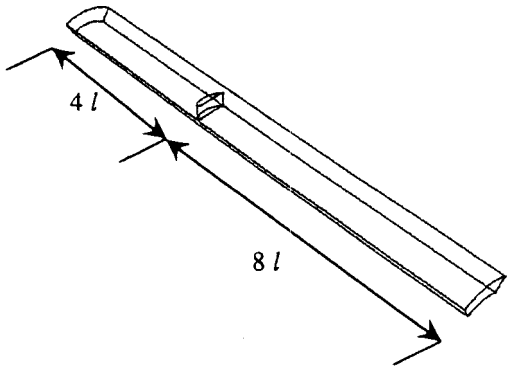

Fig. 2 Computational domain

The attack angle varies between 0 deg and its maximum value in phase with the oscillating flow. In the course of the cycle the experimental C_A value (broken line) during acceleration of axial velocity (increasing α_R), is lower than that during deceleration (decreasing α_R), and then a counterclockwise hysteretic loop appears as shown in Fig. 4(*a*). As is evident from Fig. 4(*b*), a similar hysteretic loop is also observed in the experimental value of the torque coefficient C_T. If the hysteretic behavior was caused by the dynamic stall of blade, a clockwise hysteretic loop would be seen, [5–8]. Therefore, the mechanism of hysteretic behavior of the Wells turbine should be different from the mechanism of the dynamic stall.

As for the agreement of the calculated values with the experimental data in Fig. 4, good agreement is obtained, although the calculated values are a little smaller than the experimental data for both C_A and C_T. Maximum values of the calculated results of C_A and C_T agree well with the experiment quantitatively. As for the grid dependency of C_A, C_A values for finer grids are a little (0.1 of C_A in the maximum case) larger than the values for the objective grids in the accelerating flow, but the maximum C_A value and the C_A values in the decelerating flow for finer grids is almost the same as the C_A values for the objective grids. The grid dependency of C_T is similar to the one of C_A. The calculation of the objective grids can qualitatively simulate the hysteretic phenomenon of the Wells turbine in spite of comparably small numbers of grid points in the tip clearance. In the following description, the mechanism of the hysteretic characteristics of the Wells turbine is considered through the examination of the calculated flow fields.

Figure 5 shows the circumferential velocity contours at mid span, where the numbers at the centerline are the attack angle α_R, and the air flows left to right. For $\alpha_R = 6 \sim 15$ deg, the contour lines near the suction surface of the blade are denser than the ones near the pressure surface, which means that the boundary layer along the suction surface is thicker than the one along the pressure surface. Comparing the figures in the decelerating flow with the ones in the accelerating flow for $\alpha_R = 6$ or 12 deg, the boundary layer along the suction side surface in the accelerating flow is thicker. In each figure, the region where the contour lines are dense exists in the area from the upstream side of the periodic boundary to a location a little distant from the suction surface of the blade, which is considered the wake formed by the front side blade in the rotational direction. The thickness of the wake in the accelerating flow is larger than that in the decelerating flow for $\alpha_R = 6$ deg.

Figure 6 shows the streamlines near the suction surface starting from the leading edge of the blade. For $\alpha_R = 6$ deg, the flow near the hub surface separates more upstream than the flow near the tip side in the accelerating flow. This region of separation cannot be seen for $\alpha_R = 6$ deg in the decelerating flow. In addition, some of

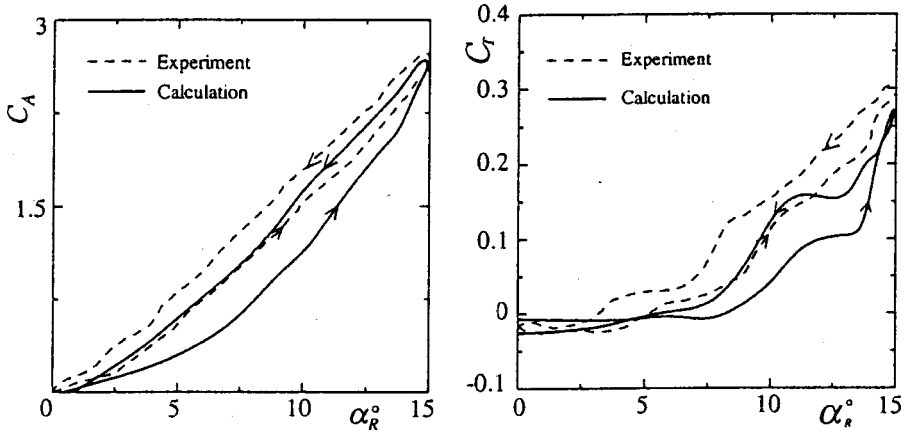

Fig. 4 Comparison of calculated results with experimental data by Inoue et al. [2]

the streamlines near the trailing edge go away from the suction surface in the tip-side region, due to the effect of the tip leakage flow. For $\alpha_R = 12$ deg, the separation region is extended in both accelerating and decelerating flows. The separation region in the accelerating flow becomes more enlarged than the one in the decelerating flow.

Figure 7 shows the streamlines starting from the trailing edge of the blade. The streamlines crossing over the blade suction surface come from the trailing edge of the left side blade. A clockwise vortex exists near the hub, which is caused by the strong downward flow near the trailing edge. The clearest vortex can be seen in the accelerating flow for $\alpha_R = 6$ deg among the four cases in Fig. 7.

Figure 8 shows the pressure contour maps on the suction surface of the blade. The minimum and maximum values are located near the leading edge and the trailing edge, respectively. The pressure difference between the leading edge and the trailing edge in the decelerating flow is larger than that in the accelerating flow for both $\alpha_R = 6$ and 12 deg. This fact is consistent with the larger values of C_T in the decelerating flow. The region where the contours are coarse is enlarged around the center of the blade surface in the accelerating flow for both $\alpha_R = 6$ and 12 deg, corresponding to the separation region in Fig. 6.

Figure 9(*a*) shows the velocity vectors around the blade for $\alpha_R = 6$ deg. The numbers at the center of the figure are the nondimensional radiuses $r^*(=(r-r_h)/(r_t-r_h))$. At $r^* = 0.5$ (mid-

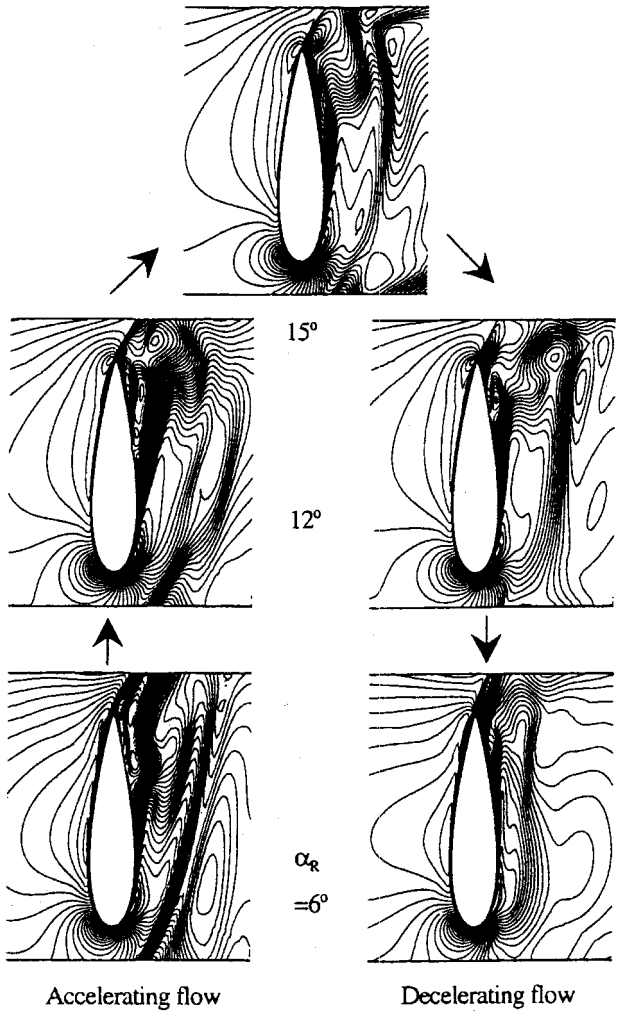

Fig. 5 Circumferential velocity contours at midspan

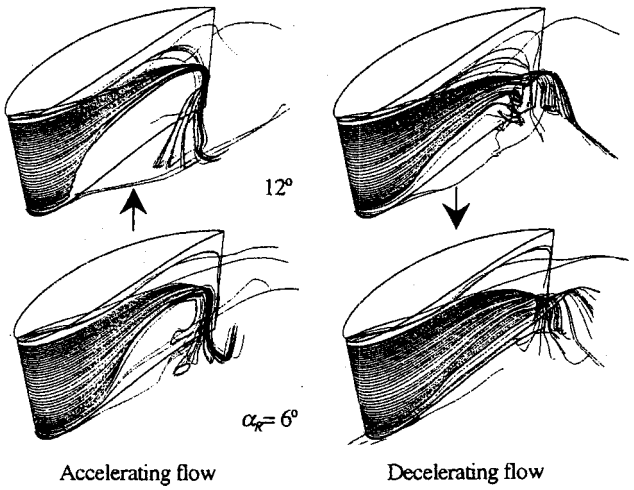

Fig. 6 Streamlines near the suction surface

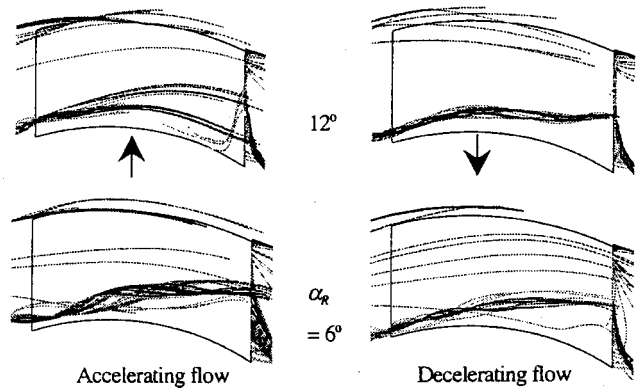

Fig. 7 Streamlines starting from the trailing edge

span), the boundary layer is thicker near the trailing edge of the suction surface, and the wake from the front side blade appears more clearly in the accelerating flow. In addition, near the hub surface of $r^*=0.1$, the velocities are overall smaller in the accelerating flow, which means that a lot of low-energy fluids gather near the hub surface in the accelerating flow. Figure 9(*b*) shows velocity vector map for $\alpha_R=12$ deg. At $r^*=0.1$ the flows are largely separated near the suction surface in both increasing and decelerating flow. At $r^*=0.5$, the flow separates near the side of the trailing edge of the suction surface in the accelerating flow, while the flow in the decelerating flow does not separate.

Figure 10(*a*) shows the velocity diagram on the plane perpendicular to the chordwise direction for $\alpha_R=6$ deg. The numbers at the center of the figure are the distance from the leading edge normalized by the chord length. The clockwise vortex mentioned in Fig. 7 can be seen in Fig. 10(*a*) in the accelerating flow. This vortex moves from hub to tip according to the mainstream. In addition, a counterclockwise vortex can be seen on the corner of the suction surface and hub surface for $x/l=0.9$ for both $\alpha_R=6$ and 12 deg. No clockwise vortex can be seen in the decelerating flow. Figure 10(*b*) shows the similar figure as Fig. 10(*a*) for $\alpha_R=12$ deg. The clockwise vortex is not seen around the region of the wake for both $\alpha_R=6$ and 12 deg.

The change in the intensity of the clockwise vortex in Fig. 10(*a*) seems to result in the hysteretic characteristics. By the increased intensity of this clockwise vortex in the accelerating flow, the low-energy fluids in the separation region near the suction side of the hub surface migrate toward the mid span region and the torque of the rotor reduces. In the decelerating flow, the intensity

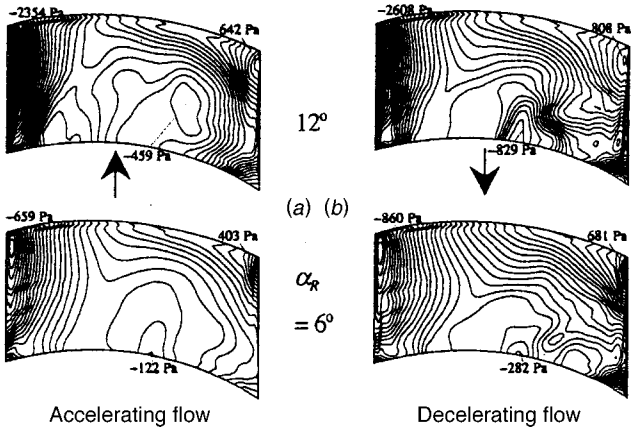

Fig. 8 Pressure contours on the suction surface

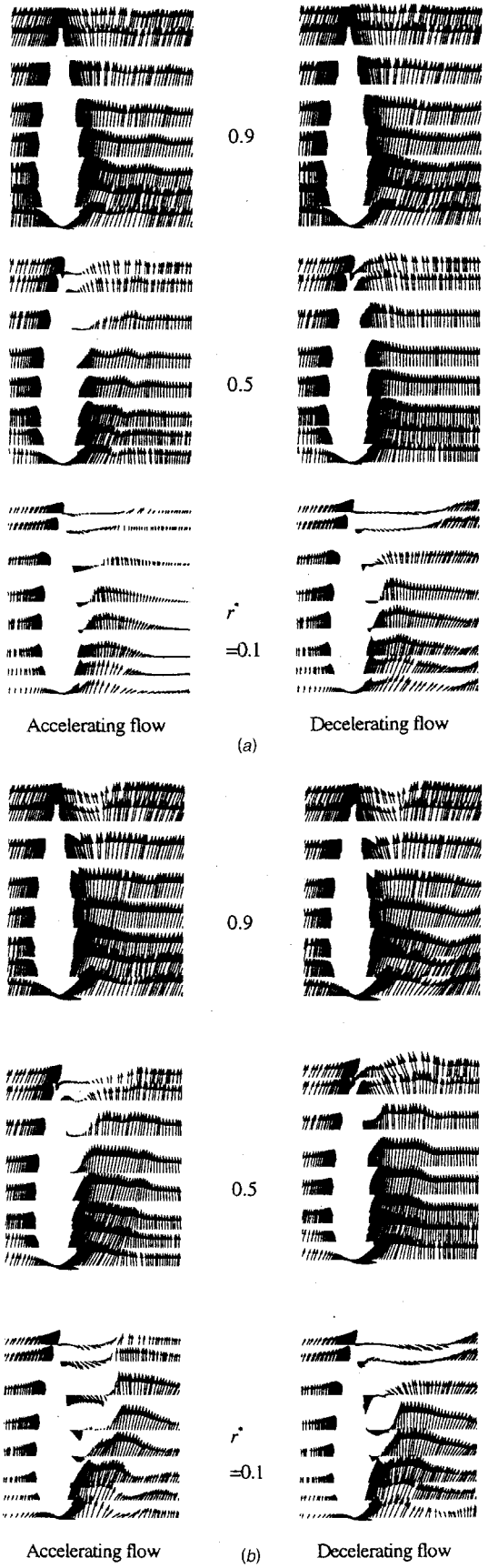

Fig. 9 (*a*) Velocity diagram around the blade for $\alpha_R=6$ deg; (*b*) velocity diagram around the blade for $\alpha_R=12$ deg

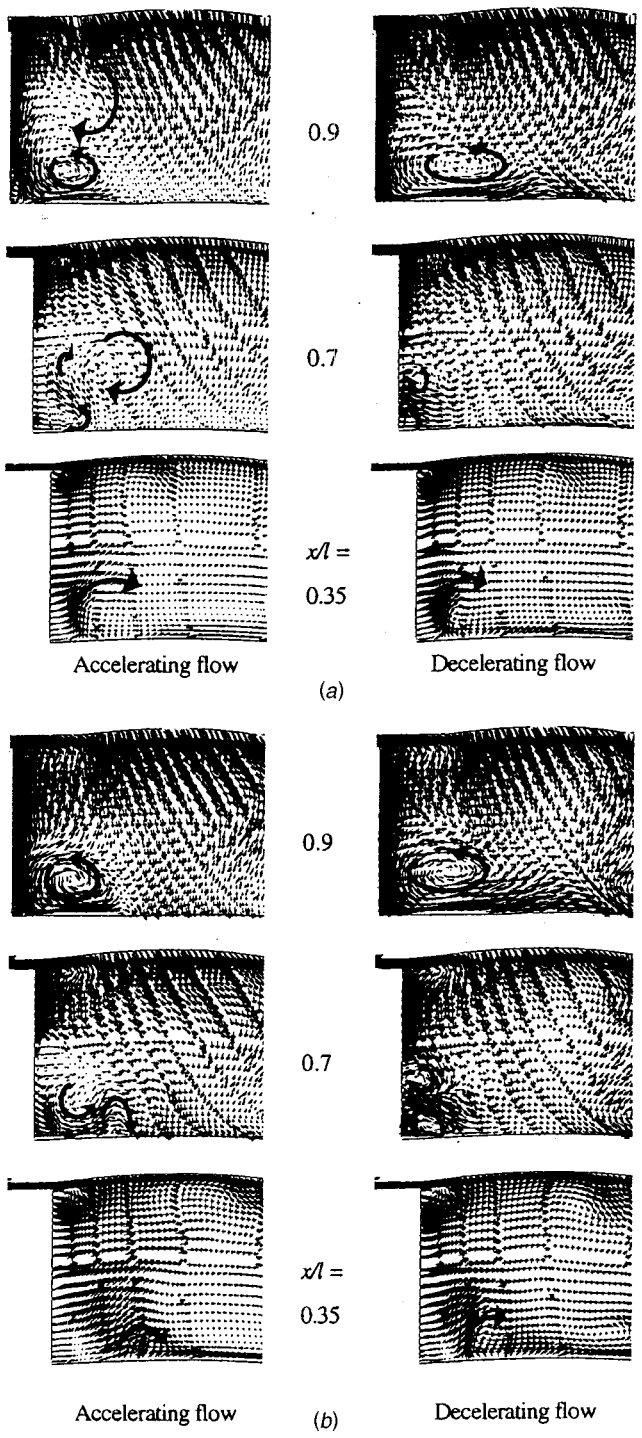

Fig. 10 (*a*) Velocity diagram on the plane perpendicular to the chordwise direction for α_R=6 deg; (*b*) velocity diagram on the plane perpendicular to the chordwise direction for α_R=12 deg

of this clockwise vortex is so small that the low-energy fluids are confined near the hub surface and the torque remains larger.

Mechanism of Hysteretic Characteristics

As shown in Fig. 4, the performance of the Wells turbine has a hysteretic loop in which the values of C_T and C_A in the accelerating flow are smaller than that in the decelerating flow. This behavior cannot be explained by the dynamic stall of an airfoil. As mentioned above, however, it seems to be associated with the intensity of the vortical flow appearing near the blade suction

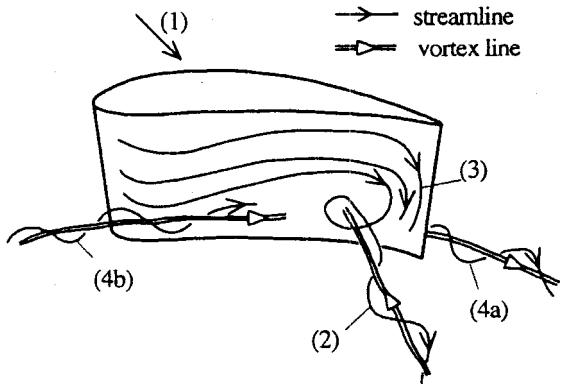

Fig. 11 Illustrations of the flow structure in blade suction side

surface. In this section, the mechanism to vary the vortex intensity in the accelerating and the decelerating flow will be discussed based on the vortex theorem.

Figure 11 shows an illustration of the flow structure obtained by the present numerical simulation. At high angles of attack a separation vortex (2) appears on the blade suction surface in the hub side to reduce the blade circulation, because of the excessive angle of attack near the hub. A strong downward flow (3) is induced by the separation vortex near the trailing edge. It brings about the clockwise vortical wake flow (4a), which enlarges the flow separation on the adjacent blade suction surface (4b). The intensity of the vortical flow varies in the accelerating and the decelerating flow process for the following reason.

Figure 12 illustrates how the unsteady trailing vortices that are shed affect the vortical wake flow. In the accelerating flow process, as the blade circulation increases, vortices opposite to the blade circulation are shed from the trailing edge according to Kelvin's theorem. The stronger vortices are shed at a larger radius

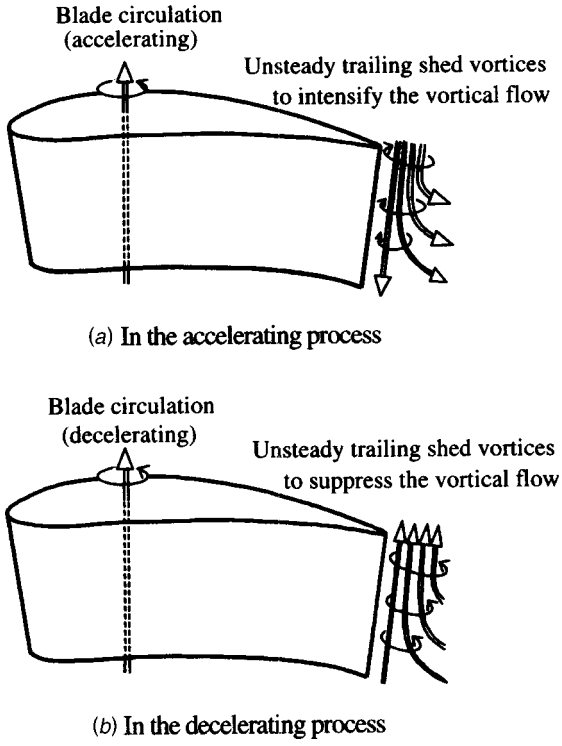

Fig. 12 Illustration of unsteady trailing shed vortices to affect the vortical wake flow

because the blade circulation increases more than at a smaller radius. Then, the clockwise trailing vortices are generated according to Helmholtz's theorem, as illustrated in Fig. 12(*a*). Therefore, the clockwise vortical flow is intensified by these vortices. In the decelerating flow process where the blade circulation decreases, the shed vortices are in the same direction of the blade circulation. They form counterclockwise trailing vortices as shown in Fig. 12(*b*), which suppress the vortical wake flow. Since the stronger vortical wake flow enlarges the separation on the suction surface of the adjacent blade, the performance in the accelerating flow process becomes lower than in the decelerating flow process.

Conclusions

In order to elucidate the mechanism of hysteretic characteristics of the Wells turbine, unsteady, three-dimensional Navier-Stokes numerical simulations were conducted using the commercial code of FLUENT5 for the case of an axial velocity changing sinusoidally. Conclusions are summarized as follows.

1. The calculated results using the RNG-SGS model reveal the hysteretic behavior which agrees well with the experimental results qualitatively.
2. In the accelerating flow, the boundary layer is thicker along the suction side surface, the separation region is more enlarged, and the wake of the front side blade in the rotating direction is clearer than in the decelerating flow.
3. The flow is downward near the trailing edge of the suction surface and a clockwise vortex exists in the wake. This vortex is intensified when the attack angle increases rapidly (in the accelerating flow process for $\alpha_R = 6$ deg).
4. The cause of hysteretic behavior is associated with this clockwise vortex. In the accelerating flow, the increased intensity of the clockwise vortex extends the separation region on the blade suction surface toward the mid span region, which leads to the reduction of the torque coefficient and the total pressure coefficient. In the decelerating flow, the separation region is reduced as the vortex is weakened.
5. The mechanism to change the vortex intensity in the wake can be explained based on the vortex theorem. The vortex is intensified by the clockwise trailing shed vortices (due to increase in the blade circulation) in the accelerating flow process, while it is suppressed by the counterclockwise vortices (due to decrease in the blade circulation) in the decelerating flow process.

Nomenclature

b = span of the blade, m
C_A = total pressure coefficient (Eq. (1))
C_T = torque coefficient (Eq. (2))
l = chord length, m
r = radius, m
T = torque generated by rotor, Nm
U = circumferential velocity, m/s
v_a = axial velocity, m/s
x = distance from the leading edge, m
z = number of blades
α = angle of attack, degree
ΔP_0 = total pressure drop between settling chamber and atmosphere, Pa
ρ = density of air, kg/m^3

Subscripts

h = hub
R = midspan
t = tip

References

[1] Inoue, M., Kaneko, K., Setoguchi, T., and Simamoto, K., 1985, "Studies on Wells Turbine for Wave Power Generator (4th Report, Starting and Running Characteristics in Periodically Oscillating Flow)," Trans. Jpn. Soc. Mech. Eng., Ser. B, **51**(468), pp. 2746–2751 (in Japanese).
[2] Inoue, M., Kaneko, K., Setoguchi, T., and Koura, F., 1987, "Hysteretic Characteristics of Wells Turbine in Reciprocating Flow," Trans. Jpn. Soc. Mech. Eng., Ser. B, **53**(496), pp. 3699–3704 (in Japanese).
[3] Setoguchi, T., Kaneko, K., Hamakawa, H., and Inoue, M., 1990, "Measurement of Hysteresis on Wells Turbine Characteristics in Reciprocating Flow," *Proc. 1st International Symposium on Experimental and Computational Aerothermodynamics of Internal Flows*, ISECAIF, Beijing, China, pp. 537–543.
[4] Alcorn, R. G., and Beattie, W. C., 1998, "Observations of Time domain Data on Wells Turbine in the Islay Wave-Power Plant," *Proc. 8th International Offshore and Polar Engineering Conference*, ISOPE, Cupertino, CA, **1**, pp. 81–85.
[5] Ericsson, L. E., and Reding, J. P., 1987, "Fluid Dynamics of Unsteady Separated Flow, Part II. Lifting Surfaces," Prog. Aerosp. Sci., **24**, pp. 249–356.
[6] Shida, Y., Kuwahara, K., Ono, K., and Takami, H., 1987, "Computation of Dynamic Stall of a NACA-0012 Airfoil," AIAA J., **25**(3), pp. 408–413.
[7] Carr, L. W., 1988, "Progress in Analysis and Prediction of Dynamic Stall," J. Aircr., **25**(1), pp. 6–17.
[8] Leishman, J. G., 1990, "Dynamic Stall Experiments on the NACA 23012 Aerofoil," Exp. Fluids, **9**, pp. 49–58.
[9] Yakhot, V., and Orszag, S. A., 1986, "Renormalization Group Analysis of Turbulence (I. Basic Theory)," J. Sci. Comput., **1**(1), pp. 3–51.

Comparison of Semi-Empirical Correlations and a Navier-Stokes Method for the Overall Performance Assessment of Turbine Cascades

C. Cravero

A. Satta

DIMSET–Università di Genova,
via Montallegro n. 1,
16145 Genova, Italy

Turbomachinery flows can nowadays be investigated using several numerical techniques to solve the full set of Navier-Stokes equations; nevertheless the accuracy in the computation of losses is still a challenging topic. The paper describes a time-marching method developed by the authors for the integration of the Reynolds averaged Navier-Stokes equations in turbomachinery cascades. The attention is focused on turbine sections and the computed aerodynamic performances (outlet flow angle, profile loss, etc.,) are compared to experimental data and/or correlations. The need for this kind of CFD analysis tools is stressed for the substitution of standard correlations when a new blade is designed. [DOI: 10.1115/1.1539869]

Introduction

The two-dimensional analysis of turbomachinery cascades is still an interesting field of investigation both from a numerical and from an experimental point of view. The interest is motivated by the need for profiles with increasing load (less blade number that means less weight in aeronautical applications) and high efficiency. In the past the experimental analysis of profiles was the only feasible way to optimize the performance of the cascade in a two-dimensional arrangement and the results have been generalized with correlations, [1–3], for use of profile design not too different from the original data. The use of compressible time-marching techniques coupled with boundary layer calculations has pioneered the analysis of two-dimensional cascades with some account for losses and deviation, [4,5]. More recently the impressive evolution of CFD has significantly modified the industrial approach in designing new turbomachinery components. Many codes are in current use in industry for the two-dimensional and three-dimensional analysis of turbomachinery, [6–8]. The overall features of the flowfield are captured pretty well but there is still room for the improvement of the CFD techniques in the evaluation of losses. Nowadays correlations for deviation in axial turbines can be optimized with three-dimensional Navier-Stokes codes to give the designer an efficient tool, [9], for a quick definition of a new blade. Nevertheless a similar approach for losses is still more difficult. The paper presents a Navier-Stokes solver developed by the authors for two-dimensional blade sections analysis and the attention is focused on turbine applications. An algebraic turbulence model has been introduced because it did show the ability of reproducing the overall physics of the turbulent flow in cascades, [10]. Some modifications have been introduced in the standard model of Baldwin-Lomax following Boyle [11]. Several turbine blade sections have been analyzed and the computed performances are compared to existing experimental data and correlations. Many correlations have been proposed over the years for turbine blade performance prediction, but they have not usually been updated in the open literature following the advances in turbine design methods. The correlation from Ainley-Mathieson, [12], has been frequently updated and the last version from Kacker-Okapuu, [2], has been considered to compute the total pressure loss coefficient. Moreover the accuracy of the above correlation, discussed by the authors, [2], for the prediction of turbine stage efficiency (± 1.5 percent) has been considered sufficient for the present work. The correlation originally proposed by Ainley-Mathieson, [12], has been used for the evaluation of the outlet flow angle.

Many papers have been presented in the past to show the ability of a given CFD method to accurately predict the flow field in different turbomachinery cascades, [11,13]. Nevertheless the attention has been mainly focused on blade load distribution (isoentropic Mach number or static pressure) or on detailed flow features (i.e., heat transfer along the blade profile) rather than on overall cascade performances. Some comparisons have been published for the computed versus experimental total pressure loss coefficient for compressor, [14], or turbine, [15], cascades, but the analysis has been restricted to one family of aerodynamic profiles. In this paper, after a critical verification of the accuracy of the flow solver, the comparison is extended to turbine profiles with very different characteristics and the ability of both the Navier-Stokes method and standard semi-empirical correlations in obtaining the overall performances is checked.

Navier-Stokes Solver

The two-dimensional Reynolds-averaged equations are written in conservative form

$$\frac{\partial}{\partial t}Q+\frac{\partial}{\partial x}F+\frac{\partial}{\partial y}G=\frac{1}{\mathrm{Re}}\left(\frac{\partial}{\partial x}F_v+\frac{\partial}{\partial y}G_v\right) \tag{1}$$

where

$$Q=\begin{pmatrix}\rho\\ \rho u\\ \rho v\\ \rho e\end{pmatrix}\quad F=\begin{pmatrix}\rho u\\ \rho u^2+p\\ \rho uv\\ \rho uh_t\end{pmatrix}\quad G=\begin{pmatrix}\rho v\\ \rho uv\\ \rho v^2+p\\ \rho vh_t\end{pmatrix}$$
$$F_v=\begin{pmatrix}0\\ \tau_{xx}\\ \tau_{xy}\\ \Pi_x\end{pmatrix}\quad G_v=\begin{pmatrix}0\\ \tau_{xy}\\ \tau_{yy}\\ \Pi_y\end{pmatrix} \tag{2}$$

Contributed by the Fluids Engineering Division for publication in the JOURNAL OF FLUIDS ENGINEERING. Manuscript received by the Fluids Engineering Division July 24, 2000; revised manuscript received Oct. 23, 2002. Associate Editor: B. Schiavello.

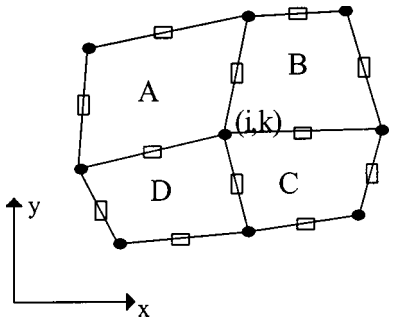

Fig. 1 Control volume

and

$$\Pi_x = \tau_{xx}u + \tau_{yx}v + \frac{\mu}{(\gamma-1)\mathrm{Pr}}\frac{\partial}{\partial x}(c^2)$$

$$\Pi_y = \tau_{xy}u + \tau_{yy}v + \frac{\mu}{(\gamma-1)\mathrm{Pr}}\frac{\partial}{\partial y}(c^2) \tag{3}$$

$$\frac{\mu}{\mathrm{Pr}} = \frac{\mu_L}{\mathrm{Pr}_L} + \frac{\mu_T}{\mathrm{Pr}_T}.$$

The stress tensor is computed in the standard way using Stokes's hypothesis, [16]. The ''total'' energy per unit mass $\overline{e}$ in vector Q is defined as

$$\overline{e} = e + \frac{1}{2}V^2. \tag{4}$$

A cell-vertex finite volume technique with an explicit Runge-Kutta integration method and Jameson artificial dissipation scheme has been used, as accurately described in previous papers, [17,18].

The numerical technique is second-order accurate in both time and space. The control volume shown in Fig. 1 is considered; the conservative variables are stored in the grid vertices (black circle) while the diffusive terms are calculated in the auxiliary midpoints (white rectangle). This arrangement simplifies the computation of boundary points keeping a second order accuracy with skewed grids.

Structured H-Type Grids. Structured H-type grids with orthogonal lines at the wall boundaries are generated by integrating a biharmonic system as described by Cravero [19]. The biharmonic system consists of two fourth-order differential equations (one for each coordinate direction) that can be split into four second-order Poisson equations. Increasing the order of the system permits to impose as boundary conditions both the points distribution and the line orthogonality along the boundaries.

Several point stretching functions are implemented in the code to distribute the points along the blade profile in order to generate an H-type orthogonal mesh in turbine sections with a strong curvature or/and thick leading and trailing edges.

The numerical procedure has demonstrated very strong stability properties and flexibility in generating boundary orthogonal H grids when applied to several profiles typical of turbine sections.

The grids are periodic upstream and downstream the profile and allow a straightforward implementation of the periodicity boundary condition for turbomachinery flow analysis. Downstream the trailing edge the mesh is inclined according to the outlet blade metal angle; this simplifies the implementation of the algebraic turbulence model and improves its accuracy in the wake region.

In order to asses the grid quality, the line orthogonality at the boundaries is checked after the grid is generated and a maximum difference of ten degree, with respect to the geometrical orthogonal local direction, is accepted.

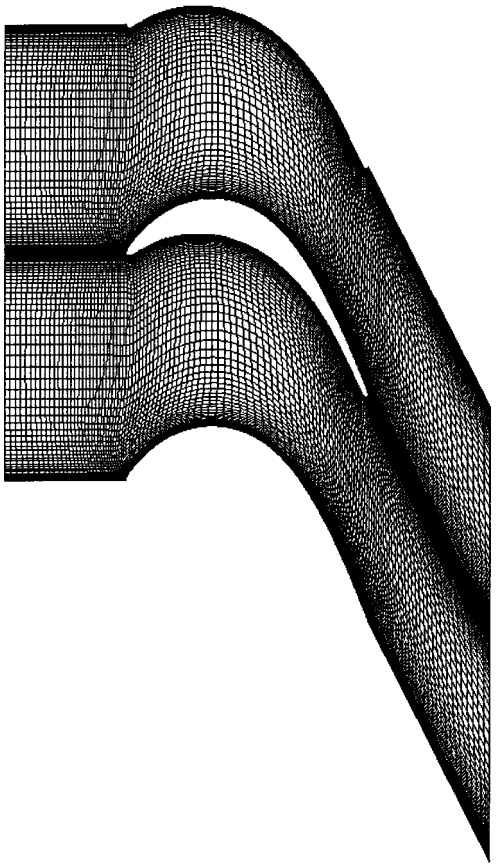

Fig. 2 Boundary orthogonal grid–ECA6 cascade; 121×95 grid points

For Navier-Stokes analysis the grid lines are stretched to the wall boundary in order to have a value of y^+ less then ten. The distribution of y^+ at the wall is checked after the computation and if values higher then the above-mentioned limit are detected a new grid is generated.

In Fig. 2 a sample grid for the ECA6 turbine blade profile, [20], is shown. The grid consists of 121×95 points in the x and y-direction respectively.

Inlet and Outlet Boundary Conditions. Different sets of quantities can be fixed at inlet or outlet according to the axial inlet Mach number. For turbomachinery computations it is known that the best set of values to fix is composed by total pressure, total temperature, and flow angles at the inlet and static pressure at the outlet. This is for subsonic inlet axial velocity, while for supersonic inlet axial Mach number an additional quantity is fixed at the inlet and all the values are extrapolated at the outlet.

At the inlet, in case of axial Mach number less than unity, total pressure, total temperature and flow angle are fixed and the static density is extrapolated from the interior point. To update all the conservative variables in the first axial section, the one-dimensional Riemann invariants have been considered.

At the outlet the static pressure is fixed while density and the Riemann invariants are extrapolated from the interior points using a local one-dimensional approximation.

Wall Boundary Conditions. The cell-vertex finite volume technique is directly applied at the wall boundary points using a half-control volume for the point lying on the surface. When viscous flows are computed the nonslip condition at the wall is implemented and the adiabatic wall ($\partial T/\partial n = 0$) is enforced using the neighboring points to the wall. In case of heat transfer analysis

Table 1 Wall-damping functions

Option	A^+
$A^+=26$	standard
$A^+=\dfrac{25}{C_{km}P^++1}$	Kays-Moffat, [22]
$A^+=\dfrac{26}{\sqrt{11.8P^++1}}$	Cebeci-Smith, [23]

the static temperature value is fixed at the wall. The code has the option to solve an inviscid flow. In this case the slip condition for velocity at the wall point is implemented as described in Ref. [18]. In the applications presented in this paper only viscous adiabatic wall boundary condition has been used.

Turbulence Model. The Baldwin-Lomax algebraic turbulence model, [21], is implemented to compute the turbulent viscosity and some modifications to the standard model have been introduced as additional options for the near-wall damping and the turbulent Prandtl number evaluation. The dynamic turbulent viscosity is computed with the two-layers model:

$$\mu_T=\rho\varepsilon \quad \varepsilon=\varepsilon_{\text{inner}} \quad \text{if } n\leqslant\overline{n} \text{ or } \varepsilon=\varepsilon_{\text{outer}} \quad \text{if } n>\overline{n},$$

$\overline{n}$ being the normal distance to the wall where $\varepsilon_{\text{inner}}=\varepsilon_{\text{outer}}$.

The standard option for the *inner layer* is the Prandtl-van Driest formulation with the following mixing-length model:

$$\varepsilon_{\text{inner}}=l^2|\omega|, \tag{5}$$

ω being the vorticity and 1 the mixing length according to

$$l=kn[1-e^{-n^+/A^+}] \quad k=0.4(\text{Von Karman}) \tag{6}$$

with $n^+=n\sqrt{\rho_W|\tau_W|}/\mu_W=n\rho u_{\tau\max}/\mu_L$ and $u_{\tau\max}$ is the maximum value of $u_\tau=\sqrt{\mu_L|\omega/\rho|}$ along the boundary layer profile. The wall-damping functions of Table 1 can be selected.

P^+ is the pressure gradient computed as $P^+=\nu U^3/\rho(C_f/2)^{1.5}\partial p/\partial s$ while $C_{\text{km}}=30.2$ for $P^+\leqslant 0.0$ otherwise $C_{km}=20.6$. The turbulent Prandtl number can be either fixed (0.9 in case of air) or computed following Boyle [11] for heat transfer analysis:

$$\text{Pr}_T=\left[\frac{0.5}{\text{Pr}_{T\infty}}+\frac{0.2\mu_T}{\mu_L}\frac{\text{Pr}_L}{\sqrt{\text{Pr}_{T\infty}}}-0.04\left(\frac{\mu_T\text{Pr}_L}{\mu_L}\right)^2\times\left(1-\exp\left(-\frac{5\mu_L\text{Pr}_L}{\mu_T\sqrt{\text{Pr}_{T\infty}}}\right)\right)\right]^{-1} \tag{7}$$

being $\text{Pr}_{T\infty}=0.86$. The variable Prandtl number model allows a slight improve in the heat transfer predictions for turbine blades, as discussed by Boyle [11], and it has been therefore included as an option in the present code. Without heat transfer analysis the constant Prandtl number option shows no differences with respect to the model of Eq. (7).

The *outer layer* is computed with the complete formulation including the function F_{wake} for the wake region analysis:

$$\varepsilon_{\text{outer}}=0.02688F_{\text{wake}}F_{\text{Kleb}} \tag{8}$$

$$F_{\text{wake}}=\min\left[n_{\max}F_{\max},C_2(U_{\text{mam}}-U_{\min})^2\frac{n_{\max}}{F_{\max}}\right], \tag{9}$$

$U_{\max}$ and $U_{\min}$ being the maximum and the minimum values of the velocity profile and $n_{\max}$ the value of n where the maximum value of the following function is reached:

$$F=n|\omega|[1-e^{-n^+/A^+}]. \tag{10}$$

The function of Klebanov is

$$F_{\text{kleb}}=[1+5.5(0.3n/n_{\max})^6]^{-1}. \tag{11}$$

In the near wall region $U_{\min}$ is equal to zero while in the wake region the turbulent viscosity is computed with the outer value.

The simple transition criterion of the original Baldwin-Lomax model, [21], has been retained, as in other codes, [8], without any intermittency function effect, [11].

Applications

The computational technique has been applied to a set of turbine cascades from different profile families. All the computations presented have been performed with a four-stage Runge-Kutta scheme with standard coefficients (1/4,1/3,1/2,1), standard values for the second and fourth-order artificial viscosity coefficients (1/4 and 1/64, respectively). The adiabatic wall condition and constant turbulent Prandtl number (0.9) have been fixed for the above computations. The Kays-Moffat option (see Table 1) for the wall damping function has been considered.

The convergence criterion for the iterative computation has been based on the total pressure coefficient and a tolerance of 0.1 percent for its stabilization has been introduced (this requires about 25,000 iterations starting from a uniform initial guess of the flow field).

The two-dimensional cascade obtained with the profile ECA6, [20], typical for a gas turbine rotor section, has been analyzed to compare the results obtained with the Navier-Stokes solver to the experimental data. A grid refinement study has been conducted with the cascade design conditions ($\alpha_1=37.7$ deg$-M_2=0.59$). The grids are formed by 121 lines in the axial direction (see Fig. 2) and 35/75/95 points in the tangential direction clustered to the wall. Denoting by ξ the coordinate along the grid line normal to the wall, the points are distributed on these lines according to the function $\eta=a\xi+\xi^b$ (with $a=0.02$ and $b=7$). In Fig. 3 the calculated blade load is compared to the experimental data; the agreement is rather good and the grid density has a major effect in the trailing edge region, as can be expected with an H-type grid.

In Fig. 4 the boundary layer velocity profiles at $x/C=0.85$ for the three grids are compared to the experimental distribution; the predicted velocity distribution with $ny=35$ is appreciably different from those obtained with $ny=75$ and $ny=95$ that are in reasonable agreement with the experiments. Nevertheless, even with the finest grid ($ny=95$), the model is not able to correctly capture

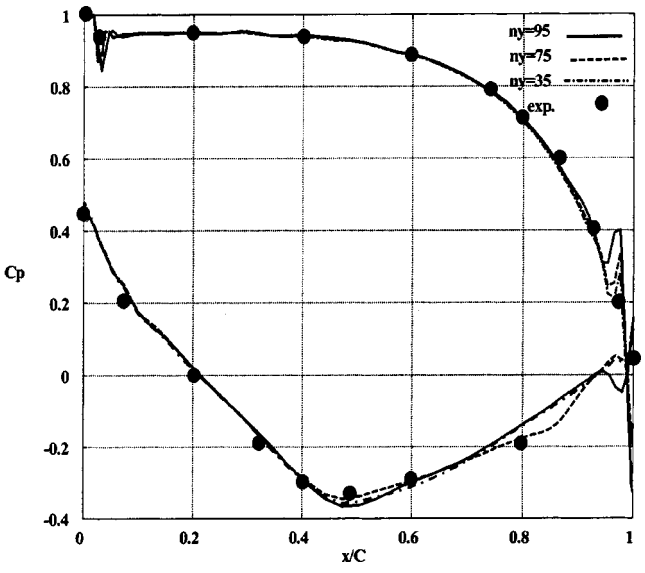

Fig. 3 Blade profile ECA6—pressure coefficient distributions along the blade with different grid densities. Comparison with experimental values *Tu*=7.0 percent (uncertainty for *Cp* =±0.005).

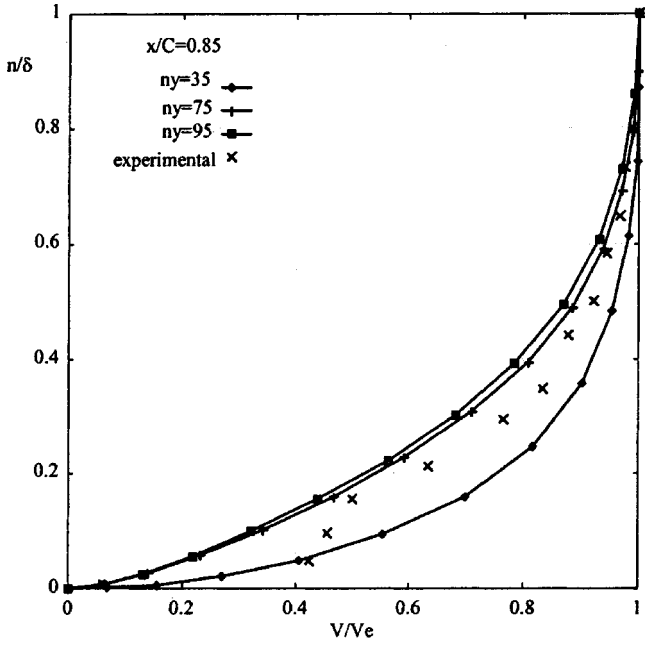

Fig. 4 Blade profile ECA6—boundary layer velocity profiles at $x/C=0.85$ with different grid densities. $Tu=0.8$ percent (uncertainty for $V\leqslant 5$ percent).

the separation bubble that is experimentally detected on the suction side surface. The physics of the separation bubble is dominated by the pressure distribution on the blade profile, that is not extremely well predicted by the viscous flow solver at $0.8<x/Cax<1.0$ (see Fig. 3).

The computed outlet flow angle (63.2 deg) matches the experimental value and it is not influenced by the grid density. The calculated total pressure loss coefficients are 0.0270, 0.0259, 0.0251 with $ny=35$, 75 and 95 points, respectively, while the experimental value is 0.0223. The grid effect is not too strong and even the worst value (0.0270) obtained with the coarsest grid is closer to the experimental data then the value of 0.038 obtained with semi-empirical correlations, [2].

In Figs. 5–7 the computed boundary layer profiles with $ny=95$ at $x/C=0.65$, 0.75, 0.85 are, respectively, shown and compared to the experimental distributions obtained with different values of the turbulence intensity Tu (0.8,5.0,7.1 percent). The separation bubble, and the associated boundary layer profile,

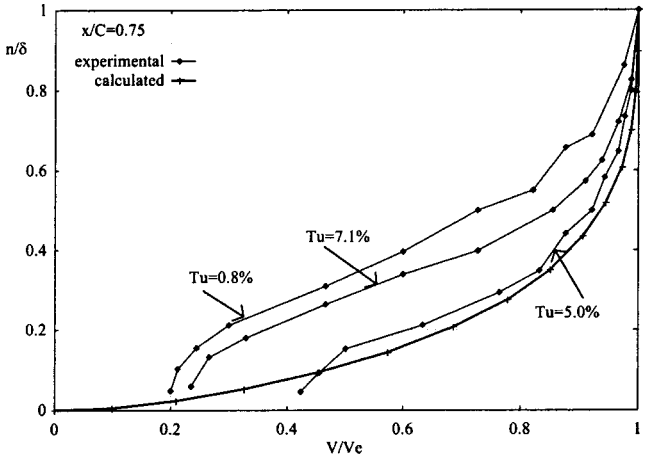

Fig. 6 Blade profile ECA6—boundary layer velocity profiles at $x/C=0.75$ (uncertainty for $V\leqslant 5$ percent)

previously discussed (Fig. 4), are strongly affected by the freestream turbulence level, that is not considered by the algebraic model. In fact, as discussed in Ref. [24], transition occurs, for the same blade profile, on the suction side surface in the region $0.75<x/C<0.95$, depending on the turbulence level. With the lowest inlet turbulence level of 0.8 percent a laminar separation bubble is detected at $x/C=0.85$.

This flow condition is not easy to represent with a CFD analysis even with more sophisticated turbulence models. In Ref. [25] the computational results for the ECA6 cascade in a three-dimensional configuration have been obtained with k-ε and k-ω turbulence closures in a low-Reynolds formulation, but without any transition modeling. Only fully turbulent flows have been computed and massive flow separations on the suction side and stability problems have been reported with purely laminar flows. With a two-dimensional low-Reynolds k-ω formulation the separation bubble has been detected with the lowest turbulence intensity (0.8 percent), [26], but the need for an external transition model has been highlighted for higher turbulence levels. In fact, the correct boundary layer profiles on the ECA6 suction side surface can be correctly computed, with different turbulence intensity, after the inclusion of the transition model (based on experimental correlations) proposed by Mayle [27] into a standard k-ω formulation, [28].

The algebraic turbulence closure implemented into the present code does not take into account the effects of turbulence intensity

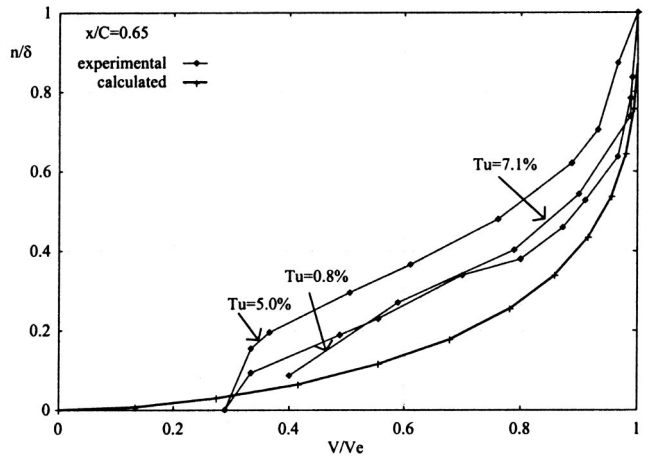

Fig. 5 Blade profile ECA6—boundary layer velocity profiles at $x/C=0.65$ (uncertainty for $V\leqslant 5$ percent)

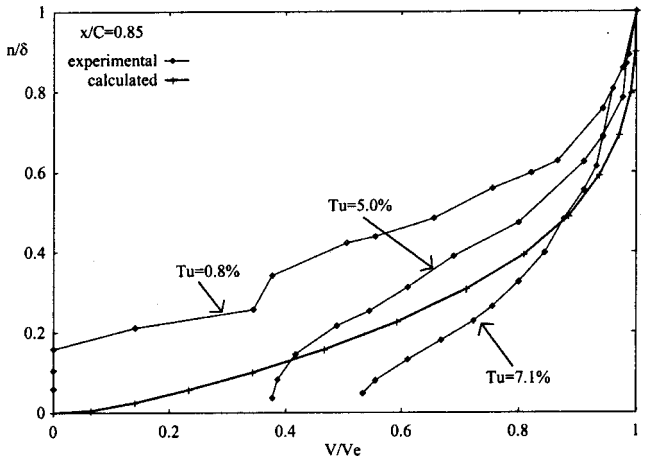

Fig. 7 Blade profile ECA6—boundary layer velocity profiles at $x/C=0.85$ (uncertainty for $V\leqslant 5$ percent)

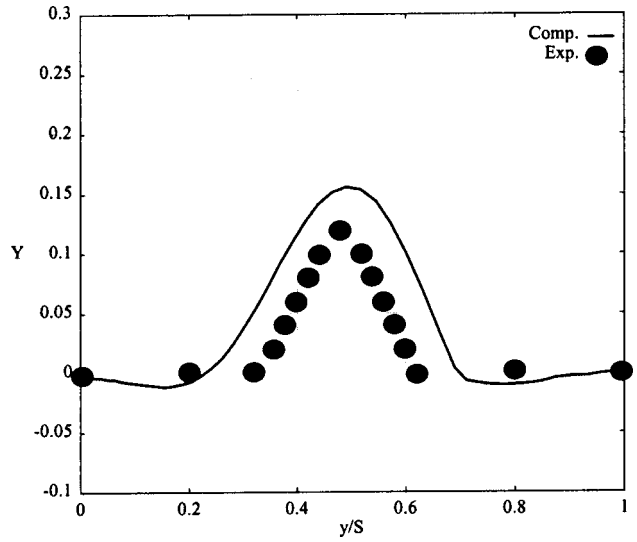

Fig. 8 Computed versus experimental wake profile at $x/Cax = 1.40$. $Tu = 5.0$ percent (uncertainty for $Y = \pm 0.001$)

and therefore the best agreement with the experimental results can be expected with high turbulence levels outside the transition and separation bubble regions.

In Fig. 8 the computed wake profile at $x/Cax = 1.40$ is compared to the experimental data, [20]; the local total pressure loss coefficient is plotted against the normalized tangential direction. The wake model for the algebraic turbulence closure (Eq. (9)) is rather rough and it is difficult to implement in the trailing edge region where both wall and wake effects are present, [16]. The shape and the symmetry of the wake are well represented by the viscous solver, but the width is overestimated. This can explain the overestimation of the computed loss coefficient. In fact, in case of subsonic flow, the mixing loss, that occurs downstream the trailing edge, accounts for a high percentage (about 50 percent) of the total profile loss, [29]. The accurate computation of the mixing loss depends on the correct representation of the blade wake development. Owing to the approximate modeling of the wake in the algebraic turbulence closure and the difficulties of a correct implementation of the model for a turbomachinery cascade, the mixing loss is not quantitatively well represented.

From the above analysis it is shown that the main cascade performances (blade load, outlet flow angle) are not significantly influenced by the grid density, but when the attention is focused on the profile loss the grid has some effect. Nevertheless the loss value obtained with the coarsest grid is more accurate than standard correlations. A more detailed inspection into the flow field (boundary layer profiles and wake shape) shows the weaknesses of the turbulence model.

A set of turbine cascades has been calculated using the profiles of Fig. 9 and the overall performances (outlet flow angle and loss coefficient) have been compared to existing experimental data and/or correlations, [2]. The experimental data and design flow conditions have been obtained from Fottner [20] and Sieverding [30]. In Table 2 the flow boundary conditions (inlet flow angle and outlet Mach number) are reported for the set of cascades together with the outlet flow angle obtained with the Navier-Stokes calculation, the experiments and correlations. The profile named VKI-A in Table 2 is similar to the ECA8 blade (see Fig. 9) and the full set of geometrical data and experimental results can be found in [31].

The agreement between the Navier-Stokes code and the experimental data is good and within 1 deg, while the correlation values compared to experimental data show a lower accuracy (especially for high subsonic–transonic flows when the outlet flow angle deviates from the cosine rule).

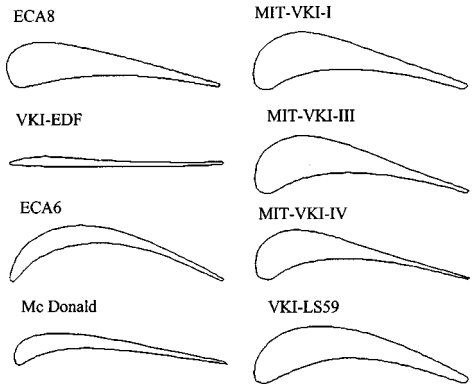

Fig. 9 Different turbine blade sections

The total pressure loss for a two-dimensional cascade can be split into three different contributions correlated to the flow physics [29]: (a) boundary layer loss, (b) shock loss, and (c) mixing loss. The capability of a simulation tool (correlations or Navier-Stokes analysis) to accurately predict the profile loss is directly linked to its accuracy in modeling the above-mentioned loss mechanisms. With a systematic analysis of turbomachinery cascades in a wide range of operating conditions, the blade profile parameters that have a direct impact on the loss mechanisms, and therefore on the total profile loss, can be identified and discussed, [32]. From the above analysis three quantities can be extracted to form the basis for a loss model: (a) the evolution of the boundary layer on the profile suction side (momentum thickness at the trailing edge), (b) the trailing edge thickness, and (c) the base pressure. The accuracy of a loss model therefore depends on its accuracy in representing and modeling the above quantities. The ability and the limits of the Navier-Stokes code to analyze the evolution of the blade boundary layers have been previously discussed.

In Table 3 the value of the base pressure obtained with the code is compared to the experimental value [30] for different cascades. The agreement is rather good and the discrepancies can be mainly attributed to the difficulties in modeling the trailing edge region with an H-type grid. Attempts have been made to improve the accuracy of an H-type grid in the trailing edge region [33], but the proposed grid modification has not been taken into account because it makes the grid boundary orthogonality almost impossible at the trailing edge. In order to build a successful structured H-type grid for Navier-Stokes analysis in turbomachinery cascades a compromise between grid orthogonality, trailing edge geometrical representation and grid shape in the wake region has to be considered. In the present work the grid orthogonality and the grid alignment with the wake have been considered more im-

Table 2 Outlet gas angle—comparison between Navier-Stokes, correlations and experiments (uncertainty for $\alpha = \pm 0.5$ deg)

Profile	α_1 (deg)	M_2	α_{2NS} (deg)	$\alpha_{2\,exp}$ (deg)	α_{2corr} (deg)
ECA6	37.7	0.59	63.2	63.2	60.4
ECA8	2.0	0.96	79.6	79.8	80.5
VKI-LS59	30.0	0.83	66.5	67.0	66.6
VKI-A	0.0	0.87	72.0	72.2	71.0
MIT-VKI-I	30.0	0.60	66.1	65.0	68.3
MIT-VKI-III	30.0	0.68	66.1	65.0	69.0
MIT-VKI-IV	30.0	0.60	66.0	65.0	68.0
Mc Donald (a)	24.0	0.68	72.8	72.0	70.5
Mc Donald (b)	24.0	1.06	71.7	72.0	70.4
VKI-EDF	66.0	0.75	67.77	···	70.4

Table 3 Base pressure p_b at the trailing edge—comparison between Navier-Stokes and experiments (uncertainty for $p_b = \pm 0.5$ percent)

Profile	$(p_b/p_{t1})_{NS}$	$(p_b/p_{t1})_{\exp}$
VKI-LS59	0.60	0.58
MIT-VKI-I	0.75	0.76
MIT-VKI-III	0.61	0.68
MIT-VKI-IV	0.75	0.76
Mc Donald (a)	0.65	0.70
Mc Donald (b)	0.30	0.39
VKI-EDF	0.54	0.61

portant in order to improve the accuracy of the wall boundary condition and the implementation of the turbulence model in the wake region.

The final comparison among Navier-Stokes, experiments and correlation is presented in Table 4 for the total pressure loss coefficient. The viscous computations and the experimental values agree reasonably well. But it is clear from Table 4 that the Navier-Stokes computation and the correlations don't show a common trend.

The profile loss coefficient, as in the original Ainley-Mathieson correlation, [12], is computed by interpolating the profile loss of two reference blade types: impulse blade and reaction blade. The interpolation is based on the inlet blade metal angle, the outlet flow angle, and the cascade pitch/chord ratio. Correction terms are then introduced, [2], to improve the accuracy of the original correlation taking into account viscous and compressibility effects. The cascade parameters used to compute this terms are: maximum profile thickness/chord, trailing edge thickness/throat opening, and inlet and outlet Mach numbers. As can be noticed, very few blade profile and cascade parameters are involved to model the profile loss that results from the viscous and compressible flow in a turbine cascade. Actually the boundary layer growth (and stability) and the shock loss are highly affected by local geometry and flow conditions. The difference between the value of the profile loss computed with correlations and Navier-Stokes method is higher at higher Mach numbers (Tables 2–4). In these conditions the effects of compressibility are important and they are very roughly modeled using correlations. A correction term, based on the profile exit to inlet Mach number ratio, is introduced into correlation to reduce the profile loss. This should model the boundary layer thinning and suppression of local flow separations close to sonic exit velocities in an accelerating flow passage. Moreover a very simple shock loss model, based on inlet and outlet Mach numbers, is implemented into correlations, [2], but it cannot represent the actual shock wave loss that is highly dependent on the local profile geometry and cascade parameters (i.e., suction side blade curvature and area increase in the supersonic part of the blade channel).

Nevertheless it should be noted that correlations are calibrated to give a reliable value for the overall loss coefficient composed by profile, secondary, and tip/hub clearance loss values in a three-dimensional cascade. Actually the model for the single loss coefficient (profile, secondary or tip/hub clearance) is not necessarily optimized to give the best value. From the above Navier-Stokes computations only the profile loss has been investigated.

Table 4 Profile loss coefficient—comparison between Navier-Stokes, correlations and experiments (uncertainty for $Y = \pm 0.001$)

Profile	Y_{NS}	$Y_{\exp}$	Y_{corr}	Re
ECA6	0.025	0.022	0.038	5×10^5
ECA8	0.070	0.065	0.079	1×10^6
VKI-LS59	0.048	0.054	0.080	7×10^5
VKI-A	0.024	0.022	0.030	1×10^6
MIT-VKI-I	0.062	⋯	0.069	5×10^5
MIT-VKI-III	0.053	⋯	0.050	5×10^5
MIT-VKI-IV	0.056	⋯	0.043	5×10^5
Mc Donald (a)	0.059	⋯	0.036	3×10^5
Mc Donald (b)	0.063	⋯	0.038	4×10^5
VKI-EDF	0.066	⋯	0.056	7×10^5

Conclusions

The proposed numerical technique to solve the Navier-Stokes equations in turbomachinery cascades has shown a good accuracy in capturing the main performances of the blade section. Maximum error for the outlet flow angle of 1.1 deg (average of 0.6 deg) and for total pressure loss coefficient of 13 percent. After a deeper analysis of the flow field some structural inaccuracies of the simple algebraic turbulence model arise when comparing the experimental and the computed boundary layer profile for different positions on the blade suction side, especially in the separation bubble zone. These inaccuracies can be mainly attributed to the absence of the turbulence intensity effect, the rough estimation of transition and the simplified wake model. Nevertheless the value of the total pressure profile loss coefficient computed with the code compares well to the experimental data (average error of about 10 percent); the comparison with the value predicted using correlations shows some discrepancies. From the above, analysis can be concluded that current CFD techniques for Navier-Stokes equations, even with simple turbulence modeling, can safely substitute the correlations in the design process for a new blade profile.

Nomenclature

C = blade chord
C_f = wall friction coefficient
C_p = pressure coefficient $(p_{t1}-p)/(p_{t1}-p_2)$
c = sound speed
e = internal energy
$\overline{e}$ = total internal energy
F, G = convective flux vectors
F_v, G_v = diffusive flux vectors
h = enthalpy
Ma_{is} = isentropic Mach number
n = normal distance to the wall
ny = points number in y-direction
p = static pressure
$\mathrm{Pr}_L, \mathrm{Pr}_T$ = laminar, turbulent Prandtl numbers
P^+ = static pressure gradient
Q = conservative flow variables vector
R = gas constant
Re = Reynolds Nr (based on blade chord)
s = surface distance along the profile
S = cascade pitch
t = time
T = static temperature
Tu = turbulence intensity
u, v = Cartesian components of velocity
V = velocity (sqrt(u^2+v^2))
$x, y,$ = Cartesian coordinates
Y = loss coefficient $(p_{t1}-p_{t2})/(p_{t1}-p_2)$

Greek

α = yaw flow angle
δ = boundary layer thickness
γ = specific heat ratio
μ_L, μ_T = laminar and turbulent viscosities
ρ = density

Subscript

ax = axial
e = external to the boundary layer
L = laminar
t = total quantity

T = turbulent
w = value at the wall
1,2 = inlet, outlet blade sections

References

[1] Baljé, O. E., and Binsley, R. L., 1968, "Axial Turbine Performance Evaluation. Part A—Loss-Geometry Relationships," ASME J. Eng. Gas Turbines Power, **90**, pp. 341–348.
[2] Kacker, S. C., and Okapuu, U., 1982, "A Mean Line Prediction Method for Axial Flow Turbine Efficiency," ASME J. Eng. Gas Turbines Power, **104**, pp. 111–119.
[3] Chen, S., 1987, "A Loss Model for the Transonic Flow Low-Pressure Steam Turbine Blades," IMechE Paper No. C269/87.
[4] Qiang, K. F., and Chen, N. X., 1982, "New Correlations of the Two-Dimensional Turbine Cascade Aerodynamic Performance," ASME J. Eng. Gas Turbines Power, **104**, pp. 458–466.
[5] Benvenuto, G., and Pittaluga, F., 1983, "Sul calcolo delle perdite di schiere di pale transoniche," 38th Congresso ATI, Bari, Italy.
[6] Dawes, W. N., 1983, "Computation of Viscous Compressible Flow in Blade Cascades Using an Implicit Iterative Replacement Algorithm," TPRD/M/1377/N83.
[7] Chima, R. V., 1987, "Explicit Multigrid Algorithm for Quasi-Three-Dimensional Flow in Turbomachinery," AIAA J. Propul. Power, **3**(5), pp. 397–405.
[8] Arnone, A., Liou, M. S., and Povinelli, L. A., 1992, "Navier-Stokes Solution of Transonic Cascade Flows Using Non-Periodic C-Type Grids," AIAA J. Propul Power, **8**(2), pp. 410–417.
[9] Islam, A. M. T., and Sjolander, S. A., 1999, "Deviation in Axial Turbines at Subsonic Conditions," ASME Paper No. 99-GT-026.
[10] Croce, G., and Satta, A., 1996, "Calcolo numerico delle prestazioni termofluidodinamiche di schiere di pale di turbina," Turbomacchine '96, July 11–12, Genova.
[11] Boyle, R. J., 1991, "Navier-Stokes Analysis of Turbine Blade Heat Transfer," ASME J. Turbomach., **113**, pp. 392–403.
[12] Ainley, D. G., and Mathieson, G. C. R., 1951, "A Method of Performance Estimation for Axial-Flow Turbines," Aeronautical Research Council of Great Britain, Reports and Memoranda No. 2974.
[13] Sato, T., Aoki, S., and Nagayama, T., 1986, "Extensive Verification of the Denton New Scheme From the User's Point of View; Part I–II," ASME J. Turbomach., **108**, pp. 162–179.
[14] Davis, R. L., Hobbs, D. E., and Weingold, H. D., 1988, "Prediction of Compressor Cascade Performance Using a Navier-Stokes Technique," ASME J. Turbomach., **110**, pp. 520–531.
[15] Xu, L., and Denton, J. D., 1988, "The Base Pressure and Loss of a Family of Four Turbine Blades," ASME J. Turbomach., **110**, pp. 9–17.
[16] Chiari, P., Cravero, C., and Satta, A., 1998, "Un codice di calcolo per l'integrazione delle equazioni di Navier-Stokes nelle schiere di pale bidimensionali delle turbomacchine," IMSE Internal Report 3/98, University of Genova, Genova.
[17] Cravero, C., and Satta, A., 1995, "Three-Dimensional Numerical Solutions of Turbomachinery Annular Cascade Flow," ASME Cogen Turbo Power, Vienna, Austria, Aug.
[18] Cravero, C., and Satta, A., 1995, "An Algorithm for the Numerical Computation of Convective Fluxes in a Finite Volume Method for Complex Configurations," Fluid Machinery Forum, ASME Summer Meeting, Hilton Head, Aug.
[19] Cravero, C., 1997, "Generazione di magliature ortogonali al contorno tramite l'integrazione di equazioni biarmoniche," 15th UIT National Heat Transfer Conference, June 19–20, Torino.
[20] Fottner, L., 1990, "Test Cases for Computation of Internal Flows in Aero Engine Components," AGARD Propulsion and Energetics Panel, AGARD AR 275.
[21] Baldwin, B. S., and Lomax, H., 1978, "Thin Layer Approximation and Algebraic Model for Separated Turbulent Flows," AIAA Paper No. 78-257.
[22] Kays, W. M., and Moffat, R. J., 1975, "The Behavior of Transpired Boundary Layers," *Studies in Convection, Vol. 1: Theory, Measurement, and Application*, B. E. Launder ed., Academic Press, London.
[23] Cebeci, T., and Smith, A. O. M., 1974, *Analysis of Turbulent Boundary Layers*, Academic Press, New York.
[24] Hoheisel, H., Kiock, R., Lichtfuss, H. J., and Fottner, L., 1987, "Influence of Free-Stream Turbulence and Blade Pressure Gradient on Boundary Layer and Loss Behavior of Turbine Cascades," ASME J. Turbomach., **109**, pp. 210–219.
[25] Hildebrandt, T., and Fottner, L., 1999, "A Numerical Study of the Influence of Grid Refinement and Turbulence Modeling on the Flow Field Inside a Highly Loaded Turbine Cascade," ASME J. Turbomach., **121**, pp. 709–716.
[26] Cravero, C., and Perelli, L., 2001, "Aerodynamic Performance Prediction of Gas Turbine Cascades Using a k-ω Turbulence Closure," ECCOMAS Computational Fluid Dynamics Conference 2001, Sept. 4–7, Swansea.
[27] Mayle, E., 1991, "The Role of Laminar-Turbulent Transition in Gas Turbine Engines," ASME J. Turbomach., **113**, pp. 509–537.
[28] De Palma, P., 2001, "Accurate Numerical Simulation of Compressible Turbulent Flows in Turbomachinery," AIAA Paper No. 2001-2926.
[29] Mee, D. J., Baines, N. C., Oldfield, M. L. G., and Dickens, T. E., 1992, "An Examination of the Contributions to Loss on a Transonic Turbine Blade in Cascade," ASME J. Turbomach., **114**, pp. 155–162.
[30] Sieverding, C., 1976, "Transonic Flows in Axial Turbomachinery," VKI-LS 84, Rhode Saint Genese, Belgium.
[31] Arts, T., and Lambert de Rouvroit, M., 1992, "Aero-Thermal Performance for a Two-Dimensional Highly Loaded Transonic Turbine Nozzle Guide Vane: A Test Case for Inviscid and Viscous Flow Computations," ASME J. Turbomach., **114**, pp. 147–154.
[32] Denton, J. D., 1993, "Loss Mechanisms in Turbomachines," ASME Paper No. 93-GT-435.
[33] Knight, C. J., and Choi, D., 1989, "Development of a Viscous Cascade Code Based on Scalar Implicit Factorization," AIAA J., **27**(5), pp. 581–594.
[34] Stock, H. W., and Haase, W., 1989, "Determination of Length Scales in Algebraic Turbulence Models for Navier-Stokes Methods," AIAA J., **27**(1), pp. 5–14.
[35] Boyle, R. J., and Ameri, A. A., 1997, "Grid Orthogonality Effects on Predicted Turbine Midspan Heat Transfer and Performance," ASME J. Turbomach., **119**, pp. 31–38.

J. Hernández
Professor,
Departamento de Mecánica
ETSII, UNED,
E-28040 Madrid, Spain
e-mail: jhernandez@ind.uned.es

J. López
Associate Professor,
e-mail: Joaquin.lopez@upct.es

F. Faura
Professor,
e-mail: felix.faura@upct.es

Departamento de Ingenieriá de Materiales y Fabricación,
ETSII, Universidad Politécnica de Cartagena,
E-30202 Cartagena, Spain

P. Gómez
Assistant Professor,
Departamento de Mecánica,
ETSII, UNED,
E-28040 Madrid, Spain
e-mail: pgomez@ind.uned.es

Analysis of the Flow in a High-Pressure Die Casting Injection Chamber

The flow in the injection chamber of pressure die casting machines is analyzed using a model based on the shallow-water approximation which takes into account the effects of wave reflection against the end wall of the chamber. The governing equations are solved numerically using the method of characteristics and a finite difference grid based on the inverse marching method. The results of the model for wave profiles, volume of air remaining in the injection chamber at the instant at which the molten metal reaches the gate to the die cavity, and optimum values of the parameters characterizing the law of plunger motion, are compared with the numerical results obtained from a finite element code, which solves the two-dimensional momentum and mass conservation equations, taking into account nonhydrostatic and viscous effects. We found that, although the shallow-water model does not provide a very accurate estimation of the mass of entrapped air in the injection chamber for certain ranges of working conditions, it does describe reasonably well the influence of the acceleration parameters and the initial filling fraction on the entrapped air mass, and can be of help in selecting operating conditions that reduce air entrapment while keeping the injection chamber filling time as low as possible. [DOI: 10.1115/1.1538627]

1 Introduction

In the pressure die casting processes considered in this work the molten metal is injected into a die cavity from a horizontal injection chamber, in which the metal is pushed by a plunger (Fig. 1). The chamber is partially filled with the volume of molten metal that corresponds to the size of the die cavity, and the plunger then moves the length of the chamber, causing the formation of a surface wave. This process, which is the most commonly used process for manufacturing near-net shape cast aluminum components, provides closer dimensional tolerances and better surface finish than most alternative casting processes and allows very high production rates. On the other hand, one of the most important problems encountered in die casting manufactured parts is porosity, which adversely affects their mechanical properties, and makes it difficult to apply, or even prevents, heat treatment or welding. The control of casting porosity requires extensive study of different aspects of the process, [1], among them appropriate injection conditions that can contribute to minimizing air entrapment. To reduce the porosity of the manufactured parts caused by the initial air in the die cavity and injection chamber being trapped in the molten metal, the injection process usually consists of slow and fast shot stages. The study described in this paper focuses on the slow injection stage, during which the plunger usually first forces the molten metal to rise and fill the upper section of the injection chamber, and then moves at a constant critical speed until the injection chamber is completely filled, [2]. This operational procedure in the slow stage attempts to avoid air entrapment effects due to the roll over of the wave front caused by the reflection of the wave against the injection chamber ceiling (which might occur if plunger speed is too high) and to prevent premature wave reflection against the end wall of the chamber (which may also occur if the plunger remains below the critical speed and might produce air entrapment in front of the plunger or along the chamber ceiling). To reach the critical speed, the plunger must be initially accelerated, and the evolution of the wave profile will obviously depend on the plunger acceleration law, [3,4]. To reduce the amount of entrapped air, the wave must be prevented from breaking inside the chamber and possible air entrapment effects due to the wave reflecting off the end wall and ceiling of the chamber should be minimized. It is very difficult to estimate accurately the contribution of the amount of air entrapped in the injection chamber at the time the molten metal reaches the gate to the die cavity, to the porosity level of manufactured pieces. This porosity level will depend on (among other factors) not only the amount of air that is entrained into the liquid within the injection chamber, where it forms small air bubbles (as a consequence, for example, of wave breaking, if the operating conditions are far from the optimal), but also on the air entrained during the injection of the metal into the die cavity. However, it is highly probable that the larger the amount of air in the chamber at the instant the molten metal reaches the gate to the die cavity and begins to flow through the runner, the larger the amount of air that will be entrained when the molten metal enters the die cavity. Lindberg et al. [5] discussed the importance of reducing this amount of entrapped air, and showed experimentally that large amounts of entrapped air may even cause interruptions in the flow of metal in the runner due to solidification effects.

Until recently, little attention had been paid to investigating the flow of molten metal in the injection chamber, and the published experimental data in this area, [2,6], are still limited. Among the theoretical works that have helped to provide a better physical understanding of the overall behavior of the molten metal in the chamber are those of Thome and Brevick [7,8], Tszeng and Chu [3], and López et al. [4], although none of them has considered effects of wave reflection against the end wall of the chamber. The numerical simulations of the slow injection stage that have been carried out are scarce, although it is interesting to mention the studies of Backer and Sant [9], Kuo and Hwang [10], Khayat [11], and López et al. [12]. The difficulties and limitations involved in the numerical simulation of the flow in the injection chamber arise from the complex behavior that the molten metal may exhibit in

Contributed by the Fluids Engineering Division for publication in the JOURNAL OF FLUIDS ENGINEERING. Manuscript received by the Fluids Engineering Division November 28, 2001; revised manuscript received September 18, 2002. Associate Editor: G. Karniadakis.

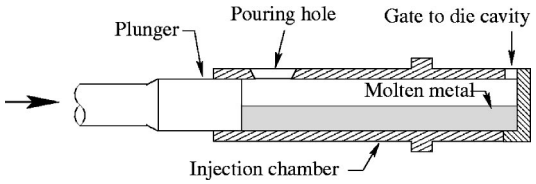

Fig. 1 Schematic representation of the injection chamber of a die casting machine

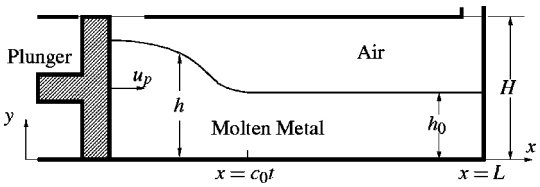

Fig. 2 Schematic representation of the problem and coordinate system

some operating conditions. Phenomena, such as those involved in wave breaking processes, the interaction of the molten metal with the chamber ceiling and wave reflection against the chamber walls, may require grid sizes that allow solution of the small-scale viscous and capillary effects, and this would require very high computational resources, even in the case of two-dimensional flows. However, it should be easier to describe the evolution of the free surface in operating conditions close to the optimal. For such conditions, simpler models, such as that based on the shallow-water approximation described by López et al. [4], could be very useful.

The main objective of this work was to carry out an analysis of the flow in the injection chamber using a model based on the shallow-water approximation which takes into account effects of wave reflection against the end wall of the chamber. In previous works, [4,13,14], a model based on the shallow-water approximation that neglected wave reflection effects was applied to cases for a wide range of the relevant parameters. In this work, this model will be extended to include wave reflection effects. Some preliminary results were presented in [12]. The proposed model will be applied to situations where the effects of the molten metal wave reflecting off the injection chamber end wall may be relevant. Results for the wave profile, the amount of air trapped in the molten metal and optimum values of the parameters characterizing the piston's movement will be presented. These results will be compared with those obtained numerically using a CFD code, which solves the two-dimensional momentum and mass conservation equations and takes into account nonhydrostatic and viscous effects. We will assume that the flow phenomena occurring in the injection chamber are sufficiently fast (the duration of the slow stage is typically of the order of 1 s) to make heat transfer and phase change effects negligible. Only operating conditions relatively close to the optimal, in which wave breaking would only occur in very early stages, will be considered. For these conditions, surface tension effects are expected to have very little influence on the free-surface dynamics, and have therefore been neglected. A detailed numerical simulation of wave breaking processes in the injection chamber was carried out by Gómez et al. [15], in whose work only plunging breakers (and no spilling breakers) were found to appear for typical operating conditions in the injection chamber.

2 Model Based on the Shallow-Water Approximation

In this section a simplified model of the flow in the injection chamber based on the shallow-water approximation will be briefly described. Further details of an analytical study based on this model of cases in which wave reflection effects were neglected can be found in [4,13]. In this work, the governing equations are solved numerically to take into account wave reflection effects.

2.1 Governing Equations. We shall assume that viscous effects are negligible and that the typical value of the free-surface height, $h(x,t)$, is much smaller than the typical horizontal length scale of the wave, so that shallow-water approximation can be used. With this approximation, which will be justified below, the vertical component of acceleration can be neglected when compared with gravitational acceleration, g. Introducing the shallow-water approximation into the two-dimensional Euler equations, it can be deduced that the pressure distribution in the molten metal can be considered as hydrostatic and the horizontal velocity component, u, becomes independent of the vertical coordinate y at any time, so that $u=u(x,t)$ (see Fig. 2). The governing equations can then be written as, [16],

$$\left[\frac{\partial}{\partial t}+(u+c)\frac{\partial}{\partial x}\right](u+2c)=0, \tag{1}$$

$$\left[\frac{\partial}{\partial t}+(u-c)\frac{\partial}{\partial x}\right](u-2c)=0, \tag{2}$$

where $c(x,t)=(gh)^{1/2}$ is the speed of a small-amplitude wave, relative to the fluid, for a depth h. Using the method of characteristics, these equations reduce to the statement that

$$u\pm 2c=\text{constant} \tag{3}$$

along characteristic curves defined by

$$\frac{dx}{dt}=u\pm c. \tag{4}$$

When wave reflection effects are not considered, the velocity and all other magnitudes can be obtained analytically (see López et al. [4]) as an implicit function of x and t:

$$x=X(t_1)+\left[\frac{3}{2}X'(t_1)+c_0\right](t-t_1), \tag{5}$$

$$u=X'(t_1), \tag{6}$$

where $X(t)$ is the location of the plunger face and $X'(t)$ the plunger speed. Boundary conditions will be applied at the plunger surface, where the velocity of molten metal is taken to be equal to the plunger speed $X'(t)$, and at the end wall of the chamber, where $u=0$. Two different plunger speed laws are considered in this work: a time-exponential law,

$$X'(t)=\alpha\beta(e^{\alpha t}-1), \quad t\leqslant t_H, \tag{7}$$

where α and β are positive constants, and where

$$t_H=\frac{1}{\alpha}\ln\left[\frac{2(\sqrt{gH}-\sqrt{gh_0})}{\alpha\beta}+1\right] \tag{8}$$

is the time which the molten metal takes to reach the chamber ceiling at the plunger face, [4], and a law given by

$$X'(t)=2(gh_0)^{1/2}\left[\left(1-\frac{(gh_0)^{1/2}t}{l}\right)^{-1/3}-1\right], \quad t\leqslant t_H, \tag{9}$$

where l is a positive constant, and where

$$t_H=\frac{l}{(gh_0)^{1/2}}[1-(h_0/H)^{3/2}]. \tag{10}$$

Notice that, for sufficiently large values of t, Eq. (7) gives a plunger speed that is proportional to the distance traveled by the plunger. A motion law of this kind can be considered as representative of die casting machines where the plunger speed is programmed as a function of plunger position, [14]. On the other hand, when l is equal to the injection chamber length, L, the

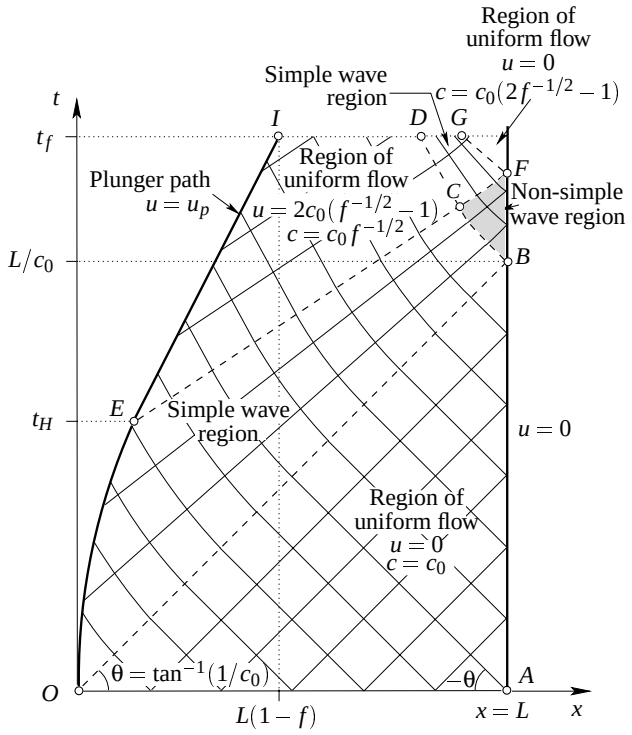

Fig. 3 Characteristic curves and flow regions in the x-t–plane

shallow-water model predicts that the plunger speed law of Eq. (9) will produce a vertical wave profile at the end wall of the chamber at $t=L/c_0$, so that all the initial air volume will be forced out without being entrapped, [4,14]. In both types of laws, for $t>t_H$,

$$X'(t)=2[(gH)^{1/2}-(gh_0)^{1/2}]. \tag{11}$$

Figure 3 shows the characteristic curves and the different flow regions in the $x-t$ plane. In the simple-wave region OBCE, since all the negative characteristics come from a region where the molten metal is at rest, it can be deduced from Eq. (3) that both u and c are constant along each positive characteristic. When the simple compression wave (comprising the positive characteristics emerging from the plunger between points O and E) impinges on the end wall of the chamber (at $t=L/c_0$), a simple compression wave is reflected from the wall, and a nonsimple wave interaction region (BFC) is formed. In this region, neither the slopes of the positive or negative characteristics are constant, and Eqs. (3) and (4) are solved numerically in order to obtain the wave profile as a function of time. The solution of Eqs. (3) and (4) may develop a singularity after a given time, for which the derivatives become unbounded and the solution ceases to exist. This singularity represents the beginning of wave breaking. A systematic study of the place and time of singularity formation in waves of molten metal within the injection chamber when wave reflection effects are not present can be found in the analytical study of López et al. [4].

2.2 Numerical Procedure. Equations (3) and (4) are solved using a deformable finite difference grid in the $x-t$ plane and an algorithm based on the inverse marching method, in which the locations of solution points are specified a priori. The characteristic curves through each solution point are extended rearwards to intersect the line of constant time on which the points from previous calculations are located. The characteristic curves between the solution point and the intersection points (initial-data points) are approximated by straight lines. The finite difference equations resulting from the discretization of Eqs. (3) and (4) are solved by using the modified Euler predictor-corrector method. In the predictor step, the coefficients in the finite difference equations are calculated at the initial-data points, where the flow properties are determined from a natural cubic spline interpolation based on previous solution points. In the corrector step, the coefficients are calculated from the average values of the dependent variables along each characteristic curve. The number of spatial grid nodes is kept constant with time. At each time step, a uniform grid step size Δx is calculated, and a ratio $\Delta x/\Delta t$ is chosen to satisfy the CFL stability condition.

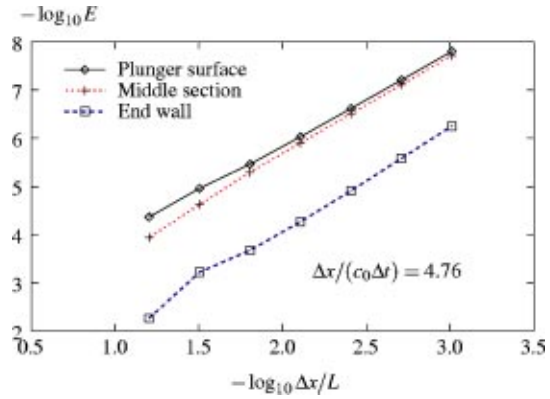

Fig. 4 Relative grid refinement error of Eq. (12) as a function of dimensionless grid size $\Delta x/L$, in different chamber sections and at $tc_0/L=1.08$ ($f=0.25$, $\xi=3$ and $L/\beta=9.46$)

The Richardson extrapolation method was applied to check the accuracy of the numerical model. As an example, Fig. 4 shows the approximate relative grid refinement error defined by

$$E=|(c_{\text{ext}}-c_{\Delta x})/c_{\text{ext}}|. \tag{12}$$

($c_{\Delta x}$ and c_{ext} are, respectively, the approximate and the extrapolated numerical solutions, [17], for the wave speed), as a function of the dimensionless grid spacing at $t=0$, $\Delta x/L$, for the time-exponential plunger speed law with $\xi=2c_0/(3\alpha\beta)=3$ (where c_0 is the wave speed corresponding to h_0) and $L/\beta=9.46$, and an initial filling fraction $f=0.25$. Notice that the parameter ξ is the inverse of a Froude number. The curves in Fig. 4 correspond to an instant $tc_0/L=1.08$ (i.e., after wave reflection has begun) and to three different locations: the plunger surface, the end-wall of the injection chamber, and the intermediate section between both. The order of convergence rate of the method calculated at these locations was found to be 1.97, 2.24, and 2.01, respectively. The finest grid used in the convergence test corresponded to $\Delta x/L=10^{-3}$. Notice in Fig. 4 that the relative error is higher at the end wall of the chamber, where the reflection occurs. All the results in Fig. 4 were obtained using a value of 4.76 for $\Delta x/(c_0\Delta t)$ at the beginning of plunger motion. Using 500 nodes along the x-coordinate ensured that the solution was independent of the grid in most cases presented in this paper. A more detailed discussion about the numerical accuracy and validation of a similar numerical scheme, which was applied to the evacuation of air through vents in pressure die casting processes using a fixed grid, can be found in [18].

3 CFD Model

The Navier-Stokes equations were solved numerically using the finite element Wrafts code, [19]. A two-dimensional model, which requires much less computational resources than a three-dimensional model and where the governing equations can be written as

$$\frac{\partial u}{\partial x}+\frac{\partial v}{\partial y}=0, \tag{13}$$

$$\frac{\partial u}{\partial t}+u\frac{\partial u}{\partial x}+v\frac{\partial u}{\partial y}=-\frac{1}{\rho}\frac{\partial p}{\partial x}+\nu\left(\frac{\partial^2 u}{\partial x^2}+\frac{\partial^2 u}{\partial y^2}\right), \tag{14}$$

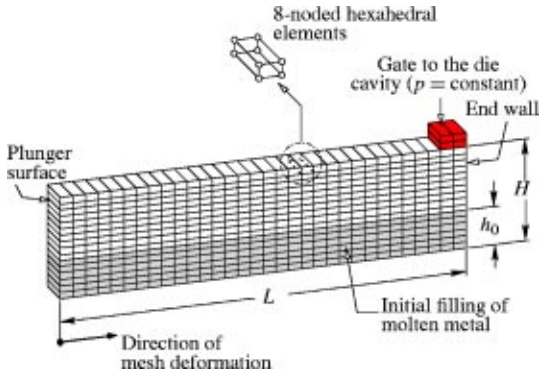

Fig. 5 Schematic representation of the computation grid in the injection chamber

$$\frac{\partial v}{\partial t}+u\frac{\partial v}{\partial x}+v\frac{\partial v}{\partial y}=-\frac{1}{\rho}\frac{\partial p}{\partial y}+\nu\left(\frac{\partial^2 v}{\partial x^2}+\frac{\partial^2 v}{\partial y^2}\right)-g, \qquad (15)$$

was used. It is expected that the wave profiles in the symmetry plane of an injection chamber of circular cross-section will be similar to those in an equivalent two-dimensional configuration. A discussion on the shape of the free-surface profile outside the symmetry plane in real injection chambers can be found in [3]. The momentum equations were solved using an explicit time integration for the velocities, and the pressure was calculated from a Poisson equation at each time step, using a projection method, [20]. A volume of fluid (VOF) method, [21], was used to describe the evolution of the free surface, and the mesh was moved and deformed using a technique similar to the arbitrary Lagrangian-Eulerian method, [22]. As already mentioned in the Introduction, surface tension effects were neglected. The problem was treated using a one-element-thick computational mesh with eight-noded hexahedral elements, with symmetry conditions applied to the lateral surfaces (Fig. 5). A no-slip condition was imposed at the chamber walls and the pressure was fixed at the gate to the die cavity. The dynamic viscosity and density of pure aluminum at its freezing point (1.3×10^{-3} Pa s and 2385 kg m^{-3}, respectively), and a chamber height of 5.08 cm were used in all computations. At the plunger surface, a horizontal velocity given by Eqs. (7) or (9) for $t\leqslant t_H$, and by Eq. (11) for $t>t_H$ was imposed.

Different grids were used to check the grid-dependency of the solution, [13,14]. As an example, Fig. 6 shows, for an injection chamber with $L/H=9$ and $H=5.08$ cm, three wave surface profiles computed with Wrafts code for a case involving the plunger speed law of Eq. (9), with $L/l=0.8$, and $f=0.254$. The results were obtained using three different grids with 250×64, 350×90, and 500×130 elements. The difficulty in obtaining grid-independent results increased for times after the beginning of wave breaking. At earlier times, for which most of the results presented in this paper were obtained, grid independency was generally achieved for a number of grid elements within a range of around 350×90 and 500×130, which were used to obtain most of the results reported in this paper. At later times, the grid sizes required to ensure grid independence were considerably greater. Nevertheless, attention in this work was focused on conditions close to the optimal, for which air entrapment would be minimized and wave breaking effects were not expected to appear. Typical time steps in the cases simulated in this work varied from 1 ms at the beginning of plunger movement to less than 0.01 ms during wave breaking.

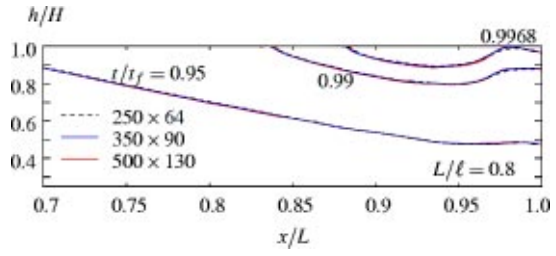

Fig. 6 Dependence of computed wave surface profiles on grid size. Plunger speed law of Eq. (9), with $L/l=0.8$, and $f=0.254$.

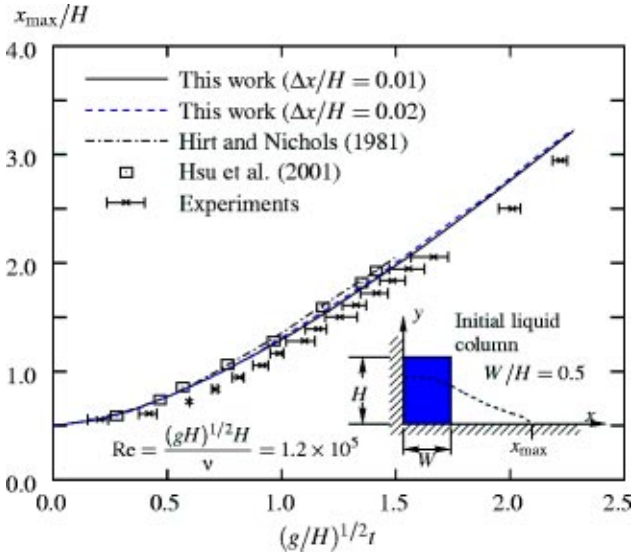

Fig. 7 Dimensionless water front location as a function of dimensionless time during the collapse of a water column. Comparison between Wrafts results and other numerical and experimental results.

Hernández et al. [13] compared some of the results of the CFD model with the experimental results of Duran et al. [2], finding a good qualitative agreement. Although the quantitative agreement was also acceptable in cases where the experimental uncertainty seemed to be least, the small number of experimental data available and the uncertainty of most of them made it difficult to obtain a more conclusive experimental validation.

In order to assess the performance of the CFD model, extensive calculations were carried out for different test problems. As an example, the results of the CFD model for the water front location as a function of time during the collapse of a water column, obtained for two different grid spacings, are compared in Fig. 7 with different numerical and experimental results. The present results agree well with the data of Martin and Moyce [23], the differences being of a similar magnitude to those reported elsewhere, [21,24]. Figure 8 shows results for the free-surface profiles at different times during the collapse of a water column of a width/height ratio (W/H) of 10. The Wrafts results are in good agreement with those obtained numerically by Hsu et al. [24], and also with the analytical results predicted by the model based on the shallow-water approximation, which, in this case, because of the large W/H ratio, is justified. In these simulations, as well as in those presented below, the CFD model faithfully conserved mass, with mass errors lower than 0.5% in all cases. The excellent agreement between the CFD results and some of those predicted by the shallow-water model presented in the next section for conditions for which the shallow-water approximation holds very accurately, constitutes an additional test of the code for such conditions.

4 Discussion of Results

4.1 Validity of the Shallow-Water Approximation. Before presenting and discussing the results obtained in this work, we will briefly examine the validity of the shallow-water approxima-

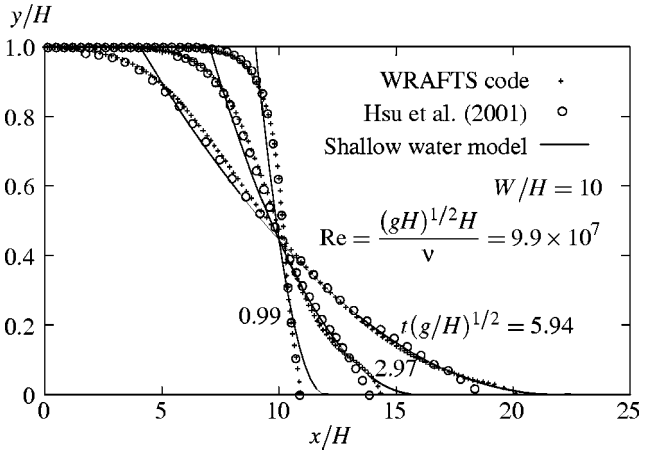

Fig. 8 Free-surface profiles at different instants during the collapse of a water column with a width/height ratio of 10 (the vertical scale has been enlarged by a factor of 15)

tion for typical operating conditions and geometries of the injection chamber. If plunger acceleration ceases at t_H, the characteristic horizontal length scale of the wave can be estimated as $t_H c_0 - X(t_H)$. Then, the shallow-water approximation will be justified if $\varepsilon = h_0/(t_H c_0 - X(t_H)) \ll 1$, a condition that, for the plunger motion law of Eq. (9), for example, is satisfied provided that $\varepsilon = H/3l[1-(h_0/H)^{0.5}] \ll 1$. As an example, for the cases corresponding to the results of Figs. 9(*a*) and 9(*b*), which correspond to the plunger speed law of Eq. (9), and where $f=0.254$ and 0.5, respectively, $l/H=9$ and the injection chamber has a length $L=1.56l$ (for which there are no wave reflection effects against the end wall of the chamber), $\varepsilon=0.075$ and 0.126, respectively, and so the shallow-water approximation is reasonable. This is confirmed by the overall good agreement between numerical and analytical results, despite some slight discrepancies (particularly for large values of f), which are more noticeable around the foremost tip of the wave profile and (especially) near wave breaking. On the other hand, the discrepancies are more important in the cases of Figs. 9(*c*) and 9(*d*) (notice the smaller enlargement factor indicated in the caption), which correspond to the plunger speed law of Eq. (9), and where $f=0.254$ and $f=0.5$, respectively, $l/H=3$ and the injection chamber has a length $L=1.56l$, for which $\varepsilon=0.225$ and 0.379, respectively, and so the shallow-water approximation is less justified. Whatever the case, although the predictions of the shallow-water model are still fairly accurate, the chamber aspect ratio of this case is not typical of real die casting machines, and, for all the cases for which results are presented in this section, the shallow-water approximation may be considered appropriate (except obviously for conditions near wave breaking).

4.2 Wave Surface Profiles

Plunger Motion With a Time-Exponential Speed Law. Figures 10(*a*) and 10(*b*) show a comparison between results for the wave-surface profiles obtained with the model based on the shallow-water approximation and those predicted with the Wrafts code. They correspond to the time-exponential plunger speed law of Eq. (7), a chamber aspect ratio $L/H=9$ (typical of real machines, [2,3]), for which the shallow-water approximation is expected to be acceptable, and initial filling fractions of 0.25 and 0.4, respectively. All the combinations of the dimensionless parameters ξ and L/β in the depicted profiles satisfy the condition that, in accordance with the shallow-water model, the wave reflected from the end wall of the chamber begins to break (i.e., the wave profile first has a vertical tangent) just at the instant at which the molten metal reaches the gate to the die cavity (this instant corresponds to the

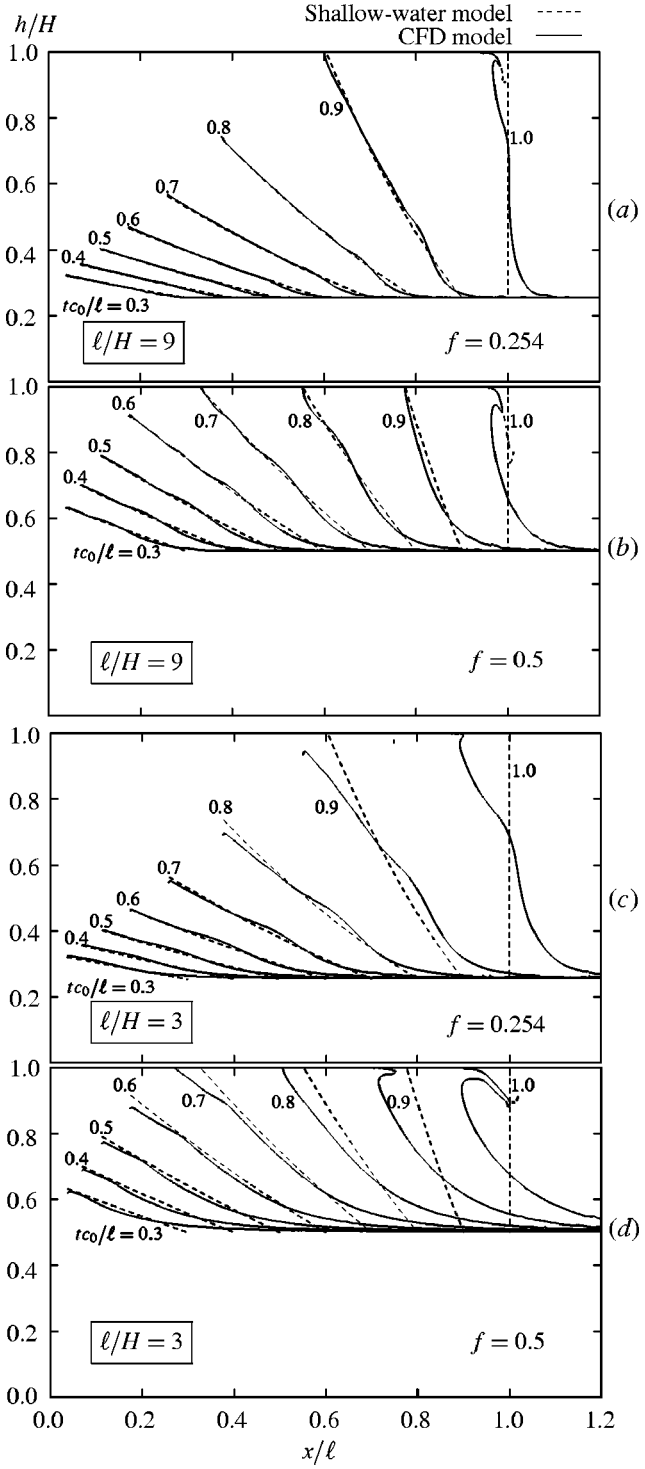

Fig. 9 Comparison between analytical and computed wave-surface profiles for the plunger speed law of Eq. (9). (*a*) $l/H=9$, $f=0.254$, (*b*) $l/H=9$, $f=0.5$, (*c*) $l/H=3$, $f=0.254$, (*d*) $l/H=3$, $f=0.5$. The vertical scale has been enlarged by a factor of 6.5 in (*a*) and (*b*), and 2.2 in (*c*) and (*d*). The time has been made dimensionless with the time required to fill a chamber with $L/l=1$.

value of t/t_f of the last profile obtained, where t_f is the time that the molten metal would take to fill the injection chamber if it were not possible for the metal to flow out of the chamber). It was expected that, for a given value of ξ, a local minimum volume (area) of entrapped air in the injection chamber would be obtained

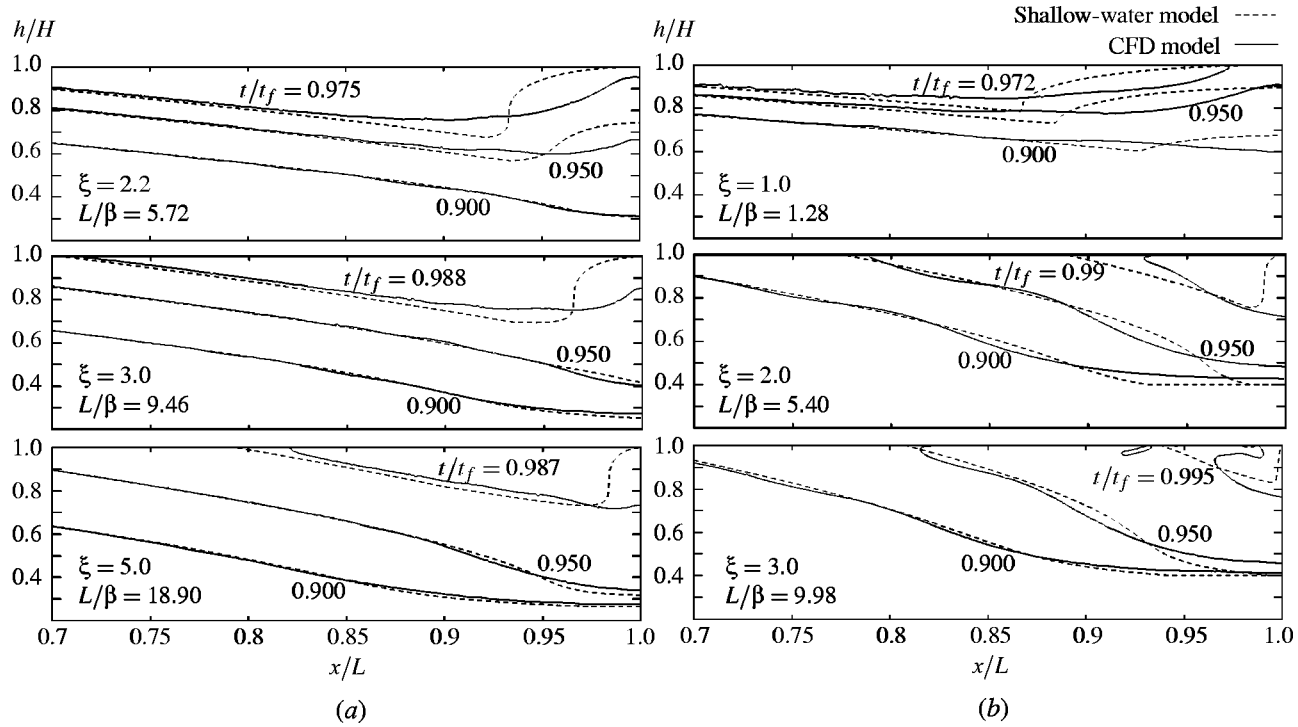

Fig. 10 Comparison between results for the wave profiles obtained with the shallow-water model and from the CFD model, for the time-exponential plunger speed law with different values of ξ, and the conditions described in the text. (*a*) $f=0.25$, (*b*) $f=0.4$.

for this condition. From the results of Fig. 10, it can be observed that in all cases sufficiently far from the end wall of the chamber, there is very good agreement between both types of results, although the CFD model predicts slightly later wave breaking and smoother wave profiles. In the vicinity of the end wall, wave reflection accentuates the differences between the results of the two models, particularly as regards the instant at which the molten metal reaches the gate to the die cavity for large values of ξ, which is delayed in the CFD results. For conditions relatively far from the optimal, regions of high curvature in the free surface can be observed in the figures, and so a more detailed analysis of the flow would have to take into account surface tension effects. However, it is expected that the optimum operating conditions that would be obtained from this analysis, for which no small-scale motions are expected to appear, will not be significantly different from those obtained in this work.

Plunger Motion With the Speed Law of Eq. (9). Figures 11(*a*) and 11(*b*) show a comparison between the wave surface profiles obtained with the shallow-water and CFD models for the plunger speed law of Eq. (9). The results correspond to initial filling fractions $f=0.254$ and 0.4, a chamber aspect ratio $L/H=9$, and different values of L/l, including $L/l=1$, for which the volume of entrapped air would be minimum (zero), in accordance with the shallow-water model. In each case, the last profile depicted corresponds to the instant at which the CFD model predicts that the molten metal reaches the gate to the die cavity, except for the case where $f=0.4$ and $L/l=0.9$, for which the shallow-water model predicts that the molten metal reaches the gate to the die cavity at an earlier instant, and so the last profile represented corresponds to this instant. Also notice that, for the case where $L/l=1.05$, the last profile obtained from the shallow-water model represented in Fig. 11(*a*) is vertical, and only a profile obtained with the CFD model is represented for later instants.

There is good agreement between both types of results in Fig. 11, and, in the vicinity of the end wall of the chamber, even better than in the cases of the time-exponential motion law considered in the previous section. At the instant $t/t_f=0.95$, for an initial filling fraction $f=0.254$, the mean slopes of the free surface over $x \leqslant c_0 t$ predicted by the CFD model are 0.92% and 7.87% lower than those predicted by the shallow-water model for $L/l=0.9$ and $L/l=1.05$, respectively. For $f=0.4$, these differences are 3.91% and 7.36% for $L/l=0.9$ and $L/l=1$, respectively. For instants before those represented in Fig. 11, the agreement is excellent, particularly for low initial filling fractions, as can be observed from Figs. 9(*a*) and 9(*b*).

4.3 Volume (Area) of Entrapped Air in the Injection Chamber. In this section we present results for the dimensionless area occupied by the air in the injection chamber when the molten metal reaches the gate to the die cavity, $A/(HL)$. As mentioned in the Introduction, a considerable fraction of the porosity of the manufactured part is expected to be caused by this entrapped air. The variation of $A/(HL)$ with the parameters defining the plunger motion law can be explained, as discussed below, by considering the different phenomena that may give rise to air entrapment: wave breaking, wave interaction with the injection chamber ceiling, and wave reflection against the end wall of the injection chamber. The figures presented in what follows, which depict the variation of $A/(HL)$ with the mentioned parameters, allow a sensitivity analysis to be made for the parameters in the neighborhood of the optimum operating conditions.

Plunger Motion With a Time-Exponential Speed Law. Figures 12 and 13, which correspond to initial filling fractions of 0.25 and 0.4, respectively, show results for $A/(HL)$ as a function of L/β, for different values of ξ, which were obtained with both the shallow-water and CFD models. In the upper part of these figures, the dimensionless filling time of the injection chamber, $t_f c_0/L$, has also been represented. We will first discuss the results of the shallow-water model.

It can be observed from Figs. 12 and 13 that, except when $f=0.25$ and $\xi=2$, for a given ξ there is a local maximum of entrapped air for a value of L/β that increases with ξ. This maxi-

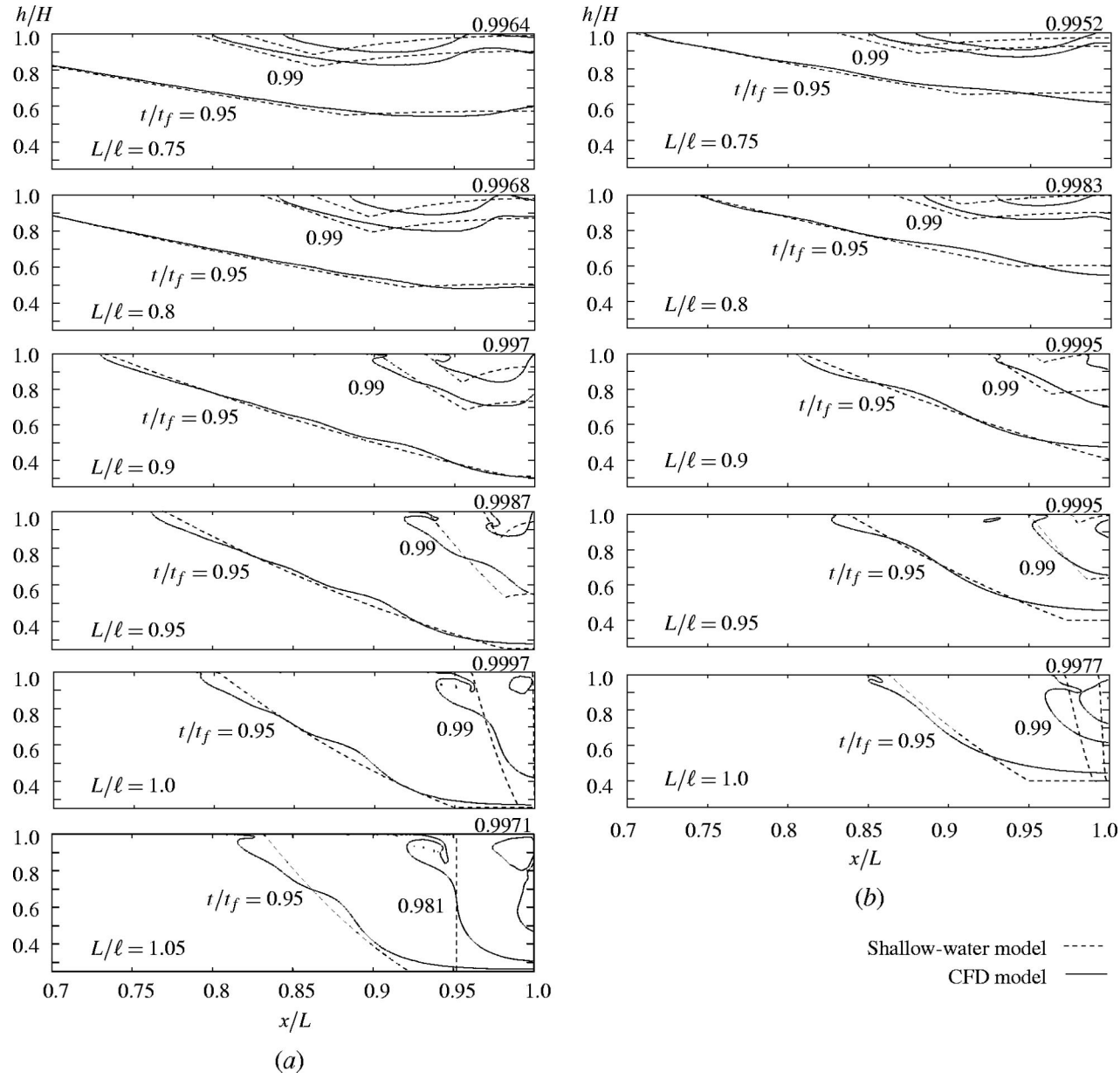

Fig. 11 Wave profiles for the plunger speed law of Eq. (9) and different values of L/l. (*a*) $f=0.254$, and (*b*) $f=0.4$.

mum decreases as ξ increases. In each curve, for a given value of ξ, the black circle denotes the value $(L/\beta)_{\text{opt}}$ that makes the wave reflected from the end wall of the chamber begin to break just at the instant at which the molten metal reaches the gate to the die cavity, the same condition which is satisfied by the wave profiles represented in Figs. 10(*a*) and 10(*b*). Notice that this point lies to the right of the maximum. For a given value of ξ, when L/β increases above $(L/\beta)_{\text{opt}}$, the wave would break earlier and the molten metal would reach the gate to the die cavity earlier, so that an increase in entrapped air is to be expected. Therefore, a local minimum of entrapped air would exist around $(L/\beta)_{\text{opt}}$. Furthermore, the filling time is also minimum at $(L/\beta)_{\text{opt}}$ within the range $L/\beta \leqslant (L/\beta)_{\text{opt}}$, so that, for a given value of ξ, $(L/\beta)_{\text{opt}}$ will be the correct choice when a low filling time is an essential requirement. On the other hand, it is worth noting that, for a given ξ, a smaller amount of entrapped air could be obtained by selecting a sufficiently low value of L/β to the left of the maximum, although at the cost of considerably higher filling times (see the upper part of Figs. 12 and 13).

In Figs. 12 and 13 we have also indicated (by a vertical dashed short line) the value equivalent to $(L/\beta)_{\text{opt}}$ predicted analytically by the shallow-water model when wave-reflection effects are neglected, [4,13]. With this simplification, the ''optimum'' value of L/β for a given value of ξ was assumed to be that which satisfied the condition that the wave profile becomes vertical exactly at the end wall of the chamber. It can be observed in Figs. 12 and 13 that the values of L/β thus determined for different ξ values are very close to those obtained in this work (denoted by black circles). However, the interest of the present work in this regard is justified by the need to analyze in detail variations in the volume (area) of entrapped air using acceleration parameters around the ''optimal,'' and this can only be done by retaining wave reflection effects.

Taking into account the simplifications involved in the shallow-water model, we can consider that the results of this model are in reasonable agreement with those of the CFD model represented in Figs. 12 and 13. However, the CFD model in general predicts substantially smaller amounts of entrapped air (particularly for high values of ξ). It can also be observed that, in the CFD results,

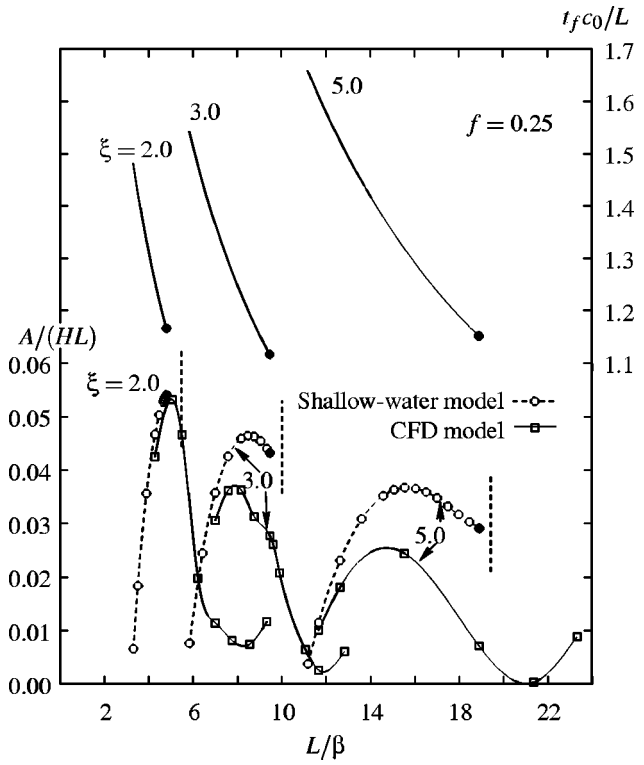

Fig. 12 Dimensionless area occupied by the air when the molten metal reaches the gate to the die cavity and dimensionless filling time as a function of L/β, for the plunger speed law of Eq. (7), $L/H=9$, $f=0.25$ and different values of ξ. The vertical dashed lines indicate the optimum conditions predicted by the shallow-water model when wave reflection effects are not taken into account, [4].

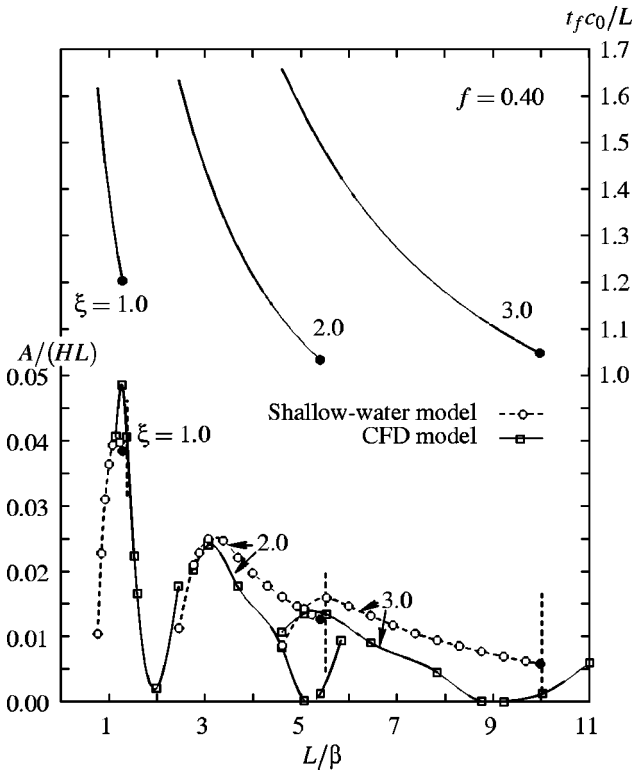

Fig. 13 Dimensionless area occupied by the air when the molten metal reaches the gate to the die cavity and dimensionless filling time as a function of L/β, for the plunger speed law of Eq. (7), $L/H=9$, $f=0.4$ and different values of ξ. The vertical dashed lines indicate the optimum conditions predicted by the shallow-water model when wave reflection effects are not taken into account, [4].

the local maximum of $A/(HL)$ in general moves slightly towards lower values of L/β. On the other hand, for a given ξ, these results show a local minimum of $A/(HL)$ for a value of L/β relatively close to the value $(L/\beta)_{\text{opt}}$ predicted by the shallow-water model. This value of L/β is higher than $(L/\beta)_{\text{opt}}$ for sufficiently small values of f and ξ, so that the amount of entrapped air calculated from the CFD model will be minimum for plunger accelerations greater than those predicted by the shallow-water model. However, note that when $f=0.4$ and $\xi=2$ or 3 (as represented in Fig. 13), the local minimum of $A/(HL)$ in the CFD results is reached for a value of L/β slightly lower than $(L/\beta)_{\text{opt}}$. This is due to the formation of wall jets along the chamber ceiling that bring forward the breaking of the wave and the closure of the gate to the die cavity (see case for $\xi=3$ in Fig. 10(*b*)).

A relevant finding of this work is that there are some combinations of parameters which, in accordance with the CFD results, allow the volume of entrapped air to be reduced to levels well below those predicted by the shallow-water model. The discrepancies between both types of results for the minimum values of the entrapped air volume, as shown in Figs. 12 and 13, are due, on one hand, to the fact that the shallow-water model predicts wave breaking (and therefore is not applicable) for values of $L/\beta > (L/\beta)_{\text{opt}}$, and, on the other, to the already mentioned delay, predicted by the CFD code, in the molten metal reaching the gate to the die cavity for large values of ξ, which can be observed in the wave profiles of Fig. 10.

In spite of the above discrepancies, the relatively good agreement between the predictions of both models regarding the combinations of parameters which minimize the volume of entrapped air while keeping the filling time sufficiently low, suggests that the shallow-water model may be a useful tool in the selection of optimum operating conditions.

Plunger Motion With the Law of Eq. (9). Figure 14 shows results of the shallow-water and CFD models for the dimensionless area $A/(HL)$ as a function of L/l, for six values of the initial filling fraction, $f=0.15$, 0.2, 0.254, 0.3, 0.35, and 0.4, when the plunger moves with the law of Eq. (9). As in the previous section, we will firstly discuss the results of the model based on the shallow-water approximation.

The shallow-water results of Fig. 14 clearly show that the minimum volume (zero) of entrapped air is obtained for $L/l=1$, which is to be expected, and that this volume increases almost linearly with decreasing values of L/l, with a slope that decreases with f. This increase is due to the reflection of the wave against the end wall of the chamber, which results in an elevation of the free surface at this wall and brings forward the closure of the gate to the die cavity by the molten metal (see Fig. 11). For $L/l>1$, the wave profile becomes vertical at a certain distance before the end wall, so that the volume of entrapped air can be expected to increase with L/l due to wave breaking effects (although, obviously, the shallow-water model is no longer applicable). Also, notice that an L/l of 1 would not only produce, according to the shallow-water model, the minimum entrapped air volume, but also the minimum filling time in the range $L/l\leqslant 1$ (note that the filling time decreases monotonically with L/l).

Figure 14 also shows the results of the CFD model for $A/(HL)$, which follow some of the general trends exhibited by the shallow-water results, although the CFD model in general predicts higher volumes of entrapped air. Of particular interest is the relatively close agreement in the prediction of the optimum value of L/l, especially for intermediate values of f. The quantitative agreement between both types of result is better for L/l values around this optimum when f is large, and for $L/l<0.9$ in the cases with f

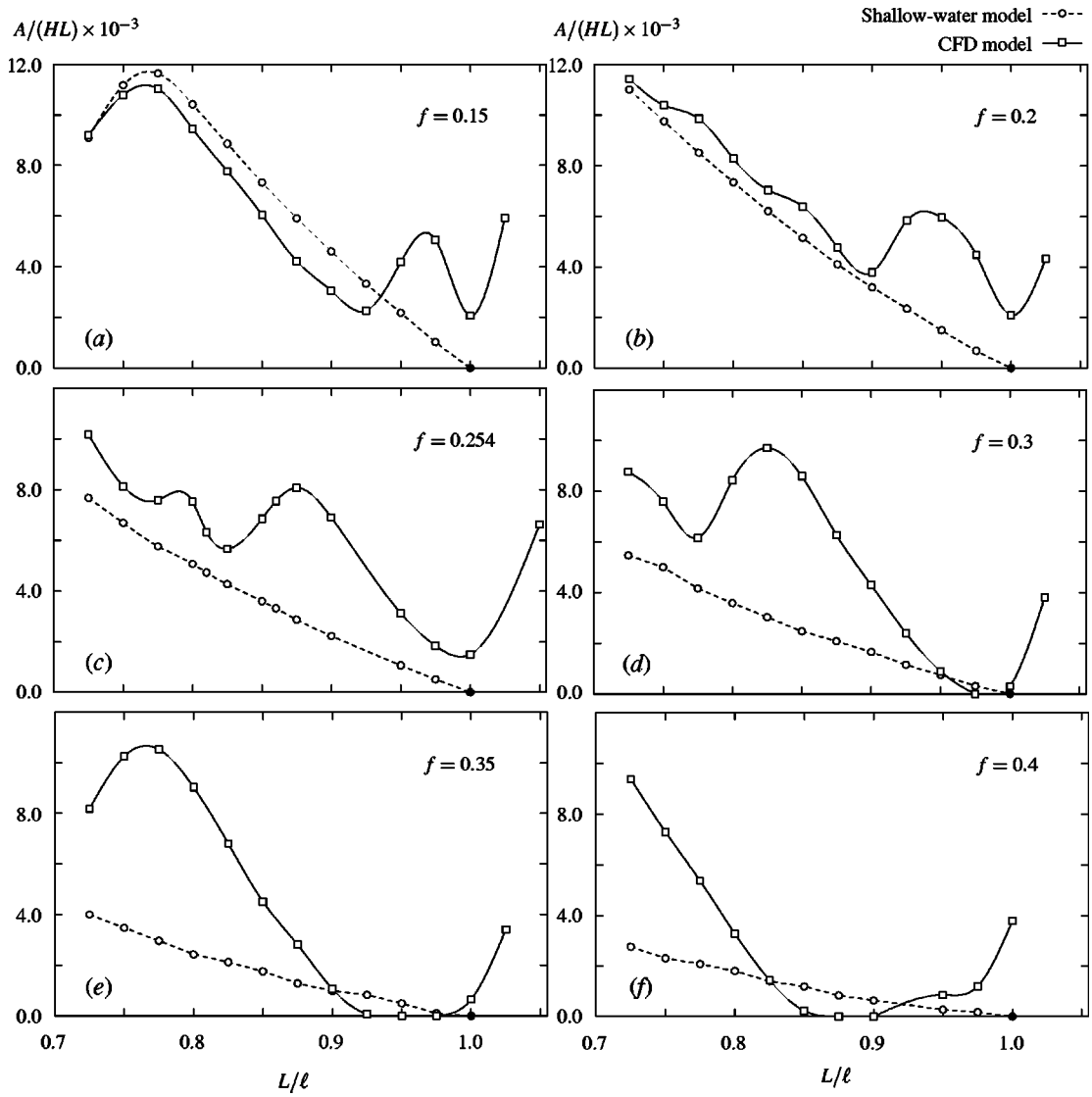

Fig. 14 Dimensionless area $A/(HL)$ as a function of L/l for the plunger speed law of Eq. (9) and different values of the initial filling fraction

$=0.15$ and 0.2. For large f values there is a range of L/l for which the CFD model predicts very low or zero values of $A/(HL)$, which are lower than those predicted by the shallow-water model. This range is always below $L/l=1$, becomes narrower with decreasing values of f, and can be explained by reference to the corresponding wave profiles of Fig. 11. This means that, for sufficiently large f values, the minimum amount of entrapped air calculated from the CFD model is reached for plunger accelerations lower than those predicted by the shallow-water model, as happens in the case of the time-exponential law for sufficiently large values of f and ξ. These lower plunger accelerations avoid the formation of wall jets along the chamber ceiling that would otherwise bring forward the closure of the gate to the die cavity. It can also be observed from Fig. 14 that, for small values of f, the minimum value of $A/(HL)$ predicted by the CFD code is not equal to zero, and that the local minimum of $A/(HL)$ to the left of the optimum decreases with decreasing f. Finally, it is worth noting that the increase in the values of $A/(HL)$ predicted by the CFD model for values of L/l to the right of the optimum can be attributed to wave breaking effects (see, e.g., the case in Fig. 11 for $L/l=1.05$), whereas the nonmonotonic variation of $A/(HL)$ with L/l for L/l values to the left of the optimum is due to wave reflection effects against the end wall of the chamber. This nonmonotonic behavior is not predicted by the shallow-water model except for small values of f.

Some of the simplifications used in both shallow-water and CFD models require further investigation. For example, the assumption that the molten metal is initially at rest, which is not very realistic (given the short time elapsed from the pouring of the chamber with molten metal and the beginning of the injection process), and the two-dimensional description of the flow. Another drawback of the CFD model is that it may require tremendous computational resources to describe in detail the very complex flow patterns that can occur in the injection chamber (particularly when operating conditions are far from the optimum and a three-dimensional model is used). In connection with this, it should be taken into account that the limitations in the numerical accuracy of the results introduce uncertainties into the small values of the volume of entrapped air predicted around the optimum conditions. The possible formation of small wall jets at the ceiling, particularly at the end of the chamber filling process, but also at earlier instants, and at the end wall of the chamber as a result of wave reflection, introduces difficulties in the modeling that contribute to

reduce the accuracy of the results. However, despite all the above difficulties and limitations, the results obtained in this work may help understand and evaluate the overall characteristics of the flow in the injection chamber in many practical situations, and provide general guidelines for the selection of operating conditions during the slow stage of the injection process.

5 Conclusions

The flow of molten metal inside the injection chamber of a high-pressure die casting machine was analyzed using a two-dimensional finite element model and a simpler model based on the shallow-water approximation. Results for wave profiles, the volume (area) of air remaining in the injection chamber at the instant at which the molten metal reaches the gate to the die cavity, and optimum values of the parameters characterizing the law of plunger motion are presented. The following conclusions can be drawn:

1 Despite the simplicity of the shallow-water model, the wave profiles predicted by both types of model are in relatively good agreement. As expected, discrepancies are greatest near the end wall of the chamber, where some substantial deviations are found.

2 These discrepancies may give rise, for certain operating conditions, to differences in the predicted instant at which the molten metal reaches the gate to the die cavity, and, as a result, to important quantitative differences in the predicted volume of residual air in the injection chamber at that instant.

3 Despite its limitations regarding the quantitative prediction of the mass of entrapped air, the shallow-water model describes reasonably well the influence of acceleration parameters and the initial filling fraction on the entrapped air volume. Predictions of the operating conditions that minimize the volume of entrapped air are in reasonable agreement with those obtained with the CFD model.

4 Therefore, taking all the above into account, we can conclude that, despite its limitations, the shallow-water model can be regarded as a simple and useful tool for the selection of optimum operating conditions in high-pressure die casting machines, which at present are usually determined by experimental trial and error methods.

In a future work, the two-dimensional assumption will be relaxed, and the influence of surface tension effects will be investigated.

Acknowledgment

The authors gratefully acknowledge the support of the Spanish Comisión Interministerial de Ciencia y Tecnología (CICYT) under grants TAP97-0489 and PB98-0007, and the CICYT and the European Commission under grant 1FD97-2333.

Nomenclature

A = area occupied by air when molten metal reaches the gate to the die cavity
c = speed relative to the fluid of a small-amplitude wave for a depth h
c_0 = speed relative to the fluid of a small-amplitude wave for a depth h_0
E = relative grid refinement error defined by Eq. (12)
f = initial filling fraction of the injection chamber, h_0/H
g = gravitational acceleration
h = height of the free surface
h_0 = initial depth of molten metal
H = height of the injection chamber
L = length of the injection chamber
l = length in the plunger speed law of Eq. (9)
p = pressure
t = time
t_f = filling time of the injection chamber
t_H = time at which the molten metal reaches the chamber ceiling
u = horizontal velocity component of molten metal
v = vertical velocity component of molten metal
x, y = coordinates (Fig. 2)
X = location of the plunger face
α, β = parameters in the exponential plunger speed law of Eq. (7)
ν = kinematic viscosity
ρ = density
ξ = dimensionless parameter, $2c_0/3\alpha\beta$

References

[1] Campbell, J., 1991, *Castings*, Butterworth-Heinemann, Oxford, UK.
[2] Duran, M., Karni, Y., Brevick, J., Chu, Y., and Altan, T., 1991, "Minimization of Air Entrapment in the Shot Sleeve of a Die Casting Machine to Reduce Porosity," Technical Report ERC/NSM-C-91-31, The Ohio State University, OH.
[3] Tszeng, T. C., and Chu, Y. L., 1994, "A Study of Wave Formation in Shot Sleeve of a Die Casting Machine," ASME J. Eng. Ind., **116**, pp. 175–182.
[4] López, J., Hernández, J., Faura, F., and Trapaga, G., 2000, "Shot Sleeve Wave Dynamics in the Slow Phase of Die Casting Injection," ASME J. Fluids Eng., **122**(2), pp. 349–356.
[5] Lindberg, B., Hansen, P. N., and Hansen, S. F., 1991, "High Speed Filming of Mold Filling Process of Al Alloys in High Pressure Die Casting," *Modeling of Casting, Welding and Advanced Solidification Processes V*, M. Rappaz, M. R. Özgü, and K. W. Mahin, eds., TMS, Warrendale, PA, pp. 763–769.
[6] Karni, Y., 1991, "Selection of Process Variables for Die Casting," Ph.D. thesis, The Ohio State University, OH.
[7] Thome, M. C., and Brevick, J. R., 1993, "Modeling Fluid Flow in Horizontal Cold Chamber Diecasting Shot Sleeves," AFS Transactions, **101**, pp. 343–348.
[8] Thome, M. C., and Brevick, J. R., 1995, "Optimal Slow Shot Velocity Profiles for Cold Chamber Die Casting," NADCA Congress and Exposition, Indianapolis, paper T95-024.
[9] Backer, G., and Sant, F., 1997, "Using Finite Element Simulation for the Development of Shot Sleeve Velocity Profiles," NADCA Congress and Exposition, Minneapolis, MN, Paper No. T97-014.
[10] Kuo, T.-H., and Hwang, W.-S., 1998, "Flow Pattern Simulation in Shot Sleeve During Injection of Diecasting," AFS Trans., **106**, pp. 497–503.
[11] Khayat, R. E., 1998, "A Three-Dimensional Boundary Element Approach to Confined Free-Surface Flow as Applied to Die Casting," Eng. Anal. Boundary Elem., **22**, pp. 83–102.
[12] López, J., Hernández, J., Faura, F., and Gómez, P., 2000, "Effects of Shot Sleeve Wave Reflection on Air Entrapment in Pressure Die Casting Processes," 2000 ASME Fluids Engineering Division Summer Meeting, Symposium on Flows in Manufacturing Processes, Boston, MA.
[13] Hernández, J., López, J., Gómez, P., and Faura, F., 1999, "Influence of Non-Hydrostatic and Viscous Effects on Shot Sleeve Wave Dynamics in Die Casting Injection," ASME/JSME Fluids Engineering Conference. Forum on Advances in Free Surface and Interface Fluid Dynamics, San Francisco, CA.
[14] Faura, F., López, J., and Hernández, J., 2001, "On the Optimum Plunger Acceleration Law in the Slow Shot Phase of Pressure Die Casting Machines," Int. J. Mach. Tools Manuf., **41**, pp. 173–191.
[15] Gómez, P., Hernández, J., López, J., and Faura, F., 2002, "Numerical Simulation of Breaking Waves Using a Level Set Method," 2002 ASME FEDSM, Forum on Advances in Free Surface and Interface Fluid Dynamics, Montreal, Canada.
[16] Lamb, H., 1945, *Hydrodynamics*, Dover, New York.
[17] Celik, I., and Zhang, W., 1995, "Calculation of Numerical Uncertainty Using Richardson Extrapolation: Application to Some Simple Turbulent Flow Calculations," ASME J. Fluids Eng., **117**, pp. 439–445.
[18] Hernández, J., López, J., and Faura, F., 2001, "Influence of Unsteady Effects on Air Venting in Pressure Die Casting," ASME J. Fluids Eng., **123**, pp. 884–892.
[19] Sant, F., and Backer, G., 1995, "Application of WRAFTS Fluid Flow Modeling Software to the Bench Mark Test Casting," *Modeling of Casting, Welding and Advanced Solidification Processes VII*, M. Cross and J. Campbell, eds., TMS, Warrendale, PA, pp. 983–990.
[20] Chorin, A. J., 1969, "On the Convergence of Discrete Approximations of the Navier-Stokes Equations," Math. Comput., **23**, pp. 341–353.
[21] Hirt, C. W., and Nichols, B. D., 1981, "Volume of Fluid (VOF) Method for the Dynamics of Free Boundaries," J. Comput. Phys., **39**, pp. 201–225.
[22] Hirt, C. W., Amsden, A. A., and Cook, J. L., 1974, "An Arbitrary Lagrangian-Eulerian Computing Method for all Flow Speeds," J. Comput. Phys., **14**, pp. 227–253.
[23] Martin, J. C., and Moyce, W. J., 1952, "An Experimental Study of the Collapse of Liquid Columns on a Rigid Horizontal Plane," Philos. Trans. R. Soc. London, Ser. A, **244A**, pp. 312–324.
[24] Hsu, M.-H., Chen, C.-H., and Teng, W.-H., 2001, "An Arbitrary Lagrangian-Eulerian Finite Difference Method for Computations of Free Surface Flows," J. Hydraul. Res., **39**(4), pp. 1–11.

Experimental Investigation of Two Cylindrical Water Columns Subjected to Planar Shock Wave Loading

D. Igra

K. Takayama

Shock Wave Research Center,
Institute of Fluid Science,
Tohoku University,
Japan

Two water columns with identical initial diameters of 4.8 mm were placed 30 mm apart inside a shock tube test section and were loaded by a shock wave of Mach number 1.47 in atmospheric air. The Weber and Reynolds numbers corresponding to these flow conditions are 6900 and 112,000, respectively. Double-exposure holographic interferometry was used to visualize the shock/water columns interaction. The process of the water columns deformation, displacement, and acceleration was well visualized and hence the drag coefficient of shock loaded water columns was evaluated. The front water column behaved virtually the same as a single water column under the same flow conditions. However, the displacement and acceleration of the rear water column was less significant than that of the front one. Hence, its drag coefficient is less. These results show that the front water column has affected the flow field around the rear water column.
[DOI: 10.1115/1.1538628]

Introduction

Stripping-type breakup occurs when a shock wave interacts with a liquid column, which occurs usually for Weber numbers ranging from 100 to 20,000 (Wierzba and Takayama [1]). A survey of droplet breakup was done by Wierzba and Takayama [1], while Wierzba and Takayama [2] studied stripping-type breakup of droplet exposed to shock wave loading. This range of Weber numbers corresponds to high-speed flows which appear in modern propulsion systems. Spherical droplet breakup is a topic that has been studied by many researchers employing various methods to visualize the breakup. Some employed a shadowgraph, for example, Ranger and Nicholls [3] and Simpkins and Bales [4], while a recent work of Joseph et al. [5] used a high-speed camera to visualize the breakup sequence.

The observed shape of the droplet breakup depends on the method used for flow visualization. Yoshida and Takayama [6] demonstrated the usefulness of holographic interferometry. In the past, the Schlieren method or a shadowgraph have been implemented to visualize the droplet breakup process, in which the shape of disintegrating spherical droplets resembles a fire ball. On these photographs the internal structure of the disintegrating spherical droplets, such as shattering mist clouds and wakes, were hardly observable. The patterns of disintegrating droplets visualized on double-exposure holographic interferograms were found to be different from those appearing on their unreconstructed holograms which are equivalent to shadowgraphs. The images so far recorded are substantially equivalent to those observed in direct shadowgraphs.

However, the mechanism of three-dimensional droplet disintegration when subjected to shock wave loading is still unclear. In order to understand the fundamental mechanism of droplet disintegration, it will be helpful to visualize quantitatively shock wave interaction with a liquid column which will hopefully help to simulate complex wave interactions over and inside droplets. The advantages of studying the breakup of a water column is that during the breakup process it is possible to visualize the wave motion inside it. In addition, the shape of the water column is clearly seen during the entire breakup process as shown in Igra and Takayama [7].

An engineering example in which droplet breakup plays an important role is in propulsion systems. In such cases several droplets exist in the flow field and they interact with each other, therefore it is important to study such interactions. The interaction results in more complex flow fields since the breakup of each droplet is influenced by droplets surrounding it.

Raju and Sirignano [8] have conducted a numerical investigation of the interaction of two vaporizing droplets. Their investigation was carried out for Reynolds number of about 200. The flow around the droplets was laminar and the droplets shape was retained spherical throughout the calculation. Their results for the case of two droplets with an identical initial size showed that their stand off distance decreased with elapsing time.

Yoshida et al. [9] investigated experimentally the interaction of two spherical droplets of 1.4 mm in diameter positioned in tandem. Their initial separation distance was 8.8 mm. A shock wave of Mach number 1.4 hit the droplets head on. They concluded that the displacement of the front droplet was more remarkable than that of the rear droplet.

In the present work the deformation and displacement of tandem cylindrical water columns have been studied. Based on these results, their accelerations and drag coefficients were evaluated. In addition the shape of the micro mist and its structure can be visualized clearly. Finally the water columns deformations and displacements are compared between the two cases; a case of tandem water columns and a case of a single water column when both experience the same initial conditions.

It should be noted here that the considered two-phase flow is very complex. As shown subsequently the acceleration of the front water column due to its head-on collision with the incident shock wave is significant. The acceleration and deformation of the rear water column is affected not only by the strength of the incident shock wave and the water column geometry but mostly by the induced flow generated behind the front water column. This highly nonsteady flow is affected by the shape of both water columns, their relative separation distances (the ratio between the water column diameter to the separation distance) and the character of the local flow. Covering *all* these effects is beyond the scope

Contributed by the Fluids Engineering Division for publication in the JOURNAL OF FLUIDS ENGINEERING. Manuscript received by the Fluids Engineering Division April 25, 2001; revised manuscript received July 1, 2002. Associate Editor: A. K. Prasad.

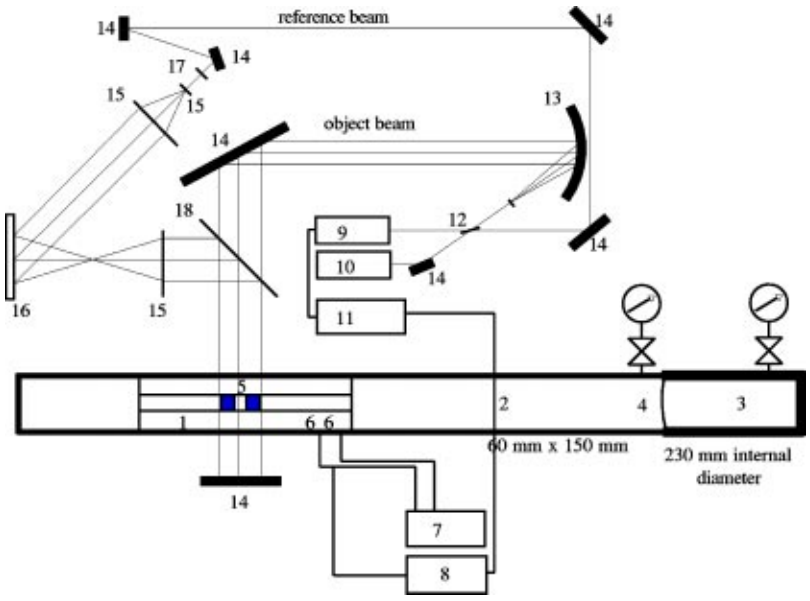

Fig. 1 Experimental setup and optical arrangement. 1–test section, 2–driven section, 3–driver, 4–diaphragm, 5–water columns, 6–pressure transducers, 7–universal counter, 8–delay, 9–ruby laser, 10–He-Ne laser, 11–power supply, 12–beam splitter, 13–paraboloidal schlieren mirror, 14–plane mirrors, 15–lens, 16–film holder, 17–filter, 18–half mirror

of the present paper. Being a first attempt at investigating such a complex two-phase flow we centered our attention on a comparison between two different cases. One case is a tandem geometry while the other is a single water column when both are exposed to the same incident shock and have the same geometry. Future investigations should explore details regarding the tandem geometry and changes in the strength of the incident shock wave.

Experimental Setup

The low-pressure channel of the shock tube had a cross section of 60 mm×150 mm and was approximately 5 m long. It is made of 25-mm-thick steel plates, the surface of which was finished with surface roughness of 10 μm. The discrepancy of surface flange section was about 50 μm. The high pressure chamber is 230-mm-dia., 1.5-m-long thick wall steel tube. A smooth transition section was inserted downstream of the diaphragm section. Diaphragms were Mylar films of 0.1 mm in thickness. The test gas was atmospheric air and the driver gas was nitrogen. The 150-mm wide side wall was placed in the horizontal position so as to accommodate the water columns, at the observation window of the test section, in the vertical position.

The optical arrangement is shown in Fig. 1. It consists of a paraboloidal schlieren mirror of 300-mm dia. and 3-m in focal length, a planar mirror, a beam splitter that transmits 60% of laser beam intensity to the object beam OB and 40% for the reference beam RB, and auxiliary planar mirrors and lenses. An object lens was used to obtain a sharply focused image of the object on a holofilm. A Q-switched ruby laser (Apollo Lasers Inc. 22HD, 2 J/pulse and 25 ns pulse duration) was used as the light source. This optical arrangement was in principle identical with that of the shadowgraph. However, the light path of RB was combined so as to make its path length identical with that of OB. OB and RB were superimposed on the holofilm. The source laser was oscillated for the first exposure just before the arrival of shock wave at the test section and the second exposure was synchronized with the arrival of shock wave at the test section. Hence infinite fringe interferograms were obtained. In order to take sequential interferograms the experiments were repeated by varying the delay time while retaining identical initial conditions. The scattering in the shock wave Mach number was about 0.5%.

A cookie cutter of 4 mm in height was inserted into the test section, so as to make the cross section of the test section of 4 mm×150 mm. It was confirmed in preparatory tests (see Igra and Takayama [7] for details) that the shock wave propagating inside the 4-mm-high passage was only very slightly perturbed when it encountered the cookie cutter. A water column, whose diameter is nearly the same as its height, was created inside the cookie cutter. A syringe was used to create the water columns by slowly injecting water at the center of the upper glass plate of the test section. As soon as the hemispherical water droplet touched the bottom glass plate, it became a cylindrical shape of 4.8 mm dia. The water column is shown, in a side view photo, in Fig. 2. The shape of the water column is not exactly cylindrical due to the water surface tension. This results in a slightly larger wet area at the bottom as compared with the top. The variations in the water column diameter during an experiment was less than 4%. The water column had a volume of approximately 80 mm^3. The water

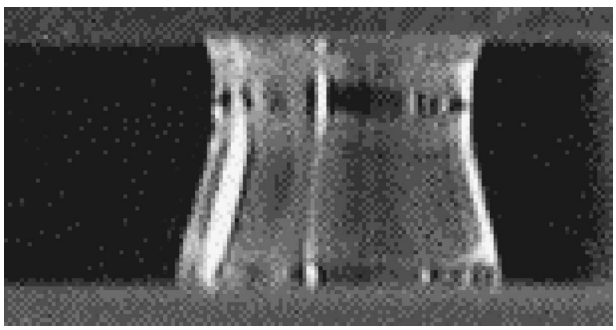

Fig. 2 The shape of water column view from the side

columns were placed 30 mm apart in tandem and then exposed to a planar shock wave. The variation of the initial distance between the water columns was about 4%.

Although the produced water column is not a perfect cylinder, due to surface tension, except for its upper and lower regions (connected to the glass windows) its central region is very close to a cylinder. The corresponding Weber and Reynolds numbers to these values are 6900 and 112,000, respectively. The shock wave Mach number was 1.47 in air. Upon the shock wave loading the density inside the water column changes. These changes can be evaluated from the fringes distribution inside the column, similarly to the evaluation of isopycnics in an infinite fringe interferograms in air.

Experimental Results

Interferograms taken at various stages of the breakup process are shown in Fig. 3. These interferograms where taken form a top view. The ''dark ring'' seen in these interferograms is a result of water surface curvature due to surface tension. Starting with Fig. 3(*a*) it can be seen that initially the front water column begins to deform while the rear water column retains its initial shape. This can be detected by comparing the thickness of the ''dark ring'' surrounding the front water column. In Fig. 3(*a*) one side of the ''dark ring'' is thicker than the other, this indicates that the water column is slightly deformed. Compared to the rear water column whose ''dark ring'' has a uniform thickness. In Fig. 3(*b*) the deformation of the front water column can be clearly seen. At this time the rear water column is just beginning to deform. With elapsing time the two water columns continue to deform, as seen in Fig. 3(*c*). Boundary layer stripping has begun over the front water column. Later, micro mist was generated over the water columns as clearly seen in Fig. 3(*d*). The wake behind the rear water column is smaller than that behind the front one. This trend continues until the last interferogram. In addition, the rate of deformation of the rear water column is slower than that of the front water column. This can be seen by comparing the shape of the rear water column in Figs. 3(*e*) and 3(*g*) to that of the front water column shown in Fig. 3(*d*) and 3(*e*), respectively. This is due to the fact that the rear water column is placed completely inside the wake produced by the front water column. This causes the relative flow velocity over the rear water column to be smaller. Yoshida et al. [9] reported similar results for the early stage of the breakup process similar to that shown here. The front water column experiences a higher drag force than the rear one. Accordingly, the distance between the two water columns decreases with elapsing time. However, during the present experiment the water columns and their micro mists do not merge with each other as shown in Fig. 3(*h*). The wake behind the rear water column tends to reach nearly a constant width at about 350 μs after the incident shock wave impinged on it (Fig. 3(*d*)). Although this wake seems to elongate, its width remains unchanged with time. This trend is significantly different from that of the front water column.

Water Column Deformation

The interferograms were taken from the top view. The first exposure was taken prior to the shock wave loading where the initial size of the water column was measured. The second exposure was taken based on a present delay time, after the incident shock impingement upon the front water column. All measurements reported here refer to the central region of the water column, where it has a cylindrical shape. The results shown here are complied from the results taken at different time intervals and compared with the initial water column shape. The water columns deformation can be compared to that of a single water column. We define here a nondimensional time t^*, which is $t^* = tu_2/d_0$.

In Fig. 4 the time variation of the water column deformation, in the lateral direction (normal to the flow field), is shown. Up to about $t^* = 22$ the deformation of front and rear water columns is similar to that of a single water column. From $t^* = 22$ the deformation of the front water column follows the evolution of a single water column although its breakup time is slightly longer; the rear water column continues to deform. It reaches a maximum deformation of almost twice its initial diameter at about $t^* = 30$. After $t^* = 30$ its size begins to decrease. Water columns deformation behavior has similar trends to that of spherical droplets, first the water column is flattened until it reaches its maximum elongation normal to the flow direction. After this stage is reached the micro mist are striped from the water column at an increasing rate until a complete breakup is reached.

Similar results appear in the deformation in the flow direction as shown in Fig. 5. The evolution of the deformation of the front water column is found to be similar to that of a single water column. This means that the front water column in an array will deform and breakup as if it was a single water column, but the water columns downstream of the first one are affected by the water columns located upstream. The rate of change of the rear water column is smaller over the range $22 < t^* < 40$.

Variations in the relative area changes are shown in Fig. 6. The area was measured directly from the interferograms and normalized with the initial area of the water columns. Results obtained show a similar trend to that shown in Figs. 4 and 5. The area change of the front water column is similar to that observed for a single water column under the same initial conditions. The area changes in the rear water column decrease slowly. The changes in the deformations of the rear water column after $t^* = 22$ were strongly affected by the deformation of the front water column. At this time deformations in the front water column are maximal. The rear water column is contained inside the wake of the front water column and as a result deformations in the rear water column are slower. However, at $t^* = 40$ it continues to deform rapidly until its final breakup.

Water Column Displacement

The displacement of the water columns in the tandem configuration was measured at the frontal end of each water column. From interferograms taken at various times the deviation of the water columns, at each time instant relative to their initial position was measured. The position of water columns in nondimensional terms is shown in Fig. 7. The displacement of the front water column is similar to that of a single water column, whereas the displacement of the rear water column appears to be below that of the front one. It is clearly seen that the water columns are accelerated. These results are similar to those of Yoshida et al. [9] obtained for spherical water droplets. The drag force acting on the front water column is larger than that acting on the rear water column. As a result, the front water column experiences higher acceleration than the rear water column. Due to this difference in acceleration the rear water column is gradually overtaken by the front water column. This can be seen in Fig. 8. At $t^* = 46$ the separation distance between the two water columns is reduced to 72% of the initial separation distance. In Yoshida et al. [9] the micro mists of the two droplets merged. Raju and Sirignano [8] ended the numerical simulation when the separation distance between the two droplets became about one third of the initial separation. The reason why the two water columns do not merge quickly is due to the fact that the water columns were sandwiched between two glass windows. Therefore, an additional friction force, which adhere them to the glass surface existed. This force does not exist in the case of spherical droplets suspended in air. In addition, the diameter of the water columns in the present case was larger than that used in the case of spherical droplets.

Water Column Acceleration and Drag Coefficient Approximations

The displacement of spherical water droplets suspended in air was plotted by Ranger and Nicholls [3], Simpkins and Bales [4],

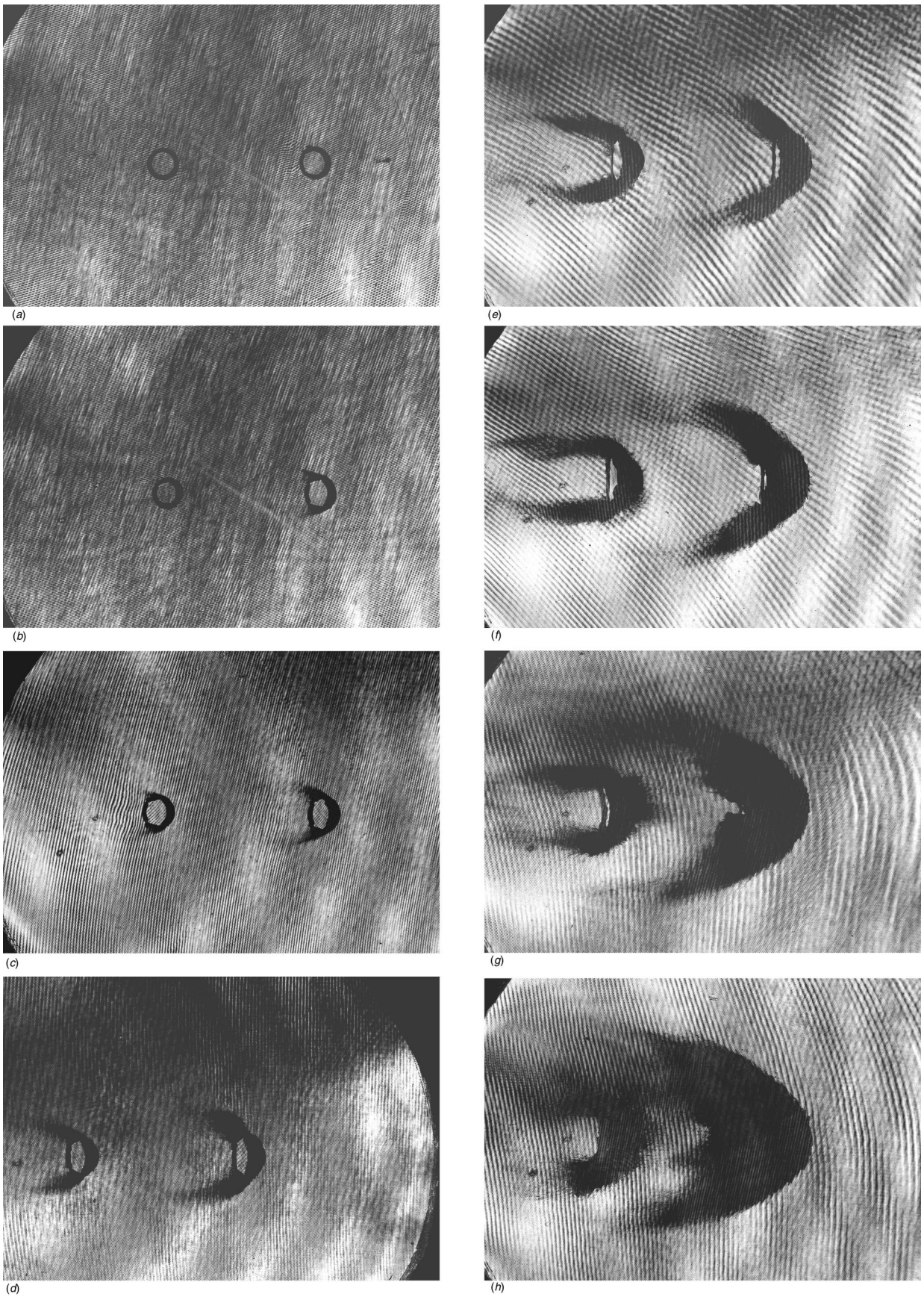

Fig. 3 Infinite fringe double exposure holographic interferogram at the time instant: (*a*) 70 μs, $t^*=3.137$: (*b*) 140 μs, $t^*=6.335$; (*c*) 210 μs, $t^*=12.578$; (*d*) 350 μs, $t^*=15.919$; (*e*) 560 μs, $t^*=25.544$; (*f*) 700 μs, $t^*=30.885$; (*g*) 910 μs, $t^*=41.285$; (*h*) 1050 μs, $t^*=47.23$

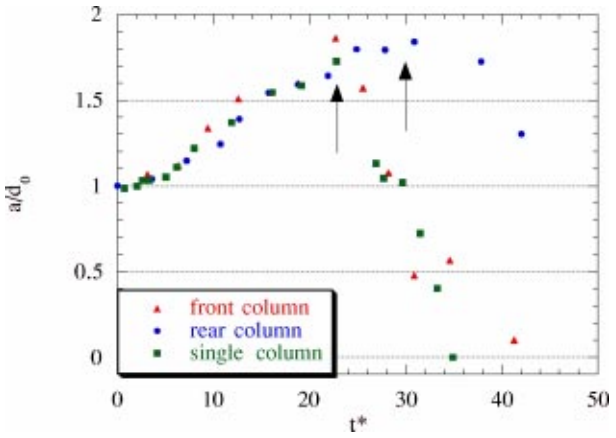

Fig. 4 Water columns deformation in the lateral direction

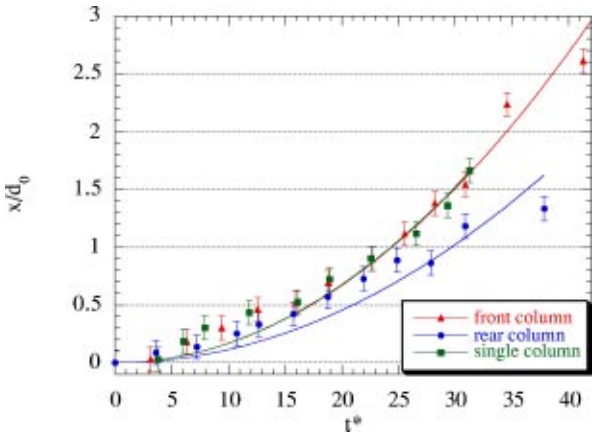

Fig. 7 Water columns trajectory

and Joseph et al. [5]. In those experiments the droplet displacement had a parabolic shape therefore, they assumed that the droplet acceleration is constant. Here, using the water columns displacements shown in Fig. 7, it is possible to approximate the water columns acceleration. The water columns displacements resemble a parabola therefore it is assumed that the water columns are subjected to constant acceleration. At initial stages of the breakup, the water columns acceleration is uniform. The displacement of the front water column is similar to that of a single water column.

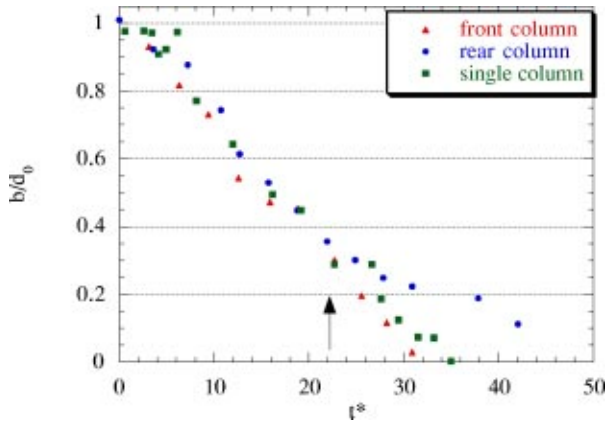

Fig. 5 Water columns deformation in the direction of the flow

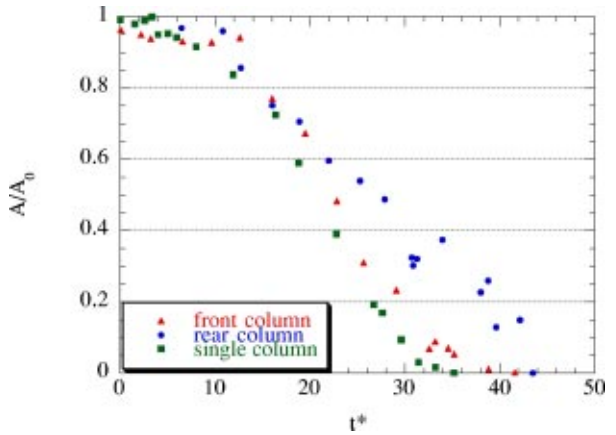

Fig. 6 Area change of the water columns

Trajectories shown in Fig. 7 can be fitted by the following equation:

$$x^* = \frac{1}{2} a_t^{*2}. \tag{1}$$

Based on this curve fit the acceleration of the front water column is about 34,000 m/s^2 and that of the rear water column is about 19,700 m/s^2. These accelerations are much smaller than that observed in the case of spherical droplets suspended in air. Obviously this is caused by lower displacement of the water columns as compared with those of spherical droplet.

Assumptions made by Ranger and Nicholls [3], while evaluating the drag coefficient of spherical droplets, are used in analyzing the cylindrical water columns. The assumptions are

1. the water column shape does not change and its mass is conserved and
2. the acceleration of the water column is constant.

Although these assumptions might seem poor in view of the actual water columns shape shown in Fig. 3, employing them can provide us with a first order estimate of the water columns drag coefficients. According to Wierzba and Takayama [1] and the references therein this method for approximating the drag coefficient has been widely employed by many researchers.

When these assumptions are combined with the equation of motion,

$$\frac{1}{2} C_D \rho_2 U^2 S = ma, \tag{2}$$

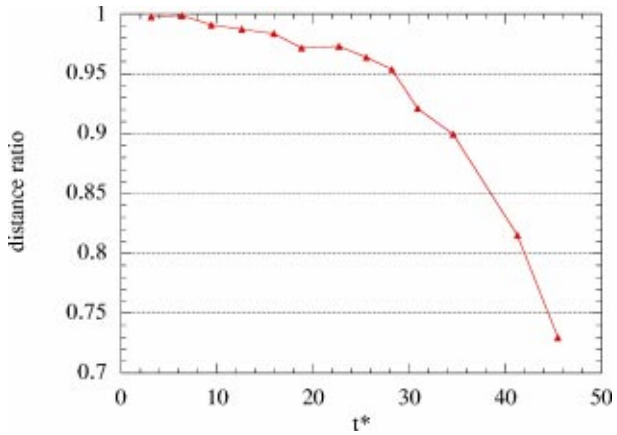

Fig. 8 Distance changes between the water columns

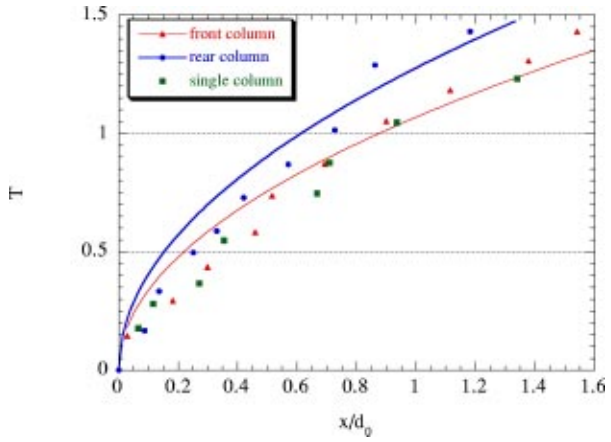

Fig. 9 Water columns drag coefficients

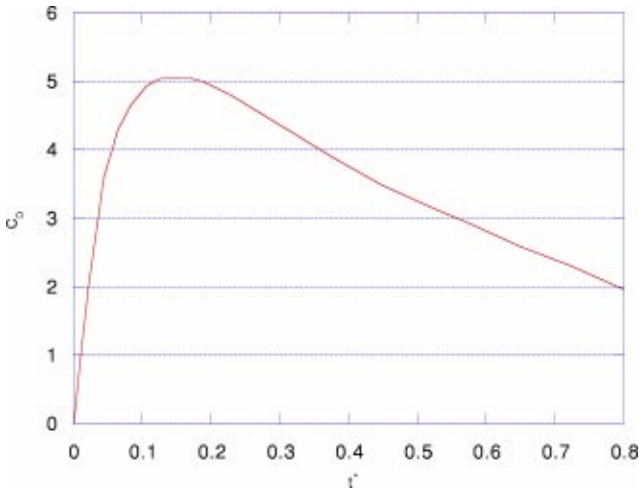

Fig. 10 Temporal variation of unsteady drag coefficient

where the acceleration is

$$a = \frac{2}{\pi}\frac{C_D}{D_0}\frac{\rho_2}{\rho_1}U^2. \tag{3}$$

Therefore, the motion of the water column under a constant acceleration would be

$$x = \frac{1}{2}at^2. \tag{4}$$

When x, t are written in dimensionless from the following equation results:

$$x^* = \frac{1}{\pi}C_D T^2. \tag{5}$$

Figure 9 shows curves described by Eq. (5). The same drag coefficient is used for a single water column and for the front water column, for both $C_D \approx 3$, whereas that of the rear water column $C_D \approx 1.93$. The value of the drag coefficient for a single water column is larger than those reported by Wierzba and Takayama [1] for spherical droplets. However, it is known that the drag coefficient of solid cylinders are much larger than that of solid spheres. In addition, in these experiments the water column is sandwiched between the glass windows which obviously contributes to increasing the friction force. Therefore, the value of drag coefficient found here is reasonable.

The analysis presented so far is for a steady drag coefficient; however, the present study deals with unsteady flows. Therefore the unsteady drag coefficient value should be evaluated as well. At the early stages of the shock wave interaction with the water column its behavior is similar to that of a solid cylinder. In Figs. 4–6 it was shown that initially there is no deformation of the water column. This behavior has been verified experimentally and numerically by Igra and Takayama [10]. In their work the unsteady drag coefficient of a water column was computed numerically and compared with the drag coefficient of a similar solid cylinder and with available experimental data. Based on these results it was found that the unsteady drag coefficient of a solid cylinder is similar to that of a water column. By employing the same numerical scheme used by Igra and Takayama [10] the unsteady drag coefficient of the front water column is evaluated based on the obtained numerical data. Figure 10 shows the temporal variations of the unsteady drag coefficient. Immediately after the incident shock wave impingement on the front water column the unsteady drag coefficient increases rapidly, it reaches a maximum of 5 at about $t^* = 0.15$. A similar pattern was found to occur in the unsteady drag coefficient of solid cylinders as well.

Conclusions

The interaction of two water columns placed in tandem configuration with a shock wave was studied. Holographic interferometry was employed to visualize the shock/water columns interaction at various stages of their breakup process. The water columns deformations and displacements were measured. It was found that the front water column behaves similarly to a single water column, in its deformation, displacement, and acceleration. The presence of the front water column affected the deformation and displacement of the rear water column, and hence its deformation, displacement and drag coefficient were lower than those of the front water column. The deformation of both water columns was similar until $t^* = 22$, at this time the front water column reached its maximum deformation in the lateral direction. Whereas the rear water column continued to deform, reaching a slightly larger maximum deformation at about $t^* = 30$.

Acknowledgments

The authors would like to express their gratitude to Mr. M. Hamamura, former Master Course student for his help in conducting a part of the experiments and also to Dr. O. Onodera and Mr. H. Ojima of the Shock Wave Research Center for their technical assistance in conducting the present work. The first author would like to acknowledge the Tohoku Kaihatsu Memorial Foundation for their financial support.

Nomenclature

a = water column size in the lateral direction
a = acceleration
A = base area of the water column
b = water column size in the flow direction
C_D = drag coefficient
d = droplet diameter
m = mass
OB = object beam
RB = reference beam
Re = Reynolds number ($\mathrm{Re} = Ud_0/\nu$)
S = water column's projected area facing the flow field
t = time
t^* = nondimensional time ($t^* = tu_2/d_0$)
T = nondimensional time ($T = (tu_2/d_0)\sqrt{\rho_2/\rho_2}$)
U = air–liquid relative velocity
We = Weber number ($\mathrm{We} = \rho U^2 d_0/\sigma$)
x = distance
x^* = nondimensional distance ($x^* = x/d_0$)

ρ = density
ν = kinematic viscosity
σ = surface tension

Subscripts

0 = reference state
l = liquid
g = gas
2 = state behind shock wave

References

[1] Wierzba, A., and Takayama, K., 1987, *Experimental Investigation Liquid Droplet Breakup in a Gas Stream*, Institute of High Speed Mechanics, Tohoku University, Sendai, Japan.

[2] Wierzba, A., and Takayama, K., 1988, ''Experimental Investigation of the Aerodynamic Breakup of Liquid Drops,'' AIAA J., **26**, pp. 1329–1335.

[3] Ranger, A. A., and Nicholls, J. A., 1969, ''Aerodynamic Shattering of Liquid Drops,'' AIAA J., **7**, pp. 285–290.

[4] Simpkins, P. G., and Bales, E. L., 1972, ''Water Drop Response to Sudden Accelerations,'' J. Fluid Mech., **55**, pp. 629–639.

[5] Joseph, D. D., Belanger, J., and Beavers, G. S., 1999, ''Breakup of a Liquid Drop Suddenly Exposed to a High-Speed Airstream,'' Int. J. Multiphase Flow, **25**, pp. 1263–1303.

[6] Yoshida, T., and Takayama, K., 1990, ''Interaction of Liquid Droplets With Planar Shock Waves,'' ASME J. Fluids Eng., **112**, pp. 481–486.

[7] Igra, D., and Takayama, K., 2001, ''Investigation of Aerodynamic Breakup of a Cylindrical Water Droplet,'' Atomization Sprays, **11**, pp. 167–185.

[8] Raju, M. S., and Sirignano, W. A., 1990, ''Interaction Between Two Vaporizing Droplets in an Intermediate Reynolds Number Flow,'' Phys. Fluids, **2**, pp. 1780–1796.

[9] Yoshida, T., Wierzba, A., and Takayama, K. 1988. ''Breakup and Interaction of Two Droplet Columns in a Shock Wave Induced High-Speed Air Flow,'' ICLASS 88, Sendai.

[10] Igra, D., and Takayama, K., 2001, ''Experimental and Numerical Study of Water Column Breakup due to Interaction With a Planar Shock Wave,'' ISSW 23.

Influence of Diffuser Angle on a Bluff Body in Ground Effect

Andreas Ruhrmann

Xin Zhang[1]

Aeronautics and Astronautics,
School of Engineering Sciences,
University of Southampton,
Southampton SO17 1BJ, UK

The forces and pressures on a generic bluff body in ground effect were investigated. The bluff-body model was equipped with interchangeable underbody diffuser ramps and side plates. Five different diffuser angles were tested: 5, 10, 15, 17, and 20 deg to the horizontal. The experiments were undertaken in a low-speed wind tunnel equipped with a moving ground. Load cells, pressure taps, and surface flow visualization were the techniques used to evaluate the flow field. The flow field is characterized by vortex flow and three-dimensional flow separation. A region of hysteresis was found for the 15, 17, and 20 deg diffusers. As the ride height is varied, five different flow types can be identified with three subtypes within the region of hysteresis. The force reduction phenomenon was found to be caused by both vortex breakdown and flow separation. [DOI: 10.1115/1.1537252]

Introduction

A symmetrical body in ground effect will generate aerodynamic force pointed to the ground (downforce). The flow between the body and the ground is accelerated leading to reduced pressure. Introducing camber to the body in the form of an upswept ramp at the rear creates a diffuser between the ground and the body. Since the diffuser exits to the base pressure of the model, the flow under the model accelerates to a greater degree than without the diffuser. This increase in downforce is accompanied by complex flow physics within the diffuser. The upsweep initiates three-dimensional flow separation which leads to vortex formation and possible flow reversal. This area of research is especially important in the automobile industry with respect to performance and safety. A complete understanding of the complex fluid flow physics is essential for the development of flow control measures.

Currently there is only limited research published in the field of diffuser flow in ground effect, [1–6]. The general principle of how a diffuser functions in ground effect is described by Sovran [3]. It is likened to a venturi, with the flow rate under the model governed mainly by the efficiency of the diffuser. As the diffuser efficiency is increased, the flow rate increases and the static pressure under the model drops leading to a rise in the level of downforce. The study completed by Cooper et al. [4] found that as the ride height is reduced down to a critical ride height, the downforce increases. Below the critical ride height, the downforce reduces rapidly. It was surmised that at this ride height, the ground and model boundary layers form a substantial proportion of the flow into the diffuser. Senior and Zhang [6] found that for a bluff body with a 17-deg diffuser, the rapid reduction in downforce was not due to the increased influence of the boundary layers as changes in the Reynolds number did not influence the critical ride height. They also found that one of the two counterrotating vortices that form in the diffuser disappears below the critical ride height resulting in an asymmetric flow pattern with flow reversal on one side. Four different types of force behavior were identified through a range of ride heights.

The goals of the present research is to further the understanding of the complex three-dimensional flow field to aid the development of improved diffuser design and methods of flow control. To aid in the understanding of the complex flow phenomena, several different diffuser ramp angles were studied to investigate the effects of area ratio, pressure gradient and ground proximity. The diffuser ramp angles investigated were 5, 10, 15, 17, and 20 deg to the horizontal. The various angles are tested to establish a database of results for comparison with computational fluid dynamics and from which flow control methods could be developed. The range of angles includes lower angles (5 and 10 deg) where no flow separation occurs in two dimensional planar diffusers. These will hopefully show the influence of the separation bubble on the force-ride height characteristics of the diffusers with larger divergence angles.

Experimental Setup

The experiments were undertaken at the University of Southampton in the low-speed closed-circuit wind tunnel with test section dimensions of 2.1 m$\times$1.5 m. The wind tunnel is equipped with a moving ground measuring 3.5 m in length and 1.5 m in width. The experiments were run at a wind and ground speed of 30 m/s at a freestream turbulence level of 0.2%. There is a boundary layer removal system ahead of the moving ground. It consists of a slot through which the boundary layer passes and a perforated plate just ahead of the belt (moving ground) through which the remainder of the boundary layer is sucked. The velocity reaches freestream values 2 mm above the belt. Further details can be found in Senior [7].

A schematic of the wind tunnel setup is shown in Fig. 1. It is mounted on a motorized main strut and tail wire (a free pivoting, thin carbon strut) configuration. The motorized struts are each powered by a stepper motor allowing the model to be moved up to a maximum ride height of 180 mm. The lowest ride height is constrained by a minimum safety clearance above the moving ground.

The bluff body of the model is constructed of carbon fiber. Using different diffuser ramps, the angle of the diffuser can be varied. The ramps are constructed of 3-mm steel sheets. The angles tested are 5, 10, 15, 17, and 20 deg. This range of angles was chosen to create a better understanding of different flow physics which occur at the different ride heights. By varying the diffuser angle, the significance of the blockage between the ground and the model underbody can be investigated as the various flow types will occur at a different ride height for each diffuser angle. Transition on the model is fixed using a 0.4-mm diameter wire placed at 100 mm from the nose of the model.

The tests conducted include force measurements, surface pressure measurements, and oil-streak flow visualisation. The forces are measured using a two component load cell (vertical and horizontal forces) on the base of the main strut and a single component load cell (vertical force) on the top of the tail wire. A total of 186 pressure taps are arranged on the underside and base of the model to give both centerline pressures and spanwise measure-

[1]To whom correspondence should be addressed.

Contributed by the Fluids Engineering Division for publication in the JOURNAL OF FLUIDS ENGINEERING. Manuscript received by the Fluids Engineering Division July 16, 2001; revised manuscript received October 7, 2002. Associate Editors: J. Bridges and J. Katz.

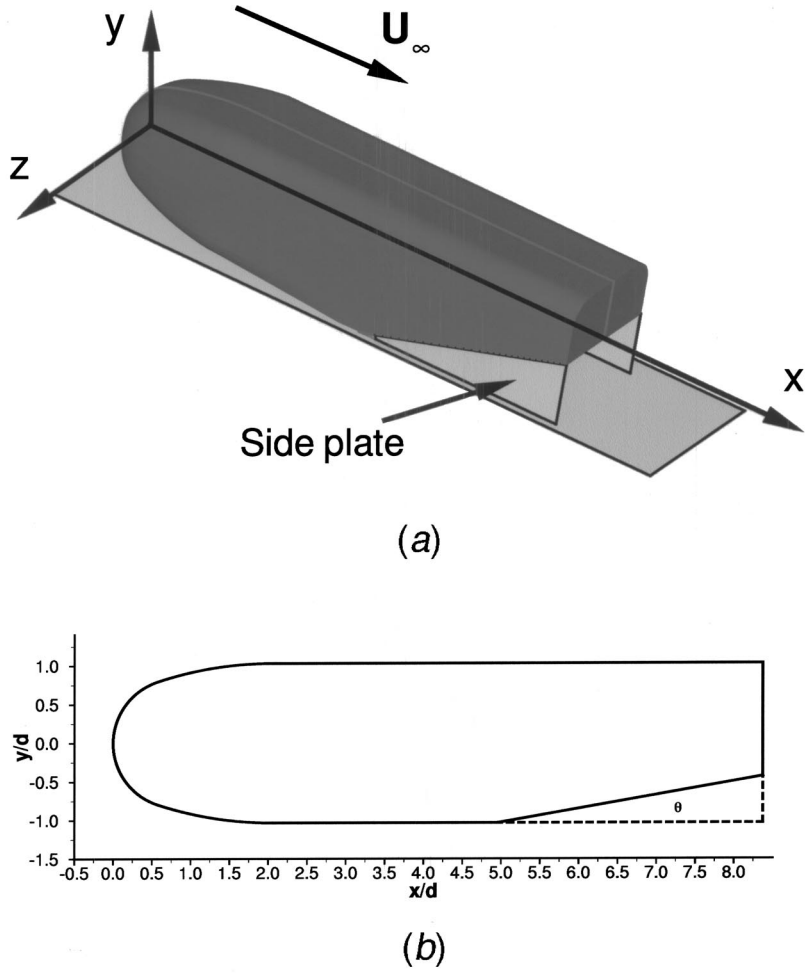

Fig. 1 Schematic of model; (*a*) a prospective view of the model, (*b*) a side view of the model

ments. The pressures were measured using a zero operate calibrate (ZOC) system. A mixture of titanium dioxide and light oil was used to visualize the surface streak lines.

Applying the procedure described by Moffat [8] the single-sample uncertainties in the experiment were calculated. The ride height was kept to within ± 0.1 mm and the yaw angle was set to ± 0.05 deg. The forces were averaged over 15 seconds at each ride height, with a one-second delay between ride height changes. The pressures on the ZOC were sampled for ten seconds on each of the two banks, also with a one second delay between ride height change. For the 20-deg diffuser at 90-mm ride height, the uncertainties in the C_L and C_D measurements are ± 0.0016 and ± 0.0008, respectively. The uncertainty in the pressure measurements in the previous configuration for a C_P of -2.0 is ± 0.0188. This uncertainty incorporates the quoted accuracy of the equipment.

Results and Discussion

Definition of Flow Regimes. The downforce and drag curves in Fig. 2 demonstrate that there are two different types of flow regimes dependent on the diffuser angle. The curves for the 15, 17, and 20 deg (high angle) diffusers have similar characteristics as do the 5 and 10 deg (low angle) diffusers. The 10-deg diffuser appears to be more of a transition angle between the two types as it contains characteristics of both. As the height above the moving ground is varied, the slopes of the curves change indicating changes in the flow physics. The high angle diffusers demonstrate the same characteristics as found by Senior and Zhang [6]. Utilizing the moving strut, one additional flow type along with extensions to three of the existing flow types in the region of hysteresis were identified. All flow types are described in Table 1. The different flow regions are shown on the downforce curve for the 15-deg diffuser in Fig. 3. Starting the wind tunnel with the model at a fixed height within the region of hysteresis, the flow always reverted to the curve of lower downforce. The high downforce portion of the hysteresis loop was found to be unstable, as any disturbances would trigger it to fall onto the low downforce curve. During the 15-second sampling period of the forces, a real time display of the measured forces indicated that the flow was unsteady in this region. The real time display of the measured forces suggested that most of region b and all of regions c, d, d′, and e were unsteady as well.

Comparing the downforce curves of the low angle diffusers to those of the high angle diffusers, distinctions between the two sets are identifiable. Although the curves are similar, the closer proximity to the ground introduces differences. There is no hysteresis loop and the sudden reduction in downforce is not as pronounced. Type a and b flow still exist, however, there is a pronounced increase in downforce through the lower portion of region b. This is clearest for the 5-deg diffuser. Type c and d flow exist only to a very limited extent for the 10-deg diffuser. Due to the lower ride heights, it is assumed that both the underbody and ground boundary layers form a considerable proportion of the flow entering the diffuser at these ride heights, causing the direct transition into type

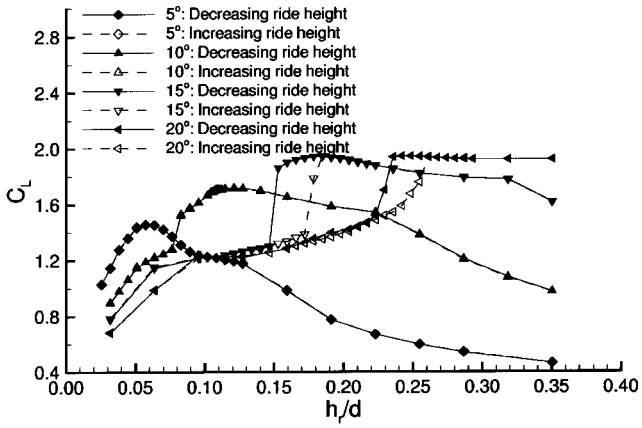

(*a*)

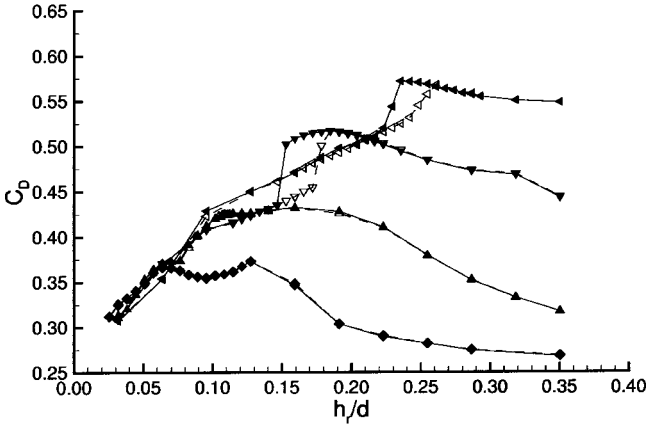

(*b*)

Fig. 2 Force curves: 30 m/s; (*a*) downforce coefficient, (*b*) drag coefficient

e flow. The underbody boundary layer is predicted to be (O)0.096 *d* from flat plate theory, although this value will certainly change with the favorable pressure gradient and increased flow velocity under the model. Measurements by Senior [7] using laser doppler anemometry supports our assertion.

Table 1 Flow types in high angle diffusers

Type	Direction	Description (see Fig. 3)
a	both	increasing downforce with reducing ride height
b	both	almost constant region high downforce, slight increase with reducing ride height
b′	down	an extension of b when the ride height is decreasing, downforce starts to reduce
c	up	rapid increase in downforce with ride height
c′	down	rapid downforce reduction with a small decrement in ride height
d	both	an almost flat region of low downforce
d′	up	an extension of d when the ride height is increasing, slow increase in downforce
e	both	a further reduction in downforce at flow ride heights

Regions b′ and c overlap (in terms of ride heights), as well as d′ and c′.

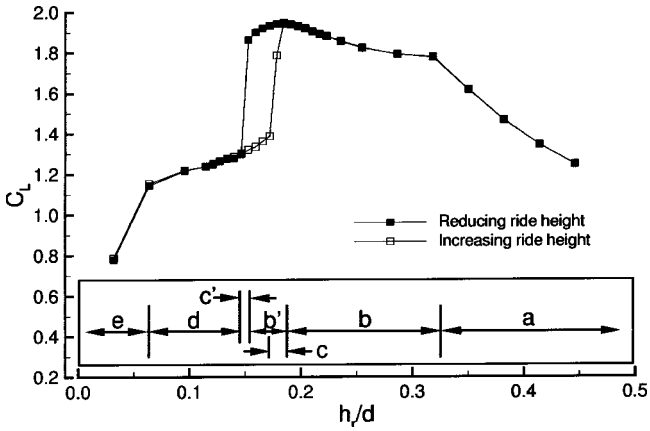

Fig. 3 Flow types for high angle diffusers: 15 deg diffuser, C_L, 30 m/s

Maximum Downforce. Reducing the normalized ride height with the diffuser angle, it becomes apparent that the maximum downforce occurs at similar values of $h_r/(d\times\theta)$ (Fig. 4), where θ is the divergence angle of the diffuser in radians. The maximum occurs at approximately 0.7 $h_r/(d\times\theta)$. Using this, the diffuser angle (or length) could be optimised with regard to expected ride heights.

Flow visualization on the ramp surfaces taken at maximum downforce as shown in Fig. 5, demonstrate some of the differences between the low and high angle diffusers. There is no separation bubble on the 5-deg ramp, although towards the end of the diffuser, the flow appears to be slow and unsteady. The flow on the 10-deg diffuser ramp demonstrates a closed separation bubble. The bubble forms somewhat downstream of the inlet and closes just ahead of the diffuser exit. Upstream of this point, the vortices appear to become wider, with a reduced swirl indicating the onset of vortex breakdown. The open separation bubble forming on the 20-deg diffuser ramp is very similar to those found on the 15 and 17 deg diffuser ramps. From the surface flow patterns downstream of the primary separation line, there appears to be only a small region where the flow is reversed. The separated flow is entrained into the vortices reducing the axial momentum. The reduced swirl of the vortices downstream of the primary separation line are an indication of vortex breakdown. In comparison to the the 10-deg diffuser, the primary flow separation line is closer to the inlet at the center of the ramp. For the 15 and 17 deg diffuser ramps, the primary flow separation line moves closer to the inlet below the maximum downforce ride height up to the point where the flow becomes asymmetrical.

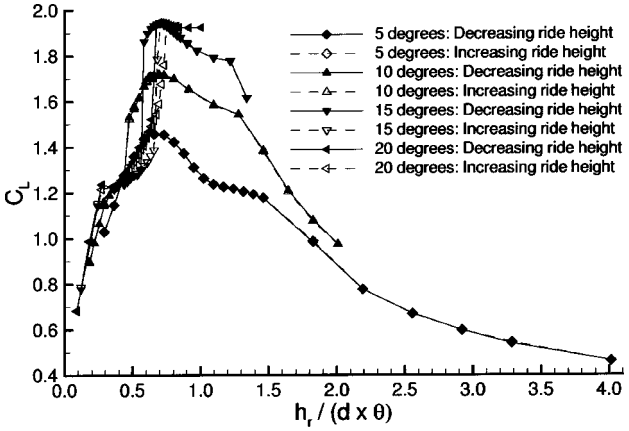

Fig. 4 Downforce coefficients: renormalized ride heights, 30 m/s

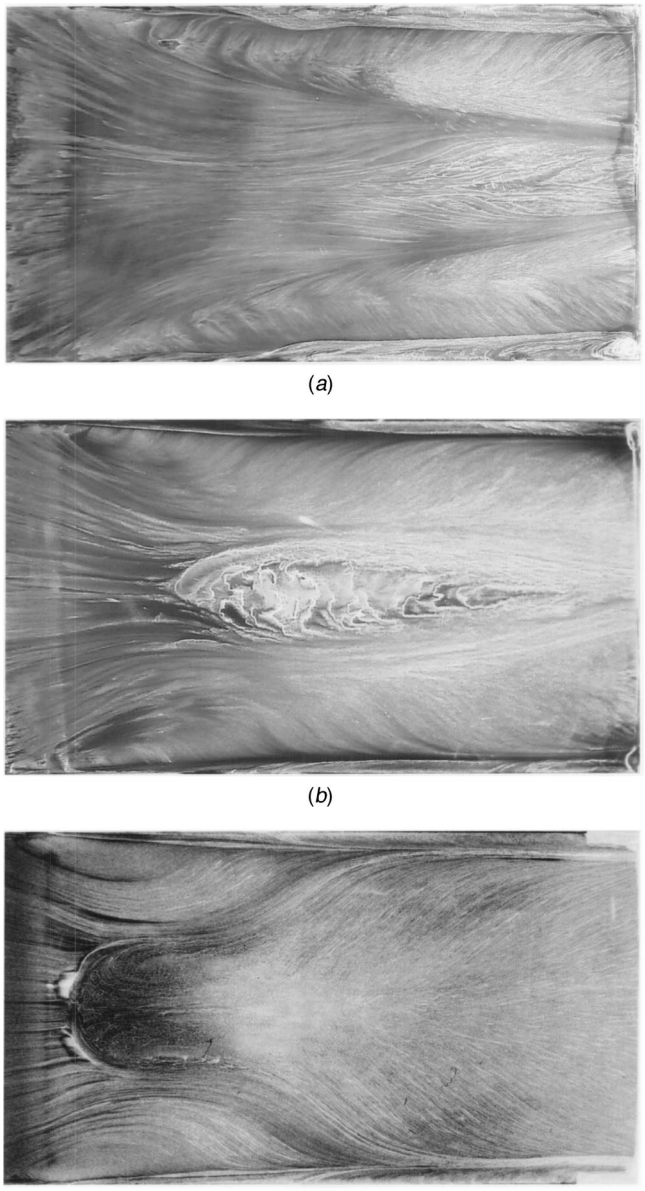

(*a*)

(*b*)

(*c*)

Fig. 5 Surface flow visualization on the ramp at maximum downforce, 30 m/s. Flow from left to right. Picture area corresponds to the ramp area. (*a*) 5-deg diffuser: $h_r/(d\times\theta)=0.657$, (*b*) 10-deg diffuser $h_r/(d\times\theta)=0.694$, (*c*) 15-deg diffuser—moving down: $h_r/(d\times\theta)=0.584$.

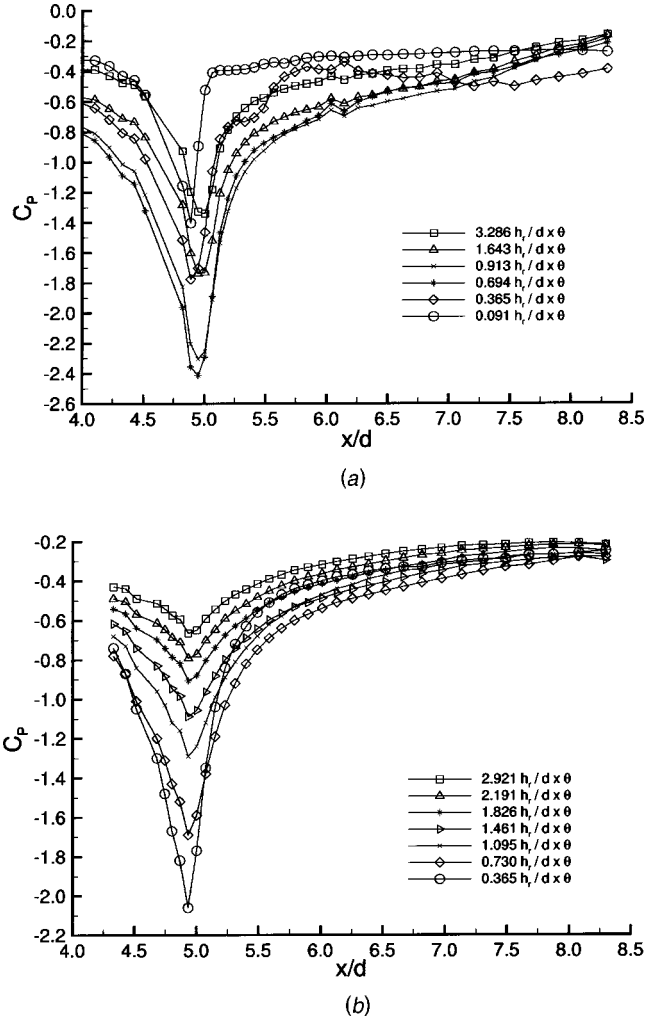

Fig. 6 Centerline pressure coefficients: 30 m/s. (*a*) 20 deg diffuser, (*b*) 5 deg diffuser.

Variation of Ride Height. At larger ride heights (type a flow), the adverse pressure gradient along the diffuser centerline is relatively weak (Fig. 6). The ratio of exit area to inlet area is low. No quasi-two-dimensional flow separation occurs in the center of the diffuser ramps. As the ride height is reduced through this region of type a flow, the area ratio (ratio of exit to inlet area of the diffuser) increases along with the effect of moving closer to the ground. The flow speed under the model rises (reduced static pressure, see Fig. 6(*a*)) resulting in increased downforce. The flow is dominated by two counter rotating vortices which prevent or limit the formation of a separation bubble. The pressure at the inlet of the diffuser reduces with ride height. Low pressure regions form in the corners of the diffuser where the vortices originate (Fig. 7). Figure 8 shows that the average base pressure of the model remains fairly constant throughout this region, although for the 5-deg diffuser, the base pressure begins to drop at a higher ride height ($h_r/(d\times\theta)=2.2$) indicating a change in the flow physics.

Reducing the ride height further in region b for the large angle diffusers, the flow field starts to change. The average base pressure of the model drops quickly (Fig. 8(*a*)) indicating a loss of pressure recovery within the diffuser. Drawing a parallel to two-dimensional planar diffusers, a reduction in pressure recovery is

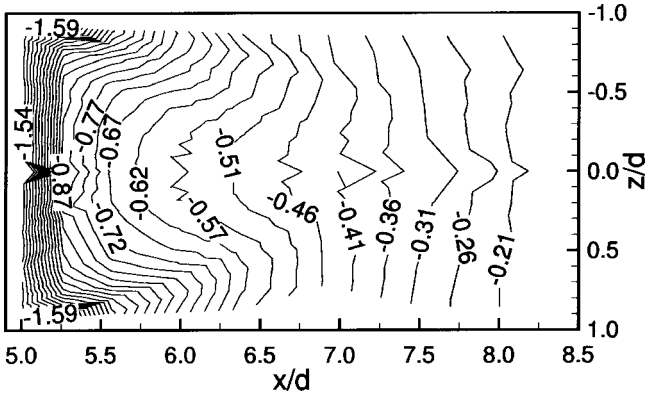

Fig. 7 Surface pressure coefficients: 20 degree diffuser, $h_r/(d\times\theta)=2.008$, 30 m/s

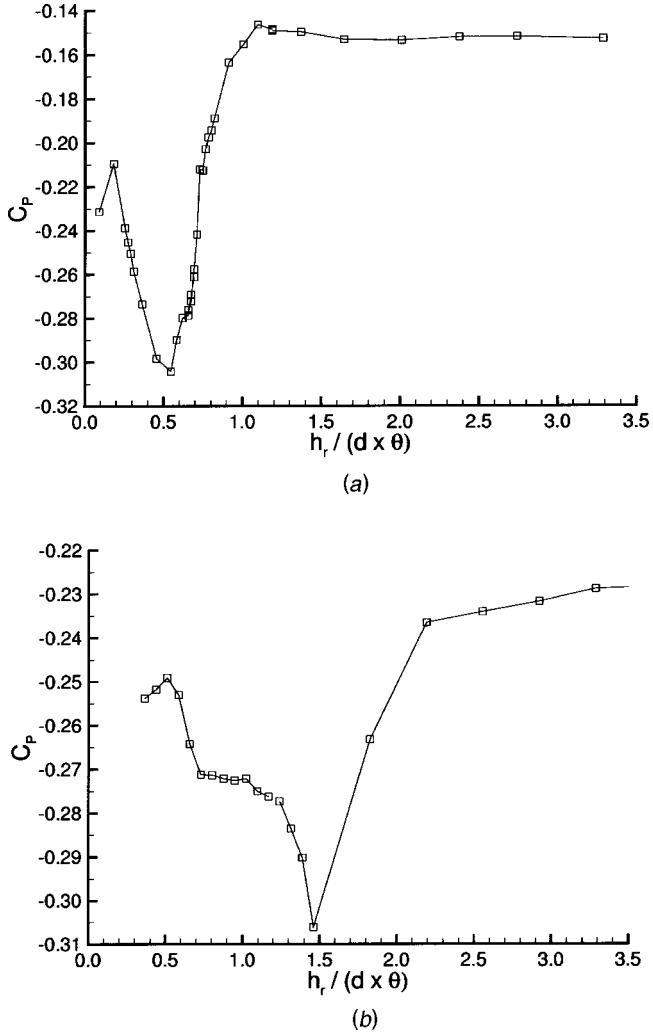

Fig. 8 Mean base pressures, 30 m/s; (*a*) 20 deg diffuser, (*b*) 5 deg diffuser

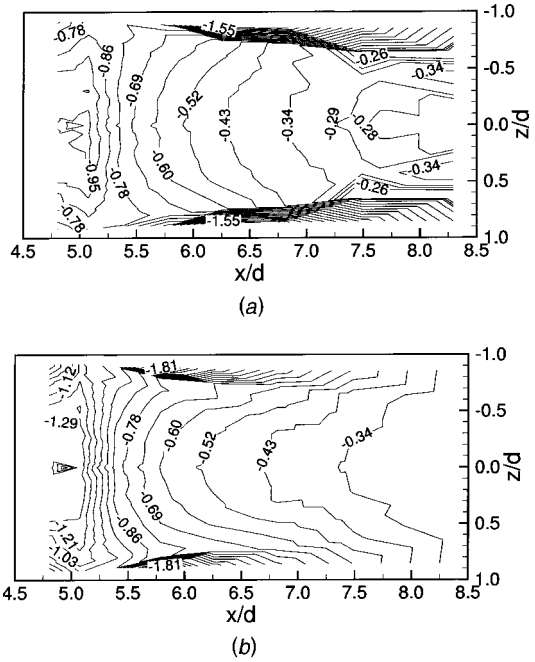

Fig. 9 Pressure contours: 5 deg diffuser, 30 m/s; (*a*) $h_r/(d \times \theta) = 1.241$, (*b*) $h_r/(d \times \theta) = 0.730$

generally associated with the onset of flow separation. In the case of the high angled diffusers, this is the case. The flow starts to separate at the inlet in the center of the diffuser. This separation bubble ceases to exist downstream as the vortices grow in diameter. However, in the case of the 5-deg diffuser, no such flow separation is apparent. The cause of this reduction in pressure recovery may be due to the onset of vortex breakdown. As a vortex begins to breakdown, the axial velocity of the core reduces. This effectively reduces the area ratio of the diffuser as the lower speed in the cores of the vortices essentially decreases the exit area of the diffuser. The velocity of the air between the vortices down the centerline appears to increase as the centerline pressure coefficients along the length of the diffuser ramp reduce (Fig. 6(*b*) when moving from an $h_r/(d \times \theta)$ value of 1.095 to 0.730. The second set of vortices present at 1.241 $h_r/(d \times \theta)$ at approximately $z/d = \pm 0.4$ towards the end of the diffuser diminish in strength to 0.730 $h_r/(d \times \theta)$ (Fig. 9). The vortices at the edge of the ramp increase in strength.

In the case of the 5-deg diffuser, the minimum base pressure occurs at the onset of type b flow. The peak in the drag curve at this point is due to the large base area of the model in this configuration. The lower diffuser angle and ride heights limit the strength and size of the vortices in the diffuser resulting in lower induced drag relative to the higher angled diffusers, as a result, the pressure drag becomes increasingly significant. An increase of base pressure beyond this point indicates that the boundary layers entering the diffuser are beginning to influence the flow to a larger degree. Whereas with the 17-deg diffuser the base pressure reduces to a minimum at the point where the hysteresis loop closes at the lower ride height, the base pressure for the 5-deg diffuser increases beyond the maximum downforce. As the boundary layers make up an increasing proportion of the diffuser inlet, the flow rate under the model decreases reducing the importance of the diffuser, moving towards the limiting case of zero ride height where no air passes under the model or through the diffuser.

The vortex observed in the current study is similar in characters to the leading edge vortex studied by Polhamus [9] using a leading-edge suction analogy and by Wentz and Kohlman [10] in a wind tunnel model test. In Fig. 10 evidence of vortex breakdown can be seen. As described in an earlier work of Lambourne and Bryer [11], the surface streaklines change downstream of the vortex bursting point. The swirl becomes less evident and the vortex becomes wider. This may also be a contributing factor to the ensuing asymmetry of the flow at lower ride heights. The apparent unsteadiness of the flow field may result in the bursting point of

Fig. 10 Surface flow visualization on the ramp: 20 deg diffuser, $h_r/(d \times \theta) = 0.694$, 30 m/s. Flow from left to right. Picture area corresponds to the ramp area.

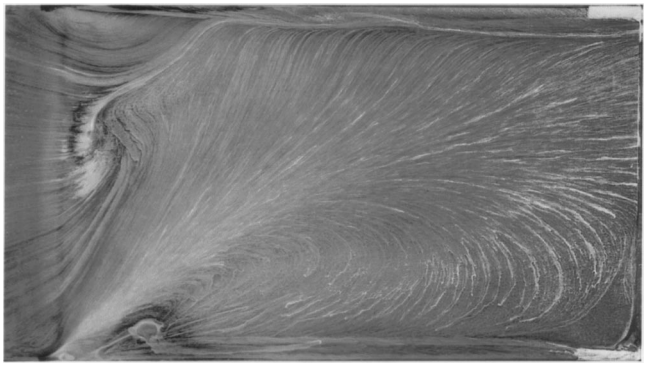

Fig. 11 Surface flow visualization on the ramp: 15 deg diffuser, $h_r/(d\times\theta)=0.560$, 30 m/s. Flow from left to right. Picture area corresponds to the ramp area.

one vortex to move further upstream momentarily, causing a disturbance to the pressure field resulting in the asymmetric flow of region d.

The importance of the separation bubble in the center of the diffuser inlet can be seen in Fig. 10. Just before the hysteresis loop closes, at the lower end of region b′, the separation bubble has almost reached the inlet of the diffuser. At the point where the hysteresis loop is closed at the lower end moving through region c′, the flow becomes asymetrical as shown in Fig. 11. Once the separation point reaches the inlet it cannot travel further upstream due to the favorable pressure gradient ahead of the inlet. Due to the extremely low pressures to either side of the inlet (Fig. 12), any disturbances will cause the large asymmetry in the flow to occur. The separation bubble gets swept to one side and a large recirculation region forms.

The direction of the asymmetry occurred randomly, but once established did not switch sides. This gives further indication that the type b flow is unstable. As found in experiments with high speed flows over axisymmetric bodies, any slight imperfection on the surface can cause asymmetries in the vortex flow field. As slight movement of the model may trigger the asymmetry in the flow field to take one direction over the other.

Progressing downwards through region d, the focus point close to the inlet of the diffuser on the side of the recirculating region (Fig. 11) moves downstream and towards the center of the diffuser. The region of recirculating flow is easily identifiable in the pressure contour plot of the 20-deg diffuser within type d flow in Fig. 13 as the large region of constant pressure. The pressure coefficients indicate that the remaining longitudinal vortex is not as strong as those at higher ride heights.

Flow type e is characterized by a steepening of the downforce curve. For the large angle diffusers this appears to occur when the ride height reaches the order of magnitude of the expected boundary layer thickness. From the pressure coefficient contour plot in Fig. 14 at a ride height of 0.091 $h_r/(d\times\theta)$ it is clear that the flow is separated over the majority of the diffuser ramp. The slight asymmetry in the contours is caused by a weak vortex forming on one side of the inlet. The centerline pressures from Fig. 6(*a*) show that the pressure spike is reduced dramatically and occurs further upstream. This indicates that there is not enough energy in the flow to overcome the adverse pressure gradient in the diffuser.

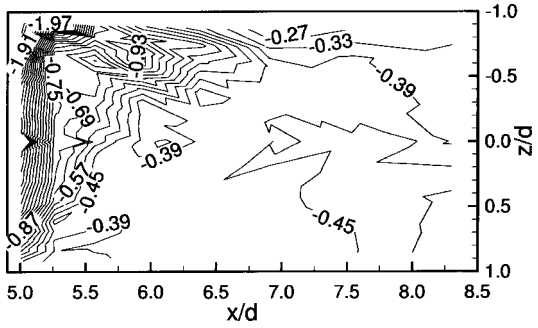

Fig. 13 Surface pressure coefficients: 20 deg diffuser, $h_r/(d\times\theta)=0.365$, 30 m/s

Further Discussion

The plot of drag variation with ride height for the 5 and 10 deg diffusers (Fig. 2(*b*) show two peaks, although the trough is better defined for the 5-deg diffuser. As can be seen with the pressure plots from the 5-deg diffuser in Fig. 9, at 1.241 $h_r/(d\times\theta)$ or 0.108 h_r/d there is a second set of vortices present, inboard of the first. These are no longer present on the pressure plot at 0.730 $h_r/(d\times\theta)$ or $0.064h_r/d$. The ouboard votices appear to increase in strength as the minimum C_P drops with reducing ride height. Between these two ride heights, the centerline pressure coefficients (Fig. 6(*b*)) also drop along the length of the diffuser, with a larger difference at the inlet and approaching the same value at the exit. Figure 8(*b*) shows an increase in the mean base pressure between these ride heights. The weakening of the inboard vortices, and the ensuing increase of the axial velocity through the diffuser cause an increase in the downforce. As the inboard vortices burst, the initial increase in downforce due to the strengthening of the outboard vortices is gradual. As the ride height is reduced, the flow through the diffuser becomes increasingly two-dimensional in nature as the aspect ratio $(2d/h_r)$ of the inlet increases to a value of 31.4 at 0.730 $h_r/(d\times\theta)$. The expansion of the axial flow region through the center of the diffuser improves the pressure recovery of the diffuser, creating the peak in the downforce at 0.730 $h_r/(d\times\theta)$. It is surmized that the dip in the drag curve is caused by the increasing base pressure and by a reduction in the induced drag due to the diminishment of the inboard vortices. The increase in drag below the trough is most

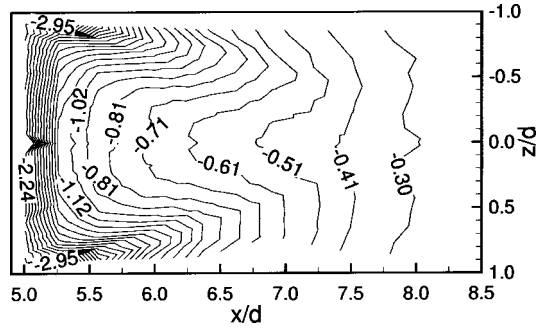

Fig. 12 Surface pressure coefficients: 20 deg diffuser, $h_r/(d\times\theta)=0.694$, 30 m/s

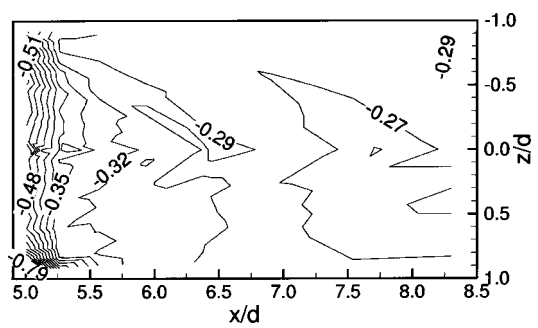

Fig. 14 Surface pressure coefficients: 20 deg diffuser, $h_r/(d\times\theta)=0.091$, 30 m/s

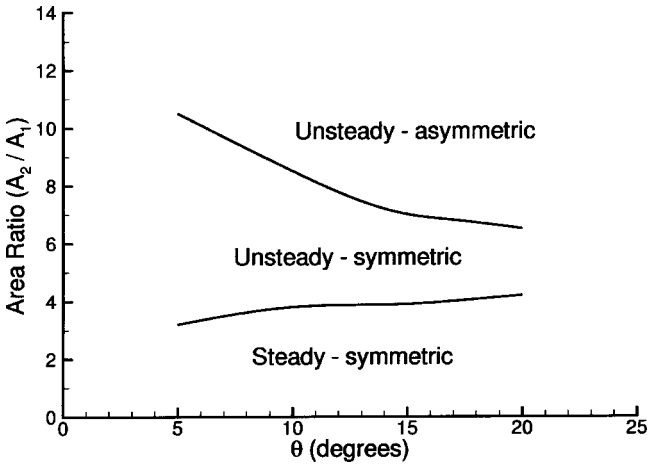

Fig. 15 Different flow regimes

likely caused by the increase of strength in the outboard vortices and the accompanying increase of induced drag. The base pressure in this region does not increase as rapidly as when the the drag reduces.

A map of diffuser performance, Fig. 15, shows the different operating regions of the different diffusers angle with respect to area ratio. The shift from steady symmetric flow (type a) to unsteady and symmetric (type b) occurs as similar area ratios for all diffuser ramp angles, indicating that it is primarily governed by the adverse pressure gradient. The narrowing of the unsteady-symmetric region towards the larger diffuser angles indicates that the streamwise adverse pressure gradient along the diffuser is not the driving factor for the transition to asymmetric flow. From the negative slope of this boundary it is clear that the underbody and ground boundary layers are not an important aspect of this transition. If the boundary layers were an influencing factor, the shift would occur at lower area ratios for the lower diffuser ramp angles as the effective inlet area would be reduced. Supporting evidence of the above observation can also be found in the wing in ground study of Zerihan and Zhang [12] and the high angle diffuser study of Senior and Zhang [6], where fixed ground tests were also performed. We have also performed fixed ground tests for all the angles. These fixed ground tests produced essentially the same observations. The effect of a fixed ground was first pointed by Burgen et al. [13] using, among other things, a bluff body in ground effect. The use of a fixed ground generally results in a downward shift in the downforce curve because of an effective reduction on mass flow rate between the ground and the model. An additional factor is the reduction in the effective ground height due to the displacement effect of the boundary layers. A change in the fundamental force characteristics does not occur above flow region e.

Summary

1. It is surmized that for the lower angled diffusers, vortex breakdown is the primary cause of force reduction. A combination of flow separation and vortex breakdown causes the force reduction for the high angle diffusers.

2. The underbody boundary layers do not appear to change the force characteristics of the diffuser at ride heights above region e, the onset of which approximately corresponds to the estimated boundary layer thickness. This occurs at a much larger ride height for the fixed ground case, [6].

3. A region of hysteresis occurs over the force reduction region for the 15, 17, and 20 degree diffusers.

4. The flow through the low angled diffusers is influenced by the underbody, and presumeably ground, boundary layers. Especially the formation and breakdown of the vortices.

5. The flow is unsteady in regions b, c, d, and e.

Acknowledgments

Andreas Ruhrmann wishes to thank British American Racing for providing a scholarship. The authors wish to thank Willem Toet and Andrea Senior for their help and suggestions.

Nomenclature

C_D = drag coefficient, $D/q_\infty S$
C_L = downforce coefficient, $L/q_\infty S$
C_P = pressure coefficient, $(p-p_\infty)/q_\infty$
D = drag
L = downforce
M = pitching moment
p = static pressure
p_∞ = freestream static pressure
q_∞ = freestream dynamic pressure, $\rho_\infty U_\infty^2/2$
U_∞ = freestream velocity
Re = Reynolds number, $\rho_\infty U_\infty l/\mu$
S = model frontal area
d = model half-width measured in y-direction
h_r = model ride height
l = length of model
x, y, z = cartesian coordinates: $x+$ve downstream, $y+$ve up, $z+$ve to port
ρ_∞ = freestream density
μ = viscosity
θ = diffuser expansion angle

References

[1] George, A. R., 1981, "Aerodynamic Effects of Shape Camber, Pitch, and Ground Proximity on Idealized Ground Vehicle Bodies," ASME J. Fluids Eng., **103**, pp. 631–638.
[2] George, A. R., and Donis, J. E., 1983, "Flow Patterns, Pressures, and Forces on the Underside of Idealized Ground Effect Vehicles," *Proceedings of the ASME, Fluids Engineering Division*, **7**, ASME, New York, pp. 69–79.
[3] Sovran, G., 1994, "The Kinematic and Fluid-Mechanic Boundary Conditions in Underbody Flow Simulation," *Proceedings of the CNR-Pininfarina Workshop on Wind Tunnel Simulation of Ground Effect*, Turin, Italy, May, National Research Council.
[4] Cooper, K. R., Bertenyi, T., Dutil, G., Syms, J., and Sovran, G., 1998, "The Aerodynamic Performance of Automotive Underbody Diffusers," SAE Paper No. 980030.
[5] Cooper, K. R., Sovran, G., and Syms, J., 2000, "Selecting Automotive Diffusers to Maximize Underbody Downforce," SAE Paper No. 2000-01-0354.
[6] Senior, A. E., and Zhang, X., 2001, "The Force and Pressure of a Diffuser-Equipped Bluff Body in Ground Effect," J. Fluid Eng., **123**, pp. 105–111.
[7] Senior, A. E., 2002, "An Investigation of a Generic 3D Diffuser in Ground Effect," Ph.D. thesis, University of Southampton, Apr.
[8] Moffat, R., 1988, "Describing the Uncertainties in Experimental Results," Exp. Therm. Fluid Sci., **1**, pp. 3–17.
[9] Polhamus, E. C., 1971, "Predictions of Vortex-Lift Characteristics by a Leading-Edge Suction Analogy," J. Aircr., **8**(4), pp. 193–199.
[10] Wentz, Jr., W. H., and Kohlman, D. L., 1971, "Vortex Breakdown on Slender Sharp-Edged Wings," J. Aircr., **8**(3), pp. 156–161.
[11] Lambourne, N. C., and Bryer, D. W., 1962, "The Bursting of Leading-Edge Vortices—Some Observations and Discussion of the Phenomenon," Aeronautical Research Council, Reports and Memoranda No. 3282.
[12] Zerihan, J., and Zhang, X., 2000, "Aerodynamics of a Single Element Wing in Ground Effect," J. Aircr., **37**(6), pp. 1058–1064.
[13] Burgin, K., Addey, P. C., and Beatham, J. P., 1986, "Wind Tunnel Tests on Road Vehicle Models Using a Moving Belt Simulation of Ground Effect," J. Wind. Eng. Ind. Aerodyn., **22**, pp. 227–236.

Mohammad I. Kilani[1]
Mechanical Engineering Department,
Florida State University,
Tallahassee, FL 32310

Paul C. Galambos
Intelligent Micromachine Department,
Sandia National Laboratories,
Albuquerque, NM 87185

Yousef S. Haik
e-mail: haik@eng.fsu.edu

Ching-Jen Chen

Mechanical Engineering Department,
Florida State University,
Tallahassee, FL 32310

Design and Analysis of a Surface Micromachined Spiral-Channel Viscous Pump

A new viscous spiral micropump which uses the surface micromachining technology is introduced. The paper outlines the design of a spiral pump fabricated in five levels of polysilicon using Sandia's Ultraplanar Multilevel MEMS Technology (SUMMiT), and presents an analytical solution of the flow field in its spiral channel. The pump characteristics are obtained experimentally for a scaled-up prototype and are found to be in good agreement with the results obtained using the analytical model.
[DOI: 10.1115/1.1524582]

1 Introduction

Several recent investigations discuss using viscous drag as the operating principle in micromachined pumps. The feasibility of this concept in the viscosity dominated microscale flow fields has been experimentally demonstrated using a rotating cylinder placed eccentrically between two parallel plates, [1], and a number of analytical and numerical simulations have followed, [2,3].

This paper introduces a planar, viscous drag, micropump, which targets the surface micromachining technology. The pump works by rotating a disk with a spiral groove at a close proximity over a stationary plate. The spiral channel resulting from this geometry produces the effect of the long channel of Couette experiment, while the rotating disk assumes the role of the moving plate.

For the purpose of analyzing the flow field in the pump, the spiral channel is ''unfolded'' into a straight channel with appropriate dimensions and boundary conditions. The paper demonstrates that this approximation is valid for typical designs and develops the relations mapping between the spiral pump geometry and the straight channel model. Analytical solution of the flow field in the straight channel model at the lubrication limit relates the flow rate of the spiral pump to rotation rate and pressure head.

The paper also describes a scaled-up spiral pump prototype developed for the purpose of verifying the spiral pumping concept and validating the presented analytical model. Pressure versus flow rate data obtained from the prototype was found to be in good agreement with the predictions of the analytical model.

2 Design

A schematic illustration of the spiral pump concept is shown in Fig. 1. A disk with a spiral groove rotates at a close proximity over a stationary plate and fluid is contained in the spiral channel created by the groove between the spiral disk and the stationary plate. Two holes at either end of the spiral channel provide the required inlet and outlet for the pumped fluid.

Due to nonslip conditions a velocity profile develops in the channel with fluid velocity increasing from zero at the stationary plate to the rotating plate velocity at the top, and viscous stresses on the upper and lower surfaces of the channel allow the fluid to be transported against an imposed pressure difference.

Figure 2 shows an example spiral micropump fabricated in Sandia Ultrplaner Multilevel MEMS Technology (SUMMiT). A compatible (also planar) comb drive microengine provides continuous rotational motion on its pinion gear, which is transmitted to the spiral disk through a 12:1 torque amplification gear train. Both the microengine and the gear train are available as pick and place components in SUMMiT technology, [4].

Figure 3 shows a cross-sectional view through the centerline of the rotating spiral disk to illustrate the interconnections between the different polysilicon levels. The disk is defined in the upper polysilicon level POLY4 and the stationary plate in the ground level POLY0. The spiral protrusion is defined in intervening POLY1, POLY2, and POLY3 levels and is connected to the POLY4 rotating disk while leaving a small gap (0.5 microns) above the stationary POLY0 level. A pin joint at the center of the disk provides rotational freedom for the spiral disk. Gear teeth on the perimeter of the disk mesh with matching teeth on the output gear of the transmission gear train and provide continuous rotation. The intricate structure around the rotating disk is a labyrinth seal for the pumped fluid. The inlet and outlet holes are created through backside of the wafer using a Bosch etching process.

The centerline curve of the spiral channel of a viscous-type spiral pump is a linear Archimedean spiral described in polar coordinates by

$$r = k\theta + r_o, \quad 0 \leqslant \theta \leqslant \Delta\theta \tag{1}$$

and satisfying the condition

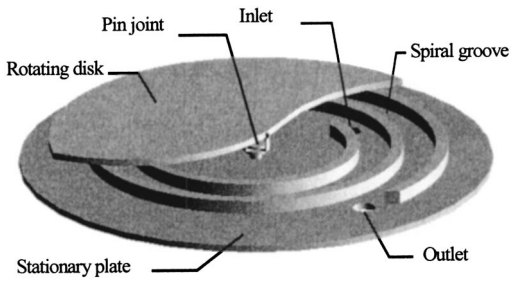

Fig. 1 The spiral pump concept

[1]Current address: Mechanical Engineering Department, University of Jordan, Amman, Jordan.

Contributed by the Fluids Engineering Division for publication in the JOURNAL OF FLUIDS ENGINEERING. Manuscript received by the Fluids Engineering Division April 9, 2002; revised manuscript received August 6, 2002. Associate Editor: J. Katz.

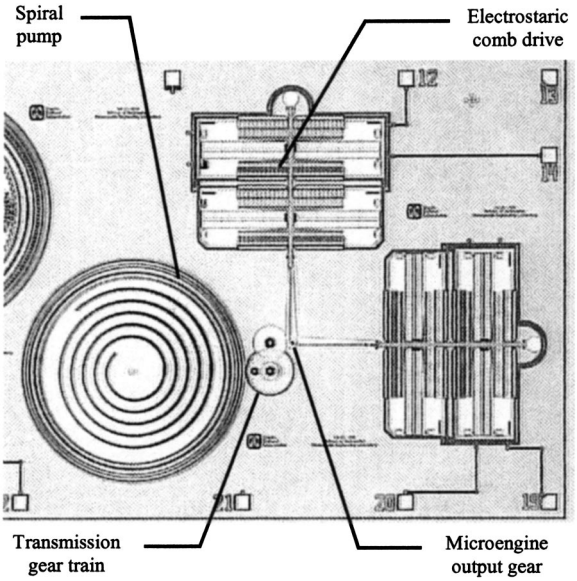

Fig. 2 An example spiral micropump fabricated in SUMMiT

$$k/r_o \ll 1 \tag{2}$$

where r_o is the starting radius of the spiral curve, k is its polar slope (change of r per θ), and $\Delta\theta$ is its angular span. Condition (2) indicates that the channel has a slight curvature at the entry and along its entire length, and when satisfied, the rotation of the spiral causes the fluid to be dragged axially along the spiral channel and not normal to the channel axis.

The values of k, r_o, and $\Delta\theta$ for the design of Fig. 2 are listed in Table 1 along with the spiral wall width w_t the spiral channel height h and the gap height h'. These six parameters completely define the spiral channel geometry.

3 Straight-Channel Approximation

Consider a disk with a spiral channel whose centerline curve is defined by Eq. (1) and satisfying Eq. (2). Let the disk rotate at an angular speed ω against a pressure head Δp between the inlet and outlet. For the purpose of analyzing the flow field in the spiral channel we propose an approximation that replaces it with a straight channel with equivalent dimensions and boundary conditions. The validity of such an approximation for flows in slightly curved geometries has been first investigated by Dean in 1927 [5]. Using a perturbation analysis of the Navier-Stokes equations it may be demonstrated that the leading-order error in the axial velocity due to the unfolding approximation is proportional to the square of Reynolds number Re, [6], which is small in the viscosity dominated microscale flow fields. The perturbation parameter in this analysis is the curvature ratio ε defined as

$$\varepsilon = w/\rho \tag{3}$$

Table 1 Spiral channel defining parameters and their values for the design of Fig. 2

Parameter	Value
Polar slope k	12 microns
Starting radius r_o	146 microns
Angular span $\Delta\theta$	8π
Wall thickness w_t	21 microns
Channel height h	10 microns
Gap height h'	0.5 microns

where w is the channel width and ρ is its radius of curvature. The unfolding approximation is valid only for small values of both Re and ε.

For a spiral channel with a centerline segment defined by Eq. (1) the curvature ratio is defined as

$$\varepsilon = \frac{2\pi k - w_t}{r} = \frac{k}{r}(2\pi - w_t/k) \tag{4}$$

where w_t is the spiral wall thickness. By virtue of condition (2), $\varepsilon \ll 1$ is satisfied unless $2\pi - w_t/k$ is much larger that unity. Since both w_t and k are positive, the upper limit on $2\pi - w_t/k$ is 2π, and $\varepsilon \ll 1$ when in addition to (2) either one of the following conditions is satisfied

$$\frac{k}{r} < \frac{1}{2\pi} \tag{5}$$

$$2\pi - w_t/k \leqslant 1. \tag{6}$$

For the design describe in Table 1, $k/r_o = 0.08$ and the unfolding approximation is valid.

Figure 4 shows the straight channel model resulting from the unfolding approximation. The height h is equal to the original height of the spiral channel. The length l is taken to be the length of the centerline curve and is determined by integrating the differential length $dl = r\,d\theta$ over the angular span, after substituting for r from Eq. (1) we obtain

$$l \approx \int_0^{\Delta\theta} (r_o + k\theta)\,d\theta = (r_o + k\Delta\theta/2)\Delta\theta = r_a\Delta\theta \tag{7}$$

where $r_a = (r_o + k\Delta\theta/2)$ is the average radius of the spiral curve.

To complete the straight channel model, we relate the boundary velocity of the straight channel u_{ch} to the angular velocity ω of the spiral channel. Using the velocity relation $u_{ch} = \omega r$, it is noted that u_{ch} is a function of x since r increases with x. A simple relation for the functional dependence of r on x may be established using the length relation in Eq. (7) to arrive at the first-order approximation $dx = r_a\,d\theta$. The coordinate x is thus related to θ and r by

$$x = \int_0^{\theta} r_a\,d\theta = r_a\theta = \frac{r_a}{k}(r - r_o) \tag{8}$$

or

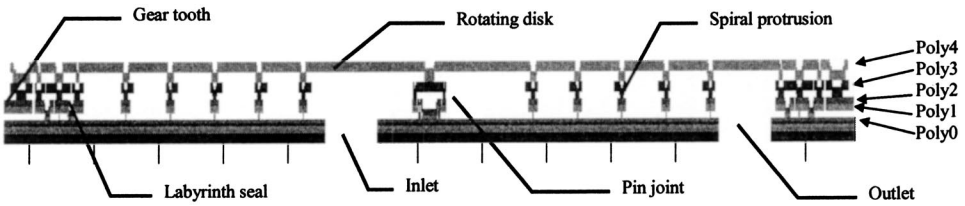

Fig. 3 A cross section through the spiral micropump (vertical dimension magnified to show film details)

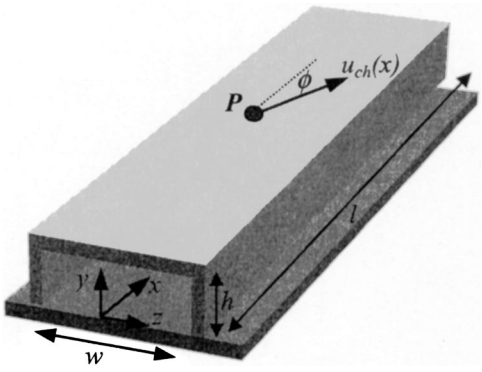

Fig. 4 Straight channel model

$$r = r_o + kx/r_a \tag{9}$$

and

$$u_{ch}(x) = \omega r_o + \frac{k\omega}{r_a} x. \tag{10}$$

To determine the direction of u_{ch} with respect to the x-direction, Fig. 5 shows a small portion of a spiral curve rotating about the origin O of the polar coordinate. As illustrated in the figure, the direction of motion of a point P on the channel makes an angle ϕ with x, which may be related to the spiral channel parameters by

$$\phi = \tan^{-1}(dr/rd\theta) = \tan^{-1}(k/r). \tag{11}$$

To conclude this section, we summarize the relations needed to map a spiral channel geometry into a straight channel model using the unfolding approximation. Given a spiral channel with height h, wall thickness w_t, and centerline curve defined by Eq. (1) and satisfying Eq. (2). If the channel is rotating at an angular velocity ω against a pressure head Δp, the flow field in the channel may be modeled by a straight model with the mapping relations listed in Table 2. The table also lists the values of the straight channel parameters for the design of Table 1.

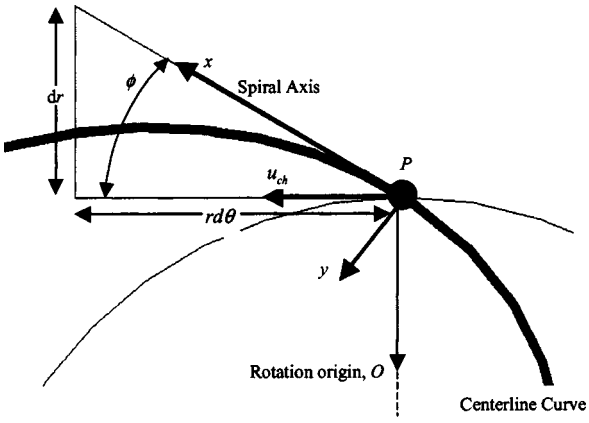

Fig. 5 Determination of the spiral angle

Table 2 Mapping from spiral geometry into a straight channel model

Straight-Channel Parameter	Formula	Value for Design in Table 1
Width	$2\pi k - w_t$	54.4 microns
Length	$r_a \Delta\theta$	7459 microns
Height	h	10 microns
Gap height	h'	0.5 microns
Angle	$\tan^{-1}(k/r)$	4.7 deg at inlet, 1.5 deg at exit.
Upper boundary velocity	$\omega r_o + k\omega x/r_a$	146,000+40x microns/s (with $\omega = 1000$ rad/s)
Pressure difference	Δp	Δp

4 Analysis

The unfolding approximation results in a straight-channel model for the flow field in the spiral channel, with the equivalence formulas for dimensions and velocities listed in Table 2. As illustrated in Fig. 5, $u_{ch}(x)$ has both an axial component $u_{ch-x} = u_{ch}\cos\phi$ along the spiral axis and a transverse component $u_{ch-y} = u_{ch}\sin\phi$ normal to the spiral direction. An order of magnitude analysis on the quantities describing the straight channel model reveals the significance of these components and allows further simplification in the model. To that end, we nondimensionalise the quantities in Table 2 by selecting the reference length to be the channel length l, and the reference velocity to be the boundary velocity of at the entrance of the channel, $u_{ch}(0) = \omega r_o$. The nondimensional upper boundary velocity u^*_{ch} and its components u^*_{ch-x} and u^*_{ch-y} are thus obtained to be

$$u^*_{ch} = 1 + (k/r_o)(l/r_a)x^* \tag{12}$$

$$u^*_{ch-x} = u^*_{ch}\cos\phi = u^*_{ch}/\sqrt{1+(k/r)^2} \tag{13}$$

$$u^*_{ch-y} = u^*_{ch}\sin\phi = (k/r)(u^*_{ch}/\sqrt{1+(k/r)^2}). \tag{14}$$

For $k/r \ll 1$, $u^*_{ch-x} \approx u^*_{ch}$ and $u^*_{ch-y} \approx 0$. The axial velocity approaches $u_{ch}(x)$, and the transverse component may be neglected, leading to symmetric geometry and boundary conditions around the $z=0$ plane. When $h \ll w$, which is usually the case in the channels considered, the flow field in the plane of symmetry represents the flow across the channel, and the problem reduces to the two-dimensional flow in that plane as shown in Fig. 6.

The relative magnitude of axial velocity gradient du^*_{ch}/dx^* may be determined from (12) to be $O(k/r_o)(l/r_a)$. While k/r_o is typically small, l/r_a is frequently large and the product is too significant to be neglected. For example, the design of Table 1 has $k/r_o = 0.08$ and $l/r_a = 25$ with the product $(k/r_o)(l/r_a) = 2$. That is, the boundary velocity at the exit, when $x^* = 1$, approaches three times its value at the inlet, precluding the possibility of obtaining a one-dimensional solution for the flow in the channel (the streamlines are not parallel). An analytical solution for the two-dimensional flow field using the lubrication approximation, however, may be obtained as shown below.

The microscale flow field of an incompressible Newtonian fluid in the thin narrow gap of the model depicted in Fig. 6 is a classical example of flow situation governed by the simplified version of the Navier-Stokes equations known as the lubrication model. The reduced Reynolds number, $\overline{\mathrm{Re}} = \mathrm{Re}(h/l)$ for the case of pumping water using the pump described in Table 1 is $2\times10^{-6}\omega$ and the lubrication model holds for a rotational speed up to 500,000 rad/s! Letting u and v denote the x and y-components of the fluid velocity, p fluid pressure and μ its viscosity, the momentum and continuity in the lubrication model are

$$\frac{\partial p}{\partial x} = \mu\frac{\partial^2 u}{\partial y^2}, \quad \frac{\partial p}{\partial y} = 0 \tag{15}$$

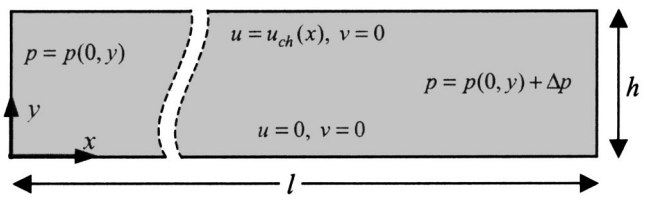

Fig. 6 Two-dimensional flow model

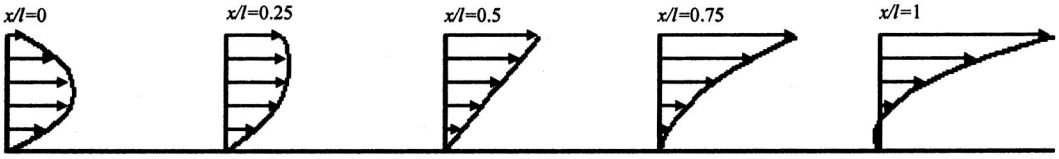

Fig. 7 Axial velocity profiles at zero pressure head

$$\frac{\partial u}{\partial x}+\frac{\partial v}{\partial y}=0 \tag{16}$$

which in the case of Fig. 6, are subject to the following boundary conditions:

$$u(x,0)=0, \quad u(x,h)=u_{ch}(x) \tag{17}$$

$$v(x,0)=0, \quad v(x,h)=0 \tag{18}$$

$$p(l,y)=p(0,y)+\Delta p. \tag{19}$$

An analytical solution for the linear system above may be obtained by eliminating p from (17) to give $\partial^3 u/\partial y^3=0$, which may be solved by repeated integration using the boundary conditions in Eq. (17) through Eq. (19). It may be verified that the closed-form solution of the above system is

$$u=u_{ch}(x)\frac{y}{h}-\left(\frac{h^2}{2\mu}\frac{\Delta p}{l}+3\delta(x)\right)\left(\frac{y}{h}-\left(\frac{y}{h}\right)^2\right) \tag{20}$$

$$v=hu'_{ch}((y/h)^2-(y/h)^3) \tag{21}$$

$$p(x)=\frac{6\mu}{h^2}\int_0^x \delta(x)dx+\Delta p\frac{x}{l}+p_o \tag{22}$$

where $u'_{ch}\equiv \partial u_{ch}/\partial x$ is the upper boundary velocity gradient, $\overline{u_{ch}}(x)\equiv 1/l\int_0^l u_{ch}(x)dx$ is the mean upper boundary velocity, and $\delta(x)\equiv u_{ch}(x)-\overline{u_{ch}}$ is the local deviation from the mean. Figure 7 shows the u profiles between $y/h=0$ and $y/h=1$ resulting from a linearly increasing upper boundary speed no imposed external pressure. The figure shows that backflow barely develops near the bottom wall.

5 Pump Characteristics

The volume flow rate per unit channel width may be estimated by evaluating the integral $\int_0^h u dy$ at any x with $x=\overline{x}$ being particularly convenient. Using Eq. (20) we obtain

$$q=\frac{h\overline{u_{ch}}}{2}-\frac{h^3}{12\mu l}\Delta p. \tag{23}$$

The quantity $h\overline{u_{ch}}$ is the per unit width flow rate in front of a plug of height h and speed $\overline{u_{ch}}$. As in the conventional Couette experiment, the zero pressure flow rate is only half that quantity and drops with pressure buildup by $h^3/12\mu l$.

Using the linear velocity relation in Eq. (10) we have $\overline{u_{ch}}=\omega r_a$ and $\delta(x)=\omega k(x/r_a-\Delta\theta/2)$. The flow rate of a spiral pump defined by the parameters listed in Table 1 is given by

$$Q=\frac{whr_a}{2}\omega-\frac{wh^3}{12\mu r_a\Delta\theta}\Delta p. \tag{24}$$

Figure 8 shows the theoretical flow rate for the case of pumping water ($\mu=1\times10^{-3}$ kg/(m.s)) using the spiral pump described in design A of Table 1 when running at speeds ranging from 1000 rad/s to 5000 rad/s against a pressure head ranging from zero to 700 kPa.

6 Experimental Tests

Experimental flow rate versus pressure head data were generated using the setup shown in Fig. 9. The spiral pump in the figure is a scaled up prototype that was built to verify the spiral pump concept and examine the correctness of the analytical model. The geometric properties the prototype pump are listed in Table 3.

Flow rate–pressure head data were obtained by running the pump at a fixed speed and measuring the flow rates while increasing the pressure head until the maximum pressure is reached. The process is repeated for three different speeds. SAE 10W30 motor oil with a density of 825 kg/m^3 and viscosity of 90.1×10^{-3} kg/m.s at 28°C was used.

7 Discussion

Figure 10 presents a comparison between the experimental data and the analytical model for the spiral pump. The flow rates of the

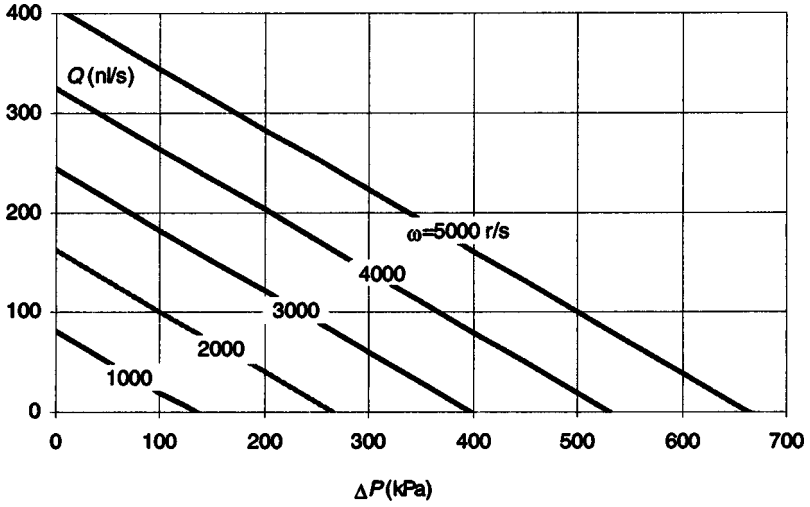

Fig. 8 Theoretical flow rate

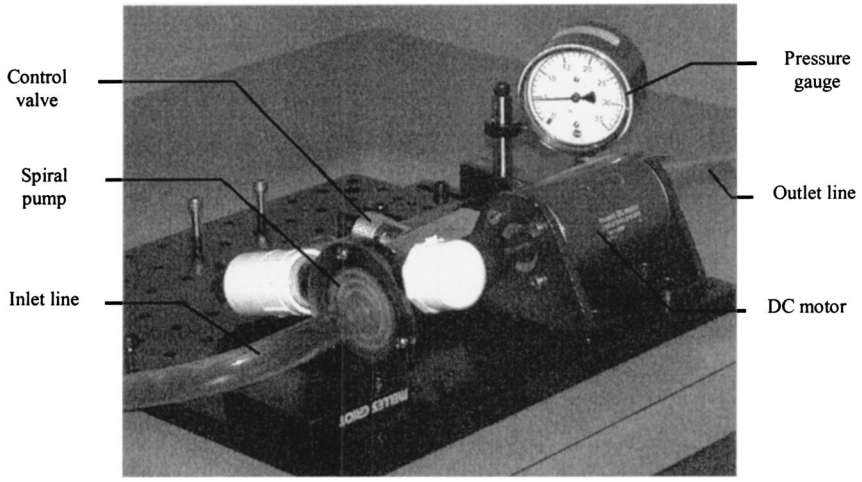

Fig. 9 Flow rate–pressure head experimental setup

prototype pump predicted by Eq. (24) are generally in good agreement with those obtained experimentally. At low speeds, the experimental flow rates are below the analytical predictions with the error increasing as the pressure head is increased. This may be attributed to the cross flow in the gap below the spiral wall, which is more pronounced at higher pressures. As the speed of the pump is increased, the centrifugal effects compensate for the cross flow loss, and when the speed is further increased, the experimental flow rate becomes larger than that predicted by the analytical solution.

The effect of gap height h' is particularly important since in addition to its effect on flow rate, due to cross flow between the flights of the spiral channel, it plays a dominant role in determining the torque and thus the power needed to operate the pump. An intersection of a moving boundary with a stationary boundary is created near the gap, and the presence of a transverse flow component further complicates the situation, as it leads to large velocity gradients and a ''scraping motion'' next to the gap. A detailed analytical solution of the flow field near the intersection of moving and fixed boundaries shows that when the intersecting boundaries make perfect geometric contact, the tangential force becomes logarithmically infinite, [7]. The presence of the clearance gap precludes this divergent solution, but the force increases as the gap is diminished. The gap clearance requires a critical tradeoff between minimizing the cross flow while also minimizing the power consumption in the pump.

Table 3 Spiral channel parameters for the prototype pump

Parameter	Value
Polar slope k, mm	0.75
Average radius r_a, mm	16.0
Angular span $\Delta\theta$	3π
Channel width w, mm	3.2
Channel height h, mm	1.0
Clearance gap h', mm	0.1

8 Conclusions

This paper introduced a new surface micromachined viscous pump concept that works by rotating a disk with a spiral protrusion over a stationary plate and outlined the implementation of this concept in the 5-level of silicon using surface micromachining. Approximating the spiral channel by an equivalent straight

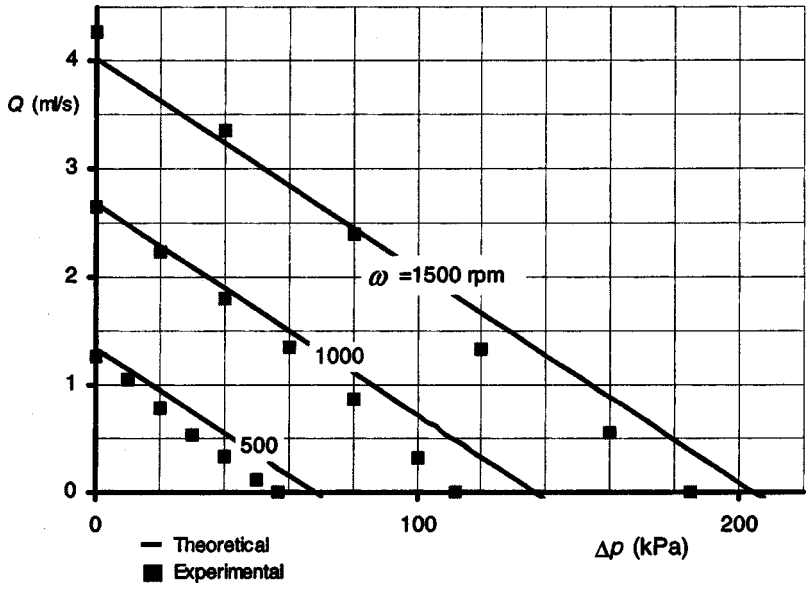

Fig. 10 Theoretical and experimental flow rates

channel, and using the lubrication model, a simple analytical solution of the flow field in the pump was obtained, which relates the flow rate to the pressure difference and rotation rate. Experimental pressure versus flow rate data obtained from a scaled-up spiral pump prototype follow the trend predicted by the analytical model, with deviation attributed to centrifugal effect and to cross flow in the gap between the spiral wall and the fixed plate.

The analysis presented above focused on the contribution of flow in the spiral channel on pump performance. The effect of spiral curvature, spiral angle, spiral wall height, gap between the spiral and stationary disk, and transverse flow on pump performance at both low and high Reynolds numbers are still open issues that need to be addressed in further research.

References

[1] Sen, M., Wajerski, D., and Gad-El-Hak, M., 1996, ''A Novel Pump for MEMS Applications,'' ASME J. Fluids Eng., **118**, pp. 624–627.

[2] Sharachandra, M. C., Sen, M., and Gad-Elhak, M., 1997, ''Navier-Stokes Simulations of a Novel Viscous Pump,'' ASME J. Fluids Eng., **119**, pp. 372–382.

[3] Day, R., and Stone, H., 2000, ''Lubrication Analysis and Boundary Integral Simulations of a Viscous Micropump,'' J. Fluid Mech., **416**, pp. 197–216.

[4] Garcia, E., and Sniegowski, J., 1995, ''Surface Micromachined Microengines,'' Sens. Actuators, **48**, pp. 203–214.

[5] Dean, W. R., 1927, ''Note on the Motion of Fluid in a Curved Pipe,'' Philos. Mag., **4**, pp. 208–219.

[6] Leal, L. G., 1992, *Laminar Flow and Convective Transport Processes: Scaling Principles and Asymptotic Analysis*, Butterworth-Heinemann, Boston, MA.

[7] Batchelor, G. K., 1967, *An Introduction to Fluid Dynamics*, Cambridge University Press, Cambridge, UK.

Nobuyuki Yamaguchi
Faculty of Sciences and Engineering,
Meisei University,
2-1-1 Hodokubo, Hino City,
Tokyo 191-8506, Japan

Keisuke Ito
Ichigaya Division,
Dai-nippon Printing Company,
1-1-1, Kagamachi,
Ichigaya, Shinjuku-ku,
Tokyo 162-8001, Japan

Masayuki Ogata
Faculty of Sciences and Engineering,
Meisei University,
2-1-1 Hodokubo, Hino City,
Tokyo 191-8506, Japan

Flutter Limits and Behaviors of Flexible Webs Having a Simplified Basic Configuration in High-Speed Flow

Fluttering conditions were analyzed for webs with a simplified basic configuration with both leading and trailing edges fixed in a uniform flow. The predicted flutter limits are expressed in terms of a ratio of fluid force to tension (σ^*), a ratio of tension to bending stiffness (τ^*), and a reduced frequency f_R. Three characteristic zones of the behavior are seen to appear depending on the magnitude of τ^*. For medium τ^* of 1×10^3 to 1×10^6, flutter-limit values of σ^* and f_R remain nearly constant, respectively. For low $\tau^*(<1\times10^3)$ effect of bending stiffness becomes significant and buckling-like instabilities tend to occur preceding the flutter. For high $\tau^*(>1\times10^6)$ ripple-like modes tend to occur and σ^* falls drastically and f_R scatters much. Experimental flutter limits obtained in the wind tunnel were seen on the average to agree with the expected ones for the tested range of $9\times10^2<\tau^*<4\times10^4$. [DOI: 10.1115/1.1537254]

1 Foreword

Long continuous belts (webs) of thin and flexible materials are frequently handled or moved at high speed in air. Such a process is, so to say, a basic and essential unit component employed in a vast area of industries and technologies; for example, webs of paper, plastic film, cloth, thin steel strips, and so forth are handled in modern information processing units, tape recorders, rotary printing machines, transmission belts, plastic film manufacturing equipment, and rolling mills in steel-making plants. Fluttering of the webs tend to occur in such processes, having undesirable effects on the quality of the product and/or the production rate of the process. If the web behavior could be stabilized, for example, in printing machines, significant improvements could be gained, such as better print quality, a higher printing speed, and a decrease in frequency of troubles such as wrinkling and folded edges.

Especially with the advent of a variety of high-speed information processing equipment and information media, practical prediction methods for web behaviors are in high demand, in order to elucidate and control the phenomena. The phenomena, however, are complicated because of the many factors involved, such as web stiffness (elasticity), inertia force, fluid force, axial force (tension), motion configuration, and so forth. Therefore, improvements and countermeasures have been mostly devised by experiences and through trial and error on site.

The situation is similar to flag-like sheet flutter phenomena. A brief historical survey on investigations on the flutter phenomena of sheets and webs was presented in the Foreword of Yamaguchi et al. [1]. They have constructed a practical prediction method of flutter limits of sheets and webs. By use of the method, Yamaguchi et al. [2] made clear the flutter limits and behaviors for sheets having the leading edge clamped and the trailing edge free in a uniform flow.

Difficulty in the problems lies in the extreme aeroelastic nature of the phenomena. The web has a very low stiffness and a very small mass ratio compared to the surrounding fluid. Therefore, the web motion tends to deviate significantly from the resonance modes in vacuum, and progressive waves appear. Investigations in the field have been relatively few in number from both analytical and experimental aspects. For the web flutter phenomena, the general tendencies or behaviors affected by governing factors have not yet been clearly understood.

Recently, the web flutter phenomena have received more attention. Kaneko et al. [3] treated a flow-induced flutter of a highly flexible sheet in a very narrow passage between rigid walls as is often seen in paper-making machines by leakage flow approximation and the finite element method based structural equation. Chang and Moretti [4] treated another kind of web flutter, the flutter of free edges in the cross machine direction which is the direction transverse to the one here.

This paper aims to predict the flutter limits of webs in a uniform flow and to elucidate the general behaviors by extending the above method, [1]. In addition, results from wind tunnel tests are included to compare with the predicted data.

2 A Simplified Basic Configurations of a Web

As shown in Fig. 1(*a*), a web is generally a continuous belt of flexible and thin plate or film running between revolving rollers, supported and tensioned by them. As additionally shown in Fig. 1(*b*), walls are often present nearby.

Although it is desirable to handle the practical situations of the webs as they are, it is too complicated to analyze them generally. So, to begin with, a very simplified situation as a basic condition of the web is assumed. A very thin two-dimensional web is swept by a two-dimensional uniform flow, with its leading and trailing edges clamped or hinged, as shown in Fig. 2.

Several differences are really present between the simplified basic configuration and the practical ones, as understood at first glance of Figs. 1 and 2, including (1) the axial movement of the web, (2) the presence of the rollers at both edges, (3) the finite width of the web (three-dimensionality of the flow), and (4) possible presence of nearby walls. These factors are expected to affect the practical phenomena to a more or less extent in addition to the basic effect. Since the magnitude of these effects are supposed to be not small, they should be the tasks for further studies.

3 Outline of the Method of Analysis

The basic concept of the analytical method employed here was already described in Yamaguchi et al. [1], which should be re-

Contributed by the Fluids Engineering Division for publication in the JOURNAL OF FLUIDS ENGINEERING. Manuscript received by the Fluids Engineering Division Nov. 6, 2001; revised manuscript received Aug. 15, 2002. Associate Editor: Y. Tsujimoto.

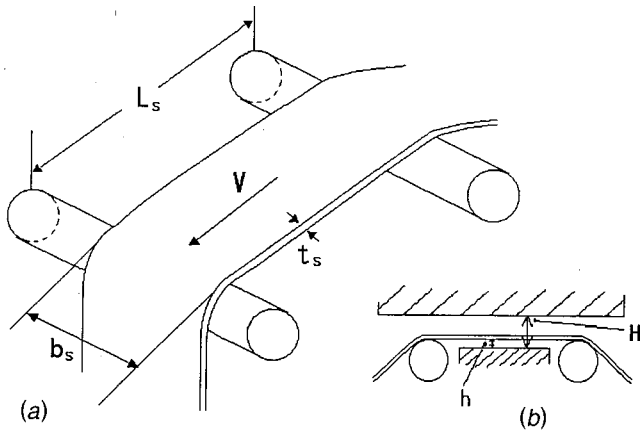

Fig. 1 (*a*) General practical situations of webs and (*b*) presence of nearby walls

ferred to for details. This paper deals with a web of very thin and flexible material in an infinitesimal perturbed motion. The web is clamped at its leading and trailing edges and swept by a uniform flow of speed U_a. It has a length of L_s and a thickness of t_s. The width b_s is so large that the situation could be assumed to be two-dimensional. As shown in Fig. 3(*a*), the web surface, being flown in *x*-direction on the average, performs a small-amplitude

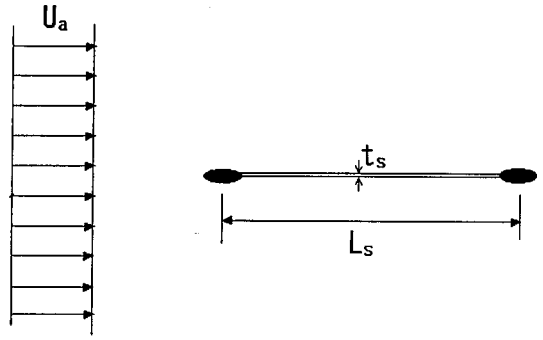

Fig. 2 The simplified basic configuration of web assumed in this simulation study

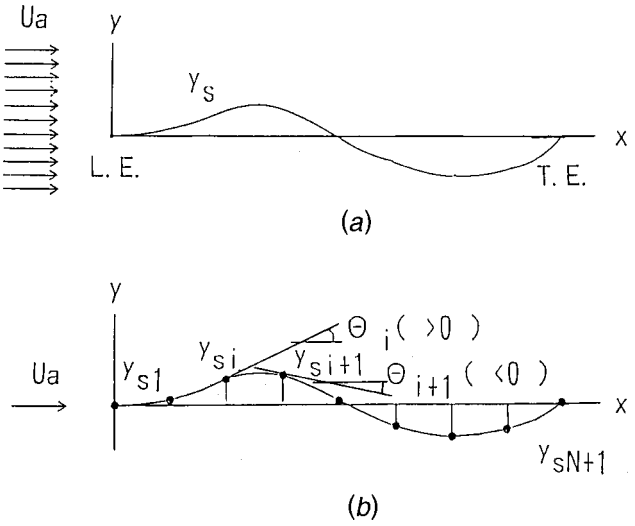

Fig. 3 Conditions of a fluttering web

oscillation in *y*-direction, whose displacement is y_s. The edges are at $x=0$ and $x=L_s$. The densities of the web and the air are ρ_s and ρ_a, respectively.

The basic equations are as follows:

(1) *Flow field*: The web is simulated by distributed vortices on the web $\Gamma(x,t)$ and free vortices $\Gamma_w(x,t)$ emitted from the trailing edge.

$$\Gamma w(x,t)=\Gamma(Ls,t-Ls/U_a) \quad \text{for } x>L_s \tag{1}$$

The unsteady pressure difference across the web plane $\Delta p(x,t)$ is determined by the following equation derived from the conservation of the vorticity and the relationship between the pressure and the velocity:

$$\Delta p(x,t)=-\rho_a\int_0^x \frac{\partial\Gamma(x,t)}{\partial t}dx-\rho_a U_a\Gamma(x,t) \quad \text{for } 0<x<L_s. \tag{2}$$

A velocity component v in the *y*-direction is estimated by Biot-Savart's law from the distributed vortices.

(2) *Web motion*: The forces acting on the web are given by the following:

$$F_D(x,t)=\Delta p(x,t)-\rho_s t_s\frac{\partial^2 y_s(x,t)}{\partial t^2}+T(x)\frac{\partial\Theta(x,t)}{\partial t}. \tag{3}$$

Here the second term and the third one on the right-hand side are the inertia force of the web and the contribution of the tension *T*, respectively.

The exerted forces are related with the beam sectional shear force as follows:

$$\frac{\partial f_B(x,t)}{\partial x}=F_D(x,t). \tag{4}$$

Based on the above relationships, the following equations give the relationships concerning the beam quantities:

$$\text{sectional shear forces: } f_B(x,t)=\int_{xo}^x F_D(x,t)dx+f_B(x_o,t) \tag{5}$$

$$\text{bending moments: } M(x,t)=\int_{xo}^x f_B(x,t)dx+M(x_o,t) \tag{6}$$

$$\text{web inclinations: } \Theta(x,t)=\frac{1}{\beta}\int_{xo}^x M(x,t)dx+\Theta(x_o,t) \tag{7}$$

$$\text{web displacements: } y_s(x,t)=\int_{xo}^x \Theta(x,t)dx+y_s(x_o,t). \tag{8}$$

Here, β is a relative stiffness, a ratio of the web stiffness on the typical flow force,

$$\beta=\frac{E_s I_s}{(\rho_a U_a^2/2)L_s^3}, \tag{9}$$

where E_s is Young's modulus, and I_s is the sectional area moment of the web. x_o is a starting point of the integration, or the joint point of each segment when the sheet is approximated by a number of short segments as described later.

(3) *Boundary conditions*: The Kutta-Joukowski equation holds at the trailing edge.

$$\Delta p(L_s,t)=0 \tag{10}$$

The web motion and the flow field are matched as follows:

$$v-\frac{\partial y_s(x,t)}{\partial t}=U_a\frac{\partial y_s(x,t)}{\partial x}. \tag{11}$$

The leading and trailing-edge conditions of simple support are

Table 1 Data for the analysis of web behavior

WEB	Material	paper
	Length L_s	1 m
	Thickness t_s	1–0.1 mm
	Density ρ_s	700 kg/m^3
	Young's Modulus E_s	3 GPa
FLOW		air
	Density ρ_a	1.2 kg/m^3
	Friction Coeff. c_{fo}	0.05

$$y_s(0,t)=0 \quad \text{and} \quad M(0,t)=0 \tag{12}$$

$$y_s(L_s,t)=0 \quad \text{and} \quad M(L_s,t)=0. \tag{13}$$

The above variables as functions of coordinate x and time t are variable separated. The time function can reasonably be expressed as $\exp(j\omega t)$, where j is the imaginary unit and ω is a complex angular frequency. A general function $g(x,t)$ is expressed as follows:

$$g(x,t)=G(x)\exp(j\omega t) \tag{14}$$

where $g(x,t)$ stands for each of $\Gamma(x,t)$, $\Delta p(x,t)$, $F_D(x,t)$, $f_B(x,t)$, $M(x,t)$, $\Theta(x,t)$, and $y_s(x,t)$. The respective functions $G(x)$ of x only exist corresponding to the above functions, respectively. They are linearized on the assumption of small perturbations.

The effects of fluid friction are taken into the analysis as follows. The local tension is given as

$$T(x,t)=T_o-2\times cf_o(\rho_a U_a^2/2)x. \tag{15}$$

Here, T_o is the tension at the leading edge, and cf_o is a fluid frictional coefficient. The multiplication factor 2 is taking account of both surfaces of the sheet.

The web is divided into N segments as shown in Fig. 3(b). The Eqs. (5)–(8) are applied to each segment. The variables at respective joining points as unknowns are related continuously with those at the neighboring junction points. Thus from the basic equations, simultaneous equations for respective segments are constructed in terms of the variables at the segment junctions, to form a system of homogeneous linear simultaneous equations. The determinant derived from the coefficient matrix of the system determines complex frequencies of the phenomena. The sign of the imaginary part indicates either the stability or instability of the web motion. The unstable condition will bring about web flutter.

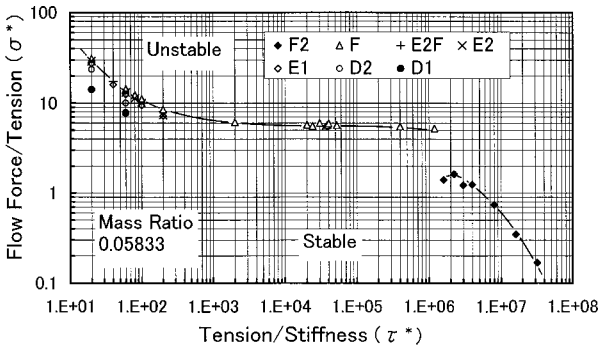

Fig. 4 Predicted flutter limits of webs under tension

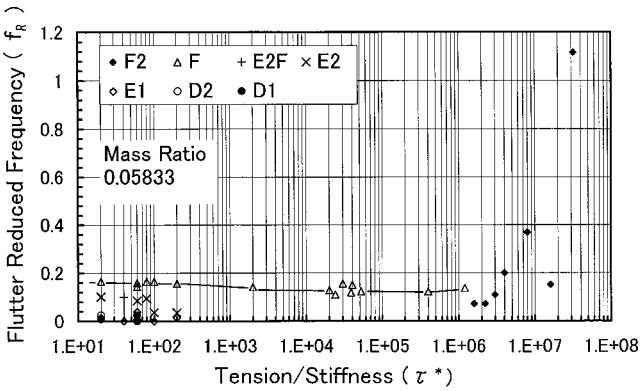

Fig. 5 Predicted reduced flutter frequency of webs under tension

4 Governing Parameters

Although the phenomena are affected by various factors in a complicated manner, the results are conveniently expressed in

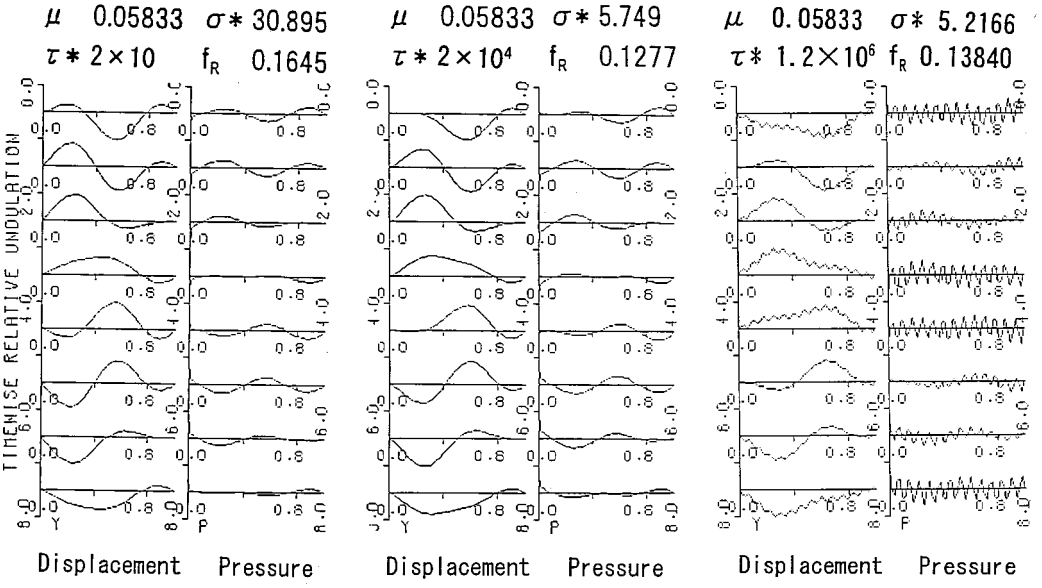

Fig. 6 Predicted vibration modes of webs and pressures for F-mode for τ^* of 2×10, 2×10^4, and 1.2×10^6

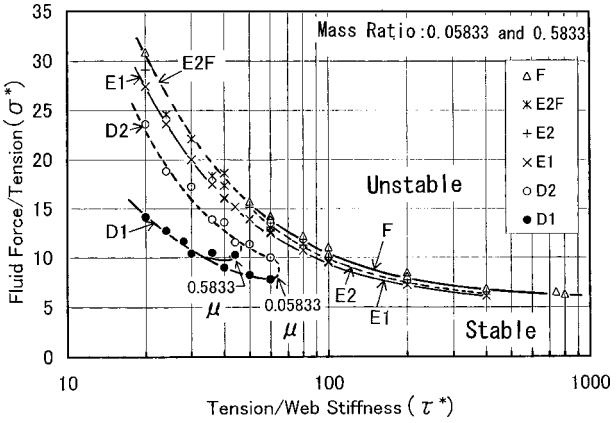

Fig. 7 Detailed behavior of flutter limit lines in low τ^* region

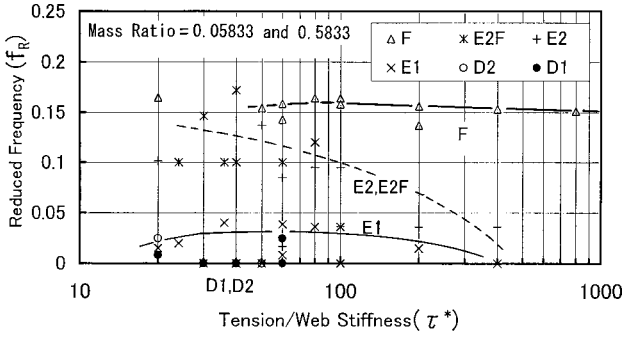

Fig. 8 Detailed behavior of flutter limit reduced frequency lines in low τ^* region

terms of the following four nondimensional quantities, which have been derived by normalization of the governing equations (Yamaguchi et al. [1]).

$$\text{tension/stiffness ratio} \quad \tau^* = TL_s^2/E_sI_s \tag{16}$$

$$\text{fluid force/tension ratio} \quad \sigma^* = (\rho_a U_a^2 L_s b_s)/T \tag{17}$$

$$\text{reduced frequency} \quad f_R = fL_s/U_a \tag{18}$$

$$\text{mass ratio} \quad \mu = \rho_s t_s/\rho_a L_s \tag{19}$$

Here T is the web tensile force (N) and is nominally taken equal to To here, and f is the flutter frequency (Hz). The first parameter τ^* is the ratio of the web tension to the web bending stiffness. It may be called a tension parameter. The second parameter σ^* is the ratio of the typical flow force to the web tension. Both include the tension term whose effects are very important in the web flutter phenomena. Hereafter these dimensionless quantities are employed to show the results.

5 Analytical Results

Web behaviors were calculated for the conditions given in Table 1 by increasing the flow speed gradually from sufficiently low value up to the one where the characteristic root became unstable. A flutter limit was defined as the condition where neutral stability was reached. The flow friction coefficient c_{fo} was assumed to be 0.05, which appeared rather high but was considered to be reasonable for the situation based on the results on sheet flutter in Yamaguchi et al. [2]. The number of the segments N approximating the webs was taken to be 50 in the analysis.

5.1 Predicted Results. Figures 4 and 5 show the predicted results. All the plotted points in the figures are the analytical ones. Figure 4 shows the predicted flutter limits in terms of fluid force/tension ratios σ^* against the tension parameter τ^* for mass ratio μ of 0.05833 ($L_s = 1$ m and $t_s = 0.0001$ m). Symbols such as D, E, F, etc., discern the oscillation modes at the respective points, which will be described later. The lower part of the figure corresponds to a stable region and the upper part to the unstable region, i.e., flutter region. Figure 5 shows the predicted reduced frequencies f_R at the flutter limits against the tension parameters τ^* for a mass ratio μ of 0.05833.

The web flutter phenomena depend mainly on the tension parameter τ^*. The effect of mass ratios and fluid frictions on the web flutter phenomena will be mainly presented in Section 6. The flutter limit σ^* proved to be relatively independent of the mass ratios and friction coefficients in the range surveyed here.

5.2 Features of the Flutter Behavior. As seen in Figs. 4 and 5, the behavior of the flutter limits shows different tendencies in the following three regions depending on the tension parameters τ^*.

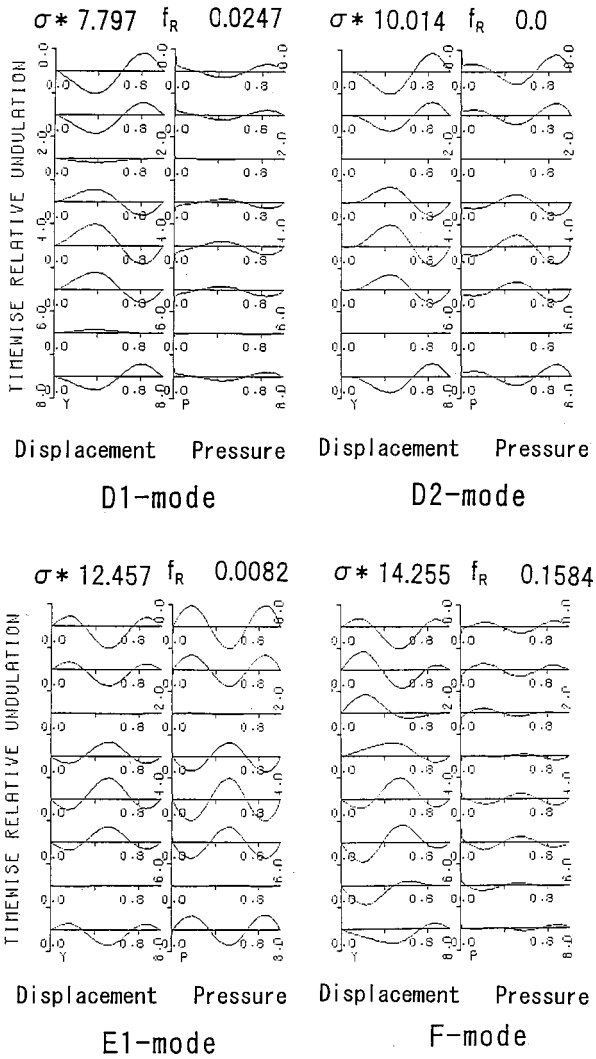

Fig. 9 Predicted vibration modes of webs and pressures in low τ^* region for $\tau^*=60$ and $\mu=0.05833$

(1) $\tau^* < 1\times10^3$ low τ^* region

(2) $1\times10^3 < \tau^* < 1\times10^6$ medium τ^* region

(3) $1\times10^6 < \tau^*$ high τ^* region

In the medium τ^* region ($1\times10^3 < \tau^* < 1\times10^6$), the flutter fluid force/tension ratios σ^* remain nearly of a constant value close to 6, and the reduced frequencies f_R lie between 0.1–0.15. The figure at the center of Fig. 6 shows a typical oscillation mode for the medium τ^* region, predicted at τ^* of 2×10^4. Eight subfigures to the left and to the right of each pair in Fig. 6 show instantaneous displacements and pressure distributions, respectively, along the web. The subfigures are at each eighth time interval of one complete cycle successively from the top to the bottom. They are normalized by the maximum absolute value of the corresponding quantity over an oscillation period and over the whole web length. The flutter modes are seen to resemble roughly the third resonance mode. The web displacements, however, show the presence of progressive waves traveling toward downstream direction. On the other hand, the pressure distributions show progressive waves traveling toward upstream. The speed of the waves is one weblength for an oscillation period. The mode is named the "F" mode hereafter.

Immediately below the upper border of the medium τ^*, for example, at τ^* of 1.2×10^6 in Fig. 6, small ripples are seen to appear superposed on the F-mode. The ripples play a major role in the adjacent high τ^* region. The ripples, however, tend to lower the analytical accuracy.

Instability conditions in the low τ^* region ($\tau^* < 1\times10^3$) are shown in an expanded scale in Figs. 7 and 8 including data for mass ratios $\mu=0.05833$ and 0.5833. Toward lower values of τ^*, the value of σ^* corresponding to the F-mode flutter limit increases gradually. The character of the oscillation and the f_R value are seen to remain unchanged. The oscillation mode shown in the left pair of Fig. 6, which is for τ^* of 20 in the low τ^* region, belongs to the F-mode and is essentially of the same form as that for the medium τ^* region.

In the low τ^* region, however, unstable zones are predicted preceding the F-mode flutter. As seen in Figs. 7 and 8, for $\tau^* < 70$, with an increase in the flow speed, a neutral point named "D1" first occurs and breaks into instability. In the zone from point D1 to D2 the web behavior is unstable. Figure 8 shows a rough tendency of the reduced frequencies. At points D1 and D2 the reduced frequencies f_R are calculated to be nearly zero. From D2 to E1 the web is stable. At point E1 instability occurs again. Above point E1 one of the following two situations occurs: (1) at point E2, stability is regained and after that the web breaks into F-mode instability, i.e., the ordinary fluttering condition, or (2) without recourse to the E2 condition, the web directly breaks into F-mode instability. The latter is named point E2F. At points E1 and E2 the reduced frequencies are relatively close to those for F-mode flutter. For $70 < \tau^* < 400$, the D-mode vanishes and E1 first occurs. The E-mode zone between lines E1 and E2 is seen to exist very close to the F-line at relatively higher values of τ^*.

As shown in Fig. 9, both D and E-modes show a manner of standing waves of the second modes and the third ones, respectively. In addition to that, their frequencies are very low, which suggests an occurrence of instability close to buckling.

In the very low τ^* region, the web tension is relatively small compared to the bending stiffness. The growing fluid force would cause such kind of oscillation against the web bending stiffness prior to the ordinary flutter occurrence. It is anticipated that this pre-flutter instability would, in practice, force the oscillation directly into a flutter without recourse to the intervening stable zones.

The upper-limit σ^* line and the lower one for the D-mode zone appear nearly independent of mass ratios. However, the upper-limit τ^* for the D-zone is affected by mass ratios, as seen in Fig. 7. The upper-limit τ^* for the D-mode zone is lower for a larger mass ratio ($\mu=0.5833$) than for a smaller mass ratio ($\mu=0.05833$). Since other mode-lines are not affected by changes in the mass ratios, the same marks are used in plotting the calculated points irrespective of mass ratios in Figs. 7 and 8.

In the high τ^* region ($1\times10^6 < \tau^*$), the magnitude of σ^* suddenly drops, namely, the flutter speed is lower toward higher values of τ^* as shown in Fig. 4. In the region, a number of unstable results tend to occur in a very crowded fashion. In practice, the flutter limits encountered will be the lowest ones which are plotted

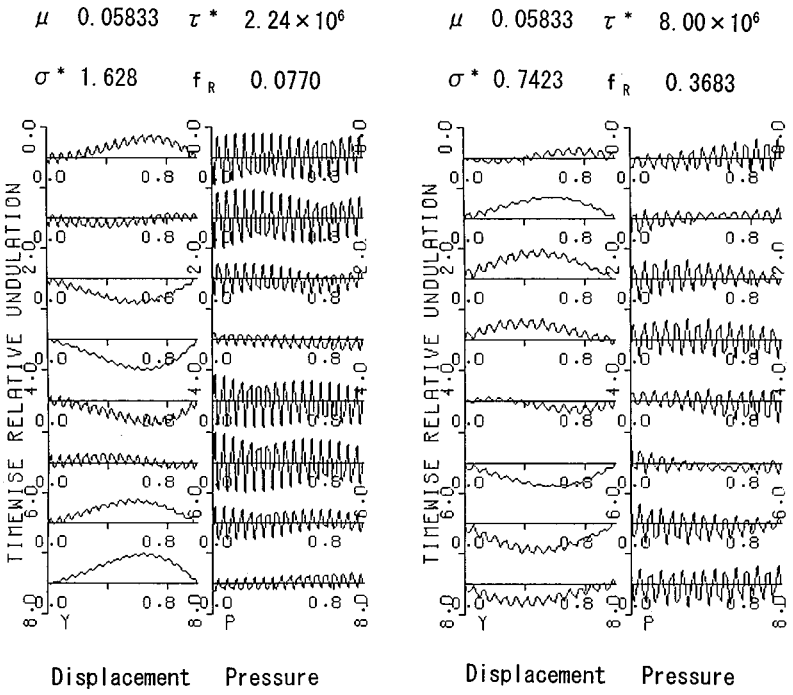

Fig. 10 Predicted vibration modes of webs and pressures for high τ^* region

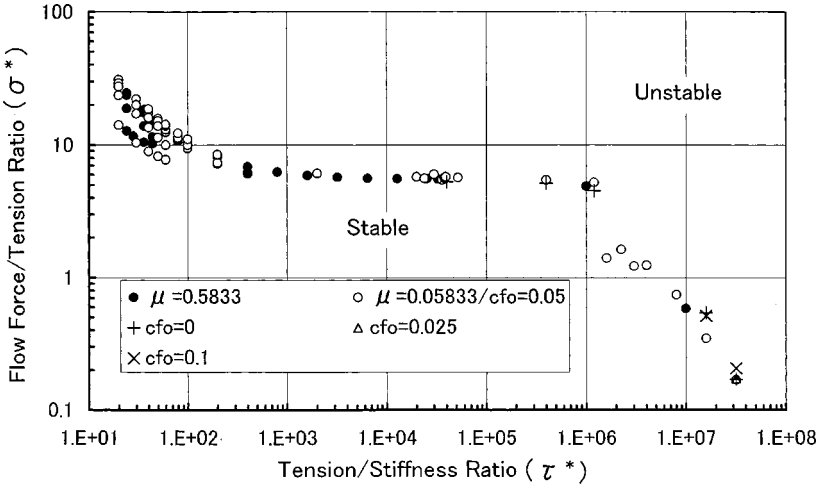

Fig. 11 Predicted effects of mass ratios and friction coefficients on the web flutter limits

in the figure. At the same time the values of the reduced flutter-frequency f_R become scattered, and many of them become higher.

The modes show oscillations of very high orders, which appear as ripples superposed on a lower mode oscillation in Fig. 10. The pressure distributions show a prevalence of the ripples. These flutter modes are named F2 as a whole.

The ripple phenomenon is attributed to a significant difference in the characteristic wavelengths for a beam-bending vibration and a tensioned-string vibration for the same frequency (*cf.* Appendix). Around τ^* of 1×10^6, the wave lengths of both vibrations are noticeably different from one another. For example, a tensioned string vibration for the third mode (1.5 waves on the string) can coexist together with a beam bending vibration for the 30th mode (15 waves on the beam). Thus ripples of the bending modes appear superposed on a lower order mode of the tensioned string vibrations. The ripples might be the major cause of the F2 instability in the high τ^* region.

Here it must be noted that the ripples of very short wavelength tend to limit the analytical accuracy owing to the limited number of the segments employed in the calculation ($N=50$). From the authors' experiences, [1], accuracy within 1 percent in the flutter speed requires roughly ten segments for a wavelength. Thus the above results in the high τ^* region should be thought to be tentative ones. The result for τ^* of 1.2×10^6 in Fig. 6 and all examples in Fig. 10 thus have rather limited accuracy.

For reference, the conditions where both of the wavelengths are comparable for the respective third modes are estimated to be for τ^* of around 100, which is within the low τ^* region. For these conditions both types of vibrations are naturally very dependent on one another through the parameters and may form an inseparably combined mode in contrast to the apparently independent modes of ripples on a long-wave mode.

6 Effects of Mass Ratio and Friction Coefficient

The effects of mass ratio and friction coefficient on the flutter behavior are summarized in Figs. 11 and 12 mainly for the medium and the high-τ^* regions. The effects of mass ratios are compared for μ of 0.05833 and 0.5833, with a friction coefficient c_{fo} of 0.05. The effects of the fluid friction coefficient are compared among c_{fo} of 0.0, 0.025, 0.05, and 0.1, all for mass ratio μ of 0.05833.

Changes in these factors are seen to have little effects on the F-mode flutter phenomena within the range surveyed here, particularly in the medium τ^* region. As to the low τ^* region, the

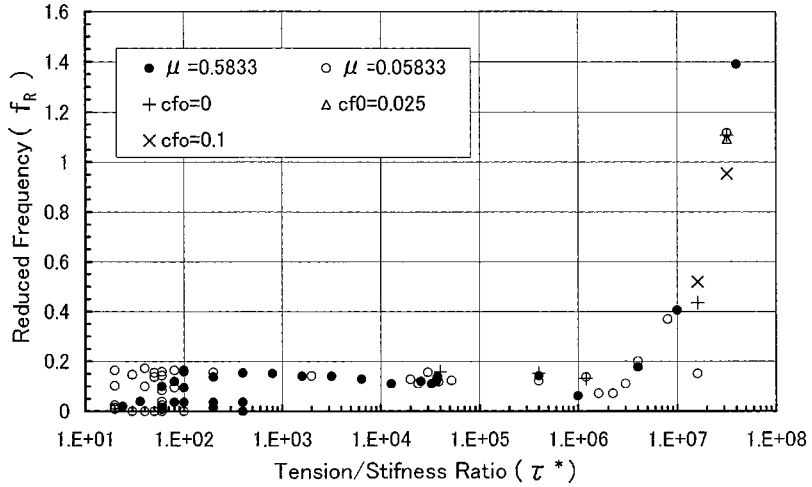

Fig. 12 Predicted effects of mass ratios and friction coefficients on the reduced flutter frequencies

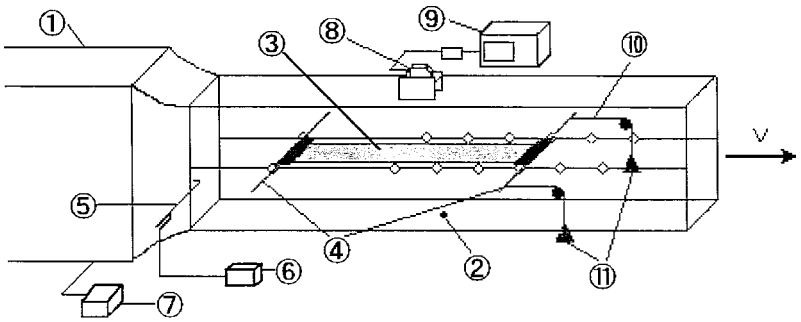

Fig. 13 Experimental arrangement for the web flutter tests

D-mode is affected by the mass ratios but the F-mode is not, as described in the preceding section. In the high τ^* region, however, prediction accuracy is lower because of the limited number of the segments for one wave at present. Therefore, for $1\times10^2<\tau^*<1\times10^6$, the above conclusion is appropriate from the analytical view.

7 Results of Wind Tunnel Tests

The analytical data above are compared with those experimentally obtained in wind tunnel tests (Ito et al. [5]).

7.1 Procedure of the Wind Tunnel Tests. Thin and flexible sheets of paper with both ends clamped were tested on their flutter limits in a uniform airflow in a wind. The dimensional data of the wind tunnel are given in Table 2.

The arrangement of the experiment is schematically shown in Fig. 13. Edge-clamping devices, as shown in Fig. 14, have a thin and streamlined two-dimensional sectional shape. They are supported horizontally on knife edges, allowing both free axial movement of the web and a horizontal tension load on the web. Tension is provided by two weight pieces of a known mass hung at the tips of two vertical wires. After a deflection in the direction via rollers, the wires transmit the tension horizontally to the trailing-edge device. The wires run outside of the wind tunnel channel walls on both sides of the web.

Procedures of the measurement are as follows: A sheet of paper for the test is fixed by the edge-clamping devices and weights of a known mass are hung at the tip of the tension wires. Then the wind tunnel fan is started and the speed is gradually increased by an inverter controller system. At each fan speed the flow velocity and the web amplitude is measured. When the amplitude increases suddenly, it is identified as a flutter speed. As shown in Fig. 13, flow velocity is measured by means of a Pitot tube and a digital differential pressure indicator. The web displacement is measured with a noncontact laser position-sensor system, whose output is analyzed by an FFT analyzer system for surveying the frequency characteristics.

The data and properties of the papers used for the tests are given in Table 3. The Young's modulus of each web specimen was estimated from the tip deflection of a sample sheet caused by the uniform loading of the sheet weight itself using the deflection formula on the uniformly loaded beam. The data are very scattered, influenced by various characteristics of the test sheet, such as which side of the paper (the face or the back) is upward, which of the paper directions (longitudinal or lateral) is for the beam fibers, etc., in addition to the geometrical data. So, many measurements were taken and averaged.

The uncertainties of the measurements are estimated as follows; mass of the sheet: 0.5 percent, thickness: 5 percent, web length: 0.5 percent, flow speed: 1.5 percent, tension: 0.01 percent, and frequency: less than 0.1 percent. The uncertainty of the Young's modulus was thus expected to be 12 percent and the experimental scatter was 10 percent within a range of very small deflections. In spite of the above, the experimental data obtained on flutter limits scattered far more than expected.

In the test, care was taken to avoid humidification of the test sheet, wrinkling or edge folding of the sheet during testing, and so on. These precautions tended to reduce the scattering of the ex-

Table 2 Dimensions of the wind tunnel

Nozzle caliber	300 mm×300 mm square
Channel length	800 mm
Jet direction	horizontal
Jet velocity	0–17 m/s
Air source	axial flow fan (0.75 Kw)
Speed control	inverter control of the fan RPM
Velocity distribution	±1.5%
Turbulence	0.5%

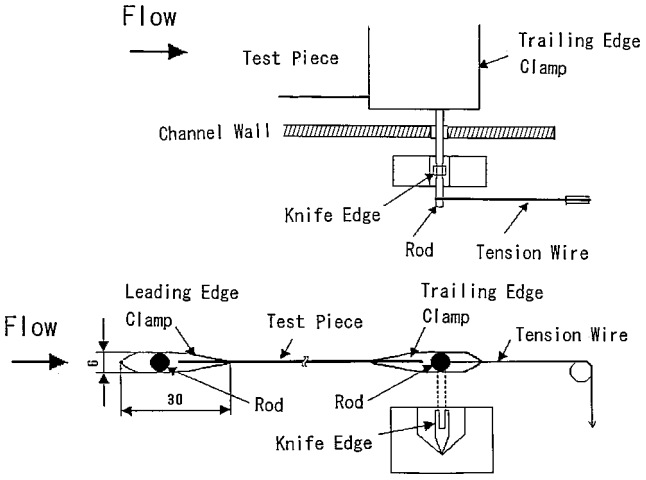

Fig. 14 Edge fixing device for the test piece

Table 3 Characteristic figures of the papers for test

Paper	Copy Paper	Simili Paper	Tracing Paper
Thickness t_s (mm)	0.098	0.082	0.062
Density ρ_s (kg/m^3)	679	808	989
Young's modulus E_s (Gpa)	1.24	2.07	2.48
Length L_s (mm)		275–775	
Width b_s (mm)		30,60,90	

perimental data somewhat, but the degree of improvement was not as much as expected. In addition to the variable properties of the papers, the gravitational effect due to the horizontal positioning of the sheets for testing, the three-dimensional effect due to the limited width, and the limited relative size of the wind tunnel, are to be pointed out as the additive major causes of the data scattering.

7.2 Results of Flutter Tests in the Wind Tunnel. The results thus obtained are plotted with respect to the flutter fluid force/tension ratio σ^* in Fig. 15 and with respect to the reduced frequency f_R in Fig. 16, against the tension-stiffness ratio τ^*. Because of the limited capacity of the experimental setup, the data are limited to a relatively narrow range of the medium τ^* region.

The nature of the frequency change near the onset of flutter occurrence are varied: in some conditions the frequency remains nearly the same; in other conditions it changes at the same time as the flutter occurrence. Here the frequency immediately after the flutter occurrence is employed as the experimental flutter frequency.

The dotted lines in Figs. 15 and 16 are the analytical results obtained in the preceding section. Compared with these predicted lines, the experimental data are seen to be very scattered. The zone of scattered data, however, includes the predicted lines. It may be said that the prediction is rather reasonable for the region surveyed in the medium τ^* region, $9\times10^2<\tau^*<4\times10^4$.

For simplicity, the data points in Figs. 15 and 16 are identified by their particular mass ratios. Each symbol represents data falling within a certain range. The data are seen in a mixed fashion within the scatter. This suggests that the effect of mass ratios is negligible for the range tested within the experimental accuracy. It agrees with the tendency predicted in Section 6.

It was attempted to maintain two-dimensional nature of the experiment, but the outbreak of flutter interfered. It was observed that the flutter speed tends to be somewhat higher for wider sheets. This tendency is thought to be similar to that of a sheet with the trailing edge free [2]. However, it was difficult to show a consistent tendency, given the few widths tested and the wide scatter of the experimental data.

The horizontal position of the web tended to droop because of gravity. When the web was pulled tightly to straighten the web, the flutter speed tended to be much higher. So, the tests were started initially with a rather slack condition with a constant tension. The tightness was difficult to control and is considered to have added to the data scatter.

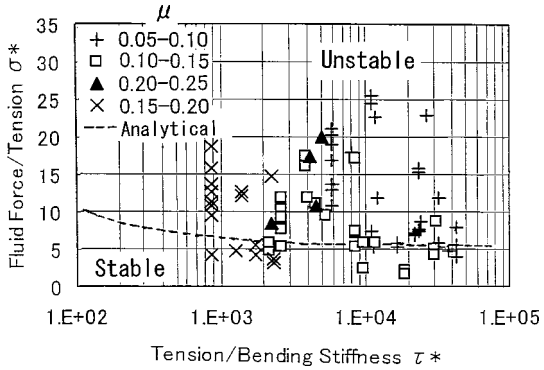

Fig. 15 Effect of tension parameter on the flutter limits

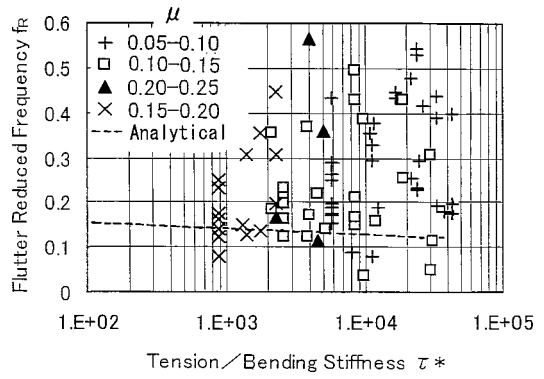

Fig. 16 Effect of tension parameter on the flutter reduced frequencies

8 Conclusion

Flutter limits of webs with a simplified basic configuration were analytically predicted and the effects of the governing parameters on the limits and behaviors were investigated. From the results a general understanding of the phenomena are gained. Three characteristic regions exist depending on the tension parameter τ^*.

The experiments suggested some degree of validity of the analytical results, though within a limited range of the medium τ^* region, $9\times10^2<\tau^*<4\times10^4$.

To improve the experimental accuracy, the authors are now constructing a vertical wind tunnel for the flutter tests.

Nomenclature

b_s = web width (m)
c_{fo} = surface fluid-friction coefficient
E_s = Young' modulus of web material (Pa)
F_D = external force on the web
f_B = sectional shear force
f_R = reduced frequency, Eq. (18)
g = a general function of both x and t
G = a general function of x only after a variable separation of a function g
I_S = sectional area moment
i = order of vibration (Appendix)
j = order of vibration (Appendix)
L_s = length of a web (m)
M = sectional bending moment
N = number of segments in approximating a web
R = ratio of resonance frequencies of a beam bending vibration and a tensioned string vibration (Appendix)
T = tension (N)
t = time (s)
t_s = web thickness (m)
U_a = velocity of the uniform flow (m/s)
v = induced velocity perpendicular to the main flow (m/s)
x = coordinate in the main flow direction (m)
y = coordinate perpendicular to the x coordinate (m)
y_s = sheet displacement (m)
β = relative stiffness
Δp = pressure difference across the sheet plane (Pa)
Γ = vortex strength
Γ_W = wake vortex strength discharged from the trailing edge
Θ = sheet surface inclination
ρ_a = fluid density (kg/m^3)
ρ_s = density of the web material (kg/m^3)
σ^* = flutter fluid force/tension ratio, Eq. (17)

τ^* = tension/stiffness ratio, Eq. (16)
μ = mass ratio, Eq. (19)
ω = angular frequency (rad/s)
$\omega^B j$ = angular frequency of the jth mode of a beam bending vibration (Appendix)
$\omega^T i$ = angular frequency of the ith mode of a tensioned string vibration (Appendix)

Appendix

Occurrence of Ripples of Higher-Order Mode in the Web Flutters. As described in the main body of the present paper, for around τ^* of 1×10^6, ripples in the web configurations become significant. The Appendix discusses the phenomenon.

Essentially, several kinds of forces act on the web in an inseparable manner, resulting in flutter. Here, for the simplicity, it is assumed that two types of resonance modes occur independently, i.e., a tension-governed string mode for a string with both ends clamped, and an elasticity-governed beam-bending mode for a beam with both ends clamped. The latter is named ''beam-bending mode'' and the former ''tensioned-string mode.''

The angular frequency of the tth resonance mode of the tensioned-string mode is given by the following equation (Burton [6]):

$$\omega_i^T = i(\pi/L_s)\sqrt{T/\rho_s t_s} \quad \text{for } i=1,2,3\ldots. \tag{A1}$$

The angular frequency of the jth resonance mode of the beam-bending mode is given by the following equation (Burton [6]):

$$\omega_j^B = j^2(\pi/L_s)^2\sqrt{(E_s I_s/\rho_s t_s)} \quad \text{for } j=1,2,3\ldots. \tag{A2}$$

A ratio of the above both is defined as R as follows:

$$R=\omega_i^T/\omega_j^B \tag{A3}$$

From Eqs. (*A*1), (*A*2), and (*A*3)

$$R=(i/j^2)\sqrt{(TL_s^2/E_s I_s)}/\pi. \tag{A4}$$

From the definition of τ^* (Eq. (16)),

$$R=(i/j^2)\sqrt{\tau^*}/\pi. \tag{A5}$$

For the condition of the same frequency for the two modes ($R=1$),

$$j=\sqrt[4]{\tau^*}\sqrt{(i/\pi)}. \tag{A6}$$

From the above, relations among i and j are as given in the following.

τ^*	10^4	10^5	10^6	10^7
$i=1$	$j=5.6$	10.0	17.8	31.7
2	8.0	14.1	25.2	44.8
3	9.8	17.3	30.9	54.9

As seen from the table, for high values of τ^*, lower modes of tensioned-string vibration and higher modes of beam-bending vibration tend to have frequencies close to each other, resulting in the appearance of ripples by the latter mode.

On the other hand, for low values of τ^*, the differences of the resonance frequencies between the tensioned string vibrations and the beam bending vibrations are small. Therefore ripples do not appear. For example, the condition for the third mode for both ($i=j=3$) is

$$\tau^*=100.$$

The condition is in the low τ^* region. Near this condition, both vibrations will merge easily.

References

[1] Yamaguchi, N., Yokota, K., and Tsujimoto, Y., 2000, ''Flutter Limits and Behaviors of a Flexible Thin Sheet in High Speed Flow—I: Analytical Method for Prediction of the Sheet Behavior,'' ASME J. Fluids Eng., **122**, pp. 65–73.
[2] Yamaguchi, N., Sekiguchi, T., Yokota, K., and Tsujimoto, Y., 2000, ''Flutter Limits and Behaviors of a Flexible Thin Sheet in High Speed Flow—II: Experimental Results and Predicted Behaviors for Low Mass Ratios,'' ASME J. Fluids Eng., **122**, pp. 74–83.
[3] Kaneko, S., Tanaka, S., and Watanabe, T., 2001, ''Leakage Flow Induced Flutter of Highly Flexible Structures,'' *Flow Induced Vibration*, Ziada and Staubli, eds., Balkema, Rotterdam, pp. 811–818.
[4] Chang, Y. B., and Moretti, P. M., 2001, ''Flow Induced Vibration of Free Edges of Thin Films,'' *Flow Induced Vibration*, Ziada and Staubli, eds., Balkema, Rotterdam, pp. 801–810.
[5] Ito, K., Yamaguchi, N., and Ogata, M., 2000, ''Experimental Flutter Limits of Webs of Flexible Media,'' JSME Int. J., Ser. I, (**00-1**), pp. 943–944.
[6] Burton, R., 1958, *Vibration and Impact*, Dover, New York, p. 224, 242.

X. Guan
Graduate Student

R. Pitchumani[1]
Mem. ASME
e-mail: r.pitchumani@uconn.edu

Department of Mechanical Engineering,
University of Connecticut,
Storrs, CT 06269-3139

Viscous Fingering in a Hele-Shaw Cell With Finite Viscosity Ratio and Interfacial Tension

A volume tracking method was developed to simulate time-dependent unstable viscous fingering in a Hele-Shaw cell. The effect of finite viscosity ratio μ_r between displacing and displaced fluids and their interfacial tension σ on finger morphology is investigated. It is shown that there exist four distinct finger patterns, depending upon the viscosity ratio, μ_r, and Ca', the modified capillary number for constant flow rate, or $\Delta P \cdot W/\sigma$, for constant driving pressure difference. Morphology diagrams are developed to identify the ranges of the dimensionless parameters corresponding to the various finger patterns. The simulation results are validated with experiments. [DOI: 10.1115/1.1524589]

1 Introduction

Viscous fingering in a Hele-Shaw cell, [1], originating from industrial oil recovery, was first studied by Saffman and Taylor [2], and the complexity of fundamentals behind the phenomenon itself has since attracted much attention. A Hele-Shaw cell consists of two parallel plates with a narrow spacing; when a less viscous fluid is driven to displace a more viscous one in the cell, an initially flat interface between the two fluids evolves into a so-called *viscous fingering* pattern. The flow is governed by the Hele-Shaw equation, [3], which, if both fluids are Newtonian, is written as

$$\mathbf{u}_i = -\frac{b^2}{12\mu_i}\nabla P_i \tag{1}$$

where i refers to each of the two fluids, $\mathbf{u}_i$ is velocity averaged over the cell thickness b, μ_i dynamic viscosity, and P_i pressure. Usually, incompressibility is assumed ($\nabla \cdot \mathbf{u}_i = 0$), which reduces Eq. (1) to a Laplacian equation for the pressure in both fluids

$$\nabla^2 P_i = 0. \tag{2}$$

Across the interface, the pressure is continuous if the two fluids are miscible; otherwise, a pressure jump condition should be met

$$P_1 - P_2 = \sigma \cdot \kappa \tag{3}$$

where σ is interfacial tension and κ the curvature of the interface projected onto the Hele-Shaw cell plane.

In most studies so far, the viscosity of the displacing fluid is neglected, which renders a uniform pressure distribution in its side. The interface then becomes part of boundaries enclosing the more viscous displaced fluid. As indicated by the experiments of Park and Homsy [4], Maxworthy [5], and Kopf-Sill and Homsy [6], in the absence of the displacing fluid viscosity the finger shape and morphology could be determined by a single parameter, the *modified capillary number*

$$Ca' = \frac{U\mu}{\sigma}\left(\frac{W}{b}\right)^2, \tag{4}$$

where U is the velocity of the finger, μ the viscosity of the displaced fluid, σ interfacial tension, W the half Hele-Shaw cell width, b the cell thickness. For low Ca', a single, long, steady finger called a *Saffman-Taylor finger* was obtained; for large Ca', unstable, branched fingers were reported, [4–6]. McLean and Saffman [7] solved for the steady finger width analytically as a function of Ca', but the mechanism, by which the finger asymptotically approaches half-cell width, was resolved later, [8,9].

Time-dependent direct simulations have also been developed to investigate both stable and unstable fingers. One approach is the *random-walker* method, of which good examples are given by Kadanoff [10], Liang [11], Tang [12], and by Arneodo and coworkers [13]. In this purely stochastic method, the solution of the Laplacian pressure equation, Eq. (2), is obtained by a probabilistic scheme. Particles released from one end of the cell, walk randomly until they encounter and stick to a cluster forming from the other end, which eventually grows into a finger-like pattern. Although the behavior of a random-walker is precisely formulated by the discretized Laplacian pressure equation, it is restricted to the case of vanishing displacing fluid viscosity. The approach can not be used to simulate viscous fingering under finite viscosity ratio between the two fluids.

Numerical solutions of the Eqs. (1)–(3) governing the viscous fingering phenomenon have been reported using boundary integral method by DeGregoria and Schwartz [14,15], Hou et al. [16,17], and Nie and Tian [18], the vortex-in-cell method by Tryggvason and Aref [19], and Meiburg and Homsy [20], and the volume tracking method by Whitaker [21]. In a particular approach of the boundary integral method, called the conformal mapping method (for example, [22]), the moving interface is transformed into a fixed boundary in a complex domain, and the interface velocities are derived from the complex boundary velocities. In the vortex-in-cell method, a vorticity form of the Hele-Shaw equation is used to obtain the interface as the only location that is not irrotational, and the velocities are reconstructed from the vorticities. Good agreement with McLean and Saffman's analytical solution, [7], for stable fingers was reported by using either of these two methods with zero displacing fluid viscosity, and the authors also extended the use of the method to selected unstable fingering cases.

Both of the above-mentioned methods feature a Lagrangian approach to tracking the interface. The volume tracking method, [21], on the other hand, employs an Eulerian formulation. Here "volume" refers to a value F assigned to each cell that forms a fixed mesh over the whole computational domain. Specifically, this value F represents the fraction of a cell that is occupied by the displacing fluid. A time-dependent advection equation, given below, is solved to obtain F throughout the computational domain, from which the interface is constructed through the cells having $0 < F < 1$.

$$\frac{\partial F}{\partial t} + \frac{\partial (uF)}{\partial x} + \frac{\partial (vF)}{\partial y} = 0 \tag{5}$$

[1]To whom correspondence should be addressed.

Contributed by the Fluids Engineering Division for publication in the JOURNAL OF FLUIDS ENGINEERING. Manuscript received by the Fluids Engineering Division February 1, 2002, revised manuscript received August 15, 2002. Associate Editor: A. K. Prasad.

The velocities, u and v, in the above equation and the pressure in each cell could be directly solved using a finite difference method without resorting to special transformations. In Whitaker's work, [21], a SLIC (simple line interface calculation) algorithm was implemented to treat the interface in each cell as lines aligned with one of the logical mesh coordinates. However, using the SLIC method, the Saffman and Taylor finger was reproduced only qualitatively, and furthermore, no significant development was reported in regard to simulation of unstable fingers.

It is evident from the foregoing discussion that numerical simulation of viscous fingering with finite viscosity ratio and finite interfacial tension between the two fluids has been the subject of relatively little attention, and it is the intent of the present study to fill this void. Specifically, the study seeks to systematically explore the influence of the viscosity ratio μ_r (defined as the ratio of displaced fluid viscosity to that of displacing one) and the interfacial tension (expressed in a suitably nondimensionalized form) on finger morphologies. A numerical method based on the volume tracking formulation coupled with a piecewise linear interface calculation (PLIC) scheme is used to simulate the evolution of the fingers with time. With the focus on Newtonian fluid systems, the results of the simulations are used to identify, for the first time, ranges of the dimensionless parameters associated with the various finger morphologies.

The paper is organized as follows: Section 2 presents a description of the numerical simulation technique based on the volume tracking method with modifications to accurately reconstruct the complex finger interfaces. Section 3 provides validation of the numerical method by considering available data in the literature, and further, details the results of the study on simulation of viscous fingering for finite viscosity ratio and interfacial tension.

2 Numerical Simulation Method

The numerical scheme used for the simulation of the viscous fingering phenomenon is the volume tracking method with modifications tailored for a reliable reconstruction of the complex finger morphologies. The essence of the volume tracking method is to design a scheme that will accurately estimate interface information, such as orientation, position, and curvature, solely based on the volume of fluid F data in each cell. The orientation and position are important to evaluation of fluid advection along the interface; the curvature is needed to calculate the local interfacial tension that could strongly affect the evolution of the interface. The volume tracking method considered here is based on the concept of piecewise linear interface calculation (PLIC) scheme introduced by Youngs [23]. In the PLIC scheme, a line defined by a slope and intercepts with the cell faces represents the local interface orientation and position. Many variants of PLIC schemes have been developed with different techniques of evaluating the slope, intercepts, and curvature, and for an elaborate description of the algorithm, the reader is referred to the work of Rider and Kothe [24].

In the scheme discussed in this section, the slope is the first information derived from the volume of fluid data, which is then used to locate the intercepts, or *boundary fractions* f_w, f_e, f_s, and f_n on the west, east, south, and north faces of the cell, respectively. The boundary fractions are, in turn, used for computing advection fluxes. The computing of the curvature, and hence the interfacial tension, is also facilitated by the slope information. Within this basic framework, modifications are introduced to account for situations where the interface experiences various abrupt changes within 3×3 grid stencils. Therefore, the scheme is rendered suitable for simulating unstable viscous fingering within the framework of the volume tracking method. The following subsections outline the various calculations involved in the numerical simulation algorithm.

2.1 Slope and Boundary Fraction Calculation. The interface orientation, or slope, can generally be obtained by finite differencing of local volume of fluid. Specifically, considering a 3×3 stencil around the cell (i, j) of interest as shown in Fig. 1(a), the volumes of fluid in each of the three columns can be summed up to give three dimensionless volume heights,

$$H_h(k,j)=\sum_{l=j-1}^{l=j+1} F(k,l), \quad k=i-1,i,i+1,$$

from which the interface slope of the cell (i, j) may be approximated, assuming equal mesh spacing in the x and y-directions, as

$$S_h(i,j)=\frac{H_h(i+1,j)-H_h(i-1,j)}{2}.$$

However, if the stencil in Fig. 1(a) were rotated by 90 deg, which corresponds to a vertical interface of the cell (i, j), the above finite differencing based on columns yields a poor estimate of the slope. It is more appropriate in this case to define three more volume heights as

$$H_v(i,l)=\sum_{k=i-1}^{k=i+1} F(k,l), \quad l=j-1,j,j+1,$$

which are simply summations of volumes of fluid in each of the three rows, and calculate an interface slope of the cell (i, j) viewed from the rotated coordinates as

$$S_v(i,j)=\frac{H_v(i,j+1)-H_v(i,j-1)}{2}.$$

The inverse of $S_v(i,j)$ is the interface slope viewed from the original coordinates, and its is a much better approximation than $S_h(i,j)$. Since the interface orientation is generally unknown a priori, both the horizontal volume height, $H_h(i,j)$, hence the horizontal slope $S_h(i,j)$, and the vertical volume height, $H_v(i,j)$, hence the vertical slope $S_v(i,j)$, are computed. Comparison of the absolute values of S_h and S_v determines if the interface is "horizontal" or "vertical," and, in turn, if S_h or S_v should be used to approximate the interface slope S. Specifically, if $|S_h|<|S_v|$, the interface is "horizontal," and S_h is a more accurate estimation of slope than S_v, thus $S=S_h$; conversely, if $|S_h|>|S_v|$, the interface is "vertical," and $S=S_v$ instead.

Note that even though only one of these two slopes is chosen to represent the real interface, the other is still important in that its sign reveals which side of the interface the displacing fluid resides. For example, in Fig. 1(a), the interface in the cell (i, j) is "horizontal," owing to the fact that $|S_h(i,j)|<|S_v(i,j)|$. Further, since $S_v(i,j)<0$, the nonzero volumes of fluid are discerned to be in the bottom area of the stencil. On the other hand, if it were a "vertical" interface in the cell (i, j), then the sign of $S_h(i,j)$ would have been used to determine whether the volumes of fluid were in the left or in the right part of the stencil. The information on which side of the interface contains the displacing (or equivalently, the displaced) fluid volume will assist in finding the cell boundary fractions, as will be explained in the following description. For the discussion below, it is convenient to define the slope that gives such information as the *auxiliary slope*, and the one that represents the real slope as the *principal slope*.

The boundary fractions may be derived from the volumes of fluid in the cells constituting the stencil. For the cell (i, j) with a "horizontal" interface illustrated in Fig. 1(a), the west and the east boundary fractions, f_w and f_e, can be obtained directly from the horizontal volume heights in the stencil. First, two boundary heights, Y_w and Y_e, which are measured on the west and the east cell faces, respectively, are defined as follows:

$$Y_w=\frac{H_h(i-1,j)+H_h(i,j)}{2}, \quad Y_e=\frac{H_h(i,j)+H_h(i+1,j)}{2}.$$

Approximating the interface in the cell (i, j) by a straight line connecting these two boundary heights from the west cell face to the east cell face, they can be readily related to f_w and f_e as

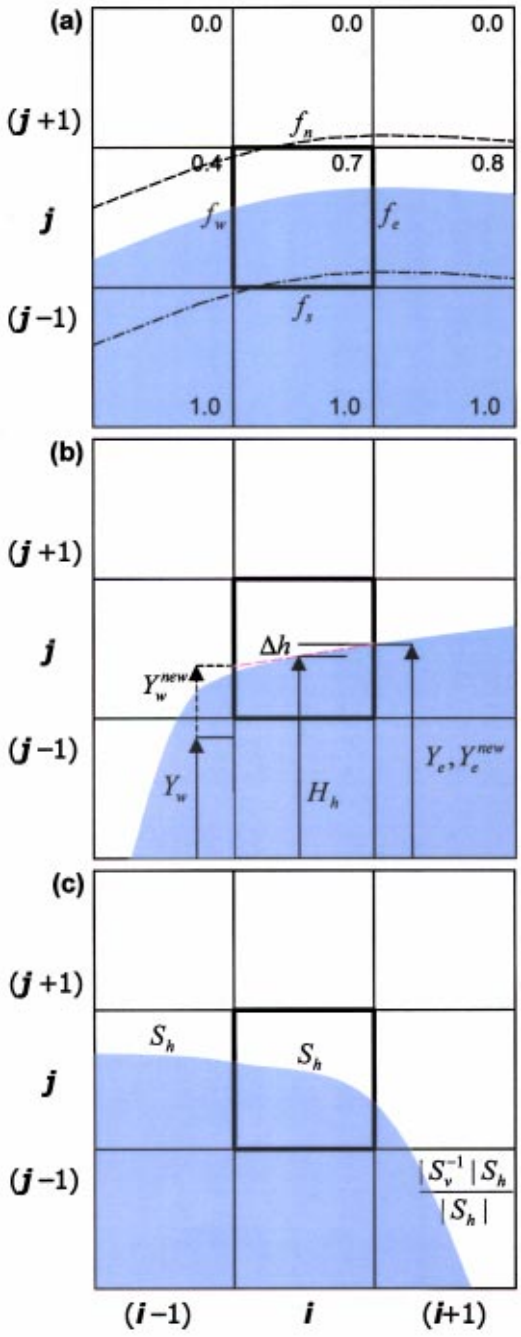

Fig. 1 (*a*) Calculation of boundary fractions and interface slope based on volume of fill fractions in a 3×3 stencil around each cell. Numerics at the upper-right corner of each cell denote the volume fractions of the displacing fluid (depicted by the shaded region). (*b*) Schematic of the "shooting" method to correct estimations on boundary fractions in situations where interface orientation has an abrupt change within a 3×3 stencil. (*c*) Choice of the appropriate neighboring interface cells for obtaining a good approximation of curvature of center cell in a 3×3 stencil.

$$f_w = \min[1, \max(0, Y_w - 1)], \quad f_e = \min[1, \max(0, Y_e - 1)]. \tag{6}$$

Note that the boundary fractions are explicitly limited in the range of 0 to 1, so that physically correct values will be obtained in all cases including those where the interface may not intersect with the west or the east cell boundary, as exemplified by the dashed and the chain-dashed lines in Fig. 1(*a*).

The calculation of the boundary fractions on the north and south faces of the cell is as follows. If the straight line described above does not intersect with either the north or the south face of the cell (i, j), then the boundary fraction of one of the faces is 0, and the other is 1. The assignment of the appropriate value depends on the sign of the auxiliary slope, which, in the case of the illustration in Fig. 1(*a*) is $S_v(i,j)$: If $S_v(i,j)$ is negative, the south boundary fraction, $f_s = 1$, and the north boundary fraction, $f_n = 0$; if $S_v(i,j)$ is positive, then their values are interchanged.

If the straight line connecting the boundary heights Y_w and Y_e runs through either the north or the south face of the cell (i, j), as indicated by the dashed and the chain-dashed lines in Fig. 1(*a*), the values of the north and the south boundary fractions rely on three factors: (1) whether the north or the south face of the cell (i, j) is intersected by the straight line, (2) the sign of the auxiliary slope, and (3) which of the boundary heights, $Y_w(i,j)$ or $Y_e(i,j)$, is larger. For instance, consider the situation where the interface intersects the north cell face as shown by the dashed line in Fig. 1(*a*). Since the sign of the auxiliary slope, $S_v(i,j)$, is negative, which corresponds to the displacing fluid being below the interface, the south boundary fraction of the cell (i, j), $f_s = 1$. Its opposite side, the north face of the cell (i, j), has a fractional boundary value between 0 and 1. For the interface configuration shown in Fig. 1(*a*), since $Y_w(i,j) < Y_e(i,j)$, the fraction of the north face to the right of the intersection with the straight line connecting the boundary heights Y_w and Y_e is taken as the north boundary fraction. If $Y_w(i,j) > Y_e(i,j)$, and factors (1) and (2) do not change, the appropriate choice of the north boundary fraction would be the fraction of the north cell face to the left of the intersection with the straight line. The north boundary fraction, f_n, will equal 0 or 1 if the interface runs through the south cell face, as denoted by the chain-dashed line in Fig. 1(*a*), and accordingly the south boundary fractions will lie in the range $0 < f_s < 1$. If the sign of the auxiliary slope is negative, i.e., the displacing fluid is below the interface, the north boundary fraction is 0; otherwise, it is 1. On the south face, the fraction to the right of the intersection with the straight line is taken as an estimate of the south boundary fraction if $Y_w(i,j) < Y_e(i,j)$; otherwise, the left fraction is used.

The value of the fractional portions are computed as the geometric intercepts with the north or the south cell face by the straight line that connects the two boundary heights, Y_w and Y_e, which, as mentioned earlier, are measured on the west and the east cell faces, respectively. With all the considerations discussed above, a generalized formulation for the north and the south boundary fractions, f_n and f_s, may be written as follows:

$$f_s = \max\left[A_1, A_2 \frac{-S_v(i,j)}{|S_v(i,j)|}\right]; \quad f_n = \max\left[A_1, A_2 \frac{S_v(i,j)}{|S_v(i,j)|}\right] \tag{7}$$

where

$$A_1 = \frac{\max(0, Y_1 - 2)}{|Y_1 - 2| + |Y_2 - 2|}; \quad A_2 = \frac{|Y_1 - 1|}{|\min(0, Y_1 - 1)| + |Y_2 - 1|}$$

$$Y_1 = \max(Y_w, Y_e); \quad Y_2 = \min(Y_w, Y_e).$$

Note that $S_v(i,j)$ is used above as the auxiliary slope, whose sign, rather than magnitude, is relevant for the calculating of the boundary fractions. The set of expressions above holds for the situation where the interface is horizontal as depicted in Fig. 1(*a*). A similar set of relationships for a vertical interface could be readily obtained by defining a pair of vertical volume heights, Y_s and Y_n, in place of Y_w and Y_e, respectively, and using $S_h(i,j)$ as the auxiliary slope. In this case, f_s and f_n are calculated using expressions similar to those in Eq. (6), while the equivalent of Eq. (7) determines f_w and f_e. In the simulations, the algorithm first determines the interface orientation, and then chooses corresponding set of

formulation to calculate all four boundary fractions for each cell. In the case of Fig. 1(*a*), the boundary fractions as computed are $f_w=0.51$, $f_e=0.75$, $f_s=1.00$, and $f_n=0.00$.

Following the foregoing procedure, each cell is assigned a set of f_w, f_e, f_s, and f_n values. However, these values do not necessarily match those calculated by the neighboring cells for the same shared boundaries. Since this is unphysical, and a boundary must have a unique boundary fraction, the value corresponding to the cell having a greater volume of fluid, F (with respect to its neighbor), is taken as the boundary fraction on their common face. This rule was generally found in the present study to yield a better estimate of boundary fractions for those cells with an interface passing through two perpendicular cell faces.

The algorithm developed so far performs well for gradual interface orientation changes. However, in unstable viscous fingers, the orientation may exhibit abrupt changes locally within 3×3 stencil, as exemplified in Fig. 1(*b*). Such a situation can be discerned by comparing the sign of $|S_h|-|S_v|$ for all the interface cells within the stencil—if the sign changes, then the orientation changes, either from horizontal to vertical, or vice-verse. In such cases, since the slopes and boundary fractions computed in the way described above may not be sufficiently accurate, a ''shooting'' correction method, as illustrated in Fig. 1(*b*), was implemented. In this method, the smaller of $|Y_w-H_h(i,j)|$ and $|Y_e-H_h(i,j)|$ is used as the amount of correction Δh to obtain a new set of Y_w^{new} and Y_e^{new} as: $Y_w^{\text{new}}=H_h(i,j)\pm\Delta h$, and $Y_e^{\text{new}}=H_h(i,j)\mp\Delta h$. The basic idea of ''shooting'' is that if the slope on the side with less orientation change (such as the right face of the cell (i, j) in Fig. 1(*b*)) is maintained towards the opposite side of the cell, the intercepts and boundary fractions calculated as such would be much closer to their real values. After this correction, the above formulation is used to obtain better estimations of the boundary fractions and the slopes.

2.2 Interface Curvature Calculation. One of the methods for curvature calculation reported in the literature is Chorin's iterative algorithm, [25], which is based on the philosophy of trying to find a circle that will cut out exact values of F for the cells in the 3×3 stencil. In the present study, since the slope information is known, as developed in Section 2.1, the curvature was determined directly, without invoking an iterative calculation. The curvature may be related to the slope as

$$\kappa=\frac{-d^2y/dx^2}{[1+(dy/dx)^2]^{3/2}} \quad \text{(for a horizontal interface)}, \tag{8a}$$

$$=\frac{-d^2x/dy^2}{[1+(dx/dy)^2]^{3/2}} \quad \text{(for a vertical interface)}. \tag{8b}$$

Such an algorithm allows for a relatively straightforward implementation, except that care must be taken in evaluating derivatives of the slopes in the above equations. The method is illustrated by the case shown in Fig. 1(*c*), where the interface runs through cells $(i-1,j)$ and (i, j) horizontally, then changes its orientation to the vertical while passing through cells $(i+1,j)$ and $(i+1,j-1)$. The curvature of the interface cell (i, j) is sought by discretizing the first of the above analytical expressions for the curvature, since the interface in the cell (i, j) is horizontal. The derivative of slope of the cell (i, j) is seen to be either

$$S(i,j)'=\frac{S(i+1,j)-S(i-1,j)}{2\Delta x}, \quad \text{or}$$

$$S(i,j)'=\frac{S(i+1,j-1)-S(i-1,j)}{2\Delta x},$$

i.e., the two interface cells in column $i+1$ could be used to evaluate $S(i,j)'$. The choice of the appropriate expression is based on the following consideration: As explained in Section 2.1, slopes calculated in those cells with an interface line cutting out corners may not be as accurate as in the other cases. Therefore, in Fig. 1(*c*), the interface cell $(i+1,j-1)$ is chosen in place of $(i+1,j)$, and the latter of the above expressions is used to calculate $S(i,j)'$. The general implementation of such algorithm is that the volumes of the cells are compared first, and if $|F(i+1,j)-0.5|<|F(i+1,j-1)-0.5|$, the former expression for $S(i,j)'$ is used; otherwise, the latter is chosen. Note that the derivative is evaluated by finite differencing of the *principal* slopes, so that in the above expressions, $S(i-1,j)$ and $S(i,j)$ are the horizontal slopes of the cell $(i-1,j)$ and (i, j), while $S(i+1,j)$ and $S(i+1,j-1)$ are the inverse of the vertical slopes of these two cells but taking the sign of their horizontal slopes.

2.3 Boundary Flux Calculation. In addition to a reliable interface reconstruction, discussed in the foregoing subsections, an accurate update of the volume of fluid fractions is equally important for an effective simulation of the flow phenomenon. The principal issue is the evaluation of advection terms in Eq. (5) once the velocity field is known. In a finite difference implementation, it is equivalent to evaluating fluxes of F over the cell faces during a time-step Δt. Two different methodologies to computing the boundary flux are reported in the literature, [24].

- *Algebraic Method*: The boundary fluxes are expressed as upwind or downwind contributions depending upon the interface orientation. If the flow is parallel to the interface, an upwind flux is used; otherwise, a downwind flux is adopted in general. A correction is added to prevent more volume than current F available in the cell, or more void than current $(1-F)$ from being fluxed out. The volume of fluid (VOF) method by Hirt and Nichols [26] features this algebraic approximation.
- *Geometric Method*: The boundary fractions f_w, f_e, f_s, and f_n are used in the calculation of the boundary fluxes in Eq. (5). In a simpler treatment, called the operator-splitting method, fluxes are swept in one direction at a time. An unsplit algorithm will consider the corner regions of the cell in much more detail, and leads to a truly multidimensional flux calculation, albeit at a greater computational investment.

A geometric method was implemented in the present study. The fluxes are approximated by the boundary fractions obtained in Section 2.1 in an operator splitting fashion, and a correction based on bounding the maximum and the minimum fluid volume fraction in a cell is employed. The operator splitting scheme was chosen, because it is accurate enough and computationally faster on the fine mesh used in the simulations. The net summation, ΔF, of the fluxes across the four faces of each cell, corrected to ensure physical consistency (i.e., $0\leqslant F\leqslant1$), is used to update the volume of fill fraction. An adjustment scheme is designed to redistribute any minute surpluses ($F_{\text{old}}+\Delta F-1.0$) or deficits ($F_{\text{old}}+\Delta F$) into the *outbound* boundary fluxes. If a cell has more than one outbound flux, then the redistributions are apportioned with respect to their velocities. The readjustment is carried out iteratively until all cells have volume of fluid fractions within the range of 0 to 1.

2.4 Velocity and Pressure Calculations. For interior areas of both fluids in a Hele-Shaw cell, a discretization of Eq. (2) yields a five-point Laplacian finite difference formula

$$P_{i-1,j}+P_{i+1,j}+P_{i,j-1}+P_{i,j+1}-4P_{i,j}=0. \tag{9}$$

For interface cells, a similar five-point formula can be obtained by utilizing Eq. (1) for the velocity. An effective viscosity for interface cells may be defined as

$$\mu^*=F\mu_1+(1-F)\mu_2, \tag{10}$$

where μ_1 is the viscosity of displacing fluid and μ_2 the viscosity of displaced fluid. Without invoking interfacial tension for the time being, a pressure driven flow is given by Hele-Shaw equation as

$$v_w=-\frac{b^2}{12\mu^*_{(i-1/2,j)}}\frac{P_{i-1,j}-P_{i,j}}{\Delta x} \tag{11a}$$

$$u_e = -\frac{b^2}{12\mu^*_{(i+1/2,j)}}\frac{P_{i,j}-P_{i+1,j}}{\Delta x} \tag{11b}$$

$$u_s = -\frac{b^2}{12\mu^*_{(i,j-1/2)}}\frac{P_{i,j-1}-P_{i,j}}{\Delta y} \tag{11c}$$

$$u_s = -\frac{b^2}{12\mu^*_{(i,j+1/2)}}\frac{P_{i,j}-P_{i,j+1}}{\Delta y} \tag{11d}$$

where u_w, u_e, u_s, and u_n are velocities at four boundaries of a cell, $\mu^*_{(i-1/2,j)}$, $\mu^*_{(i+1/2,j)}$, $\mu^*_{(i,j-1/2)}$, and $\mu^*_{(i,j+1/2)}$ are effective viscosities at four boundaries obtained by averaging the viscosities of the two neighboring cells sharing the common boundary face, and Δx and Δy are grid sizes. Since the fluids are incompressible, volume conservation for a cell at any time is given by

$$u_w\Delta y + u_s\Delta x = u_e\Delta y + u_n\Delta x. \tag{12}$$

Substituting Eqs. (11*a*)–(11*d*) into (12) yields a pressure difference formula for interface cells in the form of

$$a_wP_{i-1,j} + a_eP_{i+1,j} + a_sP_{i,j-1} + a_nP_{i,j+1} - P_{i,j} = 0. \tag{13}$$

Accounting for interfacial tension, using Eq. (3), a more general formulation of pressure results as

$$a_wP_{i-1,j} + a_eP_{i+1,j} + a_sP_{i,j-1} + a_nP_{i,j+1} - P_{i,j} = \sigma\sum\ \Delta\kappa_i \tag{14}$$

where

$$\sum\ \Delta\kappa_i = a_w(\kappa_{i-1,j}-\kappa_{i,j}) + a_e(\kappa_{i+1,j}-\kappa_{i,j}) + a_s(\kappa_{i,j-1}-\kappa_{i,j}) + a_n(\kappa_{i,j+1}-\kappa_{i,j}).$$

Note that for the noninterfacial cells, their curvatures are simply zeroes, and the formulation defaults to that in Eq. (13). The governing equations are subject to appropriate boundary conditions at the four walls of a rectangular Hele-Shaw cell, as discussed in the later sections.

The system of linear equations for pressure is solved iteratively using the *preconditioned biconjugate gradient* (PBCG) method. In order to handle cases in which the PBCG can not converge at a certain time-step, the lower-upper triangular matrix (LU) decomposition method was used as a backup solver at that time-step. The convergence criterion was based on a residual, Δ, defined from Eq. (12) as

$$\Delta = \frac{u_w + u_s - u_e - u_n}{\frac{1}{2}(|u_w| + |u_s| + |u_e| + |u_n|)}.$$

The iterative solution procedure was continued until Δ was less than 0.001 for all the cells in the computational domain. The time-step Δt for solving the advection Eq. (5) was evaluated as

$$\Delta t = \frac{1}{4}\frac{h}{|U|} \tag{15}$$

which satisfied the Courant-Friedrichs-Lewy condition $|U|\Delta t/h \leq 1$, where $|U|$ is the maximum speed of the flow at the interface, and $h = \Delta x = \Delta y$ for a square mesh used in the present study.

Viscous fingering is inherently an instability phenomenon, the simulation of which requires a certain amount of randomness to be introduced in the computation. The randomness serves to break down the symmetry in the flow pattern and to introduce unstable characteristics such as bifurcation (tip-splitting) at the finger tip. Further, the instability is sought to be introduced in the computations based on the physics of the problem rather than as purely random perturbations. With the foregoing objectives, the following simulation procedure was implemented. At each time-step during the simulation, all interface cells are assigned their normal velocities calculated from previous time-step, and the maximum velocity among them is found. For each interface cell, its normal velocity is scaled with respect to the maximum velocity to obtain the probability assigned to the interface cell. A random number between 0 to 1 is generated for each interface cell, and compared with its associated probability to determine if the interface cell is to be selected for flow advancement. The viscosities of those selected cells are changed to viscosity of invading fluid (regardless of the volume of fill fractions, F, associated with the cells), and a new pressure field is calculated for next time-step. The velocities computed based on the pressure field are used to advance the interface.

It is evident that the method uses a deterministic velocity field to update the interface, thereby ensuring mass conservation. By way of contrast, approaches based on randomization of the interface velocity, [14,20], may result in a spurious ''excess'' mass or ''deficit'' mass which are not physically realistic. It is noted that other means of randomization may also be explored, but as will be shown in the next section, the approach presented is adequate as evidenced by the comparison of simulations with experimental data. Furthermore, the introduction of randomness based on the interfacial velocity information, instead of employing a tunable noise parameter, renders the approach attractive.

3 Results and Discussion

Prior to its application to simulating viscous fingering phenomenon, the numerical method was validated against benchmark solutions, to assess the accuracy of the developed algorithm. The validation studies are discussed in Section 3.1. Subsequently, the validated model is used to explore viscous fingering in the presence of finite viscosity ratio and interfacial surface tension. The results of these studies are described in Section 3.2.

3.1 Validation of the Numerical Method. First, the curvature calculation method outlined in Section 2.2 was tested by considering a sinusoidal function, $y = \frac{1}{2} + \frac{3}{10}\sin 2\pi x$, $0 < x < 1$ on a 20×20 mesh, which was also used as the test case by Chorin [25]. Figure 2 shows a comparison of the numerically computed values of the curvature (discrete symbols) at various x values with the exact solution (shown by the continuous line) that was derived analytically for the sinusoidal function. It is seen that the curvature values computed by the present algorithm are in good agreement with the analytical solution over the entire range of the function. This provides validation of the curvature calculation algorithm, which forms the basis for incorporating the effects of surface tension in the viscous fingering simulation discussed in the next section.

A second validation of the computational technique was conducted on the simulation of steady Saffman-Taylor finger growth in a Hele-Shaw cell, for which an analytical solution of the finger width is reported by McLean and Saffman [7]. The simulations were carried out on a rectangular Hele-Shaw cell with a length-to-width ratio of 3:1, and consisting of a line inlet and a line exit located along the two shorter sides of the cell. The line inlet is described by a constant pressure boundary condition, while the line outlet on the opposite end is set with a constant efflux rate, Q. As the Saffman-Taylor finger progresses steadily, Q may be related to finger tip velocity U by

$$Q = U \cdot b \cdot \lambda_f,$$

where λ_f is the finger width, and b the cell thickness. Once the finger tip velocity U is known, the modified capillary number, Ca', can be determined using the expression provided previously (Eq. (4)). The two lengthwise side walls are treated as being impermeable with free slip boundary conditions. An initial sinusoidal interface of one period with its peak equal to 1/8th of the cell width at the centerline is introduced to initiate the growth of the steady finger, and randomness in the interface progression was not used in this validation study. The simulations were carried out

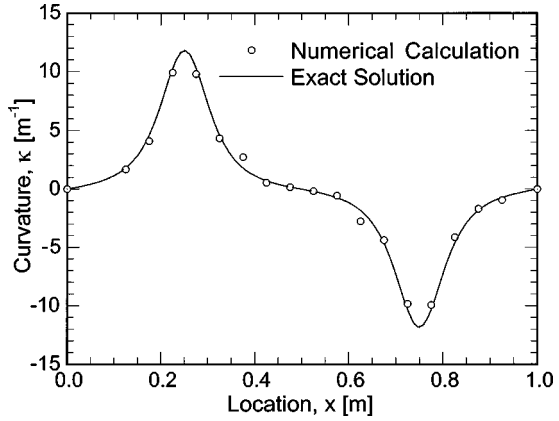

Fig. 2 Validation of curvature calculation on $y=1/2+(3/10)\sin 2\pi x$. Continuous line denotes the exact curvature as $C(x)=\pm(1.2\pi^2)\sin 2\pi x/[1+(9\pi^2/25)\cos^2 2\pi x]^{3/2}$, and the symbols represent the curvatures computed by the numerical method.

for a range of surface tension (σ), viscosity of the fluid in the cell (μ), and the efflux rate, Q. In each case, the steady width of the Saffman-Taylor finger was recorded.

The results of the validation are presented in Fig. 3, in terms of the ratio of the finger width (λ_f) to the cell width (W), λ, as a function of a dimensionless group defined by Tryggvason and Aref [19]: $2\pi(3\tau)^{1/2}$, where $\tau=(b^2/12\mu)(\sigma b/2QW)$. The continuous line in the plot denotes the solution reported by McLean and Saffman [7], expressed in terms of the dimensionless parameters, while the discrete markers represent the simulation results. The plot also identifies the modified capillary numbers, Ca', associated with the data points. It is seen that the volume tracking method used in the present study gives a good agreement with McLean and Saffman's solution for all the cases considered. For $2\pi(3\tau)^{1/2}>\sqrt{3}$, it is known from linear stability analysis, [15], that stable fingers can not be generated, which was also confirmed by the present simulations. For these cases, since a steady width can not be identified, a comparison with the benchmark solution is not possible, and they are excluded from the plot. Overall, the physical trend in the simulation data are seen to validate well with the analytical solution.

The simulation results in Fig. 3 correspond to a numerical mesh consisting of 80 grid points along the width of the cell, and 240 grid points along the length of the cell. In a separate numerical mesh convergence study, four different grid sizes of 20×60, 40×120, 80×240, and 160×480 were successively used to obtain the finger widths for the different Ca' numbers indicated in Fig. 3. The absolute errors relative to the solution by McLean and Saffman [7] were found to decrease by a factor of 4 for every doubling of the number of grid points, which suggests that the numerical method has a second-order spatial accuracy. Although not determined explicitly in this study, the temporal accuracy is expected to follow that of similar methods reported in the literature, [23,24].

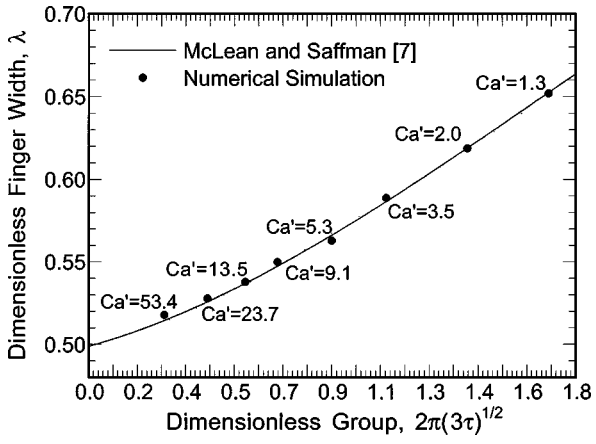

Fig. 3 Dimensionless width λ of a Saffman-Taylor finger as a function of $2\pi(3\tau)^{1/2}$. Solid line is McLean and Saffman's solution, and the symbols are simulation results using the present algorithm.

Furthermore, the mesh convergence study revealed that the 80×240 mesh was adequate to obtain converged results over the range of parameters considered. Indeed, Fig. 3 demonstrates that this discretization yields results that accurately match the McLean and Saffman solution. Further simulations presented in this article are therefore based on a discretization of 80 grid points along the cell width, and a proportional number along the mold length, based on the length-to-width aspect ratio. Although the chosen spatial discretization was based on the convergence of the stable Saffman-Taylor finger, for which a systematic mesh convergence analysis is possible, the discretization was also adequate to achieve morphological convergence in the case of unstable fingering, as discussed later in this section. For a chosen mesh size, the time step used in the simulations was determined such that the mesh Courant number was 1/4 [Eq. (15)].

It is reported based on experimental studies, [4], that the fingers exhibit tip-splitting above a critical capillary number of about 100. In the present simulations tip-splitting was observed for $Ca'>\approx60$ on a mesh of 80×240. This may be attributed to numerically induced instabilities which are difficult to curtail in the simulations—a trend also reported by Degregoria and Schwartz in their boundary-integral computations, [15]. It is worth noting that the early onset of finger tip-splitting in the simulations does not impair the exploration of unstable fingering for ranges of Ca' farther away from the transition point.

3.2 Finger Morphologies Under Finite Viscosity Ratio and Interfacial Tension. Although it is qualitatively known that the viscosity ratio μ_r defined as the displaced fluid viscosity to the displacing fluid viscosity must be "high" enough to favor viscous fingering, it is not readily evident from the literature if there exists a critical μ_r below which the fingering could not happen. Further, it is of interest to determine the variation of the critical Ca' that marks the onset of the unstable fingering, with the viscosity ratio μ_r. The goal of the present study is therefore to systematically map the various finger morphologies onto a $Ca'-\mu_r$ space. Similarly, for viscous fingers resulting from a constant pressure injection, a morphology diagram in terms of a suitably nondimensionalized pressure difference and the viscosity ratio is sought to be developed.

With the focus on the evolution of a single finger, the inlet in our simulation is set to be a narrow opening, equal to $\frac{1}{40}$th of the cell width, at the center of one of the smaller sides of the cell. Both constant pressure and constant flow-rate-based injection of the low viscosity fluid are investigated. The opposite end of the cell, directly across the injection face, is a line outlet with constant pressure. The rest of the cell boundaries are set to no-flow condition normal to the bounding surface. The cell length was considered to be twice its width, and the simulations were carried out on a 80×160 mesh with random interface progression turned on.

For the constant flow rate study, the μ in the modified capillary number, Ca', is defined as the displaced fluid viscosity μ_2. The viscosity, μ_2, and the interfacial tension, σ, were varied to obtain a wide range of μ_r and Ca' in the simulations. However, the Ca' can not be precisely determined beforehand without knowing the actual finger tip velocity, and its evaluation will be discussed later in this section. For conciseness, results of only 20 typical cases from all that were simulated are presented here in Fig. 4. They are

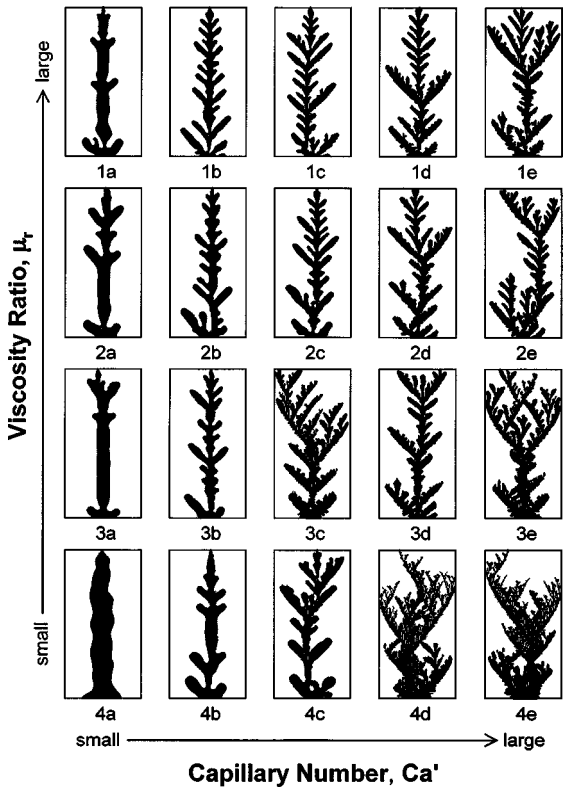

Fig. 4 Finger morphologies as a function of Ca' and μ_r for the case of constant flow rate injection. The corresponding Ca' and μ_r values for each frame are given in Table 1.

labeled 1(*a*) to 4(*e*), and are roughly arranged in the ascending order with respect to Ca' ($a \rightarrow e$) and μ_r ($4 \rightarrow 1$), as tabulated in Table 1. From Fig. 4, four distinct finger patterns are identified:

• *Saffman-Taylor-Like Finger*: This type of pattern (seen in frames 1(*a*), 2(*a*), 3(*a*), and 4(*a*) in Fig. 4) is characterized by a single, long stretching finger, as wide as one-third of the cell width, with minimal or no branching. Both its geometric features and constant progression speed, as we shall see later, resemble the steady Saffman-Taylor fingers. The interfacial tension σ plays a significant role in stabilizing the fingers, because the pattern is only found at small capillary numbers (equivalently large σ) for all viscosity ratios.

• *Dendritic Fingering*: For each μ_r, as Ca' increases, the fingers begin to split in a periodic manner, exhibiting an incipient dendritic growth. However, no secondary level of branching appears. These are exemplified by frames 1(*b*), 2(*b*), 3(*b*), and 1(*c*), 2(*c*) in Fig. 4.

• *Coalescent Fingering*: When μ_r is not high enough, and for Ca' exceeding a critical value, it is seen that growth of the tips is significantly influenced by other parts of the finger. Continuous joining and merging of finger branches leads to no distinct finger formation. The early stage of finger development in frames 4(*d*) and 4(*e*) in Fig. 4 best demonstrates this *coalescence* behavior. In the later stage of the finger, the simulation suggests that the branches tend to sever from the finger main body into many small submesh-size fluid blobs. Frames 3(*c*), 3(*d*), 3(*e*), and 4(*c*) also exhibit coalescence to various degrees. The pattern in frame 4(*b*) represents a transition from the coalescent to stable fingers, and the abovementioned critical Ca' may be defined at this transition.

• *Multiscale Fingering*: As the Ca' and the μ_r exceed certain critical values, each branching begins to occur at several length scales, resulting in an incipient (1*d*) and 2(*d*) to full arborescent pattern (1(*e*) and 2(*e*) in Fig. 4). Competition between higher level finger tips can be observed as in 2(*e*), and eventually only one prevails. The structures strongly suggest fractal characteristics that are usually found in miscible, non-Newtonian viscous finger experiments, where Ca' is infinity.

As mentioned earlier, the Ca' used to define each case was evaluated with the finger tip velocity, *U*. The velocities were obtained by linearly fitting the tip locations at multiple time instances that are readily known from the simulations. Figure 5 shows a few example cases from the set in Fig. 4. Constant finger tip velocities, as indicated by the close correspondence of the data points with the linear regression fits in Fig. 5, were achieved by the *constant flow rate injection*, and this justifies the use of Ca' as an appropriate governing parameter. In contrast, as will be discussed later in this section, the *constant pressure injection* cases are described by a different dimensionless parameter. It is also evident from Fig. 5 that the finger growth slows down with the increasing level of branching. The fastest growth is of Saffman-Taylor like fingers, such as 1(*a*), which requires only half the time needed by highly branched fingers, such as 1(*e*), to reach the same locations.

The results of all the simulated cases were categorized into one of four finger types that were identified. The simulation results were then mapped onto the $Ca' - \mu_r$ space, giving a finger morphology diagram shown in Fig. 6, which features four zones as follows:

• *Stable Zone*: It is found that in lower capillary number region, for which the characteristic upper limit is seen to be around $Ca' = 630$ and independent of the viscosity ratio, branching can hardly grow from the main finger body. As the capillary number decreases in this region, the finger gets more and more stabilized, owing to the increased interfacial tension. This trend is shown by examination of frames 1(*a*), 2(*a*), and 3(*a*) (all of which have $Ca' = 632$) with frame 4(*a*) ($Ca' = 130$) in Fig. 4 corresponding to the data points denoted by filled circles in Fig. 6. Among them, one that most resembles the Saffman-Taylor fingers is obtained around $Ca' = 130$ (frame 4(*a*) in Fig. 4). Further decrease of capillary number to less than 100, as explored in Section 3.1 and Fig. 3, will eventually yield steady state Saffman-Taylor fingers. In view of such a stabilization for $Ca' < 630$, this region is classified as the stable zone.

• *Coalescence Zone*: For $Ca' > 630$, the tip-splitting phenomenon is dominant. However, if the viscosity ratio is not high enough to exceed a critical $\mu_{r,\min} \approx 300$, the branches of fingers will always merge inwardly in their later stages to the main finger bodies. This coalescence behavior is even more pronounced as Ca' increases up to infinity, as long as the viscosity ratio is maintained below $\mu_{r,\min}$. It is seen that within this lower viscosity ratio

Table 1 Modified capillary number and viscosity ratio values (Ca', μ_r) corresponding to the simulations in Fig. 4

	a	*b*	*c*	*d*	*e*
1	632, 10^4	6320, 10^4	6.32×10^4, 1000	6.32×10^5, 1000	6.32×10^6, 1000
2	632, 3162	2000, 1000	6.32×10^3, 776	6.32×10^5, 776	6.32×10^7, 776
3	632, 1000	6320, 562	2×10^4, 316	6.32×10^5, 562	2×10^7, 316
4	130, 316	632, 316	2×10^3, 316	6.32×10^4, 100	6.32×10^5, 100

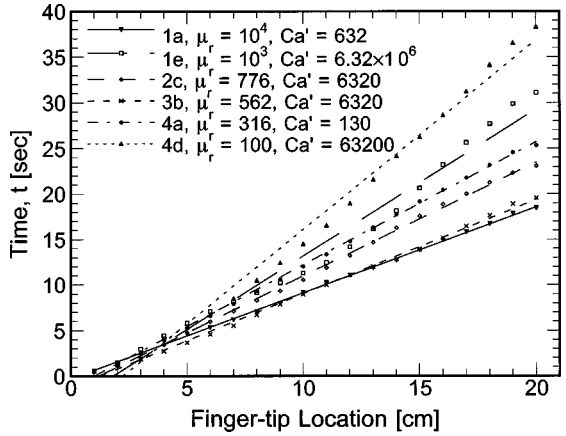

Fig. 5 Finger-tip location as a function of time for a constant flow rate injection. The labels correspond to the finger patterns in Fig. 4.

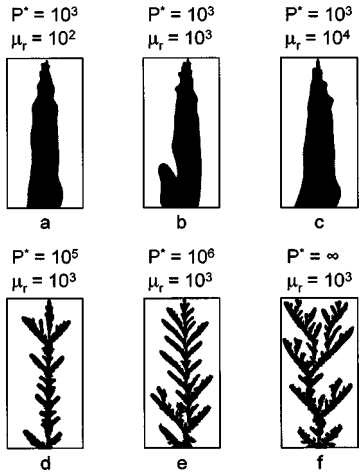

Fig. 7 Finger morphologies as a function of P^* and μ_r for select cases of constant pressure injection

region, in the case of high capillary numbers, $Ca' \geq 6.32\times10^4$ in Fig. 6, coalescence could take place at multiple levels (cf. frames 4(*d*), 4(*e*) in Fig. 4).

• *Transition Zone*: As the viscosity ratio exceeds $\mu_{r,\min}\approx300$ and the capillary number is beyond $Ca'>630$, finger branches can not only develop from the main body, but also stay apart from each other during their progression through the cell. However, the pattern shared by the cases denoted the inverted-triangle symbols in Fig. 6 are mostly of the dendritic type. At higher viscosity ratios, such patterns span a relatively narrower capillary number ranges starting from $Ca'=630$. The range is observed to be monotonically widened as the viscosity ratio decreases until another critical $\mu_{r,\max}\approx560$ is reached. At viscosity ratios from $\mu_{r,\min}$ to $\mu_{r,\max}$ and $Ca'>630$, the fingers undergo a transition from coalescence to multiscale fingering. If the dendritic finger pattern could also be viewed as a transition from the stable finger to the multiscale finger, a transition region can be identified as in Fig. 6.

• *Multiscale Zone*: When the viscosity ratio is greater than $\mu_{r,\max}=560$, the multiscale finger pattern will be reached, provided that the capillary number is also greater than some threshold values depending on the viscosity ratio. Referring to the region occupied by square markers in Fig. 6, it is seen that higher viscosity ratios favor the formation of the multiscale fingers by requiring smaller threshold Ca' values. For instance, at $\mu_r=10^4$ the multiscale finger pattern starts from $Ca'\approx6.3\times10^3$; while at $\mu_r=560$, it can not be obtained until $Ca'\approx6.3\times10^5$, which is two orders of magnitude higher. This feature is quantified in Fig. 6 by the curve that divides the multiscale zone and the transition zone.

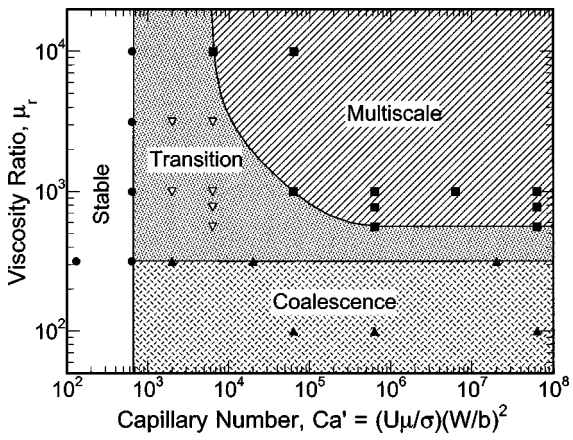

Fig. 6 Finger morphology diagram on a $Ca'-\mu_r$ space for the case of constant flow rate injection. All the simulated cases are discerned as being one of multiscale (square), coalescence (triangle), transition (inverted-triangle), and stable (circle) fingers.

It is evident from the preceding discussion that the viscous fingering phenomenon is fully characterized by the modified capillary number Ca' and the viscosity ratio μ_r when it is driven by the constant flow rate at the inlet of the Hele-Shaw cell. However, when the driving force is specified by the constant pressure difference, ΔP, between the inlet and the outlet, a nondimensionalization of the governing Eqs. (1)–(3) yields a new parameter, $P^*=\Delta P\cdot W/\sigma$, which will, along with the viscosity ratio μ_r, determine the finger morphologies.

Simulations with different P^*s and μ_rs also yielded four finger patterns that are similar to those found in the study of constant flow rate injection. As such, the detailed results, like those shown in Fig. 4, are omitted here in the interest of brevity. Six select cases are shown in Fig. 7 to exemplify some unique features. Briefly, the parameter P^*, like Ca', is a measure of the dynamic force (ΔP) relative to the stabilizing force (σ). Frames (*a*), (*b*), and (*c*), in Fig. 7 illustrate the stable morphologies with increasing μ_r for a fixed value of P^*, while frames (*d*), (*e*), and (*f*) correspond to the morphological differences for a fixed μ_r as the parameter P^* is increased. As P^* increases, while μ_r is kept constant and beyond a critical value of 560, the interface tends to be unstable, and a branched finger pattern is eventually reached. This morphology change is clearly demonstrated by frames (*b*), (*d*), (*e*), and (*f*) in Fig. 7, all of which share the same $\mu_r=1000$, but with progressively decreasing interfacial tension effects. The case of $P^*=\infty$ (frame *f*) denotes complete miscibility between the fluids, whereby $\sigma=0$.

Further, in Fig. 7, the Saffman-Taylor like fingers (*a*), (*b*), and (*c*) are seen to be tapered near their ends, and the multiscale fingers (*d*), (*e*), and (*f*) appear more branched compared to the constant flow rate cases with the same viscosity ratio μ_r (frames 1(*c*), 1(*d*), and 1(*e*) in Fig. 4). Both these effects may be explained by tip acceleration induced by the constant ΔP. Figure 8 shows the finger-tip position with time for the six cases in Fig. 7, and clearly demonstrates the pronounced finger-tip acceleration, especially in the later stages of the process. It may be recalled by way of comparison that the finger-tip progression was at a nearly uniform rate for the constant flow-rate-based injections (cf. Fig. 5). The tapering of the Saffman-Taylor-like fingers may be regarded as a reduction in the flow channel area corresponding to the in-

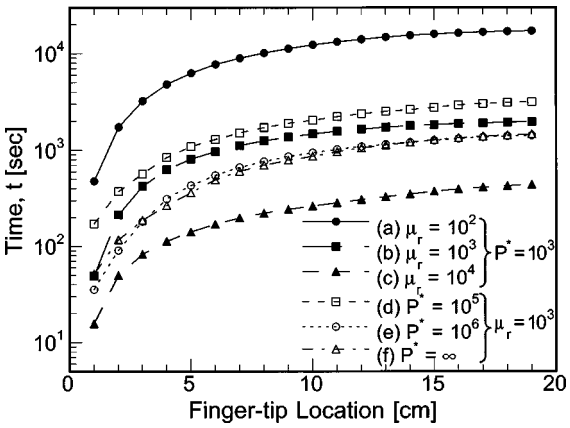

Fig. 8 Finger-tip location as a function of time for constant pressure injection, corresponding to the finger patterns in Fig. 7

creasing velocity at the finger tip so as to maintain the same volumetric flow rate. Further, since the tip acceleration is equivalent to an increasing local Ca' at the finger tip, it follows from the $Ca' - \mu_r$ morphology diagram (Fig. 6) that the fingers will exhibit a greater degree of branching.

Based on the simulation results, a morphology diagram for the constant pressure injection can be built on a $P^* - \mu_r$ space. Such a diagram is shown in Fig. 9 with all the simulated cases denoted by four different symbols representing the four different finger types. It is found from the figure that, independent of the viscosity ratio, there exists a critical $P^* = 10^4$, below which a stable zone could be classified. At higher P^* values than 10^4, the critical viscosity ratios $\mu_{r,\min} = 316$ and $\mu_{r,\max} = 560$ separating the *coalescence*, *transition*, and *multiscale* regimes are about the same as in the constant flow rate study. However, the critical values of the viscosity ratio μ_r and the P^* for dividing the multiscale zone and the transition zone are seen to be mutually independent, unlike the relationship between μ_r and Ca' found in the constant flow rate based injection. It is evident from Fig. 9 that the region $\mu_r > 1000$ and $P^* > 10^5$ represents the multiscale finger regime.

The grid size used to simulate unstable fingering is determined by a balance between the important overall physics that could be exhibited by the simulation and the cost of simulation. Due to the random nature of the instability phenomenon, an exact convergence study as in stable Saffman-Taylor finger evolution, is not possible. However, the morphologies of the unstable fingering determined by the underlying physics should be statistically invariant—i.e., the fingers should exhibit morphological convergence—with respect to the grid size, beyond a sufficient resolution. In this study, morphological convergence was found on a 80×240 grid, for the 1:3 Hele-Shaw cell aspect ratio considered. This was established by the fact that when selected cases from each morphological zone reported in Figs. 5 and 9 were simulated on a 160×480 grid, no new morphological patterns were discerned. It must be mentioned that the demarcations of the four zones in each of Figs. 5 and 9 should not be interpreted to be sharp delineations. This is owing to the inherent randomness associated with the instability phenomenon, which is also evident in experiments, where no two runs at nominally identical conditions exhibit precisely identical finger patterns. Nevertheless, the delineations serve as a general guideline for distinguishing the various regimes.

The volume tracking simulations presented in this study revealed, to within the accuracy of the simulations, the existence of multiscale and coalescent morphologies in the case of immiscible fingers. While coalescence and finger merging have been well-documented in the context of miscible fingering (for e.g., Zimmerman and Homsy [27] and Petitjeans et al. [28]) the present study demonstrates possible presence of such patterns in immiscible fingering. In order to verify the existence of the different morphologies in their relevant parameter regimes, a series of viscous fingering experiments were conducted in a Hele-Shaw cell. The experiments were performed using a regulated constant pressure injection source. Figure 10 illustrates the time evolution of a

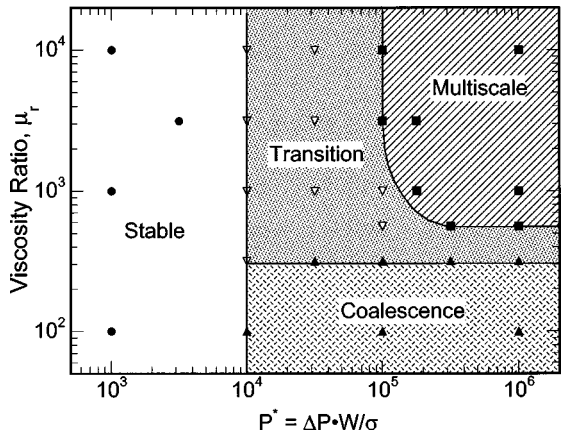

Fig. 9 Finger morphology diagram on a $P^* - \mu_r$ space for constant pressure injection. All the simulated cases are classified as being one of multiscale (square), coalescence (triangle), transition (inverted-triangle), and stable (circle) fingers.

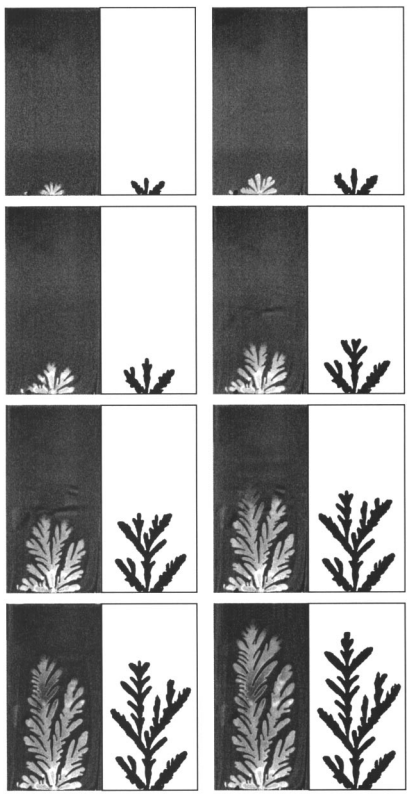

Fig. 10 Evolution of a multiscaled finger pattern in simulation and experiment for a constant pressure injection of air into glycerin. Frames with dark background and white fingers denote experiments, while frames with black fingers on a white background are the simulation results.

highly branched finger caused by constant pressure, point injection of air into glycerin. The experiment results, shown on the left half of each frame, are compared with the time-dependent simulation for the same materials, boundary conditions, and geometry as of the experiment. The dimensionless parameters for this case evaluate to $P^* = 1.08 \times 10^5$ and $\mu_r = 4.3 \times 10^4$, which falls in the multiscale zone in Fig. 9. Although the result of the simulation is limited in the amount of details, due to the finite mesh size (80×160), it presents a good qualitative resemblance of all the essential features of the multiscale finger obtained in the experiment.

A second experiment involved injection of mineral oil into glycerin, for which $\mu_r \approx 213$, and $Ca' = \infty$ since these two fluids are miscible. The morphology maps (Figs. 6 and 9) suggest the formation of coalescent fingering for these parameters. Figure 11 presents the experimental results (top frames) along with the simulated finger patterns (bottom frames) at the corresponding times. It is seen from the experiment that continuous merging of the finger arms inhibits any potential branch growth. Due to the coalescence, many isolated small areas of glycerin are formed as also suggested by the simulation of coalescent fingers. Overall, the simulations are seen to successfully reproduce the observed phenomena. The lighter shade of gray observed in the finger-tip regions of the second experiment frame signifies that glycerin, dyed with dark color, was not displaced completely by the mineral oil. Thus, strictly speaking, the two-dimensional Hele-Shaw flow model is not valid from this stage on. The simulation clearly demonstrates how the displaced fluid between initial finger branches is enclosed and trapped later by the coalescence.

With the results presented in the paper, especially the complete morphology diagrams as found, finger patterns can be easily predicted by knowing the dimensionless governing parameters, such as viscosity ratio μ_r, and the modified capillary number Ca', or $P^* = \Delta P \cdot W/\sigma$. Such quantitative knowledge is crucial in understanding many practical problems that involve the interface development between fluid components. The morphology diagram can assist in designing appropriate parameter settings that either promote or mitigate the instability phenomenon, as desired in the application. The focus of the study was on Newtonian fluids, although the numerical methodology presented may be readily extended to non-Newtonian systems as well, as will be reported in a future work.

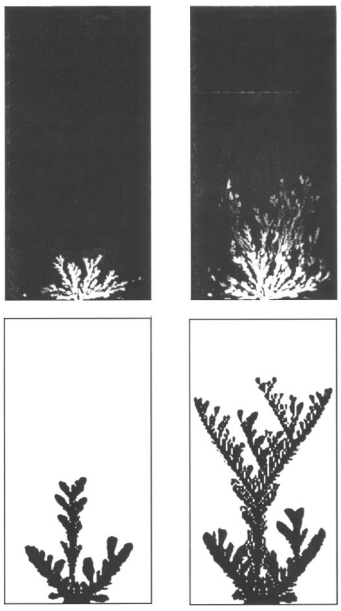

Fig. 11 Evolution of a coalescing finger pattern in simulation and experiment for injection of mineral oil into glycerin. Frames with dark background and white fingers denote experiments, while frames with black fingers on a white background are the simulation results.

4 Conclusions

A volume-tracking method capable of evolving rather complex interfaces was developed to simulate unstable viscous fingering of Newtonian fluids in a Hele-Shaw cell. The effect of finite viscosity ratio and interfacial tension on fingering morphology is found to be characterized by four distinct finger types, among which highly branched pattern and coalescent pattern are produced, for the first time, by the time-dependent simulations. Finger morphology diagrams were developed in terms of the viscosity ratio μ_r and the modified capillary number $Ca' = U\mu/\sigma(W/b)^2$ for constant injection flow rate, or $\Gamma = \Delta P \cdot W/\sigma$, for constant driving pressure difference. The effectiveness of the method was demonstrated by comparison with other viscous fingering simulations in the literature as well as with experiments conducted as part of the study.

Acknowledgments

The authors acknowledge funding for the work from the National Science Foundation through Grant Nos. DMI-9908450 and CTS-9912093.

References

[1] Hele-Shaw, H. J. S., 1898, "The Flow of Water," Nature (London), **58**, p. 34.
[2] Saffman, P. G., and Taylor, G. I., 1958, "The Pentration of a Fluid Into a Porous Medium or Hele-Shaw Cell Containing a More Viscous Liquid," Proc. R. Soc. London, Ser. A, **245**, p. 312.
[3] H., Lamb, 1932, *Hydrodynamics*, Cambridge Univ. Press, Cambridge, UK.
[4] Park, C. W., and Homsy, G. M., 1985, "The Instability of Long Fingers in Hele-Shaw Flows," Phys. Fluids, **28**(6), p. 1583.
[5] Maxworthy, T., 1987, "The Nonlinear Growth of a Gravitationally Unstable Interface in a Hele-Shaw Cell," J. Fluid Mech., **177**, p. 207.
[6] Kopf-Sill, A. R., and Homsy, G. M., 1987, "Narrow Fingers in a Hele-Shaw Cell," Phys. Fluids, **30**, p. 2607.
[7] McLean, J. W., and Saffman, P. G., 1981, "The Effect of Surface Tension on the Shape of Fingers in a Hele-Shaw Cell," J. Fluid Mech., **102**, p. 455.
[8] Shraiman, B., 1986, "Velocity Selection and the Saffman-Taylor Problem," Phys. Rev. Lett., **56**, p. 2028.
[9] Hong, D. C., and Langer, J., 1986, "Analytic Theory of the Selection Mechanism in the Saffman-Taylor Problem," Phys. Rev. Lett., **56**, p. 2032.
[10] Kadanoff, L. P., 1985, "Simulating Hydrodynamics: A Pedestrian Model," J. Stat. Phys., **39**, p. 267.
[11] Liang, S., 1986, "Random-Walk Simulations of Flow in Hele-Shaw Cells," Phys. Rev. A, **33**, p. 2663.
[12] Tang, C., 1985, "Diffusion-Limited Aggregation and the Saffman-Taylor Problem," Phys. Rev. A, **31**, p. 1977.
[13] Arneodo, A., Elezgaray, J., Tabard, M., and Tallet, F., 1996, "Statistical Analysis of Off-Lattice Diffusion-Limited Aggregates in Channel and Sector Geometries," Phys. Rev. E, **53**, p. 6200.
[14] DeGregoria, A. J., and Schwartz, L. W., 1985, "Finger Breakup in Hele-Shaw Cells," Phys. Fluids, **28**, p. 2313.
[15] DeGregoria, A. J., and Schwartz, L. W., 1986, "A Boundary-Integral Method for Two-Phase Displacement in Hele-Shaw Cells," J. Fluid Mech., **164**, p. 383.
[16] Hou, T. Y., Lowengrub, J. S., and Shelley, M. J., 1994, "Removing the Stiffness From Interfacial Flows With Surface Tension," J. Comput. Phys., **114**, p. 312.
[17] Hou, T. Y., Lowengrub, J. S., and Shelley, M. J., 2001, "Boundary Integral Methods for Multicomponent Fluids and Multiphase Materials," J. Comput. Phys., **169**, p. 302.
[18] Nie, Q., and Tian, F. R., 1998, "Singularities in Hele-Shaw Flows," SIAM (Soc. Ind. Appl. Math.) J. Appl. Math., **58**, p. 34.
[19] Tryggvason, G., and Aref, H., 1985, "Finger-Interaction Mechanisms in Stratified Hele-Shaw Flow," J. Fluid Mech., **154**, p. 287.
[20] Meiburg, E., and Homsy, G. M., 1988, "Nonlinear Unstable Viscous Fingers in Hele-Shaw Flows. II. Numerical Simulation," Phys. Fluids, **31**, p. 429.
[21] Whitaker, N., 1990, "Numerical Simulation of the Hele-Shaw Equations," J. Comput. Phys., **90**, p. 176.
[22] Dai, W.-S., and Shelley, M. J., 1993, "A Numerical Study of the Effect of Surface Tension and Noise on an Expanding Hele-Shaw Bubble," Phys. Fluids A, **5**, p. 2131.
[23] Youngs, D. L., 1982, "Time-Dependent Multi-Material Flow With Large Fluid Distortion," *Numerical Methods for Fluid Dynamics*, Academic Press, New York, p. 273.

[24] Rider, W. J., and Kothe, D. B., 1998, ''Reconstructing Volume Tracking,'' J. Comput. Phys., **141**, p. 112.
[25] Hirt, C. W., and Nichols, B. D., 1981, ''Volume of Fluid (VOF) Method for the Dynamics of Free Boundaries,'' J. Comput. Phys., **39**, p. 201.
[26] Chorin, A. J., 1985, ''Curvature and Solidification,'' J. Comput. Phys., **57**, p. 472.
[27] Zimmerman, W. B., and Homsy, G. M., 1992, ''Viscous Fingering in Miscible Displacements: Unification of Effects of Viscosity Contrast, Anisotropic Dispersion, and Velocity Dependence of Dispersion on Nonlinear Finger Propagation,'' Phys. Fluids A, **4**, p. 2348.
[28] Petitjeans, P., Chen, C.-Y., Meiburg, E., and Maxworthy, T., 1999, ''Miscible Quarter Five-Spot Displacements in a Hele-Shaw Cell and the Role of Flow-Induced Dispersion,'' Phys. Fluids, **11**, p. 1705.

J. Rafael Pacheco
Assistant Professor,
Departamento de Ingenieriá Mecánica,
Instituto Tecnológico de Monterrey,
Monterrey, NJ 64849, México
Mem. ASME,
e-mail: rpacheco@asu.edu

Arturo Pacheco-Vega
Visiting Assistant Professor,
Department of Aerospace
and Mechanical Engineering,
University of Notre Dame,
Notre Dame, IN 46556
Mem. ASME

Analysis of Thin Film Flows Using a Flux Vector Splitting[1]

We propose a flux vector splitting (FVS) for the solution of film flows radially spreading on a flat surface created by an impinging jet using the shallow-water approximation. The governing equations along with the boundary conditions are transformed from the physical to the computational domain and solved in a rectangular grid. A first-order upwind finite difference scheme is used at the point of the shock while a second-order upwind differentiation is applied elsewhere. Higher-order spatial accuracy is achieved by introducing a MUSCL approach. Three thin film flow problems (1) one-dimensional dam break problem, (2) radial flow without jump, and (3) radial flow with jump, are investigated with emphasis in the prediction of hydraulic jumps. Results demonstrate that the method is useful and accurate in solving the shallow water equations for several flow conditions.
[DOI: 10.1115/1.1538626]

Introduction

A phenomenon of interest in free-surface film flows under certain conditions is the formation of a sudden discontinuity in the depth of a flowing liquid; i.e., a hydraulic jump, as the flow in the radial direction makes a transition from supercritical to a subcritical regime. Significant back-flow may be present at the jump location with a corresponding loss of mechanical energy due to the abrupt change in depth. In general, the region of increased film thickness corresponds to a zone of substantially amplified turbulence. From a thermal standpoint, the location of the hydraulic jump is critical because of the degraded transport characteristics that exist there. This region is unsteady, and depends heavily on the drainage configuration downstream.

Thin film flows can be characterized as shallow-water flows in which the vertical dimension is much smaller than any typical horizontal length scale. Important applications of the shallow-water equations include the prediction of weather, simulation of tidal flows, storm surges, river flows, and dam-break waves.

For engineering applications numerical solution of the governing equations is a useful tool for aiding in the prediction of local flow properties of the fluid. From a numerical standpoint, a major difficulty in analyzing the hydraulic jump stems from the discontinuity of the fluid depth across the jump, which must be accurately captured by the numerical method.

Due to the similarity between the depth-averaged equations and the two-dimensional compressible Navier-Stokes equations, the methods developed to solve the compressible flow may also be used to study the shallow water equations and therefore to analyze hydraulic jumps in thin flows.

Several finite difference schemes have been developed for the simulation of gas dynamics equations and are available in the literature. The main difference among them is the way they address the problem of shock waves formation, which is of fundamental importance in the overall accuracy of the calculations. These techniques are based either on central-difference formulations, [1,2], or on upwind-difference discretizations. Though the earlier schemes give fairly accurate results in the case of smooth and weak-shocks, the precision given by the latter methods, even for problems containing strong shock waves, is superior, [3]. Representatives of upwind schemes are those by Roe [4] and Yee and Harten [5], based on flux difference splitting (FDS) techniques, and those by Steger and Warming [6], van Leer [7], and Walters et al. [8] structured on the flux vector splitting (FVS) approach.

Since the shallow-water equations have the property of being nonhomogeneous functions of the primitive variables, the application of FVS schemes to the solution of these equations has been limited, mainly due to the difficulty in finding the proper split of the flux vectors. However, a number of numerical studies for the shallow-water equations using schemes based on the FDS method have been carried out. Examples include the study of flow in a channel of infinite width, [9], the simulation of open channel flows coupled with flux limiters, [10], and the analysis of two-dimensional free-surface flow equations employing a high-order Godunov-type scheme based on monotone upstream-centered scheme for conservation laws (MUSCL) variable extrapolation and slope limiters, [11], among others.

In the current work we are interested in the analysis of free-surface thin film flows, for which a hydraulic jump may exist, using the shallow water equations as mathematical model. To this end, we use a finite difference scheme based on a new split of the flux vector to solve the governing equations. A first-order upwind differentiation is enforced at the location of the shock whereas a higher order upwind differentiation is employed elsewhere. A straight forward formulation of the governing equations is presented followed by a discussion of the split of the flux vector that accounts for the inhomogeneity of the shallow-water model. The effects of the FVS on the accuracy and consistency of the spatial discretization are studied next. Finally, three thin film problems (1) one-dimensional dam break problem, (2) radial flow without jump, and (3) radial flow with jump, are investigated with emphasis in the capability of the technique to capture discontinuities in the flow field.

Mathematical Model

Governing Equations. We present the governing Navier-Stokes and continuity equations for incompressible fluid with constant properties,

$$\nabla \cdot \mathbf{u} = 0 \tag{1}$$

$$\frac{\partial \mathbf{u}}{\partial t} + \mathbf{u} \cdot \nabla \mathbf{u} = -\nabla p + \nu \nabla^2 \mathbf{u} + g\mathbf{e}_z, \tag{2}$$

where $\mathbf{e_z}$ is the unit vector in the vertical direction; $\mathbf{u}=(u,v,w)$

[1]Address correspondence to ASU, P.O. Box 6106, Tempe, AZ 85287-6106.

Contributed by the Fluids Engineering Division for publication in the JOURNAL OF FLUIDS ENGINEERING. Manuscript received by the Fluids Engineering Division December 15, 1999; revised manuscript received October 11, 2002. Associate Editor: Y. Matsumoto.

represents the Cartesian velocity vector components; p is the pressure; ν is the kinematic viscosity; ρ is the density, and g is the gravitational acceleration. In the following, the physical space will be denoted by (x, y, z), and the computational space by (ξ, η, ζ).

Assuming that vertical acceleration, wind stresses and Coriolis effects are negligible, the bottom slope is small, and considering that the friction losses can be computed using uniform steady flow formulas, [12], the set of equations (1)–(2) can be vertically averaged to obtain the two-dimensional unsteady shallow flow equations. The depth-averaged equations of motion can be written in conservation law form as

$$\frac{\partial \mathbf{Q}}{\partial t}+\frac{\partial \mathbf{E}}{\partial x}+\frac{\partial \mathbf{F}}{\partial y}=\mathbf{S}, \tag{3}$$

where

$$\mathbf{Q}=\begin{bmatrix} h \\ hU \\ hV \end{bmatrix}; \quad \mathbf{E}=\begin{bmatrix} hU \\ hU^2+\dfrac{gh^2}{2} \\ hUV^2 \end{bmatrix}; \quad \mathbf{F}=\begin{bmatrix} hV \\ hUV \\ hV^2+\dfrac{gh^2}{2} \end{bmatrix};$$

$$\mathbf{S}=\begin{bmatrix} 0 \\ -gh\dfrac{\partial z_b}{\partial x}-\dfrac{\tau_{bx}}{\rho} \\ -gh\dfrac{\partial z_b}{\partial y}-\dfrac{\tau_{by}}{\rho} \end{bmatrix}. \tag{4}$$

Here h is the water depth measured vertically, U and V are the Cartesian depth-averaged velocity components, z_b is the channel bottom elevation, t is time, g is the gravitational acceleration, and τ_{bx} and τ_{by} are the bottom shear stress components. The bottom stress is an unknown quantity in the shallow water equations and has to be expressed in terms of the other variables in order to ''close'' the system. In the current formulation the effective stress components are neglected and the shear stress on the bottom is approximated using the Chezy formulas

$$\tau_{bx}=\frac{g}{C^2}U(U^2+V^2)^{1/2}, \quad \tau_{by}=\frac{g}{C^2}V(U^2+V^2)^{1/2}, \tag{5}$$

where C is the Chezy constant, [13]. The advantage of this approach (assuming the pressure distribution to be hydrostatic), is that leads to a considerable simplification in both the mathematical formulation and the numerical solution without degrading the accuracy of the overall solution, for most engineering applications, [14].

Equation (3) can be written in generalized coordinates as

$$\frac{\partial \hat{\mathbf{Q}}}{\partial \tau}+\frac{\partial \hat{\mathbf{E}}}{\partial \xi}+\frac{\partial \hat{\mathbf{F}}}{\partial \eta}=\hat{\mathbf{S}}, \tag{6}$$

where $\hat{\mathbf{Q}}$ represents the standard form of the conserved variables. Because of the particular structure of these equations, it is possible to write

$$\frac{\partial \hat{\mathbf{E}}}{\partial \xi}=\hat{\mathbf{A}}\frac{\partial \hat{\mathbf{Q}}}{\partial \xi} \quad \text{and} \quad \frac{\partial \hat{\mathbf{F}}}{\partial \eta}=\hat{\mathbf{B}}\frac{\partial \hat{\mathbf{Q}}}{\partial \eta}, \tag{7}$$

where $\hat{\mathbf{A}}$ and $\hat{\mathbf{B}}$ are the flux Jacobian matrices, i.e., $\hat{A}_{ij}=\partial \hat{E}_i/\partial \hat{Q}_j$ and $\hat{B}_{ij}=\partial \hat{F}_i/\partial \hat{Q}_j$. The elements of Eqs. (6)–(7) are shown in the Appendix.

The system of equations (6) is hyperbolic and therefore the direction of propagation of the information is determined by the sign of the eigenvalues of the Jacobian matrices, $\hat{\mathbf{A}}$ and $\hat{\mathbf{B}}$, which are all real. For $\hat{\mathbf{A}}$ and $\hat{\mathbf{B}}$ a similarity transformation exists such that $\hat{\mathbf{A}}=\hat{\mathbf{E}}_\lambda\hat{\mathbf{\Lambda}}\hat{\mathbf{E}}_\lambda^{-1}$ and $\hat{\mathbf{B}}=\hat{\mathbf{F}}_\gamma\hat{\mathbf{\Gamma}}\hat{\mathbf{F}}_\gamma^{-1}$, where $\hat{\mathbf{\Lambda}}$ and $\hat{\mathbf{\Gamma}}$ are the diagonal matrices of eigenvalues, and $\hat{\mathbf{E}}_\lambda$ and $\hat{\mathbf{F}}_\gamma$ the associated eigenvectors. If we define $U_c=\xi_x U+\xi_y V$, $V_c=\eta_x U+\eta_y V$ and $a=\sqrt{gh}$, the characteristic directions in the ξ and η-coordinates, respectively, can be written as

$$\lambda_1=U_c, \quad \lambda_{2,3}=U_c\pm a\sqrt{\xi_x^2+\xi_y^2} \tag{8}$$

$$\gamma_1=V_c, \quad \gamma_{2,3}=V_c\pm a\sqrt{\eta_x^2+\eta_y^2} \tag{9}$$

where U_c and V_c are the characteristic velocities.

Table 1 Boundary conditions for the shallow-water equations

Case	Condition	Number of Outward Characteristics	Number of Inward Characteristics	Number of Boundary Conditions
1	$U_c<-a\sqrt{\xi_x^2+\xi_y^2}$	0	3	3
2	$-a\sqrt{\xi_x^2+\xi_y^2}\le U_c<0$	1	2	2
3	$0\le U_c<a\sqrt{\xi_x^2+\xi_y^2}$	2	1	1
4	$U_c>-a\sqrt{\xi_x^2+\xi_y^2}$	3	0	0

Boundary Conditions. The system of equations (6) cannot be solved without assigning appropriate initial and boundary conditions. For a hyperbolic system the required number of boundary conditions is related to the behavior of the characteristics. At any point on the boundary one must specify as many conditions as there are characteristic planes entering the region. The characteristic directions of propagation are given in Eqs. (8)–(9). Considering the radial velocity as positive if the flow is outward, we may have the situations shown in Table 1. Cases 1 and 4, in the table, are concerned with supercritical flow, Fr>1 where Fr$=U/\sqrt{gh}$ is the Froude number. Supercritical flows do not occur very often. For the more frequent cases, 2 and 3 (Fr<1), we must specify either one or two boundary conditions depending on whether the flow is directed outward or inward.

For supercritical flow (Fr>1), the boundary conditions used were: (a) upstream boundary: the longitudinal velocity U, transverse velocity V and the depth h are specified and do not change during computations, and (b) downstream boundary: all the variables, i.e., U, V, and h are extrapolated from the interior points. For subcritical flow (Fr<1), the corresponding boundary conditions are (a) upstream boundary: the depth h is specified and the longitudinal velocity U is extrapolated from the interior points, and (b) downstream boundary: the velocities U and V are specified and the depth h is extrapolated from the interior points.

Splitting Scheme

The splitting of the flux vectors $\hat{\mathbf{E}}$ and $\hat{\mathbf{F}}$, in Eq. (6), can be accomplished in a number of ways. The most common choice is in accord to the sign of the eigenvalues of the system, where the flux vectors can be split into subvectors. Each subvector is associated with the positive or negative eigenvalues of the flux matrix Jacobian. Thus, $\hat{\mathbf{A}}$ can be split as $\hat{\mathbf{A}}=\hat{\mathbf{A}}^+ +\hat{\mathbf{A}}^-$ where $\hat{\mathbf{A}}^+ =\hat{\mathbf{E}}_\lambda\hat{\mathbf{\Lambda}}^+\hat{\mathbf{E}}_\lambda^{-1}$ and $\hat{\mathbf{A}}^-=\hat{\mathbf{E}}_\lambda\hat{\mathbf{\Lambda}}^-\hat{\mathbf{E}}_\lambda^{-1}$, where the elements of $\hat{\mathbf{\Lambda}}^+$ and $\hat{\mathbf{\Lambda}}^-$ are the positive and negative eigenvalues, respectively. Similarly $\hat{\mathbf{B}}=\hat{\mathbf{B}}^+ +\hat{\mathbf{B}}^-$, where $\hat{\mathbf{B}}^+=\hat{\mathbf{F}}_\gamma\hat{\mathbf{\Gamma}}^+\hat{\mathbf{F}}_\gamma^{-1}$ and $\hat{\mathbf{B}}^-=\hat{\mathbf{F}}_\gamma\hat{\mathbf{\Gamma}}^-\hat{\mathbf{F}}_\gamma^{-1}$.

In the case of the Euler equations, the fluxes associated with these Jacobians are obtained from the property of homogeneity of the flux vector $\hat{\mathbf{E}}(\hat{\mathbf{Q}})$. If the flux vector $\hat{\mathbf{E}}$ is an homogeneous function of degree one in $\hat{\mathbf{Q}}$, one has $\hat{\mathbf{E}}=\hat{\mathbf{A}}\hat{\mathbf{Q}}$. In a similar fashion, $\hat{\mathbf{F}}$ can be written as $\hat{\mathbf{F}}=\hat{\mathbf{B}}\hat{\mathbf{Q}}$. The property of homogeneity was used by Steger and Warming [6] to split the flux vector into forward and backward contributions. The eigenvalues of the Jacobian matrix of the full flux were split into non-negative and nonpositive groups. An alternate flux splitting with continuously differentiable flux contributions that lead to smoother solutions at sonic points was introduced in van Leer [7]. An important remark to be made

is that the concept of flux splitting as previously defined, is totally dependent on the fact that the fluxes are homogeneous functions of degree one in $\hat{\mathbf{Q}}$.

Although the system of equations (6) is hyperbolic and has some similarities with the Euler equations for compressible flows, there are some differences: the Jacobian matrices $\hat{\mathbf{A}}$ and $\hat{\mathbf{B}}$ of the shallow-water equations are not homogeneous functions of degree one in $\hat{\mathbf{Q}}$. Thence, the flux vectors of Eq. (6) cannot be expressed as $\hat{\mathbf{E}}=\hat{\mathbf{A}}\hat{\mathbf{Q}}$, and $\hat{\mathbf{F}}=\hat{\mathbf{B}}\hat{\mathbf{Q}}$.

It is possible to use the FVS method to solve the shallow-water equations by splitting the flux vectors $\hat{\mathbf{E}}$ and $\hat{\mathbf{F}}$ in Eq. (6) according to $\hat{\mathbf{E}}=\hat{\mathbf{E}}^{+}+\hat{\mathbf{E}}^{-}$ and $\hat{\mathbf{F}}=\hat{\mathbf{F}}^{+}+\hat{\mathbf{F}}^{-}$, where

$$\hat{\mathbf{E}}^{+}=\tilde{\hat{\mathbf{A}}}^{+}\hat{\mathbf{Q}} \quad \text{and} \quad \hat{\mathbf{E}}^{-}=\tilde{\hat{\mathbf{A}}}^{-}\hat{\mathbf{Q}}, \tag{10}$$

and

$$\hat{\mathbf{F}}^{+}=\tilde{\hat{\mathbf{B}}}^{+}\hat{\mathbf{Q}} \quad \text{and} \quad \hat{\mathbf{F}}^{-}=\tilde{\hat{\mathbf{B}}}^{-}\hat{\mathbf{Q}}. \tag{11}$$

To this end, we introduce the modified Jacobian matrices $\tilde{\hat{\mathbf{A}}}$ and $\tilde{\hat{\mathbf{B}}}$, where

$$\tilde{\hat{\mathbf{A}}}=\hat{\mathbf{E}}_{\lambda}\tilde{\hat{\mathbf{\Lambda}}}\hat{\mathbf{E}}_{\lambda}^{-1} \tag{12}$$

with the diagonal matrix of eigenvalues

$$\tilde{\hat{\mathbf{\Lambda}}}=\begin{bmatrix} \dfrac{\xi_x Q_2+\xi_y Q_3}{Q_1} & 0 & 0 \\ 0 & \dfrac{\xi_x Q_2+\xi_y Q_3+1/2Q_1\sqrt{Q_1 g(\xi_x^2+\xi_y^2)}}{Q_1} & 0 \\ 0 & 0 & \dfrac{\xi_x Q_2+\xi_y Q_3-1/2Q_1\sqrt{Q_1 g(\xi_x^2+\xi_y^2)}}{Q_1} \end{bmatrix}; \tag{13}$$

and the corresponding expression for the modified Jacobian $\tilde{\hat{\mathbf{B}}}$

$$\tilde{\hat{\mathbf{B}}}=\hat{\mathbf{F}}_{\gamma}\tilde{\hat{\mathbf{\Gamma}}}\hat{\mathbf{F}}_{\gamma}^{-1}, \tag{14}$$

with the diagonal matrix of eigenvalues

$$\tilde{\hat{\mathbf{\Gamma}}}=\begin{bmatrix} \dfrac{\eta_x Q_2+\eta_y Q_3}{Q_1} & 0 & 0 \\ 0 & \dfrac{\eta_x Q_2+\eta_y Q_3+1/2Q_1\sqrt{Q_1 g(\eta_x^2+\eta_y^2)}}{Q_1} & 0 \\ 0 & 0 & \dfrac{\eta_x Q_2+\eta_y Q_3-1/2Q_1\sqrt{Q_1 g(\eta_x^2+\eta_y^2)}}{Q_1} \end{bmatrix}. \tag{15}$$

It is now possible to obtain a well-behaved solution by splitting the spatial derivatives in two parts associated with the characteristic speeds. The flux vectors can be split into subvectors, such that each subvector is associated with positive or negative eigenvalues of the modified Jacobian matrix. Therefore, $\tilde{\hat{\mathbf{A}}}$ can be split according to $\tilde{\hat{\mathbf{A}}}=\tilde{\hat{\mathbf{A}}}^{+}+\tilde{\hat{\mathbf{A}}}^{-}$ where $\tilde{\hat{\mathbf{A}}}^{+}=\hat{\mathbf{E}}_{\lambda}\tilde{\hat{\mathbf{\Lambda}}}^{+}\hat{\mathbf{E}}_{\lambda}^{-1}$, and $\tilde{\hat{\mathbf{A}}}^{-}=\hat{\mathbf{E}}_{\lambda}\tilde{\hat{\mathbf{\Lambda}}}^{-}\hat{\mathbf{E}}_{\lambda}^{-1}$. The elements of the diagonal matrices $\tilde{\hat{\mathbf{\Lambda}}}^{+}$ and $\tilde{\hat{\mathbf{\Lambda}}}^{-}$ are the positive and negative eigenvalues of the modified Jacobian matrix. Similarly, we write for the η-coordinate $\tilde{\hat{\mathbf{B}}}=\tilde{\hat{\mathbf{B}}}^{+}+\tilde{\hat{\mathbf{B}}}^{-}$ where $\tilde{\hat{\mathbf{B}}}^{+}=\hat{\mathbf{F}}_{\gamma}\tilde{\hat{\mathbf{\Gamma}}}^{+}{}^{+}\hat{\mathbf{F}}_{\gamma}^{-1}$ and $\tilde{\hat{\mathbf{B}}}^{-}=\hat{\mathbf{F}}_{\gamma}\tilde{\hat{\mathbf{\Gamma}}}^{-}\hat{\mathbf{F}}_{\gamma}^{-1}$.

$\tilde{\hat{\mathbf{\Lambda}}}$ and $\tilde{\hat{\mathbf{\Gamma}}}$ were modified from the original eigenvalues of the Jacobians $\hat{\mathbf{A}}$ and $\hat{\mathbf{B}}$ (see the Appendix) to introduce a new splitting of the flux vectors $\hat{\mathbf{E}}$ and $\hat{\mathbf{F}}$. In a later section we will discuss the effect of modifying the characteristic speed on the consistency and accuracy of the scheme.

Discretization Schemes

The governing equations (6) are solved by marching in time from some known set of initial conditions. The general form of the time-difference approximation is given by

$$\begin{aligned} \Delta\hat{\mathbf{Q}}^{n+1}+\frac{\theta_1\Delta\tau}{1+\theta_2}\Bigg\{&\frac{\delta}{\delta\xi}[(\hat{\mathbf{A}}^{+}+\hat{\mathbf{A}}^{-})^{n}\Delta\hat{\mathbf{Q}}^{n+1}] \\ &+\frac{\delta}{\delta\eta}[(\hat{\mathbf{B}}^{+}+\hat{\mathbf{B}}^{-})^{n}\Delta\hat{\mathbf{Q}}^{n+1}]\Bigg\} \\ =&-\frac{\Delta\tau}{1+\theta_2}\left(\frac{\delta}{\delta\xi}[\hat{\mathbf{E}}^{+}+\hat{\mathbf{E}}^{-}]+\frac{\delta}{\delta\eta}[\hat{\mathbf{F}}^{+}+\hat{\mathbf{F}}^{-}]\right)^{n} \\ &-\frac{(1+\theta_1)\Delta\tau}{1+\theta_2}\hat{\mathbf{S}}^{n}-\frac{\theta_1\Delta\tau}{1+\theta_2}\hat{\mathbf{S}}^{n-1}+\frac{\theta_1}{1+\theta_2}(\hat{\mathbf{Q}}^{n}-\hat{\mathbf{Q}}^{n-1}) \end{aligned} \tag{16}$$

where the difference approximations for $\delta(\hat{\mathbf{E}}^{+}+\hat{\mathbf{E}}^{-})/\delta\xi$ are shown in the next section. For the numerical simulations presented here, an explicit scheme is chosen ($\theta_1=0$ and $\theta_2=0$) to solve Eq. (16).

Spatial Differencing Scheme. The upwind differencing of the convective terms is based on the flux splitting technique, where the spatial derivatives of $\hat{\mathbf{E}}^{+}$ and $\hat{\mathbf{E}}^{-}$ are approximated with backward and forward difference operators, respectively. Combining the standard first and second-order backward/forward differences the spatial derivatives can be expressed as

$$\left(\frac{\delta\hat{\mathbf{E}}^{+}(\mathbf{Q})}{\delta\xi}\right)_i=\frac{(\hat{\mathbf{E}}_i^{+}-\hat{\mathbf{E}}_{i-1}^{+})}{\Delta\xi}+\frac{\phi_i^{-}(\hat{\mathbf{E}}_i^{+}-\hat{\mathbf{E}}_{i-1}^{+})}{2\Delta\xi}-\frac{\phi_{i-1}^{-}(\hat{\mathbf{E}}_{i-1}^{+}-\hat{\mathbf{E}}_{i-2}^{+})}{2\Delta\xi} \tag{17}$$

and

$$\left(\frac{\delta\hat{\mathbf{E}}^{-}(\mathbf{Q})}{\delta\xi}\right)_i=\frac{(\hat{\mathbf{E}}_{i+1}^{-}-\hat{\mathbf{E}}_i^{-})}{\Delta\xi}+\frac{\phi_i^{+}(\hat{\mathbf{E}}_{i+1}^{-}-\hat{\mathbf{E}}_i^{-})}{2\Delta\xi}-\frac{\phi_{i+1}^{+}(\hat{\mathbf{E}}_{i+2}^{-}-\hat{\mathbf{E}}_{i+1}^{-})}{2\Delta\xi}. \tag{18}$$

Equation (17) can also be written as

$$\left(\frac{\delta\hat{\mathbf{E}}^{+}}{\delta\xi}\right)_i=\frac{\hat{\mathbf{E}}_{i+1/2}^{+}-\hat{\mathbf{E}}_{i-1/2}^{+}}{\Delta\xi} \tag{19}$$

with

$$\hat{\mathbf{E}}_{i+1/2}^{+}=\hat{\mathbf{E}}_i^{+}-\frac{\phi_i^{-}}{2}(\hat{\mathbf{E}}_i^{+}-\hat{\mathbf{E}}_{i-1}^{+}); \tag{20}$$

which is equivalent to obtaining the value of $\hat{\mathbf{E}}$ at the center of the cell followed by a forward extrapolation. The parameter ϕ appearing in Eqs. (17)–(18) limits the higher-order terms by acting as a nonlinear switch. ϕ enhances shock capturing by dropping from a second-order to a first-order scheme near discontinuities so that oscillations in large gradient regions such as in the vicinity of a shock are suppressed. The spatial differencing is second-order for $\phi=1$ and first-order for $\phi=0$. The value of ϕ is determined locally from

$$\phi=\left[\frac{2\|\Delta_\xi\mathbf{Q}_i\nabla_\xi\mathbf{Q}_i\|+\epsilon}{(\Delta_\xi\mathbf{Q}_i)^2+(\nabla_\xi\mathbf{Q}_i)^2+\epsilon}\right]^n \tag{21}$$

where ϵ is a small number $O(10^{-6})$, [8], and n is a positive number $(0<n\leqslant 1)$ used to capture the shock profile. The operators Δ_ξ and ∇_ξ are the standard forward and backward difference operators, respectively.

A spatial-discretization alternative is first, to extrapolate nodal point values of $\hat{\mathbf{Q}}$ toward the face of the cell, and then to obtain $\hat{\mathbf{E}}^{\pm}$ at the interfaces. This is implemented as a flux balance across the cell and leads to the following approximation:

$$\left(\frac{\delta\hat{\mathbf{E}}(\hat{\mathbf{Q}})}{\delta\xi}\right)_i=\frac{[\hat{\mathbf{E}}^{+}(\hat{\mathbf{Q}}_{i+1/2}^{-})-\hat{\mathbf{E}}^{+}(\hat{\mathbf{Q}}_{i-1/2}^{-})+\hat{\mathbf{E}}^{-}(\hat{\mathbf{Q}}_{i+1/2}^{+})-\hat{\mathbf{E}}^{-}(\hat{\mathbf{Q}}_{i-1/2}^{+})]}{\Delta\xi} \tag{22}$$

where $\hat{\mathbf{E}}^{\pm}(\hat{\mathbf{Q}}^{\mp})$ denotes $\hat{\mathbf{E}}^{\pm}$ evaluated at $\hat{\mathbf{Q}}^{\mp}$, and

$$\hat{\mathbf{Q}}_{i+1/2,\,j}^{-}=\hat{\mathbf{Q}}_{i,j}+\frac{\phi_i^{-}}{4}[(1-\kappa\phi_i^{-})\nabla_\xi+(1+\kappa\phi_i^{-})\Delta_\xi]\tilde{\mathbf{Q}}_{i,j} \tag{23}$$

$$\hat{\mathbf{Q}}_{i+1/2,\,j}^{+}=\hat{\mathbf{Q}}_{i+1,j}-\frac{\phi_{i+1}^{+}}{4}[(1+\kappa\phi_{i+1}^{+})\Delta_\xi+(1-\kappa\phi_{i+1}^{+})\nabla_\xi]\hat{\mathbf{Q}}_{i+1,\,j}. \tag{24}$$

The aforementioned method, developed by van Leer [7], is often referred as the MUSCL-type approach. In Eqs. (23)–(24), κ determines the spatial accuracy of the difference approximation. For fully upwind differencing, the choice $\kappa=-1$ is used whereas $\kappa=1/3$ corresponds to the upwind-biased third-order scheme, [15,16]. Analogous expressions to (17)–(22) may be obtained for the gradient of the fluxes $\delta(\mathbf{F}^{+}+\hat{\mathbf{F}}^{-})/\delta\eta$.

A comparison of numerical results for the dam-break problem, obtained with the discretized forms of Eqs. (17)–(18), and Eq. (22) will be presented in the section of numerical experiments.

Accuracy and Consistency Analyses. We now analyze the impact on the order of accuracy and consistency of the scheme due to the modification of the characteristic speeds (eigenvalues) of the modified Jacobian matrices $\tilde{\tilde{\mathbf{A}}}$ and $\tilde{\tilde{\mathbf{B}}}$ of our flux-splitting.

Consider for simplicity the one-dimensional shallow-water equation

$$\frac{\partial\hat{\mathbf{Q}}}{\partial\tau}+\frac{\partial\hat{\mathbf{E}}^{+}}{\partial\xi}+\frac{\partial\hat{\mathbf{E}}^{-}}{\partial\xi}=0 \tag{25}$$

discretized in space and time with the following first-order scheme as

$$\hat{\mathbf{Q}}_i^{n+1}-\hat{\mathbf{Q}}_i^{n}=-\frac{\Delta\tau}{\Delta\xi}[(\hat{\mathbf{E}}_i^{+}-\hat{\mathbf{E}}_{i-1}^{+})+(\hat{\mathbf{E}}_{i+1}^{-}-\hat{\mathbf{E}}_i^{-})]^n=-\frac{\Delta\tau}{\Delta\xi}[(\hat{\mathbf{E}}_i^{+}+\hat{\mathbf{E}}_{i+1}^{-})-(\hat{\mathbf{E}}_{i-1}^{+}+\hat{\mathbf{E}}_i^{-})]^n. \tag{26}$$

On expressing the absolute value of $\hat{\mathbf{E}}$ as $|\hat{\mathbf{E}}|=\hat{\mathbf{E}}^{+}-\hat{\mathbf{E}}^{-}=|\tilde{\tilde{\mathbf{A}}}|\hat{\mathbf{Q}}$, where $|\tilde{\tilde{\mathbf{A}}}|=\hat{\mathbf{E}}_\lambda|\tilde{\tilde{\mathbf{A}}}|\hat{\mathbf{E}}_\lambda^{-1}$, and using $\hat{\mathbf{E}}=\tilde{\tilde{\mathbf{A}}}^{+}\hat{\mathbf{Q}}+\tilde{\tilde{\mathbf{A}}}^{-}\hat{\mathbf{Q}}$ with $\tilde{\tilde{\mathbf{A}}}^{+}\hat{\mathbf{Q}}=\hat{\mathbf{E}}^{+}$ and $\tilde{\tilde{\mathbf{A}}}^{-}\hat{\mathbf{Q}}=\hat{\mathbf{E}}^{-}$, we can recast Eq. (26) as

$$\hat{\mathbf{Q}}_i^{n+1}-\hat{\mathbf{Q}}_i^{n}=-\frac{\Delta t}{2\Delta\xi}(\hat{\mathbf{E}}_{i+1}-\hat{\mathbf{E}}_{i-1})^n+\frac{\Delta\tau}{2\Delta\xi}(|\hat{\mathbf{E}}|_{i+1}-2|\hat{\mathbf{E}}|_i+|\hat{\mathbf{E}}|_{i-1})^n, \tag{27}$$

to show an artificial viscosity term proportional to the second derivative of the absolute flux value $|\hat{\mathbf{E}}|$. It can be noticed from Eq. (27) that the consistency of the scheme is maintained.

After a Taylor expansion of $(|\hat{\mathbf{E}}|_{i+1}-|\hat{\mathbf{E}}|_i)$ and $(|\hat{\mathbf{E}}|_i-|\hat{\mathbf{E}}|_{i-1})$, we can transform Eq. (27) in a form that explicits the absolute value of the modified Jacobian $|\tilde{\tilde{\mathbf{A}}}|$; e.g.,

$$|\hat{\mathbf{E}}|_{i+1}-|\hat{\mathbf{E}}|_i=|\tilde{\tilde{\mathbf{A}}}|_{i+(1/2)}(\hat{\mathbf{Q}}_{i+1}-\hat{\mathbf{Q}}_{i-1})+O(\Delta\xi)(\hat{\mathbf{Q}}_{i+1}-\hat{\mathbf{Q}}_{i-1}), \tag{28}$$

$$|\hat{\mathbf{E}}|_i-|\hat{\mathbf{E}}|_{i-1}=|\tilde{\tilde{\mathbf{A}}}|_{i-(1/2)}(\hat{\mathbf{Q}}_{i+1}-\hat{\mathbf{Q}}_{i-1})+O(\Delta\xi)(\hat{\mathbf{Q}}_{i+1}-\hat{\mathbf{Q}}_{i-1}). \tag{29}$$

Using Eqs. (28)–(29), Eq. (27) becomes, to the first-order accuracy

$$\hat{\mathbf{Q}}_i^{n+1}-\hat{\mathbf{Q}}_i^{n}=-\frac{\Delta t}{2\Delta\xi}(\hat{\mathbf{E}}_{i+1}-\hat{\mathbf{E}}_{i-1})^n+\frac{\Delta\tau}{2\Delta\xi}[|\tilde{\tilde{\mathbf{A}}}|_{i+(1/2)}(\hat{\mathbf{Q}}_{i+1}-\hat{\mathbf{Q}}_i)-|\tilde{\tilde{\mathbf{A}}}|_{i-(1/2)}(\hat{\mathbf{Q}}_i-\hat{\mathbf{Q}}_{i-1})]^n+O(\Delta\hat{\mathbf{Q}}^2). \tag{30}$$

Equations (26) and (27) are equivalent formulations of the first-order conservative upwind scheme (25) for smooth variations of $\hat{\mathbf{Q}}$. One can write Eq. (26) in terms of the numerical flux, as

$$\hat{\mathbf{Q}}_i^{n+1}-\hat{\mathbf{Q}}_i^n=-\frac{\Delta\tau}{\Delta\xi}(\hat{\mathbf{E}}_{i+1/2}-\hat{\mathbf{E}}_{i-1/2})^n \tag{31}$$

with $\hat{\mathbf{E}}_{i+1/2}=\hat{\mathbf{E}}_i^+ +\hat{\mathbf{E}}_{i+1}^-$, or up to second-order accuracy as

$$\hat{\mathbf{E}}_{i+(1/2)}=\frac{1}{2}(\hat{\mathbf{E}}_i+\hat{\mathbf{E}}_{i+1})-\frac{1}{2}\tilde{\tilde{\mathbf{A}}}_{i+(1/2)}(\hat{\mathbf{Q}}_{i+1}-\hat{\mathbf{Q}}_i)+O(\Delta\hat{\mathbf{Q}}^2). \tag{32}$$

It can be observed that the modification of the characteristic speed does not affect the order of accuracy of the scheme, as it is part of an artificial dissipation term [16].

Numerical Experiments

Three problems are solved in order to examine the proposed FVS. The first is the analysis of the well-known one-dimensional dam-breaking, the second corresponds to a radial flow within a supercritical region in the domain for which no hydraulic jump exists, and the third is a radial flow in the presence of supercritical and subcritical regions which induce a hydraulic jump.

One-Dimensional Dam-Breaking Problem. This problem consists of a dam located at the origin ($x=0$) in a rectangular channel, that extends to $\pm\infty$, in which fluid is initially at rest on both sides. The x-coordinate is in the downstream direction of the channel. The initial height of the fluid on the left ($x<0$) is 1 m while the height on the right ($x>0$) is 0.8 m. For this problem, [17] developed an exact solution based on the theory of characteristics to analyze the behavior of the fluid after the dam breaks. The numerical simulations were carried out using the proposed FVS along with four different schemes: a first-order upwind, a second-order upwind, and two different schemes that use slope limiters.

Figures 1(a)–1(d) illustrate comparisons of the results obtained from the numerical procedure with the exact solution at time t

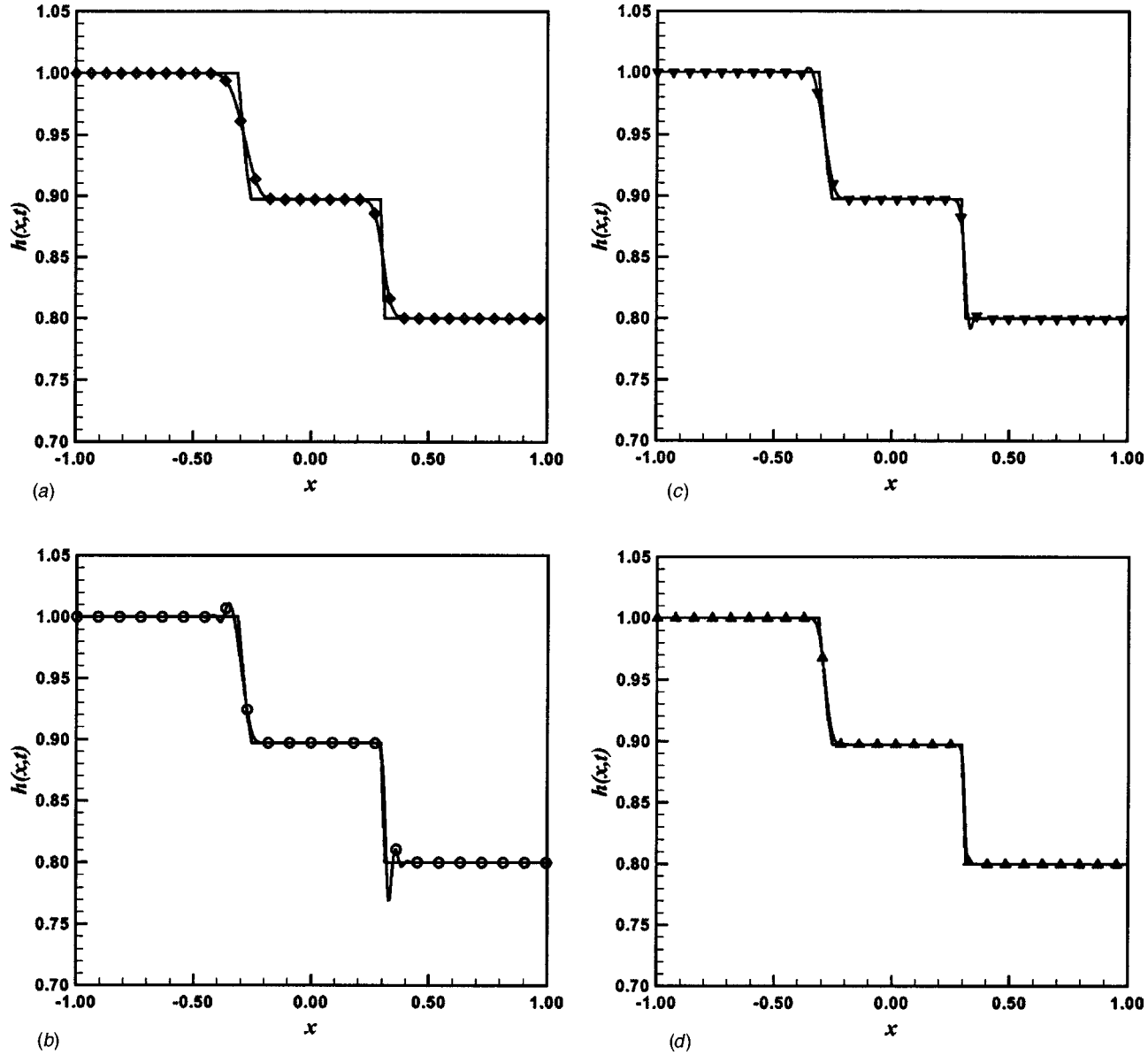

Fig. 1 Water depth of the dam-break problem in a rectangular channel at time $t=0.10$ second and 440 grid points. (*a*) Exact solution; –◇– first-order scheme. (*b*) Exact solution; –○– second-order scheme. (*c*) Exact solution; –▽– scheme based on flux extrapolation $\hat{\mathbf{E}}$ with limiter. (*d*) Exact solution; –△– scheme based on variable extrapolation $\hat{\mathbf{Q}}$ (MUSCL) with limiter.

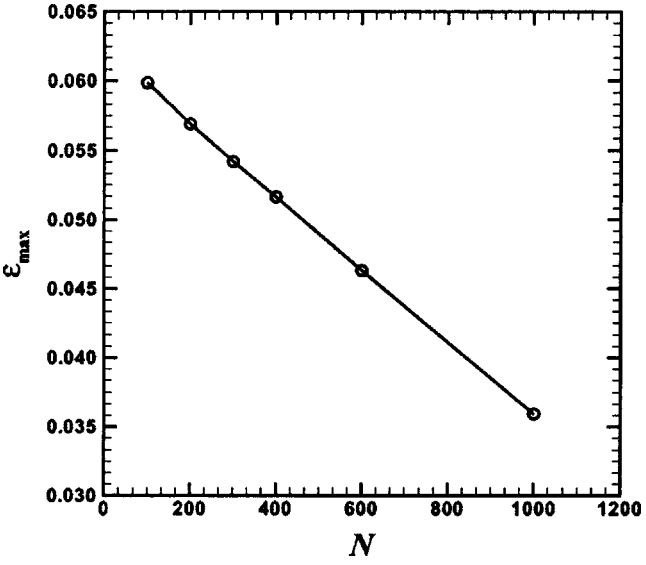

Fig. 2 Maximum relative error of h as a function of mesh refinement for the dam-break problem on a rectangular channel at time $t=0.10$ s at the points of discontinuity

$=0.10$ seconds using 440 mesh points. It can be observed from the figures that, in general, the discontinuities are captured by all the schemes, but some differences in accuracy are evident. For instance, Fig. 1(a) shows that the first-order upwind scheme has good properties of monotonicity, however it suffers from severe inaccuracies because of the high level of truncation error. On the other hand, the second-order upwind scheme, shown in Fig. 1(b), yields low levels of numerical dissipation, but steep gradients produce an oscillating behavior due to its numerical dispersion. In Fig. 1(c) the slope limiter technique based on extrapolation of the flux vector $\hat{\mathbf{E}}$ shows a substantial reduction in the amplitude of the oscillations at the discontinuities but cannot be completely suppressed. Finally, the results obtained from coupling FVS with the MUSCL technique indicate that the method is able to capture the discontinuities in a sharp way, avoiding any unrealistic oscillation as illustrated in Fig. 1(d).

The maximum relative error in h, $\epsilon_{\max}$, at the points of discontinuity and time of 0.10 s is plotted in Fig. 2 as a function of mesh refinement, for the MUSCL scheme. Similar results were obtained for the velocity U. A uniform grid was used in the computation. The time-step was refined proportional to the grid spacing. Figure 2 shows that the present method is first-order accurate at the shock locations. The maximum relative error in h at time 0.10 s away from the shock is presented in Table 2 as function of mesh refinement. The experimentally established orders or accuracy are also shown in this table as function of mesh refinement. In our computation, we used $\kappa=1/3$ which corresponds to the upwind-biased third-order scheme, [15].

Radial Flow Without Jump. We simulate the radial flow with the proposed flux vector splitting method coupled with the MUSCL technique and compare the results with the experiments

Table 2 Convergence test results for the dam-break problem away from the discontinuity region

N	$\epsilon_{\max}$ (m)	Order
100	-	-
200	2.25893928×10^{-5}	1.9716
300	8.58939347×10^{-6}	2.3847
400	3.58939360×10^{-6}	3.0327

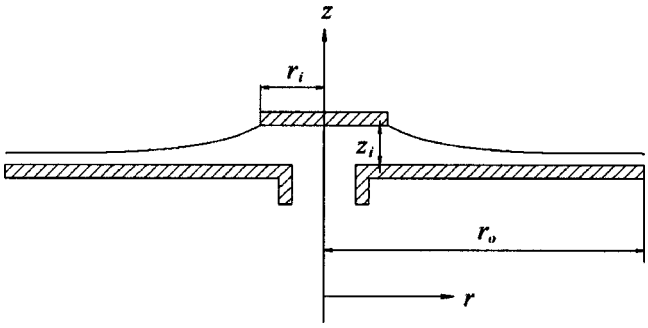

Fig. 3 Schematic of the experiment layout of Sadler and Higgins [18]

of Sadler and Higgins [18]. A layout of their experimental setup is shown in Fig. 3; the reported geometrical parameters and flow rates are presented in Table 3 as case 1. It consists of a 2.44 m (8 ft) square sheet of Plexiglas mounted horizontally on a 15.2 cm (6 in) diameter vertical pipe. Both Plexiglas and pipe were fixed to a structure. Water was discharged from a nozzle, from below, onto a 20.3 cm (8 in) diameter disk located at a height of 5 mm (3/16 in) above the sheet of Plexiglas. The water was then collected through a series of drains arranged in a circular fashion located at a distance of 68.6 cm (27 in) from the center. In the experiment, the depth of the flow was measured with a point gauge mounted on an arm under steady-state conditions.

For simulation purposes, we use a flow rate of $Q_w=0.0098$ m^3/s (0.345 cfs), as reported by Sadler and Higgins [18], and a value of the Chezy constant $C=80$, [19], which is in the range commonly used for practical engineering calculations. It must be noted that a simplification of the problem can be obtained since the flow is axisymmetric, so that a one-dimensional version of the shallow-water equations in cylindrical coordinates may be used. Nonetheless, we consider a two-dimensional discretization

Table 3 Conditions from experiments for the solution of the shallow-water equations

Case	r_i (m)	r_o (m)	z_i (m)	Q_w (m^3/s)	Experiment
1	0.102	0.686	5×10^{-3}	0.0098	Sadler and Higgins [18]
2	0.082	0.914	8×10^{-3}	0.0170	Ahmad [21]

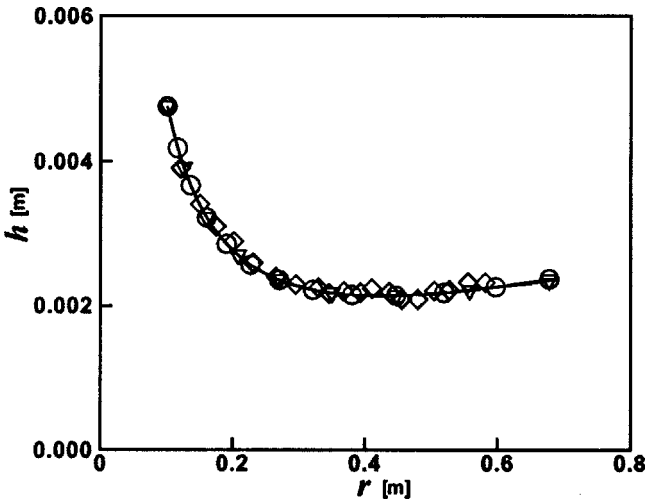

Fig. 4 Comparison of numerical solutions and experiments for $Q_w=0.0098$ m^3/s (0.345 cfs); -▽- (121×121) grid points; -○- (241×121) grid points; ◇ Sadler and Higgins [18]

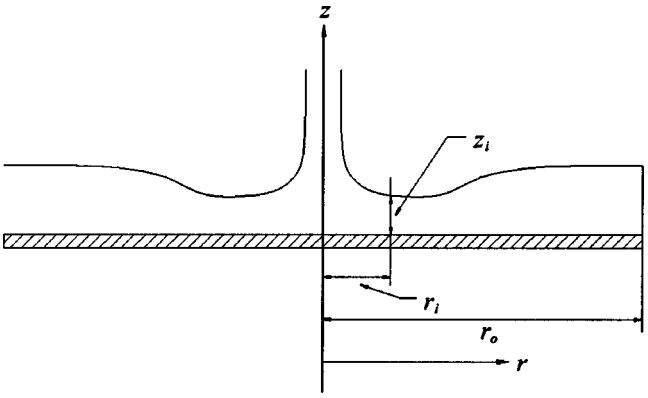

Fig. 5 Schematic of the experiment layout of Ahmad [21]

of the domain in order to illustrate potential applications of the method for nonaxisymmetric flows, [20]. The upstream values of *h*, *U*, and *V* are assigned as initial conditions for the numerical runs at all the grid points. The upstream boundary condition is of the Dirichlet type (case 1 of Table 1). Since the flow is supercritical within the domain, the boundary condition downstream corresponds to the Neumann type. Therefore the values of the variables are extrapolated using the values at the interior points. In the azimuthal direction periodic boundary conditions were implemented. The numerical scheme was tested until grid independent solutions were obtained by successively refining the mesh. Figure 4 shows the film height for two different sets of mesh points. The FVS-based model was run until steady state was reached.

A comparison between the numerical calculations obtained from the proposed FVS method and the experimental results of Sadler and Higgins [18] is presented in Fig. 4. The water surface profiles determined from the model and the surface profile found experimentally for the current analysis are shown in this figure. The numerical results display a very good agreement with experiments.

Radial Flow With Jump. The radially spreading flow of a thin liquid film is simulated in the presence of supercritical and subcritical regions. The shock-capturing capabilities of our FVS method are tested and the results are compared with the laboratory test data obtained by [21]. A schematic of the experimental layout is shown in Fig. 5. It consisted of a 2.14 m (7 ft) diameter by 2.5 cm (1 in) thickness circular plywood disc placed in a circular steel

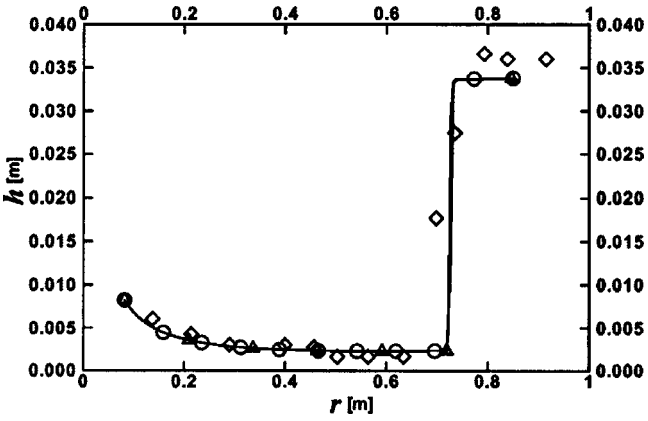

Fig. 6 Comparison of water surface profile of a hydraulic jump for Q_w=0.0170 m^3/s (0.60 cfs) between experiments and numerical solutions for different number of grid points: –△– (121×121) grid mesh; –○– (241×121) grid mesh; ◇ observed by Ahmad [21]

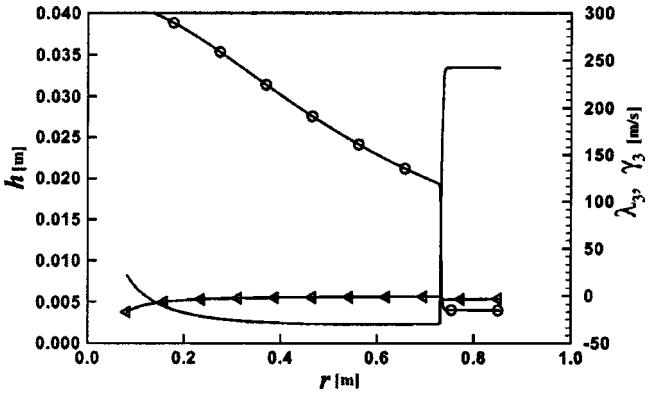

Fig. 7 Evolution of the eigenvalues and appearance of the hydraulic jump; –○– λ_3; –▷– γ_3; – height *h*. FVS with slope limiter solution; (241×121) grid points.

tank of diameter 2.29 m (7.5 ft). A ring of 1.83 m (6 ft) inside diameter, 2.14 m (7 ft) outside diameter, and 2.5 cm (1 in) thickness was placed on the plywood disk to control the downstream depth and consequently the location of the jump. A 10.2 cm (4 in) diameter pipe was used to convey the water onto the disc. The distance between the nozzle and the disc was kept at 2 cm (13/16 in).

For the numerical simulation we use the flow conditions reported by Ahmad [21] which are presented as case 2 in Table 3. Since the flow is supercritical in the upstream region, the variables *U*, *V*, and *h*, once specified, remain unchanged during the iteration process. At the downstream boundary, *U* and *V* are defined whereas *h* is extrapolated from the interior points. Periodic boundary conditions are prescribed in the azimuthal direction. For the present case, the value of the Chezy constant was chosen as $C=90$, [19], and the time-step $\Delta\tau$ was restricted to a CFL=0.5. Results from this run are shown in Fig. 6. The values of the speed of propagation (eigenvalues λ_3 and γ_3) are shown in Fig. 7 as a function of the radial position. From Fig. 7, it is clear that the change of sign of the eigenvalue λ_3 coincides with the location of the jump, as expected. It is also important to note that the location of the jump coincides at a location where the characteristics intersect. In our test, we start from an initial condition and stop the computation when the change in water depth reaches a prescribed tolerance of $\epsilon=1.0\times10^{-5}$ m.

The computed results from the proposed scheme and the measurements of Ahmad [21] are shown in Fig. 6 for comparison. From the figure it can be observed first that the film heights from the simulations using a mesh of 121×121 points, are almost identical when increasing the number of grid points in the radial-azimuthal directions to 241×121, for the same initial conditions indicating grid independence. Moreover, when comparing the numerical simulations with the experimental measurements becomes clear that the method simulates the supercritical flow accurately, and that it is able to determine the location of the jump. The sharp transition from supercritical to subcritical flow is clearly shown in Fig. 6. In the region of transition from supercritical to subcritical flow, the computed water-depth magnitude is very close to the measured height reported in the experiment. In the subcritical region where the flow is turbulent, the difference in heights between simulations and experiments becomes larger. These differences may be due on one side to experimental uncertainties which are increased in the turbulent region, and on the other, to the energy dissipated at the location of the jump, which is not accounted for in the shallow-water formulation.

Concluding Remarks

The hydraulic jump is an intriguing complex phenomenon commonly found in nature. The complexity stems from the change in

the character of the flow at the jump location with the corresponding production of distorted free surfaces and flow separation. Because of its important role in engineering applications, e.g., the design of water courses, energy dissipators, etc., it is crucial to determine accurately the characteristics of the jump such as position and thickness.

The shallow water equations are mathematically similar to the equations for compressible fluid flow. They are useful in predicting the location of shocks, at which the height of the free surface and the mean fluid velocity are discontinuous. In contrast to the compressible fluid flow equations, the shallow water equations do not posses the property of homogeneity and hence common FVS cannot be used to solve them. In this work we have introduced a new FVS that allows the analysis of thin film flows, in particular, the formation of hydraulic jumps within the flow domain using the shallow-water theory. The proposed splitting of the flux vectors was obtained by modified Jacobian matrices that account for the inhomogeneity of the system. Details of the methodology and theoretical analyses have been included to illustrate its implementation, consistency and accuracy.

The usefulness of the proposed FVS is tested by coupling the method to several finite difference schemes, two of them with slope limiters, that yield high-order accuracy away from the location of the shock. The numerical predictions have shown favorable comparisons with the theoretical solution of the dam-break problem. When the proposed FVS is used in conjunction with MUSCL, the resulting scheme is more efficient and produces accurate results in the location of the discontinuity and the height of the flow, avoiding unrealistic oscillations. An excellent agreement with laboratory experiments and analytical solutions confirmed the efficiency of the method. The technique proposed here has been successfully applied to analyze axisymmetric and nonaxisymmetric density currents, [20].

Acknowledgments

The authors would like to thank Prof. Kyle Squires for helpful discussions on this work and to Prof. Miguel Angel Arredondo of Universidad Iberoamericana, León, for access to computer facilities. We are grateful for the helpful comments of the anonymous referees which improved the quality of the manuscript.

Appendix

Expanded Vectors. We present next the expanded form of the expressions often encountered in solving the shallow-water equations. The flux vectors are given by

$$\hat{\mathbf{Q}}=\frac{1}{J}\begin{bmatrix}Q_1\\Q_2\\Q_3\end{bmatrix}=\frac{1}{J}\begin{bmatrix}h\\hU\\hV\end{bmatrix} \tag{33}$$

$$\hat{\mathbf{E}}=\frac{1}{J}\begin{bmatrix}\xi_x Q_2+\xi_y Q_3\\ \dfrac{\xi_x Q_2^2+\xi_y Q_2 Q_3}{Q_1}+\dfrac{\xi_x}{2}gQ_1^2\\ \dfrac{\xi_x Q_2 Q_3+\xi_y Q_3^2}{Q_1}+\dfrac{\xi_y}{2}gQ_1^2\end{bmatrix} \tag{34}$$

$$\hat{\mathbf{F}}=\frac{1}{J}\begin{bmatrix}\eta_x Q_2+\eta_y Q_3\\ \dfrac{\eta_x Q_2^2+\eta_y Q_2 Q_3}{Q_1}+\dfrac{\eta_x}{2}gQ_1^2\\ \dfrac{\eta_x Q_2 Q_3+\eta_y Q_3^2}{Q_1}+\dfrac{\eta_y}{2}gQ_1^2\end{bmatrix} \tag{35}$$

$$\hat{\mathbf{S}}=\frac{1}{J}\begin{bmatrix}0\\ -gQ_1\dfrac{\partial z_b}{\partial x}-\dfrac{g}{C^2}\dfrac{Q_2}{Q_1^2}\sqrt{Q_2^2+Q_3^2}\\ -gQ_1\dfrac{\partial z_b}{\partial y}-\dfrac{g}{C^2}\dfrac{Q_3}{Q_1^2}\sqrt{Q_2^2+Q_3^2}\end{bmatrix}. \tag{36}$$

The Jacobians of flux vectors are

$$\hat{\mathbf{A}}=\frac{\partial\hat{\mathbf{E}}}{\partial\hat{\mathbf{Q}}}=\begin{bmatrix}0 & \xi_x & \xi_y\\ -\dfrac{\xi_x Q_2^2+\xi_y Q_2 Q_3-gQ_1^3}{Q_1^2} & \dfrac{2\xi_x Q_2+\xi_y Q_3}{Q_1} & \dfrac{\xi_y Q_2}{Q_1}\\ -\dfrac{\xi_x Q_2 Q_3+\xi_y Q_3^2-gQ_1^3}{Q_1^2} & \dfrac{\xi_x Q_3}{Q_1} & \dfrac{\xi_x Q_2+2\xi_y Q_3}{Q_1}\end{bmatrix}. \tag{37}$$

The diagonal matrix of eigenvalues is

$$\hat{\mathbf{\Lambda}}=\begin{bmatrix}\dfrac{\xi_x Q_2+\xi_y Q_3}{Q_1} & 0 & 0\\ 0 & \dfrac{\xi_x Q_2+\xi_y Q_3+Q_1\sqrt{Q_1 g(\xi_x^2+\xi_y^2)}}{Q_1} & 0\\ 0 & 0 & \dfrac{\xi_x Q_2+\xi_y Q_3-Q_1\sqrt{Q_1 g(\xi_x^2+\xi_y^2)}}{Q_1}\end{bmatrix} \tag{38}$$

and the corresponding set of eigenvectors can be written as

$$\hat{\mathbf{E}}_\lambda=\begin{bmatrix}0 & 1 & 1\\ \xi_y & \dfrac{Q_2}{Q_1}+\dfrac{\xi_x\sqrt{(\xi_x^2+\xi_y^2)gQ_1}}{(\xi_x^2+\xi_y^2)} & \dfrac{Q_2}{Q_1}-\dfrac{\xi_x\sqrt{(\xi_x^2+\xi_y^2)gQ_1}}{(\xi_x^2+\xi_y^2)}\\ -\xi_x & \dfrac{Q_3}{Q_1}+\dfrac{\xi_y\sqrt{(\xi_x^2+\xi_y^2)gQ_1}}{(\xi_x^2+\xi_y^2)} & \dfrac{Q_3}{Q_1}-\dfrac{\xi_y\sqrt{(\xi_x^2+\xi_y^2)gQ_1}}{(\xi_x^2+\xi_y^2)}\end{bmatrix}. \tag{39}$$

The inverse of the left eigenvectors is expressed as

$$\hat{\mathbf{E}}_\lambda^{-1}=\begin{bmatrix} -\dfrac{Q_2\xi_y-\xi_xQ_3}{Q_1(\xi_x^2+\xi_y^2)} & \dfrac{\xi_y}{(\xi_x^2+\xi_y^2)} & -\dfrac{\xi_x}{(\xi_x^2+\xi_y^2)} \\ -\dfrac{\xi_yQ_3-Q_1\sqrt{(\xi_x^2+\xi_y^2)gQ_1}+\xi_xQ_2}{2Q_1\sqrt{(\xi_x^2+\xi_y^2)gQ_1}} & \dfrac{\xi_x}{2\sqrt{(\xi_x^2+\xi_y^2)gQ_1}} & \dfrac{\xi_y}{2\sqrt{(\xi_x^2+\xi_y^2)gQ_1}} \\ \dfrac{\xi_yQ_3+Q_1\sqrt{(\xi_x^2+\xi_y^2)gQ_1}+\xi_xQ_2}{2Q_1\sqrt{(\xi_x^2+\xi_y^2)gQ_1}} & -\dfrac{\xi_x}{2\sqrt{(\xi_x^2+\xi_y^2)gQ_1}} & -\dfrac{\xi_y}{2\sqrt{(\xi_x^2+\xi_y^2)gQ_1}} \end{bmatrix}. \tag{40}$$

The Jacobians of flux vectors are

$$\hat{\mathbf{B}}=\frac{\partial\hat{\mathbf{F}}}{\partial\hat{\mathbf{Q}}}=\begin{bmatrix} 0 & \eta_x & \eta_y \\ -\dfrac{\eta_xQ_2^2+\eta_yQ_2Q_3-gQ_1^3}{Q_1^2} & \dfrac{2\eta_xQ_2+\eta_yQ_3}{Q_1} & \dfrac{\eta_yQ_2}{Q_1} \\ -\dfrac{\eta_xQ_2Q_3+\eta_yQ_3^2-gQ_1^3}{Q_1^2} & \dfrac{\eta_xQ_3}{Q_1} & \dfrac{\eta_xQ_2+2\eta_yQ_3}{Q_1} \end{bmatrix}. \tag{41}$$

The diagonal matrix form of the Jacobians of flux vectors can be written as

$$\hat{\mathbf{\Gamma}}=\begin{bmatrix} \dfrac{\eta_xQ_2+\eta_yQ_3}{Q_1} & 0 & 0 \\ 0 & \dfrac{\eta_xQ_2+\eta_yQ_3+Q_1\sqrt{Q_1g(\eta_x^2+\eta_y^2)}}{Q_1} & 0 \\ 0 & 0 & \dfrac{\eta_xQ_2+\eta_yQ_3-Q_1\sqrt{Q_1g(\eta_x^2+\eta_y^2)}}{Q_1} \end{bmatrix}. \tag{42}$$

The set of eigenvectors corresponding to the eigenvalues is

$$\hat{\mathbf{F}}_\gamma=\begin{bmatrix} 0 & 1 & 1 \\ \eta_y & \dfrac{Q_2}{Q_1}+\dfrac{\eta_x\sqrt{(\eta_x^2+\eta_y^2)gQ_1}}{(\eta_x^2+\eta_y^2)} & \dfrac{Q_2}{Q_1}-\dfrac{\eta_x\sqrt{(\eta_x^2+\eta_y^2)gQ_1}}{(\eta_x^2+\eta_y^2)} \\ -\eta_x & \dfrac{Q_3}{Q_1}+\dfrac{\eta_y\sqrt{(\eta_x^2+\eta_y^2)gQ_1}}{(\eta_x^2+\eta_y^2)} & \dfrac{Q_3}{Q_1}-\dfrac{\eta_y\sqrt{(\eta_x^2+\eta_y^2)gQ_1}}{(\eta_x^2+\eta_y^2)} \end{bmatrix}. \tag{43}$$

The inverse of the set of eigenvectors is

$$\hat{\mathbf{F}}_\gamma^{-1}=\begin{bmatrix} -\dfrac{Q_2\eta_y-\eta_xQ_3}{Q_1(\eta_x^2+\eta_y^2)} & \dfrac{\eta_y}{(\eta_x^2+\eta_y^2)} & -\dfrac{\eta_x}{(\eta_x^2+\eta_y^2)} \\ -\dfrac{\eta_yQ_3-Q_1\sqrt{(\eta_x^2+\eta_y^2)gQ_1}+\eta_xQ_2}{2Q_1\sqrt{(\eta_x^2+\eta_y^2)gQ_1}} & \dfrac{\eta_x}{2\sqrt{(\eta_x^2+\eta_y^2)gQ_1}} & \dfrac{\eta_y}{2\sqrt{(\eta_x^2+\eta_y^2)gQ_1}} \\ \dfrac{\eta_yQ_3+Q_1\sqrt{(\eta_x^2+\eta_y^2)gQ_1}+\eta_xQ_2}{2Q_1\sqrt{(\eta_x^2+\eta_y^2)gQ_1}} & -\dfrac{\eta_x}{2\sqrt{(\eta_x^2+\eta_y^2)gQ_1}} & -\dfrac{\eta_y}{2\sqrt{(\eta_x^2+\eta_y^2)gQ_1}} \end{bmatrix}. \tag{44}$$

In order to show that the shallow-water equations do not have the property of homogeneity we write

$$(\hat{\mathbf{E}}_\lambda\hat{\mathbf{\Lambda}}\hat{\mathbf{E}}_\lambda^{-1})\hat{\mathbf{Q}}=\frac{1}{J}\begin{bmatrix} \xi_xQ_2+\xi_yQ_3 \\ \dfrac{\xi_xQ_2^2+\xi_yQ_2Q_3}{Q_1}+\xi_xgQ_1^2 \\ \dfrac{\xi_xQ_2Q_3+\xi_yQ_3^2}{Q_1}+\xi_ygQ_1^2 \end{bmatrix} \tag{45}$$

$$(\hat{\mathbf{F}}_\gamma\hat{\mathbf{\Gamma}}\hat{\mathbf{F}}_\gamma^{-1})\hat{\mathbf{Q}}=\frac{1}{J}\begin{bmatrix} \eta_xQ_2+\eta_yQ_3 \\ \dfrac{\eta_xQ_2^2+\eta_yQ_2Q_3}{Q_1}+\eta_xgQ_1^2 \\ \dfrac{\eta_xQ_2Q_3+\eta_yQ_3^2}{Q_1}+\eta_ygQ_1^2 \end{bmatrix}, \tag{46}$$

which are different from (34) and (35).

Nomenclature

$\hat{\mathbf{A}}$, $\hat{\mathbf{B}}$ = Jacobian matrices
$\tilde{\hat{\mathbf{A}}}$, $\tilde{\hat{\mathbf{B}}}$ = modified Jacobian matrices
$\hat{\mathbf{A}}^+$, $\hat{\mathbf{B}}^+$ = Jacobians corresponding to positive eigenvalues
$\hat{\mathbf{A}}^-$, $\hat{\mathbf{B}}^-$ = Jacobians corresponding to negative eigenvalues
a = speed of propagation (m/s)
C = Chezy constant
$\mathbf{E}$, $\mathbf{F}$, $\mathbf{Q}$, $\mathbf{S}$ = vectors in the physical domain
$\hat{\mathbf{E}}$, $\hat{\mathbf{F}}$, $\hat{\mathbf{Q}}$, $\hat{\mathbf{S}}$ = vectors in the computational domain
$\hat{\mathbf{E}}^+$, $\hat{\mathbf{F}}^+$ = split flux vector corresponding to positive eigenvalues
$\hat{\mathbf{E}}^-$, $\hat{\mathbf{F}}^-$ = split flux vector corresponding to negative eigenvalues
$\hat{\mathbf{E}}_\lambda$, $\hat{\mathbf{F}}_\gamma$ = matrices of corresponding eigenvectors
$\mathbf{e}_z$ = unit vector in the vertical direction
Fr = Froude number
g = gravitational acceleration (m/s^2)
h = film height (m)
J = Jacobian
N = number of cells
p = pressure (N/m^2)
Q_i = components of the depth-averaged variables (m/s)
Q_w = volumetric flow rate (m^3/s)
r_i = radial location of initial measurements (m)
r_o = outer radius of the disk (m)
t, τ = time (s)
U, V = depth averaged velocities (m/s)
U_c, V_c = characteristic velocities (m/s)
$\mathbf{u}$ = Cartesian velocity vector (m/s)
u, v, w = velocity components in the x, y, z-directions (m/s)
x, y, z = Cartesian coordinates (m)
z_b = reference height (m)
z_i = initial film height in experiments (m)

Greek Symbols

γ, λ = eigenvalues of the Jacobian (m/s)
δ, Δ, ∇ = finite difference operators
ϵ = error
ϕ = nonlinear limiting parameter
$\hat{\mathbf{\Lambda}}$, $\hat{\mathbf{\Gamma}}$ = diagonal matrices of eigenvalues
$\hat{\mathbf{\Lambda}}^+$, $\hat{\mathbf{\Gamma}}^+$ = diagonal matrices of positive eigenvalues
$\hat{\mathbf{\Lambda}}^-$, $\hat{\mathbf{\Gamma}}^-$ = diagonal matrices of negative eigenvalues
$\tilde{\hat{\mathbf{\Lambda}}}$, $\tilde{\hat{\mathbf{\Gamma}}}$ = diagonal matrices of modified eigenvalues
ν = kinematic viscosity (m^2/s)
ρ = density of the fluid (kg/m^3)
θ_1, θ_2 = weight function
τ_{bx}, τ_{by} = bottom shear stresses (N/m^2)
ξ, η, ζ = curvilinear coordinates (m)

Subscripts and Superscripts

i, j, k = index for the Cartesian coordinates x, y, z
max = maximum
n = index of time-step
x = x-direction, first derivative in the x-direction
y = y-direction, first derivative in the y-direction
z = z-direction
$+$ = positive eigenvalues
$-$ = negative eigenvalues

Abbreviations

CFL = Courant-Friedrich-Levy number
cfs = cubic feet per second
FVS = flux vector splitting
FDS = flux difference splitting
MUSCL = monotone upstream-centered scheme for conservation laws

References

[1] MacCormack, R. W., 1969, "The Effect of Viscosity in Hypervelocity Impact Craterings," AIAA Paper No. 69-354.
[2] Beam, R. M., and Warming, R. F., 1976, "An Implicit Finite-Difference Algorithm for Hyperbolic Systems in Conservation Law Form," Comput. Phys., **22**, pp. 87–110.
[3] Yee, H. C., 1989, "A Class of High-Resolution Explicit and Implicit Shock-Capturing Methods," technical report, von Karman Institute for Fluid Dynamics,
[4] Roe, P. L., 1981, "Approximate Riemann Solvers, Parameter Vectors, and Difference Schemes," Comput. Phys., **43**, pp. 357–372.
[5] Yee, H. C., and Harten, A., 1987, "Implicit TVD Schemes for Hyperbolic Conservation-Laws in Curvilinear Coordinates," AIAA J., **25**, pp. 266–274.
[6] Steger, J. L., and Warming, R. F., 1979, "Flux Vector Splitting of the Inviscid Gasdynamic Equation With Application to Finite Difference Methods," technical report, NASA TM-78605.
[7] Van Leer, B., 1982, "Flux-Vector Splitting for the Euler Equations," Krause E., editor, *Lecture, Notes in Physics*, E. Krause, ed., Springer, Berlin, **170**, pp. 507–512.
[8] Walters, R. W., Thomas, J. L., and Van Leer, B., 1986, "An Implicit Flux-Split Algorithm for the Compressible Euler and Navier-Stokes Equations," *Lecture Notes in Physics*, F. G. Zhuang and Y. L. Zhu, eds., Springer, Berlin, **264**, pp. 628–635.
[9] Glaister, P., 1988, "Approximate Riemann Solutions of the Shallow Water Equations," J. Hydraulic Res., **26**, pp. 293–306.
[10] Glaister, P., 1993, "Flux Difference Splitting for Open-Channel Flows," Int. J. Numer. Methods Fluids, **16**, pp. 629–654.
[11] Alcrudo, F., and Garcia-Navarro, P., 1993, "A High-Resolution Godunov-Type Scheme in Finite Volumes for the 2D Shallow-Water Equations," Int. J. Numer. Methods Fluids, **16**, pp. 489–505.
[12] Chapman, R. S., and Kuo, C. Y., 1985, "Application of the Two-Equation κ-ϵ Turbulence Model to a Two-Dimensional, Steady, Free Surface Flow Problem With Separation," Int. J. Numer. Methods Fluids, **5**, pp. 257–268.
[13] Vreugdenhill, C. B., 1993, *Numerical Methods for Shallow-Water Flows*, Kluwer, Dordrecht, Netherlands.
[14] Cunge, J., 1975, "Rapidly Varying Flow in Power and Pumping Canals," *Unsteady flow in open channels*, K. Mahmood and V. Yevjevich, eds., Water Resources Publications, Littleton, CO, pp. 539–586.
[15] Thomas, J. L., and Walters, R. W., 1985, "Upwind Relaxation Algorithms for the Navier-Stokes Equations," AIAA Paper No. 85–1501.
[16] Hirsch, C., 1990, *Numerical Computation of Internal and External Flows*, John Wiley and Sons, New York.
[17] Stoker, J. J., 1957, *Water Waves*, Wiley Interscience, New York,
[18] Sadler, C. D., and Higgins, M. S., 1963, "Radial Free Surfaces Flows," master's thesis, Massachussetts Institute of Technology, Cambridge, MA.
[19] Younus, M., and Chaudhry, M. H., 1994, "A Depth-Averaged κ-ϵ Turbulence Model for the Computation of Free Surface Flow," J. Hydraul Res., **32**(3), pp. 415–444.
[20] Hunt, J. C. R., Pacheco, J. R., Mahalov, A., and Fernando, H. J. S., 2003, "Effects of Rotation and Sloping Terrain on Fronts of Density Currents," J. Fluid Mech., (submitted).
[21] Ahmad, D., 1967, "Circular Hydraulic Jump," master's thesis, Colorado State University, Fort Collings, CO.

R. von Kaenel
Ph.D. Student
e-mail: vonkaenel@ifd.mavt.ethz.ch

N. A. Adams[1]

L. Kleiser
Professor

ETH Zurich,
Institute of Fluid Dynamics,
CH-8092 Zurich, Switzerland

J. B. Vos
Senior Research Scientist,
CFS Engineering SA,
PSE-B,
CH-1015 Lausanne, Switzerland

The Approximate Deconvolution Model for Large-Eddy Simulation of Compressible Flows With Finite Volume Schemes

The approximate deconvolution model for large-eddy simulation is formulated for a second-order finite volume scheme. With the approximate deconvolution model, an approximation of the unfiltered solution is obtained by repeated filtering, and given a good approximation of the unfiltered solution, the nonlinear terms of the Navier-Stokes equations are computed directly. The effect of scales not represented on the numerical grid is modeled by a relaxation regularization involving a secondary filter operation. A turbulent channel flow at a Mach number of $M=1.5$ and a Reynolds number based on bulk quantities of $Re=3000$ is selected for validation of the approximate deconvolution model implementation in a finite volume code. A direct numerical simulation of this configuration has been computed by Coleman et al. Overall, our large-eddy simulation results show good agreement with our filtered direct numerical simulation data. For this rather simple configuration and the low-order spatial discretization, differences between approximate deconvolution model and a no-model computation are found to be small.
[DOI: 10.1115/1.1511167]

The following article has been reprinted with corrections. It previously appeared in the Dec. 2002 issue of this publication without figure legends.

Introduction

Most flows of practical interest are turbulent, and for industrial applications it is important that these flows can be computed by numerical simulation with sufficient accuracy. However, numerical solutions of the Reynolds-averaged Navier-Stokes equations often fail to predict the proper flow behavior, in particular in cases where the flow exhibits large-scale unsteadiness, separation, or shock-turbulence interaction ([1]).

In large-eddy simulations (LES), the solution of the Navier-Stokes equations is convolved with a smoothing filter which reduces the numerical-resolution requirements for the filtered solution at the expense of a model for the resolved-scale/nonrepresented-scale interaction. Stolz and Adams [2] have developed a subgrid-scale model based on approximate deconvolution (ADM) and have demonstrated excellent performance of the model for a number of canonical flow configurations ([3,4]), including shock-turbulence interaction in a boundary layer. For flows at higher Reynolds numbers, a relaxation regularization is employed to represent the resolved-scale/nonrepresented-scale interaction. So far computations were performed with high-order (fourth-order, sixth-order) finite difference schemes and spectral schemes. Test computations with second-order finite difference schemes for isotropic turbulence have shown that the filter-cutoff wave number should be adjusted to the maximum wave number which can be considered to be well resolved by the underlying discretization scheme, employing the modified wave number concept [5]. In this paper we address the formulation of ADM for a given second-order finite volume scheme without further consideration of the resolution properties of this scheme. The objective is to test ADM for a numerical method which is being used in standard CFD design tasks of the aerospace industry.

We first introduce the governing equations and then briefly present the filtering, deconvolution and relaxation procedure. Next, we summarize the numerical method and introduce the parameters of our test case. Finally, the results of four different data sets, DNS, filtered DNS, LES with ADM, and underresolved DNS, are compared and analyzed.

Governing Equations

A flow in a plane channel with periodic boundary conditions in the streamwise ($x_1=x$) and spanwise ($x_2=y$) directions is considered. The computational domain with volume V is spanned by a Cartesian coordinate system. The flow is described by the compressible Navier-Stokes equations for an ideal gas with ratio of specific heats $\gamma=1.4$. Nondimensionalized with the wall temperature T_w, the channel half-width H, the bulk velocity $u_b=\int_V \rho u dV/(V\rho_b)$, and density $\rho_b=\int_V \rho dV/V$, the continuity, momentum and energy equations read (summation rule applies):

$$\frac{\partial \rho}{\partial t}+\frac{\partial}{\partial x_j}(\rho u_j)=0 \tag{1}$$

$$\frac{\partial}{\partial t}(\rho u_i)+\frac{\partial}{\partial x_j}(\rho u_i u_j)+\frac{\partial p}{\partial x_i}-\frac{\partial \sigma_{ij}}{\partial x_j}=-f_1\delta_{i1} \tag{2}$$

$$\frac{\partial E}{\partial t}+\frac{\partial}{\partial x_j}(E+p)u_j-\frac{\partial}{\partial x_j}(\sigma_{ij}u_i)+\frac{\partial}{\partial x_j}q_j=-f_1u_1, \tag{3}$$

with the total energy

$$E=p/(\gamma-1)+\frac{1}{2}\rho u_i u_i, \tag{4}$$

the temperature

$$T=\gamma M_0^2(p/\rho), \tag{5}$$

and the nondimensional dynamic viscosity

$$\mu(T)=T^{0.7}. \tag{6}$$

The heat fluxes and the viscous stresses are defined as

[1]Presently Professor, Technical University Dresden, Dresden, Germany.

Contributed by the Fluids Engineering Division for publication in the JOURNAL OF FLUIDS ENGINEERING. Manuscript received by the Fluids Engineering Division March 12, 2002; revised manuscript received May 31, 2002. Associate Editor: F. F. Grinstein.

$$q_j = -\frac{\mu(T)}{(\gamma-1)\mathrm{Re}\,\mathrm{Pr} M_0^2}\frac{\partial T}{\partial x_j}, \tag{7}$$

$$\sigma_{ij} = \frac{\mu(T)}{\mathrm{Re}}\left(\frac{\partial u_i}{\partial x_j}+\frac{\partial u_j}{\partial x_i}-\frac{2}{3}\delta_{ij}\frac{\partial u_k}{\partial x_k}\right), \tag{8}$$

with the Reynolds number $\mathrm{Re}=\rho_b u_b H/\mu(T_w)$, the Mach number $M_0 = u_b/\sqrt{\gamma R T_w}$, and the Prandtl number $\mathrm{Pr}=0.7$. The Kronecker symbol is used, $\delta_{ij}=1$ for $i=j$ and $\delta_{ij}=0$ otherwise. For a periodic wall-bounded flow, the addition of a driving force to the Navier-Stokes equations is necessary to compensate the wall-friction forces and to maintain a stationary flow. Following Deschamps [6], the flow is driven in the streamwise direction with a body force $f_1(t)$ adjusted to the instantaneous solution such that the total mass flow rate remains stationary. The wall boundary conditions are no-slip for the velocity and isothermal for the temperature.

Filtering Approach and Approximate Deconvolution

In most large-eddy simulation (LES) methods, filtering is performed implicitly by the projection of the equations onto the computational grid, formally including all wave numbers up to the Nyquist wave number ω_n in the solution. Since for finite difference or finite volume schemes the wave number up to which scales can be considered to be resolved is often significantly smaller than ω_n, it is desirable to suppress nonresolved solution components by application of an explicit filter operation ([5]). Even for spectral schemes the relative error at the Nyquist wave number is of order $\mathcal{O}(1)$. In the following we will distinguish between *resolved wave numbers* $|\omega|\leqslant\omega_c$, where ω_c is the primary-filter cutoff wave number, *represented wave numbers* $|\omega|\leqslant\omega_n$ which can be represented on the given mesh, and nonrepresented wave numbers $|\omega|>\omega_n$.

The governing equations of LES are obtained by applying the primary-filter operation to the Navier-Stokes equations. Any flow variable u can be decomposed as $u=\bar{u}+u'+u''$ where $\bar{u}$ represents the resolved scales, u' the represented nonresolved scales, and u'' the nonrepresented scales. The filtering operation on a domain $[\alpha\Delta, \beta\Delta]$ is defined by a convolution of the filter kernel G and the variable. We define a one-dimensional primary filter operation with compact support by

$$\bar{u}(x) = G*u = \int_{x-\beta\Delta}^{x-\alpha\Delta} G\left(\frac{x-x'}{\Delta},x\right)u(x')\frac{dx'}{\Delta}$$
$$= \int_{\alpha}^{\beta} G(z,x)u(x-\Delta z)dz, \tag{9}$$

where $z=(x-x')/\Delta$ and $\Delta=\pi h/\omega_c$ is the filter width in physical space. h is the uniform grid spacing in an equidistantly spaced computational space ξ. The mapping of x onto ξ does not need to be known explicitly. ω_c is the cutoff wave number of the primary filter, nondimensionalized with h, and $G(z,x)$ is the primary filter kernel which may depend explicitly on the location x. The extension of this one-dimensional filter to three space dimensions is obtained by applying the filter in each coordinate direction successively

$$\bar{u}(x_1,x_2,x_3) = G_1*G_2*G_3*u$$
$$= \int_{\alpha_3}^{\beta_3}\int_{\alpha_2}^{\beta_2}\int_{\alpha_1}^{\beta_1} G_1(z_1,x_1)G_2(z_2,x_2)G_3(z_3,x_3)$$
$$\times u(x_1-\Delta_1 z_1, x_2-\Delta_2 z_2, x_3-\Delta_3 z_3)dz_1 dz_2 dz_3. \tag{10}$$

The integration in this definition is discretized by an explicit quadrature, defined in one space dimension as

$$\bar{u}_i := \sum_{j=-\nu_l}^{\nu_r}\alpha_j u_{i+j} \tag{11}$$

for the grid function u_i, where $u_i = u(x_i)$. The cell centers in the finite-volume formulation are denoted as x_i. We consider discrete filters on a five-point stencil with $\nu_l+\nu_r=4$ for interior cells. A complete derivation of the coefficients α_j can be found in Refs. [3], [7]. The definition of the cutoff wave number ω_c is somewhat arbitrary for filters with smooth Fourier transform $\hat{G}(\omega)$. Here we choose the criterion $|\hat{G}(\omega_c)|=1/2$, leading to $\omega_c \approx 2/3\pi$. The represented but nonresolved scales $\omega_c < |\omega| \leqslant \omega_n$ are used to model the effect of the nonresolved scales $|\omega|>\omega_c$ on the resolved scales $|\omega|\leqslant\omega_c$. Resolved scales can be recovered by an approximate inversion of the filter (9) resulting in an approximation $u^\star$ of the unfiltered solution u. The approximate deconvolution $u^\star$ is given by applying the approximate deconvolution operator Q_N to $\bar{u}$,

$$u^\star = Q_N * \bar{u}. \tag{12}$$

Assuming that the filter G has an inverse, the inverse operator can be expanded as an infinite series of filter operators. Filters with compact transfer functions are noninvertible, but a regularized inverse operator Q_N can be obtained by truncating the series at some N, obtaining a regularized approximation ([2]) of G^{-1},

$$Q_N = \sum_{\nu=0}^{N}(I-G)^\nu \approx G^{-1} \tag{13}$$

where I is the identity operator.

Stolz et al. [3,4] found that $N=5$ was giving best results for a wide range of test cases. We therefore set $N=5$ in the following. Using (13), $u^\star$ can be computed by repeated filtering of $\bar{u}$ from

$$u^\star = Q_N*\bar{u} = \bar{u}+(\bar{u}-\bar{\bar{u}})+(\bar{u}-2\bar{\bar{u}}+\overline{\overline{\overline{u}}})+\ \ldots$$
$$= 3\bar{u}-3\bar{\bar{u}}+\overline{\overline{\overline{u}}}+\ \ldots\ . \tag{14}$$

The adaptation of the approximate deconvolution model (ADM) for a finite volume scheme is straightforward. Note that a finite volume scheme itself comprises a deconvolution when cell-face values are reconstructed from the cell averages, see, e.g., Ref. [8]. This approach which can be exploited to construct an approximate deconvolution method directly by adapting the finite volume method accordingly, is presently under investigation. Here, we treat numerical discretization and subgrid-scale modeling as separate entities and introduce ADM into the finite volume framework. For simplicity we first consider a scalar transport equation and return to the full Navier-Stokes equations later. Starting from the generic transport equation for the variable Ψ with flux function $F(\Psi)$, integrated over the computational cell V_j

$$\int_{V_j}\frac{\partial\Psi}{\partial t}dV_j + \int_{V_j}\nabla\cdot F(\Psi)dV_j = 0, \tag{15}$$

where $F(\Psi)$ is the flux, we can apply the divergence theorem so that Eq. (15) can be rewritten as

$$\int_{V_j}\frac{\partial\Psi}{\partial t}dV_j + \int_{S_j}F(\Psi)n dS_j = 0, \tag{16}$$

with n being the outward normal vector of the cell surface. On applying the filter operation to Eq. (15) and exchanging the filter operation and the volume integration one obtains, under the assumption that divergence operator and filter operator commute,

$$\int_{V_j}\frac{\partial\bar{\Psi}}{\partial t}dV_j + \int_{S_j}\overline{F(\Psi)}n dS_j = 0. \tag{17}$$

Using the approximately deconvolved solution $\Psi^\star$ of Ψ, the filtered flux term $\overline{F(\Psi)}$ can be approximated directly by replacing the unfiltered quantity Ψ by $\Psi^\star$,

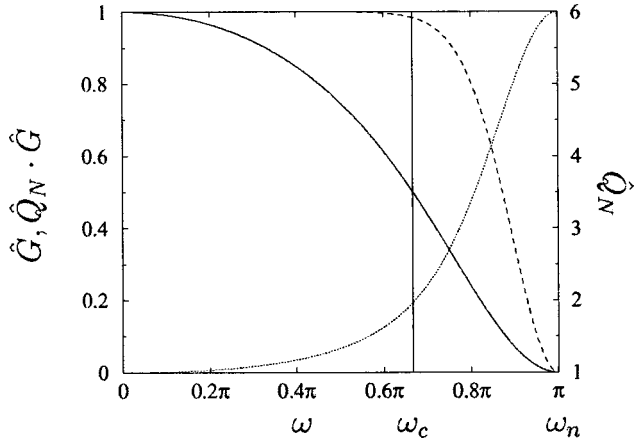

Fig. 1 Transfer functions, —— explicit primary filter for an equidistant mesh, e.g., *x* or *y* direction, · · · · approximate inverse $\hat{Q}_N$, – – – secondary filter $\hat{Q}_N \cdot \hat{G}$, for $N=5$

$$\int_{V_j} \frac{\partial \overline{\Psi}}{\partial t} dV_j + \int_{S_j} \overline{F(\Psi^\star)} n dS_j = \int_{S_j} (\overline{F(\Psi^\star)} - \overline{F(\Psi)}) n dS_j , \tag{18}$$

thus avoiding at that point the need of computing extra subgrid-scale terms.

The energy transfer to nonrepresented scales $|\omega| > \omega_n$ is modeled only partially by using $\Psi^\star$. Note that it would not be modeled at all if $\overline{\Psi}$ would be deconvolved by singular value decomposition, since the resulting Eq. (18) with $\Psi^\star$ replaced by Ψ restricted to represented scales is energy conserving. This situation corresponds to the truncated Navier-Stokes approach of Domaradzki et al. [9] without energy removal. Stolz et al. [3,4] have proposed a relaxation regularization derived from the requirement that the solution remains well-resolved within the range $|\omega| \leqslant \omega_c$. For this purpose, the integral energy of nonresolved represented scales should not increase, although energy redistribution among these scales is permitted. In order to model the energy transfer from scales $|\omega| \leqslant \omega_n$ to scales $|\omega| > \omega_n$ energy is drained from the range $\omega_c < |\omega| \leqslant \omega_n$ by subtracting a term $\chi_\Psi (I - Q_N * G)\overline{\Psi}$ from the left-hand side of the filtered differential conservation law (18). This expression, which models the nonclosed terms $\overline{F(\Psi^\star)} - \overline{F(\Psi)}$ of the right-hand side of Eq. (18), has the form of a relaxation term with a relaxation parameter $\chi_\Psi > 0$ corresponding to an inverse relaxation-time scale. Applying the finite volume discretization to the resulting equation one obtains

$$\int_{V_j} \frac{\partial \overline{\Psi}}{\partial t} dV_j + \int_{S_j} \overline{F(\Psi^\star)} n dS_j = -\int_{V_j} \chi_\Psi (I - Q_N * G) * \overline{\Psi} dV_j = -\int_{V_j} \chi_\Psi (\overline{\Psi} - \overline{\Psi}^\star) dV_j . \tag{19}$$

Since $(I - Q_N * G)$ is constructed being positive semidefinite, the relaxation term is purely dissipative. The use of the relaxation term can also be interpreted as applying a secondary filter to $\overline{\Psi}$ every $1/(\chi_\Psi \Delta t)$ time-step, Δt being the time-step of the numerical integration, which poses the approach in a relation to the truncated Navier-Stokes approach with energy removal of Domaradzki et al. [9]. The transfer function of the secondary filter $\hat{Q}_N \hat{G}$ for interior points on the equidistant mesh used in the present work is shown in Fig. 1.

To close the model without requiring an a priori parameter choice, χ_Ψ is estimated dynamically as a function of space and time. The underlying argument for determining χ_Ψ is that in order to obtain a well-resolved representation of the filtered solution no energy should accumulate during time advancement in the wave-number range $\omega_c < |\omega| \leqslant \omega_n$. The kinetic energy content of the considered wave number range can be estimated by the second-order structure function ([10,11]) applied to $\phi_\Psi = (I - Q_N * G) * \overline{\Psi}$. The discrete form of the local second-order structure function in three dimensions, which requires the value of ϕ_Ψ at the considered grid point in the computational space $\xi = (\xi_1, \xi_2, \xi_3)$ and its six next neighbors in the three computational-space coordinate directions, is given by

$$F_2(\xi, t) = \| \phi_\Psi(\xi + \mathbf{r}, t) - \phi_\Psi(\xi, t) \|^2_{||\mathbf{r}||=h} \tag{20}$$

where h is the computational-space grid spacing. Note again that the mapping of the physical space onto the computational space does not need to be known explicitly.

For an estimate of the relaxation parameter χ_Ψ we advance Eq. (19) by one Euler-forward time-step with size Δt, once using $\chi_\Psi = \chi_{\Psi 0}$ and once using $\chi_\Psi = 0$. $\chi_{\Psi 0}$ is some positive nonvanishing estimate of the parameter χ_Ψ, the value from the previous time integration step or some positive constant at time $t = 0$ for instance. The difference of the structure function $F_2(\xi, t + \Delta t)|_{\chi_\Psi = 0} - F_2(\xi, t)$ is an estimate for the integral energy generated within the time increment Δt in the range of scales with wave numbers $\omega_c < |\omega| \leqslant \omega_n$. The difference $F_2(\xi, t + \Delta t)|_{\chi_\Psi = 0} - F_2(\xi, t + \Delta t)|_{\chi_\Psi = \chi_{\Psi 0}}$ estimates how much energy would be dissipated by the relaxation term using $\chi_\Psi = \chi_{\Psi 0}$. Accordingly, χ_Ψ can be determined from

$$\chi_\Psi = \chi_{\Psi 0} \frac{F_2(\xi, t + \Delta t)|_{\chi_\Psi = 0} - F_2(\xi, t)}{F_2(\xi, t + \Delta t)|_{\chi_\Psi = 0} - F_2(\xi, t + \Delta t)|_{\chi_\Psi = \chi_{\Psi 0}}} . \tag{21}$$

In Ref. [4] this procedure is related to the requirement of no-energy accumulation in $\omega_c < |\omega| \leqslant \omega_n$. By construction, the dynamic parameter χ_Ψ is now a function of space and time. To avoid the generation of nonresolved scales due to the nonlinear product of χ_Ψ and $(I - Q_N * G) * \overline{\Psi}$, χ_Ψ is smoothed with a second-order Padé filter ([12]) whose cutoff wave number ω_c' is set to $\pi/8$. Given a time-step size Δt, an upper and a lower bound $1/100 \Delta t \leqslant \chi_\Psi \leqslant 1/\Delta t$ is imposed for numerical stability. According to previous experience, it is sufficient to update χ_Ψ every ten time-steps since it exhibits only small time variation.

Applying now the above operators to Eqs. (1), (2), and (3) we obtain the differential form of the underlying modeled conservation laws to be solved

$$\frac{\partial \overline{\rho}}{\partial t} + \frac{\partial \overline{(\rho u_j)^\star}}{\partial x_j} = -\chi_\rho (\overline{\rho} - \overline{\rho}^\star) \tag{22}$$

$$\frac{\partial \overline{\rho u_i}}{\partial t} + \overline{\frac{\partial}{\partial x_j} (\rho u_i u_j)^\star + \frac{\partial \check{p}^\star}{\partial x_i} - \frac{\partial \check{\sigma}^\star_{ij}}{\partial x_j}} = -f_1(\overline{u}) \delta_{i1} - \chi_{\rho u} (\overline{\rho u_i} - \overline{\rho u_i}^\star), \tag{23}$$

$$\frac{\partial \overline{E}}{\partial t} + \overline{\frac{\partial}{\partial x_j} (E^\star + \check{p}^\star) u_j^\star - \frac{\partial}{\partial x_j} (\check{\sigma}^\star_{ij} u_i^\star) + \frac{\partial}{\partial x_j} \check{q}_j^\star} = -f_1(\overline{u}) \overline{u}_1 - \chi_E (\overline{E} - \overline{E}^\star), \tag{24}$$

for $i, j = 1,2,3$. The superscript $\check{\bullet}^\star$ indicates that the quantities are computed from the deconvolved solution, e.g., $\check{p}^\star = (\gamma - 1)(E^\star - \rho^\star u_i^\star u_i^\star / 2)$.

$f_1(\overline{u})$ means that the forcing term is computed with the filtered velocity. Note that we use the same relaxation parameter for the three momentum equations. To this set of equations the finite volume method is applied as discretization scheme as in Eq. (19).

Numerical Method

The approximate deconvolution model (ADM) was implemented in a CFD code using a cell centered second-order finite volume method ([13–15]). The particular form of the convective terms influences the stability of the numerical scheme. We use the

Table 1 Parameters of the numerical simulation

	Coleman et al. [18]	DNS	DNS Filtered	ADM	No-Model
L_x/H	4π	4π	4π	4π	4π
L_y/H	$4\pi/3$	$4\pi/3$	$4\pi/3$	$4\pi/3$	$4\pi/3$
L_z/H	2	2	2	2	2
n_x	144	288	72	72	72
n_y	80	160	40	40	40
n_z	119	237	60	60	60
M_0	1.5	1.5	-	1.5	1.5
Re	3000	3000	-	3000	3000
u_b	1	1	-	1	1
ρ_b	1	1	-	1	1

skew-symmetric form of the convective term ([16]) instead of the divergence form. In this case the nonlinear flux term is decomposed as

$$F_l^{\text{nonlin}} = \frac{1}{2}\left(\frac{\partial u_l u_m}{\partial x_m} + u_m \frac{\partial u_l}{\partial x_m}\right). \tag{25}$$

Viscous terms are integrated with a second-order centered scheme on a shifted control volume, see Ref. [17].

Time integration is performed by an explicit four-stage Runge-Kutta scheme which is formally fourth-order accurate for linear equations but drops to second-order accuracy for a general nonlinear equation. The Courant-Friedrichs-Lewy (CFL) number is set constant and an adaptive time-stepping procedure based on a linear stability analysis computes the maximum time-step ([14]).

Application to Channel Flow

As a test case the compressible channel flow as computed by Coleman et al. [18] was considered for two reasons. First, the test case requires a correct near-wall subgrid-scale treatment. Second, reference data are available in the literature, see Ref. [19]. Three different simulations have been performed: a direct numerical simulation (DNS), a no-model computation or underresolved DNS on the same mesh as the large-eddy simulation (LES), and a LES with the approximate deconvolution model (ADM). In contrast to traditional LES where filtering is the result of the projection of the solution onto the discrete mesh, the filter operator in ADM is known explicitly and allows for filtering of the DNS data with the same filter for validation of the LES. The main parameters of the simulation are summarized in Table 1. L_x, L_y, L_z are the extents of the integration domain in the streamwise, spanwise, and the wall-normal coordinate directions, respectively, and n_x, n_y, n_z are the corresponding numbers of grid points. All four simulations have the same Reynolds number Re and Mach number M_0. The forcing term is adjusted to maintain a constant mass flow. The grid spacing is constant in the streamwise and spanwise directions and is stretched with a hyperbolic tangent function in the wall-normal direction. Except for the DNS, all simulations were initialized with a laminar profile with a random velocity disturbance superimposed in each of the three coordinate directions. The initial density was $\rho(t=0)=1$ and the initial temperature was computed according to the laminar distribution $T(t=0)=1+1/3(\gamma-1)\text{Pr}M_0^2 u_{1\,\max}(1-(z-1)^4)$ where $u_{1\,\max}$ is the maximum nondimensional laminar velocity which is equal to 1.5. To save computational time, the DNS simulation was started from a turbulent profile obtained with the coarse-grid no-model computation, interpolated to the fine DNS mesh. The boundary conditions are periodic in the two homogeneous directions. Isothermal conditions with wall temperature $T_w=1$ and no-slip conditions are prescribed at the walls.

Results

Starting from the disturbed laminar solution, the computation is advanced for all large-eddy simulation (LES) cases for 380 time units $t_b = tu_b/H$. Transition from laminar to turbulent flow is observed between time $t_b=50$ and $t_b=120$. Because certain quantities, such as the temperature, attain a stationary state only rather slowly, the statistics presented here are sampled between time $t_b=300$ to $t_b=380$ with a sampling interval of 0.2. The statistics of the direct numerical simulation (DNS) were obtained after an initial transient of $t_b=160$ during 140 time units with a sampling interval of 1. The filtered DNS data were computed from 29 DNS samples of the DNS evenly spaced between time $t_b=160$ and $t_b=300$. The number of samples was found to be sufficient for the computed statistics to be symmetric across the channel halves. The filtered DNS data are generated by interpolating the DNS to the LES mesh and subsequent filtering. All statistics presented here are averaged over wall-parallel planes and over both channel halves.

Figure 2 gives a qualitative impression of the instantaneous flow close to the wall. Shown are iso-contours of the wall-normal vorticity in a near-wall plane. Clearly visible are the near-wall streak structures. Each simulation represents another realization of this flow, so that the agreement of these flow snapshots can only be qualitative.

In Table 2 averaged flow quantities measured at the wall and at the channel center are given. There are slight differences between the DNS of Coleman et al. and our DNS results. In our case the friction-velocity Reynolds number $\text{Re}_\tau = \text{Re}\, u_\tau \rho_w/(u_b\rho_b)$ is smaller and the centerline velocity u_c is larger. Also, a larger centerline temperature T_c and a smaller centerline density ρ_c are observed. These differences may be due to the different numerical method, but may also be related to differences in the implementation of the forcing f_1. For the mean flow variables the agreement between filtered DNS and DNS is good which confirms that the constructed filter leaves the mean flow essentially unchanged even on a distorted mesh. This requirement leads to moment conditions in real space on the filter as shown in Ref. [3]. A comparison of

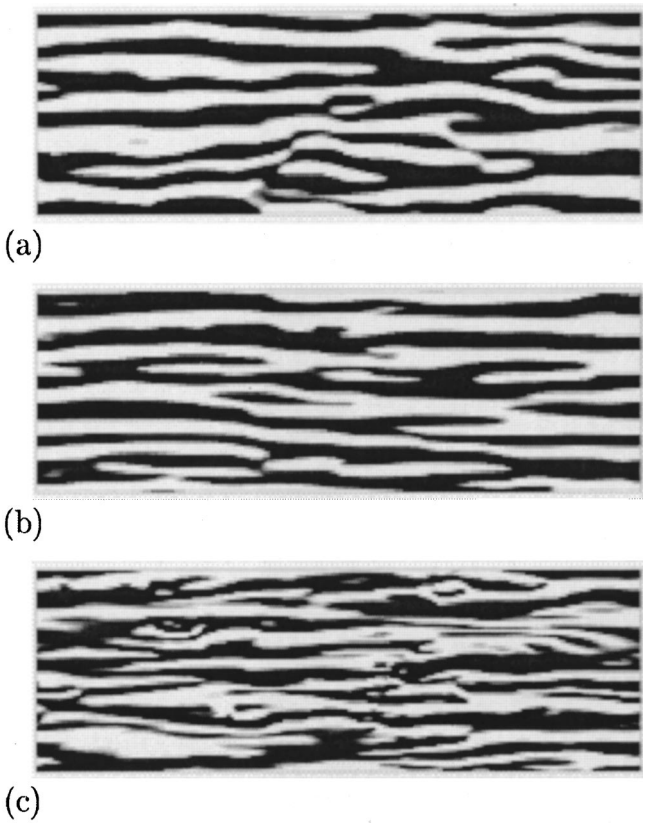

Fig. 2 Contours of instantaneous wall-normal vorticity ω_z in (x,y)-plane at $z^+\approx 10$, (*a*) ADM, (*b*) no-model, (*c*) DNS; $\omega_z \geq 0$ in light regions, $\omega_z < 0$ in dark regions

Table 2 Mean flow variables

	Coleman et al. [18]	DNS	DNS Filtered	ADM	No-Model
Re_τ	222	216	214	224	217
τ_w	12.12	11.41	11.35	12.44	11.61
u_τ	0.0545	0.0529	0.0530	0.0554	0.0534
Δ_x^+	19	9.4	37	39	38
Δ_y^+	12	5.6	22	23	23
$\Delta_z^+\|_w$	0.1	0.38	1	1	1
u_c	1.16	1.18	1.18	1.18	1.19
T_c	1.378	1.39	1.39	1.40	1.41
ρ_c	0.980	0.977	0.977	0.979	0.977
ρ_w	1.355	1.359	1.359	1.353	1.360

approximate deconvolution model (ADM) results with filtered DNS shows that all quantities of Table 2 are within a reasonable error margin, e.g., the Reynolds number Re_τ differs by 4.7% from the filtered DNS.

We find that the near-wall velocity gradient is slightly overpredicted by the LES, resulting in a larger Reynolds number Re_τ. The centerline velocity u_c is not affected by the near-wall velocity gradient since the forcing f_1 is adjusted such that the initial mass-flux is kept constant throughout the simulation. We find that probably due to the different initial conditions for the DNS and the LES, the stationary value of the mass flux differs by about 0.5%. As shown in Figs. 3 and 4, the mean velocity, density and temperature are predicted accurately. The temperature profile computed with the ADM shows a better agreement with the filtered DNS than the no-model computation with the DNS. For the velocity profile, a steeper slope near the wall can be seen which is responsible for the larger Reynolds number Re_τ with ADM. A similar overprediction of u_τ is responsible for the difference of the mean streamwise velocity profile in wall units between ADM and filtered DNS in the outer layer as can be seen from the van Driest transformed profiles $\langle u_{VD}\rangle^+$ (Fig. 4(*b*)) which are computed as

$$\langle u_{VD}\rangle^+ = \int_0^{\langle u\rangle^+} \sqrt{\frac{\overline{\rho}}{\rho_w}}\, d\langle u\rangle^+. \tag{26}$$

The von Karman constant is, however, predicted accurately. Interesting are the comparably good results obtained with the no-model computations. For the velocity fluctuations and Reynolds stress (Fig. 5 and 6) trends are somewhat more difficult to determine. Generally, ADM results show a similarly good agreement with the filtered DNS data as the no-model computation does with the DNS.

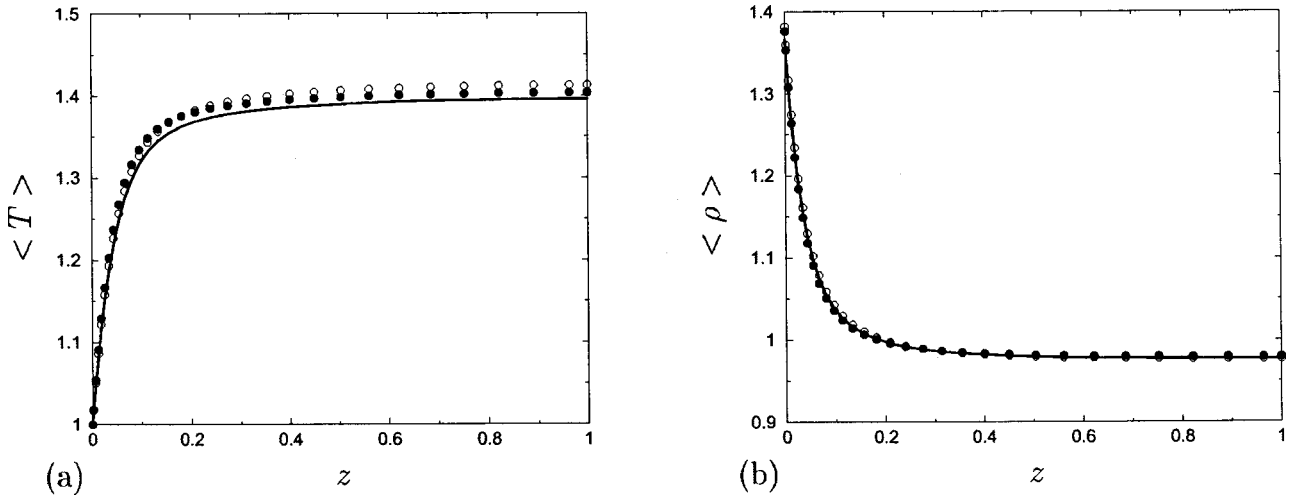

Fig. 3 (*a*) Mean temperature profile, (*b*) mean density profile, ——DNS, ● ADM, —— filtered DNS, ○ no-model

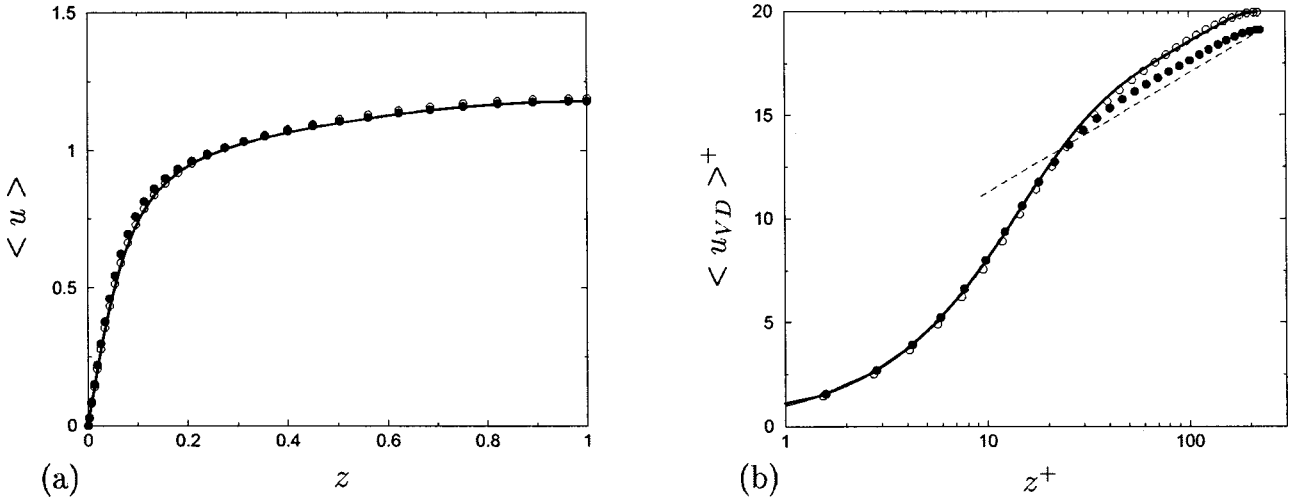

Fig. 4 Mean velocity profile, (*a*) linear plot, (*b*) van Driest transformed logarithmic plot, —— DNS, ● ADM, —— filtered DNS, ○ no-model, – – – 2.5 ln z^++5.5

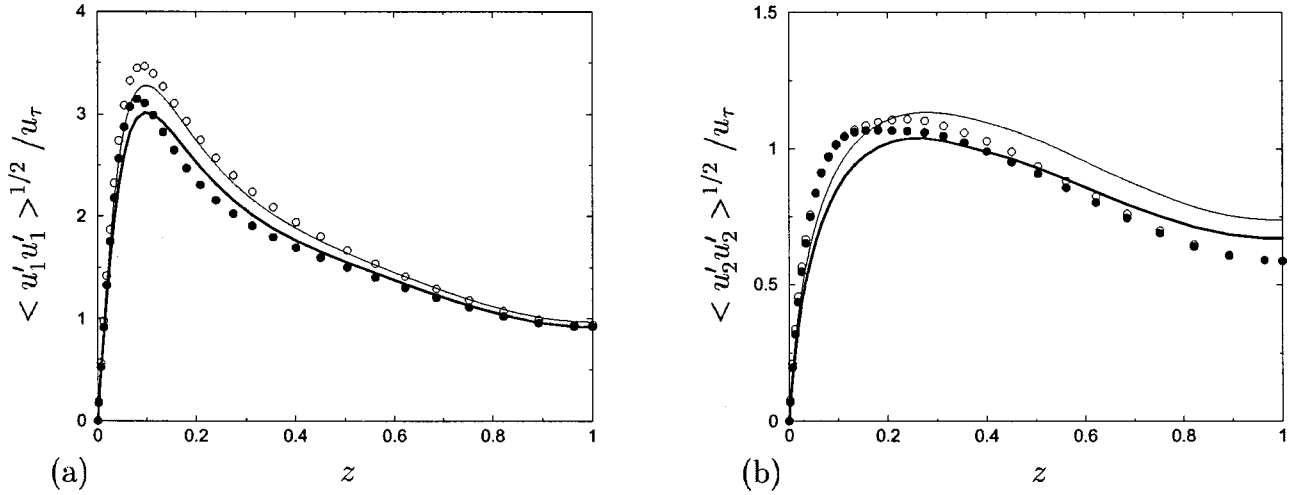

Fig. 5 Velocity fluctuations, (*a*) streamwise velocity, (*b*) spanwise velocity, —— DNS, ● ADM, —— filtered DNS, ○ no-model

Lenormand et al. [19] recently have evaluated several subgrid-scale (SGS) models for the same channel flow configuration. They discretized the convective terms in skew-symmetric form with a fourth-order finite difference scheme whereas the diffusive terms were discretized with a second-order scheme. Six different subgrid-scale models were tested on a coarse and a fine mesh (only these latter results will be considered here). Different from our computations, the streamwise extent of the computational domain was only of 2π. The number of grid points in the wall-normal direction was two times larger ($n_z = 119$) than in our case and the spanwise number of grid points was 3/2 times larger. Two of the tested SGS models are based on the Smagorinsky model, whereas the four others are based on a newly proposed mixed scale model, which estimates the subgrid-scale kinetic energy by means of a test filter and scale-similarity arguments. Linear hybridization with a Bardina-type model ([20,21]) is also considered, together with the use of a turbulent scale selection function. A priori tests suggest the use of the hybrid models, and a comparison of these models with the DNS data (nonfiltered) of Coleman et al. [18] shows results of similar quality as ours. The mean quantities are predicted accurately except for the temperature where, as in our case, the LES slightly overpredicts the temperature in the channel center. Clear trends for the velocity fluctuations and the Reynolds stress are also difficult to determine, but differences in the peak magnitude and location are visible. We can conclude that even with a lower order numerical scheme and on a coarser mesh, ADM gives results of similar quality as other SGS models on finer meshes with higher-order schemes.

Conclusions

The approximate deconvolution model was formulated to be used with a second-order finite volume method. The convective terms are discretized in their skew-symmetric form using a second-order centered scheme while the viscous terms are computed using a second-order scheme on a shifted control volume. Time integration is performed with a four-stage Runge-Kutta method. Compared to other channel flow large-eddy simulation (LES) with similar numerical discretizations, the mesh used here is coarser up to a factor of two in the wall-normal direction and of 2/3 in the spanwise direction. The model is based on an approximate deconvolution of the filtered quantities by a truncated series expansion of the inverse filter. This approximation is used to compute the nonlinear terms in the Navier-Stokes equations avoiding the need to compute subgrid-scale terms explicitly, except for a relaxation term. A relaxation term models the resolved-scale/nonrepresented-scale interaction by draining energy from the range of nonresolved represented scales $\omega_c < |\omega| \leq \omega_n$. The ap-

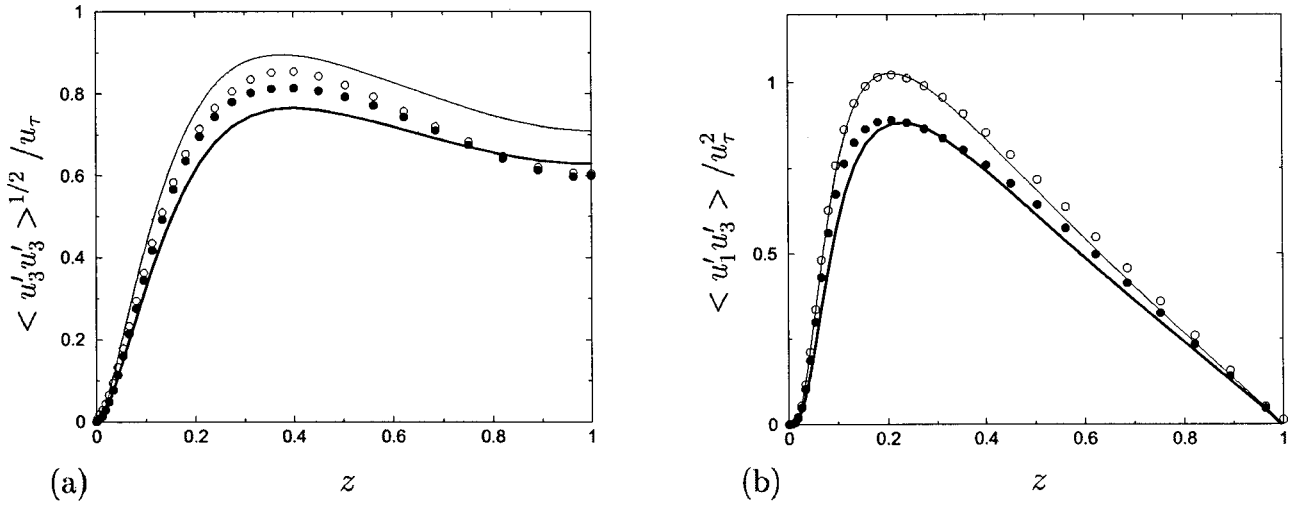

Fig. 6 (*a*) Velocity fluctuations in wall-normal direction, (*b*) Reynolds-stress, —— DNS, ● ADM, —— filtered DNS, ○ no-model

proximate deconvolution part alone of the approximate deconvolution model (ADM) is a generalized scale-similarity or tensor diffusivity model which can both be cast as special cases of ADM ([2,3]). It shares the advantages and disadvantages of these models: on the one hand a good prediction of inhomogeneous turbulent flows, on the other hand an insufficient modeling of nonrepresented scales. To cope with the latter, the relaxation term has been formulated.

Validation of the implemented model was performed for the case of a supersonic isothermal-wall channel flow. A good agreement between filtered direct numerical simulation (DNS) and LES was found for the mean flow. For the turbulence statistics, the no-model results are of the same quality as the ones with ADM. Since our observations were quite different when comparing no-model coarse-grid computations and LES with ADM for incompressible channel flow using a spectral method ([3]), we believe that the main source of error in the ADM simulations with the present primary-filter choice does not come from the subgrid-scale model but rather from the numerical discretization. Similar observations were made by Mossi [22] and Garnier et al. [23] who also found that the effect of different subgrid-scale models employed with the present numerical method was rather small. Filtering of the no-model computation would probably give results very close to ADM which suggests a small influence of the model in this particular case. Considering, however, the already good quality of the no-model computation, the ADM results can be seen positively compared to other subgrid-scale models which proved even to deteriorate results ([22]). The interplay between the numerical discretization and the subgrid-scale model has not been investigated further in the frame of this work and we refer to Ref. [16] for an analysis of the skew-symmetric form of the convective fluxes and to Stolz et al. [24] for an analysis of the effect of the discretization order on ADM.

The good results of the no-model computations can be attributed to the particular form of the truncation error induced by the skew-symmetric formulation ([16]) of the convective fluxes and to the relatively simple channel flow configuration considered here. No-model coarse-grid computations with the divergence form of the convective terms were found to be unstable for the channel flow—ADM remained stable but the results were slightly less accurate. No-model computations of more complex flows such as shock-turbulence interaction were found to be unstable. In this case the regularizing effect of the skew-symmetric form is insufficient and the benefit of ADM, providing a unified modeling of turbulent and nonturbulent subgrid scales (shocks) ([4]), should be more clearly visible.

Acknowledgments

The authors would like to acknowledge Benjamin Rembold (ETH), Dr. Steffen Stolz (ETH), and Prof. Michel Deville (EPFL) for stimulating discussions. Computations were performed on the NEC-SX5 of the Swiss Center of Scientific Computing.

References

[1] Dolling, D. S., 2001, ''Fifty Years of Shock-Wave/Boundary-Layer Interaction Research: What Next?'' AIAA J., **39**, p. 1517.
[2] Stolz, S., and Adams, N. A., 1999, ''An Approximate Deconvolution Procedure for Large-Eddy Simulation,'' Phys. Fluids, **11**, pp. 1699–1701.
[3] Stolz, S., Adams, N. A., and Kleiser, L., 2001, ''An Approximate Deconvolution Model for Large-Eddy Simulation With Application to Incompressible Wall-Bounded Flows,'' Phys. Fluids, **13**, pp. 997–1015.
[4] Stolz, S., Adams, N. A., and Kleiser, L., 2001, ''An Approximate Deconvolution Model for Large-Eddy Simulations of Compressible Flows and Its Application to Shock-Turbulent-Boundary-Layer Interaction,'' Phys. Fluids, **13**, pp. 2985–3001.
[5] Stolz, S., Adams, N. A., and Kleiser, L., 2000, ''LES of Shock-Boundary Layer Interaction With the Approximate Deconvolution Model,'' *Advances in Turbulence, Proceedings of the 8th European Turbulence Conference*, C. Dopazo et al., eds., CIMNE, Barcelona, pp. 715–718.
[6] Deschamps, V., 1988, ''Simulation Numérique de la Turbulence Inhomogène Incompressible dans un Ecoulement de Canal Plan,'' ONERA, TR 1988-5, Châtillon, France.
[7] Stolz, S., 2000, ''Large-Eddy Simulation of Complex Shear Flows Using an Approximate Deconvolution Model,'' Diss. ETH No. 13861.
[8] Adams, N. A., 2001, ''The Role of Deconvolution and Numerical Discretization in Subgrid-Scale Modeling,'' *Direct and Large-Eddy Simulation IV*, B. Geurts, R. Friedrich, and O. Métais, eds., Kluwer, Dordrecht, The Netherlands.
[9] Domaradzki, J. A., Loh, K. C., and Yee, P. P., 2001, ''Large Eddy Simulations Using the Subgrid-Scale Estimation Model and Truncated Navier-Stokes Dynamics,'' submitted for publication.
[10] Lesieur, M., and Métais, O., 1996, ''New Trends in Large-Eddy Simulations of Turbulence,'' Annu. Rev. Fluid Mech., **28**, p. 45.
[11] Batchelor, G. K., 1953, *The Theory of Homogeneous Turbulence*, Cambridge University Press, Cambridge, UK.
[12] Lele, S. K., 1992, ''Compact Finite-Difference Schemes With Spectral-Like Resolution,'' J. Comput. Phys., **103**, p. 16.
[13] Jameson, A., Schmidt, W., and Turkel, E., ''Numerical Solution of the Euler Equations by Finite-Volume Methods Using Runge-Kutta Time Stepping Schemes,'' AIAA Paper No. 81-1259, July.
[14] Vos, J. B., Leyland, P., Lindberg, P. A., van Kemenade, V., Gacherieu, C., Duquesne, N., Lotstedt, P., Weber, C., Ytterström, A., and Saint Requier, C., 2000, ''NSMB Handbook,'' Technical Report 4.5, EPF Lausanne, KTH, CERFACS, Aérospatiale, SAAB, EPF Lausanne, Switzerland.
[15] Vos, J. B., Rizzi, A. W., Corjon, A., Chaput, E., and Soinne, E., 1988, ''Recent Advances in Aerodynamics Inside the NSMB (Navier-Stokes Multi-Block) Consortium,'' AIAA Paper No. AIAA-98-0225.
[16] Ducros, F., Laporte, F., Soulères, T., Guinot, V., Moinat, P., and Caruelle, B., 2000, ''High-Order Fluxes for Conservative Skew-Symmetric-Like Schemes in Structured Meshes: Application to Compressible Flows,'' J. Comput. Phys., **161**, pp. 114–139.
[17] Peyret, R., and Taylor, T. D., 1983, *Computational Methods for Fluid Flows*, Springer-Verlag, New York.
[18] Coleman, G. N., Kim, J., and Moser, R. D., 1995, ''A Numerical Study of Turbulent Supersonic Isothermal-Wall Channel Flow,'' J. Fluid Mech., **305**, pp. 159–183.
[19] Lenormand, E., Sagaut, P., Ta Phuoc, L., and Comte, P., 2000, ''Subgrid-Scale Models for Large-Eddy Simulations of Compressible Wall Bounded Flows,'' AIAA J., **38**, pp. 1340–1350.
[20] Bardina, J., Ferziger, J. H., and Reynolds, W. C., 1983, ''Improved Turbulence Models Based on Large-Eddy Simulation of Homogeneous, Incompressible, Turbulent Flows,'' Thermosciences Div., Rept. TF-19, Department of Mechanical Engineering, Stanford University, Stanford, CA.
[21] Bardina, J., Ferziger, J. H., and Reynolds, W. C., 1980, ''Improved Subgrid Scale Models for Large-Eddy Simulation,'' AIAA J., **80**, p. 1357.
[22] Mossi, M., 1999, ''Simulation of Benchmark and Industrial Unsteady Compressible Turbulent Fluid Flows,'' Thèse EPFL No. 1958.
[23] Garnier, E., Mossi, M., Sagaut, P., Comte, P., and Deville, M., 1999, ''On the Use of Shock-Capturing Schemes for Large-Eddy Simulation,'' J. Comput. Phys., **153**, pp. 273–311.
[24] Stolz, S., Adams, N. A., and Kleiser, L., 2002, ''The Approximate Deconvolution Model for Compressible Flows: Isotropic Turbulence and Shock-Boundary-Layer Interaction,'' R. Friedrich and W. Rodi, eds., *Advances in LES of Complex Flows*, Kluwer, Dordrecht, The Netherlands.

Journal of Fluids Engineering

Technical Briefs

Exact Solution of the Navier-Stokes Equations for the Fully Developed, Pulsating Flow in a Rectangular Duct With a Constant Cross-Sectional Velocity[1]

S. Tsangaris
e-mail: sgt@fluid.mech.ntua.gr

N. W. Vlachakis

Department of Mechanical Engineering, National Technical University of Athens, Fluids Section, 15710 Zografou, Athens, Greece

The Navier-Stokes equations have been solved in order to obtain an analytical solution of the fully developed laminar flow in a duct having a rectangular cross section with two opposite equally porous walls. We obtained solutions both for the case of steady flow as well as for the case of oscillating pressure gradient flow. The pulsating flow is obtained by the superposition of the steady and oscillating pressure gradient solutions. The solution has applications for blood flow in fiber membranes used for the artificial kidney. [DOI: 10.1115/1.1537250]

Introduction

The velocity distribution for the laminar, developed, steady flow in a duct with rectangular cross section has been given by J. V. Boussinesq (1914), as referred to in Part II (Chap. 2) of the excellent reviews of H. L. Dryden et al. [1] and R. Berker [2].

Laminar, developed, oscillating flow in straight ducts with a constant cross section and impermeable wall is treated in the literature for cases between parallel plates, [2], and for a duct of rectangular cross section, [3–5].

In the bibliography only a small number of exact solutions of the Navier-Stokes equations exist, concerning steady and periodic flow in ducts with porous walls. An analytic solution has been given by A. S. Bearman [6] for the steady flow between parallel walls with porous walls, and constant velocities of the imposed suction and injection. C. Y. Wang [7] extended the work of A. S. Bearman with an analytic solution for the case of the pulsating flow in a porous channel between parallel walls. An analytical solution of the steady and oscillating flow in the straight duct with rectangular cross section and porous walls is sought in the present paper and is successfully given in a series form.

Methodology and Solution

As governing equations the Navier-Stokes equations, for unsteady flow of an incompressible fluid of constant viscosity, are used as a system with the continuity equation, both written in cartesian coordinates. We seek the analytical solution for both steady and oscillating flow conditions for the case of a straight duct with rectangular cross section $(2a\times 2b)$, having porous the two opposite walls $(x=\pm a)$. By assuming a constant transverse velocity component U in the x-direction, due to the porosity of the walls and a vanishing velocity component in the y-direction $u=U$, $v=0$, the continuity equation is satisfied when developed flow conditions across the z-axis of the straight duct are imposed: $w=w(x,y,t)$. We are interested here in the cases of the flow due to an oscillating pressure gradient:

$$\frac{1}{\rho}\frac{\partial p}{\partial z}=-\mathrm{Pe}^{i\omega t}. \tag{1}$$

P is the imaginary amplitude of the imposed pressure gradient while ω is the cyclic frequency of the oscillating pressure gradient. For $\omega=0$, Eq. (1) leads to the case of steady flow solution.

For the w-component of the velocity, using the corresponding Navier-Stokes equation, the following partial differential equation should be satisfied:

$$\beta^2\frac{\partial\tilde{w}}{\partial\tilde{t}}+\mathrm{Re}\,\frac{\partial\tilde{w}}{\partial\tilde{x}}=e^{i\tilde{t}}+\left(\frac{\partial^2\tilde{w}}{\partial\tilde{x}^2}+\frac{\partial^2\tilde{w}}{\partial\tilde{y}^2}\right). \tag{2}$$

The dimensionless variables to be introduced are the following:

$$\tilde{x}=\frac{x}{b},\quad \tilde{y}=\frac{y}{b},\quad \tilde{t}=t\omega,\quad \lambda=\frac{a}{b},\quad \tilde{w}=\frac{w}{Pb^2}\nu,$$

$$\beta=b\left(\frac{\omega}{\nu}\right)^{1/2},\quad \mathrm{Re}=\frac{Ub}{\nu}. \tag{3}$$

β is the reduced frequency and Re the cross flow Reynolds number.

The boundary conditions that have to be fulfilled are the nonslip condition at the walls of the rectangular cross section for the w component of the velocity:

$$\tilde{w}(\pm\lambda,\tilde{y},\tilde{t})=0, \tag{4a}$$

$$\tilde{w}(\tilde{x},\pm 1,\tilde{t})=0. \tag{4b}$$

In order to define periodic and steady solutions we assume that $\tilde{w}$ is periodic so that

$$\tilde{w}(\tilde{x},\tilde{y},\tilde{t})=\tilde{W}(\tilde{x},\tilde{y})e^{i\tilde{t}}. \tag{5}$$

[1]In memory of Athanassios Fidas.

Contributed by the Fluids Engineering Division for publication in the JOURNAL OF FLUIDS ENGINEERING. Manuscript received by the Fluids Engineering Division Sept. 28, 2001; revised manuscript received Sept. 24, 2002. Associate Editor: I. Celik.

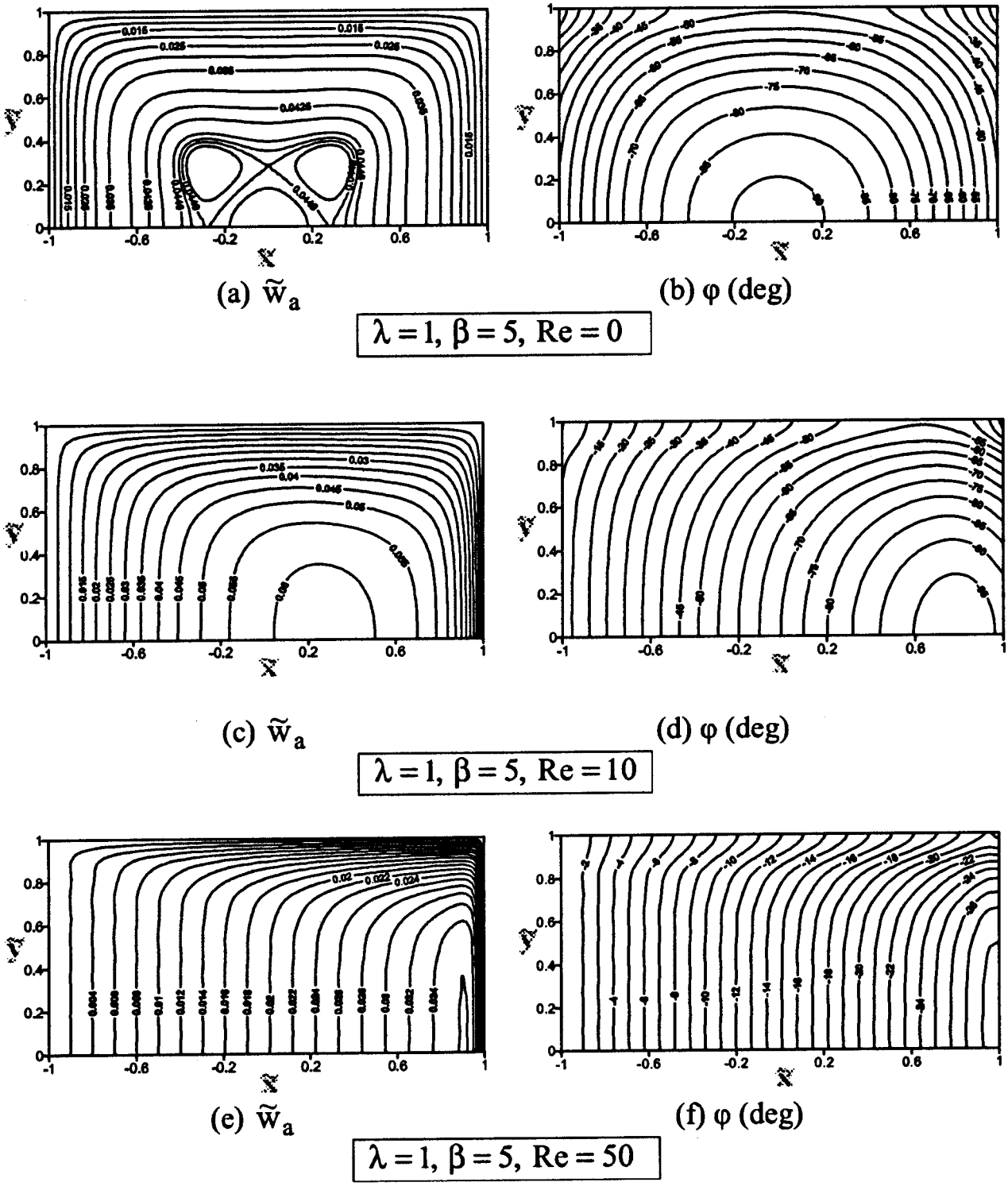

Fig. 1 Iso-amplitude $\tilde{w}_a$ (left) and iso-phase angle φ (right) plots of the velocity in the cross section of a square duct (λ=1), for oscillating flow with a reduced frequency β=5 and for three different Reynolds numbers of the cross flow (Re=0,10,50)

Equation (2) together with Eq. (5) reduces to a nonhomogeneous Helmholtz equation. The boundary conditions for $\tilde{W}$ result by using the boundary conditions for the velocity (4) and the equation for oscillating flow assumption (5).

For Eq. (2), the analytical solution, which satisfies the boundary conditions (4), can be determined by using first a Fourier series analysis of $\tilde{W}$ for $\tilde{y}$. This expansion should satisfy the symmetry of the solution for the plane x-z, as well as the boundary condition (4*b*) for $\tilde{W}$ at $\tilde{y}=\pm 1$. The Fourier series expansion is $\tilde{W}(\tilde{x},\tilde{y})=\Sigma_{n=0}^{\infty}A_n f_n(\tilde{x})\cos(2n+1/2\pi\tilde{y})$. The functions $f_n(\tilde{x})$ then satisfy a nonhomogeneous ordinary differential equation with constant coefficients. The solutions of the above equation can be obtained as the sum of a partial solution and the solution of the homogeneous differential equation. By using the boundary condi-

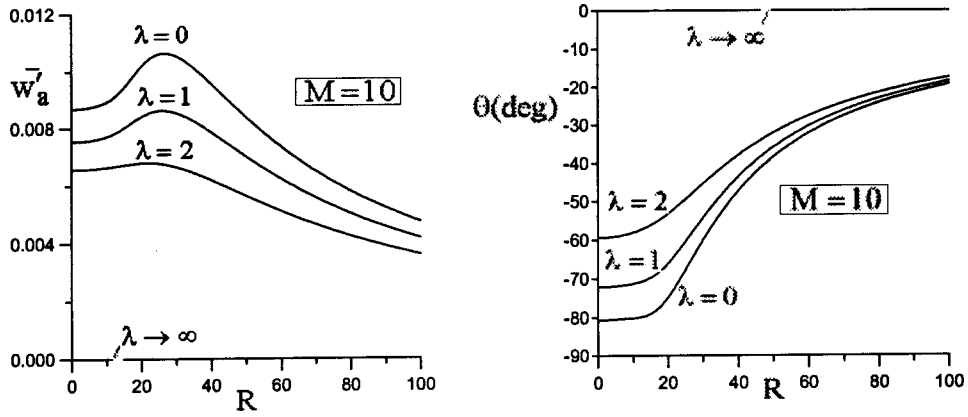

Fig. 2 Mean over the rectangular cross section amplitude $\bar{w}'_a$ (left) and phase angle θ (right) of the velocity as function of the cross flow Reynolds number R, for four different values of the aspect ratio ($\lambda\to 0.$, $\lambda=1$, $\lambda=2$, $\lambda\to\infty$) and for the value of the reduced frequency $M=10$

tions (4*a*) for $\tilde{W}$ at $\tilde{x}=\pm\lambda$, the final expression for the solution of $\tilde{W}$ is obtained:

$$\tilde{W}(\tilde{x},\tilde{y})=\frac{4}{\pi}\sum_{n=0}^{\infty}\frac{(-1)^n}{(2n+1)p^2}\times\left\{1+\frac{1}{\sinh(D\cdot\lambda)}\left[e^{\frac{\mathrm{Re}+D}{2}\tilde{x}}\sinh\left(\frac{\mathrm{Re}-D}{2}\lambda\right)-e^{\frac{\mathrm{Re}-D}{2}\tilde{x}}\sinh\left(\frac{\mathrm{Re}+D}{2}\lambda\right)\right]\right\}\cos\left(\frac{2n+1}{2}\pi\tilde{y}\right)\qquad(6)$$

where

$$p^2=i\beta^2+\left(\frac{2n+1}{2}\pi\right)^2,\quad D=(\mathrm{Re}^2+4p^2)^{1/2}.\qquad(7)$$

We have to multiply the former expression of $\tilde{W}$ by $e^{i\omega t}$ in order to determine the imaginary expression of the dimensionless velocity component $\tilde{w}$.

For a periodic imposed pressure gradient of the form

$$-\frac{1}{\rho}\frac{\partial p}{\partial z}=P\cos(\omega t),\qquad(8)$$

the resulting periodic velocity is

$$\tilde{w}=\tilde{w}_a\cos(\omega t+\varphi),\qquad(9)$$

where $\tilde{w}_a(\tilde{x},\tilde{y})$ is the amplitude and $\varphi(\tilde{x},\tilde{y})$ the phase angle resulting from the expression of $\tilde{W}(\tilde{x},\tilde{y})$ as follows:

$$\tilde{w}_a=(\tilde{W}_r^2+\tilde{W}_i^2)^{1/2},\quad \varphi=\arctan\frac{\tilde{W}_i}{\tilde{W}_r}.\qquad(10)$$

$\tilde{W}_r$, $\tilde{W}_i$ are the real and the imaginary parts of the expression of $\tilde{W}$.

The defined analytic solution of the problem (6) contains both the oscillatory as well as the steady solution of the problem. The steady solution can be obtained by taking the limit of the expression for $\beta\to 0$. The steady-state solution is obtained for $\beta=0$ and has the following form:

$$\tilde{w}(\tilde{x},\tilde{y})=\frac{8}{\pi^3}\sum_{n=0}^{\infty}\frac{(-1)^n}{(2n+1)^3}\times\left\{1+\frac{1}{\sinh(D\cdot\lambda)}\left[e^{\frac{\mathrm{Re}+D}{2}\tilde{x}}\sinh\left(\frac{\mathrm{Re}-D}{2}\lambda\right)-e^{\frac{\mathrm{Re}-D}{2}\tilde{x}}\sinh\left(\frac{\mathrm{Re}+D}{2}\lambda\right)\right]\right\}\cos\left(\frac{2n+1}{2}\tilde{x}\tilde{y}\right)\qquad(11)$$

with

$$D=\left(\mathrm{Re}^2+\left(\frac{2n+1}{2}\pi\right)^2\right)^{1/2}.\qquad(12)$$

Results and Discussion

The obtained solutions for both steady ($\beta=0$) and oscillating flow ($\beta\neq 0$) in a rectangular duct of aspect ratio λ with constant cross flow velocity can be reduced to the corresponding analytic solutions for nonporous walls (Re=0) given by J. V. Boussinesq [1] (steady, $\beta=0$) and D. G. Drake [3] (oscillating, $\beta\neq 0$). The oscillating flow solution given by D. G. Drake [3] can be shown to be equivalent to the solution of C. Fan and B. D. Chao [4] and V. O'Brien [5].

The obtained solution here (Re≠0) contains as a limit both the steady ($\beta\to 0$) as well as the oscillatory flow solution ($\beta\neq 0$) for the case of equally porous parallel walls ($\lambda\to 0$) obtained by A. S. Bearman [6] and C. Y. Wang [7], respectively.

An example of the amplitude and phase angle distributions over the rectangular duct cross section is shown in Fig. 1, for the oscillating flow with a reduced frequency $\beta=5$ and three values of the transverse Reynolds number Re=0, 10, 50. In the case of the absence of transverse flow (Re=0), both the amplitude and phase angle are nearly constant in the central part of the duct's cross section except for a region close to the walls, which shows a boundary layer behavior (Figs. 1(*a*) 1(*b*)). In the region of the constant velocity, the flow behaves inviscid showing amplitude $\tilde{w}_a=1/\beta^2$ and phase angle $\varphi=-90$ deg. This behavior is typical for the oscillating flows of high frequencies. The phase angle at the walls far from the apexes and for high values of β takes a value near to −45 deg, which is also typical for such kind of flows (Fig. 1(*b*)). There are four local maxima, clearly shown in Fig. 1(*a*). Related flow phenomena are expected, and are discovered for the pipe of circular cross section by E. G. Richardson and E. Tyler (1929) and are known as "annular effect" [2].

By increasing the cross flow Reynolds number (Re=10) the effect of flattening of the velocity profile in the central region of

the cross section is suspended, while, due to the convection, the maximum velocity, which increases, is shifted to the suction side (Fig. 1(*c*)). In parallel, the phase angle increases and approaches the value $\varphi=0$ at the injection side of the duct (Re=50), where the flow is convection dominated and so the viscous effects are suppressed, while at the suction side the phase angle decreases by increasing Re (Fig. 2(*f*)). The following relations can approximate the amplitude of the velocity and phase angle for the convection-dominated flows at the injection side,

$$\tilde{w}_a=\frac{2}{\beta^2}\sin\left[\frac{\beta^2}{2\ \mathrm{Re}}(\tilde{x}+\lambda)\right],\quad \varphi=-\frac{\beta^2}{2\ \mathrm{Re}}(\tilde{x}+\lambda), \tag{18}$$

as can be shown using the unsteady inviscid flow equations with the convection term and applying the nonslip condition at the injection wall. For the case of $\beta^2/\mathrm{Re}\to 0$, which practically means small values of β and high values of Re then the velocity amplitude has a linear distribution as in the case of steady flow $\tilde{w}_a=(\tilde{x}+\lambda)/\mathrm{Re}$. The relations (18) confirm the above claims, for small β and high Re values.

The mean over the rectangular cross section velocity can be calculated by integration of the velocity distribution (6) over the cross section. It can be found in dimensionless form by the following expression:

$$\tilde{\tilde{w}}=\tilde{\tilde{W}}e^{i\omega t},\quad \tilde{\tilde{W}}=2\sum_{n=0}^{\infty}\frac{1}{\left(\frac{2n+1}{2}\pi\right)^2 p^2}\times\left\{1+\frac{D}{2p^2\lambda}\frac{\cosh(\mathrm{Re}\,\lambda)-\cosh(D\lambda)}{\sinh(D\cdot\lambda)}\right\}. \tag{13}$$

Using the relations (10), the amplitude $\tilde{\tilde{w}}_a$ and the phase angle symbolized as θ can be calculated. In order to find the association of the present solution to the corresponding problem of Wang's solution for the oscillating flow between two parallel porous walls [7], we are obliged to choose other nondimensional variables defined as follows:

$$w'=\frac{w}{P(2a)^2}\ \nu=\tilde{w}\frac{1}{4\lambda^2},\quad M=2a\left(\frac{\omega}{\nu}\right)^{1/2}=2\lambda\beta,$$

$$R=\frac{U2a}{\nu}=2\lambda\ \mathrm{Re}. \tag{14}$$

Using the expression for w' and taking the limit for $\lambda\to 0$, we end up with the solution of C. Y. Wang [7]. In Fig. 2 the mean-velocity amplitude and phase angle are shown as functions of the cross flow Reynolds number R (0 to 100) for the value of the reduced frequency $M=10$ and for four different values of the aspect ratio ($\lambda\to 0$, $\lambda=1$, $\lambda=2$, $\lambda\to\infty$). The value $\lambda=0$ is identical to the curves of the solution of C. Y. Wang [7]. The truncation error for the Fourier series expression of the amplitude [Eq. (13)] is of the order of $2\ 10^{-7}$ for $n=12$, we used for the calculations of Fig. 2.

References

[1] Dryden, H. L., and Murnaghan, F. D., and Bateman, H., 1956, *Hydrodynamics*, Dover, New York.

[2] Berker, R., 1963, ''Integration des Equations du Mouvement d'un Fluide Visqueux Incompressible,'' *Handbuch der Physik*, **VIII/2**, Springer-Verlag, Berlin, p. 70.

[3] Drake, D. G., 1965, ''On the Flow in a Channel Due to a Periodic Pressure Gradient,'' Q. J. Mech. Appl. Math., **18**(1), pp. 1–10.

[4] Fan, C., and Chao, B. T., 1965, ''Unsteady, Laminar, Incompressible Flow Through Rectangular Ducts,'' Z. Angew. Math. Phys., **16**, pp. 351–360.

[5] O'Brien, V., 1975, ''Pulsatile Fully Developed Flow in Rectangular Channels,'' J. Franklin Inst., **300**(3), pp. 225–230.

[6] Bearman, A. S., 1958, ''Laminar Flow in an Annulus With Porous Walls,'' J. Appl. Phys., **29**(1), pp. 71–75.

[7] Wang, C. Y., 1971, ''Pulsatile Flow in a Porous Channel,'' ASME J. Appl. Mech., **38**, pp. 553–555.

Prediction of Turbulence Statistics Behind a Square Cylinder Using Neural Networks and Fuzzy Logic

P. K. Panigrahi[1]
e-mail: panig@iitk.ac.in

Manish Dwivedi

Vinay Khandelwal

Department of Mechanical Engineering, Indian Institute of Technology, Kanpur, UP 208016, India

Mihir Sen
Department of Aerospace Engineering, University of Notre Dame, Notre Dame, IN 46556

Experiments are carried out behind a square cylinder mounted in the freestream of a wind tunnel, and hot-wire anemometry is used to determine the profiles of the mean and statistical turbulence quantities. Artificial neural networks and fuzzy-logic models successfully predict the statistical quantities like mean velocity profiles and Reynolds stresses. The fuzzy-logic modeling is more convenient to use, is less computationally intensive, and gives a higher correlation coefficient in comparison to the neural network. [DOI: 10.1115/1.1537251]

1 Introduction

Artificial neural networks (ANN) and fuzzy logic modeling (FLM) have been used in recent years in many applications in thermal and fluids engineering (Sen and Goodwine [1]). There is little, however, on the prediction of turbulent flow characteristics using these methods. These techniques have the advantage that they can be continuously updated in a learning mode such that recently acquired data can be quickly incorporated into prediction models. This would be particularly useful for the design of turbulence control systems that should adapt to changing circumstances. To test this idea a series of hot-wire anemometer measurements were performed behind a cylinder of square cross section mounted in the freestream of a subsonic wind tunnel. The techniques of analysis are developed and tested on data from these experiments.

2 Experimental Facilities

The experiments were carried out in an open-circuit wind tunnel with a 2-m long test section and a nominal cross section of 40 cm×40 cm. A square cylinder made of perspex with a 25 mm×25 mm cross section and 40 cm in length was mounted spanning the width of the wind tunnel. The wind velocity was kept as 5.3 m/sec with the corresponding Reynolds number based on $h=25$ mm equal to 8543. A DANTEC model 56C17 Constant Temperature Anemometer and DANTEC X-wire probe were used for the velocity measurements. The details of the experimental technique with uncertainty have been discussed in Dutta et al. [2].

[1]To whom correspondence should be addressed.

Contributed by the Fluids Engineering Division for publication in the JOURNAL OF FLUIDS ENGINEERING. Manuscript received by the Fluids Engineering Division March 19, 2002; revised manuscript received August 28, 2002. Associate Editor: G. Karniadakis.

Table 1 Multiple correlation coefficients R^2 for velocity and fluctuation data when (*a*) the same data, and (*b*) different data are used for training and testing

	Same Training & Testing Data		Different Training & Testing Data	
Quantity	ANN	FLM	ANN	FLM
u	0.979	0.996	0.968	0.972
v	0.953	0.991	0.845	0.979
u_{rms}	0.957	0.992	0.943	0.963
v_{rms}	0.968	0.991	0.958	0.973
$\overline{u'v'}$	0.968	0.992	0.925	0.964

3 Artificial Neural Network

The feed-forward or multilayer perceptron configuration is used in this work. A multilayer perceptron can learn when presented with measured input and output pairs. Here the input are the downstream and cross stream locations, X and Y respectively. The output are the turbulent statistics such as the mean velocity u, v in the X and Y directions, respectively, the rms of the fluctuations u_{rms} and v_{rms}, and the Reynolds stress $\overline{u'v'}$. Learning or training involves modifying the connection weights and biases until the network is capable of reproducing the target output for the respective input. Training takes place in an iterative fashion: Each cycle consists of a forward propagation step with the weights and biases being modified by the back propagation method. More details regarding the ANN technique used here are in Panigrahi et al. [3].

4 Fuzzy-Logic Model

The FLM procedure has four elements: (i) a membership function, (ii) internal functions, (iii) rules, and (iv) output. The membership function characterizes a fuzzy set which takes values and converts them to [0,1] through a process of fuzzification, where 0 indicates no contribution of the variable and 1 is full contribution. The output of the FLM corresponding to the input pair is obtained

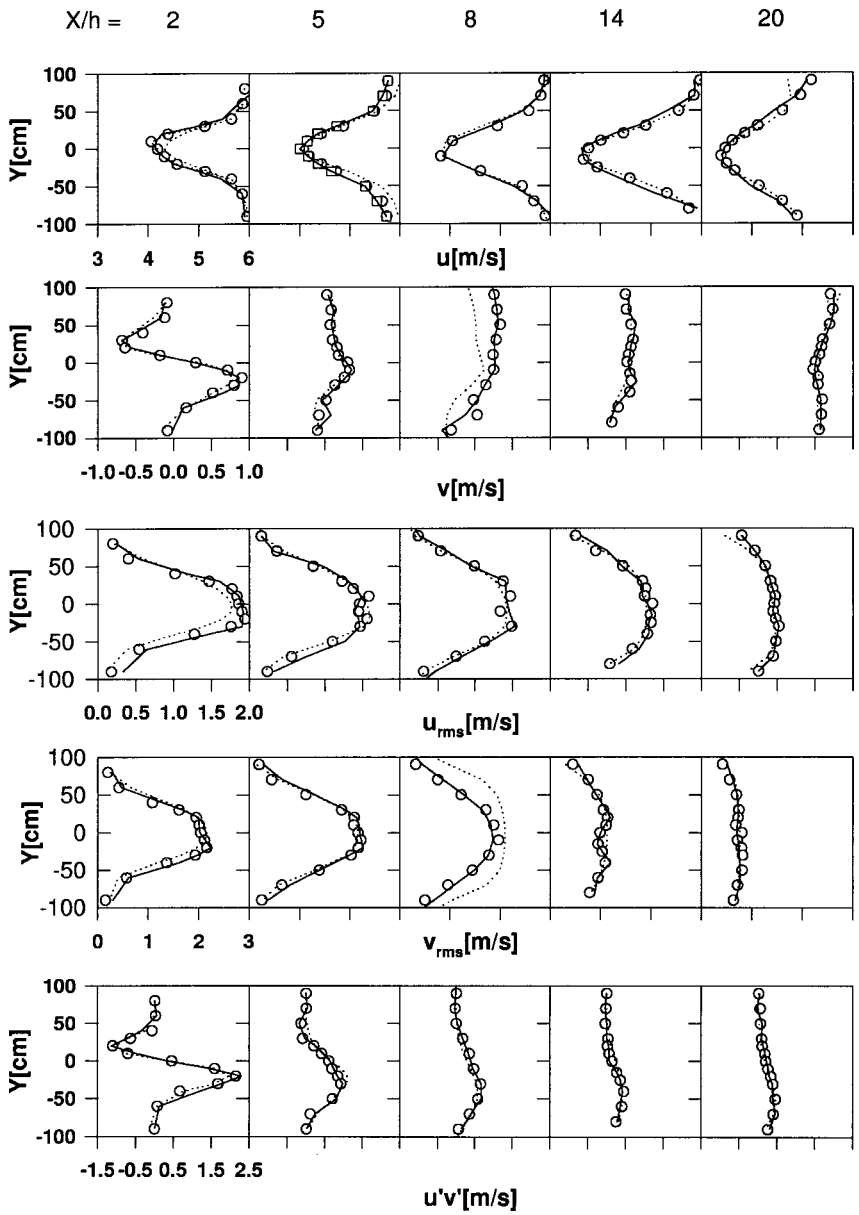

Fig. 1 Comparison of u, v, u_{rms}, v_{rms}, and $\overline{u'v'}$ data at various X/h-locations with ANN and FLM predictions. Symbols correspond to experimental data, solid line to FLM and dotted line to ANN. Different data are used for training and testing.

by defuzzifying the model. The model output is compared to the input data to calculate the internal function coefficients which are modified using Newton's method. Triangular membership functions are used in this work. The overall procedure employed here is similar to the one reported by Xie et al. [4].

5 Results and Discussion

For the ANN, the number of nodes in each layer, the initial assignment of weights and biases, the learning rate, and the momentum factor were decided on the basis of numerical experimentation. For v_{rms}, u_{rms} and u, a 2-5-1 configuration was used, while v and $\overline{u'v'}$ were analyzed with 2-8-6-1. For FLM, the membership function was observed to influence the correlation coefficient depending on the type of turbulent statistics being modeled. The largest correlation coefficient was obtained using 12 membership functions.

The testing of the ANN and FLM was carried out in two stages. In the first series of tests, the same data were used for testing and training, while in the second 50% of the data were used for training and the rest for testing (alternate data were selected for training and testing, respectively). The goodness of the modeling is verified by using the multiple correlation coefficient defined as

$$R^2 = 1 - \frac{\sum_{j=1}^{m} (\hat{y}_j - y_j)^2}{\sum_{j=1}^{m} (y_j - \overline{y})^2} \tag{1}$$

where $\overline{y}$ is the sample mean of the m data, and m is the number of datapoints.

The correlation coefficients obtained are presented in Table 1. For both ANN and FLM, the R^2 values are smaller when using different data for training and testing in comparison to when the same data are used. The output from the ANN and FLM model are compared with the experimental data in Fig. 1. The FLM is observed to be satisfactory in modeling at all spatial locations. The ANN also has satisfactory prediction at all locations except at $X/h=8$. The overall performance of the FLM is observed to be superior in comparison to the ANN. It may be noted that Rediniotis and Chrysanthakopoulos [5] also observed the FLM to outperform the ANN for the calibration of a seven-hole probe.

6 Conclusions

The ANN and FLM techniques for modeling the statistics of turbulence have been compared. To meet this objective, experiments were carried out for the measurement of flow behind a square cylinder mounted in the free stream of a subsonic tunnel with a hot-wire anemometer. The back-propagation ANN and FLM using internal functions were used for modeling. Both techniques are successful in modeling the turbulence statistics well. Overall, the performance of the FLM is superior to the ANN. The ANN requires a number of trials for proper choice of the parameters of the network. In comparison, the FLM is more convenient to use and is less computationally intensive than the ANN.

Acknowledgments

M.S. is grateful for a Fulbright Visiting Lecturership and the hospitality of I.I.T, Kanpur which made possible his stay there.

References

[1] Sen, M., and Goodwine, J. W., 2001, "Soft Computing in Control," *The MEMS Handbook*, M. Gad-el-Hak, ed., CRC Press, Boca Raton, FL, Chap. 14, pp. 1–37.

[2] Dutta, S., Muralidhar, K., and Panigrahi, P. K., 2002, "Influence of the Orientation of a Square Cylinder on the Wake Properties," Exp. Fluids, in press.

[3] Panigrahi, P. K., Khandelwal, V., and Sen, M., 2002, "Prediction of Turbulent Statistics Behind a Rib Using Artificial Neural Network," *Proceedings of the Fifth ISHMT/ASME Heat & Mass Transfer Conference & Sixteenth National Heat & Mass Transfer Conference*, Calcutta, Jan. 3–5, Tata McGraw-Hill, pp. 676–681.

[4] Xie, H., Mahajan, R. L., and Lee, Y., 1995, "Fuzzy Logic Models for Thermally Based Microelectronic Manufacturing Processes," IEEE Trans. Semicond. Manuf., **8**(3), pp. 219–226.

[5] Rediniotis, O. K., and Chrysanthakopoulos, G., 1988, "Application of Neural Networks and Fuzzy Logic to the Calibration of the Seven-Hole Probe," ASME J. Fluids Eng., **120**, pp. 95–101.

A Linear Stability Analysis for an Improved One-Dimensional Two-Fluid Model

Jin Ho Song
Korea Atomic Energy Research Institute, P.O. Box 105
Taejon 305-600, Korea.
e-mail: dosa@kaeri.re.kr

A linear stability analysis is performed for a two-phase flow in a channel to demonstrate the feasibility of using momentum flux parameters to improve the one-dimensional two-fluid model. It is shown that the proposed model is stable within a practical range of pressure and void fraction for a bubbly and a slug flow.

[DOI: 10.1115/1.1537256]

1 Introduction

It is still an unresolved issue that the basic form of the governing differential equations for the one-dimensional two-fluid model is mathematically ill-posed, though there have been efforts to improve it, [1–3]. Recently, Song and Ishii [4] suggested an improvement of the model by considering the void fraction and velocity profile in the flow channel. However, as the analysis was limited to the characteristic analysis, which considers only a very short wavelength disturbance, it is challenging to perform a linear stability to figure out the general applicability of the proposed model.

A two-phase flow in a channel is described by the one-dimensional two-fluid model as indicated below, [4,5],

$$\alpha\rho_g \partial u_g/\partial z + \rho_g \partial\alpha/\partial t + \rho_g u_g \partial\alpha/\partial z = 0 \tag{1}$$

$$\alpha_f\rho_f \partial u_f/\partial z - \rho_f \partial\alpha/\partial t - \rho_f u_f \partial\alpha/\partial z = 0 \tag{2}$$

$$\alpha\rho_g \partial u_g/\partial t + \alpha\rho_g(2C_{vg}-1)u_g \partial u_g/\partial z + \rho_g(C_{vg}-1)u_g^2 \partial\alpha/\partial z = -\alpha\partial p/\partial z + \alpha\rho_g g - F_I + M_{ig} \tag{3}$$

$$\alpha_f\rho_f \partial u_f/\partial t + \alpha_f\rho_f(2C_{vf}-1)u_f \partial u_f/\partial z - \rho_f(C_{vf}-1)u_f^2 \partial\alpha/\partial z = -\alpha_f\partial p/\partial z + \alpha_f\rho_f g + F_I + M_{if} \tag{4}$$

where $\alpha_f = 1-\alpha$, F_I is the interphase drag, and M_{ig} and M_{if} are the generalized drag force, and C_{vf} and C_{vg} are the momentum flux parameters, [4,5]. In a two-phase flow, the momentum flux parameters for the gas and liquid phase do not only indicate the effect of velocity profile but also the coupling between the velocity and void fraction profile. It is fundamentally different from a single-phase flow.

2 A Linear Stability Analysis and Stability Criteria

By defining a vector $\varphi = (\alpha, u_g, u_f, p)$, Eqs. (1)–(4) are written as

Contributed by the Fluids Engineering Division for publication in the JOURNAL OF FLUIDS ENGINEERING. Manuscript received by the Fluids Engineering Division Apr. 25, 2001; revised manuscript received Sept. 25, 2002. Associate Editor: I. Celik.

$$\mathbf{A}\partial\boldsymbol{\varphi}/\partial t+\mathbf{B}\partial\boldsymbol{\varphi}/\partial z+\mathbf{C}=0 \tag{5}$$

where **A**, **B**, and **C** are matrices. A linear stability analysis considering a traveling wave-type disturbance $\delta\boldsymbol{\varphi}=\delta\boldsymbol{\varphi}_o\exp[i(kz-\omega t)]$, where $\delta\boldsymbol{\varphi}_o$ denotes the initial amplitude of the perturbation, indicates that the stability of the system is determined from the roots $\lambda=\lambda_R+i\lambda_I=\omega_R/k+i\omega_I/k$ of the following equation:

$$\text{determinant of } (\mathbf{A}\lambda-\mathbf{B}+i/k\mathbf{D})=0 \tag{6}$$

where $\mathbf{D}=(\partial\mathbf{C}/\partial\boldsymbol{\varphi})_o$. To compare these results with those of Pokharna et al. [6], a simple Darcy model for the interfacial drag by Ishii and Zuber [7] is used:

$$F_I=K\alpha\rho_f u_r^2. \tag{7}$$

Then, for a two-phase flow in a horizontal channel, the matrices **C** and **D** become

$$\mathbf{C}=[0,0,K\alpha\rho_f u_r^2,-K\alpha\rho_f u_r^2] \tag{8}$$

$$D_{11}=D_{12}=D_{13}=D_{14}=D_{21}=D_{22}=D_{23}=D_{24}=0 \tag{9}$$

$$D_{31}=K\rho_f u_r^2,\quad D_{32}=2K\alpha\rho_f u_r,\quad D_{33}=-D_{32},\quad D_{34}=0 \tag{10}$$

$$D_{41}=-D_{31},\quad D_{42}=-D_{32},\quad D_{43}=D_{32},\quad D_{44}=0 \tag{11}$$

where C_D and K are constants and $u_r=u_g-u_f$. Let $\Phi^*=iD_{31}/k$, $\Omega^*=iD_{32}/k$. The determinant is calculated as

$$\begin{aligned}f(\lambda,k)=&-\alpha\rho_g\alpha_f\rho_f[\rho_g\alpha_f(\lambda^2-2C_{vg}u_g\lambda+C_{vg}u_g^2)\\&+\alpha\rho_f(\lambda^2-2C_{vf}u_f\lambda+C_{vf}u_f^2)]-\rho_g\rho_f[\Omega^*\alpha_f(\lambda-u_g)\\&+\Omega^*\alpha(\lambda-u_f)]-\alpha\rho_g\alpha_f\rho_f\Phi^*.\end{aligned} \tag{12}$$

For a finite ω/k in the limit $k\to\infty$, Eq. (6) reduces to the characteristic equation

$$\begin{aligned}f(\lambda)=&-\alpha(1-\alpha)\rho_g\rho_f[(1-\alpha)\rho_g(\lambda^2-2\lambda C_{vg}u_g+C_{vg}u_g^2)\\&+\alpha\rho_f(\lambda^2-2C_{vf}u_f\lambda+C_{vf}u_f^2)]=0.\end{aligned} \tag{13}$$

In the case of the conventional model, where $C_{vg}=C_{vf}=1$, the model becomes mathematically ill-posed since it can have real roots only if $\lambda=u_g=u_f$,. However, if the momentum flux parameters satisfy the following equation, we can have real roots for λ:

$$\begin{aligned}P^*=&(\alpha_f\rho_g C_{vg}u_g+\alpha\rho_f C_{vf}u_f)^2-(\alpha_f\rho_g+\alpha\rho_f)\\&\times(\alpha_f\rho_g C_{vg}u_g^2+\alpha\rho_f C_{vf}u_f^2)\geqslant 0.\end{aligned} \tag{14}$$

This provides the necessary condition for stability as discussed in Song and Ishii [4].

Let's consider the general case where the wave number k is finite. The solution for $f(\lambda,k)=0$ is determined from the real and imaginary parts as

$$\begin{aligned}&\rho_g\alpha_f(\lambda_R^2-2C_{vg}u_g\lambda_R+C_{vg}u_g^2-\lambda_I^2)\\&\quad+\alpha\rho_f(\lambda_R^2-2C_{vf}u_f\lambda_R+C_{vf}u_f^2-\lambda_I^2)-\Omega/k\lambda_I=0\end{aligned} \tag{15}$$

$$\begin{aligned}&2\rho_g\alpha_f\lambda_I(\lambda_R-C_{vg}u_g)+2\alpha\rho_f\lambda_I(\lambda_R-C_{vf}u_f)\\&\quad+[\lambda_R\Omega-\Omega\alpha_f u_g-\Omega\alpha u_f]/k+\Phi/k=0\end{aligned} \tag{16}$$

where $\Omega=D_{32}/(\alpha\alpha_f)=2K\rho_f u_r/\alpha_f$ and $\Phi=D_{31}$.

For convenience, let $\rho\alpha=\rho_g\alpha_f+\alpha\rho_f$, $\alpha u=u_g\alpha_f+\alpha u_f$. A dispersion relation between the wave number k and the growth factor ω_I is obtained by combining the above two equations:

$$\begin{aligned}g(\omega_I,k)=&4\rho\alpha^3\omega_I^4+8\rho\alpha^2\Omega\omega_I^3+5\rho\alpha\Omega^2\omega_I^2+\Omega^3\omega_I\\&+k^2(4\rho\alpha\omega_I^2P+4\Omega\omega_IP^*-Q^*)=0\end{aligned} \tag{17}$$

where P^* is the same as in Eq. (14) and Q^* is defined as

$$\begin{aligned}Q^*=&\alpha_f\rho_g[(\Omega\alpha u-\Phi)^2-2C_{vg}u_g(\Omega\alpha u-\Phi)\Omega+\Omega^2C_{vg}u_g^2]\\&+\alpha\rho_f[(\Omega\alpha u-\Phi)^2-2C_{vf}u_f(\Omega\alpha u-\Phi)\Omega+\Omega^2C_{vf}u_f^2].\end{aligned} \tag{18}$$

Then, the solution of ω_I for $g(\omega_I,k)=0$ at a given wave number k is determined by the intersection of the following two curves:

$$\begin{aligned}g1(x)&=4\Omega^4/\rho\alpha x(x^3+2x^2+5/4x+1/4)\\&=4\Omega^4/\rho\alpha(x+1/2)^2(x+1)x=0\end{aligned} \tag{19}$$

and

$$\begin{aligned}g2(x,k)&=-k^2(4\rho\alpha\omega_I^2P^*+4\Omega\omega_IP^*-Q^*)\\&=-k^2\{4P^*\Omega^2/\rho\alpha(x+1/2)^2-P^*\Omega^2/\rho\alpha-Q^*\}\end{aligned} \tag{20}$$

where $x=\omega_I\rho\alpha/\Omega$ represents the growth factor.

In the case of the conventional model, where $C_{vf}=C_{vg}=1$, $P^*=-\alpha_f\rho_g\alpha\rho_f(u_g^2-u_f)^2$, and $Q^*=\alpha_f\rho_g[(\Omega\alpha u-\Phi)-\Omega u_g]^2+\alpha\rho_f[(\Omega\rho u-\Phi)-\Omega u_f]^2$, the functions $g1(x)$ and $g2(x,k)$ are always positive at positive value x. So, they intersect at positive value of x. This means that the growth factor is positive and the system is always unstable. As the function $g1(x)$ is proportional to Ω^4, while $g2(x,k)$ is proportional to Ω^2, the growth factor decreases as $\Omega=2K\rho_f u_r/\alpha_f$ increases. These results are basically the same as that of Pokharna et al. [6].

Let's consider an improved model with appropriate momentum flux parameters, which satisfy the necessary condition that P^* is positive. The shape of the function $g1(x)$ remains the same as that of the conventional model, while the shape of the function $g2(x,k)$ changes from concave to convex and has a maximum value of k^2Q^* at $x=0$. The curves $g1(x)$ and $g2(x,k)$ will intersect at a positive value of x if Q^* is positive. If Q^* is negative, they would not intersect at the positive value of x. Under that condition, the growth factor would not grow with time, and the flow is stable. Therefore, it can be claimed that a sufficient condition for stability is for Q^* to be negative.

$$\begin{aligned}Q=&\alpha_f\rho_g[(\Omega\alpha u-\Phi)^2-2C_{vg}u_g(\Omega\alpha u-\Phi)\Omega+\Omega^2C_{vg}u_g^2]\\&+\alpha\rho_f[(\Omega\alpha u-\Phi)^2-2C_{vf}u_f(\Omega\alpha u-\Phi)\Omega+\Omega^2C_{vf}u_f^2]\leqslant 0\end{aligned} \tag{21}$$

The first criterion in Eq. (14) makes the system of governing differential equations hyperbolic, which enables the propagation of void fraction wave. The second criterion in Eq. (21) determines whether the flow is stable to the small perturbations or not.

3 Application of Proposed Arguments to a Bubbly Flow and a Slug Flow

We can put the stability criteria in nondimensional forms by introducing $S=u_g/u_f$ and $R=\alpha\rho_f/((1-\alpha)\rho_g)$ as

$$\begin{aligned}P(\alpha,\rho_g/\rho_f)=P^*/(\alpha\rho_f u_f)^2=&(C_{vg}S/R+C_{vf})^2-(1/R+1)\\&\times(C_{vg}S^2/R+C_{vf})\geqslant 0\end{aligned} \tag{22}$$

$$\begin{aligned}Q(\alpha,\rho_g/\rho_f)=&Q^*/(\alpha\rho_f\Omega^2u_f^2)\\=&0.25(1/R+1)(1+\alpha+\alpha_fS)^2\\&-S/R[1-\alpha(S-1)]C_{vg}-[S+\alpha(1-S)]C_{vf}\leqslant 0.\end{aligned} \tag{23}$$

By using these two criteria, we can investigate the adequacy of the improved one-dimensional two-fluid model in describing a bubbly or a slug flow in a channel.

By using a correlation for a volumetric distribution parameter, [8], and the experimental results of Welle [9], Song and Ishii [4]

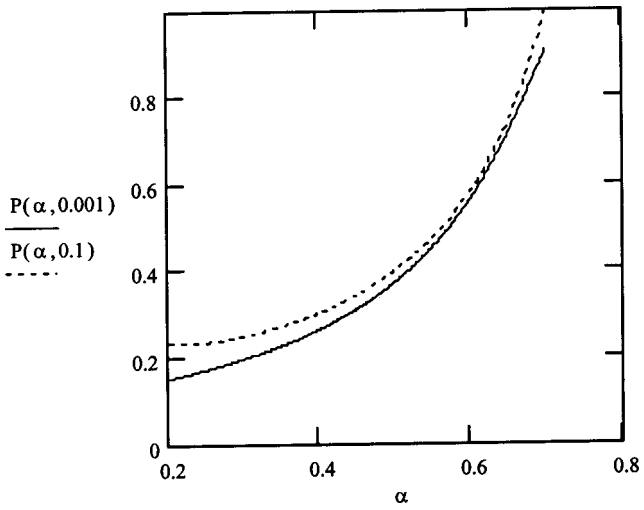

Fig. 1 Plots of *P* for bubbly and slug flow at density ratio of 0.1 and 0.001

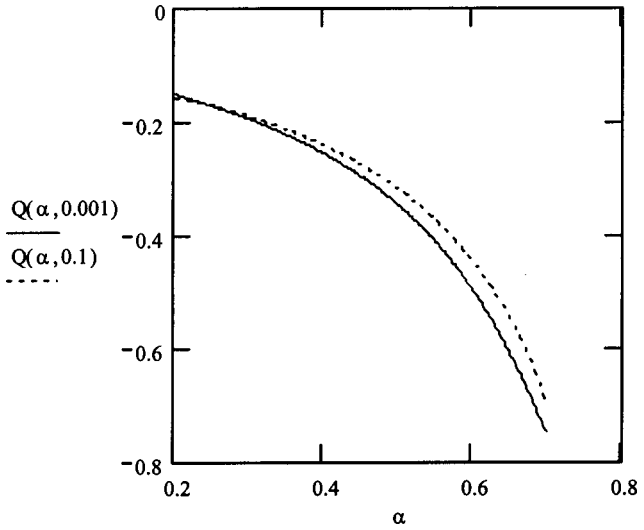

Fig. 2 Plots of *Q* for bubbly and slug flow at density ratio of 0.1 and 0.001

constructed a bubbly flow and a slug flow in the void fraction range of 0.2–0.7. By following the same procedure we can detemine *R, S,* and momentum flux parameters as a function of void fraction and density ratio. It enabled us to calculate *P* and *Q* as a function of void fraction and density ratio.

Figure 1 shows the nondimensional quantity $P(\alpha,\rho_g/\rho_f)$. The density ratio is chosen between 0.01 and 0.001, which is between the system pressure of the nuclear reactor and atmospheric pressure. It is shown that $P(\alpha,\rho_g/\rho_f)$ is always positive, which satisfies the first stability criterion. Figure 2 shows the nondimensional quantity $Q(\alpha,\rho_g/\rho_f)$. It shows that $Q(\alpha,\rho_g/\rho_f)$ is always negative, which meets the second stability criterion.

The fact is that the proposed model is applicable in a wide range of void fraction and the density ratio is very important, as previous improvements had a very limited range of application, [1–3].

4 Discussions

The argument above indicates that we can significantly improve the one-dimensional two-fluid model by considering the coupling of velocity and void profile. The proposed model is mathematically well-posed and can describe the propagation of the void fraction wave in bubbly flow and slug flow within a wide range of void fraction and density ratio. It is consistent with the existence of bubbly and slug flow regime in the real world, while the conventional basic form of the one-dimensional two-fluid model causes unphysical instability.

Acknowledgment

The authors appreciate the support from the Ministry of Science and Technology of the Korean Government.

References

[1] Ramshaw, J. D., and Trapp, J. D., 1978, "Characteristics, Stability, and Short-Wavelength Phenomena in Two-Phase Flow Equation Systems," Nucl. Sci. Eng., **66**, pp. 93–102.

[2] Stuhmiller, J. H., 1977, "The Influence of Interfacial Pressure Forces on the Character of Two-Phase Flow Model Equations," Int. J. Multiphase Flow, **3**, pp. 551–560.

[3] Lahey, R. T., Cheng, L. Y., Drew, D. A., and Flaherty, J. E., 1980, "The Effect of Virtual Mass on the Numerical Stability of Accelerating Two-Phase Flow," Int. J. Multiphase Flow, **6**, pp. 281–294.

[4] Song, J. H., and Ishii, M., 2001, "On the Stability of a One-Dimensional Two-Fluid Model," Nucl. Eng. Des., **204**, pp. 101–115.

[5] Ishii, M., and Mishima, K., 1984, "Two-Fluid Model and Hydrodynamic Constitutive Relations," Nucl. Eng. Des., **pp.** 107–126.

[6] Pokharna, H., Mori, M., and Ransom, V. H., 1997, "Regularization of Two-Phase Flow Models: A Comparison of Numerical and Differential Approaches," J. Comput. Phys., **134**, pp. 282–295.

[7] Ishii, M., and Zuber, N., 1979, "Drag Coefficient and Relative Velocity in Bubbly, Droplet or Particulate Flows," AIChE J., **25**(5), pp. 843–855.

[8] Ishii, M., 1977, "One Dimensional Drift-Flux Model and Constitutive Equations for Relative Motion between Phases in Various Two-Phase Flow Regimes," Paper No. ANL-77-47.

[9] Van der Welle, R., 1985, "Void Fraction, Bubble Velocity, and Bubble Size in Two-Phase Flow," Int. J. Multiphase Flow, **11**(3), pp. 17–34.

Periodic Flow Between Low Aspect Ratio Parallel Jets

Elgin A. Anderson
e-mail: eanderson@mae.usu.edu

Deryl O. Snyder

Jonathan Christensen

Mechanical and Aerospace Engineering Department, Utah State University, Logan, UT 84322

The behavior of symmetric parallel jets was investigated experimentally. Two-component hot-wire surveys of the velocity field were performed over a jet region extending from the nozzle plate to a distance seven times the spacing between the nozzles. The objective of this study was to investigate an observed periodic behavior in the near-field region between parallel jets that increases in frequency as the nozzle widths decrease. This behavior was found to occur in parallel jets where nozzle widths are greater than 0.5 times the jet spacer width. The phenomena are attributed to bluff body shedding in the near field and a confining effect of the outer shear layers. [DOI: 10.1115/1.1537257]

Introduction

The current study focuses on a parallel planar jet flow with relatively large nozzle widths *w* compared to the width of the

Contributed by the Fluids Engineering Division for publication in the JOURNAL OF FLUIDS ENGINEERING. Manuscript received by the Fluids Engineering Division June 20, 2002, revised manuscript received Oct. 22, 2002. Associate Editor: M. V. Ötügen.

spacer separating the two jets d, specifically $w/d > 0.6$. For those configurations a periodic, bluff-body-type shedding behavior was detected between the two jets with the spacer between the jets serving as the bluff body. In previous studies on smaller w/d ratios this periodic behavior is not detected and is instead dominated by a pair of counterrotating recirculation cells, [1–7]. The objective of the present work is to experimentally investigate the vortex shedding phenomenon for parallel jets with $0.6 \leqslant w/d \leqslant 2.0$.

Experimental Procedure

The schematic shown in Fig. 1 defines the relevant parameters and coordinate system for the parallel jet configuration. Experiments were conducted over a nozzle exit velocity range of 3–35 m/s which gave a Reynolds number range based on d of $\mathrm{Re}_d = 3{,}900–108{,}000$. The origin of the two-dimensional coordinate system was located where the symmetry plane intersects the jet plate. Mean velocity and frequency spectra data were obtained for $w/d = 0.6$, 0.8, 1.2, 1.6, and 2.0 utilizing three nozzle spacings of $d = 2.7$, 3.18, and 3.81 cm. Measurements were obtained at a consistent w/d for each spacer by varying the nozzle width. The lengthwise span of the nozzle, L was fixed at 20.32 cm.

The flowfield was surveyed with an x-type hot-wire probe. A recirculation flow was present in the cavity region between the jet inner shear layers that extended in the streamwise direction to approximately $x/d = 1.5$. Data in that region are not included due to the probes inability to detect reverse flow.

There were two aspect ratios of interest for this problem; the nozzle aspect ratio, w/L, and the spacer aspect ratio, d/L. For large w/d and large d the two aspect ratios were quite small, e.g., $w/L = 2.67$ and $d/L = 5.33$. This condition is a practical consequence of the facility dimensions and measurement resolution for large w/d. For nozzle aspect ratios greater than 5 the midspan flow demonstrated a nominally two-dimensional character. This was verified by measurements near the symmetry plane which showed negligible spanwise gradients in the mean flow. However, when the spacer aspect ratio decreased below 5 the jet end conditions began to influence the midspan flow. A more three-dimensional mean flow was produced that caused the periodic behavior to become progressively more irregular. In the current study the data only reflect configurations with spacer aspect ratios greater than 5. Small nozzle aspect ratios did not introduce any significant change in character to the mean flow in the regions surveyed.

Results

Mean flow profiles are presented in Figs. 2(a) and 2(b) at five axial stations for a representative Reynolds number, $\mathrm{Re}_d = 20{,}000$ and for $w/d = 0.6$ and 1.4, respectively. These figures illustrate that the flowfield had both jet-like and wake-like characteristics. That is, studying only the inner two shear layers, the profiles resemble the wake behind a bluff body with dimension d. This is most clearly shown in Fig. 2(b). However, studying only the outer two shear layers, the profile behavior is more typical of a planar jet. In the far field the merged jets have the mean flow characteristics of a single turbulent jet. At a given w/d the mean flow profiles are similar and independent of scale.

The periodic nature of the flow was investigated by measuring the axial flow at a stationary point and performing a Fourier analysis of the data. The location of the probe was chosen to be a streamwise distance of $x/d = 1.5$ and transverse distance $y/d = 0.5$ directly downstream of the inner lip of the jet nozzle. The streamwise location corresponded to the location of maximum normal stress along the centerline for all configurations. One should note that definition as the one typically used for the vortex formation length in a bluff-body flow, cf. Bloor [8]. The dominant frequency mode detected along the symmetry plane ($y/d = 0$) was twice the value measured at $y/d = 0.5$. That result supports the claim that periodic vortex shedding occurred between the two jets. Flow visualization provided additional evidence to confirm the vortex shedding behavior. However, those results are omitted due to the inability of still images to adequately describe dynamic events.

Figure 3 shows jet exit velocity versus the product of shedding frequency and spacer width, fd for $w/d = 0.6$ and $d = 3.18$ cm. Superimposed on the plots are the frequency (fd) spectra positioned adjacent to the corresponding velocity point. The vertical positioning of each scale is arbitrary and chosen so that the dominant peak was aligned with the appropriate U_o versus fd datapoint. The spectra are included only to illustrate the presence and shape of the dominant peak and although it is important to note that the vertical scales are logarithmic with a consistent range, they are arbitrary and therefore omitted to improve the overall clarity of the chart. It is emphasized that the power spectra scale is omitted and should not be confused with the displayed velocity scale. The dotted line shown on the plot represents the best linear fit of the U_o versus fd data. This choice of parameter grouping was selected because the inverse of the slope of the linear fit, fd/U_o defines a Strouhal number or, reduced frequency of the periodic motion.

Some general trends were identified. For all configurations the data accurately matched the linear fit. This indicated that the reduced frequency was independent of Reynolds number over the range measured. Also, the slope of the linear fit was constant at a given w/d and independent of d. That result is consistent with the mean velocity profiles which govern the periodic behavior and show that for a given w/d the profile shape and streamwise evolution did not depend on d.

For each w/d the data representing all velocities and spacer widths could be described by a single linear trend as shown in Fig. 4. The average reduced frequency for each w/d is presented in Table 1 and shows that it decreased as w/d increased. The correlation coefficients for the linear regression curve fits are also presented in Table 1 and give a strong indication of the linearity of the data trend. The data in Table 1 are plotted in Fig. 5 and show that the relationship between the reduced frequency and w/d was nonlinear and consistent with an asymptote limit for large w/d. The asymptote value of approximately 0.20–0.24 is in the range of Strouhal numbers reported for similar D-shaped bodies in wind tunnel experiments, cf., Bearman and Tombazis [9].

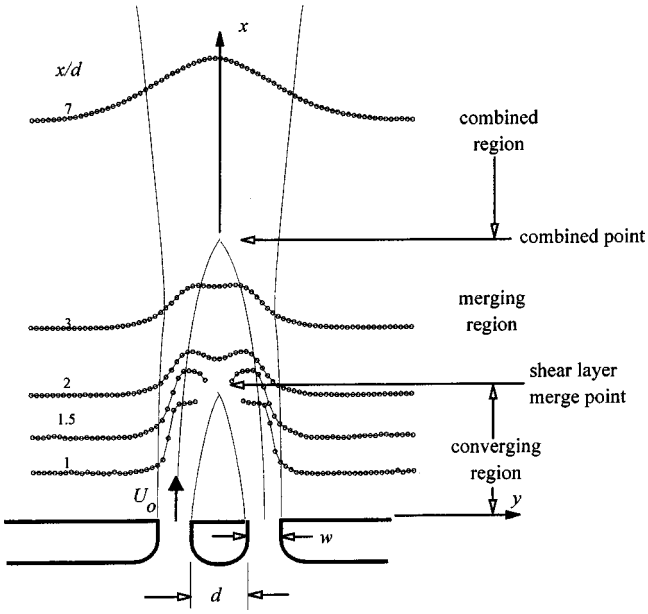

Fig. 1 Description of parallel jet flowfield parameters and coordinates

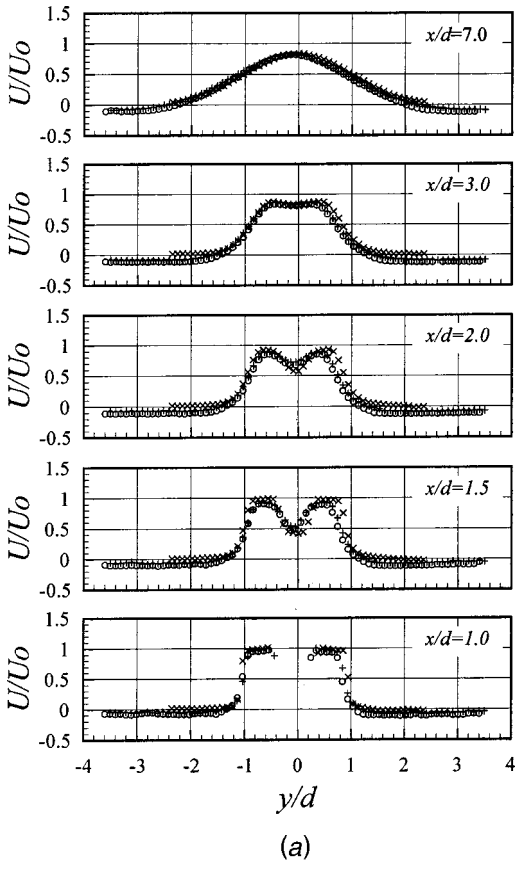

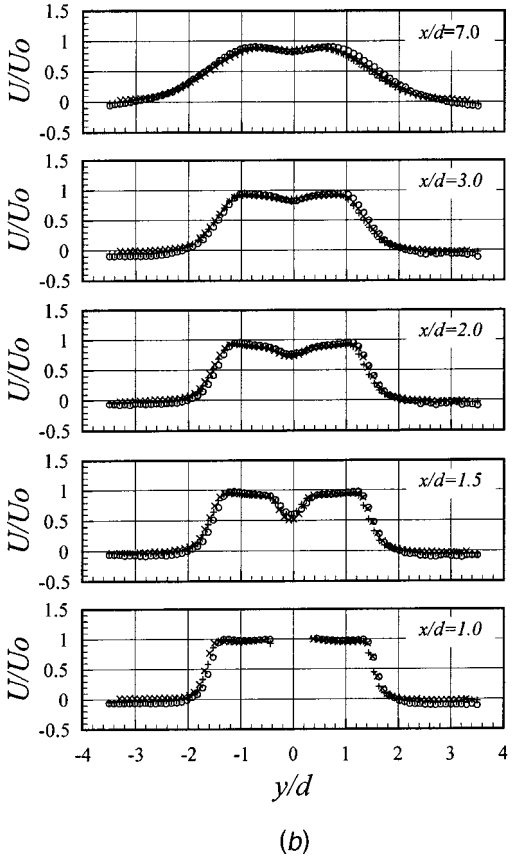

Fig. 2 Mean velocity profiles at Re_d=20,000. d=2.70 cm, ×; d=3.18 cm, +; d=3.81 cm, ○.

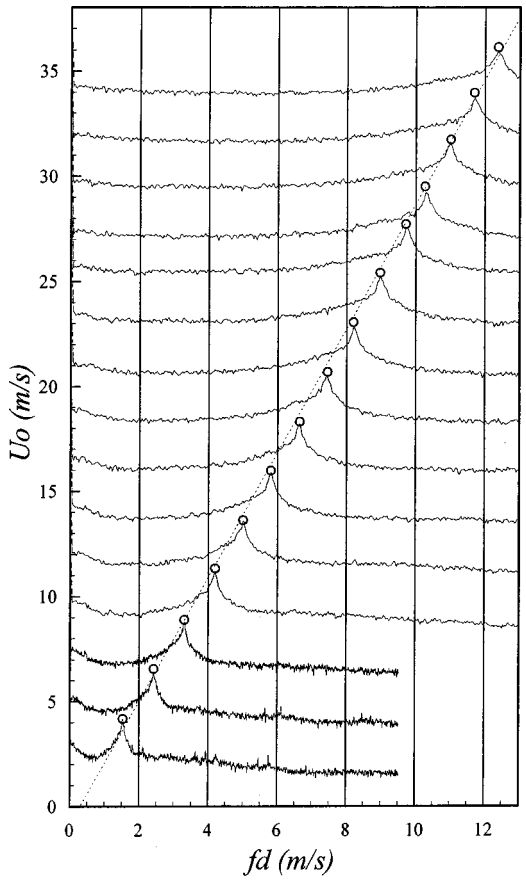

Fig. 3 w/d=0.6 jet exit velocity versus fd superimposed over the frequency spectra. Dotted line indicates best linear fit. d =3.18 cm. The log scales for the spectra are hidden.

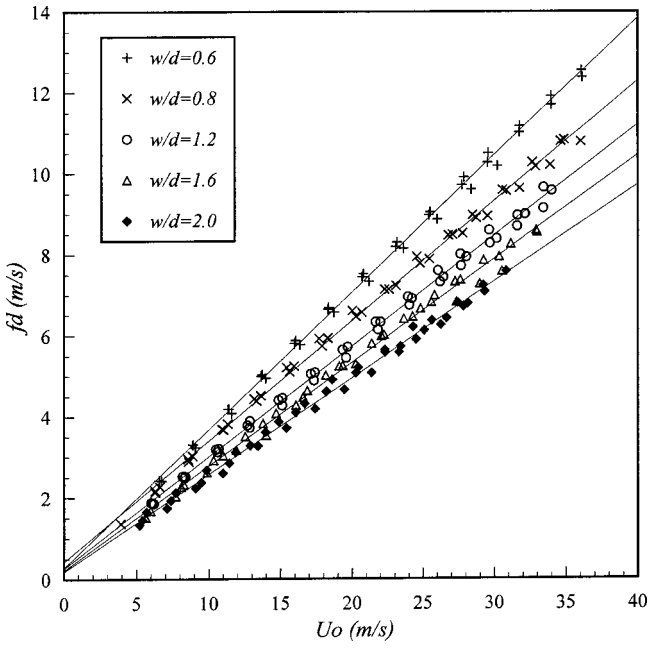

Fig. 4 Product of shedding frequency and spacer width, fd as a function of jet exit velocity. Lines indicate the best linear fit of data at consistent w/d.

Table 1 Reduced frequency and linear curve fit correlation coefficients, R^2 averaged over all spacer widths and velocities

w/d	fd/U_o	R^2
0.6	0.334	0.998
0.8	0.297	0.998
1.2	0.270	0.998
1.6	0.261	0.995
2.0	0.243	0.995

The increase in reduced frequency with decreasing w/d may be explained by the confining effect of the outer shear layers. As w/d decreased the outer shear layers were brought closer to the bluff-body shedding region between the jets. This had an effect similar to that of the confining walls in a wind tunnel being brought closer to a bluff body. The walls of the wind tunnel alter the trajectory of the streamlines from that which would exist in an unconfined configuration resulting in an increase in the shedding frequency. For the parallel jet, each of the outer shear layers produce a sheet of vorticity whose integrated influence on the cavity between the jets is an induced velocity with a component directed toward the symmetry plane. The induced velocity will influence the interior streamlines and impede the free expansion of the wake envelope in a manner similar to the walls of a wind tunnel. The influence of the outer shear layers on the flow near the symmetry plane is increased as their distance from the shedding region is decreased (smaller w/d) and therefore produced a progressive increase in shedding frequency. For large w/d the outer shear layer influence is diminished and the reduced frequency approached a constant unconfined value.

Progressive decreases in w/d below 0.6 showed a rapid transition away from the periodic shedding and below $w/d=0.5$ there was no detection of periodic behavior. Hence, that range indicated a transition region between a vortex shedding regime, the focus of the current study, and the recirculation cell regime reported in the many previous studies, [1–7].

The data in Fig. 4 correlated well with the linear fit despite a seemingly large variation in the geometric parameters. For example, the increase in d at a fixed w/d produced a change in the spacer aspect ratio from 4.57 to 7.52. In addition, the different spacer widths describe bluff-body shapes which were not geometrically similar. Both of these effects are expected to slightly alter a bluff-body shedding frequency. However, despite those variations in geometric parameters the linear fit provided an accurate description of the data trends over the entire parameter space. That indicates that the confining effect of the outer shear layers had a much stronger influence on the shedding behavior than the variations in geometry used in the current study.

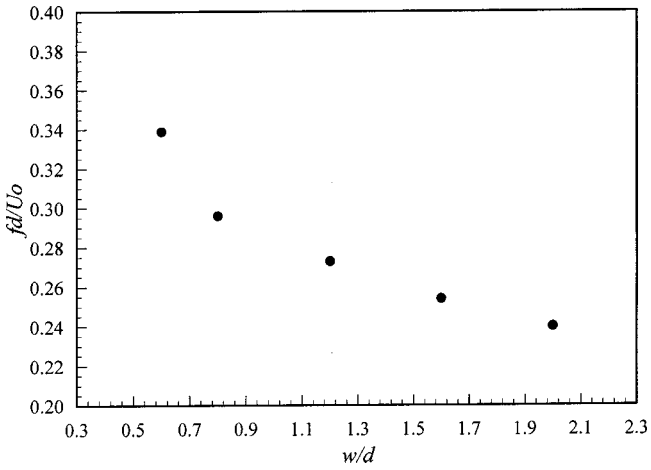

Fig. 5 Relationship between the reduced frequency and *w/d*

Conclusions

The mean flow and periodic behavior of low aspect ratio parallel jets was experimentally investigated for $w/d=0.6–2.0$ over a jet exit velocity range covering approximately 2–34 m/s. The flow demonstrated a vortex shedding behavior in the near-field region between the jets similar to that which would be expected from a bluff-body. That is contrary to the behavior at smaller w/d's where periodic flow is not detected. Both the mean flow and the periodic behavior were found to be similar for all d and Re_d when compared at a consistent w/d. A progressive increase in reduced frequency was found to correspond to a decrease in w/d consistent with the increasing influence of the outer shear layers. Likewise, the reduced frequency of the periodic flow was found to decrease toward a constant value for large w/d consistent with a diminished effect of the outer shear layers.

References

[1] Tanaka, E., 1970, "The Interference of Two-Dimensional Parallel Jets (1st Report, Experiments on Dual Jet)," Bull. JSME, **13**(56), p. 272.

[2] Tanaka, E., 1974, "The Interference of Two-Dimensional Parallel Jets (2nd Report, Experiments on the Combined Flow of Dual Jet)," Bull. JSME, **17**(109), p. 920.

[3] Elbanna, H., Gahin, S., and Rashed, M. I. I., 1983, "Investigation of Two Plane Parallel Jets," AIAA J., **21**(7), p. 986.

[4] Lin, Y. F., and Sheu, M. J., 1990, "Investigation of Two Plane Parallel Unventilated Jets," Exp. Fluids, **10**, p. 17.

[5] Lin, Y. F., and Sheu, M. J., 1991, "Interaction of Parallel Turbulent Plane Jets," AIAA J., **29**, p. 1372.

[6] Nasr, A., and Lai, J. C. S., 1997, "Comparison of Flow Characteristics in the Near Field of Two Parallel Plane Jets and an Offset Plane Jet," Phys. Fluids, **9**(10), p. 2919.

[7] Anderson, E. A., and Spall, R. E., 2001, "Experimental/Numerical Investigation of Two-Dimensional Parallel Jets," ASME J. Fluids Eng., **123**, p. 401.

[8] Bloor, M. S., 1964, "The Transition to Turbulence in the Wake of a Circular Cylinder," J. Fluid Mech., **19**, p. 290.

[9] Bearman, P. W., and Tombazis, N., 1992, "The Effects of Three-Dimensional Imposed Disturbances on Bluff-Body Near Wake Flows," Second International Colloquium on Bluff-Body Aerodynamics and Applications, Melbourne, Australia. Dec. 7–10.